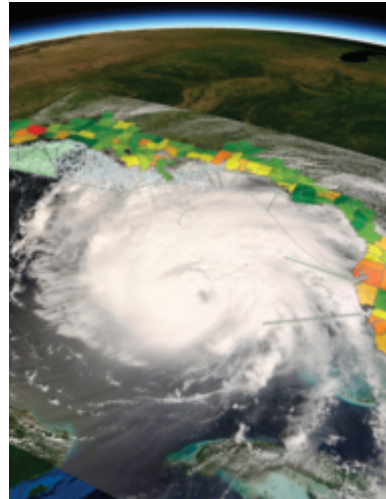


A dramatic view of Hurricane Gustav is shown in the Coastal Online

Assessment and Synthesis Tool (COAST) geobrowser being developed at NASA's Applied Sciences Program at Stennis Space Center. COAST is being used to integrate previously disparate coastal datasets from NASA and other sources into a common desktop tool that provides new data visualization and analysis capabilities for the coastal researcher. Built upon the popular NASA open-source World Wind geobrowser from NASA Ames Research Center, COAST allows direct data import and overlay of accessible online geo-image and vector datasets, temporal image overlay animation, and transparency control over the data layers. The image depicted on the cover is a COAST view of Hurricane Gustav as it bears down upon the oil and gas infrastructure laden coasts of Louisiana and Texas on August 31, 2008. NASA Moderate Resolution Imaging Spectroradiometer (MODIS) 500-meter resolution Blue Marble imagery with bathymetry from NASA's Jet Propulsion Laboratory forms the background image with a NASA Aqua MODIS visible truecolor image of Gustav superimposed (image courtesy of MODIS Rapid Response Project at NASA Goddard Space Flight Center). Overlaid vector data includes oil industry infrastructure from the National Oceanic and Atmospheric Administration and the 2007 population density by county from the U.S. Census Bureau.



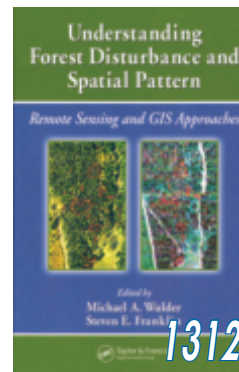
Highlight Articles

- 1286 Guidelines for Procurement of Professional Aerial Imagery, Photogrammetry, Lidar and Related Remote Sensor-based Geospatial Mapping Services
- 1297 ASPRS Ten-Year Remote Sensing Industry Forecast – Phase V
Charles Mondello, George Hepner, and Richard Medina



Columns & Updates

- 1307 Grids and Datums – Arab Republic of Egypt
- 1312 Book Review – *Understanding Forest Disturbance and Spatial Pattern: Remote Sensing and GIS Approaches*
- 1311 Mapping Matters
- 1315 Headquarters News
- 1317 Industry News



Announcements

- 1314 Call for Papers – 22nd Biennial Workshop on Aerial Photography, Videography, and High Resolution Digital Imagery for Resource Assessment
- 1439 ASPRS 2009 Annual Conference – *Reflection of the Past, Vision for the Future*
- 1424 Call for Papers – MultiTemp 2009 – Fifth International Workshop on the Analysis of Multitemporal Remote Sensing Images

Departments

- 1308 Certification List
- 1309 New Member List

- 1315 Region of the Month
- 1316 ASPRS Member Champions
- 1320 Who's Who in ASPRS
- 1321 Sustaining Members
- 1323 Instructions for Authors
- 1342 Forthcoming Articles
- 1412 Calendar
- 1441 Classifieds
- 1442 Professional Directory
- 1443 Advertiser Index
- 1444 Membership Application

PE&RS

November 2008 Volume 74, Number 11

PHOTOGRAMMETRIC ENGINEERING & REMOTE SENSING
The official journal for imaging and geospatial information science and technology

JOURNAL STAFF

Publisher

James R. Plasker
jplasker@asprs.org

Editor

Russell G. Congalton
russ.congalton@unh.edu

Executive Editor

Kimberly A. Tilley
kimt@asprs.org

Technical Editor

Michael S. Renslow
renslow76@comcast.net

Assistant Director – Publications

Rae Kelley
rkelley@asprs.org

Publications Production Assistant

Matthew Austin
maustin@asprs.org

Manuscript Coordinator

Jeanie Congalton
jcongalton@asprs.org

Circulation Manager

Sokhan Hing, sokhanh@asprs.org

Advertising Sales Representative

The Townsend Group, Inc.
asprs@townsend-group.com

CONTRIBUTING EDITORS

Grids & Datums Column

Clifford J. Mugnier
cjmce@isu.edu

Book Reviews

Bradley C. Rundquist
bradley_rundquist@und.nodak.edu

Mapping Matters Column

Qassim Abdullah
Mapping_Matters@asprs.org

Web Site

Martin Wills
willsm@missouri.edu



Immediate electronic access to all peer-reviewed articles in this issue is available to ASPRS members at www.asprs.org. Just log in to the ASPRS web site with your membership ID and password and download the articles you need.

Peer-Reviewed Articles

- 1325 Habitat Mapping in Rugged Terrain Using Multispectral Ikonos Images**
Janet Nichol and Man Sing Wong
A multi-level object-oriented and decision-tree classifier for detailed habitat mapping in rugged terrain.
- 1335 Estimation of Forest Stand Characteristics Using Spectral Histograms Derived from an Ikonos Satellite Image**
Jussi Peuhkurinen, Matti Maltamo, Lauri Vesa, and Petteri Packalén
The potential of Ikonos satellite images for estimating forest stand characteristics studied in boreal conditions.
- 1343 Pixel-based Minnaert Correction Method for Reducing Topographic Effects on a Landsat-7 ETM+ Image**
Dengsheng Lu, Hongli Ge, Shizhen He, Aijun Xu, Guomo Zhou, and Huaqiang Du
A pixel-based Minnaert correction approach is developed for reducing the topographic effects on a Landsat ETM+ image.
- 1351 Orthogonal Transformation of Segmented SPOT5 Images: Seasonal and Geographical Dependence of the Tasseled Cap Parameters**
Eva Ivits, Alistair Lamb, Filip Langar, Scott Hemphill, and Barbara Koch
Tasseled Cap parameters were derived for the SPOT5 sensor from different seasons and geographical locations; differences were observed in the Greenness and Wetness parameters while the Brightness was proven relatively stable.
- 1365 A Polygonal Approach for Automation in Extraction of Serial Modular Roofs**
Yair Avrahami, Yuri Raizman, and Yerach Doytsher
A novel approach for automation in roof extraction from aerial images based on the assumption that roofs are composed of several spatial polygons, and automation in extracting these polygons can lead to automation in roof extraction.
- 1379 Conterminous U.S. and Alaska Forest Type Mapping Using Forest Inventory and Analysis Data**
B. Ruefenacht, M.V. Finco, M.D. Nelson, R. Czaplowski, E.H. Helmer, J.A. Blackard, G.R. Holden, A.J. Lister, D. Salajanu, D. Weyermann, and K. Winterberger
Classification-trees were used to map forest types and forest type groups for the conterminous United States and Alaska using Forest Inventory and Analysis data.
- 1389 Leaf Area Index (LAI) Change Detection Analysis on Loblolly Pine (*Pinus taeda*) Following Complete Understorey Removal**
J.S. Iames, R.G. Congalton, A.N. Pilant, and T.E. Lewis
Investigation of the confounding effect of understorey contributions to satellite-derived estimates of LAI on two loblolly pine (*Pinus taeda*) plantations (ages 19 and 23 years) located in Virginia and North Carolina, USA.
- 1401 An Initial Study on Vehicle Information Extraction from Single Pass QuickBird Satellite Imagery**
Zhen Xiong and Yun Zhang
A direct location algorithm to calculate vehicle's ground position from its image position based on a Digital Elevation Model.
- 1413 A Comparison of Coincident Landsat-5 TM and Re-sourcesat-1 AWiFS Imagery for Classifying Croplands**
David M. Johnson
Testing the suitability of AWiFS imagery with TM as a benchmark for deriving row crop focused cover type maps over highly cultivated regions of the central U.S.
- 1425 Using a Binary Space Partitioning Tree for Reconstructing Polyhedral Building Models from Airborne Lidar Data**
Gunho Sohn, Xianfeng Huang, and Vincent Tao
A complex building model, which includes a mixture of flat and sloped planes, is simultaneously reconstructed using a coarse-to-fine approach accomplished by recursively partitioning an initial building region with data-driven linear features into a set of convex planar polygons having maximal co-planarity.

PHOTOGRAMMETRIC ENGINEERING & REMOTE SENSING is the official journal of the American Society for Photogrammetry and Remote Sensing. It is devoted to the exchange of ideas and information about the applications of photogrammetry, remote sensing, and geographic information systems.

The technical activities of the Society are conducted through the following Technical Divisions: Geographic Information Systems, Photogrammetric Applications, Primary Data Acquisition, Professional Practice, and Remote Sensing Applications. Additional information on the functioning of the Technical Divisions and the Society can be found in the Yearbook issue of *PE&RS*.

Correspondence relating to all business and editorial matters pertaining to this and other Society publications should be directed to the American Society for Photogrammetry and Remote Sensing, 5410 Grosvenor Lane, Suite 210, Bethesda, Maryland 20814-2160, including inquiries, memberships, subscriptions, changes in address, manuscripts for publication, advertising, back issues, and publications. The telephone number of the Society Headquarters is 301-493-0290; the fax number is 301-493-0208; email address is asprs@asprs.org.

PE&RS. *PE&RS* (ISSN0099-1112) is published monthly by the American Society for Photogrammetry and Remote Sensing, 5410 Grosvenor Lane, Suite 210, Bethesda, Maryland 20814-2160. Periodicals postage paid at Bethesda, Maryland and at additional mailing offices.

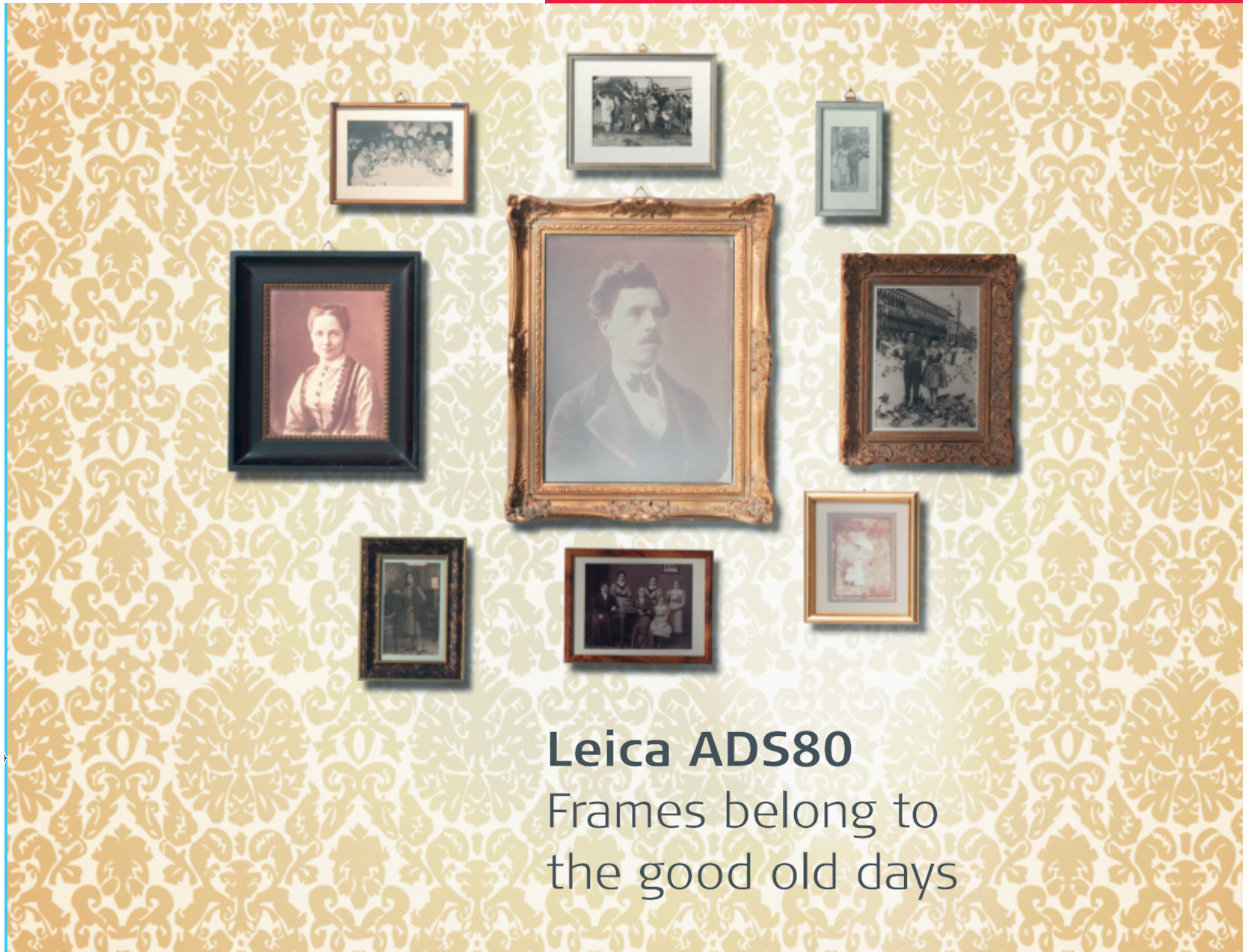
SUBSCRIPTION. Effective January 1, 2008, the Subscription Rate for non-members per calendar year (companies, libraries) is \$320 (USA); \$389 for **Canada Airmail** (includes **6% for Canada's Goods and Service Tax (GST#135123065)**); \$385 for all other foreign.

POSTMASTER. Send address changes to *PE&RS*, ASPRS Headquarters, 5410 Grosvenor Lane, Suite 210, Bethesda, Maryland 20814-2160. CDN CPM # (40020812)

MEMBERSHIP. Membership is open to any person actively engaged in the practice of photogrammetry, photointerpretation, remote sensing and geographic information systems; or who by means of education or profession is interested in the application or development of these arts and sciences. Membership is for one year, with renewal based on the anniversary date of the month joined. Membership Dues include a 12-month subscription to *PE&RS* valued at \$60. Subscription is part of membership benefits and cannot be deducted from annual dues. Annual dues for Regular members (Active Member) is \$120; for Student members it is \$45; for Associate Members it is \$80 (see description on application in the back of this Journal). An additional postage surcharge is applied to all International memberships: Add \$40 for **Canada Airmail**, and **6% for Canada's Goods and Service Tax (GST #135123065)**; all other foreign add \$60.00.

COPYRIGHT 2008. Copyright by the American Society for Photogrammetry and Remote Sensing. Reproduction of this issue or any part thereof (except short quotations for use in preparing technical and scientific papers) may be made only after obtaining the specific approval of the Managing Editor. The Society is not responsible for any statements made or opinions expressed in technical papers, advertisements, or other portions of this publication. Printed in the United States of America.

PERMISSION TO PHOTOCOPY. The appearance of the code at the bottom of the first page of an article in this journal indicates the copyright owner's consent that copies of the article may be made for personal or internal use or for the personal or internal use of specific clients. This consent is given on the condition, however, that the copier pay the stated per copy fee of \$3.00 through the Copyright Clearance Center, Inc., 222 Rosewood Drive, Danvers, Massachusetts 01923, for copying beyond that permitted by Sections 107 or 108 of the U.S. Copyright Law. This consent does not extend to other kinds of copying, such as copying for general distribution, for advertising or promotional purposes, for creating new collective works, or for resale.



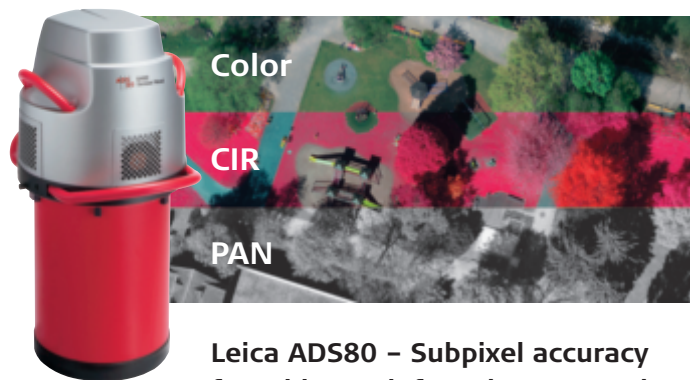
Leica ADS80 Frames belong to the good old days

When you need real performance from your large-format digital imagery and a workflow that gives you highest productivity, frames belong indeed to the good old days.

The new Leica ADS80 Airborne Digital Sensor features advanced line sensor technology and acquires imagery with equal resolution across all bands for all applications from photogrammetry to remote sensing. There is no need for pan-sharpening and no need for virtual frames.

In addition, the new Leica XPro line sensor workflow speeds up your flight data processing, is easy to use and saves you time and money.

Leica Geosystems AG
Switzerland
www.leica-geosystems.com



**Leica ADS80 – Subpixel accuracy
from blue to infrared, processed
at the speed of flight.**

- when it has to be **right**

Leica
Geosystems



Guidelines for Procurement of Professional Aerial Image, Lidar and Related Remote Sensor-based Geospatial

The following material is considered DRAFT FOR REVIEW and is being published at this time to encourage wide dissemination and comment. Comments should be forwarded via email to guidelines@asprs.org no later than January 15, 2009. The current plan is to review all comments and finalize the document for ASPRS Board approval at its March 13, 2009 meeting.

Executive Summary

These *Guidelines* were prepared by the ASPRS Procurement Guidelines Committee, an ad hoc committee appointed by the ASPRS leadership. The Committee includes representation from the ASPRS Professional Practices Division, ASPRS members from state and federal government, the Management Association for Private Photogrammetric Surveyors (MAPPS) and the American Congress on Surveying and Mapping (ACSM). These *Guidelines* were formally approved by the ASPRS Board of Directors at their meeting on [TBD].

The intent of these *Guidelines* is to provide public agencies, researchers, private entities and other organizations with a resource that they can use as a guide to help determine the best approach and methodology for procuring photogrammetry and related remote sensor-based geospatial mapping services.

This Executive Summary highlights the key issues, considerations, recommendations and conclusions that are addressed in detail in the *Guidelines* document.

Definition of Professional Services

- "Professional" services are those services that require specialized knowledge and skill; require independent judgment; and have an expectation of ethical conduct and professional expertise such that the resulting services will represent the best interests of the client and public. Professional photogrammetry and related geospatial mapping services produce geospatial mapping deliverables and information where there is an expectation of spatial or thematic accuracy.
- Professional photogrammetry and related geospatial mapping services are broad in scope and are not limited to those tasks that are regulated or licensed by states or other agencies. State laws vary widely and are not consistent in their definitions of which geospatial mapping services require a license. Further, licensure is intended to ensure a minimal level of competence to protect the public from serious harm. Procurement guidelines should meet a higher standard and seek to acquire services that are going to result in a successful project that best meets overall public interests.
- The level of automation or standardization does not by itself distinguish professional services from technical services or products. Professional services may include automated or standardized processes that require the supervision of a qualified professional.
- This broad definition of "professional" services includes the vast majority of

continued on page 1288

I. Background and Intent

The **American Society for Photogrammetry and Remote Sensing** (ASPRS) is the leading scientific professional organization representing the photogrammetry and remote sensing professions. These *Guidelines* represent the best effort of the ASPRS at defining and clarifying the key issues that affect an organization's procurement of image and sensor-based geospatial mapping services.

These *Guidelines* were prepared by the ASPRS Procurement Guidelines Committee, an ad hoc committee appointed by the ASPRS leadership. The committee includes two representatives from the ASPRS Professional Practices Division, an ASPRS representative from the federal government, an ASPRS representative from state government, two representatives from the Management Association for Private Photogrammetric Surveyors (MAPPS) and two representatives from the American Congress on Surveying and Mapping (ACSM). These *Guidelines* were formally approved by the ASPRS Board of Directors at their meeting on [TBD]. These *Guidelines* supersede the now outdated ASPRS document originally adopted in 1986, entitled "Guidelines for Procurement of Photogrammetric Services from Private Professional Sources."

By better defining specific aspects of photogrammetric mapping and related geospatial services that are professional in nature, these *Guidelines* aim to support public and private end users who need to procure geospatial mapping services. The intent of these *Guidelines* is to

gery, Photogrammetry, Mapping Services

provide public agencies, researchers, private entities and other organizations with a resource that they can use as a guide to help determine the best approach and methodology for procuring photogrammetry and related remote sensor-based geospatial mapping services.

The specific goals of these Guidelines are to:

1. Provide a clear and updated definition of which remote sensor-based geospatial mapping services are considered by members of this profession to be professional level services.
2. Endorse qualifications-based selection (QBS) procurement consistent with similar professions where services are professional in nature and affect public well being.
3. Recognize existing state and federal laws regulating this profession and distinguish between:
 - i) licensed activities that are defined by state law; and ii) professional services that may or may not require a license, but are defined by the ultimate use of the services, level of skill required and accepted standards of practice.
4. Distinguish between professional services and technical services or products that may fall outside the scope of that definition.
5. Provide broad-based definitions and guidance that will apply to both current and future technologies.

II. Definition of Remote Sensing and Photogrammetry

Remote sensing is defined as the process of gathering and processing information about an object without direct physical contact. Photogrammetry is that branch of remote sensing which is defined as the art, science, and technology of obtaining reliable information about physical objects and the environment through the processes of recording, measuring,

and interpreting photographic images, patterns of electromagnetic radiant energy and other phenomena. Photogrammetry employs the use of both interpretive techniques and mensuration methods.

Historically, photogrammetric methods and technologies were limited to the use of photographic film. With advancements in technology, the profession has expanded to apply its expertise in interpretation and mensuration of remotely-sensed data to a wide variety of other sensors. Other sensors currently used by photogrammetric professionals include both passive sensors that record specific or multiple bands of electromagnetic radiant energy (such as digital cameras and multi-spectral sensors) and active sensors, which emit and then record the returned electromagnetic energy (such as lidar and radar). Sensors may be attached to vehicles such as vans or boats, airborne in manned or unmanned aircraft, or satellite based.

III. Scope of Services Addressed by These Guidelines

These *Guidelines* are specifically intended to apply to those photogrammetry and remote sensing services that are associated with acquiring, interpreting, processing or analyzing remotely-sensed imagery and data to create geospatial mapping deliverables. This includes services associated with measuring, locating and preparing maps, charts, or other graphical or digital presentations depicting the location of natural and man-made physical features and phenomena of the Earth.

Photogrammetry and remote sensing are applied in a variety of industries and professions for a very broad range of applications. Many of those applications are not related to geospatial mapping and are not addressed herein.

The term "professional geospatial mapping services" is used throughout this document. This term refers to a much broader scope of geospatial mapping services than those that involve photogrammetry and remote sensing. It is the opinion of ASPRS that the principles and recommendations presented in this document apply equally to all geospatial mapping services that would meet the broad definition of "professional services" used herein. However, specifically determining or identifying all geospatial mapping services that should be considered "professional services" is beyond the scope of expertise of the Procurement Guidelines Committee and is beyond the scope of this document. While this document presents broad-based recommendations that could also apply to many other sectors of the geospatial mapping profession, the primary focus of the document is on the photogrammetry, remote sensing and image-based GIS services that constitute the primary area of expertise of ASPRS and its membership.

IV. General Definition of Professional Geospatial Mapping Services

ASPRS considers professional geospatial mapping services to be those geospatial mapping services that:

1. Require specialized knowledge derived from academic education, on-the-job training, and practical experience;
2. Produce mapping deliverables and information where there is an expectation or representation of geospatial or thematic accuracy;
3. Require independent judgment, ethical conduct and professional expertise to ensure that the resulting products derived from these services represent the best interests of the client and public; and,

continued on page 1288

continued from page 1286

photogrammetry, remote sensing and related sensor-based geospatial mapping services. Off-the-shelf products and technical services fall outside the scope of this definition of professional services. Technical services include conventional aerial photography with no direct geo-referencing, imagery for display only purposes, rote digitizing and similar processes.

- Professional level photogrammetry, remote sensing and related sensor-based geospatial mapping services can be divided into two categories: 1) authoritative mapping that depicts the authoritative location of features, and 2) referential mapping that meets only general accuracies and does not depict or represent authoritative locations. Authoritative mapping is defined as “surveying” by the National Council of Examiners for Engineering and Surveying (NCEES) Model Law and in many state laws. Referential mapping is not “surveying” by the NCEES definition. Federal and state procurement laws may apply differently to surveying and non-surveying services. Both types of services require independent judgment and professional expertise and are considered by these *Guidelines* to be professional services for procurement purposes.
- Detailed matrices are included as attachments to these *Guidelines* to further distinguish between professional authoritative mapping services, professional referential mapping services, technical services and products.

Procurement Guidelines and Recommendations

- The professional photogrammetry, remote sensing and related sensor-based geospatial mapping services addressed by these *Guidelines* play a critical role in the success of the engineering, architecture, surveying, planning, natural resources, agriculture, emergency response, disaster recovery and other applications that they support. Procurement methods should consider potential impacts to the intended end application.
- Qualifications-based procurement methods are the most appropriate means to ensure that public interests are best represented when procuring professional photogrammetry, remote sensing and related sensor-based geospatial mapping services. Even if there is a detailed scope of service, rigid inspection and strict client quality control process in place, these types of professional services involve too many variables and complexities to facilitate the kind of low bid process that is used for construction services, product purchases or similar price-based procurements. Independent judgment and independent oversight by the contractor are critical to the success of the project.
- When price is evaluated concurrently with qualifications and influences the final selection, responding firms often are forced to design their approach to a lower standard that meets only the very minimum requirements outlined in the scope of work. This may not be the approach that serves the best overall interest of the client and public. Quality may be compromised and advanced technologies, innovation for the best techniques, and the most cost-effective overall approach may not be implemented.
- The federal law commonly known as the Brooks Act outlines the best model for qualifications based selection. The Brooks Act process ranks firms according to qualifications only. Cost is not a factor in the initial selection of the top ranked firm. After the top ranked firm is selected based on qualifications and capability to best perform the work, an acceptable scope of work and fair and reasonable cost are negotiated. If a fair and reasonable cost cannot be agreed on with the top ranked firm, negotiations are initiated with the next most qualified service provider. The process continues until a fair and reasonable price can be negotiated.
- The Brooks Act qualifications-based selection (QBS) process is required by law as defined in Federal Acquisition Rule (FAR) Part 36 for all federal procurement of architecture, engineering and related surveying and mapping services.
- Contracting and procurement personnel should contact the State Board of Examiners for surveying and engineering in the state(s) in which the work is to be performed to confirm what aspects of existing survey and engineering statutes apply to their projects. Specific aspects of photogrammetric mapping and related geospatial mapping services

continued on page 1290

continued from page 1287

4. Could potentially affect public welfare or result in harm to the public if not performed to professional standards.

V. Professional Nature of Photogrammetry and Remote Sensing

Photogrammetric and remote sensing professionals apply the rigorous principles of measurement science and remote sensing interpretation to develop reliable geospatial data. Photogrammetric mapping professionals utilize their knowledge and training to employ the appropriate methods and technologies to image, measure, calculate, reduce, and integrate geospatial and attribute data. They then transform this data into mapping products such as vector and image maps, charts, and other graphical or digital representations.

Photogrammetrists and remote sensing specialists must have in-depth knowledge and expertise of the general principles of geomatics, the sensor technologies employed, the specific processes to be implemented and the final application of the published data. Several universities offer undergraduate and graduate programs that include photogrammetry and remote sensing; many professional photogrammetrists and remote sensing specialists have specifically studied photogrammetry at the undergraduate or graduate level. Many others have more varied backgrounds in surveying, engineering, geography or related professions that rely on similar principals of science and measurement. The specific applications of these principals to photogrammetry requires many years of practical experience and on-the-job training.

The photogrammetry and remote sensing profession has well established certification programs, accuracy standards and expectations of ethical conduct that apply to professional practitioners. ASPRS maintains certification programs for Certified Photogrammetrist and Certified Mapping Scientist. These certifications are available to qualified photogrammetry and remote sensing professionals. These certification programs have rigorous requirements for testing, references from other professionals and experience history. Applicants must demonstrate professional level experience, a history of competence and ethical conduct, and an overall level of professional excellence that exceeds minimum levels of competence. APSRS has published a strict code of ethics that applies to mapping professionals. Several map accuracy standards have been developed by federal

agencies and professional organizations. The National Standard for Spatial Data Accuracy (NSSDA), developed and published by the Federal Geographic Data Committee, is the most comprehensive and current map accuracy standard that applies to professional photogrammetric mapping. This standard incorporates the Map Accuracy Standards for Large Scale Maps that were developed by ASPRS in 1990. References for these documents are provided in the references section.

Photogrammetric mapping data are frequently used to make critical decisions that require accurate and reliable information about the location of features on the Earth. Professional photogrammetric mapping professionals may provide services and data directly to the public or may work in cooperation with other experts such as surveyors, engineers, architects, land managers and planners, remote sensing specialists, cartographers, geographers, GIS specialists, and IT professionals. The photogrammetrist in direct responsible charge of acquiring and producing the mapping data are often the only professional involved in the process that has a full understanding of what is required to meet the accuracies and quality necessary to support the intended uses of the data. Following are specific examples of some of the many areas of use where the accuracy and quality of photogrammetric mapping data directly affects decisions that could potentially impact public welfare:

1. Engineering of roads, bridges and public facilities;
2. Water resources planning and design;
3. Natural hazards assessment, including landslide assessment, dam site/reservoir assessment and flood hazard mapping;
4. Emergency services applications;
5. Municipal planning;
6. Disaster recovery;
7. Transportation planning.

VI. Qualifications Based Selection as the Accepted Method for Procurement of Professional Services

Qualifications-based selection (QBS) is the widely accepted method for procurement of architecture, engineering and related professional services. Federal law, as prescribed by Public Law 92-582, commonly referred to as the Brooks Act, and state laws in at least 47 of the 50 states require QBS procurement of architecture, engineering, survey and related services (commonly referred to as A/E services).

The QBS process, as outlined by the Brooks

Act and similar state laws, requires that an agency or private party first select a professional services firm based solely on an evaluation of that firm's qualifications to complete the work. Cost and price are not a factor in the initial ranking of firms. Under the QBS process, costs are negotiated with one firm at a time, starting with the highest ranked firm. If a fair and reasonable cost cannot be negotiated with the highest ranked firm, then, and only then, cost and price are negotiated with the next most qualified firm.

QBS is endorsed for procurement of professional services by many other professional organizations including the American Institute of Architects (AIA), National Society of Professional Engineers (NSPE), American Public Works Association (APWA), American Water Works Association (AWWA), American Bar Association (ABA) and the Associated General Contractors of America (AGC). QBS is the best means of promoting competition for professional services. Competition among professionals is healthy and desirable and ensures that project dollars are well spent. QBS provides a level playing field that promotes fair and open competition, guaranteeing that only skilled, experienced, and able professionals are selected before price is negotiated and determined. As a result, organizations acquire the services of the most qualified firm possible while obtaining a price that is fair and reasonable.

Many professional photogrammetric mapping and remote sensing services are directly related to architecture and engineering or are otherwise relied upon to determine the authoritative geospatial location of features or topography. This application of photogrammetric mapping and related remote sensing technologies to provide products similar in nature to the type of information provided by field surveyors, would be considered surveying by most definitions. In recent years, many other geospatial applications of photogrammetric and remote sensing mapping technologies have developed that may not be directly related to architecture, engineering or the authoritative location of features typically associated with professional surveying. Examples include thematic mapping for land cover, photogrammetric mapping for GIS centerline coverages, disaster recovery assessment and similar work.

While some applications of current photogrammetric mapping technologies may not have a direct tie to architecture or engineering, they share a very similar level of reliance on the professional practitioner to implement sound

judgment, exceptional professional expertise and professional ethics in order to develop mapping products that can be relied on to make decisions that often impact public welfare. While these tasks may not require the same level of authoritative accuracy required for architecture, engineering and survey applications, there is still an expectation of general accuracy and a level of quality and standard of performance that requires a professional level service.

With regards to a regulatory standard, states typically use the test of actual potential for harm to public health, safety and welfare to determine the minimum level of activities that should require a license. However, from a procurement guidelines perspective, the bar should not be placed at the minimum level. Rather, procurement guidelines should set the standard to achieve what is in the best interest of the public, and what is most likely to ensure a successful project.

Procuring professional photogrammetry services is vastly different from procuring basic supplies or even construction services. Often, the photogrammetric mapping professional is the only professional involved in the process that fully understands the specifications, accuracies, methodologies and approach that will support the intended end use of the data. Determining what to include in a comprehensive request for proposal (RFP) for geospatial mapping data is a complicated task. As a result, RFPs are often vague and missing key information. When an RFP lacks sufficient detail, each firm competing for the work will interpret it differently. Consequently, proposals vary widely in scope and detail, creating an "apples and oranges" disparity in project details. When price is a key selection criteria, firms often use the lowest-cost approach, which often means discounting advanced technologies, the best techniques, and the most effective overall project design. QBS improves the procurement process and, in so doing, improves service to private entities, public agencies and taxpayers.

QBS, as outlined by the Brooks Act, is widely used for architecture, engineering and surveying services procurement. Professional organizations, federal, and state lawmakers have long recognized that these kinds of services critically affect the public welfare. The QBS procurement approach best protects the taxpayers' and clients' interest and at the same time best safeguards public health and safety. The professional level photogrammetric mapping services outlined in these *Guidelines* share many characteristics with, are of similar nature to, and are of similar

continued on page 1290



continued from page 1288

are considered surveying and require a license to practice in many states. Many states also have "mini-Brooks Act" bills that require the Brooks Act or similar process be used for the procurement of all architecture, engineering or surveying services as defined by state law.

- State laws vary widely in their definitions of surveying and mapping. Statutes may specifically license photogrammetry, remote sensing and similar sensor-based geospatial mapping practices; or they may regulate this kind of mapping under the broader definitions of surveying or engineering.
- The FAR Part 36 definition includes many of the geospatial mapping services addressed by these *Guidelines*. Services licensed as architecture, engineering or surveying under state law in the state where the work is being performed require Brooks Act procurement under the FAR 36 definition. Further, in the absence of specific statutory language or precedent for enforcement addressing geospatial mapping services in a given jurisdiction, ASPRS considers the National Council of Examiners for Engineering and Surveying (NCEES) Model Law, Model Rules and associated NCEES documents to be the best definitive guideline for determining which geospatial services should be considered "surveying" services that require a professional license. The NCEES Model Law and Model Rules are only guidelines for the purpose of assisting state governments in the implementation and interpretation of state licensing laws. The Model Law and Model Rules do not represent enacted legislation and do not have any specific legal authority, unless so enacted in a given state.
- ASPRS endorses Brooks Act and similar QBS methods as the best process for procurement of all professional photogrammetry and related geospatial mapping services, including both surveying and non-surveying services. The Brooks Act QBS process is widely accepted by other professional organizations; encourages innovation and design; encourages competition among the most qualified firms; fosters a relationship of trust between the client and provider; and is designed to ensure the most appropriate scope of work at a fair and reasonable cost. Further, in many states, licensed professionals are prohibited from submitting a cost or bid for public work; therefore, procurement methods that do not follow Brooks Act-like procedures may eliminate many of the most qualified firms from competing in a price-based procurement.
- It is recognized that geospatial services may be procured within the scope of a more extensive project, wherein the specific professional geospatial mapping services would be considered incidental to the project. Regardless of the method of procurement for the larger project, or the size of the geospatial mapping component of the project, ASPRS recommends that these *Guidelines* be implemented for all subcontracted geospatial mapping services.
- ASPRS recognizes that QBS is not required by law in all cases, particularly for services acquired by organizations not subject to federal or state procurement laws, or in cases where the proposed services do not meet state or federal definitions of surveying and mapping as related to architecture and engineering. ASPRS recognizes there will be instances where an organization will choose to use an alternative procurement method other than the Brooks Act QBS process. In those cases, ASPRS recommends that specific minimum guidelines be implemented:
 1. Qualifications should be the primary selection factor and should not be influenced by cost.
 2. The scope of work must be well defined and have been developed by a professional who is qualified to ensure that the scope of work will best serve the public interests.
 3. Projects that have a significant element of design, and where the service provider's professional judgment and experience are required to develop the scope of work, should not include cost as a selection criteria.
 4. If cost data are to be required for the selection process, they should be submitted separately and considered only after firms are ranked based on qualifications.
 5. A qualified professional (either on the client's staff or hired as a consultant) needs to be involved to ensure the work best meets the end user and public interests.
- These *Guidelines* for professional geospatial services apply equally to future technologies and are not limited to existing technologies or "tool-based" definitions.

continued from page 1289

importance to the public well being as the engineering, architecture, surveying, planning, natural resources, emergency services and disaster recovery services that they support.

For these reasons, ASPRS endorses QBS procurement methods and recommends the Brooks Act or similar QBS procurement process be used for all procurement of professional photogrammetry and related geospatial mapping services, including both surveying and non-surveying services.

VII. Federal and State Regulations Affecting Procurement Licensure

ASPRS recognizes that the practice and procurement of many aspects of professional photogrammetric services are regulated by federal, state and local laws. These *Guidelines* are not intended to be an interpretation of local, state or federal law, nor are they intended to imply that all professional level services defined herein require a licensed professional. These *Guidelines* outline those services which, in the opinion of ASPRS, are professional in nature and therefore warrant consideration for procurement methods that use qualifications, and not cost, as the primary selection criteria.

Many states regulate and, by statute, require a license for some aspects of professional photogrammetric services. Services outlined in this document may or may not be covered by licensure statute for a given state.

State licensing laws must particularly be considered in the procurement of selected professional geospatial services. For instance, many states require a license to practice specific aspects of photogrammetric mapping and other geospatial services. Definitions and regulations vary widely from state to state. State statutes may refer specifically to photogrammetric mapping or may regulate mapping under broader definitions of surveying or engineering. Contracting personnel who are more accustomed to the procurement of other types of goods and services, even including more conventional engineering or surveying work, are not always knowledgeable about state laws that apply to geospatial services. Contracting and procurement personnel should contact the State Board of Examiners for surveying and engineering in the state(s) in which the work is to be performed to confirm what aspects of existing survey and engineering statutes apply to their projects. Procurement practices need to comply with any and all state licensing laws.

State legislatures periodically review and modify their licensing laws, and State Boards of Examiners periodically modify regulations in order to address developing technologies and evolving professional practices. To support this process, the National Council of Examiners for Engineering and Surveying (NCEES) has developed a Model Law and associated Model Rules that serve as a guide when modification of applicable statutes is deemed appropriate. The NCEES Model Law and Model Rules consider the application and intent of the work, and not the tools used, as the determining factor in distinguishing between geospatial services that should be licensed and referential services that do not require a license. The NCEES model identifies “surveying” services as any work, regardless of the tool used, that represents an authoritative location or measurement of features on or relative to the Earth, and which results in a “survey” product. This includes many remote sensing and photogrammetric services, such as controlled aerial photography, stereo feature extraction, orthophotography, lidar surveys and similar tasks.

NCEES documents are considered by ASPRS to be the best definitive guideline for determining which geospatial services should require a professional license. In the absence of specific statutory licensing language or precedent for enforcement in a given jurisdiction, procurement personnel are encouraged to use the NCEES Model Law and Model Rules as guidelines to evaluate which services may potentially be regulated under state law. However, the NCEES Model Law and Model Rules are only guidelines for the purpose of assisting state governments in the implementation and interpretation of state licensing laws. The Model Law and Model Rules do not represent enacted legislation and do not have any specific legal authority, unless so enacted in a given state.

The NCEES Model Law was developed to address licensing, not procurement. The term “professional services” is broader than, and not synonymous with, “licensed” or “regulated” services. The procurement recommendations outlined in these *Guidelines* are not limited to those “licensed” services identified by state licensing laws or NCEES Model Law recommendations. These *Guidelines* recognize that there are many geospatial mapping applications that require professional knowledge and skill, and that affect public well being, that are not directly tied to engineering, architecture or surveying, and that may not be regulated by licensing laws. Qualifications-based selection

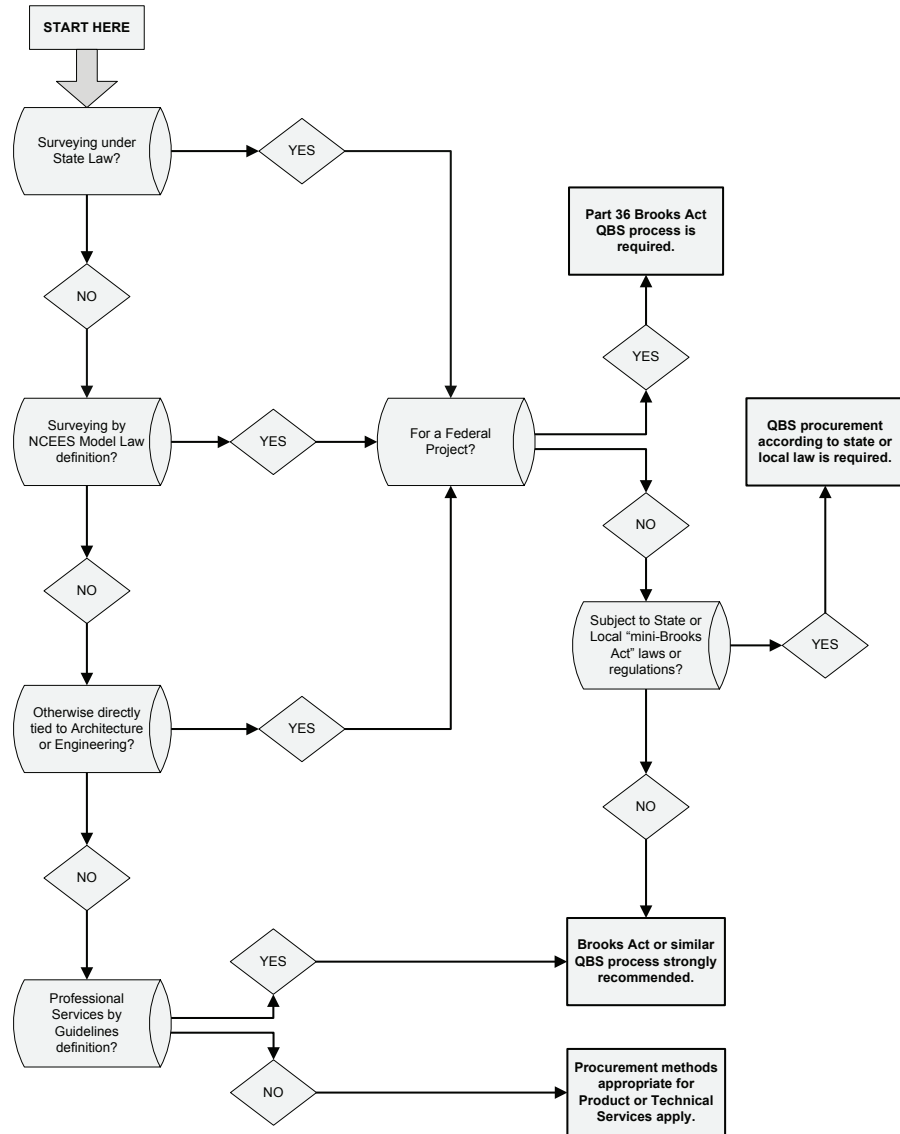


Figure 1. Professional Geospatial Services Procurement Decision Model

is appropriate for all professional geospatial services and not just services that require a professional license. It should also be noted that licensed individuals are not always more qualified to perform a specific “professional service” than unlicensed individuals and qualifications evaluation criteria should be applied appropriately to all qualified geospatial service providers.

Federal procurement is regulated by the Federal Acquisition Rules. Surveying and mapping services are included in the federal definition of architecture and engineering services subject to Subpart FAR 36.6 which requires the Brooks Act QBS procurement process for those services. It is the opinion of ASPRS, that Subpart FAR 36.6 would, at minimum, apply to all federal procurement of photogrammetry

and remote sensing services that are defined as surveying by individual states and, in the absence of such definition, by the NCEES Model Law and Model Rules. Subpart FAR 36.6 may apply to a broader range of photogrammetry services, depending on the definition of surveying and licensing requirements applicable in the specific state or states in which the work is to be performed.

Many states and local jurisdictions have enacted laws and rules, based on the Federal Brooks Act laws, which require the use of QBS for procurement of A/E services for local jurisdictions and state agencies. Furthermore, many state registration boards require their licensees (architects, engineers and surveyors) to adhere to the rules of QBS when responding to procurement announcements issued by agencies covered by

continued on page 1292

the public law or state/local equivalents. In states where such laws and rules apply, licensees who do not obey those rules when responding to procurement announcements can be individually disciplined by their licensing board.

The recommended decision process for determining the procurement approach that is the most appropriate for a specific procurement scenario, is outlined in Figure 1, "Professional Geospatial Services Procurement Decision Model."

VIII. Guidelines for Other Procurement Methods

ASPRS recognizes that the Brooks Act QBS process is not required by law in all cases, particularly for services acquired by organizations not subject to federal or state procurement laws, or in cases where the requested services may not meet the test for authoritative accuracy as used by the NCEES model and many state laws to distinguish between surveying services and other referential mapping services. When Brooks Act or similar QBS procurement practices are not required by law or regulation, procuring organizations have the autonomy to select other procurement methods.

ASPRS recommends that Brooks Act QBS or similar methods be used for procurement of all professional geospatial mapping services, regardless of whether or not a professional license is required or whether or not the Brooks Act process is specifically required by law or regulation. However, ASPRS recognizes there will be instances when an organization will choose to use a procurement method other than the Brooks Act process and that in many cases cost will be one of the selection criteria. In those cases, ASPRS emphasizes the importance of selecting procurement criteria that ensure that qualifications, not cost, is the primary selection factor. ASPRS recommends the following guidelines be applied to any procurement method that does not adhere to the preferred process outlined by the Brooks Act.

1. Qualifications should always be the primary selection factor.
2. Qualifications rankings should not be influenced by cost.
3. The scope of work must be well defined and have been developed by a professional who has extensive knowledge of the work to be performed and is qualified to ensure that the scope of work will best serve the client's interests.
4. Projects that have a significant element of design, and where the service provider's

professional judgment is relied on to develop the scope of work, methodology or approach, should always use Brooks Act QBS and should not include cost as selection criteria.

5. A registered, certified or otherwise qualified professional with specific knowledge or expertise with the services being procured (either on the client's staff or hired as a consultant) should have a significant role in the review of both the technical proposal and any cost proposals in order to ensure that the work best meets the end user and public interests.
6. If cost data are to be considered in the selection process, it should be submitted separately and considered only after firms are ranked based on qualifications.

IX. Subcontracted Services

It is recognized that geospatial services may be procured within the scope of a more extensive project, wherein the specific geospatial services would be considered "incidental" to the project. In cases where the total dollar value of the geospatial component of the project is small, it is understood that other procurement processes may reasonably apply. However, regardless of the method of procurement for the larger project, or the size of the geospatial component of the project, if the primary contractor utilizes one or more subcontractors to acquire specialized geospatial services, then those geospatial subcontracts are also considered to be subject to these *Guidelines*.

X. Specific Examples of Professional Photogrammetric Services

This section provides examples of specific task items that meet the definition of "professional" photogrammetric services. Some implementations of the tasks listed may be considered surveying by state law, depending on the nature of the work and end use of the data; other implementations may not meet state law or NCEES definitions of surveying, but still require the level of professional expertise and ethical conduct that define professional service. In the opinion of ASPRS, projects and contracts that include any of the following services should always use procurement methods that rely on qualifications as the primary selection criteria; the best example of which is the Brooks Act QBS process.

1. **Ground Control.** Remote sensing imagery is often combined with the geospatial

coordinates of identifiable points, known as ground control, to accurately georeference the imagery using photogrammetric techniques. Defining the location, distribution, accuracy requirements and number of ground control points is critical to achieving the required geospatial accuracy for subsequent mapping tasks. Selection of the appropriate geospatial datum and mapping projection is also essential.

2. **Flight Layout for Orthophotography and Photogrammetric Mapping.** Aerial imagery that is intended to be the source for orthophoto or photogrammetric mapping with an expectation of geospatial accuracy is considered a professional service. Flight coverage, equipment/calibration requirements, flight altitude, flight window, overlap and other acquisition specifications directly affect the quality and accuracy of all subsequent mapping tasks.
3. **Directly Georeferenced Aerial Image Acquisition (airborne-GPS, Inertial Measurement Unit/IMU or similar technologies).** These technologies involve the direct determination, during image acquisition, of some or all of the image georeferencing parameters. Imagery acquisition for which specific coordinate and orientation parameters are required as a deliverable implies an expectation of accuracy and requires professional services to ensure reliable results that will support intended applications.
4. **Aerial Triangulation.** This process combines the ground control with the sensor metric parameters, and then applies precise photogrammetric measurements to accurately georeference the imagery. The accuracy and reliability of the aerial triangulation process affects all subsequent mapping tasks.
5. **Determination of Topographic, Elevation Model, or Planimetric Feature Mapping.** Point and feature extraction from remotely-sensed data for the purposes of mapping topographic features, planimetric features or development of elevation and terrain models have an expectation of accuracy and affect subsequent decisions and activities that affect the public welfare. Feature extraction requires precise photogrammetric orientations and measurements, specific knowledge and skill using the photogrammetric mapping technologies and a broad understanding of the intended applications. Professional expertise is

critical to adequately represent planimetric, topographic and elevation model features within expected accuracies.

6. **Digital Orthophoto Mapping.** A digital orthophoto by definition is an image that has been differentially rectified to within a specific 2-dimensional (2D) geospatial accuracy and resolution. Rectifying and georeferencing remote sensing imagery to systematically correct for image orientation parameters, distortion, and earth surface topography requires rigorous knowledge of photogrammetric mapping principles and technologies. Production of orthophotography is considered a professional level service if the resulting orthophotography is to be published for use by the public or other professionals in any application where the reliability of the geospatial accuracy is of critical importance. Such uses may include planning, engineering, natural resources, agriculture, disaster recovery, emergency services, and development of other mapping layers or other similar applications.
7. **Lidar Acquisition and Processing.** Lidar is an active remote sensor that emits short wave electromagnetic energy (light), records the reflected return signal, and provides a direct measurement of the location and elevation of features on the Earth. The lidar sensor must be continuously georeferenced during its operation by use of airborne-GPS and IMU. Extensive knowledge of all these systems, their calibration and operational integration, and related mathematical and physics necessary to post process the data are essential for accurate 3-dimensional (3D) measurement and representation of the Earth's surface. Lidar may be employed from a ground station, aircraft, moving vehicle or other platform.
8. **Radar Measurements for Topographic Mapping.** This well-established technology is similar to lidar in being an active system that directly measures features on the Earth. Modern remote sensing radar systems emit polarized long wave electromagnetic (radio) energy, with the ability to penetrate cloud cover, and record the return signal to create an image of the landscape below. Radar systems have been extensively developed so that they are now measurement systems as well. Utilizing complex technologies such as synthetic apertures and interference pattern measurements, radar topographic data have been collected from aircraft,

satellites, and the Space Shuttle. This technology requires specialized knowledge in its use and application for geospatial mapping.

9. **Image Interpretation and Thematic Mapping.** Image interpretation and thematic mapping services involve elements of thematic accuracy rather than geospatial accuracy. These applications of remote sensing technology would not be considered surveying by the Model Law definition and, in the absence of a specific state law that may include these services, would not be subject to the federal laws that govern architecture and engineering procurement. However, these services do share the elements of knowledge, skill, expertise, professional judgment and potential impact to the public welfare that define a professional level service. While not services subject to Model Law licensure, these services would be considered professional level services as defined in this document.

XI. Future Technologies

Geospatial mapping, remote sensing and photogrammetry are very dynamic fields. As new technologies become available in the future, photogrammetric mapping professionals will continue to develop new ways of implementing photogrammetry and remote sensing principles and processes to produce geospatial mapping data.

Within the past two decades, new sensors, new software and vastly improved computer processing capabilities have dramatically transformed the level of automation in photogrammetric mapping. Many tasks that had required a highly skilled technician with many years of training can now be either partially or fully automated to the extent that a much less skilled individual can perform that same task. This trend will undoubtedly continue.

However, while specific technical tasks will continue to become more automated with future technologies, the correct and prudent implementation of these new technologies will always require the level of knowledge, expertise, ethical standards and professional conduct outlined in these *Guidelines*. As new technologies develop and become commonplace in the mapping industry, it is the intent of these *Guidelines* that the professional nature of those services be judged by the same general criteria that have been applied herein to the current technologies that have been identified.

XII. Technical Services and Products

ASPRS recognizes that there are some applications for geospatial mapping and imagery that do not fall within the scope of professional level services as outlined herein. Alternate, and in some cases, less stringent procurement requirements may be appropriate in many of those instances. Specifically, this would apply to technical services and product sales.

Technical Services

Not all geospatial services require independent professional judgment or have the same element of potential public harm that warrants professional level work. This would include services wherein the data are not to be presented to the public in any way that would imply an expectation of authoritative geospatial or thematic accuracy and where misrepresentation of geospatial or thematic accuracy will not result in potential harm to the public welfare or to the business purpose of the client. Some resource aerial photography acquisition, image processing for display only purposes and processing or formatting of existing data for referential purposes fall into this category. Nevertheless, knowledge of geospatial services, accuracy specifications, and the impact on the public is itself, is required to make a determination as to whether or not the services requested require professional expertise. Therefore, ASPRS encourages consultation with an ASPRS Certified Photogrammetrist, licensed professional or other qualified professional with expertise in the geospatial field to assist in such evaluations.

Services that meet all of the following criteria would be considered technical services that may not require professional level services or procurement methods:

1. The client/purchaser is a qualified professional, is taking responsibility for all project design, layout, specifications and quality control assurance and assumes all liability that the final products and deliverables will meet project requirements.
2. The data are not going to be presented to the public in a manner that would imply an expectation of geospatial accuracy for measurement or the location of features on the Earth.
3. There is minimal risk of harm to the public.
4. The client is responsible for final quality control and can easily verify that the data meet contract specifications.

Examples of technical photogrammetry and remote sensing services include:

1. Reference mapping that does not have published coordinates or coordinate grid;

continued on page 1294

Table 1. Comparison of Professional Services, Products and Technical Services

| Offering Type/ Differentiators | Professional Service | Product | Technical Service |
|-------------------------------------|--|---|---|
| Level of Standardization | Varies Service varies from client to client and from project to project. Service standards are established in some vertical markets. Service provider exercises independent professional judgment and quality control. | High Standardization Provider offers a set of standard features from which the client may choose. | High Standardization Provider offers a standardized service. Specific methodology prescribed solely by client. Service provider exercises only a minimal level of independent judgment. |
| Specifications | Set by Client with critical input from service provider | Set by Provider | Set by Client with minimal or no input from service provider |
| Ownership | In most cases, the client owns all resulting work and deliverables. | In most cases, the provider owns the data and they are offered under license to the client. | In most cases, task is to support subsequent work by the client and client owns all resulting work and data. |
| Certification / Warranty | Typically certified by a professional in responsible charge of the work, such as a land surveyor, photogrammetrist, engineer or GIS professional. Professional registration or licensure may not be required to oversee the work, as state licensure laws vary widely. | No professional seal or certification. Warranty may be offered by provider that the product meets specified standards. | No professional seal or certification. Client is solely responsible for quality control and for verifying that products meet specifications and expectations. |
| Protection of Public Welfare | Professional liability may apply Provider is responsible for quality control and ensuring products meet specifications and expectations. Provider is expected to comply with ethical and professional standards to protect public interest. | Product liability applies Product developer is responsible for ensuring deliverables meet stated specifications and requirements. | No professional liability Client is responsible for quality control, ensuring products meet expectations and ensuring products protect the best interest of the public. |
| Procurement Method | Qualifications based selection | Primarily cost based | Either an evaluation of both cost and qualifications or qualifications based |
| Pricing | Typically negotiated between provider and client based on level of effort and negotiated rates. May be contracted as fixed price or as cost plus fixed fee. | Published pricing. Total price determined as a function of units times a standard price of the unit. | Estimates may be negotiated based on labor hours times hourly rate or as published pricing per unit. |

- Aerial photography or mosaics for reference or resource use (not georeferenced); and,
- Digitizing, scanning or formatting of existing photogrammetry or remote sensing data, where the data are to be published only for referential, and not authoritative, purposes.

Product Sales

Some geospatial mapping products are sold as existing or custom-order products and not procured on a professional basis. Products are developed to the provider’s specifications and standards, not necessarily the purchaser’s or user’s. Therefore, QBS procurement methods may not be practical or required for these types of purchases. Products often are sold under license to the client (the client does not own source data, work products, or data). Products are not typically certified by a professional, but may be warranted to meet specific standards.

Products are subject to product liability not professional liability.

Supporting Documents

- *Executive Summary* (Side Bar)
- *Comparison of Professional Services, Products and Technical Services* (Table 1)
- *Examples of Professional Photogrammetric Services* (Table 2)
- *Professional Geospatial Services Procurement Model* (Figure 1)

References

Brooks Act Procurement Process, FAR 36.6 http://www.acquisition.gov/far/current/html/Subpart%2036_6.html.
American Institute of Architecture, 2003 Summary of “Mini-Brooks Act” State QBS Laws http://www.aia.org/static/state_local_resources/projectdelivery/QBS_matrix.pdf.

American Public Works Association Position Statement http://www.apwa.net/Documents/Advocacy/Positions/Advocacy/Qualifications_Based_Selec_Prof_Svs_Consult.pdf.
U.S. Army Corps of Engineers Engineer FAR Supplement (EFARS) (Definition of survey and mapping / refer to section 36.601-4 “Implementation”) <http://www.hq.usace.army.mil/cepr/efars/part36.pdf>.
American Bar Association Model Procurement Code for State and Local Government (Document can be purchased from: <http://www.abanet.org>).
National Standard for Spatial Data Accuracy (NSSDA) <http://www.fgdc.gov/standards/projects/FGDC-standards-projects/accuracy/part3/chapter3>.
ASPRS Code of Ethics http://www.asprs.org/membership/certification/appendix_a.html.
ASPRS Certification Program <http://www.asprs.org/membership/certification/index.html>.

Table 2. Examples of Professional Photogrammetric Services

| Service Type | PROFESSIONAL SERVICE | | TECHNICAL SERVICE |
|--|--|---|---|
| | Surveying, as Defined by NCEES Model Law and Model Rules | May not be Surveying, Depending on State Law | |
| Aerial imagery (Not Rectified) | <p>IMU or airborne GPS data that are represented to meet a specific authoritative accuracy statement.</p> <p>Conventional aerial photography for photogrammetric mapping where service provider is responsible for project design.</p> <p>Controlled aerial photography where service provider provides ground control or aerotriangulation.</p> | <p>Controlled aerial photography (conventional, IMU or airborne GPS) when used as an intermediate product solely to produce purely referential imagery which is not represented to meet a specific or authoritative accuracy.</p> <p>This application is rare; a majority of all controlled aerial imagery meets the Model Law definition of surveying.</p> | <p>Resource photography or mosaics with no published coordinates or geo-reference data.</p> <p>Conventional aerial photography where all flight layout and project design is the sole responsibility of the client or professional in charge.</p> |
| Orthophotography and Rectified Imagery | <p>Orthophotography or rectified imagery that is published or represented to meet a specific accuracy.</p> <p>Includes the majority of all common applications of orthophotography. Specifically would include any orthophotography or other rectified imagery when used for engineering, planning, natural resources and related work where the geospatial accuracy influences decisions that affect public welfare.</p> | <p>Imagery that is rectified solely for referential purposes and is not represented as a survey product or expected to meet any specific or authoritative accuracy.</p> <p>As the terms "orthophotography" and "rectified" imagery imply true map scale accuracy, a clear disclaimer that the final work products cannot be used for the measurement or location of features is required to distinguish this work from a Model Law surveying service.</p> | <p>Approximate scale enlargement or rubber-sheeted imagery for display only purposes and where there is no expectation of accuracy or professional judgment.</p> |
| Feature Extraction | <p>Vector and feature data that are published or represented to meet a specific accuracy.</p> <p>Includes the majority of all planimetric, topographic and digital terrain model feature extraction from imagery, lidar or other remotely sensed data. Specifically includes applications for engineering, planning, natural resources and related work where geospatial accuracy influences decisions that affect public welfare.</p> | <p>Vector and feature data extracted solely for referential purposes that are not represented as a survey product or expected to meet any specific or authoritative accuracy.</p> <p>Includes referential GIS layers such as inventory maps, resource management boundaries, GIS centerline data and similar applications; must be accompanied by an appropriate disclaimer stating that the mapping should not be used for measuring or locating features.</p> | <p>Feature extraction of easily distinguished features, solely for referential purposes, and as an intermediate process where a professional on the client's staff or hired by the client is responsible for all project design, quality control and final map preparation.</p> |
| Lidar, Radar Acquisition and Terrain Modeling | <p>Data are represented to meet a stated or implied authoritative accuracy.</p> <p>Includes the vast majority of all applications of terrain modeling using photogrammetry or active sensors such as airborne lidar, ground based lidar, and radar.</p> | <p>Terrain modeling or terrestrial scanning solely for display or referential purposes.</p> <p>Non-survey applications of lidar and terrain modeling are rare. Nearly all air-borne lidar projects have an element of authoritative accuracy and are considered survey services.</p> | <p>None. Terrain modeling applications require professional judgment.</p> |
| Digitizing, Scanning and Processing of Existing Photogrammetry or Remote Sensing Maps or Data | <p>Published for use by the public and represented as survey or mapping data depicting the authoritative location of features or boundaries.</p> | <p>Scanning, digitizing or formatting existing mapping data, not intended to be survey data, but where the service provider is expected to exercise professional judgment and interpretation to ensure final products are suitable for intended purpose.</p> | <p>Scanning, digitizing or formatting of existing mapping data to client specifications where minimal professional judgment or interpretation is required.</p> |
| Image Interpretation and Thematic Mapping | <p>Only if boundaries or feature locations are published or represented as meeting a specific geospatial accuracy statement to depict the authoritative locations of features or boundaries.</p> | <p>Thematic mapping or image interpretation where final deliverables have an element of thematic accuracy that requires professional judgment and expertise. This includes a majority of thematic mapping projects.</p> | <p>Routine classification of easily distinguished features where minimal professional judgment or interpretation is required.</p> |

NCEES link to State Engineering/Surveying Boards http://www.ncees.org/licensure/licensing_boards/.

NCEES Model Law http://www.ncees.org/introduction/about_ncees/ncees_model_law.pdf.

NCEES Model Rules http://www.ncees.org/introduction/about_ncees/ncees_model_rules.pdf.

NCEES Multi-Organization Task Force Materials and Reports <http://www.asprs.org/news/ncees/>.

ASPRS, 1987. Guidelines for procurement of photogrammetric services from private professional sources, *PE&RS*, 53(2), pp. 207-212.

Geo™

GeoProfessional™

GeoStereo™

A perfect vision of what you expect in geospatial intelligence.

No matter which of our products you choose, GeoEye's reputation as a trusted industry leader ensures you'll get the image accuracy and quality you want. And we will deliver it right the first time.

For geospatial intelligence served intelligently, talk to us. www.GeoEye.com/clear



ASPRS TEN-YEAR REMOTE SENSING INDUSTRY FORECAST

PHASE V

Charles Mondello, Chair ASPRS Ten-Year Remote Sensing Industry Forecast, *Pictometry International*

George Hepner, *University of Utah*

Richard Medina, *University of Utah*

Executive Summary

Phase V of the ASPRS Ten-Year Remote Sensing Industry Forecast is an extension of the previous four phases with respect to topical foci on industry workforce needs, economic conditions, evolving technology, and governmental policy. In addition, Phase V explicitly opened up to the international remote sensing community.

An internet survey was the primary tool for sampling from the combined membership rosters of the ASPRS and the ISPRS. The sample used for the analysis consisted of 512 responses from 58 nations. The majority of the respondents reside in North America and Europe having advanced degrees in remote sensing, geography, GIS and photogrammetry. Many of the respondents work outside of their resident nations, most in East Asia and South America.

Undergraduate and master's degrees are the most desired for new employees. The knowledge and technical areas most desired for new employees were application GIS tools, spatial database understanding, cartography/visualiza-

tion, verbal and communication skills, and photogrammetry.

In relationship to Phase IV, Phase V results still show a strong percentage unsure of the future; however, the out years no longer highlight an expectation of a spending decline. When the responses are segmented by region, responses from most regions of the world indicate modest expenditures for the 2010 year.

Previous Forecast reports highlight that demand for the highest levels of resolution was clearly not met; data users wanted higher resolution content. Phase V shows that this trend continues in the global market. Digital aerial sensors, as well as the continued operation of high-resolution satellite systems have expanded the global demand for better than half meter data. Provision of data lower in spatial resolution than half meter is now an area of potential overcapacity.

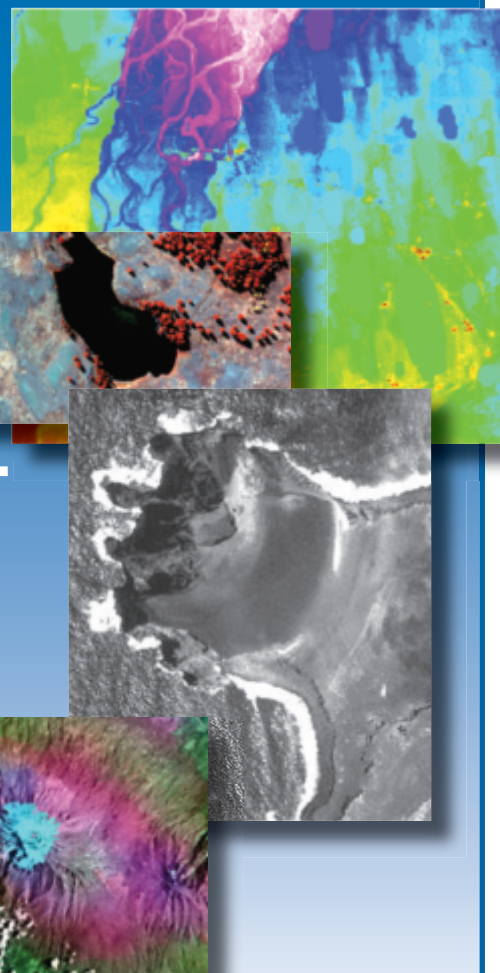
Lidar, hyperspectral and IFSAR were identified as the three data sources that need exceeded current use. Data fusion appears to be considered more in these results than reliance on a single sensor or data source.

Satellite sources of data versus aerial

sources are used more in developing regions of the world. Landsat 7 was the most utilized by respondents (74%), followed by Landsat 5 (66%), GeoEye-Ikonos and Digital Globe-Quickbird (both at 62%) and MODIS and SPOT 5 with about 44% of the respondents citing usage.

Restrictions on remote sensing data were viewed as a hindrance in every region of the world. However, the survey indicated that respondents from East and South Asia, Africa and Oceania felt that effects of restrictions on data, licensing and governmental controls most limiting on their activities.

The most significant issues that continue to represent large challenges and opportunities with the industry are: the demand versus cost in an uncertain economy for high spatial resolution and new sensor data, both aerial and satellite, meeting the increase in demand for a higher levels of education in GIS and newer imaging technologies and the conflicting roles of national governments in developing remote sensing platforms and products while limiting access and use of data.



continued on page 1298

Introduction

Phase V of the ASPRS Ten-Year Remote Sensing Industry Forecast seeks to extend the results of the first four phases in order to determine whether or not the trends noted in the first phases are continuing. The Phase V survey was extended explicitly to the larger international community. We hope that the results of this survey will inform and stimulate discussion about the industry. Given the limited nature of the survey, the results cannot be used to make explicit predictions, but do provide important information and indicate trends of interest.

In particular, ASPRS carried out the Phase V survey in order to obtain current statistical information and future expectations from a representative sample of the international remote sensing/geospatial community regarding:

- Use of and needs for specific requirements in geospatial information
- Workforce hiring needs and requirements
- The international marketplace of the industry
- The role of government policy in the geospatial industry.

These objectives formed the basis of a questionnaire that extended information gained from similar topics and questions in Phases I-IV and questions designed to elicit new information regarding the international creation and use of geospatial information.

Description of Sample and Internet Survey

The survey was implemented in late 2007 to members of ASPRS and the ISPRS. The initial roll out of the survey was announced at the ISPRS conference in Kuala Lumpur, Malaysia in November, 2007. The members with email addresses of both ASPRS and ISPRS were requested by email to complete the internet survey. ASPRS has approximately 6000 members, with nearly equal representation from the government, private sector and academia. ISPRS's email roster of members is approximately 5,000 individuals. Potential respondents were notified by email two times throughout this period with a request to complete the on-line survey. Five hundred and twelve (512) individuals responded to the internet survey, which amounts to slightly less than 5% of the target population.

Limitations on Interpretation

This report summarizes responses to the questionnaire and thus presents general trends occurring in the industry, not specific statistical information with confidence sufficient for prediction. The sufficiency of the sample size issue is confounded by the inability to control properly for assumptions of sampling theory (random, unbiased samples) that would allow rigorous statistical procedures. The internet delivery of the survey does not allow rigorous sampling protocols as it depended on voluntary response of the sample population. Unlike Phases I-III, Phase V relies solely on an internet survey for data. Also, this survey primarily represents the views of respondents from the civilian sector (non-military) of the geospatial-remote sensing industry. Interpretations should be viewed with the survey limitations in mind. Although there was no means to randomize sampling for various sectors or geographic regions, the results provide a useful stratification according to variations in responses between these sectors and regions.

Respondents were asked to indicate the nation in which they lived. These responses were aggregated into regions for presentation of responses to various questions in this study. The task of regionalization is never easy, and certainly the schema used in this study has its peculiarities. For example, Mexico is included with North America as there was only one response from Mexico and the nations of Central America were

combined into South America. The 13 responses from Turkey were included in Europe as Turkey is an associate member of the EU and fits better into the Europe region scientifically and economically than in other adjacent regions.

The world maps of the survey results require some qualification as well. For example, Greenland is included in the European region on the global maps. However, the level of place of work activity, for instance, is at a level far below the rest of Europe.

Profile of Respondents

The sample had a total of 512 individual respondents from 58 nations. Of those individual respondents, 295 (58%) identified themselves as end users of remote sensing data/information. Two hundred and seventeen (42%) specified that their primary job was managing productivity in their remote sensing/geospatial organization.

The respondents were asked to indicate the primary sector in which they were employed. The leading categories were General Mapping (20%), and Environmental (19%). Civil government and Other were the next largest employment areas, of which 6% of the total listed education/academic within the Other category.

The majority of respondents had advanced degrees with the largest category having master's degrees (38%), followed by 35% of the respondents having Ph.D. degrees. Six percent had postgraduate certificates.

The largest group of respondents (119 or

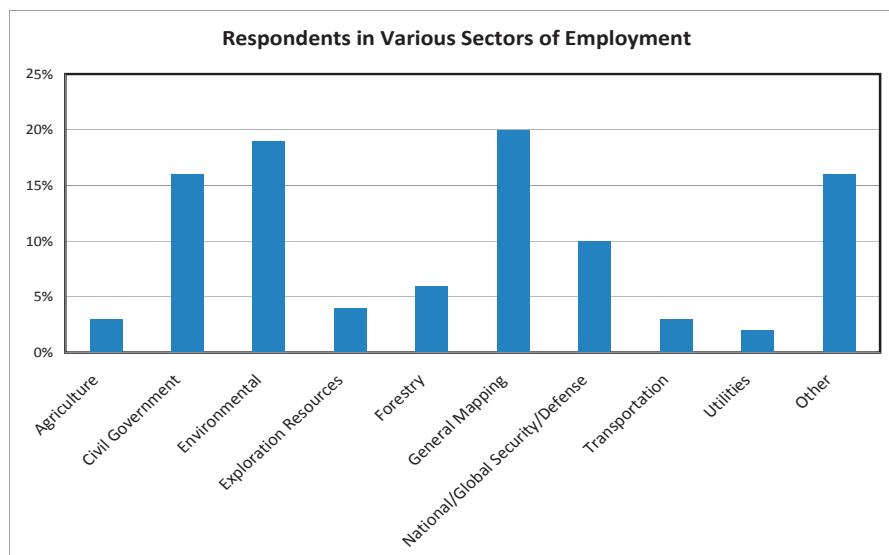


Figure 1. Question 3: In which of the following Sectors and Sub-Sectors do you work? Select one (primary)

Also important other: Academia/Education – 6%

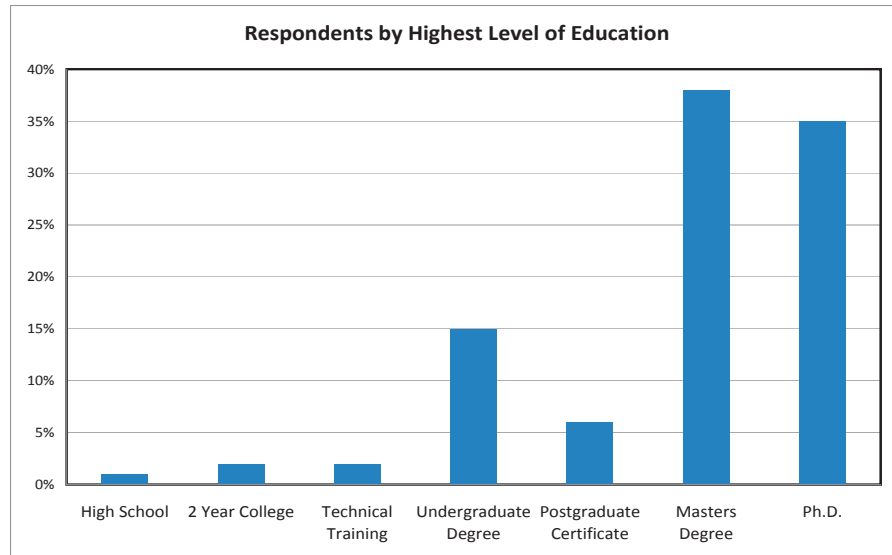


Figure 2. Question 6: What is your highest level of education?
n = 486

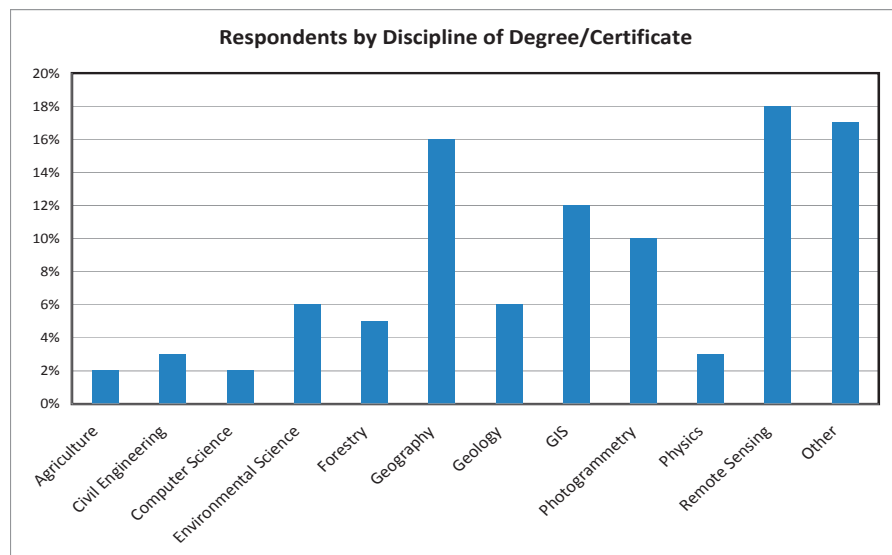


Figure 3. Question 7: In what discipline is your degree/certificate?
n = 677 (more than one category chosen)

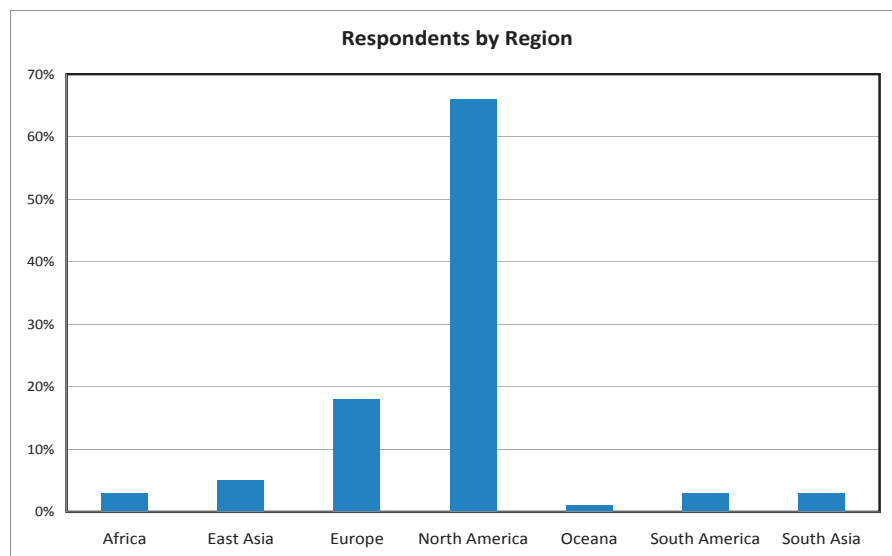


Figure 4. Question 4: In what country do you live?
n = 492

18%) to this question listed Remote Sensing as their primary discipline. This was followed by Other at 17% (113), which included numerous other disciplines from atmospheric science to urban planning. Geography was listed as the third largest disciplinary category at 16% (106). This result indicates the greater international prevalence of specific degrees in remote sensing. This is opposed to a North American prevalence of comprehensive academic programs in remote sensing and geospatial information being centered in university geography departments. Unlike some industries, persons of diverse disciplinary backgrounds are successful in the multidisciplinary geospatial business.

Most of the respondents (66%) lived in North America, with 18% from Europe, five percent from East Asia, and three percent from Africa, South Asia and South America.

The map of the where the respondents worked indicates the global nature of the industry. One can see that many of the current industry projects, as evidenced by where respondents are working, are in the regions of the developing world. North America and Europe are magnified as places where respondents are working, since the majority of respondents live in these regions and, therefore, specified these regions as where they work. Future analysis will focus on diminishing the bias to identify those regions outside of North America and Europe that have most project activity.

One interesting derivative question from the survey is how many North Americans and Europeans are working in regions of the world. If one examines the regions that respondents are working excluding their resident region, a different map of project activity results. Since the size of the group being examined is different, one should focus the relative percentages between the two maps, as well as absolute numbers. East Asia increases from 7% (135) to 14% (112) of the total indicating that when East Asians are not counted for the region, a large number of non-residents respondents have projects in East Asia. The same is true for the other regions. The greatest decline in respondents eliminating residents between the two maps is in North America. Specific conclusions are difficult, but the trend appears to be that a large number of North Americans are working in other regions of the world.

continued on page 1300

continued from page 1299

WorkForce Issues

Response to Question 21 regarding the level of education most desired by organizations for their remote sensing workforce revealed a slight difference between our more international response in Phase V and the previous solely North American response in Phase IV. The Phase V respondents cited the need for more undergraduate degrees for students followed by the need for a workforce educated to the master's degree level. Phase IV had the master's degree as the preferred level of education for the workforce and the educational community is not meeting the industry need for master's and Ph.D. level graduates, and for graduates with technical training and geospatial certificates.

The survey asked the respondents to identify the knowledge and skills most needed by new employees in the future. The 399 respondents could list more than one type of knowledge or skill. Taking those types of knowledge and skills cited by more than 50% of the respondents, new hires should possess knowledge of application GIS tools (66%), spatial database understanding (57%), cartography/visualization (55%), verbal and communication skills (54%), and photogrammetry (50%). These results (similar to Phase I-IV) reveal that the most needed skill areas involve the development of applications, especially in the GIS realm, rather than more basic areas of a particular sensor technology or related skill set. Interestingly, cartography (visual communication of information using maps) and verbal and communication skills are two of the most needed skills surpassing all of the other technical areas associated with remote sensing. This provides valuable insight into the apparent inability of current employees to speak, write and communicate effectively. It indicates the need for a broader education that focuses on analytic and communications skills as well as technical training. Photogrammetry was listed with a 50% response, a bit more than in similar questions in Phases I-IV. This may reflect the greater emphasis on photogrammetry within the international community.

Spending Trends

In most purchasing categories, Phase IV respondents expected the level of total purchases to decline in future years. Further, they expressed increasing uncertainty about estimated future purchases with time. Phase V still shows a strong percentage unsure of

Regions Where Respondents are Working (Percent)

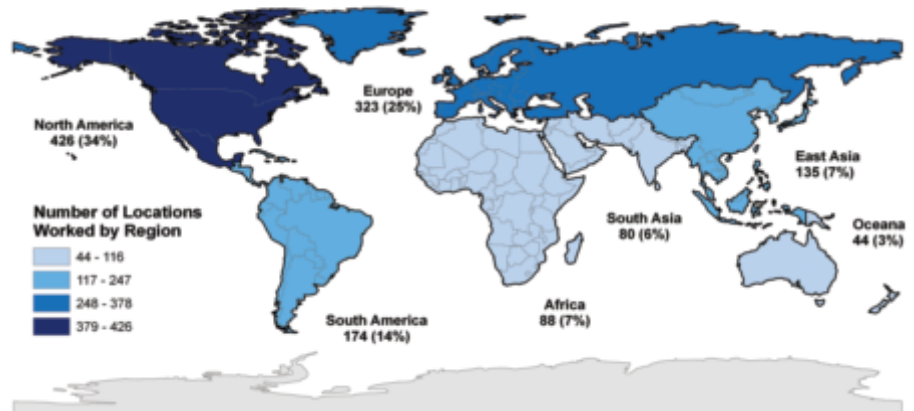


Figure 5. Question 5: In what country or countries do you work (please check all that apply)? n = 492. Total exceeds number of respondents since many work in more than one region.

Regions Where non-Resident Respondents are Working (Percent)

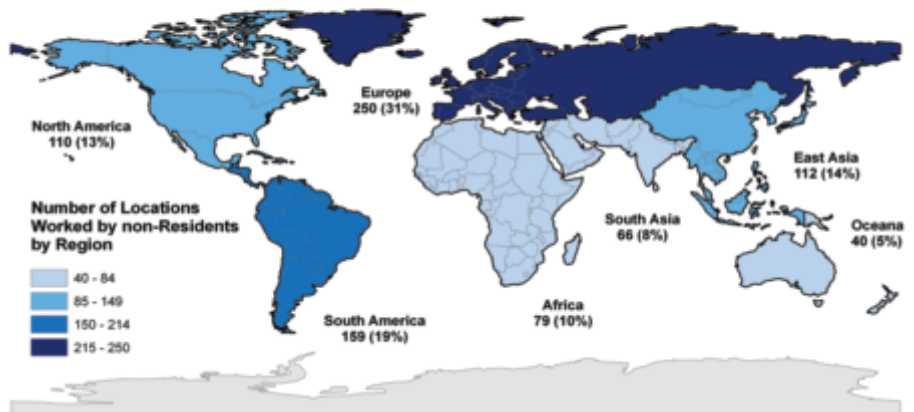


Figure 6. Regions that respondents are working, excluding their resident region n = 492. Total exceeds number of respondents since many work in more than one region.

Appropriate Education Needed for Majority of Respondents' Workforce

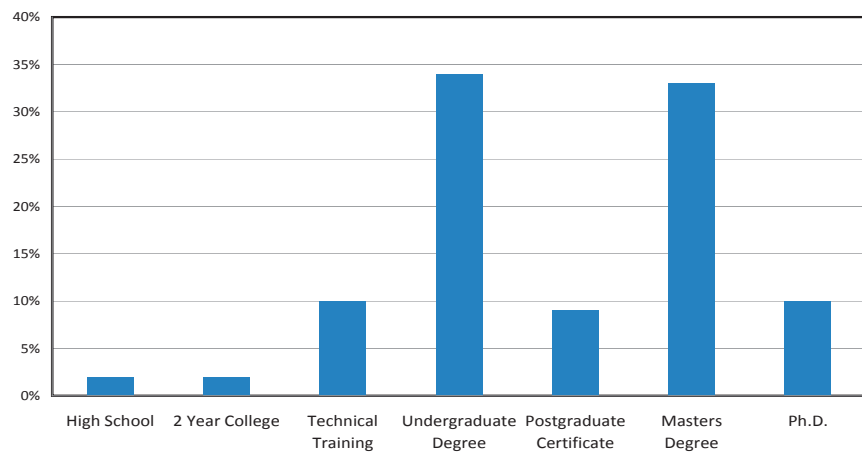


Figure 7. Question 21: For your agency or firm's needs, which level of education is appropriate for the majority of your workforce? n = 398

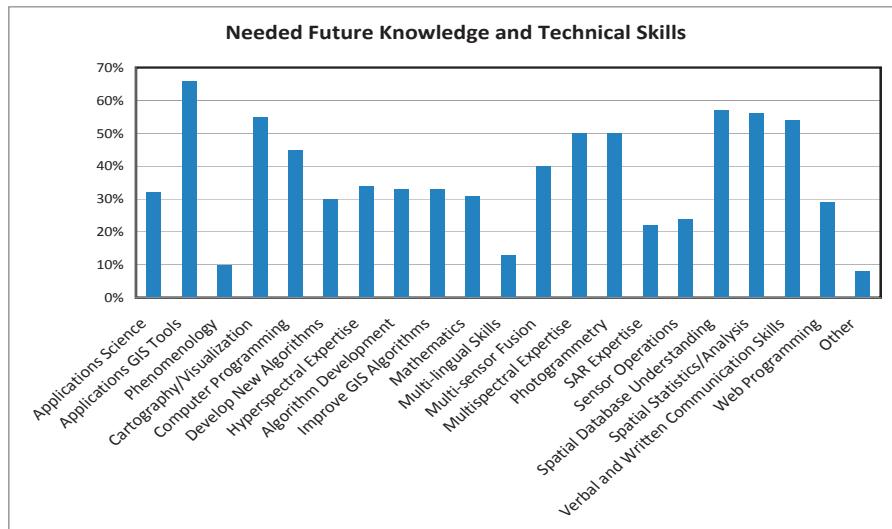


Figure 8. Question 22: What are the knowledge and technical skills that are most needed by your employees for the future? Please check all that apply. Percentages reflect the number of respondents, where n = 399.

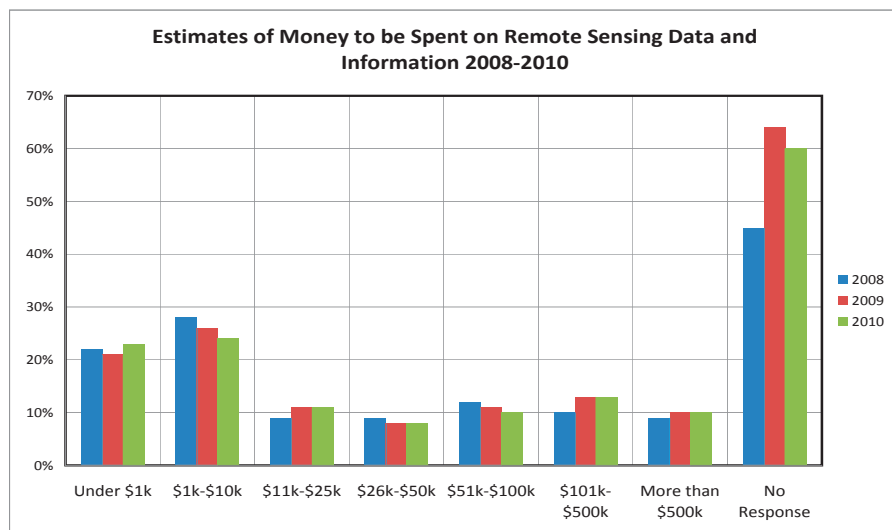


Figure 9. Questions 10-11: For the years 2008, 2009 and 2010, about how much money will you spend or authorize to acquire remotely sensed data or information, in US Dollars?

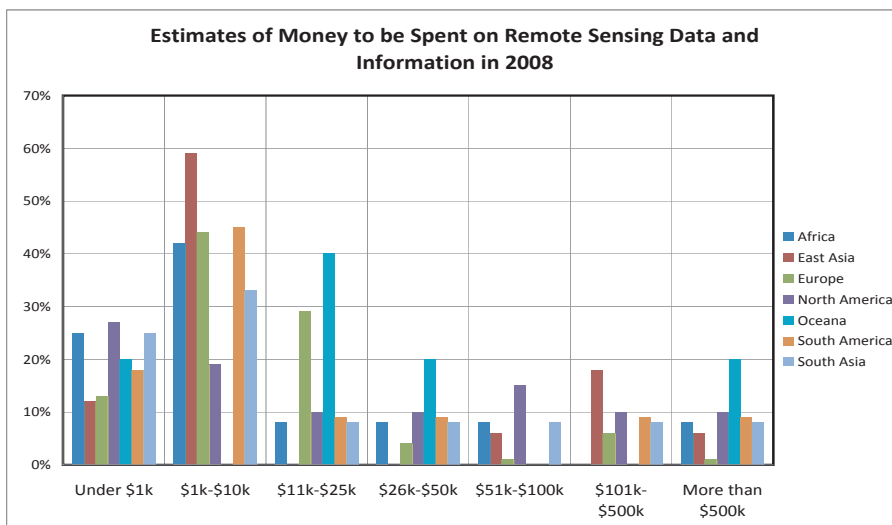


Figure 10. Question 10: For the year 2008, about how much money will you spend or authorize to acquire remotely sensed data or information, in US Dollars?

the future, however the out years no longer highlight a spending decline. These results may represent an expected modification in economic spending due to political change.

The overall spending at mid levels noted here shows a level trend. This survey has increased international participation versus previous studies and reflects the desire of many firms to perform work internationally. Commercial firms continue to outsource many core industry products and services internationally to achieve lower cost of goods sold.

In review of the data segmented by region a much stronger bias is seen in spending at the lower end of the spectrum with the largest data consumption under \$10K USD, this may be highlighting data required to complete outsourcing tasks. It is also apparent that this spending trend is maintained through the near future, with some locals considering additional spending by 2010.

Technology Application Areas

Phase V of the Forecast provides a follow-up assessment of the technology areas which firms utilize to conduct business. Technology areas polled in Phase V are similar to those found in the previous phases of the Forecast. This has been done to allow the user to trend data over time. It MUST be noted however that population and regional sampling have changed. Overall trend data may still be compared.

Data Characteristics

As in previous phases key attributes in remotesensing were sampled:

- Spatial Resolution* *Geospatial Accuracy*
- Vertical Accuracy* *Image Types*
- Currency* *Air versus Space*

Phase V continued this enquiry using a regional breakdown of the data. Two points stand out in the relative importance of the attributes. Data currency is clearly continuing to increase in relative importance. As global change escalates the demand for timely data continues to rise. The lack of international interest in data licensing is worthy of note. Data licensing barely registered as a point of concern in the study. While this often appears as an area of discussion, those participating in Phase V do not seem to share in this significance.

continued on page 1302

Data Characteristics: Spatial Resolution

The question about spatial resolution “needed” versus the resolution of the data “used” reflects the continued demand for high resolution data worldwide. Past surveys highlight that demand for the highest levels of resolution was clearly not met; data users wanted higher resolution content. Phase V shows that this trend continues in the global market. Digital aerial sensors, as well as the continued operation of high-resolution satellite systems have expanded the global demand for better than half meter data. This “used” versus “needed” transition point has shifted to higher quality data from previous surveys. Provision of data lower in resolution than half meter is now the area of potential overcapacity. The industry confirms this argument in price reductions for course resolution orthophotography.

Data Characteristics: Geospatial & Vertical Accuracy

Past industry surveys indicate that high quality geospatial and vertical accuracy data as an end product is in high demand, even with the cost associate premiums. With the growth in automated aero-triangulation, lidar, and direct geo-registration, much of this demand is well served. Each of these technologies drives improvement in data overall. The new imaging sensors with superior resolution and dynamic range require timely and current positional data to complete their data georegistration processing. Ground sample distances (GSD) of 6” and better continue to offer users the ability to focus on smaller and smaller targets, each requiring better positional data for production. Phase V validates the overall shape of the trend worldwide.

Vertical accuracy source data pushes overall quality in many imaging systems that are now classified as DEM-limited in performance. The greatest error source in pixel placement for these systems is that associated with the source elevation data. Phase V of the Forecast shows that technology has closed the previous gap in elevation data supply versus demand at the half meter level. While the best levels of performance still show unmet demand, the overall match in “used” versus “needed” worldwide indicates a greater shortfall than in the US only Phase IV. The adoption of automated elevation extraction and lidar still shows strong potential globally.

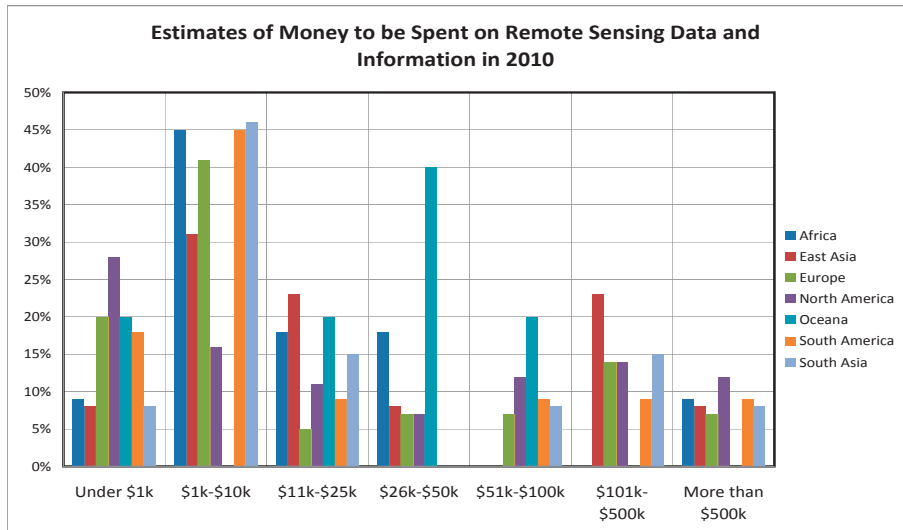


Figure 11. Question 11: For the years 2009 and 2010, about how much money will you spend or authorize to acquire remotely sensed data or information, in US Dollars?

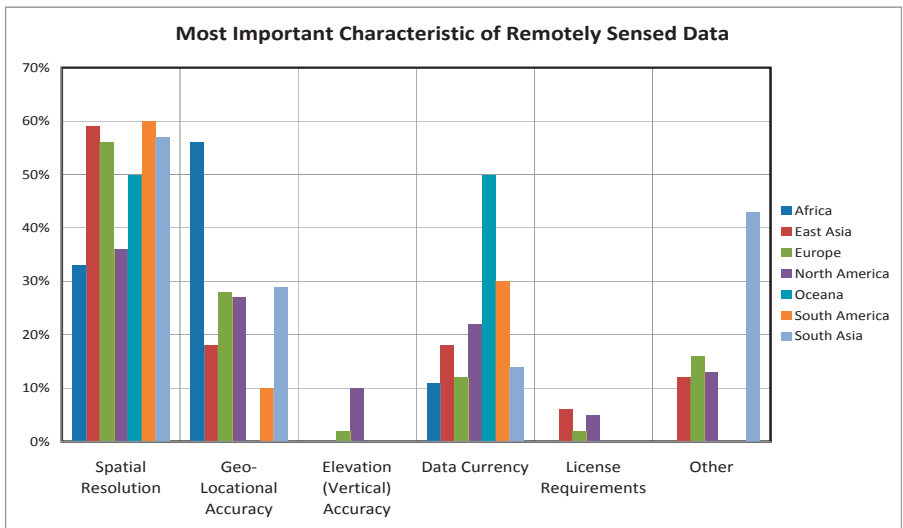


Figure 12. Question 12: For your job requirements, which is the most important characteristic of remotely sensed data or information?

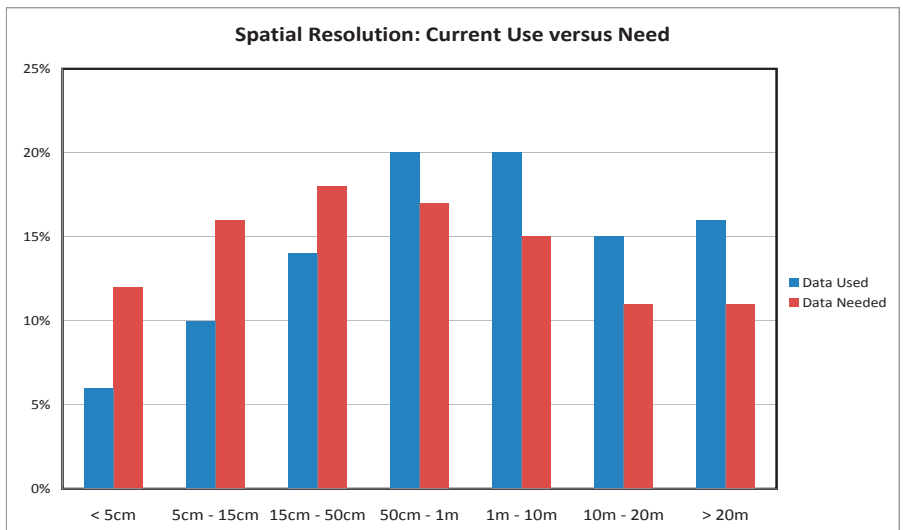


Figure 13. Question 13: What levels of Spatial Resolution do you currently WORK WITH today? What levels of Spatial Resolution do you NEED most to do your job? (Could be the same – check all that apply)

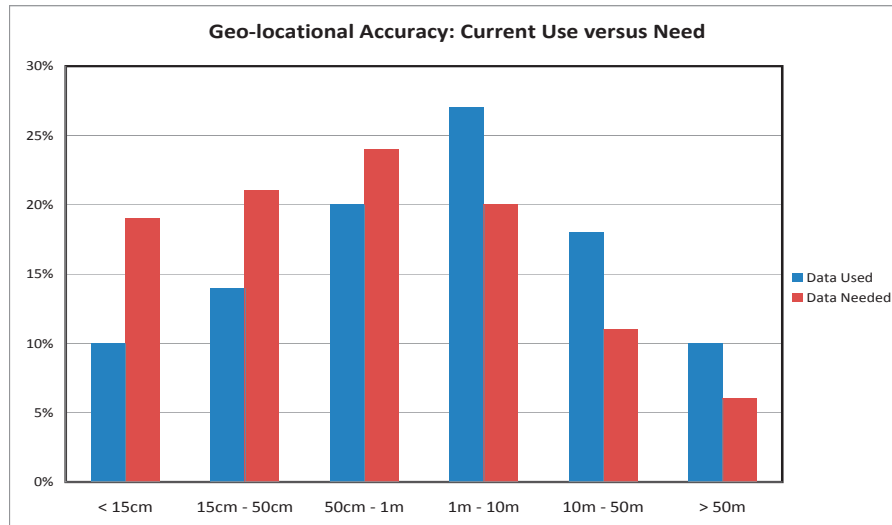


Figure 14. Question 14: What levels of geo-locational accuracy do you currently WORK WITH today? What levels of geo-locational (horizontal) accuracy do you NEED most to do your job? (Could be the same – check all that apply)

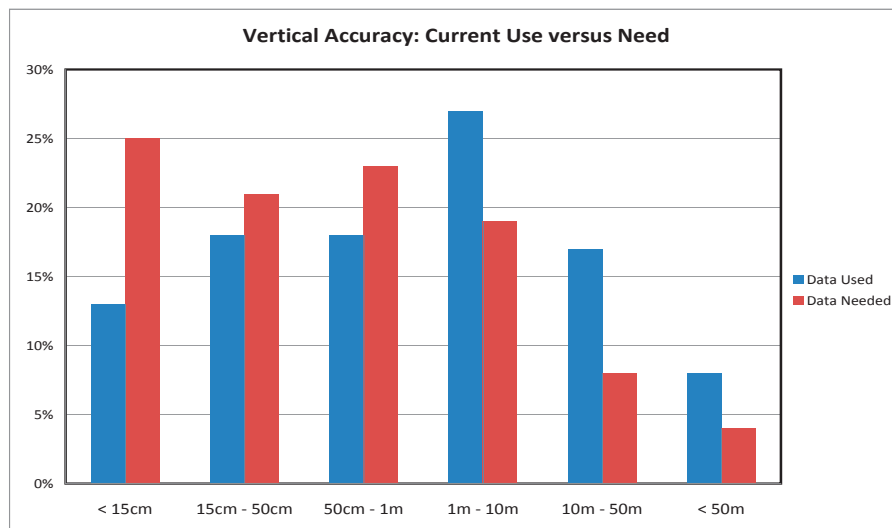


Figure 15. Question 15: What levels of elevation (vertical) accuracy do you currently WORK WITH today? What levels of elevation (vertical) accuracy do you NEED most to do your job? (Could be the same - check all that apply)

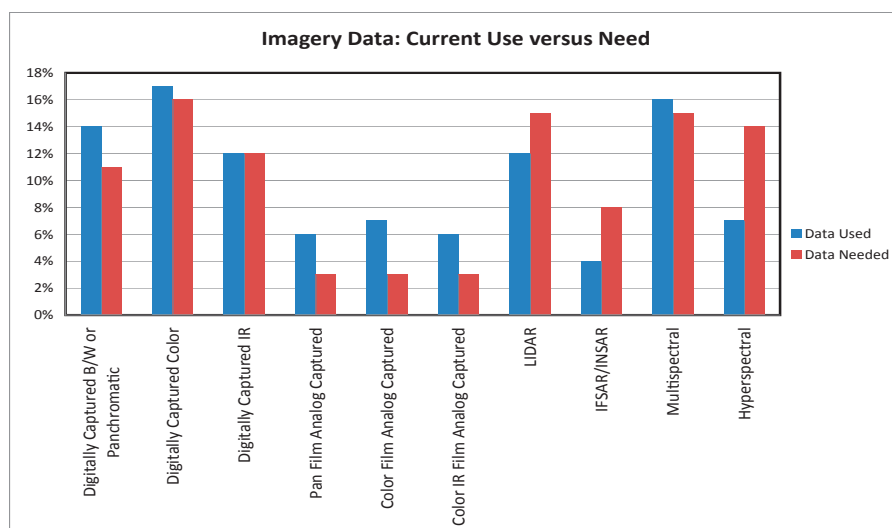


Figure 16. Question 16: What image/sensor types do you currently WORK WITH today? What image types do you NEED most to do your job? (Could be the same - check all that apply)

Data Characteristics: Image Types

The industry continues its utilization of technologies comparable to those of previous studies. Film-based image acquisition has shown a steady decline since the inception of the Forecast; Phase V confirms this but does show a slightly higher use rate worldwide than U.S. only data. Phase V continues the track of film versus digital transition in consumer and professional imaging markets. Phase V also confirms the overcapacity of digital sensors first seen in Phase IV. Only hyperspectral, IFSAR, and lidar appear to still drive industry demand.

Phase V confirmed the degree of data fusion and integration. This fusion had been qualified but not quantified. Clearly the demand for high quality resolution in concert with elevation is seen in the near 70% usage of fused data sets.

Data Characteristics: Currency

While resolution, accuracy and sensor type define the technologies employed, currency defines a critical component of the service aspect of the geospatial industry. The demand for “current” data is influenced heavily by global events. After the September 11, 2001 terrorist attacks, and again due to Hurricane Katrina, a strong increase was noted in demand for real time and near real time data. Users understood the value of near real time data in the assessment of disaster, triage, and rapid response. Commercial vendors have multiple price points for new, versus archival, data. As data pedigree ages to greater than one year its overall demand significantly decreases for many applications.

Data Characteristics: Air versus Space

If one examines the aerial-satellite question on a regional basis, the clear pattern is that satellite data is utilized more in the developing regions of the world. Only in North America does the use of aerial exceed satellite data usage. The likely reasons are the large area coverage needs in some regions, the lack of aerial coverage in many regions and the availability of lower cost aerial data in North America.

High-resolution satellites have proven themselves now in multiple generation commercial devices. Consolidation has occurred

continued on page 1304

continued from page 1303

both in air and space based data vendors. The proportional use of satellite data has steadily increased compared to the aerial segment since the inception of the ASPRS Ten-Year Remote Sensing Industry Forecast. This study phase shows a leveling of both technologies.

Relatively few respondents indicated that restrictions were not an issue in their region. Respondents from Africa, East Asia and Oceania report the highest levels of data licensing and sharing restrictions. Forty percent of South Asian respondents indicated that government posed the greatest restrictions on access.

Landsat 7 was the most utilized by respondents (74%), followed by Landsat 5 (66%), GeoEye-Ikonos and Digital Globe-Quickbird (both at 62%) and MODIS and SPOT 5 with about 44% of the respondents citing usage. These results indicate the clear demand for both the moderate and high spatial resolution data. Other important data sources were Terra-ASTER (37%), AVHRR (30%), SPOT 4 (28%), Radarsat (25%) and Orbview and EO-1 (25 and 24%). These results indicate the clear dependency of respondents from all regions of the world on U.S. supported satellites and data.

View to the Future

Phase V of the ASPRS Ten-Year Remote Sensing Industry Forecast had a relatively high response with limited, but still useful responses from every region of the world. Phase V reinforced trends identified in Phases I-IV and recalibrated these trends based on the uncertainty of the financial situation and the increasing distribution of new technologies across the world.

Several areas of investigation need to be addressed in future phases, in addition to the extension of the lines of inquiry already developed in Phases I-V. These new areas for investigation are 1) the role of information firms, such as Google and Microsoft in the dynamics and traditional business models of the remote sensing industry; 2) the nature of the relationships between military and intelligence demand for imagery data, especially in the high resolution arena and the economic situation of imagery providers and the civilian sector's ability to acquire imagery to meet increasing demand; and, 3) the increasing role of many nations in providing satellite imagery with a multitude of capabilities and restrictions.

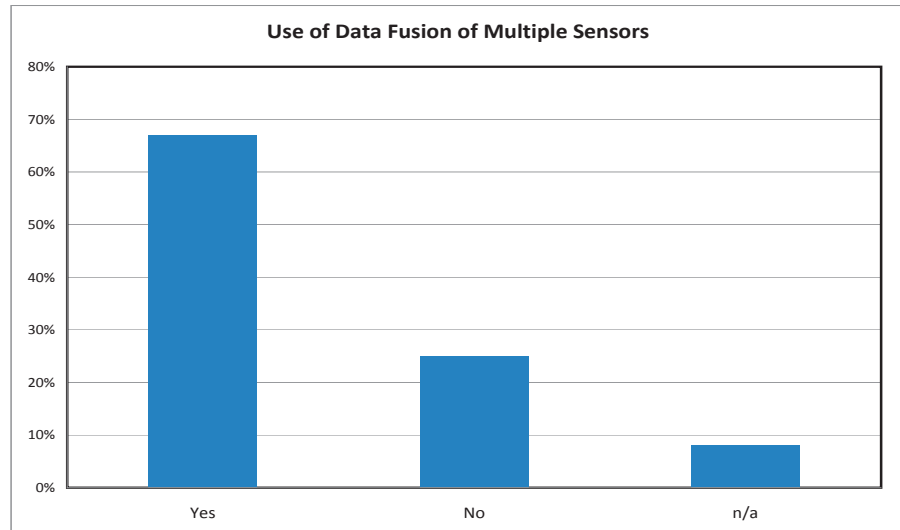


Figure 17. Question 17: Do you use data fusion of multiple sensor types you have selected above?

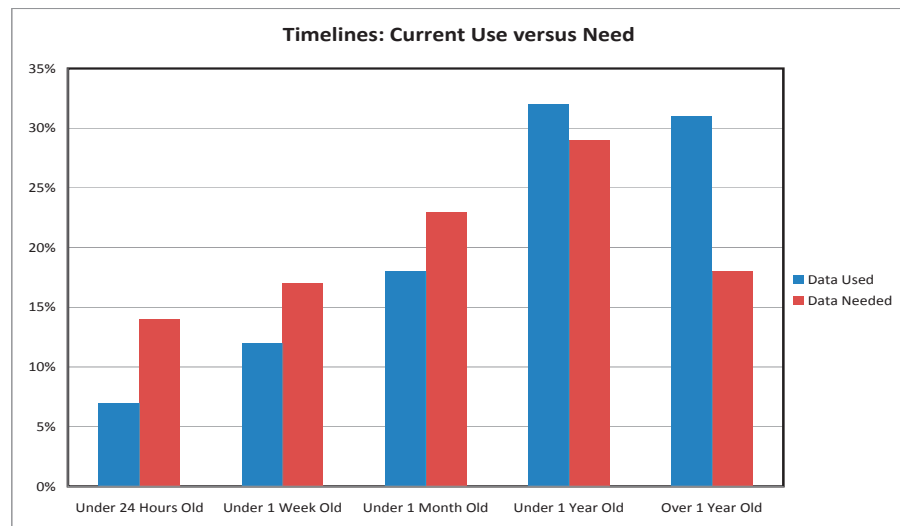


Figure 18. Question 18: How current are the data sets that you WORK WITH? How current do you NEED your data to be?

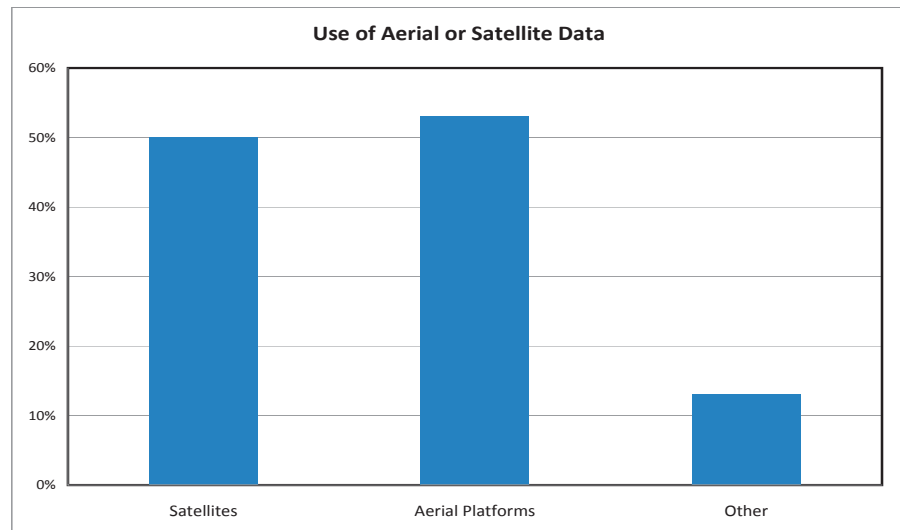


Figure 19. Question 19: What proportion of you remote sensing data/information is collected by aerial platforms vs. space-based collection? Your responses must add to 100%.

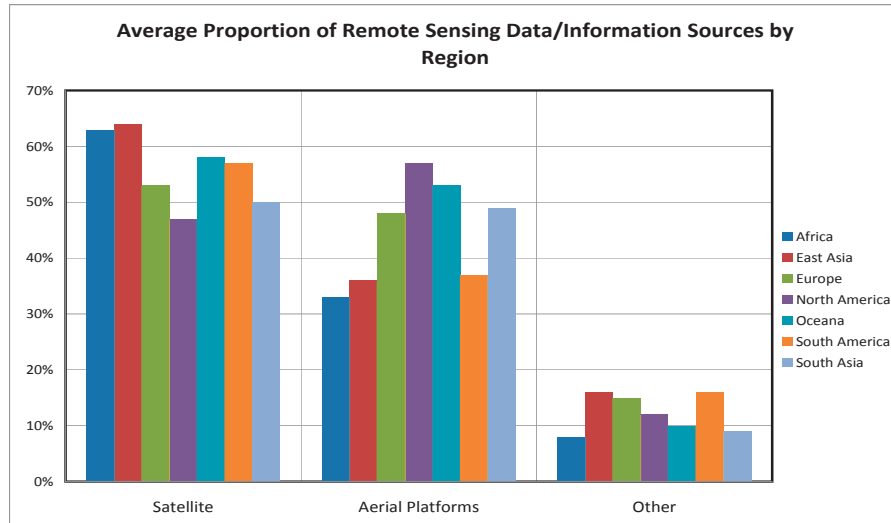


Figure 20. Question 19: What proportion of your remote sensing data/information is collected by aerial platforms vs. space-based collection? Your responses must add to 100%.

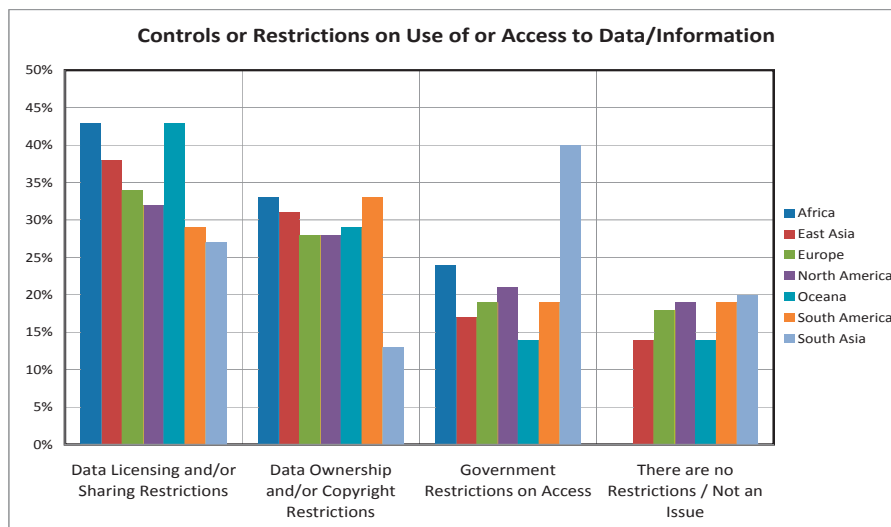


Figure 21. Question 20: What controls or restrictions on the use of, or access to, data/information most affect your work? Select all that apply.

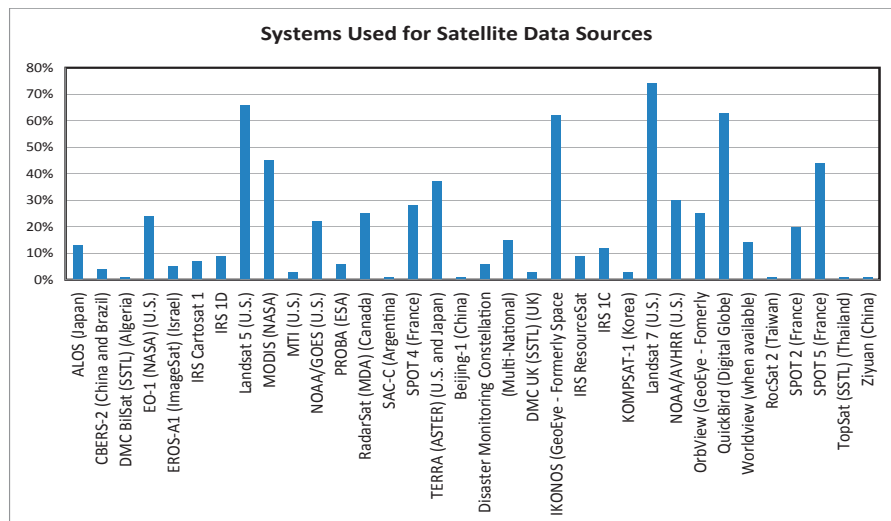


Figure 22. Question 26: Which sources provide satellite data utilized by your company/organization?
n = 2302 (More than one category chosen)

References

- Charles Mondello, George Hepner, and Ray A. Williamson, "10-Year Industry Forecast: Phases I-III -- Study Documentation," *Photogrammetric Engineering and Remote Sensing*, Vol. 70, No. 1, January 2004, pp. 7-58.
- Charles Mondello, George Hepner and Ray A. Williamson, "Ten Year Forecast of the U.S. Remote Sensing Industry Phase IV," *Photogrammetric Engineering and Remote Sensing*, 72-9 (September, 2006) pp. 985-1000.

Cover Caption

The NASA Applied Sciences Program within the Earth Science Division of the Science Mission Directorate has historically demonstrated practical applications of NASA Earth science observations and research. Through the NASA Scientific Purchase (Highlight Article, PE & RS, February, 2008), implemented by the NASA Commercial Remote Sensing Program (now the Applied Science and Technology Project Office) commercially available remotely sensed data was acquired and used to benefit many NASA research and application studies. Some examples from these valuable studies are represented in the images on page (x).

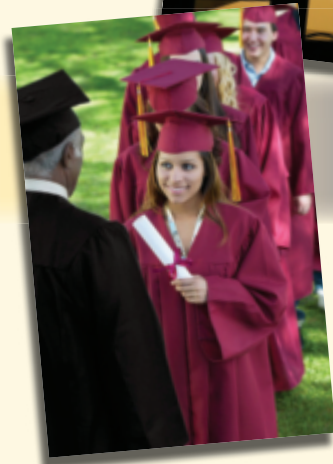
EarthWatch/Intermap STAR-3i DEM data over Alaska enabled essential detailed hydrologic analysis and modeling for large scale Arctic watersheds used in permafrost research studies (includes material ©Earth-Watch and/or its suppliers, Longmont, CO). (upper right)

Positive Systems ADAR 5500 high-resolution aerial imagery over Wyoming was used to evaluate and monitor ecosystems, including streams and riparian areas, in Yellowstone National Park for watershed analysis studies (includes material © Positive Systems, Inc.). (upper left)

IKONOS imagery (this image acquired over Faial Island) was used to observe highly sensitive and previously inaccessible oceanic island landscapes, and to quantify the sensitivity of landscape systems to different forcings and climate change (image courtesy of Space Imaging, LLC). (lower right)

An orthorectified Landsat TM image of Mount Kilimanjaro in East Africa, used for sustainable development projects; this data has also been utilized as a significant baseline dataset for assessing global and local land cover change (Courtesy of NASA and Earth Satellite Corporation). (lower left)

Your life is an ongoing series of changes...



...Make sure you're prepared for what comes next.

A new family, a new house, a new baby, your own business, retirement...

Life is filled with changes, some of which are not planned. And with each change, come new responsibilities and a new reason to think about your financial future.

That is why it is important to take some time today to help make sure that your family is prepared for the unexpected.

Through the ASPRS Group Insurance Program, you can choose from a broad range of insurance plans to help keep you and your family's financial future protected when changes occur. And, since most plans are available at Group rates that are negotiated on behalf of ASPRS members, we're confident that our rates are competitive.

- Group Term Life
- Group 10-Year Level Term Life
- Group High-Limit Accident
- Dental Discount Plan
- Health Insurance
- Professional Liability

For information, including plan features, costs, eligibility, renewability, limitations and exclusions, call the Administrator toll-free:

1-800-424-9883



This program is administered by Marsh Affinity Group Services, a service of Seabury & Smith, CA#0633005. Some plans may vary or not be available in all states. The Group Term Life, 10-Year Level Term Life, and High-Limit Accident Insurance Plans are underwritten by New York Life Insurance Company, 51 Madison Ave., New York, NY 10010 on Policy Form GMR. The Dental Discount Plan is provided by The United States Life Insurance Company in the City of New York, a subsidiary of American International Group, Inc. (AIG). The Professional Liability Insurance Plan is underwritten by Certain Underwriters at Lloyd's of London.

35490
AG-6551
11/08

©Seabury and Smith, Inc. 2008

Grids & Datums

ARAB REPUBLIC OF EGYPT

by Clifford J. Mugnier, C.P., C.M.S.

The roots of Egyptian civilization go back more than 6,000 years to the beginning of settled life along the banks of the Nile River. "The regularity and richness of the annual Nile River flood, coupled with semi-isolation provided by deserts to the east and west, allowed for the development of one of the world's great civilizations. A unified kingdom arose circa 3200 B.C., and a series of dynasties ruled in Egypt for the next three millennia. The last native dynasty fell to the Persians in 341 B.C., who in turn were replaced by the Greeks, Romans, and Byzantines. It was the Arabs who introduced Islam and the Arabic language in the 7th century and who ruled for the next six centuries. A local military caste, the Mamluks took control about 1250 and continued to govern after the conquest of Egypt by the Ottoman Turks in 1517. [The Mamluks were such fierce and respected fighters that the U.S. Marine Corps adopted their ivory-hilted sword design for their officers' ceremonial dress – Ed.] Following the completion of the Suez Canal in 1869, Egypt became an important world transportation hub, but also fell heavily into debt. Ostensibly to protect its investments, Britain seized control of Egypt's government in 1882, but nominal allegiance to the Ottoman Empire continued until 1914. Partially independent from the U.K. in 1922, Egypt acquired full sovereignty with the overthrow of the British-backed monarchy in 1952. The completion of the Aswān High Dam in 1971 and the resultant Lake Nasser have altered the time-honored place of the Nile River in the agriculture and ecology of Egypt (CIA World Factbook, 2008)."

Egypt is bordered by the Gaza Strip (11 km), Israel (266 km) (PE&RS, August 2000), Libya (1,115 km) (PE&RS, June 2006), and Sudan (1,273 km); its coastline on the Mediterranean Sea and on the Red Sea totals 2,420 km. Slightly more than three times the area of New Mexico, the terrain is comprised mainly of a vast desert plateau interrupted by the Nile River Valley and its delta. The lowest point is the Qattara Depression (–133 m), and the highest point is Mount Catherine (2,629 m).

The first serious mapping of Egypt on modern lines was undertaken in 1798 by Napoleon for his survey of Egypt. A Topographic Section was formed which consisted of four officers, an astronomer, and four "intelligent soldiers." Bases were measured at Alexandria and Cairo by the "Service Topographique de l'Armée d'Égypte," and topographic maps were compiled with a 10 km grid with an origin at the great pyramids of the North in Memphis, "Le centre de la projection correspond à l'axe de la grande pyramide du Nord à Memphis." Referenced to the Plessis ellipsoid where $a = 6,375,738.7$ m, and $1/f = 334.29$, the projection was the ellipsoidal Bonne, the "standard" projection for Europe at the time. The maps of Egypt and the Palestine were later published in 1808 (The Lebanese Republic in PE&RS, October 2002).

In 1874 a number of expeditions were led by British scientists to various European colonies in Africa and the Indian Ocean in order to simultaneously observe the transit of Venus for the purpose of precisely determining differences in longitude. Locations included Mauritius, (PE&RS, February 1999), Rodrigues, Réunion, St. Paul and Egypt. Helwān Observatory situated on Az Zahra Hill in the Al Moqattam Hills, Qalyūbiya of Cairo was utilized for the observations,

and the station was termed "F₁" where: $\Phi_0 = 30^\circ 01' 42.8591''$ N, $\Lambda_0 = 31^\circ 16' 33.6''$ East of Greenwich, the initial LaPlace azimuth being measured from Station O₁ (Helwān) to Station B₁ (Saccara), $\alpha_0 = 72^\circ 42' 01.20''$ from South, and $H_0 = 204.3$ m, based on mean sea-level at Alexandria. This is considered the origin of the "Old Egypt Datum of 1907." A point of much heated contention among geodetic surveyors has been the "rumor" that the Clarke 1866 ellipsoid was once used in Egypt.

It just so happens that M. Sheppard, director general of the Survey of Egypt, reported (*in French*) to the Secretary General of the Geodesy Section of the International Union of Geodesy and Geophysics that the initial geodetic work performed in Egypt was computed on the Clarke 1866 ellipsoid where "a, demi-grande axe équatoriale = 6.378.206^m. (sic), $\alpha = 1/295,0$. (sic)." Sheppard went on to say that all cultivated lands in the Nile Valley that were based on 2nd and 3rd order triangulations (for cadastral applications) initially used this ellipsoid, but that a later controlling chain of triangulation spanning the length of the Nile Valley was computed with the later adopted Helmert (1906) ellipsoid where $a = 6.378.200$ m, $1/f = 1/298,3$. Everything was later re-calculated on the Helmert ellipsoid and also on the International 1924 ellipsoid where $a = 6,378,388$ m, $1/f = 297$ (Bulletin géodésique, no. 8, 1925).

"A point of much heated contention among Geodetic Surveyors has been the "rumor" that the Clarke 1866 ellipsoid was once used in Egypt.

"Although a great deal of survey work of various kinds had been done in Egypt from time immemorial up to 1907, and this, as regards the Framework, culminated in a certain amount of modern triangulation of secondary order executed between the years 1898 and 1907, it was not until the latter year that a triangulation of the first order was undertaken. The secondary triangulation was necessary to control the modern Cadastral Survey, but the urgency with which the latter had to be completed made it impracticable to undertake work of full first-order accuracy at the beginning. Accordingly, although the existing Survey of Egypt, as founded by the late Sir Henry Lyons, dates from 1898, the geodetic survey proper may be said not to have started until 1907 (Geodesy in Egypt, Empire Survey Review, No. 60)."

The British established a number of grid systems in 1929 for the Old Egypt Datum of 1907, each Gauss-Krüger Transverse Mercator Belt being designated with a different color: **Purple Belt** – Central Meridian (λ_0) = 27°E, Latitude of Origin (ϕ_0) = 30°N, Scale Factor at Origin (m_0) = 1.0, False Easting = 700 km, False Northing = 200 km, and South of the False Origin add 1,000 km to the northings; **Red Belt** – Central Meridian (λ_0) = 31°E, Latitude of Origin (ϕ_0) = 30°N, Scale Factor at Origin (m_0) = 1.0, False Easting = 615 km, False Northing = 810 km and South of the False Origin add 1,000 km to the northings; **Green Belt** – Central Meridian (λ_0) = 35°E, Latitude

continued on page 1308

continued from page 1307

of Origin (ϕ_0) = 30°N, Scale Factor at Origin (m_0) = 1.0, False Easting = 300 km, False Northing = 100 km and South of the False Origin add 1,000 km to the northings.

In 1930, after a re-adjustment of the classical network, the New Egypt Datum of 1930 was published, also referenced to the Helmert 1909 ellipsoid. The Purple, Red, and Green Belts were retained with no modifications. The common abbreviation for the new datum is "EG30." This remains the current classical system used in Egypt for civilian mapping purposes.

After WWII, the U.S. Army Map Service (AMS) undertook the re-computation of all classical datums that covered lands involved in the European Theater of War, including all of North Africa. That new unified system was the European Datum of 1950 (ED50), and was referenced to the International 1924 ellipsoid. The longitude of F_1 , Venus Station at Helwān, was changed to $\Lambda_0 = 31^\circ 16' 37.05''$ East of Greenwich as a result of observations for the deflection of the vertical, but this change was only with respect to its re-computation on the International 1924 ellipsoid. All coordinates on ED50 for Egypt were published on the UTM Grid and generally are considered useful

only for military mapping purposes, not for civilian use. A number of datum shift algorithms on the complex plane were developed by AMS to convert directly from the Purple, Red and Green Belts to the UTM ED50 Grids. Although classified Secret at the time, they were declassified in 1956.

TR8350.2 lists a couple of datum shifts from classical to the WGS84 Datum. **From** Old Egyptian 1907 **to** WGS84: $\Delta X = -130 \text{ m} \pm 3 \text{ m}$, $\Delta Y = +110 \text{ m} \pm 6 \text{ m}$, and $\Delta Z = -13 \text{ m} \pm 8 \text{ m}$, and is based on 14 stations used in the derivation. This compares favorably with my own computations, but using fewer stations. **From** ED50 **to** WGS84, $\Delta X = -130 \text{ m} \pm 6 \text{ m}$, $\Delta Y = -117 \text{ m} \pm 8 \text{ m}$, and $\Delta Z = -151 \text{ m} \pm 8 \text{ m}$, and is *also* based on 14 stations used in the derivation.

Using the full Molodensky 7-parameter datum shift model (including the datum origin coordinates) with 23 points, I derived the following **From** Egyptian 1930 **to** WGS84: $\Delta X = -137.5 \text{ m} \pm 0.5 \text{ m}$, $\Delta Y = +105.0 \text{ m} \pm 0.4 \text{ m}$, and $\Delta Z = -18.1 \text{ m} \pm 0.4 \text{ m}$, $\delta s = +4.38 \times 10^{-6} \pm 1$, $R_x = -5.0'' \pm 0.70''$, $R_y = +1.59'' \pm 0.48''$, $R_z = +1.51'' \pm 0.26''$. A solution with 19 differentially weighted points and 5 check points for a much larger area of

**Stand out from the rest—
earn ASPRS Certification**

ASPRS congratulates these recently Certified and Re-certified individuals:

Certified Photogrammetrists
Kelly Francis, Certification # 1372, effective 9/17/2008, expires 9/17/2013
Forrest Gladding, Certification # 1373, effective 9/17/2008, expires 9/17/2013
John S. Hrivnak, Certification # 1371, effective 9/18/2008, expires 9/18/2013
Karl Jensen, Certification # 1374, effective 9/17/2008, expires 9/17/2013
Eugene Levin, Certification # 1369, effective 9/1/2008, expires 9/1/2013

Re-certified Photogrammetrists
Christopher D. Aldridge, Certification # R1163, effective 9/18/2008, expires 9/18/2013
Jeffery Joseph Armstrong, Certification # R1086, effective 9/18/2008, expires 9/18/2013
Jeff Bandt, Certification # R1070, effective 9/18/2008, expires 9/18/2013
James Cannistra, Certification # R850, effective 9/18/2008, expires 9/18/2013
Don Cleveland, Certification # R481, effective 9/18/2008, expires 9/18/2013
Terry A. Curtis, Certification # R1128, effective 9/18/2008, expires 9/18/2013
William T. Faunce, Certification # R1104, effective 9/18/2008, expires 9/18/2013
Bradley S. Fugate, Certification # R1084, effective 9/18/2008, expires 9/18/2013
Richard R. Hudson, Certification # R902, effective 9/18/2008, expires 9/18/2013
James Lufes, Certification # R1224, effective 9/18/2008, expires 9/18/2013

Certified Photogrammetric Technologist
Debbie A. Hornsby, Certification # 1370PT, effective 9/1/2008, expires 9/1/2011

Certified Mapping Scientist GIS/LIS
Lindi J. Quackenbush, Certification # GS205, effective 9/1/2008, expires 9/1/2013

Certified Mapping Scientist Remote Sensing
Lindi J. Quackenbush, Certification # RS162, effective 9/1/2008, expires 9/1/2013

ASPRS certification is available in:

- Photogrammetrist
- Mapping Scientist - GIS/LIS
- Remote Sensing Technologist
- Mapping Scientist - Remote Sensing
- Photogrammetric Technologist
- GIS/LIS Technologist

For more information on ASPRS Certification, visit <http://www.asprs.org/membership/certification/>

Egypt yielded the following 7-parameter Bursa-Wolfe model From Egyptian 1930 to WGS84: $\Delta X = -88.832 \text{ m} \pm 0.02 \text{ m}$, $\Delta Y = +186.714 \text{ m} \pm 0.03 \text{ m}$, and $\Delta Z = +151.82 \text{ m} \pm 0.01 \text{ m}$, $\delta s = -6.413 \times 10^{-6} \pm 1.84$, $R_x = -1.305'' \pm 2.21''$, $R_y = +11.216'' \pm 1.57''$, $R_z = -6.413'' \pm 1.84''$ (Shaker, Prof. A.A., et al., *Remove-Restore Technique for Improving The Datum Transformation Process, FIG Working Week 2007, Hong Kong, 13-17 May 2007*).



The contents of this column reflect the views of the author, who is responsible for the facts and accuracy of the data presented herein. The contents do not necessarily reflect the official views or policies of the American Society for Photogrammetry and Remote Sensing and/or the Louisiana State University Center for Geoinformatics (C⁴G).

It's all about... *career*
your future
society...

ASPRS would like to welcome the following new members!

At Large
Shilu Tang*

Central US
Tyler Waters

Columbia River
Tyler Bax
Allen Bruce Martin

Eastern Great Lakes
Susan F. Benston*
Matthew Hay*
Sudhagar Nagarajan*

Mid-South
Seth Adams*
Megan Maureen Burke*

Michael A. Duncan
Reginald S. Fletcher
John Michael Harrison
Lisa D. Keys-Mathews
Thomas Francis Nance*

North Atlantic
Leonard Bundra
Laura Calandra*

Northern California
Lynne Marie Baumgras
Nicolas Damien Ramirez*

New England
Lynn Carlson

Potomac
Timothy W. Ault
Cary M. Cox*

Jonathan Dandois*
Antoine De Chassy
Stephen Louis DiCicco
William Kyle Mears
William Clarence Moffitt
Ted J. Mugnier
Prasad Avinash Pathak*
Andrew Peters
Michael Benjamin Pogue
Suzy Stensland
Jennifer J. Swenson
Silvia Terziotti

Puget Sound
Erica Capuana*
Meghan Halabisky*
Peter Nicol

Rocky Mountain
Tanya Holtz
Kristen Kaczynski*

Saint Louis
Sara J. Johnson*
Justin Patrick Thomas*

Southwest US
Steven S. Amesbury*
Reginald S. Archer*
Alfredo R. Huete
Leslie Tomlinson*

Western Great Lakes
Jonathan Hanes*

*denotes student membership

working together to advance the practice of geospatial technology

For more information on ASPRS membership,
visit <http://www.asprs.org/membership/>

DiMAC
DIGITAL MODULAR AERIAL CAMERA

TRUE COLOR ■ TRUE FMC
UPGRADEABLE
MODULAR ■ COST EFFECTIVE

True modularity for
both mapping & ortho

A NEW range of solutions
scaled to your project and budget

DiMAC WIDE
Our large format DiMAC 2.0
(10 500 x 7 200 Mp)
now equipped with our
new compact IT Rack

DiMAC LIGHT
Our medium format
DiMAC 2.0
(7 200 x 5 400 Mp)
fully upgradeable
to DiMAC WIDE

DiMAC ULTRALIGHT
Our medium format
camera (39 Mp) in
a compact and
inexpensive package

We offer the only MEDIUM
FORMAT cameras WITH FMC

fulfilling
the promises of
digital aerial
imagery

DiMAC SYSTEMS

Europe Office:
Luxemburg
Tel + 352 26 51 21 66

North America Office:
Colorado, USA
Tel: +1 303 651 2018

info@dimacsystems.com
www.dimacsystems.com

THE CHALLENGES OF MAPPING URBAN HOLLAND. AS SEEN BY NOVATEL'S GPS+INS TECHNOLOGY.

Moerdijk, Oostflakkee or wherever; you can now map cities as if you're right there. Thanks to Cyclomedia's 360-degree panoramic digital mapping with NovAtel precise positioning technology onboard, the world appears in 3-D because, well, it is. Incorporating NovAtel's SPAN GPS+Inertial Measurement Unit system, accurate and robust positioning data is possible even in challenging urban conditions where GPS alone is limited.

3-D mapping is just one of many worldwide applications successfully utilizing NovAtel's precise positioning products.

To learn more about the products that powered this application, navigate your way to novatel.com.

NovAtel's precise thinking makes it possible.



1-800-NOVATEL (U.S. & Canada) or 403-295-4900 | Europe +44 (0) 1993 852-436 | SE Asia & Australia +61 (2) 8668 4073 | sales@novatel.com

Mapping Matters

By Qassim A. Abdullah, Ph.D., PLS, CP**

Your Questions Answered

The layman's perspective on technical theory and practical applications of mapping and GIS

Q1: In Aerial Triangulation, once a least-squares adjustment has been run, the results have been found to be acceptable with no blunders or residuals out of tolerance, there is a decision to be made: Do you overwrite the given ground control values with the adjusted coordinates or do you keep the original coordinates provided by the land surveyor?

Jon Martin, CP, Texas DOT

Dr. Abdullah: I would like to quote part of Jon Martin's message that accompanied his question as he brings up a very interesting discussion on the topic that the reader needs to know about. In his message, Martin elaborated as follows:

"I've run this question by a number of colleagues. Among State DOTs, it appears that about half overwrite and half don't. Dr. Hintz has suggested that the proper procedure is to overwrite the given ground control with the adjusted values. I tend to agree with Dr. Hintz because mathematically, it doesn't seem to make much sense to not overwrite. Doing so means that you end up with a mix of best-fit tie points with non-adjusted survey control. In the big scheme of things, it shouldn't make a lot of difference. However, some software, like the software that displays imagery in stereo, runs a second least-squares adjustment on the data set coming out of the analytical triangulation process to form the stereo model. It seems that this second adjustment would be more accurate if all of the points used were part of a best-fit solution rather than a mix. My Land Surveyor colleagues feel that the ground control has to be held as a fixed value. I don't agree with this opinion. Unlike the survey world, we aren't going to "re-occupy" an aerial photo derived map. Our map product is a final product and no subsequent mapping (or surveying) is going to be done using our map as a coordinate basis. I believe that the most accurate mapping is done using least-squares, best-fit solution. Could you please weigh in on this issue?"

run least squares adjustments of geodetic control networks. Blunderous points need to be identified and removed by the survey adjustment process, and good control from a professional survey firm need to have been redundantly measured, adjusted and certified as to their accuracy at a given precision. The control survey should be magnitudes stronger than the air-trig, so the air-trig cannot supersede the values on any control point. That's not to say the erroneous control doesn't show up, and if held fixed would cause problems. So, the air-trig is not intended to "prove" the surveyor correct, but errors are errors. And if the control doesn't fit, that may indicate some other problem with the bundle as well."

Colleague #2, Land Surveyor: "This is an age old question without a known solution. In my view, the points must be adjusted with the rest in order to preserve the integrity of the adjustment. The surveyor's control is not gospel; they are prone to many types of errors, but would not be adjusted if held in place [Sic]. Thus, my solution is to preserve a copy of the original surveyor's points to document what was provided and used and then adjust the points with the solution provided that the solution does in fact meet the tolerance requirements. The bottom line is that the probability that the surveyor would measure his points one day and then measure the same points the next day with two different answers is great. Therefore, beyond good field techniques, redundancy in a least square adjustment is the key to a good solution. One man's view."

"The combination of the added constraints due to the GPS-controlled principal point, the minimal ground control points (perhaps one control point for every 20 photos), and the high density of pass/tie points, has definitely weakened the effect of ground control points on the final computation or re-computation of the exterior orientation parameters."

The question and the comments given above represent very common arguments within the aerial triangulation community. I myself wanted to survey my colleagues in the field on their response to a question like this. Here are the different responses I got on the same question:

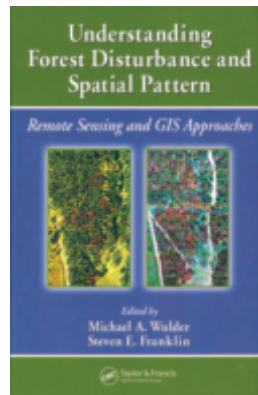
Colleague #1, Land Surveyor: "Absolutely, overwrite and hold fixed unless there is evidence of blunder. The way that I believe it works is: The bundle adjustment is run minimally constrained with only one control point fixed and all others free or to very low weights. As the control is evaluated, those with low (acceptable) residuals should then be held fixed, infinite weight, per the surveyor, not allowing for any adjustment to those data points. This has been how I have

He then added the next day, "I awoke thinking on this issue this morning and I have one additional point to add. When we are speaking of surveyor's points, what order of control are we speaking of? First order or CORS points or ground control as provided by the surveyor? I believe there may be a difference in how the two should be treated."

Colleague #3, Aerial Triangulation Specialist: "I say that you would overwrite with the adjusted control values for the main reason that individual measurements most likely would have inherent error even with their residuals being within tolerance. Using the adjusted coordinates would account for your network's normal distribution of error. Just a thought. I'm not a surveyor or a CP."

continued on page 1313

Book Review



Understanding Forest Disturbance and Spatial Pattern: Remote Sensing and GIS Approaches

Michael E. Wulder and Steven E. Franklin, Editors. CRC Press: Boca Raton, FL. 2007. xvi and 246 pp., diagrams, maps, photos, images, index

ISBN 978-0-8493-3425-2

Hardcover. \$109.95

Reviewed by

Kin M. Ma, Assistant Professor, Geography and Planning Department, Grand Valley State University, Allendale, Michigan

The stated goal of this book's editors is to consider forest disturbance and spatial pattern from an ecological point-of-view within the context of structure, function, pattern and change. *Understanding Forest Disturbance and Spatial Pattern: Remote Sensing and GIS Approaches* "guides the reader from a landscape ecological context of forest disturbance, to remote sensing and GIS technological approaches, through to pattern description and analysis" (p. vii). The intended audiences are the scientific and resource management communities, comprised of forest researchers, conservation biologists, and forest management professionals. There are nine chapters including an introduction and conclusion. Experts in the fields of forestry, remote sensing, and landscape ecology contributed. Each chapter is well-organized and includes an individual detailed table of contents.

In Chapter 1, Linke *et al.* describe the structure, function, and change

in forested landscapes from the perspective of landscape ecology. There is a balanced in-depth discussion of how various broad-scale disturbances will shape the future structure of these landscapes. Broad-scale fire and wind damage versus smaller-scale insect defoliation events are illustrated. A large number of figures showing forest disturbance and ecological succession are especially useful. It is well known that remotely-sensed imagery is effective in monitoring forest disturbance, and Chapter 2 provides a detailed guide to spatial and temporal resolution issues across various scales and sensors. A variety of radiometric and geometric techniques, such as Principal Components Analysis, are used to identify and describe forest disturbance. In Chapter 3, Healy *et al.* build upon these techniques to detect forest harvest patterns such as regeneration harvest, thinning and salvage. A case study of areas in the Pacific Northwest forest compares whether the unsupervised or

continued on page 1314

Reach new heights with
DAT/EM Systems International *Summit Evolution*
advanced softcopy digital stereoplottor



Summit Evolution is a user-friendly digital photogrammetric stereo workstation for 3D feature collection directly into ArcGIS, AutoCAD and MicroStation and includes the following:

- >Capture for ArcGIS, AutoCAD or MicroStation
- >Map Editor for AutoCAD or MicroStation

With its flexible orientation tools, **Summit Evolution** fits into any production workflow:

- >Automatic interior and relative orientation
- >Project overview and management
- >Built-in coordinate transformation
- >Terrain Visualizer (on-the-fly contours)
- >Easy-to-use Orthophoto and Mosaic generation tools
- >Quick frame sequential imaging

For more information, visit our web page at:
www.datem.com
Tel: +907.522.3681
Fax: +907.522.3688
E-mail: sales@datem.com



Colleague #4, Aerial Triangulation Specialist: "I would say not to overwrite because the adjusted values means they adjusted according to given actual control values and it shows you how the actual control network should be. As per Colleague #3, it is also correct that adjusted coordinates would account for your network's normal distribution of error since with the residuals being within tolerance, it will not make much difference if you overwrite".

I hope you agree with me that this issue has been a point of contention between professionals in the field of mapping and surveying since the beginning of analytical aerial triangulation. My view on this goes along with many of the opinions given above on the theoretical aspects of network controls and constraints. However, experience has taught me that what may sound theoretically correct may not necessarily be the only acceptable solution. We currently collect an average of 100 to 200 auto-correlated pass/tie points per frame, most of which are of excellent quality. In addition, most if not all of triangulation today is performed with the help of the airborne GPS-measured camera position. The introduction of airborne GPS has changed the requirements for ground control and only a sparse control network is needed when an aerial triangulation project is planned. The combination of the added constraints due to the GPS-controlled principal point, the minimal ground control points (perhaps one control point for every 20 photos), and the high density of pass/tie points, has definitely weakened the effect of ground control points on the final computation or re-computation of the exterior orientation parameters. In my opinion, the question on whether to overwrite or not overwrite the original controls points used in the bundle block solution can be answered in two ways, as follows:

1. If the aerial triangulation software restricts you to the production of the exterior orientation parameters derived from the airborne GPS-controlled bundle block adjustment only, then you have no choice and the adjusted coordinates of the ground control will be used in the solution. This is the case when you adjust the block using airborne GPS, the ground control points, and possibly the IMU-derived orientations, and you then use the exterior orientation derived from this solution for stereo compilation or ortho rectification.
2. If the software routinely re-computes the exterior orientation parameters of each frame after the final bundle block adjustment has been performed and accepted and all the tie/pass points' coordinates are replaced with the final adjusted ground values, then the issue of overwriting will depend on the number of the pass/tie points used in each frame. Examples of different methods of re-computing the exterior orientation parameters vary with the software and user preferences. For example, Albany performs a space resection solution, while ISAT of Intergraph performs a so-called bulk orientation. Some users prefer to perform additional conventional adjustment using the adjusted pass/tie points following the original airborne GPS adjustment. With the introduction of softcopy aerial triangulation, the subject using the original surveyed coordinates or the adjusted coordinates for the ground control points has become irrelevant to a certain degree. To simplify the matter further, previously when we used only three principal pass points per photo, the entire frame during orientation (space resection) was controlled by an average of

nine pass, tie, and perhaps a few control points. In this case the control had a higher weight in the least squares adjustment and using adjusted coordinates versus original surveyed coordinates for ground control points could have a drastic impact on the photo orientation during mapping. This is not the case with the auto-correlated collection of tie/pass points. Most softcopy aerial triangulation packages perform either space resection or bulk orientation after all the pass/tie points are adjusted and densified into control points. Therefore, having one surveyed control point, if any, between hundreds of pass/tie-turned into control points has minimized the effect of the original ground control on the final exterior orientation computation for that individual frame. The individual control point or two present between hundreds of photo controls will have minimal weight and it will be outweighed by the presence of the dense network of densified pass/tie points in the final exterior orientation computation.

Based on the above, my recommendation is that if you are performing aerial triangulation today with hundreds of adjusted pass/tie points and you are re-computing the exterior orientation parameters again after the final bundle block adjustment was finalized and accepted, it does not really matter whether you overwrite or not. However, if the aerial triangulation was performed 20 years ago, then it will be a different story.

Finally, as for the question on whether one should on a routine basis overwrite the given ground control values with the adjusted coordinates or keep the original surveyed coordinates as provided by the land surveyor, I believe that the adjusted coordinates should be used for all subsequent computations or orientation. This is due to the fact that the mathematical and statistical models have found the best fit for that ground control within the different elements of the block. Introducing a different set of coordinates (in this case the one provided by the land surveyor) will offset that balance or fit assuming that all of the measurements and values used in the aerial triangulation were of high quality. To provide an example for this argument, assume that there is one control point that the mathematical model found to be erroneous by about 40 cm. The new adjusted value, which is off by 40 cm from the surveyed value, desirably fits the entire network of the block. Introducing the original value (erroneous according to the math model) in any subsequent computations of the network or part of it will cause misfit between that control point and the adjacent points.

Please send your question to Mapping_Matters@asprs.org and indicate whether you want your name to be blocked from publishing.

Answers for all questions that are not published in *PE&RS* can be found on line at [www.asprs.org/Mapping Matters](http://www.asprs.org/Mapping_Matters).

***Dr. Abdullah is the Chief Scientist at Fugro EarthData, Inc, Frederick, MD.*



The contents of this column reflect the views of the author, who is responsible for the facts and accuracy of the data presented herein. The contents do not necessarily reflect the official views or policies of the American Society for Photogrammetry and Remote Sensing and/or Fugro EarthData, Inc.

continued from page 1312

supervised classification algorithm is more efficient in measuring the regeneration of post-harvest forest stands. A significant source of forest disturbance comes from insect defoliators, and Chapter 4's discussion of the six most common insect defoliators in North America provides an in-depth analysis of the link between the insects' adverse physiological effects on the vegetation and spectral response. The most significant forest disturbance event is fire and Chapter 5 provides a guide to the most common burn-mapping approaches and illustrates the use of the Normalized Burn Ratio (NBR) for measuring the burn severity from the large 2004 Payson, Arizona, Willow fire. To illustrate more clearly the use of remote sensing techniques, the entirety of Chapter 8 discusses the analysis of a series of Landsat 5 (TM) and Landsat 7 (ETM+) images for timber harvest and fire disturbance by utilizing the middle-infrared corrected Normalized Difference Vegetation Index (NDVIC) and the NBR in Cooney Ridge, Montana.

When monitoring forest change/disturbance, Rogan and Miller in Chapter 6 argue that the integration of GIS data as environmental variables with remote sensing imagery is vital to increasing the accuracy of forest change detection. They write frankly that the potential errors of omission and commission limit the map accuracy of forest change detection, though there is evidence from recent studies showing that the integration of GIS data will better capture and represent disturbance over a range of scales. The characterization of the spatial pattern of forest disturbance and the interplay with remote sensing is covered by Chapter 7. Gergel provides a detailed review of landscape pattern characterization with the corresponding metrics, and argues for new directions and landscape pattern indices to advance fine-scale pattern analyses. With the inexpensive nature of disk storage space, a shift from the "standard" Landsat 30 m pixel, to 1 m high-resolution images will alter the combination of landscape metrics and influence the search for new categorizations.

Overall, almost all of the figures, graphic images, and maps, excellently illustrate the disturbance and spatial patterns that were discussed in each of the chapters. However, several color figures were challenging to interpret. For example, in Fig. 3.4, because of the dark background of the Pacific Northwest forested region, the choropleth colors for the specific fire events and harvest periods are difficult to visually distinguish from one another. Either enlarging the Pacific Northwest graphic or removing the image background of the forested region would improve the map. Despite these small shortcomings, this book seriously integrates the use of remote sensing and GIS techniques to help forestry researchers, resource management professionals, and conservation biologists meet the challenges of capturing and characterizing forest disturbance and their spatial patterns. The book rightly argues that the combination and integration of remote sensing and GIS data is important for analyzing patterns of fire severity, insect defoliation, and timber harvest. Their arguments are strengthened within each chapter with numerous case studies and examples that utilize remote sensing and GIS technology methods to characterize various types of forest disturbance. The authors rely on the most recent studies to bolster their arguments and a majority of the authors are doing this highly valued integrated research. This book is well-researched and makes a significant contribution to the forestry, remote sensing and landscape ecology bodies of literature.

Wulder and Franklin's concluding chapter highlights and weaves the many strands of the forestry mosaic of chapters into an integrated whole. Each of the chapters is well-referenced and provides the reader with ample background materials to explore in more depth any of the methods or studies discussed. Wulder and Franklin have each written numerous articles that relate remote sensing to forests. They have once again succeeded in combining their expertise and distilling the knowledge of forestry, remote sensing and landscape ecology experts by guiding readers from understanding the landscape ecological patterns of forests and then to integrate the remote sensing and GIS methods to better characterize forest disturbance and their spatial patterns.

Announcement and Call for Papers

22nd Biennial Workshop on Aerial Photography, Videography, and High Resolution Digital Imagery for Resource Assessment

March 17-19, 2009 • Lubbock, Texas, USA

Abstract deadline: December 22, 2008

Sponsored By:

Texas Tech University Department of Plant and Soil Science
International Center for Arid and Semi-Arid Lands Studies (ICASALS)
American Society for Photogrammetry and Remote Sensing (ASPRS)

Hosted By:

Texas Tech University

Organized By:

Stephan J. Maas (Chairperson), Dept. of Plant and Soil Science, Texas Tech
Aderbal C. "A.C." Correa, Director, ICASALS
Seiichi Nagihara, Department of Geosciences, Texas Tech

The purpose of the Biennial Workshop is the dissemination and documentation of advances in remote sensing made using sensors with high spatial resolution (typically less than 30 meters). Relevant studies involve a wide variety of sensors, including aerial photography, imaging spectroradiometers, hyperspectral imagers, lidar, analog video cameras, digital cameras, and high-resolution satellite systems like IKONOS and QuickBird. While the scope of sensors addressed in this workshop is restricted by spatial scale, the application of the sensors is very broad. The program of the Biennial Workshop welcomes reports involving the application of high-resolution remote sensing to a wide variety of natural and managed resources. Reports are organized into one of four general topic areas: Agriculture (crops, orchards, pastures, rangeland, soils, and water), Natural Resources (forests, wetlands, wildlife habitats, water bodies, coastal regions, and geology), Infrastructure and Human Impacts (urban environments, transportation, landscaping, disturbed lands, pollution, and archaeology), and Systems (sensors, analytical procedures, calibration, image processing, integration with GIS, and technology transfer). The Biennial Workshop regularly draws researchers and students from a wide variety of disciplines. The opportunity for individuals from different disciplines to interact has been one of the main strengths of this workshop.

The deadline for submitting an abstract for a presentation at the Biennial Workshop is December 22, 2008. Information on submitting abstracts, workshop registration, and other details regarding the workshop can be obtained at the Biennial Workshop website,

http://users.sptc.net/smaas/ASPRS/ASPRS_announcement.htm

ASPRS Vice Presidential Candidates for 2009

This is a notice regarding the Official Nomination for the office of ASPRS Vice President for 2009, and the requirements for nomination by petition. The ASPRS Nominating Committee is pleased to announce its candidates for the office of ASPRS Vice President, to take office in March 2009.

Gary Florence
Photo Science
St. Petersburg, Florida

Dr. A. Stewart Walker
BAE Systems
San Diego, California

Additional nominees for Vice President from the Private Sector should be submitted to the ASPRS Executive Director, 5410 Grosvenor Lane, Suite 210, Bethesda, MD 20814-2160, no later than 14 weeks prior to the 2009 ASPRS Annual Conference. These nominations must be made by a nominating letter signed by not less than 250 voting members of ASPRS and must contain a biographical sketch of the nominee.

Deadline for nominations by petition:
November 17, 2008

ASPRS Nominating Committee:
Marguerite Madden, Chair
Kari Craun
Karen Schuckman
Russell Congalton
Donald Lauer

Thank you to all the ASPRS regions that participated in the Region of the Month contest.



**AND THE
WINNER FOR
SEPTEMBER
IS THE...**

POTOMAC REGION

The Potomac Region sponsored 12 new members during the month of September.

In recognition of their commitment to the Society, they receive the following:

- A certificate from ASPRS acknowledging their work in membership recruitment.
- ASPRS Buck\$ vouchers valued at \$50 to be used toward merchandise in the ASPRS Bookstore.
- This special recognition in this issue of *PE&RS* of their designation as "Region of the Month," a true display of their commitment to the Society.

Bravo!! Potomac Region

This is an ongoing regional recruitment campaign. We hope other regions will be listed here in future months.

Editor PE&RS,

Regarding the pertinent of
Give us your feedback!

in geospa today's published educational
As you read *PE&RS* each month if you have comments or questions about the articles and papers that you read we want to hear from you. Please include your name and contact information with each Letter to the Editor. Your name will be printed with your letter but the contact information will not be published. Please send your letters to kimt@asprs.org.

BE AN ASPRS MEMBER CHAMPION

ASPRS is recruiting new members and YOU benefit from each new member YOU champion. Not only can you contribute to the growth of ASPRS, but you can earn discounts on dues and merchandise in the ASPRS Store.

Member Champions by Region as of September 30, 2008

Central New York

Thomas E. Henderson
Ricardo Lopez-Torri
James Mower
Jeff Walton

Central US

Jackson Cothren

Columbia River

Christopher Aldridge
Michelle Kinzel
Steven Lennartz
Brian Miyake
Robert S. Peckyno
Mike Renslow

Eastern Great Lakes

James S. Bethel
Phyllis Ullery

Florida

Tarig A. Ali
Brian Murphy

Inter-Mountain

Lloyd H. Blackburn
Keith T. Weber

Mid-South

Marguerite Madden
Sorin C. Popescu
Wubishet Tadesse

North Atlantic

Kenneth W. Potter

New England

Daniel L. Civco

Northern California

Steven Steinberg
Carolyn S. Tate

Potomac

Barry Haack
Clifford Mugnier
Veronique Payan

Elizabeth M. Smith
Yogendra P. Singh

Puget Sound

Monika Moskal

Rocky Mountain

Lloyd P. Queen

Saint-Louis

David Kreighbaum

Southwest US

Stuart E. Marsh

Western Great Lakes

David Hart
Thomas Lillesand

Member Champions By number of new members recruited

Recruited from 1 to 4 New Members

Christopher Aldridge
Tarig A. Ali
James S. Bethel
Lloyd H. Blackburn
Jackson Cothren
Barry Haack
David Hart
Thomas E. Henderson
Michelle Kinzel
David Kreighbaum
Steven Lennartz
Thomas Lillesand
Ricardo Lopez-Torri
Marguerite Madden
Stuart E. Marsh
James Mower
Clifford Mugnier
Veronique Payan
Robert S. Peckyno
Sorin C. Popescu
Kenneth W. Potter

Lloyd P. Queen
Mike Renslow
Yogendra P. Singh
Elizabeth M. Smith
Steven Steinberg
Wubishet Tadesse
Carolyn S. Tate
Phyllis Ullery
Keith T. Weber

Recruited 5 through 10 New Members

Daniel L. Civco
Brian Miyake
Brian Murphy
Monika Moskal

REMEMBER! To receive credit for a new member, the CHAMPION'S name and ASPRS membership number must be included on the new member's application.

CONTACT INFORMATION

For Membership materials, contact us at: 301-493-0290, ext. 109/104 or email: members@asprs.org.

Individuals who want to join ASPRS may sign up on-line at <https://asprs.org/application>.

RECRUIT

1 new member, earn a 10% DISCOUNT off your ASPRS DUES and \$5 in ASPRS BUCKS.

5 new members, earn a 50% DISCOUNT off your ASPRS DUES and \$25 in ASPRS BUCKS.

10 or more new members in a calendar year and receive the Ford Bartlett Award, one year of complimentary membership, and \$50 in ASPRS BUCKS.

All newly recruited members count toward the Region's tally for the Region of the Month Award given by ASPRS.

Those eligible to be invited to join ASPRS under the Member Champion Program are:

- Students and/or professionals who have never been ASPRS members.
- Former ASPRS members are eligible for reinstatement if their membership has lapsed for at least three years

ASPRS BUCK\$ VOUCHERS are worth \$5 each toward the purchase of publications or merchandise available through the ASPRS web site, catalog or at ASPRS conferences.



DIGITAL CAMERAS
VARIETY OF
APPLICATIONS

Aerial Stereo Camera
High Oblique Camera
Single Lidar Camera

WEHRLI & ASSOCIATES
7 Upland Drive, Valhalla, New York
Tel: 914.831.9821 www.wehriassoc.com info@wehriassoc.com

Business

Seoul-based JiguSoft Inc. has been appointed the master distributor of **ERDAS Inc.** for the Republic of Korea. This relationship allows ERDAS to participate more effectively in the Korean market, as JiguSoft will facilitate expedited processing of resellers' orders. Additionally, resellers will avoid the additional shipping and handling charges that may increase the cost of orders shipped directly from the United States. JiguSoft Inc. will provide marketing, technical support, and training to organizations within the Korean ERDAS reseller network. The reseller network comprises Geomonitoring, SOMAF, R&G World, and DOSA, and it will continue to offer sales, software customization, and project consulting directly to Korean customers. For information, visit www.erdas.com.

GeoEye, Inc. had a successful launch and deployment of GeoEye-1 on September 6, 2008. GeoEye's ground station in Norway relayed the downlink signal it received from GeoEye-1 confirming that the satellite successfully separated from the second stage of the launch vehicle and began automatically initializing its onboard systems. GeoEye-1 is part of the National Geospatial Intelligence Agency's (NGA) NextView program. The NextView program is designed to ensure that NGA has access to commercial imagery in support of its mission to provide timely, relevant and accurate geospatial intelligence in support of national security. GeoEye-1 will simultaneously collect 0.41-meter ground resolution black-and-white (panchromatic)



PHOTOGRAMMETRIC ENGINEERING & REMOTE SENSING

images and 1.65-meter color (multispectral) images. Designed to take digital images of the Earth from 423 miles (681 kilometers) and moving at a speed of about four-and-a-half miles (seven kilometers) per second, the satellite camera can distinguish objects on the Earth's surface as small as 0.41-meter or 16 inches in size. Due to U.S. licensing restrictions, commercial customers will get access to imagery at half-meter ground resolution. For information, visit www.geoeye.com.

ITT Corporation celebrated the successful launch of the GeoEye-1 satellite and its ITT-built imaging payload. The satellite has the ability to collect images at 0.41-meter panchromatic (black and white) and 1.65-meter multispectral (color) resolution. Furthermore, GeoEye-1 can precisely locate an object to within three meters of its true location on the Earth's surface, an unprecedented level of geolocation accuracy for a commercial satellite imaging system. The satellite will also be able to collect up to 700,000 square kilometers of panchromatic imagery per day, ideal for large scale mapping projects. For information, visit www.ssd.itt.com.

A declaratory action filed by GEOSPAN Corporation against **Pictometry International Corp.** earlier this year has been dismissed by the U.S. District Court of Minnesota. Citing a lack of subject matter jurisdiction, the District Court's decision to dismiss GEOSPAN's claim was among the first judgment of its kind to reference lowered declaratory judgment standards as defined recently by the U.S. Supreme Court. GEOSPAN filed the declaratory action earlier this year following a business inquiry by Pictometry into GEOSPAN's technology and its relation to Pictometry's patent. For information, visit www.pictometry.com.

The new **Riegl USA Inc.** website is now live. The new site has a refined look and is loaded with quality photos, easy to navigate menus and an abundance of product information. The homepage has six clearly defined menus, most with submenus, that take users to the information they need more efficiently than before. These menus include applications, where they can find out when and how Riegl products are used, and news and events where users can stay posted on new product releases and trade shows that Riegl will be attending. Visit www.rieglusa.com.

Contracts

Fugro EarthData, Inc., has been awarded over USD1.9 million in multiple task orders by the U.S. National Guard Bureau (NGB) for updated mapping over thirty-one domestic military installations through 2009. The work, which includes orthoimagery as well as planimetric and topographic mapping, is being issued through the company's existing indefinite delivery contract with the U.S. Army Corps of Engineers and will support military training, environmental management, and real property assessment. The 2008 task orders represent a shift in the National Guard's digital land base mapping program, which has moved toward all-digital mapping technologies. For information, visit www.fugroearthdata.com.

Clark County, Nevada recently selected **The Sidwell Company** to help modernize their internal land records and mapping operations to support accurate GIS analysis and ease of maintenance. The County needed to improve the efficiency of their operation and their ability to better serve a greater number of users within the jurisdiction. Sidwell will begin work with the County to thoroughly define a target workflow, and establish a new Geodatabase design, which will streamline the process of restructuring their existing Geodatabase to optimize it for cadastral editing. Sidwell's team will provide a county-wide geodatabase with restructured cadastral data, a parcel inventory database with both current and historical parcel records, all necessary plotting files, and on-site installation and configuration of the completed geodatabase. For information, visit www.sidwellco.com.

Western Air Maps, Inc. has been awarded an \$8 million large business contract by the U.S. Army Corps of Engineers – Northwest Division – Kansas City District. The Indefinite Delivery contract, awarded through a full and open Qualifications-Based Selection process, is projected to last 5 years. Through the contract, the U.S. Army Corps of Engineers issues task orders to Western Air Maps for aerial photography, photogrammetry, remote sensing, lidar, topographic mapping, boundary surveying, hydrographic surveying, and CADD/GIS onsite services and implementation for civil works, military and environmental projects primarily within the district. Services will also be rendered for the Corps of Engineers in the Omaha District

continued on page 1319

Industry News

continued from page 1317

and the Northwest Division. Other federal agencies may also utilize Western Air Map's services through the same contract. For information, visit www.westernair.com.

Education

The **University of Denver** is now offering a **master's degree in Geographic Information Sciences** through a partnership between University College, the school of professional and continuing studies, and the Department of Geography at the University of Denver. This new degree recognizes the emerging importance of geographic information science and the importance of integrating advanced study in geographic information systems, remote sensing, and global positioning systems with traditional studies in human, cultural, and physical geography. This degree is unique in that students in the program will take online classes exclusively and will complete the first half of the degree by taking classes offered through the University College graduate certificate program in Geographic Information Systems and the second half by taking classes offered through the Department of Geography's Master of Science in Geographic Information Sciences. The master's degree in Geographical Information Science will consist of a total of 48 credit hours. For information visit www.universitycollege.du.edu.

People

David A. Sprenkle, P.E.

has been appointed Chief Operating Officer (COO) of Merrick & Company. In his new role, Sprenkle will be responsible for overseeing the accomplishment of the firm's \$75 million annual portfolio of professional services. Sprenkle has twice served on the firm's Board of Directors for a total of 18 years and is currently a senior vice president with the company. He is also chairman of the board for Merrick Advanced Photogrammetry of the Americas (MAPA), a wholly-owned subsidiary of Merrick & Company, and chairman of the board for MMI/ETOH, Inc., another subsidiary of the company that owns an ethanol plant that provides biofuel processing for Molson Coors Brewing Company. Prior to taking on this new appointment, Sprenkle managed Merrick's corporate and



project support department, where he oversaw the financial and administrative aspects of the firm as a senior vice president. During his 28-year tenure with Merrick, Sprenkle has held other key positions including business unit leader and project manager.

Products

CICADE is joining forces with **DIMAC Systems** to conceive and produce the only oblique photogrammetric camera that makes possible the acquisition of vertical views at the same time as oblique images both using the unique TRUE FMC. DIMAC Systems is providing CICADE with the DiMAC^{COBBLIQUE}, a unique aerial digital camera that includes six camera modules, two of them performing the vertical acquisition with an image footprint of 10,500 by 7,200 pixels while four camera heads acquire the oblique views (North/South/West/East). For information, visit www.cicade.com.

DAT/EM Systems International has released Version 4.5 for SUMMIT EVOLUTION™. In this latest release, which is available at no cost to all users who have a current support contract, Summit Evolution is now easier, faster, and better. With many new features and product improvements, this upgrade and maintenance release extends the functionality already available within both Summit Evolution and DAT/EM Capture™. Summit Evolution Professional for all CAD/GIS highlights include: a Quick Options toolbar to toggle on and off popular features; improved mosaic boundary management and creation; expanded coordinate conversion database; a new, editable 2D Super Imposition setting in the status bar; merge/Extract Summit project management tool; and, the Leica Topomouse™ USB input device. For information, visit www.datem.com.

DIMAC Systems has unveiled its latest generation IT Rack, the centralized image acquisition system of DIMAC™ (Digital Modular Aerial Camera). The IT Rack has been designed to be fitted on any type of aircraft, from small single engine planes to large bi-turbo ones. Its design, size (HxWxD: 44x27x36cm /17x11x14 in) and weight (35kg/75lbs) make this tailor-made anti-vibration rack easy to install and remove from any aircraft. The IT Rack is made of three high-quality components: the Master Computer Unit, the Slave Computer Unit and

the Removable Storage Unit. The Master Computer Unit manages and synchronizes the camera module settings, the electromechanical shutter, and the TRUE FMC system that is unique to the DiMAC camera. Each Camera Module (CM) is connected to a Slave Computer Unit that acquires



exposures. Up to 4 CMs can be fitted into a single protective Cylindrical Camera Frame (CCF). Each CM takes individual pictures allowing for multi-spectral and/or infrared exposures and simultaneous production of up to 4 individual or 2 merged images. The Removable Storage Unit contains one pressurized hard drive per CM that records up to 10,000 pictures. Once on the ground, the plug-and-play Removable Storage Unit can easily be disembarked and the image data quickly downloaded. For information, visit www.dimacsystems.com.

QCoherent Software has released LP360 v1.6 and LP360 Classify v1.6. With an advanced architecture for accessing and processing lidar points, LP360 is the lidar tool of choice for integrating and processing lidar point clouds in ArcGIS. LP360 v1.6 provides ESRI GIS users with an uncompromised ability to leverage enormous lidar point cloud datasets. New features in LP360 v1.6 include: LAS 1.2 Support; Enhanced Export Features; Quick Display Filters and Copy Legend Options; Draped Profile Lines by Point Source (flight line) attribute; Integrated ArcGIS Breakline Digitizing tools; and, On-The-Fly Topology Corrections for Breaklines. For information and a free software trial, visit www.QCoherent.com.

The Sidwell Company recently announced the release of Parcel Builder™ Version 3.3. Parcel Builder was first introduced in the GIS marketplace in 2002. A software product developed exclusively by Sidwell, Parcel Builder is the premier parcel mapping solution for ArcGIS® 9.3 software from ESRI. Parcel Builder provides users with a comprehensive GIS-based land records management solution that is fully compliant with the newest technology from ESRI. Parcel Builder features simplified interfaces, significantly streamlines

most common cadastral mapping tasks, and provides complete integration for GIS, Tax and CAMA workflows, all supported in an ESRI geodatabase. For information, visit www.sidwellco.com.

Services

ESRI announced that ArcGIS users now have access to a new premium map service in ArcGIS Online. The USA Prime Imagery premium service includes i-cubed's Nationwide Prime 1-meter or better resolution imagery for the continental United States. Included with this imagery are i-cubed's 15-meter eSAT imagery at medium-to-large scales and the National Aeronautics and Space Administration's (NASA) Blue Marble: Next Generation 500-meter resolution imagery at small scales. The 2D maps and 3D globe services of i-cubed can be leveraged by ArcGIS users to author and publish maps and perform situational analysis. ArcGIS Online services, a family of Web-based data products, is now available to ArcGIS Desktop, ArcGIS Explorer, and ArcGIS Server users. ArcGIS Online gives users the ability to access online map content as well as make their own content available to other users from their own server. For information, visit www.esri.com/arcgisonline/services.

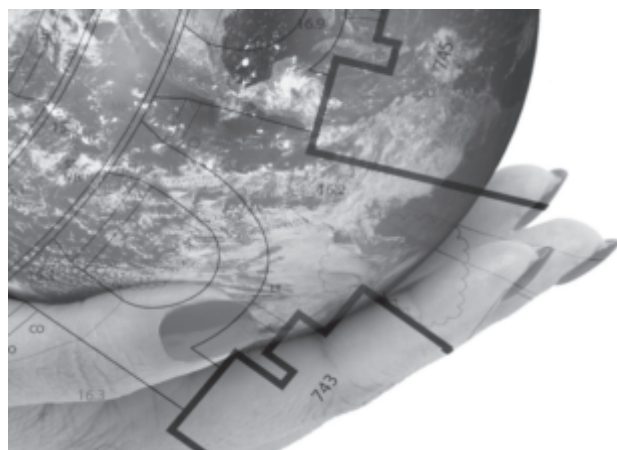
Pictometry International Corp. has captured, processed and delivered new oblique imagery to six Texas counties recently damaged by Hurricane Ike. The imagery was captured and processed within days of the devastating storm and will be used by county officials for damage assessment, recovery efforts and public communications. As part of Pictometry's Economic Alliance Partnership (EAP), Pictometry customers in Galveston,

Harris, and Montgomery counties (all part of the Houston Galveston Area Council) as well as Liberty, Orange and San Jacinto counties were immediately eligible to receive a new imagery without additional cost. Pictometry typically captures EAP imagery within hours of a natural disaster or catastrophic event. The imagery is immediately processed and

can be delivered within days or made immediately available with Pictometry Online. Either way, users are able to easily access relevant, high resolution imagery featuring 3D-like views of locations from multiple angles. For information, visit wpictometry.com.



Before (top) and after (bottom) imagery of a water tower damaged by Hurricane Ike in Crystal Beach, TX.



Vr Mapping

The NEW Standard in photogrammetric software

- VrOne
- VrTwo
- VrLite
- VrOrtho
- VrAirTrig
- VrMosaic
- VrBalance
- VrVolumes

386-439-2525 www.cardinalsystems.net

Cardinal Systems

Board of Directors

Officers

President

Kass Green*
AltaVista Company
Berkeley, CA 94708
kassgreen@earthlink.net

President-Elect

Bradley D. Doorn*
U.S. Department of Agriculture
York, PA 1740303
brad.doorn@usda.gov

Vice President

Carolyn J. Merry*
The Ohio State University
Columbus, OH 43212
merry.1@osu.edu

Past President

Marguerite Madden*
University of Georgia
Athens, GA 30602-2503
mmadden@uga.edu

Treasurer

Donald T. Lauer*
U.S. Geological Survey (Emeritus)
Reno, NV 89521
lauer@usgs.gov

Board Members

Alaska Region — 2010

Paul D. Brooks*
AERO-METRIC Anchorage
Anchorage, AK 99501-4116
pbrooks@aerometric-ak.com

Central New York Region — 2011

John T. Boland
ITT Industries Space Systems Division
Fairport, NY 14450
john.boland@itt.com

Central Region — 2011

Barry Budzowski
Western Air Maps
Overland Park, KS 66207
barryb@westernair.com

Columbia River Region — 2011

Chris Aldridge, CP
I-TEN Associates, Inc
Portland, OR 97214
chris.aldrige@i10assoc.com

Eastern Great Lakes Region — 2011

Charles K. Toth
The Ohio State University
Columbus, OH 43212
toth@cfm.ohio-state.edu

Florida Region — 2010

Thomas J. Young
Pickett & Associates
Bartow, FL 33830
tjyoung@pickett-inc.com

Geographic Information Systems Division — 2009

Paula Smit
Raytheon IIS
Denver, CO 80011
pfsmit@raytheon.com

Intermountain Region — 2010

Lucinda A. Clark
Draper, UT 84020
cclark@utah.gov

Mid-South Region — 2010

Lawrence R. Handley*
U.S. Geological Survey
Lafayette, LA 70506-3154
larry_handley@usgs.gov

New England Region — 2009

Claire Kiedrowski
Bangor, ME 04401
Claire@kappamap.com

North Atlantic Region — 2010

David Stolarz
East Meadow, NY 11554-1934
dstolarz@att.net

Northern California Region—2009

Lorraine Amenda
Towill, Inc.
San Francisco, CA 94103
Lorraine.Amenda@towill.com

Photogrammetric Applications Division — 2010

Rebecca A. Morton
Towill, Inc.
San Francisco, CA 94103
becky.morton@towill.com

Potomac Region — 2011

Allan Falconer
George Mason University
Fairfax, VA 22030
afalcon1@gmu.edu

Primary Data Acquisition Division — 2009

Robert Eadie
Spatial Wave, Inc.
Legwood, CO 80228
readie@spatialwave.com

Professional Practice Division — 2010

Douglas Lee Smith
David C. Smith and Assoc., Inc.
Portland, OR 97202
Doug@davidsmithmapping.com

Puget Sound Region — 2009

Terry A. Curtis*
WA DNR, Resource Map Sect.
Olympia, WA 98504-7032
terry.curtis@wadnr.gov

Remote Sensing Applications Division — 2010

John S. Iiames, Jr.
US EPA
Raleigh, NC 27612
iiames.john@epa.gov

Rocky Mountain Region — 2009

Allen E. Cook*
Parker, CO 80134
frostbite@awai.com

Southwest U.S. Region — 2011

A. Stewart Walker
BAE Systems
San Diego, CA 92127
stewart.walker2@baesystems.com

St. Louis Region — 2009

David W. Kreighbaum
US Army Corps of Engineers
Saint Louis, MO 63125-2535
David.W.Kreighbaum@mvs02.usace.army.mil

Sustaining Members Council Chair – 2009

Michael E. Flynn
M. J. Harden Associates, Inc.
Mission, KS 66202-2402
flynn.michael@geoeye.com

Western Great Lakes Region — 2010

Qihao Weng
Indiana State University
Terre Haute, IN 47809-0001
qweng@indstate.edu

Division Officers

Primary Data Acquisition

Director: Robert C. Eadie
Assistant Director: Gregory Stensaas
USGS EROS Data Center
stensaas@usgs.gov

Remote Sensing Applications

Director: John S. Iiames, Jr.
Assistant Director: Joseph F. Knight
joe@chromomorph.com

Professional Practice

Director: Douglas Lee Smith
Assistant Director: Anne K. Hillyer
Bonneville Power Administration (USDOE)
akhillyer@bpa.gov

Photogrammetric Applications

Director: Rebecca A. Morton
Assistant Director: Lewis N. Graham
GeoCue Corp.
lgraham@niirs10.com

Geographic Information Systems

Director: Paula Smit
Assistant Director: Maribeth Price
South Dakota School of Mines & Technology
maribeth.price@sdsmt.edu

Sustaining Members Council

Chair: Michael E. Flynn
Vice Chair: Mark Stanton
LandPixx, LLC
mstanton@pixxures.com

*Executive Committee Member

3001, Inc
Fairfax, Virginia
www.3001inc.com
Member Since: 12/2004

Aerial Cartographics of America, Inc. (ACA)
Orland, Florida
www.aca-net.com;
www.mv-usa.com
Member Since: 10/1994

Aerial Data Service, Inc.
Tulsa, Oklahoma
www.aerialdata.com
Member Since: 8/1993

Aerial Services, Inc.
Cedar Falls, Iowa
www.AerialServicesInc.com
Member Since: 5/2001

AERO-METRIC, Inc.
Sheboygan, Wisconsin
www.aerometric.com
Member Since: 1/1974

AeroTech Mapping Inc.
Las Vegas, Nevada
www.atmlv.com
Member Since: 8/2004

AGFA Corporation
Ridgefield Park, New Jersey
www.agfa.com
Member Since: 1/1990

Airborne Hydrography AB
Jönköping, Sweden
www.airbornehydro.com
Member Since: 9/2007

Air Photographics, Inc.
Martinsburg, West Virginia
www.airphotographics.com
Member Since: 1/1973

Airborne 1 Corporation
El Segundo, California
www.airborne1.com
Member Since: 7/2000

Airborne Data Systems, Inc
Wabasso, Minnesota
www.airbornedatasystems.com
Member Since: 1/2001

American Surveyor Magazine Frederick, Maryland
www.TheAmericanSurveyor.com
Member Since: 12/2004

Applanix Corporation
Ontario, Canada
www.applanix.com
Member Since: 7/1997

Applied Imagery
Silver Spring, Maryland
www.appliedimagery.com
Member Since: 4/2005

ASD Inc.
(formally Analytical Spectral Devices)
Boulder, Colorado
www.asdi.com
Member Since: 1/1998

Axis GeoSpatial, LLC
Easton, Maryland
www.axisgeospatial.com
Member Since: 1/2005

Ayres Associates, Inc.
Madison, Wisconsin
www.AyresAssociates.com
Member Since: 1/1953

BAE SYSTEMS
Mount Laurel, New Jersey
www.baesystems.com/gxp
Member Since: 7/1995

Bohannon Huston, Inc.
Albuquerque, New Mexico
www.bhinc.com
Member Since: 11/1992

Booz Allen Hamilton
Mc Lean, Virginia
www.boozallen.com
Member Since: 10/2004

Cardinal Systems, LLC
Flagler Beach, Florida
www.cardinalsystems.net
Member Since: 1/2001

CH2M HILL
Redding, California
www.ch2m.com
Member Since: 1/1974

Clark Labs | Clark University
Worcester, Massachusetts
www.clarklabs.org
Member Since: 10/1997

COL-EAST, Inc.
North Adams, Massachusetts
www.coleast.com
Member Since: 1/1976

CRC Press - Taylor & Francis Group
Boca Raton, Florida
www.crcpress.com
Member Since: 9/2006

DAT/EM Systems International
Anchorage, Alaska
www.datem.com
Member Since: 1/1974

DEFINIENS
Boulder, Colorado
www.definiens.com
Member Since: 12/2005

DeLorme
Yarmouth, Maine
www.delorme.com
Member Since: 11/2001

Dewberry
Fairfax, Virginia
www.dewberry.com
Member Since: 1/1985

Digital Aerial Solutions, LLC
Tampa, Florida
www.digitalaerial.com
Member Since 10/2006

Digital Mapping, Inc.
Huntington Beach, California
www.admap.com;
www.gisbank.com
Member Since: 4/2002

DigitalGlobe
Longmont, Colorado
www.digitalglobe.com
Member Since: 7/1996

DIMAC SYSTEMS, LLC
Longmont, Colorado
www.dimacsystems.com
Member Since: 1/2004

DMC International Imaging Ltd.
Guildford, Great Britain
www.dmcii.com
Member Since: 3/2008

Dudley Thompson Mapping Corp. (DTM)
Surrey, BC, Canada
www.dtm-global.com
Member Since: 9/2006

Dynamic Aviation Group, Inc.
Bridgewater, Virginia
www.dynamicaviation.com
Member Since: 4/2003

E. Coyote Enterprises, Inc.
Mineral Wells, Texas
www.ecoyote.com
Member Since: 1/1978

EADS Defence and Security Systems, SA
Cedex, France
www.geomatics-eads.net
Member Since: 8/1994

Eagle Mapping, Ltd
British Columbia, Canada
www.eaglemapping.com
Member Since: 1/1999

Eastdawn Corporation
Beijing, China
www.eastdawn.com.cn/english
Member Since: 1/2008

Eastern Topographics
Wolfeboro, New Hampshire
www.e-topo.com
Member Since: 8/1995

Environmental Research Incorporated
Linden, Virginia
www.eri.us.com
Member Since: 8/2008

ERDAS, Inc.
Norcross, Georgia
www.erdas.com
Member Since: 1/1985

ESRI Environmental Systems Research Institute, Inc.
Redlands, California
www.esri.com
Member Since: 1/1987

EUROSENSE
Wemmel, Belgium
www.eurosense.com
Member Since: 1/1982

Federal Geographic Data Committee
Reston, Virginia
www.fgdc.gov
Member Since: 1/1998

Fugro EarthData, Inc. (was EarthData, Inc.)
Frederick, Maryland
www.earthdata.com
Member Since: 1/1994

Fugro Horizons, Inc. (was Horizons, Inc.)
Rapid City, South Dakota
www.fugrohorizons.com
Member Since: 1/1974

Furnas Centrais Eletricas S/A
Botafogo, Brazil
Member Since: 1/2007

GeoCue Corporation (NIIRS10, Inc.)
Madison, Alabama
info@geocue.com
Member Since: 10/2003

GeoEye (was ORBIMAGE Inc.)
Dulles, Virginia
www.geoeye.com
Member Since: 4/1995

Geographic Resource Solutions
Arcata, California
www.grsgis.com
Member Since: 12/2006

Geolas Consulting
Poing, Germany
www.geolas.com
Member Since: 1/2002

Geospace Inc.
Albuquerque, New Mexico
www.geospaceinc.com
Member Since: 3/2008

GRW Aerial Surveys, Inc.
Lexington, Kentucky
www.grwinc.com
Member Since: 1/1985

Groupe ALTA
Sainte-Foy, QC Canada
www.groupealta.com
Member Since: 7/1/2003

HAS Images, Inc.
Dayton, Ohio
www.hasimages.com
Member Since: 2/1998

HJW GeoSpatial, Inc.
Oakland, California
www.hjw.com
Member Since: 11/1992

INPHO GmbH
Stuttgart, Germany
www.inpho.de
Member Since: 4/1994

Institute for the Application of Geospatial Technology (IAGT)
Auburn, New York
www.iagt.org
Member Since: 3/2001

Intergraph Corporation (Z/I Imaging)
Madison, Alabama
www.intergraph.com
Member Since: 1/1951

Intermap Technologies, Inc.
Englewood, Colorado
www.intermap.com
Member Since: 1/1987

International Institute for Geo-Information Science and Earth Observation (ITC)
Enschede, Netherlands
www.itc.nl
Member Since: 1/1992

ITRES Research Limited
Calgary, Canada
www.itres.com
Member Since: 1/2003

ITT (was RSI) Visual Information Solutions
Boulder, Colorado
www.itvis.com
Member Since: 1/1997

Kenney Aerial Mapping
Phoenix, Arizona
www.kam-az.com
Member Since: 1/2000

asprs

Sustaining Members

Keystone Aerial Surveys, Inc.
Philadelphia, Pennsylvania
www.keystoneaerialsurveys.com
Member Since: 1/1985

Kim Geomatics Corporation
Manotick, Ontario, Canada
bryerson@kimgeomatics.com
Member since: 9/2007

KLT Associates, Inc.
Peabody, Massachusetts
www.kltassoc.com
Member Since: 11/1993

Kucera International
Willoughby, Ohio
www.kucerainternational.com
Member Since: 1/1992

**L-3 Communications
Titan Group Enterprise
Geospatial Solutions**
Portland, Oregon
www.L-3com.com
Member Since: 11/1999

L. Robert Kimball & Associates
Ebensburg, Pennsylvania
www.lrkimball.com
Member Since: 1/1965

**LaFave, White & McGivern,
L.S., P.C.**
Theresa, New York
www.lwmlspc.com
Member Since: 1/1987

Land Data Technologies Inc.
Edmonton, Canada
www.landdatatech.com
Member Since: 1/1987

LizardTech, Inc.
Seattle, Washington
www.lizardtech.com
Member Since: 10/1997

**Lockheed Martin Corporation
Geospatial Intel Solutions**
Fairfax, Virginia
www.lockheedmartin.com
Member Since: 1/1995

LPA Systems, Inc.
Fairport, New York
www.lpasystem.com
Member Since: 1/2005

M.J. Harden Associates, Inc.
Mission, Kansas
www.mjharden.com
Member since 1/1976

Martinez Corporation
Eagan, Minnesota
www.mtzcorp.com
Member Since: 1/1979

MDA Geospatial Services, Inc.
Richmond, Canada
www.mdacorporation.ca
Member Since: 1/1992

MDA Federal Inc.
Rockville, Maryland
www.mdafederal.com
Member Since: 1/1983

Merrick & Company
Aurora, Colorado
www.merrick.com/gis
Member since: 4/1995

Michael Baker Jr., Inc.
Beaver, Pennsylvania
www.mbakercorp.com
Member Since: 1/1950

NavCom Technology, Inc.
Torrance, California
www.navcomtech.com
Member Since: 3/2004

New Tech Services, Inc.
Sugarland, Texas
www.nts-info.com
Member since: 3/2006

North West Group
Calgary, Canada
www.nwgeo.com
Member Since: 1/1998

**Northrop Grumman Information
Technology**
Chantilly, Virginia
www.northropgrumman.com
Member Since: 1/1989

NSTec, Remote Sensing Laboratory
Las Vegas, Nevada
www.bechtelnevada.com
Member Since: 7/2005

Observera, Inc.
Chantilly, Virginia
www.observera.com
Member Since: 7/1995

Office of Surface Mining
Denver, Colorado
www.tips.osmre.gov
Member Since: 3/2008

Optech Incorporated
Toronto, Canada
www.optech.ca
Member Since: 1/1999

Optimal Geomatics Inc.
Vancouver, BC, Canada
www.optimalgeo.com
Member Since: 2/2006

**PAR Government Systems
Corporation**
Rome, New York
www.pargovernment.com
Member Since: 5/1992

PCI Geomatics
Ontario, Canada
www.pcigeomatics.com
Member Since: 1/1989

Photo Science, Inc.
Lexington, Kentucky
www.photoscience.com
Member Since: 7/1997

Pickett & Associates, Inc.
Bartow, FL 33830
www.pickett-inc.com
Member since: 4/2007

Pictometry International Corp.
Rochester, New York
www.pictometry.com
Member Since: 5/2003

Pinnacle Mapping Technologies, Inc.
Indianapolis, Indiana
www.pinnaclemapping.com
Member Since: 7/2002

Pixoneer Geomatics
Taejon South Korea
www.pixoneer.com
Member since: 6/2005

Pixxures, Inc.
Arvada, CO
www.pixxures.com
Member Since: 8/2006

POB Magazine
Troy, Michigan
www.pobonline.com
Member since: 7/2006

QCoherent Software LLC
Colorado Springs, Colorado
www.qcoherent.com
Member Since: 9/2006

Radman Aerial Surveys
Sacramento, California
radlaerial@aol.com
Member Since: 1/1971

**Reed Business-Geo
(was GITC America, Inc. & GITC bv)**
Frederick, Maryland
www.reedbusiness-geo.com
Member Since: 1/1998

Riegl USA, Inc.
Orlando, Florida
www.rieglusa.com
Member Since: 11/2004

Robinson Aerial Survey, Inc. (RAS)
Hackettstown, New Jersey
www.robinsonaerial.com
Member Since: 1/1954

Rollei Metric GmbH
Braunschweig, Germany
www.rollei-metric.com
Member since: 7/2007

Rolta International, Inc.
Alpharetta, Georgia
www.roлта.com
Member Since: 3/2003

Sanborn
Colorado Springs, Colorado
www.sanborn.com
Member Since: 9/1984

**Science Applications International
Corporation**
Mc Lean, Virginia
www.saic.com
Member Since: 1/1987

The Sidwell Company
St. Charles, Illinois
www.sidwellco.com
Member Since: 1/1973

SPADAC Inc.
Mc Lean, Virginia
www.spadac.com
Member since: 2/2008

Spatial Data Consultants, Inc.
High Point, North Carolina
www.spatialdc.com
Member Since: 12/2004

Stewart Geo Technologies, Inc.
Irvine, California
www.stewartgeotech.com
Member Since: 1/1978

Surdex Corporation
Chesterfield, Missouri
www.surdex.com
Member Since: 1/1979

Surveying and Mapping (SAM), Inc.
Austin, Texas
www.saminc.biz
Member Since: 12/2005

TerraSim, Inc.
Pittsburgh, Pennsylvania
www.terrasim.com
Member Since: 9/2003

Terratec AS
Lysaker, Norway
www.terratec.no
Member Since: 9/2004

Total Aircraft Services, Inc.
Van Nuys, California
www.taaircraft.com
Member Since: 3/2007

Towill, Inc.
San Francisco, California
www.towill.com
Member Since: 1/1952

Track'Air BV
Ej Oldenzaal, Netherlands
www.trackair.com
Member Since: 6.2001

Urban Robotics, Inc.
Portland Oregon
www.urbanrobotics.net
Member Since: 3/2008

U.S. Geological Survey
Reston, Virginia
www.usgs.gov
Member Since: 4/2002

**USDA/National Agricultural
Statistics Service**
Fairfax, Virginia
www.nass.usda.gov
Member Since: 6/2004

Valtus Imagery Services
Boulder, Colorado
www.valtus.com
Member Since: 11/2006

Virtual Geomatics
Austin, Texas
www.virtualgeomatics.com
Member Since: 2/2008

VXServices, LLC
Longmont, Colorado
www.vxservices.com
Member Since: 6/2001

Watershed Concepts
Charlotte, North Carolina
www.watershedconcepts.com
Member Since: 8/2003

Wehrli & Associates Inc.
Valhalla, New York
www.wehrliassoc.com
Member since: 5/1994

WeoGeo
Tampa, Florida
www.weogeo.com
Member Since: 2/2008

Western Air Maps, Inc.
Overland Park, Kansas
www.westernair.com
Member Since: 12/1999

**Wilson & Company, Inc.,
Engineers & Architects**
Albuquerque, New Mexico
www.wilsonco.com
Member Since: 3/2007

Woolpert, Inc.
Dayton, Ohio
www.woolpert.com
Member Since: 1/1985

XEOS Imaging Inc.
Quebec, Canada
www.xeosimaging.com
Member Since: 11/2003

Photogrammetric Engineering and Remote Sensing (*PE&RS*)

Submitting a Manuscript for Peer Review Instructions for Authors

Authors submitting a new manuscript for peer review MUST follow these instructions. Failure to do so will result in the manuscript being returned to the author.

INTRODUCTION: The American Society for Photogrammetry and Remote Sensing (ASPRS) seeks to publish in *Photogrammetric Engineering & Remote Sensing (PE&RS)* theoretical and applied papers that address topics in photogrammetry, remote sensing, geographic information systems (GIS), the Global Positioning System (GPS) and/or other geospatial information technologies. Contributions that deal with technical advancements in instrumentation, novel or improved modes of analysis, or innovative applications of these technologies in natural and cultural resources assessment, environmental modeling, or the Earth sciences (atmosphere, hydrosphere, lithosphere, biosphere, or geosphere) are especially encouraged.

REVIEW PROCEDURES: Manuscripts are peer reviewed and refereed by a panel of experts selected by the Editor. A blind review procedure is used. The identities and affiliations of authors are not provided to reviewers, nor are reviewers' names disclosed to authors. The *PE&RS* goal is to provide authors with completed reviews within 90 days of receipt of a manuscript by the Editor. Manuscripts accepted for publication will be returned to the author(s) for final editing before being placed in the queue for publication. Manuscripts not accepted will either be (1) rejected or (2) returned to the author(s) for revision and subsequent reconsideration by the review panel. Authors who do not revise and return a "to-be-reconsidered" manuscript within 90 days from receipt of reviews may have their manuscript withdrawn from the review process.

ENGLISH LANGUAGE: Authors whose first language is not English should have their manuscripts reviewed by an English-speaking colleague or editor to refine use of the English language (vocabulary, grammar, syntax). At the discretion of the Editor, manuscripts may be returned for English language issues before they are sent for review.

COVER LETTER: All submissions must also include a separate cover letter with the names, complete mailing addresses, and email addresses of all the authors and any special instructions about the paper. Papers can not be submitted for review until this information is received by the editor. Also, please verify in the cover letter that this paper is original work and is currently not being considered for publication in any other journal.

PREPARING A MANUSCRIPT FOR REVIEW: Authors must submit papers electronically in PDF format. Care must be taken to remove the authors name from the electronic document. Please remove all author identification from the Properties of Microsoft Word before creating the PDF. Verify under Properties in Adobe Reader that your identity has been removed.

FORMAT REQUIREMENTS: Manuscripts submitted for peer review must be prepared as outlined below. Manuscripts that do not conform to the requirements described below will be returned for format revisions before they are sent for review.

- 1 TYPING:** All pages must be numbered at the bottom of the page. In addition, manuscripts must be double-spaced. An 11 or 12-point font such as Times New Roman or Arial is preferred. Authors should use 8.5 by 11-inch or A4 International (210- by 297-mm) paper size, with 30-mm (1.25 inch) margins all around. For review purposes every part of the manuscript must be double-spaced, including title page/abstract, text, footnotes, references, appendices and figure captions. Manuscripts that are single-spaced or have no page numbers will be returned to authors.
- 2 PAPER LENGTH:** Authors are encouraged to be concise. Published papers are generally limited to 7-10 journal pages. A 27-page manuscript (including tables and figures), when typed as indicated above, equals about 7 journal pages. **Authors of published papers will be charged \$125/page for each page exceeding 7 journal pages. These page charges must be paid before publication.**
- 3 TITLE PAGE/ABSTRACT:** Authors should strive for titles no longer than eight to ten words. The title page shall include a short title, a one-sentence description of the paper's content to accompany the title in the *PE&RS* Table of Contents, and the abstract. To facilitate the blind review process, authors' names, affiliations, and addresses must be provided only in a separate cover letter, not on the title page. Authors should indicate both their current affiliation and, if different, their affiliation at the time the research was performed. Following the title and one-sentence and on the same page must be the abstract. All manuscripts submitted for peer review must include an abstract of 150 words or less. The abstract should include information on goals, methods and results of the research reported.
- 4 FIGURES AND TABLES:** All figures and tables must be cited in the text. Authors should note that figures and tables will usually be reduced in size by the printer to optimize use of space, and should be designed accordingly. For purposes of peer review, figures and tables can be embedded in the manuscript. However, it should be noted that papers, once accepted, will require that all figures be included as separate files (see instructions for accepted papers) If the manuscript contains copyrighted imagery, a copyright statement must be included in the caption (e.g. ©SPOT Image, Copyright [year] CNES).
- 5 COLOR ILLUSTRATIONS:** Authors should use black and white illustrations whenever possible. Authors who include color illustrations will be charged for the cost of color reproduction. These costs must be paid before an article is published. Details on color costs can be found at <http://www.asprs.org/publications/pers/index.html> (see *PE&RS Color Order Form*).
- 6 METRIC SYSTEM:** The metric system (SI Units) will be employed throughout a manuscript except in cases where the English System has special merit stemming from accepted conventional usage (e.g., 9- by 9-inch photograph, 6-inch focal length). Authors should refer to "Usage of the International System of Units," *Photogrammetric Engineering & Remote Sensing*, 1978, 44 (7): 923-938.

7 EQUATIONS: Authors should express equations as simply as possible. They should include only those equations required by an average reader to understand the technical arguments in the manuscript. Manuscripts that appear to have excessive mathematical notation may be returned to the author for revision. Whenever possible, authors are encouraged to use the Insert and Symbol capabilities of Microsoft Word to build simple equations. If that is not possible, the author must indicate in the letter of transmittal which software was used to create the equations. *Microsoft Equation*, *Microsoft Equation Editor*, or *MathType* format should be used only if absolutely necessary. Equations must be numbered, but unlike tables, figures, color plates, and line drawings should be embedded in the text file.

8 ELECTRONIC JOURNAL: The ASPRS Journal Policy Committee discourages lengthy appendices, complex mathematical formulations and software programs. These will ordinarily not be published in the hardcopy version of *PE&RS*. However, these materials may be made available on the ASPRS web site (<http://www.asprs.org/>). Authors wishing to have supplemental material posted on the website after their paper is published should submit this material along with their manuscript. All supplemental material must be clearly labeled as *supplemental material*.

9 REFERENCES: A complete and accurate reference list is essential. Only works cited in the text should be included. Cite references to published literature in the text by authors' last names and date, as for example, Jones (1979), Jones and Smith (1979) or (Jones, 1979; Jones and Smith 1979), depending on sentence construction. If there are more than two authors, they should be cited as Jones *et al.* (1979) or (Jones *et al.*, 1979). Personal communications and unpublished data or reports should not be included in the reference list but should be shown parenthetically in the text (Jones, unpublished data, 1979). Format for references will be as follows:

BOOKS:

Falkner, E., 1995. *Aerial Mapping: Methods and Applications*, Lewis Publishers, Boca Raton, Florida, 322 p.

ARTICLES (OR CHAPTERS) IN A BOOK:

Webb, H., 1991. Creation of digital terrain models using analytical photogrammetry and their use in civil engineering, *Terrain Modelling in Surveying and Civil Engineering* (G. Petrie and T.J.M. Kennie, editors), McGraw-Hill, Inc., New York, N.Y., pp. 73-84.

JOURNAL ARTICLES:

Meyer, M.P., 1982. Place of small-format aerial photography in resource surveys, *Journal of Forestry*, 80(1):15-17.

PROCEEDINGS (PRINTED):

Davidson, J.M., D.M. Rizzo, M. Garbelotto, S. Tjosvold, and G.W. Slaughter, 2002. Phytophthora ramorum and sudden oak death in California: II. Transmission and survival, *Proceedings of the Fifth Symposium on Oak Woodlands: Oaks in California's Changing Landscape*, 23-25 October 2001, San Diego, California (USDA Forest Service, General Technical Report PSW-GTR-184, Pacific Southwest Forest and Range Experiment Station, Berkeley, California), pp. 741-749.

PROCEEDINGS (CD-ROM):

Cook, J.D., and L.D. Ferdinand, 2001. Geometric fidelity of Ikonos imagery, *Proceedings of the ASPRS 2001 Annual Convention*, 23-27 April, St. Louis, Missouri (American Society for Photogrammetry and Remote Sensing, Bethesda, Maryland), unpaginated CD-ROM.

THESIS AND DISSERTATIONS:

Yang, W., 1997. *Effects of Spatial Resolution and Landscape Structure on Land Cover Characterization*, Ph.D. dissertation, University of Nebraska-Lincoln, Lincoln, Nebraska, 336 p.

WEBSITE REFERENCES:

Diaz, H.F., 1997. Precipitation trends and water consumption in the southwestern United States, USGS Web Conference, URL: <http://geochange.er.usgs.gov/sw/changes/natural/diaz/>, U.S. Geological Survey, Reston, Virginia (last date accessed: 15 May 2002).

10 ACKNOWLEDGMENTS: In keeping with the process of blind reviews, authors are asked not to include acknowledgments in manuscripts submitted for peer review. An acknowledgment may reveal a considerable amount of information for reviewers that is not necessary or desirable for their evaluation of the manuscript. After a manuscript is accepted for publication, the lead author will be encouraged to insert appropriate acknowledgments.

14 INFORMATION ON MANUSCRIPT REVIEW PROCEDURES: Corresponding authors of manuscripts submitted for review will receive an e-mail from the Editor acknowledging receipt of the manuscript. Details on *PE&RS* Manuscript Review Procedures can be found at http://www.asprs.org/society/committees/jpc/jpc_manu.html

MANUSCRIPT SUBMISSION: All peer-reviewed manuscripts should be emailed to:

Dr. Russell G. Congalton

Editor-in-Chief, *Photogrammetric Engineering and Remote Sensing*

4 Ryan Way

Durham, NH 03824

E-mail: russ.congalton@unh.edu

Tel.: (603) 862-4644

NOTE: Authors should NOT MAIL MANUSCRIPTS TO ASPRS HEADQUARTERS. This will cause the review to be delayed.

***Instructions last updated May 30, 2008*

Habitat Mapping in Rugged Terrain Using Multispectral Ikonos Images

Janet Nichol and Man Sing Wong

Abstract

Due to the significant time and cost requirements of traditional mapping techniques, accurate and detailed habitat maps for large areas are uncommon. This study investigates the application of Ikonos Very High Resolution (VHR) images to habitat mapping in the rugged terrain of Hong Kong's country parks. A required mapping scale of 1:10 000, a minimum map object size of 150 m² on the ground, and a minimum accuracy level of 80 percent were set as the mapping standards. Very high quality aerial photographs and digital topographic maps provided accurate reference data for the image processing and habitat classification. A comparison between manual stereoscopic aerial photographic interpretation and image classification using pixel-based and object-based classifiers was carried out. The Multi-level Object Oriented Segmentation with Decision Tree Classification (MOOSC) was devised during this study using a suite of image processing techniques to integrate spectral, textural, and spatial criteria with ancillary data. Manual mapping from air photos combined with fieldwork obtained the best result, with 95 percent overall accuracy, but both this and the MOOSC method, with 94 percent, easily met the 80 percent specified accuracy standard. The MOOSC method was able to achieve similar accuracy aerial photographs, but at only one third of the cost.

Introduction

Biodiversity conservation strategies call for comprehensive information on the distribution of species and their habitats as well as their changes over time. However, wildlife habitat mapping, as a discipline has suffered from several major challenges including:

1. the need to map at detailed level, usually over large areas,
2. often indistinct boundaries between relevant vegetation classes, requiring a large element of subjectivity (Green and Hartley, 2000; Alexander and Millington, 2000),
3. the requirement for high levels of accuracy due to the slow rate of change,
4. many wildlife reserves occupy mountainous terrain, and
5. lack of readily applicable automated methodologies because, even within the same climatic zone, vegetation communities may be highly variable, thus mapping methodologies cannot be extrapolated outside a particular study area.

Traditionally, manual air photo interpretation has been used to extrapolate field observations over large areas. Since stereo viewing is often necessary to identify habitat structure, especially on steep slopes, it is time-consuming (Green

et al., 1993). Even with digital photography, large area coverage would require orthorectification of individual images, resulting in potentially prohibitive costs.

The first ever habitat survey covering the whole 1,100 km² of Hong Kong at 1:20 000 scale was undertaken by the Worldwide Fund for Nature in 1993 (Ashworth *et al.*, 1993), using a combination of fieldwork and air photo interpretation. The resulting accuracy was low (R. Corlett, personal communication), and the maps were little used. Another such project, the 1:10 000 scale habitat survey of Northumberland National Park, which was part of the Phase I national survey of Great Britain (Walton, 1993), was carried out by air photo interpretation and required a total of 717 people-days. The exercise was deemed too expensive to be repeated (Mehner *et al.*, 2004) given the low accuracy (Brookes *et al.*, 2000).

Attempts to improve accuracy and costs using satellite images have been limited by insufficient spatial resolution of medium resolution sensors such as those on Landsat and SPOT1 through SPOT4. The low overall accuracy (approximately 50 percent) obtained by a recent habitat survey covering the whole of Hong Kong using SPOT4 and Landsat images (Environmental Protection Department, 2003) appears to have been due to inadequate resolution, combined with differences in solar illumination on opposite slopes. For example, the accuracy of many cover types such as grassland, shrubby grassland and wetland, when referenced against field GPS data, was below 40 percent (Environmental Protection Department, 2003). Generally up to the present time, high accuracy in habitat mapping is difficult to achieve (Brookes *et al.*, 2000).

If the problem of differential illumination in mountainous terrain can be solved, the new generation of VHR satellite sensors such as Ikonos with its 4 m multispectral resolution has greater potential (Slater and Brown, 2000). However, it is recognised that image processing techniques specific to these sensors are required. Mather (1999) recommends the addition of texture to pixel-based classifiers due to the detection of micro-scale texture properties at high-resolution (see for example, Keramitsoglou *et al.* (2005)). Furthermore, since on VHR sensors, natural habitats are composed of many different reflectance surfaces, pixel-based classifiers are inappropriate. Thus, recent habitat mapping projects have used object-based classifiers with VHR airborne, (Ehlers *et al.*, 2003) and satellite sensors (Bock *et al.*, 2005; Kobler *et al.*, 2006). These have the ability to group pixels into discrete

Photogrammetric Engineering & Remote Sensing
Vol. 74, No. 11, November 2008, pp. 1325–1334.

0099-1112/08/7411-1325/\$3.00/0
© 2008 American Society for Photogrammetry
and Remote Sensing

Department of Land Surveying and GeoInformatics, The
Hong Kong Polytechnic University, (lsjanet@polyu.edu.hk).

objects, or segments, based on both spectral details and spatial criteria such as size, shape, and local texture, and segments may be defined at different scales (Batz and Schäpe, 2000). The method of image segmentation has also been applied successfully to stand level forest inventories (Pekkarinen, 2002; Wulder *et al.*, 2004).

Subsequently, segments may be allocated to classes using an automated approach. For example, Kobler *et al.* (2006) devised a machine learning algorithm with a decision tree structure to allocate segments to habitat classes; and Bock *et al.* (2005) used a nearest neighbor algorithm to allocate segments derived from QuickBird images to habitat classes. Only low to moderate accuracy was achieved from these fully automated methods however, with Kappa classification accuracy of 0.6 by Kobler *et al.*, (2006) and 0.75 by Bock *et al.* (2005). A study by Ehlers *et al.* (2003) combining spatial and spectral image parameters with a semi-automated, rule-based hierarchical procedure was able to achieve much higher accuracy, of well over 90 percent for some classes. However, the latter study was based on detailed airborne data with 0.15 m ground resolution over flat terrain, and there is no indication that similar accuracy could be achieved using satellite images over large areas of rugged terrain as in the present study.

This study evaluates a semi-automated approach to habitat mapping using Ikonos multispectral images in mountainous terrain by comparing the results with manual methods using high-resolution, stereo air photos and fieldwork. The specified mapping scale of 1:10 000 and a minimum object size of 100 m² on the ground are initially set as attainable with the 4 m spatial resolution of Ikonos. Thus, five Ikonos pixels would comprise such an object. A minimum class accuracy standard of 80 percent was also specified, following the recommendations of the USGS-NPS Vegetation Mapping Program for national scale mapping (USGS, 2006).

Three secondary objectives of the study include:

1. a comparison between pixel-based and object-based classifiers,
2. an assessment of the overall accuracy achievable from the image processing approach, and
3. a cost benefit analysis comparing manual and digital techniques.

The Study Area and Images Used

The study area comprises an 11 km × 11 km area of mountainous terrain containing the Tai Mo Shan and Shing Mun country parks of the central New Territories, Hong Kong, at 22°2'N, 114°1'E (Figure 1). Flat urban areas near the coast give way to steep convex slopes rising to the mountain top of Tai Mo Shan at 900 m only 3 km from the coast and the Shing Mun reservoir in the south-east occupies steep-sided valleys with slopes commonly 40° to 50°.

The climax vegetation of the south China region is evergreen broadleaf forest. Due to massive clearance during WWII, Hong Kong's forests are regenerating upslope from lowland valleys (Dudgeon and Corlett, 2005). Shrub, which is generally transitional to forest, and grasslands cover upper slopes and ridges (Dudgeon and Corlett, 2005), and both are found at lower elevations following fire. In the study area, both vertebrate and invertebrate fauna show distinct preferences for either forest, grassland, or shrub habitats, while the invasion of shrubs into grassland is accompanied by a dramatic increase in fauna due to the patches of cover offered by perennial shrubs within seasonal grassland. Thus, as habitat succession proceeds to increased shrub and tree cover, the vertebrate community becomes more diverse and includes more sensitive species such as thrushes, coucals, robins, and leaf warblers (Dudgeon and Corlett, 2005). Many



Figure 1. Location of Tai Mo Shan and Shing Mun country parks in Hong Kong.

animals also show a distinct preference for altitude, either high or low, and forest above 600 m is classified as montane forest (Dudgeon and Corlett, 2005). Planting of non-native evergreen genera such as *Acacia*, *Eucalyptus*, *Lophostemon*, and *Castanopsis* has taken place throughout the area, but due to invasion by native lowland forest species, many plantations are not distinguishable. Only the deciduous paper bark tree *Melaleuca quinquinervia*, which occurs in pure stands, is clearly identifiable (D in Figure 2).

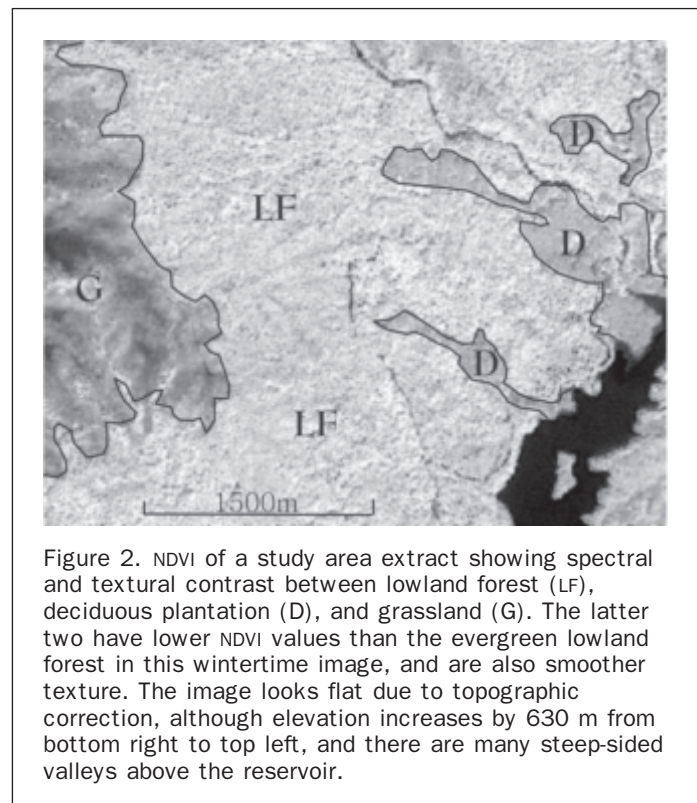


Figure 2. NDVI of a study area extract showing spectral and textural contrast between lowland forest (LF), deciduous plantation (D), and grassland (G). The latter two have lower NDVI values than the evergreen lowland forest in this wintertime image, and are also smoother texture. The image looks flat due to topographic correction, although elevation increases by 630 m from bottom right to top left, and there are many steep-sided valleys above the reservoir.

Wintertime images are considered more useful due to greater contrast between the main structural cover types, broadleaf evergreen forest and plantations, deciduous plantations, shrub, and grassland. While forest maintains high photosynthesis during the winter dry season, grassland, mainly occupying summits (G in Figure 2) dies back and exhibits lower Near Infra-Red (NIR) and green, and higher red reflectance. Shrublands also become semi-senescent during the winter dry season due to a less established root system, with reflectance values mid-way between that of grassland and forest.

A multispectral Ikonos image from 28 January 2003 having a sun elevation angle of 40° at the mid-morning image collection time was used for the study. In order to provide a frame of reference, the habitats were also manually interpreted using 38 true and false color stereo photographs, ranging in scales from 1:6 000 to 1:18 000 (e.g., Plate 1c). The boundaries were delineated onto a color digital orthophoto of 0.20 m resolution. This high quality aerial photographic resource, where individual tree and even shrub canopies could be identified (Plate 1d), compensated for the inaccessibility of many areas in the field. At least two dates and times of photos were available thus compensating for terrain shadows on some images.

Methods

Image Preprocessing

Due to the relief of the study area, geometric and topographic illumination corrections were undertaken prior to habitat classification. Orthorectification of Ikonos imagery was undertaken using Toutin and Cheng's (2000) rigorous model with 61 GCPs from 1:1 000 scale digital maps from the Hong Kong Lands Department with known accuracy within 1 meter. Accuracy of the rectified image based on the mean accuracy of 20 checkpoints at all elevations proved to be within half a pixel, i.e., 2 m.

The extremely low sun elevation angle in mid-January of 40° resulted in dark shadows over north and north-west-facing slopes (Plate 1a), which were especially severe in the NIR band. This band is particularly important for vegetation discrimination, especially since the remaining three Ikonos bands are highly correlated. Illumination correction was done using the Empirical Slope Matching technique (Nichol *et al.*, 2006) which was devised to correct for the extremes of steep terrain and low (40°) sun angle combined. The DEM was created from contours, spot heights, and shorelines on digital maps of 1:5 000 scale with accuracy of not more than 10 percent of elevations tested being in error of greater than 5 m. A grid size of 2 m was chosen for interpolating the DEM to resemble the 4 m resolution of the multispectral Ikonos images, and the Sibson with slope method of interpolation was used (Dakowicz and Gold, 2003; Nichol and Law, 2008). Plate 1a and 1b show that the correction has removed most of the dark shadows in the image, resulting in a near flat surface representation of the original (Plate 1b and Figure 2). Although these procedures do impact the DN values, they led to a 7 percent increase in classification accuracy in a previous study (Nichol *et al.*, 2006). Atmospheric correction was not undertaken since only one date of Ikonos imagery was used.

Selection of the Mapping Classes

The approach to class selection was study area specific, since classification schemes for sub-tropical regions are not well developed. Habitats were classified on a structural

rather than floristic basis for three reasons; (a) since Hong Kong is on the edge of the tropics, plant communities are heterogeneous and are thus more easily recognized and delineated according to physiognomic life form, as well as their growth habit (evergreen or deciduous) (Raunkiaer, 1937), (b) evolving paradigms for the use of satellite images for vegetation mapping are based on vegetation structure (Lewis, 1994; Millington and Alexander, 2000), and (c) observed plant-animal interactions generally (Wiens, 1989; Imhoff *et al.*, 1997), as well as in the study area (see Study Area section above). Based on the structural approach, young forest plantations on grassy slopes, which would be classified floristically as forest, were classified according to physical structure (since ecologically they function as shrubs within grassland) and allocated to shrubby grassland or shrubland. Furthermore, deciduous plantation comprising the species *Melaleuca quinquinervia* was also assigned a separate class, since growth habit is a plant structural characteristic, and because it is easily separable from the evergreen forest species on this dry season imagery (Figure 2). However, evergreen plantations, many of which have merged with the evergreen lowland forest were mapped as forest, since they are similar in terms of both structure and function. Nine classes, based on the plant-animal dependencies described (see Study Area section) were selected (Table 1).

Air Photo Interpretation and Fieldwork

The habitats throughout the study area were mapped using stereoscopic interpretation of large-scale air photos (Plate 1c), supported by fieldwork. Boundaries were first drawn onto hardcopy prints and then transferred to the digital orthophoto as the mapping base by on-screen digitizing. The size of mapping unit, 100 to 150 m² on the ground was larger than the initially specified minimum of 100 m² because some classes are mixed areal units which, by definition must be larger than either of the constituent types. Six man months were required for fieldwork, mapping, and accuracy assessment using 332 GPS points. The number of points in each habitat was allocated in proportion to its area, with a purposive random sampling approach (McCoy, 2005), whereby inaccessible points were discarded. However, due to impenetrable terrain, the majority of those remaining were located adjacent to roads and footpaths, on disturbed ground and along habitat edges. Therefore, in order to avoid the problem of mixed pixels, only homogeneous areas larger than 4*4 pixels (256 m²) in size were retained. Since the air photo mapping proved to be highly accurate, the accuracy of the digital mapping from Ikonos was tested using both these 332 GPS points as well as 215 additional checkpoints located on the air photos, evenly distributed over the study area, using systematic unaligned sampling (McCoy, 2005).

Pixel-based Classification: Maximum Likelihood Classification (MLC) and MLC with Texture Measures

Battacharya Distance measurements from an unsupervised classification of the multispectral Ikonos image suggested low spectral separability between habitat types, therefore, only seven classes were input to the Maximum Likelihood Classifier (MLC) (Table 1). However, since a low accuracy was obtained from MLC, and previous work had noted improved results with the addition of textural measures to MLC for vegetation mapping (Hay *et al.*, 1996; Zhang, 2001; Coburn and Roberts, 2004; Bock *et al.*, 2005; Keramitsoglou *et al.*, 2006; Kobler *et al.*, 2006) these were tested. This was done using a 3*3 Grey Level Co-occurrence Matrix (GLCM) with texture values representing Dissimilarity, Mean, and Standard Deviation. This window size was selected after

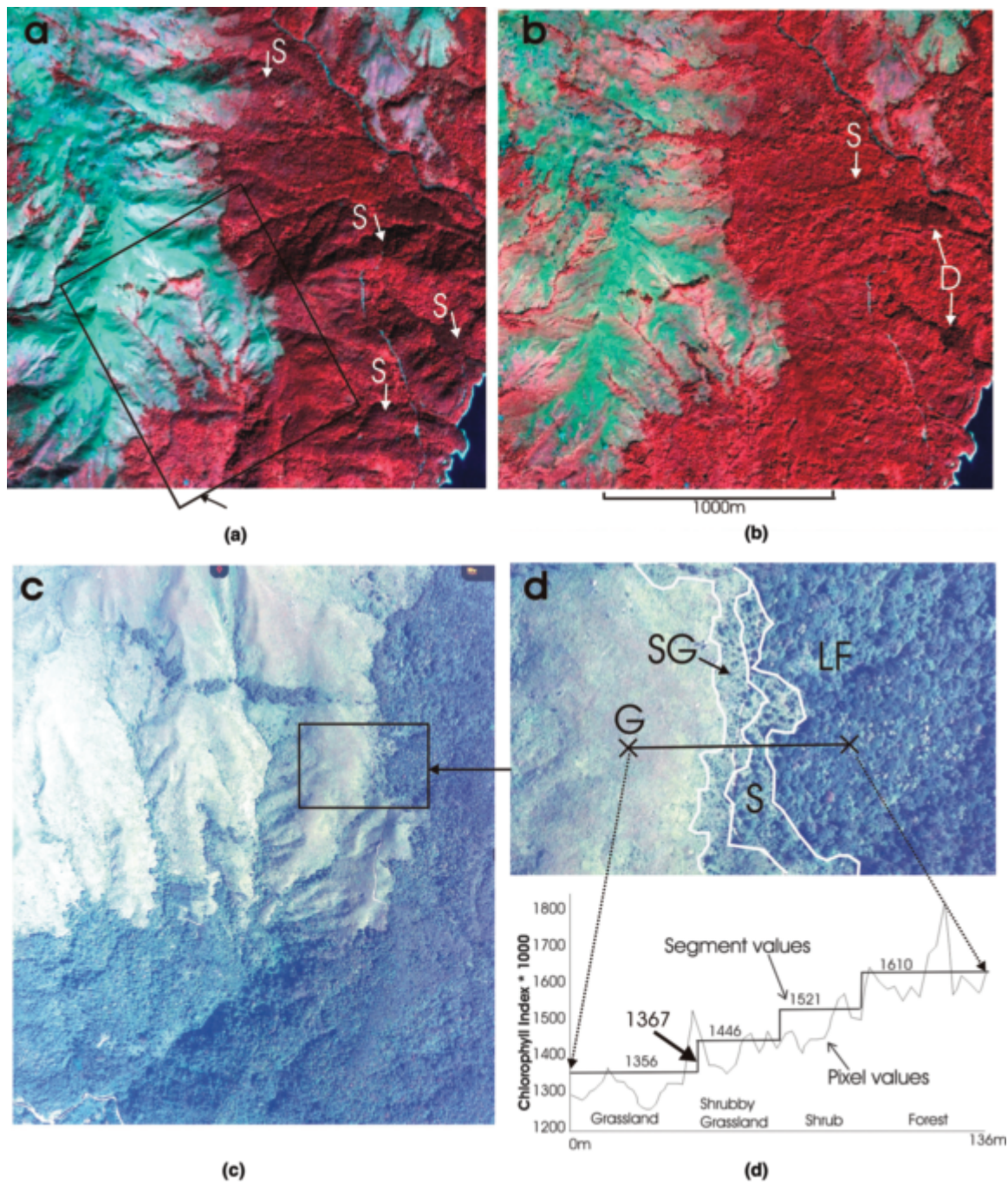


Plate 1. (a) Ikonos false color, 5 km² extract of study area before illumination correction with linear contrast stretch. From bottom right to top left, a distance of approximately 3 km, elevation rises from 170 m to 800 m. Many forested north-facing slopes (S) are in shadow; (b) Ikonos image extract following illumination correction with linear contrast stretch. Shadows on north-facing slopes have been removed except for small areas in absolute shadow (S), and deciduous plantations of *Melaleuca quinquenervia* (D) are the only remaining extensive dark areas in the image.; (c) Color air photo of August 2002 at 1:8 000 scale, showing the high quality of air photos used. The area covered is outlined on the Ikonos image (Plate 1b); and (d) Enlarged extract of Plate 1b, showing the grassland to forest ecotone with a traverse across the habitat types, grassland (G), shrubby grassland (SG), shrubland (S) and lowland forest (LF). Traverse values represent the Chlorophyll Index values derived from the Ikonos image; thin line represents pixel values and thick line represents segment values.

TABLE 1. THE NINE HABITAT CLASSES OF MOOSC. MONTANE FOREST AND SHRUBBY GRASSLAND WERE NOT INCLUDED IN THE TWO PIXEL-BASED CLASSIFICATIONS, MLC, AND MLC WITH TEXTURE

Habitat classes for MOOSC mapping

Lowland forest (includes evergreen planted spp.)
 Montane forest*
 Shrubland
 Shrubby grassland (>25% shrub in grassland)*
 Grassland
 Deciduous plantation
 Soil
 Urban
 Water

*not input to the MLC classifier

investigating the “optimum scale lengths” (Marceau *et al.*, 1994) of each mapping class, which corresponds to low spectral variability within the class. This provides a guideline as to the best resolution for identifying that class spectrally (Marceau *et al.*, 1994), or by inference, texturally. This was using Moran’s I measure of spatial autocorrelation applied to the Ikonos 1 m resolution panchromatic band.

To further increase the dimensionality of the data input to MLC, a nine-band image was created using these three texture bands, the four original Ikonos bands, the Normalized Difference Vegetation Index (NDVI), and Chlorophyll Index (CI) (Kanemasu, 1974). The latter two have greater ability than the raw bands and other vegetation indices in separating the more vigorous evergreen forest from partially senescent grass, shrub, and deciduous plantation on dry season imagery in Hong Kong (Nichol and Lee, 2005). However, although these procedures resulted in some improvement in accuracy, the results were well below the minimum acceptable accuracy standard of 80 percent, and it was recognized that a method for reducing the spectral overlap between classes as well as further reducing the high spectral variation within classes was required.

Multi-level Object-Oriented Segmentation with Decision-tree Classification (MOOSC)

The Multi-level Object-Oriented Segmentation with Decision-tree Classification (MOOSC) devised during this study is a suite of existing procedures which groups image pixels into segments at different scales and allocates segments to classes using a decision-tree approach. Image segmentation was implemented using a region-based, bottom-up approach in eCognition® (Definiens, 2004). The input image contained ten bands, including the original four Ikonos multispectral bands, the NDVI and CI, the three texture bands, and a DEM elevation band. Pixels were grouped into segments at five levels, based on homogeneity and heterogeneity of color, shape, compactness, smoothness, and scale, and the minimum polygon size was approximately 150 m². In this study, an interactive approach was used to investigate the appropriate settings for the parameters by visual comparison with the air photos. The method of allocating segments to classes is similarly interactive in that thresholds are applied to the ten bands by examination of training area statistics at each level (Figure 3). For example, at the lowest level (level 1) of the decision tree, the MLC class statistics were examined to determine the threshold in the NIR band to separate land from water. Thus, since the branches of the tree were constructed interactively at each level, there was no redundancy in the tree structure.

At level 3, the chlorophyll index, a ratio of the red and green bands (Kanemasu, 1974) was found to be suitable for the threshold placement between the senescent herbaceous (grass)

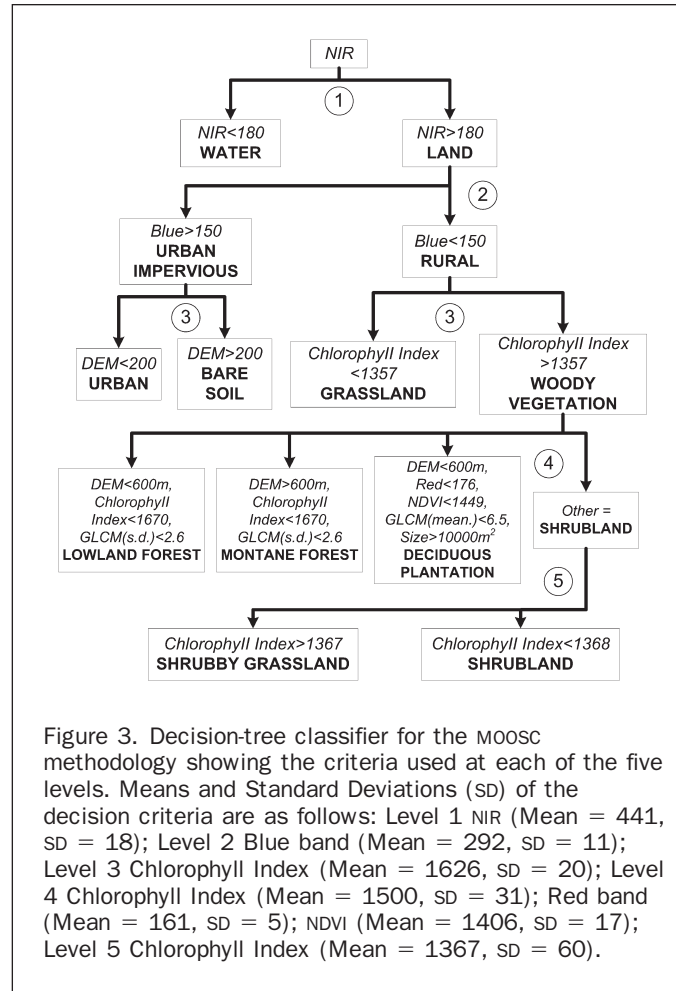


Figure 3. Decision-tree classifier for the MOOSC methodology showing the criteria used at each of the five levels. Means and Standard Deviations (SD) of the decision criteria are as follows: Level 1 NIR (Mean = 441, SD = 18); Level 2 Blue band (Mean = 292, SD = 11); Level 3 Chlorophyll Index (Mean = 1626, SD = 20); Level 4 Chlorophyll Index (Mean = 1500, SD = 31); Red band (Mean = 161, SD = 5); NDVI (Mean = 1406, SD = 17); Level 5 Chlorophyll Index (Mean = 1367, SD = 60).

and woody vegetation classes. Additionally, two morphological operators, elevation and size, were introduced to eliminate some remaining spectral overlap between the darkest areas of lowland forest in terrain shadow (S in Plate 1b), and deciduous plantation (D in Plate 1b), the latter having very low NIR response due to leaf loss. The overlap was due to the inability of the illumination correction algorithm to address areas of absolute shadow in the terrain model of this wintertime image. Such areas have a cos (*i*) value of zero and cannot be corrected. This in turn leads to the failure of the NDVI threshold condition in the decision tree classifier which is used to separate evergreen forest from deciduous plantation. Since the misclassified forest segments are much smaller than the plantations, and plantations do not occur above 600 m, they were re-allocated to forest (Plate 1c) using both a size and an elevation threshold. The DEM was also used at level 4 to separate montane forest (above 600 m) from lowland forest. Level 4 distinguishes between the three arboreal habitats (Figure 3) and the only remaining unclassified area corresponded to the transition zone between grassland and shrubland, which is situated on upper slopes above forest and below the summit grasslands.

Fuzzy Boundary Placement by Segment Unmixing

Using the CI band, grassland and forest occur at the extreme ends of a spectrum representing ecological succession from grass, through shrub to forest. This transition can be seen clearly on the air photos (Plates 1c and 1d). Due to the

wildlife importance of shrub succession in grassland (Dudgeon and Corlett, 2004), it was decided to use this band, to determine the thresholds for an additional class, shrubby grassland having a 25 percent proportion of shrub within grassland. The threshold between grassland and shrubby grassland was computed theoretically using *pure* forest and grassland endmembers taken from training areas on the image. The 4 m pixel size of Ikonos facilitates this, as pure pixels representing the endmembers are available at this resolution. Thus, for example, the CI value of a segment containing 75 percent grass and 25 percent forest, computed from the weighted endmember mean values is 1,367, and visual comparison with the air photos confirmed it to be realistic (Plate 1d).

Results

The aerial photo mapping achieved very high overall accuracy of 95 percent ($Kappa = 0.93$), which is probably a conservative estimate due to the sub-optimal location of the field GPS points near habitat boundaries. In fact, during the study it became clear that the aerial photographs, on which even small shrubs could be identified, gave better visualization of habitat boundaries than fieldwork, due to the obstructed viewing perspectives of fieldwork in the steep terrain, and the fuzzy nature of many boundaries, which require a large field of view. The much higher accuracy obtained than previous air photo mapping projects (Ashworth *et al.*, 1993; Mehner *et al.*, 2001) is not surprising in view of the high quality of the air photo cover, the use of the digital orthophoto as the mapping base, expertise, and the 100 days taken for the interpretation and mapping.

Of the automated methods, the MLC classified image obtained a low accuracy of 66 percent due partly to high within class variability typical of VHR sensors (Hay *et al.*, 2001; Pekkarinen, 2002; Wulder *et al.*, 2004). This can be seen on Plate 2a where there are many isolated “salt and pepper” pixels within homogeneous forest tracts. Additionally, areas of lowland forest (dark green) are incorrectly allocated to the class deciduous plantation (turquoise). This confusion between the darkest areas of lowland forest and deciduous plantation is explained above. Much of the “salt and pepper” variability was eliminated by the addition of texture to MLC (Plate 2b) using a 3*3 (i.e., 12 m) window size. The window size was based on observed scale lengths of 11 to 13 m for grassland, 14 to 15 m for plantation, and 13 to 16 m for forest from the Moran’s I assessment. The texture Mean function was particularly effective for distinguishing grassland and deciduous plantations from lowland forest and shrub, the former two being much smoother than the latter (see deciduous plantation (D) on Plate 1b, and grassland (G), shrub (S), and lowland forest (LF) on Plate 1d; also see Figure 2). However, spectral confusion between many classes remained, and although the addition of texture increased the overall accuracy by 8 percent to 74 percent, this was still well below the project’s specified minimum accuracy of 80 percent.

The MOOSC method achieved a high overall accuracy of 94 percent ($Kappa = 0.92$) (Table 2, and compare Plates 2a, 2b, and 2c). It was able to remove all of the confusion between lowland forest and deciduous plantation by the application of five decision criteria, namely texture (GLCM), NDVI, Red band, size, and DEM (elevation) at different levels of the decision tree (Figure 3). Of the 6 percent error, approximately 4 percent occurs at the boundaries between the three transitional classes: grassland, shrub, and shrubby grassland (Table 3). The lowest accuracies achieved are still above the specified minimum accuracy level of 80 percent;

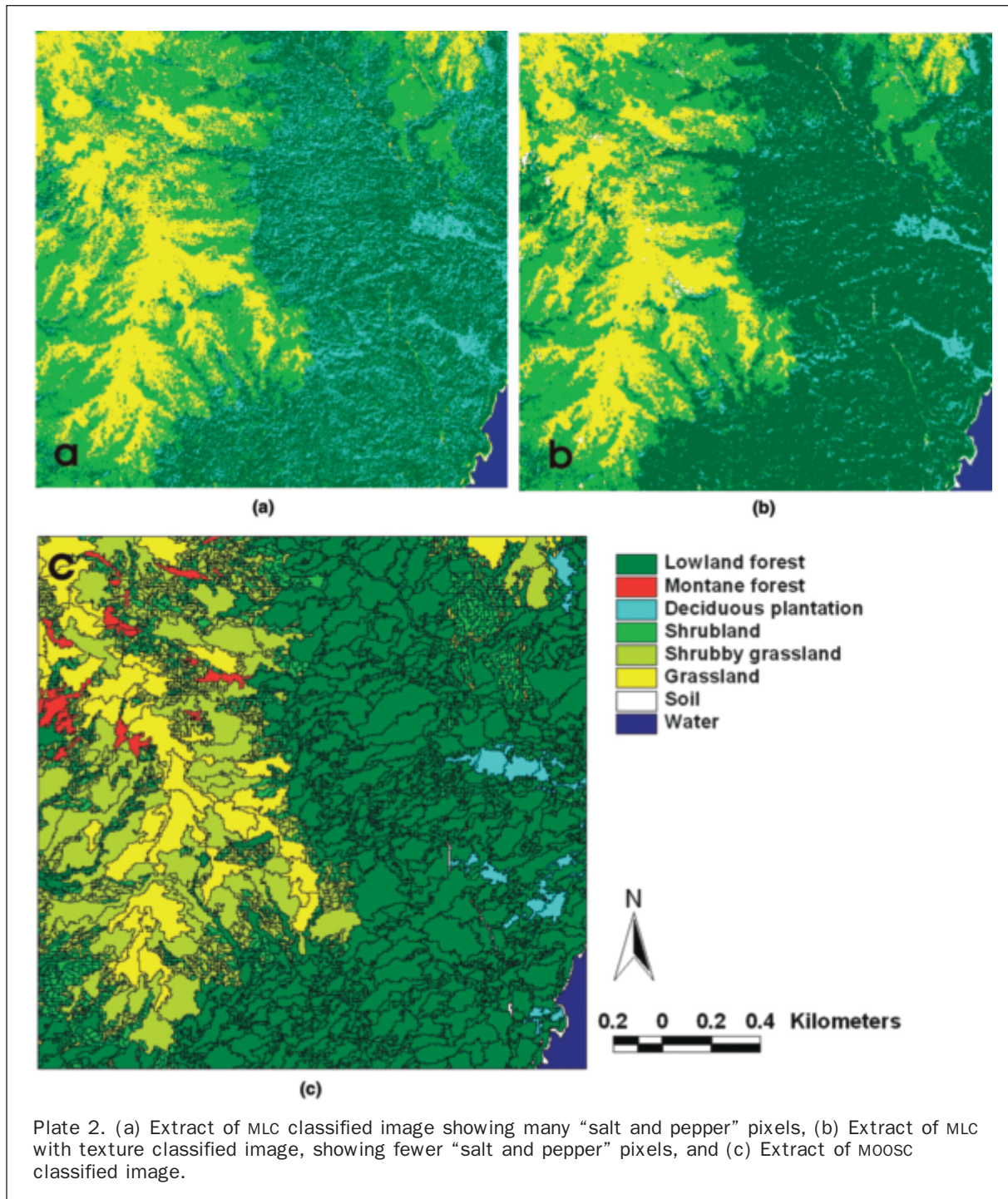
these were the users accuracy of 84 percent for shrubland, which is due to approximately 16 percent of the shrubby grassland areas being misclassified as shrubland, and the producers accuracy of 84 percent for shrubby grassland, which is due to 16 percent of the shrubby grassland areas being misclassified as shrub. Higher accuracy may be difficult to obtain since not all shrubs are evergreen, therefore high spectral contrast with the dormant grassland cannot always be assumed. Plate 1d illustrates the operation of segment unmixing to determine the spectral threshold between grassland and shrubby grassland. It compares the nature of the grassland-to-forest ecotone on an air photo with the Ikonos CI values along a traverse. Pixel values (thin line) across the ecotone are noisy, and placement of the boundary between grassland and shrubby grassland is arbitrary. Segment values however, (thick line) are discrete, and a segment with CI value of 1,446 would be allocated to shrubby grassland using the segment unmixing method, since it is greater than the weighted endmember threshold of 1,367.

Overall, 150 man days were required for the air photo mapping, compared with 44 days for MOOSC (Table 4). If both manpower and image costs are considered, the MOOSC method is almost three times cheaper than the manual air photo method, but has similar accuracy.

Discussion

All the methods used in the study to classify Ikonos images achieved higher accuracy than a previous study using medium resolution sensors. However, although the addition of texture to MLC was able to eliminate much of the “salt and pepper” variability in the pixel-based classification, it was unable to reduce the spectral overlap between classes. The accuracy level of 74 percent ($Kappa = 0.7$) accords generally with the 60 percent and 80 percent for winter and summertime Ikonos images, respectively, for pixel-based mapping in the UK at 1:10 000 scale, achieved by Mehner *et al.* (2004). The superiority of MOOSC over the pixel-based classifiers is due to the reduction of intra-class variation using segmentation, as well as the ability to incorporate ancillary data into the decision-making process. Additionally, the decision tree method used to classify the segments performs well because spatial and spectral variability is progressively eliminated leaving the most difficult classes to be examined at higher levels using more sensitive discriminators.

The semi-automated approach of MOOSC, requiring operator intervention at each level to identify the relevant discriminating parameters, appears more successful than fully automated techniques such as those used by Bock *et al.* (2005) and Kobler *et al.* (2006). This may be because natural habitats, especially in rugged terrain, are infinitely variable and cannot be identified with a rule-based approach. Thus, the USGS (2006) states “vegetation mapping requires . . . considerable ecological knowledge of the area to be mapped, including the ability to identify . . . vegetation types, and the relationship of these types to – topography, soil types, and moisture gradients within the mapping area.” The need for operator intervention however, does not compromise the transferability of MOOSC to other study areas, since the interactive approach to setting the segmentation criteria followed by operator decisions, is not different from the approach used in so-called automated methods of supervised and unsupervised classification. All are study area specific and interactive. As a complete habitat mapping methodology, MOOSC works well and is still only approximately one third of the cost of manual, aerial photo-based mapping. Since the aerial photo cover is actually cheaper than Ikonos, the difference in cost is due to the much



greater manpower required for the manual method compared with the semi-automated MOOSC method. Moreover, the time-cost advantages of MOOSC would increase with increasing study area size, since the individual aerial photos to be georeferenced, mosaiced, and stereoscopically examined would not be matched by any significant increase in the number of Ikonos images to be processed.

Segments are unquestionably more effective than pixels for fuzzy boundary placement due to the patchy nature of shrub cover within grassland. The boundary positions of shrubby grassland in automated mapping are dependent on

the mapping scale, resolution, and segment size. However, the accuracy of the endmember thresholds for allocating segments is difficult to verify due to the lack of distinct boundaries in the field. Accordingly, the majority of the inter-class confusion of the MOOSC method is observed at level 5, and occurs between the transitional classes of grass, shrubby grassland, and shrub. In spite of these uncertainties due to the fuzzy nature of the boundary, the grassland class appears to be over 90 percent accurate, and shrubby grassland and shrub classes well over 80 percent. As with the MOOSC methodology as a whole, the advantage of using segments and endmembers for

TABLE 2. MOOSC ACCURACY ASSESSMENT

| | Lowland Forest | Shrub land | Shrubby Grassland | Grass land | Montane forest | Decid. Plantation | Rock/soil | Urban | Water | Row Total |
|-------------------|----------------|------------|-------------------|------------|----------------|-------------------|-----------|-------|-------|-----------|
| Lowland forest | 145 | 2 | 0 | 0 | 1 | 3 | 0 | 0 | 0 | 151 |
| Shrubland | | 43 | 9 | 1 | 1 | 0 | 0 | 0 | 0 | 54 |
| Shrubby grassland | 0 | 1 | 69 | 3 | 0 | 0 | 0 | 0 | 0 | 73 |
| Grassland | 0 | 3 | 4 | 104 | 0 | 0 | 3 | 0 | 0 | 114 |
| Montane forest | 0 | 0 | 0 | 0 | 26 | 0 | 0 | 0 | 0 | 26 |
| Decid. plantation | 0 | 0 | 0 | 0 | 0 | 42 | 0 | 0 | 42 | |
| Rock/Soil | 0 | 0 | 0 | 0 | 0 | 0 | 20 | 0 | 0 | 20 |
| Urban | 0 | 0 | 0 | 0 | 0 | 0 | 0 | 29 | 0 | 29 |
| Water | 0 | 0 | 0 | 0 | 0 | 0 | 0 | 0 | 28 | 28 |
| Column total | 145 | 49 | 82 | 108 | 28 | 45 | 23 | 29 | 28 | 537 |

| Class | User's Accuracy | Producer's accuracy |
|-------------------|-----------------|---------------------|
| Lowland forest | 95 | 100 |
| Shrubland | 84 | 88 |
| Shrubby grassland | 95 | 84 |
| Grassland | 91 | 96 |
| Montane forest | 100 | 93 |
| Decid. plantation | 100 | 93 |
| Rock/Soil | 100 | 87 |
| Urban | 100 | 100 |
| Water | 100 | 100 |

NB. Overall accuracy = 94%; Kappa = 0.9

TABLE 3. ACCURACY OF DIFFERENT MAPPING TECHNIQUES

| Method | No. of Reference points used | Overall Accuracy | Kappa Coefficient |
|------------------|------------------------------|------------------|-------------------|
| API | 322 | 95% | 0.93 |
| MLC | 547 | 66% | 0.58 |
| MLC with texture | 547 | 74% | 0.7 |
| MOOSC | 547 | 94% | 0.92 |

boundary placement lies in their objectivity, such that the same criteria and spectral thresholds may be used in repeat studies to identify ecosystem change.

Conclusions

This study demonstrates improvements in both cost and accuracy for habitat mapping which are an order of magnitude higher than previous similar projects in Hong Kong, and reflects the state of the art in satellite image technology and methodology. Mehner *et al.* (2004) conclude that VHR sensors such as Ikonos can provide a useful tool, offering the potential for mapping upland vegetation in UK at the same mapping scale as this project, i.e., 1:10 000. The results presented here suggest that the MOOSC method, based on rigorous exploitation of the spatial and spectral characteristics of Ikonos multispectral imagery may be used to replace traditional manual interpretation, at a level of accuracy far exceeding US vegetation mapping standards. This high level of accuracy has been achieved in a challenging environment, namely using wintertime images in

TABLE 4. RELATIVE COSTS (\$US) OF DATA ACQUISITION AND PROCESSING FOR HABITAT SURVEY FOR 100 KM² AT 1:10 000 SCALE

| | Color Aerial Photographs | Ikonos |
|--------------------------------------|--------------------------|-------------|
| No. of images | 70* | 1 + 70** |
| Resolution (m) | 0.2 | 4 |
| Material cost of images (US\$) | 960 | 2,460 |
| Time (h)/cost*** | 250/5,000 | 6/120 |
| georeferencing & mosaicing | | |
| Time/cost topographic correction | NA | 24/480 |
| Time/cost interpretation and mapping | 800/16,000 | 160/3,200 |
| Time/cost fieldwork | 160/3,200 | 160/3,200 |
| Total man days | 150 | 44 |
| Total job cost | 25,160 | 9,460 |
| Cost with image acquisition added | 33,160**** | 12,460***** |

*50 air photos for stereo viewing, and creation of Digital Orthophoto as mapping base, and 20 additional prints of different date, to compensate terrain shadow

**one Ikonos image plus air photos to assist accuracy assessment

***time in hours is costed at US \$20 per hour

****aircraft one day \$6,475

*****tasking of Ikonos \$3,000

mountainous terrain. The MOOSC method is flexible enough to be applied to any study area, since it accommodates an interactive approach to the placement of spatial and spectral thresholds. Moreover, MOOSC is more repeatable than manual techniques, and the same image-based thresholds can be used at a future date.

In view of the greatly reduced cost, repeatability, and similar accuracy to manual techniques obtained from the MOOSC methodology, the results strongly recommend VHR multispectral satellite imagery, such as Ikonos, as the best choice for habitat mapping at 1:10 000 scale.

Acknowledgments

The assistance and advice of Professor Richard Corlett of the Department of Ecology and Biodiversity, the University of Hong Kong were invaluable in devising the field strategy for this project, and Miss Tang Yuen-fun helped with the field mapping. The authors would also like to acknowledge financial support from Grant PolyU 5166/03E from the Hong Kong Research Grants Council.

References

- Ashworth, J.M., R.T. Corlett, D. Dudgeon, D.S. Melville, and W.S.M. Tang, 1993. *Hong Kong Flora and Fauna: Computing Conservation*, World Wide Fund for Nature.
- Baatz, M., and A. Schäpe, 2000. Multiresolution segmentation – An optimization approach for high quality multi-scale image segmentation, *Angewandte Geographische Informationsverarbeitung XII* (T. Strobl, T. Blaschke, and G. Griesebner, editors), Beiträge zum, AGIT-Symposium Salzburg, Kerlsruhe: Herbert Wichmann Verlag.
- Barnsley, M.J., and S.L. Barr, 1996. Inferring urban land use from satellite sensor images using kernel-based spatial reclassification, *Photogrammetric Engineering & Remote Sensing*, 62(10):949–958.
- Bock, M., P. Xofis, J. Mitchley, G. Rossner, and M. Wissen, 2005. Objected-oriented methods for habitat mapping at multiple scales-Case studies from Northern Germany and Wye Downs, UK, *Journal for Nature Conservation*, 13:75–89.
- Brookes, A.M., Furse, M.T., and Fuller, R.M., 2000. An assessment of the land cover map of Great Britain within headwater stream catchments for four river systems in England and Wales (R. Alexander and A. Millington, editors), *Vegetation Mapping*, Wiley, Chichester, UK, pp.177–192.
- Coburn, C.A., and A.C.B. Roberts, 2004. A multiscale texture analysis procedure for improved forest stand classification, *International Journal of Remote Sensing*, 25:4287–4308.
- Corlett, R.T., 2000. Environmental heterogeneity and species survival in degraded tropical landscapes, *The Ecological Consequences of Environmental Heterogeneity* (M.J. Hutchings, Elizabeth A. John, and Alan J.A. Stewart, editors), Blackwell Science, Oxford, 434 p.
- Dakowicz, M., and C. Gold, 2003. Extracting meaningful slopes from terrain contours, *International Journal of Computational Geometric Applications*, 13:339–357.
- Definiens, 2004. *eCognition User Guide 4*, Definiens Imaging GmbH, Munich.
- Dudgeon, D., and R.T. Corlett, 2004. *The Ecology and Biodiversity of Hong Kong*, Friends of the Country parks, 336 p.
- Ehlers, M., M. Gähler, and R. Janowsky, 2003. Automated analysis of ultra high resolution remote sensing data for biotope type mapping: New possibilities and challenges, *ISPRS Journal of Photogrammetry and Remote Sensing*, 57:315–326.
- Environmental Protection Department, 2003. *Environmental Baseline Survey: Ranking Based on Conservation Value*, URL: http://www.epd.gov.hk/epd/english/environmentinhk/eia_planning/sea2005/terresthab.html, Environmental Protection Department, The Government of Hong Kong Special Administration Region (last date accessed: 04 July 2008).
- Green, D.R., R. Cummins, R. Wright, and J. Miles, 1993. A methodology for acquiring information on vegetation succession from remotely sensed imagery, *Landscape Ecology and GIS* (R. Haines-Young, D.R. Green, and S. Cousins, editors), Taylor & Francis, London, pp. 111–128.
- Green, D.R., and S. Hartley, 2000. Integrating photo-interpretation and GIS for vegetation mapping: Some issues of error *Vegetation Mapping* (R. Alexander and A. Millington, editors), Wiley, Chichester, pp.103–135.
- Hay, G.J., K.O. Niemann, and G.F. McLean, 1996. An object-specific image-texture analysis of H-resolution forest imagery, *Remote Sensing of Environment*, 55:108–122.
- Hay, D.S., D.J. Marceau, P. Dube, and A. Boulard, 2001. A multi-scale framework for landscape analysis: Object specific analysis and upscaling, *Landscape Ecology*, 16:471–490.
- Imhoff, M.L., T.D. Sisk, A. Milne, G. Morgan, and T. Orr, 1997. Remotely sensed indicators of habitat heterogeneity: Use of synthetic aperture radar in mapping vegetation structure and bird habitat, *Remote Sensing of Environment*, 60:217–227.
- Kanemasu, E.T., 1974. Seasonal canopy reflectance patterns of wheat, sorghum and soyabean, *Remote Sensing of Environment*, 3:43–47.
- Keramitsoglou, I., H. Sarimveis, C.T. Kiranoudis, C. Kontoes, N. Sifakis, and E. Fitoka, 2006. The performance of pixel window algorithms in the classification of habitats using VHSR imagery, *ISPRS Journal of Photogrammetry and Remote Sensing*, 60:225–238.
- Kobler, A., S. Džeroski, and I. Keramitsoglou, 2006. Habitat mapping using machine learning-extended kernel-based reclassification of an Ikonos satellite image, *Ecological Modelling*, 19:83–95.
- Lewis, M.M., 1994. Species composition related to spectral classification in an Australian spinifex hummock grassland, *International Journal of Remote Sensing*, 15:3223–3239.
- Marceau, D.P., P.J. Howarth, and D. Gratton, 1994. Remote sensing and the measurement of geographical entities in a forest environment: 1. The scale and spatial aggregation problem, *Remote Sensing of Environment*, 49:93–104.
- Mather, P.M., 1999. *Computer Processing of Remotely Sensed Images: An Introduction*, London: John Wiley & Sons, 292 p.
- McCoy, R.M., 2005. *Field Methods in Remote Sensing*, The Guilford Press, New York, 159 p.
- Mehner, H., M.E.J. Cutler, D. Fairbairn, and G. Thompson, 2004. Remote sensing of upland vegetation: The potential of high spatial resolution satellite sensors, *Global Ecology and Biogeography*, 13:359–369.
- Millington, A., and R.W. Alexander, 2000. Vegetation mapping in the last three decades of the twentieth century, *Vegetation Mapping* (R. Alexander and A. Millington, editors), Wiley, Chichester, UK, pp. 321–332.
- Nichol, J.E., and C.M. Lee, 2005. Urban vegetation monitoring in Hong Kong using high resolution multispectral images, *International Journal of Remote Sensing*, 26(5):903–919.
- Nichol, J.E., K.H. Law, and M.S. Wong, 2006. Empirical correction of low sun angle images in steeply sloping terrain: A slope matching technique, *International Journal of Remote Sensing*, 27:629–635.
- Nichol, J.E., and K.H. Law, 2008 The influence of DEM accuracy on topographic correction of Ikonos satellite images, *Photogrammetric Engineering & Remote Sensing*, 74(1):47–53.
- Pekkarinen, A., 2002. A method for the segmentation of very high spatial resolution images of forested landscapes, *International Journal of Remote Sensing*, 27:629–635.
- Raunkiaer, C., 1937. *Plant Life Forms*, Clarendon Press, Oxford, UK.
- Slater, J., and R. Brown, 2000. Changing landscapes: Monitoring environmentally sensitive areas using satellite imagery, *International Journal of Remote Sensing*, 21:2753–2767.
- Toutin, T., and P. Cheng, 2000. Demystification of Ikonos, *Earth Observation Magazine*, 9, URL:http://www.eonline.com/Common/Archives/2000jul/00jul_touin.html, GITC America, Inc. Articles, USA, (last date accessed: 04 July 2008).
- USGS, 2006. USGS-NPS Vegetation Mapping Program, U.S. Geological Survey. URL: <http://biology.usgs.gov/npsveg/>, USGS (last date accessed: 04 July 2008).
- Walton, D.D., 1993. *Northumberland National Park Phase One Habitat Survey*, Report of survey results presented to NNPA

and English Nature, Northumberland National Park Report, Berwick-upon-Tweed.

Wiens, J.A., 1989. *The Ecology of Bird Communities*, Cambridge University Press, New York.

Wulder, M.A., R.S. Skakun, W.A. Kurz, and J.C. White, 2004. Estimating time since forest harvest using segmented Landsat ETM1 imagery, *Remote Sensing of Environment*, 93:179–187.

Zhang, Y., 2001. Texture-integrated classification of urban treed areas in high-resolution color-infrared imagery, *Photogrammetric Engineering & Remote Sensing*, 67(11):1359–1365.

(Received 04 August 2006; accepted 13 November 2006; revised 20 February 2007)

ASPRS Code of Ethics

Honesty, justice, and courtesy form a moral philosophy which, associated with mutual interest among people, should be the principles on which ethics are founded.

Each person who is engaged in the use, development, and improvement of the mapping sciences (Photogrammetry, Remote Sensing, Geographic Information Systems, and related disciplines) should accept those principles as a set of dynamic guides for conduct and a way of life rather than merely for passive observance. It is an inherent obligation to apply oneself to one's profession with all diligence and in so doing to be guided by this Code of Ethics.

Accordingly, each person in the mapping sciences profession shall have full regard for achieving excellence in the practice of the profession and the essentiality of maintaining the highest standards of ethical conduct in responsibilities and work for an employer, all clients, colleagues and associates, and society at large, and shall . . .

1. Be guided in all professional activities by the highest standards and be a faithful trustee or agent in all matters for each client or employer.
2. At all times function in such a manner as will bring credit and dignity to the mapping sciences profession.
3. Not compete unfairly with anyone who is engaged in the mapping sciences profession by:
 - a. Advertising in a self-laudatory manner;
 - b. Monetarily exploiting one's own or another's employment position;
 - c. Publicly criticizing other persons working in or having an interest in the mapping sciences;
 - d. Exercising undue influence or pressure, or soliciting favors through offering monetary inducements.
4. Work to strengthen the profession of mapping sciences by:

- a. Personal effort directed toward improving personal skills and knowledge;
 - b. Interchange of information and experience with other persons interested in and using a mapping science, with other professions, and with students and the public;
 - c. Seeking to provide opportunities for professional development and advancement of persons working under his or her supervision;
 - d. Promoting the principle of appropriate compensation for work done by person in their employ.
5. Undertake only such assignments in the use of mapping sciences for which one is qualified by education, training, and experience, and employ or advise the employment of experts and specialists when and whenever clients' or employers' interests will be best served thereby.
 6. Give appropriate credit to other persons and/or firms for their professional contributions.
 7. Recognize the proprietary, privacy, legal, and ethical interests and rights of others. This not only refers to the adoption of these principles in the general conduct of business and professional activities, but also as they relate specifically to the appropriate and honest application of photogrammetry, remote sensing, geographic information systems, and related spatial technologies. Subscribers to this code shall not condone, promote, advocate, or tolerate any organization's or individual's use of these technologies in a manner that knowingly contributes to:
 - a. deception through data alteration;
 - b. circumvention of the law;
 - c. transgression of reasonable and legitimate expectation of privacy.

Estimation of Forest Stand Characteristics Using Spectral Histograms Derived from an Ikonos Satellite Image

Jussi Peuhkurinen, Matti Maltamo, Lauri Vesa, and Petteri Packalén

Abstract

The aim of this paper was to examine the potential of Ikonos satellite images for estimating boreal forest stand characteristics using frequency distributions of radiometric values. The spectral features selected for use in the estimation were medians, standard deviations, and the parameters of the two-parametric Weibull distribution derived from the standwise spectral histograms of the Ikonos image. Ancillary map information, such as land-use and peatland classes, was also included. The method of estimation was non-parametric *k*-most similar neighbors (*k*-MSN) method. The most accurate results were achieved using spectral features that were derived from the multispectral images. The lowest RMSEs for the mean total stem volume, basal area, and mean height were 52.2 m³/ha (31.3 percent), 5.6 m²/ha (25.3 percent), and 3.1 m (20.6 percent), respectively. When only the panchromatic image was used in the analysis, the RMSEs for the mean total stem volume and basal area were about 3 percentage points higher. No differences in the mean height estimates were observed between the multispectral and panchromatic images. The most efficient predictor variables were the medians and the scale parameters of the Weibull distribution. The use of classified map information did not improve the results. The findings suggest that Ikonos satellite images can be used in to estimate forest stand characteristics giving an accuracy that corresponds to that achieved with aerial photographs.

Introduction

Valid information on forest resources and characteristics is essential for the planning forest use and management. Intensive field inventories for collecting stand-level information are expensive and time-consuming. However, recent progress made in remote sensing technology, e.g., the better availability of higher-resolution satellite images, offers an opportunity to acquire the necessary information at lower costs and in a reasonably short time.

Numerical interpretation of remote sensing material at the stand level includes the extraction of stand-level features and their use for defining variables in models that predict the stand attributes of interest. There have been several studies concerning the estimation of forest stand characteristics from

remote sensing material of different kinds in recent decades the most commonly used approaches being regression models (e.g., Hyypä *et al.*, 2000; Næsset, 2004; Kayitare *et al.*, 2006) and non-parametric methods (e.g., Holmgren *et al.*, 2000; Muinonen *et al.*, 2001; Anttila, 2002). Non-parametric methods do not rely on the estimation of parameters (such as the mean or the standard deviation) describing the distribution of the variable of interest in the population.

Using medium resolution (pixel size 10 to 30 meters) satellite imagery's spectral information, the estimation accuracies of stand level forest characteristics achieved in boreal conditions have not been in sufficient level for forest planning purposes. The standard errors of volume estimates have varied from 36 percent (Holmgren *et al.*, 2000) to 56 percent (Hyypä *et al.*, 2000). Basal area estimates' accuracies have been from 24 percent (Holmgren *et al.*, 2000) to 47 percent (Hyypä *et al.*, 2000) and those for the mean tree height 36 to 39 percent (Hyypä *et al.*, 2000). Holmgren *et al.* (2000) used the non-parametric *k*-nearest neighbor (*k*-NN) method whereas Hyypä *et al.* (2000) utilized multiple regression and neural networks.

Digitized aerial photographs have been widely studied in forest stand characteristics prediction (e.g., Muinonen *et al.*, 2001; Anttila, 2002; Coueron *et al.*, 2005). Muinonen *et al.* (2001) used the *k*-most similar neighbor (*k*-MSN) method to estimate mean forest stand volumes from a scanned aerial photograph. They achieved RMSE of 25 percent using only spectral information and 18 percent using additional textural information. Anttila (2002) used the same method with a larger dataset that contained several aerial photographs. He reported the RMSE of mean volume 37 percent as its best. Using only spectral information the RMSE was slightly worse (39 percent). Coueron *et al.* (2005) used two-dimensional Fourier analysis for obtaining characterization of canopy texture in tropical forests. The used remote sensing material was black and white aerial photographs with one-meter pixel size, which can be considered very similar to Ikonos panchromatic imagery. They reported significant correlations between the obtained canopy structure index and tree density, diameter of the tree of mean basal area, and mean canopy height.

The use of Ikonos imagery in forest characteristics estimation has been studied using textural features

Jussi Peuhkurinen, Matti Maltamo, and Petteri Packalén are with the University of Joensuu, P.O. Box 111, FI-80101 Joensuu, Finland (jussi.peuhkurinen@joensuu.fi).

Lauri Vesa is with Company LTV Forest, Koski-Jaakonkatu 15, FI-80230 Joensuu, Finland.

Photogrammetric Engineering & Remote Sensing
Vol. 74, No. 11, November 2008, pp. 1335–1341.

0099-1112/08/7411-1335/\$3.00/0
© 2008 American Society for Photogrammetry
and Remote Sensing

(Franklin *et al.*, 2001; Kayitakire *et al.*, 2006), joined use of spectral and textural features (Astola *et al.*, 2004) and spectral features with spatial variables (Chubey *et al.*, 2006). Franklin *et al.* (2001) reported that it was possible to discriminate Douglas-fir stands of different age classes using first- and second-order texture values. Astola *et al.* (2004) used Ikonos multispectral and panchromatic imagery to estimate the forest variables using automatic segmentation and unsupervised clustering. The estimates were produced as weighted sums of the input sample class probabilities. The RMSE for the total stem volume was 39 percent when using only spectral features and 37 percent with additional texture information. Kayitakire *et al.* (2006) applied panchromatic Ikonos imagery in estimation of forest stand variables for homogenous Norway spruce stands using texture features and linear regression. They achieved relative errors of 10 percent and 16 percent for top height and basal area, respectively. Chubey *et al.* (2006) applied decision trees in identifying relationships between the image object metrics extracted from the Ikonos multispectral and panchromatic images and forest inventory parameters. The classification results were at their best when different combinations of spectral and spatial properties of the image objects were used.

Non-parametric estimation methods like K-NN and K-MSN have found to be effective in retrieving forest stand variables from both aerial and medium resolution satellite imageries (e.g., Holmgren *et al.*, 2000; Muinonen *et al.*, 2001). However, these methods have not been tested with the Very High Resolution (VHR) satellite data. Although textural features extracted from the Ikonos panchromatic imagery have proved to contain information from the forest structure, the multispectral imagery's main information is probably included in the spectral features.

The principal aims of the work reported here was to examine the potential of Ikonos satellite images for use in estimating forest stand characteristics by the K-MSN method based on spectral features derived from standwise spectral histograms. The forest stand characteristics to be estimated were mean total stem volume, basal area, and mean height. A second aim of this paper was to investigate the usability of the parameters of the two-parametric Weibull distribution derived from the standwise spectral histograms for estimating forest stand characteristics.

Material

The Test Area

The test area located in Lieksa, Eastern Finland (about 30°80'E, 63°10'N) included parts of the Patvinsuo National

Park and the surrounding unprotected forestland, which is managed by the Finnish Forest and Park Service. The national park was established in 1982 and is the largest contiguous wilderness area in southern Finland, with a total area of 100 km² (Suomen kansallispuistot, 1994). The dominant tree species on the forested land is Scots pine (*Pinus Sylvestris* L.), but Norway spruce (*Picea abies* (L.) Karst) and broad-leaved species, mainly birch (*Betula pubescens* Ehrh. and *Betula pendula* Roth.) are also abundant. The forest stands in the area vary from young, homogenous managed stands to over-mature, heterogeneous stands that have been unmanaged for several decades. The stand structure is similar in the Patvinsuo National Park and in the surrounding areas, however.

Field Data

The field data as a whole consisted of 471 forest stands assessed by staff of the Finnish Forest and Park Service. The stand register data was collected using conventional compartment-wise forest inventory carried out in Finland (e.g., Haara, 2003). Because of the subjective method employed in this inventory (e.g., Laasasenaho and Päivinen, 1986) a total of 91 stands were chosen as test data and tallied again systematic plot sampling during the year 2002 in order to obtain more reliable stand data. The selection of the test stands was done with stratified sampling based on main tree species and development class information of the stands extracted from the database of the Finnish Forest and Park Service. The reference data (380 stands) included the rest of the non-sapling forest stands of the study area, which were inventoried in 2000 to 2002. Information on stand boundaries and peatland and land-use classes for the reference and test stands was extracted from the database of the Finnish Forest and Park Service.

The test stands were distributed into peatland classes, with 68 stands located on heathland, 16 on spruce mires and seven on pine bogs. A total of 47 stands were located inside the Patvinsuo National Park and 44 in managed forests outside the park. The characteristics of the test stands are described in the Table 1. The distribution of reference stands by peatland classes was that 336 stands were located on heathland, 26 on spruce mires, and 18 on pine bogs. The characteristics of the reference stands are described in Table 2; 303 of the reference stands are inside the Patvinsuo National Park and 77 in the managed forests.

Satellite Data

The satellite data consisted of two adjacent partially overlapping Ikonos multispectral four-band images with four-meter spatial resolution and two panchromatic images with

TABLE 1. DESCRIPTION OF THE FIELD DATA ON THE TEST STANDS. THE NUMBER OF STANDS IS 91

| | Mean | Minimum | Maximum | Standard Deviation |
|--|-------|---------|---------|--------------------|
| Area (hectares) | 4.4 | 0.9 | 17.9 | 3.3 |
| Volume (m ³ /hectare) | 166.9 | 48.6 | 380.9 | 68.0 |
| Basal Area (m ² /hectare) | 22.1 | 10.0 | 40.6 | 6.5 |
| Mean tree height (m) | 15.2 | 8.7 | 21.7 | 3.1 |
| Mean age (years) | 62 | 32 | 146 | 22 |
| Volume of pine (m ³ /hectare) | 82.2 | 0 | 244.9 | 65.6 |
| Volume of spruce (m ³ /hectare) | 52.9 | 0 | 264.0 | 66.3 |
| Volume of broad-leaved species (m ³ /hectare) | 31.6 | 0 | 150.5 | 34.7 |
| Volume of decaying tall wood (m ³ /hectare) | 8.6 | 0 | 52.7 | 11.3 |

TABLE 2. DESCRIPTION OF THE FIELD DATA FOR THE REFERENCE STANDS. THE NUMBER OF STANDS IS 380

| | Mean | Minimum | Maximum | Standard Deviation |
|--|-------|---------|---------|--------------------|
| Area (hectares) | 4.4 | 1.0 | 19.9 | 3.8 |
| Volume (m ³ /hectare) | 181.4 | 35.0 | 423.0 | 62.9 |
| Basal Area (m ² /hectare) | 20.6 | 7.0 | 36.0 | 5.0 |
| Mean tree height (m) | 17.2 | 7.0 | 26.0 | 3.6 |
| Mean age (years) | 103 | 21 | 226 | 46.2 |
| Volume of pine (m ³ /hectare) | 149 | 0 | 354.0 | 70.3 |
| Volume of spruce (m ³ /hectare) | 24.2 | 0 | 306.0 | 52.5 |
| Volume of broad-leaved species (m ³ /hectare) | 8.2 | 0 | 200.0 | 18.6 |
| Volume of decaying tall wood (m ³ /hectare) | 7.5 | 0 | 184.0 | 16.2 |

one-meter spatial resolution. The spectral ranges of Ikonos multispectral imagery are: band 1 (blue) 0.45 to 0.90 μm , band 2 (green) 0.51 to 0.60 μm , band 3 (red) 0.63 to 0.70 μm , and band 4 (near infrared) 0.76 to 0.85 μm . Panchromatic imagery's spectral range is 0.45 to 0.90 μm (GeoEye, 2007). The images had been acquired during the same orbital pass in July 2001. The level of processing of the images was "standard geometrically corrected." The image acquisition parameters are described in the Table 3.

The images were processed further to achieve adequate geometric and radiometric accuracy and the correct format for further analysis. The processing included rectification of the images, calibration, and mosaicing of adjacent images and rescaling. The images were rectified to the map coordinate system by means of ground control points assembled using differential GPS. The radiometric calibration of adjacent images was carried out by the robust regression method, so that each band was calibrated separately (see Tokola *et al.*, 1999). The calibrated images were mosaiced to one multispectral image and one panchromatic image. The original radiometric resolution of the Ikonos satellite image is in 11-bits, but as the further analysis required the use of 8-bit data, the merged images were rescaled between 0 and 255 by the method based on standard deviations using following algorithm:

$$DN_{out} = Min_{out} + \frac{[DN_{in} - Mean(DN_{in}) + NTSD * SD(DN_{in})] * (Max_{out} - Min_{out})}{2 * NTSD * SD(DN_{in})} \quad (1)$$

where DN_{out} = value of the pixel after rescaling, DN_{in} = original value of the pixel, Min_{out} = minimum value of the output raster, Max_{out} = maximum value of the output raster, $Mean(DN_{in})$ = mean value of the input raster, $SD(DN_{in})$ = standard deviation of the input raster, and $NTSD$ = number of the standard deviations. The algorithm forces the fringe areas to minimum or maximum and

TABLE 3. ACQUISITION PARAMETERS OF THE IMAGES USED

| Parameter | Image 1 (western) | Image 2 (eastern) |
|------------------------------|--------------------|--------------------|
| Acquisition date/time | 07 July 2001, 0935 | 07 July 2001, 0935 |
| Nominal collection azimuth | 341.55° | 0.86° |
| Nominal collection elevation | 81.13° | 71.80° |
| Sun angle azimuth | 170.24° | 170.42° |
| Sun angle elevation | 49.08° | 49.08° |

does not take them into account in adjusting the range of scale. The rescaling was performed using two as the number of standard deviations. The majority of the spectral histogram values were within this range and the isolated minimum or maximum values did not wider the range of scale.

Methods

Extraction of Standwise Spectral Histograms

Standwise spectral histograms were extracted for each band separately. Due to the possible errors in the subjective delineation of the stand boundaries (see Næsset, 1999) and possible geometric incompatibilities between the satellite images and stand boundaries, a ten meter inward buffer was used and only the pixels inside the compartment polygon (limited by the buffer zone) were selected for further analysis.

Estimation of Standwise Spectral Features

The standwise spectral features used in the estimation were medians, standard deviations and the parameters of the two-parametric Weibull distribution derived from standwise spectral histograms for each band separately. The two-parametric Weibull distribution density function is as follows:

$$f(x) = \frac{c}{b} \left(\frac{x}{b}\right)^{c-1} \exp\left(-\left(\frac{x}{b}\right)^c\right), \quad (2)$$

where b = scale parameter and c = shape parameter (or slope) (Bailey and Dell, 1973). In this case, variable x denotes spectral histogram values. A change in the scale parameter has the same effect on the distribution as a change in the abscissa scale. The scale parameter is highly correlated with the median value of the distribution while the shape parameter specifies the skewness or slope of the distribution. The parameters of the Weibull distributions were estimated by the maximum likelihood method (see e.g., Silvey, 1975).

Estimation of Stand Characteristics

The stand characteristics were estimated by the k-most similar neighbors (K-MSN) method which is based on finding K-MSN observations using indicator attributes (in this case spectral features) and using these to calculate distance-weighted means for the design attributes (in this case mean total stem volume, basal area and mean height). The K-MSN observations are identified by means of the approach presented by Moeur and Stage (1995).

The k-MSN method is related to the k-NN method but it differs in the way how the distance to the neighbors is measured. The MSN similarity function derived from canonical correlation analysis (Moeur and Stage, 1995) is as follows:

$$D_{uj}^2 = (X_u - X_j) \Gamma \Lambda^2 \Gamma' (X_u - X_j)', \quad (3)$$

where D_{uj}^2 = squared distance between observations u and j , X_u = indicator variable of observation u , X_j = indicator variable of observation j , Γ = matrix of canonical coefficients of indicator variables (pxs), Λ^2 = diagonal matrix of squared canonical correlations (sxs), s = number of canonical correlations used, p = number of indicator attributes, and u, j = observations.

The weighting matrix in the MSN similarity function, (Moeur and Stage, 1995) is given by:

$$W = \Gamma \Lambda^2 \Gamma'. \quad (4)$$

The k-most similar observations are identified by sorting the distances and finding the k minimum values (Muinonen *et al.*, 2001) taking each test stand as target stand (j). The weight w_{uj} of a reference stand (u) belonging to the set of k-most similar observations for stand j was then (Muinonen *et al.*, 2001):

$$w_{uj} = \frac{1}{(D_{uj}^2)}, \quad (5)$$

where D_{uj}^2 = similarity measure from Equation 3.

Using the weights w_{uj} in Equation 5, the estimate for forest stand characteristic y in stand j (\hat{y}_j) (Muinonen *et al.*, 2001) is given by:

$$\hat{y}_j = \frac{\sum_{u=1}^k w_{uj} y_u}{\sum_{u=1}^k w_{uj}}. \quad (6)$$

The advantage of the MSN method is that it retains the full range of variability of the data and preserves the covariance among the estimates for the multivariate design attributes (Moeur and Stage, 1995). However, if more than one neighbor is averaged and used to estimate the values of design attributes, some combinations of estimates may occur that do not exist in real world. Also, the variance in the estimates declines as more neighbors are averaged (LeMay and Temesgen, 2005).

The design attributes were estimated simultaneously in order to preserve the covariance structure. To examine the effect of different indicator attributes and find the most effective combinations, 22 feature sets were formulated so that it was possible to compare which bands and features were the most informative ones in the estimation procedure. The effect of k was examined by varying the number of neighbors from 1 to 10.

The accuracies of the estimates for the stand characteristics were measured by RMSE, in which each forest stand was given equal weight:

$$RMSE = \sqrt{\frac{\sum_{i=1}^n (y_i - \hat{y}_i)^2}{n}}, \quad (7)$$

where n = number of forest stands, y_i = the measured (correct) value of stand variable y of stand i , and \hat{y}_i = the estimated value of stand variable y of stand i . Relative RMSEs were calculated by dividing the absolute RMSEs by the true mean of the stand characteristic under consideration. The biases of the stand characteristic estimates were calculated as:

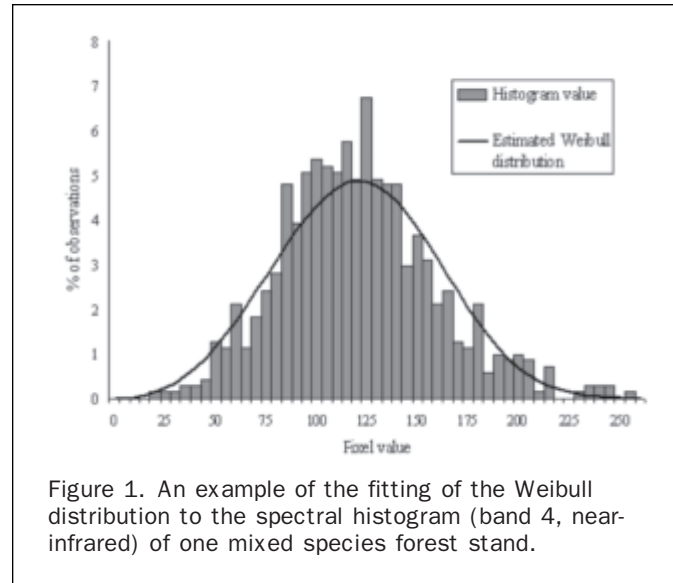


Figure 1. An example of the fitting of the Weibull distribution to the spectral histogram (band 4, near-infrared) of one mixed species forest stand.

$$bias = \frac{\sum_{i=1}^n (y_i - \hat{y}_i)}{n}. \quad (8)$$

Results

Since the standwise spectral histograms were unimodal, use of the two-parameter Weibull distribution was justified. Visual examination suggests that the estimated Weibull distributions seem to fit well with the extracted spectral histograms (Figure 1).

The accuracies of the estimates improved significantly when the number of most similar neighbors was increased from 1 to 3 after which they remained quite stable (Figure 2). The lowest RMSEs were achieved using 4 to 10 neighbors; the most accurate results on average being achieved using a k value of 10. The lowest RMSEs were 31.3 percent (52.2 m³/ha, feature set number 3) for mean total stem volume, 25.3 percent (5.6 m²/ha, feature set number 5) for basal area, and 20.6 percent (3.1 m, feature set number 9) for mean tree height. The main results achieved using the value of k that gave the minimum RMSE are given in Table 4.

The biases of the mean total stem volume estimates started to increase after 3 most similar neighbors but those

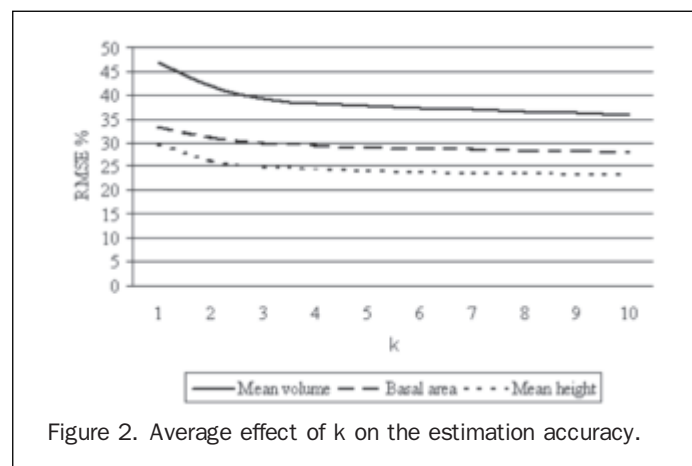


Figure 2. Average effect of k on the estimation accuracy.

TABLE 4. MAIN ESTIMATION RESULTS. THE LOWEST RMSE'S ARE PRINTED IN BOLD. NEGATIVE SIGN IN BIAS VALUE MEANS OVERESTIMATION

| Feature Set Number | Imagery | Features | Mean Volume | | Basal Area | | Mean Tree Height | |
|--------------------|------------|--|-------------|----------------------|-------------|----------------------|------------------|---------|
| | | | RMSE% | Bias, m ³ | RMSE% | Bias, m ² | RMSE% | Bias, m |
| 1 | MS and pan | W _b , W _c , med, stdev, pc,luc | 35.5 | -17.7 | 27.8 | 1.5 | 24.3 | -2.2 |
| 2 | MS and pan | W _b , W _c , med, stdev | 35.6 | -12.7 | 28.9 | 1.6 | 23.0 | -1.8 |
| 3 | MS | W _b , W _c , med, stdev | 31.3 | -10.1 | 26.4 | 1.9 | 21.7 | -1.7 |
| 4 | MS | W _b , W _c | 32.1 | -12.8 | 25.5 | 1.5 | 21.3 | -1.8 |
| 5 | MS | med | 32.4 | -8.4 | 25.3 | 1.7 | 23.8 | -1.5 |
| 6 | MS | stdev | 35.9 | -14.6 | 27.2 | 1.6 | 23.4 | -1.9 |
| 7 | pan | W _b , W _c , med, stdev | 35.2 | -18.2 | 27.9 | 1.2 | 22.4 | -1.9 |
| 8 | pan | W _b , W _c | 34.2 | -13.9 | 27.8 | 1.6 | 22.4 | -2.0 |
| 9 | pan | med | 34.3 | 9.1 | 28.7 | 2.3 | 20.6 | -0.7 |
| 10 | pan | stdev | 51.3 | -12.0 | 35.9 | 1.8 | 30.2 | -2.0 |
| MS_avg | MS | | 33.1 | -12.3 | 26.0 | 1.6 | 22.3 | -1.7 |
| Pan_avg | pan | | 37.3 | -10.9 | 29.3 | 1.6 | 23.3 | -1.8 |

MS = Ikonos multispectral image (all bands), pan = Ikonos panchromatic image, W_b = scale parameter of the Weibull distribution, W_c = shape parameter of the Weibull distribution, med = median, stdev = standard deviation, pc = peatland class, luc = land-use class, MS_avg = average accuracy using multispectral imagery, and pan_avg = average accuracy using panchromatic imagery.

of the basal area and mean tree height remained stable despite changes in k (Figure 3). The mean volume estimates were overestimations in most of the stands. For example when using feature set 4, which gave on the average comparable good results, about in one fourth of the stands the overestimation of the mean volume was more than 50 m³/ha (Figure 4). Using the same feature set, only in less than 10 percent of the stands the estimation error was over 50 m³/ha underestimation. The biases occurred mainly due to differences between the reference and test stands and different field data collection methods. According to the systematic plot sampling data the average biases of the compartment-wise forest inventory in the study area were 10 m³/ha overestimation, 3 m²/ha underestimation, and one-meter overestimation for mean total volume, basal area, and mean tree height, respectively. Reference stands were on average of greater volume, but the volume range of the reference stands was supposed to be extensive enough to encompass the whole variation of test stands' volume range.

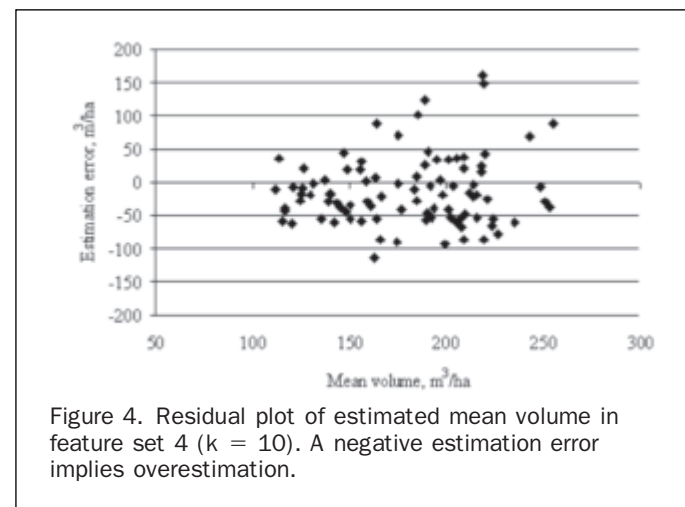
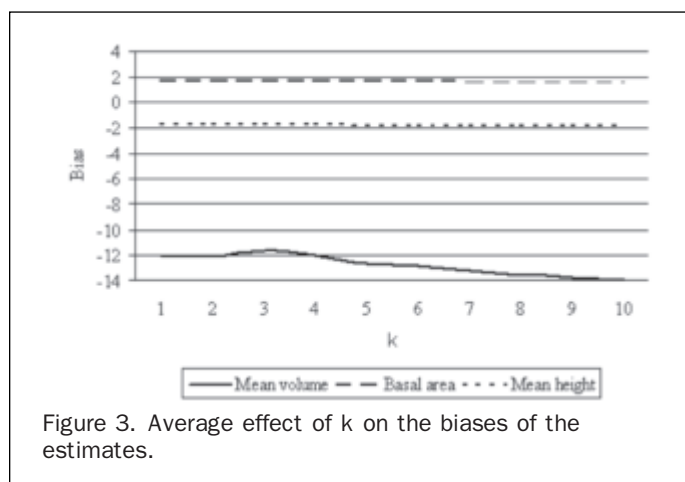
On average, the use of all the multispectral bands (excluding PAN) gave more accurate results than any single

band or the panchromatic image alone. The parameters of the Weibull distribution were slightly more informative than medians with respect to the average results but the standard deviations were considerably less powerful as indicator attributes than the medians or the parameters of the Weibull distribution. The use of ancillary map information did not improve the accuracy.

Discussion

The first commercial VHR earth observation satellite, Ikonos, started operation in 1999 and was soon followed by two other VHR satellites, QuickBird-2 and OrbView-3. Several even more accurate VHR satellites are planned to enter service in the near future. VHR instruments provide images in which the spatial resolution approaches that of aerial images but other characteristics are congruent with those of traditional satellite images. It is therefore justified to compare VHR images as a data sources with both aerial photographs and other satellite imagery systems.

The most obvious difference between VHR images such as Ikonos and traditional satellite images such as Landsat is



the spatial resolution achieved, which means that VHR data may be used on a much finer scale than Landsat or other coarser-resolution systems. It is not obvious, however, that the use of VHR data alone with the same interpretation methods as previously will increase the accuracy of interpretation.

The minor bi-directional reflectance effect (BRDF) is one advantage of VHR data over aerial photographs. In aerial photographs, the BRDF effect can be perceived as a variation of brightness arising from the fact that the tree crowns in the direction of incoming radiation have their shady sides towards the camera and those in the opposite direction have their illuminated sides exposed. Due to the considerably higher capturing altitude (approximately 680 km), BRDF is not a major issue in VHR data, i.e., the illumination within a scene is more even. There are still many applications, however, for which the spatial resolution of VHR images is not sufficient.

The estimation accuracies presented here were better than those achieved using satellite images of lower spatial resolution (Holmgren *et al.*, 2000; Hyypä *et al.*, 2000). Correspondingly, studies based on aerial photographs without ancillary data have produced higher RMSEs (Anttila, 2002; Hyypä *et al.*, 2000), with the exception of the work of Muinonen *et al.* (2001). Furthermore, the RMSE for mean volume obtained here was lower than that reported by Astola *et al.* (2004), who used similar Ikonos material in different method of estimation. On the contrary, Kayitakire *et al.* (2006) reported notably better results using texture information extracted from panchromatic Ikonos imagery, although the test data they used was limited to homogenous Norway spruce stands. However, other studies also mentioned here have shown that the use of texture improves the estimation accuracy of forest stand variables. Texture features can be implemented in MSN analysis as indicator variables, which probably would have improved the estimation results also in the present study.

As a conclusion, it can be said that the accuracy achieved here was comparable to or even better than that reported in previous studies based on optical remote sensing imagery. It was nevertheless considerably worse than those recorded using airborne laser scanning (lidar) (e.g., Næsset *et al.*, 2004). This difference is of great importance since the error tolerance of stand volume predictions in practical forest inventories conducted by compartments in Finland, for example, is about 20 to 25 percent, a level which could not be attained using the present material, although it can easily be achieved with lidar.

Lidar uses an entirely different principle from that of spectral instruments; it measures the heights of laser hits, which have proved to be very closely correlated with forest characteristics such as mean volume, mean height, or basal area. Thus, several recent studies have shown the suitability of lidar for forest inventory purposes (e.g., Næsset *et al.*, 2004). On the other hand, it does not provide sufficient information about tree species. One interesting possibility would be to combine very high-resolution satellite imagery with lidar information for practical forest inventory purposes. In principle, accurate estimates of the tree stock could be obtained by lidar, whereas tree species information in particular could be derived from Ikonos imagery. As shown here, a non-parametric methodology could be used in this.

Acknowledgments

This research has been funded by the European Union and is a contribution to research project Earth Observation for Natura 2000+. We wish to thank the Finnish Forest and Park Service for providing forest planning data. Thanks also to Doctor Perttu Anttila who carried out some of the fieldwork.

References

- Anttila, P., 2002. Nonparametric estimation of stand volume using spectral and spatial features of aerial photographs and old inventory data, *Canadian Journal of Forest Research*, 32(10):1849–1857.
- Astola, H., C. Bounsaythip, J. Ahola, T. Häme, E. Parmes, L. Sirro, and B. Veikkanen, 2004. Highforest-Forest parameter estimation from high resolution remote sensing data, *Proceedings of the International Society for Photogrammetry and Remote Sensing Twentieth Congress*, 12–23 July, Istanbul, Turkey, pp. 355–340.
- Bailey, R.L., and T.R. Dell, 1973. Quantifying diameter distribution with the Weibull-function, *Forest Science*, 19:97–104.
- Chubey, M.S., S.E. Franklin, and M.A. Wulder, 2006. Object-based analysis of Ikonos-2 imagery for extraction of forest inventory parameters, *Photogrammetric Engineering & Remote Sensing*, 72(3):383–394.
- Couteron, P., R. Pélissier, E. Nicolini, and D. Paget, 2005. Predicting tropical forest stand structure parameters from Fourier transform of very high resolution canopy images, *Journal of Applied Ecology*, 42:1121–1128.
- Franklin, S.E., M.A. Wulder, and G.R. Gerylo, 2001. Texture analysis of Ikonos panchromatic data for Douglas-fir forest age class separability in British Columbia, *International Journal of Remote Sensing*, 22:2627–2632.
- GeoEye, 2007. *IKONOS Imagery Products*, URL: http://www.geoeye.com/CorpSite/assets/docs/brochures/IKONOSImagery_bifold2007_v2.pdf (last date accessed: 16 July 2008).
- Holmgren, J., S. Joyce, M. Nilsson, and H. Olsson, 2000. Estimating stem volume and basal area in forest compartments by combining satellite image data with field data, *Scandinavian Journal of Forest Research*, 15:103–111.
- Haara, A., 2002. Comparing simulation methods for modelling the errors of stand inventory data, *Silva Fennica*, 37(4):477–491.
- Hyypä, J., H. Hyypä, M. Inkinen, M. Engdahl, S. Linko, and Y.-H. Zhu, 2000. Accuracy comparison of various remote sensing data sources in the retrieval of forest stand attributes, *Forest Ecology and Management*, 128:109–120.
- Kayitakire F., C. Hamel, and P. Defourny, 2006. Retrieving forest structure variables based on image texture analysis and IKONOS-2 imagery, *Remote Sensing of Environment*, 102:390–401.
- Laasasenaho, J., and R. Päivinen, 1986. Kuvioittaisen arvioinnin tarkistamisesta, *Folia Forestalia*, 664, 19 p.
- LeMay, V., and H. Temesgen, 2005. Comparison of nearest neighbor methods for estimating basal area and stems per hectare using aerial auxiliary variables, *Forest Science*, 51(2):109–119.
- Moeur, M., and A.R. Stage, 1995. Most similar neighbor: An improved sampling inference procedure for natural resource planning, *Forest Science*, 41(2):337–359.
- Muinonen, E., M. Maltamo, H. Hyppänen, and V. Vainikainen, 2001. Forest stand characteristics estimation using a most similar neighbor approach and image spatial structure information, *Remote Sensing of Environment*, 78:223–228.
- Næsset, E., 1999. Assessing the effect of erroneous placement of forest stand boundaries on the estimated area of individual stands, *Scandinavian Journal of Forest Research*, 14:175–181.

Næsset, E., 2004. Practical large-scale forest stand inventory using a small airborne scanning Laser, *Scandinavian Journal of Forest Research*, 19:164–179.

Næsset, E., T. Gobakken, J. Holmgren, J. Hyyppä, H. Hyyppä, M. Maltamo, M. Nilsson, H. Olsson, Å. Persson, and U. Söderman, 2004. Laser scanning of forest resources: The Scandinavian experience, *Scandinavian Journal of Forest Research*, 19:482–499.

Silvey, S.D. 1975. *Statistical Inference, Monographs on Statistics and Applied Probability*, Chapman and Hall, 191 p.

Suomen kansallispuistot, 1994. Metsähallitus, Luonnonsuojelu, Helsinki, 94 p.

Tokola, T., S. Löfman, and A. Erkkilä, 1999. Relative calibration of multitemporal Landsat data for forest area change detection, *Remote Sensing of Environment*, 68:1–11.

(Received 21 September 2006; accepted 13 December 2006; revised 10 January 2007)

Sustaining Member Benefits

One Full Membership — You may designate one person to receive the Individual Active Membership that entitles them to full voting membership.

Sustaining Member profile — A 300-word introductory profile of your company and logo will appear in the first available issue of Photogrammetric Engineering & Remote Sensing (PE&RS) as well as a continuous monthly listing of your company and e-mail or web site address as a Sustaining Member of ASPRS: The Imaging & Geospatial Information Society. You will receive a Sustaining Member certificate.

Listing in the “Resource Book” — An updated description of your company with logo will be profiled in the Resource Book that is published annually in PE&RS. Your company products, services and geographic locations will be listed on the ASPRS web site. This listing is also on our website for easy searches by anyone interested in obtaining your company’s products and/or services.

Additional Subscriptions to PE&RS — Copies of the world’s leading Journal in the photogrammetry and remote sensing fields, will be mailed to three employees of your choice at any address.

Free hot link or e-mail link — This benefit provides Sustaining Members with a free web site hot link or e-mail link in their corporate description on the ASPRS web site. Now when a customer is looking for a particular product or service and sees your listing, they will be able to contact you immediately.

Sponsored Memberships — Demonstrate your company’s commitment to your client’s continuing education and awareness of current issues in the photogrammetry, remote sensing, GIS, and GPS industries, by participating in the ASPRS Sponsored Membership program. Every month your sponsored members will receive their personal copy of PE&RS. Sponsored memberships are available for ASPRS Sustaining Members at substantially reduced prices.

ASPRS web site advertisements — Reach thousands of new potential customers by placing your advertisement on the ASPRS web site. The web site contains over 175 pages of information on the Society, new publications, upcoming conferences, professional certification, and numerous industry-related web links. ASPRS Sustaining Members receive a 15% discount on web site advertisements.

Free copies of ASPRS Proceedings — From ASPRS conferences as well as Member rates on all Society publications.

Discounts on the ASPRS Mailing List — A 50% discount on the Mailing List Service.

Reduced advertising rates — Receive discounts on display ads and limited free Classified Ad space in the ASPRS Journal, PE&RS, read by 9,500 members and subscribers worldwide each month.

Preferential treatment and reduced rate on exhibit space — ASPRS Sustaining Members receive a discount on exhibit booth space rental at ASPRS conferences.

Partners in Education — Eligibility to become an ASPRS Partner in Education. The Partner in Education Program was initiated to support the Society’s effort to educate students from K through 14, as well as the public, about the modern uses of remote sensing, Geographic Information Systems (GIS), and photogrammetry. Through the Partners in Education Program, ASPRS Sustaining Members provide direct support to the ASPRS education agenda through tax-free donations. A company’s support is highlighted on the ASPRS web site and through press releases.

Conference Discounts — Individuals who are listed under the company membership may register at any ASPRS conference at the discounted member rate; a significant savings.

Participation in the Career Fair at ASPRS Conferences

ASPRS: The Imaging & Geospatial Information Society
5410 Grosvenor Lane, Suite 210, Bethesda, Maryland 20814
301-493-0290 | 301-493-0208 (fax)
membership@asprs.org • www.asprs.org

Forthcoming Articles

- Ming-Jer Huang, Shiahn-Wern Shyue, Liang-Hwei Lee, and Chih-Chung Kao*, A Knowledge-based Approach to Urban Feature Classification Using Aerial Imagery with Lidar Data.
- Lauri Markelin, Eija Honkavaara, Jouni Peltoniemi, Eero Ahokas, Risto Kuittinen, Juha Hyyppä, Juha Suomalainen, and Antero Kukko*, Radiometric Calibration and Characterization of Large Format Digital Photogrammetric Sensors in a Test Field.
- Hongxing Liu, Jaeyhung Yu, Zhiyuan Zhao, and Kenneth C. Jezek*, Incorporation of Flow Stripes as Constraints for Calibrating Ice Surface Velocity Measurements from Interferometric SAR Data.
- John H. Lowry, Jr., R. Douglas Ramsey, Lisa Langs Stoner, Jessica Kirby, and Keith Schulz*, An Ecological Framework for Evaluating Map Errors Using Fuzzy Sets.
- Jen-Jer Jaw and Nei-Haur Perng*, Line Feature Correspondence Between Object Space and Image Space.
- Yongwei Sheng*, Modeling Algorithm-induced Errors in Iterative Mono-plotting Process.
- Sharaf Alkheder and Jie Shan*, Calibration and Assessment of Multi-temporal Image-based Cellular Automata for Urban Growth Modeling.
- Manuel A. Aguilar, Fernando J. Aguilar, and Francisco Agüera*, Assessing Geometric Reliability of Corrected Images from Very High Resolution Satellites.
- Mang Lung Cheuk and May Yuan*, Assessing Spatial Uncertainty of Lidar-derived Building Model: A case Study in Downtown Oklahoma City.
- Stephen V. Stehman, James D. Wickham, Timothy G. Wade, and Jonathan D. Smith*, Designing a Multi-objective, Multi-support Accuracy Assessment of the 2001 National Land Cover Data (NLCD 2001) of the Conterminous United States.
- Xin Huang, Liangpei Zhang, and Pingxiang Li*, Classification of Very High Resolution Imagery Based on the Fusion of Edge and Multispectral Information.
- Scott A. Soenen, Derek R. Peddle, Craig A. Coburn, Ronald J. Hall, and Forrest G. Hall*, Canopy Reflectance Model Inversion in Multiple Forward Mode: Forest Structural Information Retrieval from Solution Set Distributions.
- Keiji Kushida, Kunihiko Yoshino, Toshihide Nagano, and Tomoyasu Ishida*, Automated 3D Surface Model Extraction from Balloon Stereo Photographs.
- Tiejun Wang, Andrew K. Skidmore, Albertus G. Toxopeus, and Xuehua Liu*, Understorey Bamboo Discrimination Using a Winter Image.
- Peng Hu, Xiaohang Liu, and Hai Hu*, On the Errors in DEMs Interpolated from Topographic Maps: Accuracy Assessment Based on Approximation Theory.
- Ben Somers, Stephanie Delalieux, Willem W. Verstraeten, and Pol Coppin*, A Conceptual Framework for the Simultaneous Extraction of Sub-pixel Spatial Extent and Spectral Characteristics of Crops.
- Jung-Kung Liu, Rongxing Li, Sagar Deshpande, Xutong Niu, and Tian-Yuan Shih*, Estimation of Blufflines Using Topographic Lidar Data and Orthophotos.
- Leena Matikainen, Juha Hyyppä, and Harri Kaartinen*, Comparison Between First Pulse and Last Pulse Laser Scanner Data in the Automatic Detection of Buildings.
- Alexandre Beaulieu and Daniel Clavet*, Accuracy Assessment of Canadian Digital Elevation Data Using ICESat.
- Peijun Li, Tao Cheng, and Jiancong Guo*, Multivariate Image Texture by Multivariate Variogram for Multispectral Image Classification.
- Shengli Huang, Stacey A. Hager, Kerry Q. Halligan, Ian S. Fairweather, Alan K. Swanson, and Robert L. Crabtree*, A Comparison of Individual Tree and Forest Plot Height Derived from Lidar and InSAR.
- John R. Jensen, Michael E. Hodgson, Maria Garica-Quijano, and Jungho Im*, A Remote Sensing and GIS-assisted Spatial Decision Support System for Hazardous Waste Site Monitoring.
- Randy M. Hamilton, Rick E. Foster, Timothy J. Gibb, Christian J. Johannsen, and Judith B. Santini*, Pre-visible Detection of Grub Feeding in Turfgrass Using Remote Sensing.
- Laure Chandelier and Gilles Martinot*, A Radiometric Aerial Triangulation for the Equalization of Digital Aerial Images and Orthoimages.
- Jun Pan, Mi Wang, Deren Li, and Jonathan Li*, A Robust Approach for Repairing Color Composite DMC Images.
- Nizar Abo Akel, Sagi Filin, and Yerach Doytsher*, Reconstruction of Complex Shape Buildings from Lidar Data Using Free Form Surfaces.
- D.G. Milledge, S.N. Lane, and J. Warburton*, Optimization of Stereo Matching Algorithms Using Existing DEM Data.
- Selim Aksoy, Krzysztof Koperski, Carsten Tusk, and Giovanni Marchisio*, Land Cover Classification with Multi-Sensor Fusion of Partly Missing Data
- Ellen Schwalbe, Hans-Gerd Maas, Manuela Kenter, and Sven Wagner*, Hemispheric Image Modeling and Analysis Techniques for Solar Radiation Determination in Forest Ecosystems.
- Yonghak Sing and Jie Shan*, An Adaptive Approach to Topographic Feature Extraction from Digital Terrain Models.
- Hua Liu and Qihao Weng*, Scaling Effect on the Relationship between Landscape Pattern and Land Surface Temperature: A Case Study of Indianapolis, United States.
- Kourosh Khoshelham*, Role of tie points in integrated sensor orientation for photogrammetric map compilation.
- Joachim Höhle*, DEM Generation Using a Digital Large Format Frame Camera.
- Umamasheswaran Rajasekar and Qihao Weng*, Application of Association Rule Mining for Exploring the Relationship between Urban Land Surface Temperature and Biophysical/Social Parameters.
- Yaguang Xu, Brett G. Dickson, Haydee M. Hampton, Thomas D. Sisk, Jean A. Palumbo, and John W. Prather*, Effects of Mismatches of Scale and Location between Predictor and Response Variables on Forest Structure Mapping.
- Jonathan Cheung-Wai Chan, Rik Bellens, Frank Canters, and Sidharta Gautama*, An Assessment of Geometric Activity Features for Per-pixel Classification of Urban Man-made Objects using Very High Resolution Satellite Imagery.
- Toshihiro Sakamoto, Cao Van Phung, Nhan Van Nguyen, Akihiko Kotera, and Masayuki Yokozawa*, Agro-ecological interpretation of rice-cropping systems in flood-prone areas using MODIS imagery.
- Karsten Raguse and Christian Heipke*, Synchronization of Image Sequences - A Photogrammetric Method.
- Chenghai Yang, James H. Everitt, Reginald S. Fletcher, Ryan R. Jensen, and Paul W. Mausel*, Evaluating AISA+ Hyperspectral Imagery for Mapping Black Mangrove along the South Texas Gulf Coast.
- Zhangquan Shen, Jianguo Qi, and Ke Wang*, Modification of Pixel-swapping with Initialization of Sub-pixel/pixel Model.
- Janet Nichol*, An Emissivity Modulation Method for Spatial Enhancement of Thermal Satellite Images in Urban Heat Island Analysis.
- Qingmin Meng, Bruce E. Borders, Chris J. Cieszewski, and Marguerite Madden*, Closest Spectral Fit for Removing Clouds and Cloud Shadows.
- F. Maselli, L. Massi, M. Pieri, and C. Santini*, Spectral Angle Minimization for the Retrieval of Optically Active Seawater Constituents from MODIS Data.
- Oh-ig Kwoun and Zhong Lu*, Multi-temporal RADARSAT-1 and ERS Backscattering Signatures of Coastal Wetlands in Southern Louisiana.
- Selim Aksoy, Krzysztof Koperski, Carsten Tusk, and Giovanni Marchisio*, Land-cover Classification with Multi-sensor Fusion of Partly Missing Data
- In-seong Jeong and James Bethel*, A Study of Trajectory Models for Satellite Image Triangulation.
- Hubo Cai and William Rasdorf*, Accuracy Evaluation and Sensitivity Analysis of Estimating 3D Centerline Length Using Lidar and NED.
- Konstantinos Karantzalos and Demetre Argialas*, A Region-based Level Set Segmentation for the Automatic Detection of Manmade Objects from Aerial and Satellite Images.

Pixel-based Minnaert Correction Method for Reducing Topographic Effects on a Landsat 7 ETM+ Image

Dengsheng Lu, Hongli Ge, Shizhen He, Aijun Xu, Guomo Zhou, and Huaqiang Du

Abstract

The topographic effect on land surface reflectance is an important factor affecting quantitative analysis of remotely sensed data in mountainous regions. Different approaches have been developed to reduce topographical effects. Of the many methods, the Minnaert correction method is most frequently used for topographic correction, but a single global Minnaert value used in previous research cannot effectively reduce topographic effects on the remotely sensed data, especially in the areas with steep slopes. This paper explores the method to develop a pixel-based Minnaert coefficient image based on the established relationship between Minnaert coefficients and topographic slopes. A texture measure based on homogeneity is used to evaluate the topographic correction result. This study has demonstrated promising in reducing topographic effects on the Landsat ETM+ image with the pixel-based Minnaert correction method.

Introduction

The topographic effect has long been recognized as a problem for quantitative analyses of remotely sensed data (Teillet *et al.*, 1982; Ekstrand, 1996; Tokola *et al.*, 2001), therefore, topographic correction has become one of the important image preprocessing steps in the application of remotely sensed data in mountainous regions. Common atmospheric calibration models, such as the 6S (Second simulation of the satellite signal in the solar spectrum) model (Vermote *et al.*, 1997) and image-based dark object subtraction models (Chavez, 1996), are based on the assumption that the surface is a flat horizon with a cloud-free atmosphere. These models can eliminate the impacts caused by sensor instruments, solar irradiance, solar zenith angle, atmospheric scattering, and absorption, but cannot eliminate the topographic impacts. In order to reduce topographic effects on remotely sensed data,

Hongli Ge, Aijun Xu, Guomo Zhou, and Huaqiang Du are with the School of Environmental Technology, Zhejiang Forestry University, Lin'An, Zhejiang, China 311300 (jghlhlx@sina.com).

Dengsheng Lu is with the School of Environmental Technology, Zhejiang Forestry University, Lin'An, Zhejiang, China, and the Anthropological Center for Training and Research on Global Environmental Change (ACT), Indiana University, Bloomington, IN 47405.

Shizhen He is with the East China Institute of Forest Inventory and planning, State Forestry Administration, Jinhua, Zhejiang, China.

considerable research with Thematic Mapper (TM) and Satellite Probatoire d'Observation de la Terre (SPOT) data has been conducted in mountainous areas (Teillet *et al.*, 1982; Jones *et al.*, 1988; Leprieur *et al.*, 1988; Civco, 1989; Itten and Meyer, 1993; Meyer *et al.*, 1993; Sandmeier and Itten, 1997; Gu and Gillespie, 1998; Gu *et al.*, 1999; Allen, 2000; Tokola *et al.*, 2001; Blesius and Weirich, 2005; Gitas and Deverux, 2006). Methods used for reducing topographic effects include (a) band ratio (Holben and Justice, 1980), (b) topographic correction models, such as Minnaert correction model and statistical-empirical approach (Civco, 1989; Colby, 1991; Allen, 2000; Bishop and Colby, 2002; Riano *et al.*, 2003), (c) integration of digital elevation model (DEM) data and remote-sensing data (Walsh *et al.*, 1990; Franklin *et al.*, 1994), and (d) a combined correction model of atmospheric and topographic effects (Conese *et al.*, 1993; Richter, 1997; Sandmeier and Itten, 1997). Although different approaches have been used for topographic correction in previous research, an effective approach to reduce topographic effects is not available.

Topographic effects result from the differences in illumination due to the position of the sun and the angle of the terrain. This causes variation in brightness values. A steep slope often produces serious shadows in the aspect facing away from the sun resulting in significant variation of illumination for areas with different slopes and aspects. A simple approach to reduce the topographic effects is to use the cosine model (Jensen, 1996), which assumes that the surface reflects incident solar energy uniformly in all directions, i.e., a Lambertian reflector. Any variations in land surface reflectance are caused by the amount of incident radiation. However, the cosine model only models direct irradiance of a pixel on the ground. It ignores diffuse sky light that may weakly illuminate a shadowed area. This implies that weakly illuminated areas in the terrain receive a disproportionate brightness when the cosine model is applied. Teillet *et al.* (1982) noted that the cosine model is not particularly useful in areas of steep terrain where incident angles may approach 90°. Allen (2000) also indicated that shaded and weakly illuminated slopes may appear white, and almost all north-facing slopes become over-illuminated using the cosine model. An alternative way to account for non-Lambertian behavior is the use of a Minnaert-correction model which makes use of

Photogrammetric Engineering & Remote Sensing
Vol. 74, No. 11, November 2008, pp. 1343–1350.

0099-1112/08/7411-1343/\$3.00/0
© 2008 American Society for Photogrammetry
and Remote Sensing

a Minnaert constant k . However, the k value depends on the nature of land-cover, topographic factor, and wavelength. In areas with large incident angles, the k value can prevent a division by small values, thereby evading overcorrection as in the cosine model (Meyer *et al.*, 1993).

Different ways for computing k value have been developed. A simple way is to use a single global k value for an entire image, which is used in most previous research (Colby and Keating, 1998; Garcia-Haro *et al.*, 2001; Mitri and Gitas, 2004; Gitas and Deverux, 2006) based on the assumption that the anisotropic nature of reflectance is homogenous over the study area. However, this assumption is not valid because the topographic effects and land-cover variations generate k variation spatially (Bishop and Colby, 2002). In reality, a global k value cannot result in accurate correction for all slopes and aspects (Ekstrand, 1996; Bishop and Colby, 2002) because of differences in topographic impacts on the land surface reflectance. The second approach for k computation is related to land-cover classes, assuming that land covers have strong influences on anisotropic reflectance (Bishop and Colby, 2002; Bishop *et al.*, 2003). Three land-cover classes (snow, vegetation, and non-vegetation) are first classified with an unsupervised method based on the normalized difference vegetation index (NDVI) image. The classes are then used as stratifications, and k values are developed based on each class (Bishop and Colby, 2002; Bishop *et al.*, 2003). A similar approach for computation of multiple k values is based on the stratification of such zones as relative flat regions and mountainous regions (Blesius and Weirich, 2005).

In addition to the Minnaert correction method, other models have also been explored in previous research. For example, the statistical-empirical approach assumes that differential illumination is the same for all cover types and a linear relationship exists between illumination and spectral reflectance (Teillet *et al.*, 1982; Allen, 2000). Teillet *et al.* (1982) introduced an additional adjustment to the cosine function called the C-correction model, which the constant C was used to weaken overcorrection of faintly illuminated pixels. Riano *et al.* (2003) reviewed the major approaches for topographic normalization related to Lambertian and non-Lambertian assumption. A combined correction model of atmospheric and topographic effects (Conese *et al.*, 1993; Sandmeier and Itten, 1997) has been also used for topographic correction, such as the atmospheric and topographic correction (ATCOR) model. A detailed description of this model is provided by Richter (1997).

An evaluation of the topographic correction result is often required in order to understand the performance of the methods which are used for reducing topographic effects. Riano *et al.* (2003) summarized four possible methods, i.e., analysis of changes in spectral characteristics, graphic analysis of reflectance before and after topographic correction, standard deviation for each class, and the accuracy comparison of classification images. Most of previous research in evaluating the topographic correction effects is based on the comparison of classification accuracies between before and after topographic correction. Some research has indicated that topographic correction is helpful in improving classification accuracy (Civco, 1989; Meyer *et al.*, 1993; Tokola *et al.*, 2001), but other research did not show the capability in improving the classification accuracy (Blesius and Weirich, 2005). In reality, many factors may affect the classification accuracy. Thus, classification accuracy is not a good indicator for the evaluation of topographic correction effects (Bishop and Colby, 2002). Another approach is based on semivariogram analysis (Bishop and Colby, 2002; Bishop *et al.*, 2003) based on the assumption that spectral variation within the same land-cover should be reduced after topographic correction.

To date, topographic correction is still a challenge, and no universal approach is available yet. The Minnaert correction method is most frequently used in previous research, but a single global Minnaert value has demonstrated its poor ability in reducing the topographic effects. Another challenge is the assessment of topographic correction results. Hence, the objective of this paper is to develop a pixel-based Minnaert coefficient image for topographic correction of Landsat ETM+ image in a mountainous region in Zhejiang, China, and to explore a texture based approach for evaluation of the topographic correction effects.

Study Area and Dataset

The study area is located in Lin'An County, northwest Zhejiang province, China (Figure 1). The terrain undulates greatly, ranging from a highest elevation of 1,787 m in northwest to a lowest elevation of 9 m in east of Lin'An County. The elevations in northwest and southwest mountainous areas are often greater than 1,000 m, but they are less than 50 m in the plain in the east part of this county. In the selected study area, the highest elevation is 1,580 m with an average value of 360 m. The majority of slope is less than 50 degrees with an average value of 21.5 degree (Figure 2). The complex topographic condition in this study area is ideal for understanding the topographic impacts on land-cover reflectance and for exploring topographic correction methods to reduce the topographic effects.

Digital elevation model (DEM) data with 25 m spatial resolution and a Landsat-7 enhanced Thematic Mapper Plus (ETM+) image (path/row: 119/39), which was acquired on 26 May 2003 cloud-free were used in this research. The solar azimuth and elevation angles were 133.49 and 52.20 degrees, respectively, when the ETM+ image was captured. The ETM+ image was rectified with 37 control points which were collected from 1:50 000 topographic maps. The root mean square error (RMSE) was 0.4802 (x : 0.3447, y : 0.3343) pixels. A nearest-neighbor algorithm was used to resample the ETM+ image into a pixel size of 25 m by 25 m in order to match the spatial resolution of selected DEM data. After geometric rectification, the ETM+ digital numbers were converted to at-sensor reflectance with an apparent reflectance model (Markham and Barker, 1987; Chavez, 1989) in order to eliminate the impacts of sensor instruments and solar zenith angle.

Methods

The Minnaert correction method is frequently used in previous research, and thus is tested in this research. The Minnaert correction model can be expressed as Equation 1:

$$L_H = L_T \cos e / (\cos e \cos i)^k \quad (1)$$

where L_H is the equivalent reflectance on a flat surface with incident angle of zero, L_T is the measured radiance in the remotely sensed data, k is a Minnaert constant, e is slope, and i is the solar incident angle in relation to the normal of a pixel. The cosine of the incident solar angle ($\cos i$), referred to as *illumination*, is calculated using Equation 2 (Holben and Justice, 1980; Smith *et al.*, 1980):

$$\cos i = \cos \theta \cos e + \sin \theta \sin e \cos(\phi_m - \phi_s), \quad (2)$$

where θ and ϕ_m are solar zenith angle and azimuth, and e and ϕ_s are slope and aspect of the terrain. In order to solve k , Equation 1 can be reorganized as Equation 3:

$$\log(L_T \cos e) = \log L_H + k \log(\cos e \cos i). \quad (3)$$

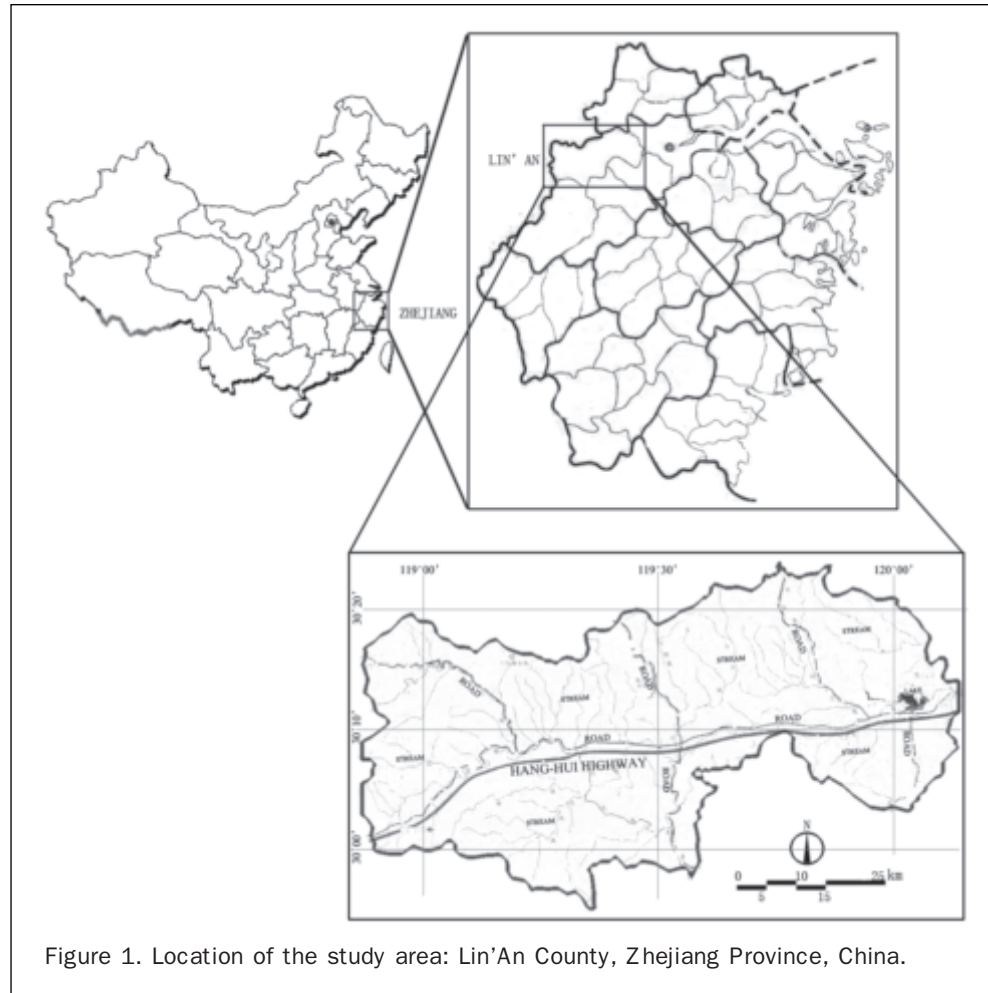


Figure 1. Location of the study area: Lin'an County, Zhejiang Province, China.

This formula indicates that the k value is equivalent to the slope of a regression line. Thus, the k value can be found from the regression analysis for each band based on the selected sample data (Meyer *et al.*, 1993; Jensen, 1996).

Equations 2 and 3 indicate slope, aspect, solar zenith angle, and azimuth are the required parameters used in the Minnaert correction model. The DEM data are used to compute slope and aspect images. The solar zenith angle and azimuth are from the ETM+ metadata. The above four parameters are used to compute illumination ($\cos i$) with Equation 2. The ETM+ image, illumination, and slope images are then stacked into one file. Sample data are extracted at every ten pixels from the entire image on the stacked file. After the samples with slopes less than one degree are removed, a total of 67,008 samples are used for the development of Minnaert coefficients for each band. The selected samples are separated into 10 groups based on slope ranges, as shown in Table 1. Because very limited samples have slopes greater than 50 degrees, the samples with slopes greater than 45 degrees were merged as the tenth group. A regression analysis based on Equation 3 is conducted for each slope group in order to develop the k value for each ETM+ band corresponding to each slope group.

A scatterplot between computed k values and the middle values in the slope ranges is first explored to examine their relationships (Figure 3). Because of the nonlinear relationships illustrated in Figure 3, nonlinear algorithms, such as logarithmic, exponential, and polynomial, are tested where k is used as a dependent variable, and slope as an independent

variable. The coefficient of determination (R^2) is used as an indicator for the selection of best models.

When the slope is less than one degree, no topographic effect on land surface reflectance is assumed; thus, no topographic correction is conducted. When the slope is greater than 50 degrees, no specific k values are developed because of the limited number of samples. So with pixels with slopes of greater than 50 degrees, the k value derived from slope of 50 degrees is used with the consideration of model limitation in extrapolation. After the model for each band is developed, this model is then used to estimate the k image for each band. Equation 1 is finally used to correct the topographic effects for each band.

The evaluation of topographic correction results is conducted based on texture images, which are derived with the homogeneity texture measure and a window size of 5 pixels by 5 pixels for each corrected image. The homogeneity texture measure measures the spectral variation within the selected window size. The higher homogeneity values represent less spectral variation within the window size. Because topographic correction reduces the topographic effects on the surface reflectance, the spectral variation within the same land-cover in the topographic correction result should be decreased. The homogeneity is calculated with Equation 4:

$$\text{HOM} = \sum_{i,j=0}^{n-1} \frac{P_{ij}}{1+(i-j)^2}, \text{ and } P_{ij} = \frac{V_{ij}}{\sum_{i,j=0}^{n-1} V_{ij}} \quad (4)$$

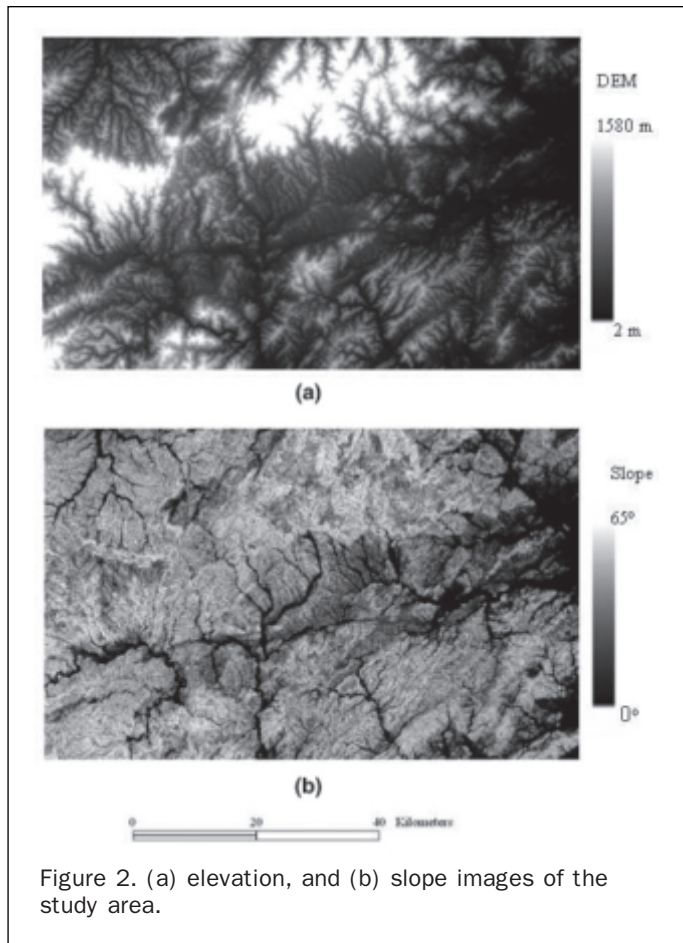


Figure 2. (a) elevation, and (b) slope images of the study area.

where $V_{i,j}$ is the value in the cell i, j (row i and column j) of the moving window, and n is the number of rows or columns.

In order to explore the effects of slope on topographic correction results, a mean homogeneity value for each slope is calculated with Equation 5:

$$M_s = \left(\sum_{i=1}^N HOM_{si} \right) / N \quad (5)$$

where M_s is the mean value of homogeneity at the slope s , and N is the number of samples in the slope s . Higher M_s values indicate more homogenous. A scatterplot illustrating the relationship between M_s and slope is then used to assess

TABLE 1. SUMMARY OF SELECTED SAMPLES FOR EACH SLOPE GROUP

| No. | Slope Range | Median Slope | No. of Samples |
|-----|-------------|--------------|----------------|
| 1 | 1–5 | 2.5 | 3,433 |
| 2 | 5–10 | 7.5 | 4,776 |
| 3 | 10–15 | 12.5 | 6,455 |
| 4 | 15–20 | 17.5 | 8,438 |
| 5 | 20–25 | 22.5 | 10,695 |
| 6 | 25–30 | 27.5 | 10,853 |
| 7 | 30–35 | 32.5 | 9,926 |
| 8 | 35–40 | 37.5 | 7,411 |
| 9 | 40–45 | 42.5 | 3,722 |
| 10 | 45–65* | 47.5 | 1,299 |

Note: *very limited pixels have slopes greater than 50 degrees.

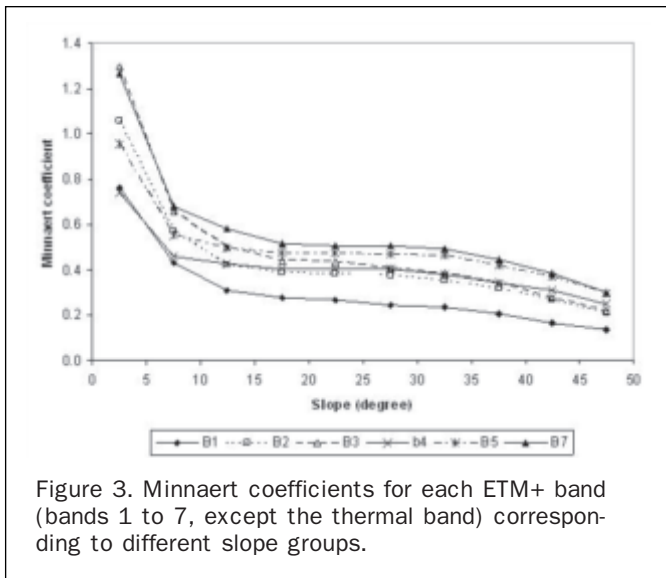


Figure 3. Minnaert coefficients for each ETM+ band (bands 1 to 7, except the thermal band) corresponding to different slope groups.

the topographic correction effects through a comparison of before and after topographic correction images.

Results

The Minnaert k value is wavelength-dependent and related to slopes. As Figure 3 shows, the k value has a similar trend for each band, i.e., the k values decrease as slope increases with nonlinear trends. The k values decrease rapidly in the slope ranges between 1 and 15 degrees, and then gradually become stable when slopes are in the ranges of 15 to 35 degrees, and finally decrease slightly when slopes are greater than 35 degrees. This trend confirms that a single global k value is not suitable for an entire image, especially for the areas with very low or very high slopes, because of different impacts of topographic conditions on the remotely sensed data. Generally, k value increases as wavelength increases, as band 1 has lowest k values and band 7 has highest k values at the same slope.

A comparison of different nonlinear regression models, such as logarithmic, polynomial, and exponential, indicates that the polynomial regression models can successfully simulate the trend of k values as the slope changes for each ETM+ band, which the coefficient of determination (R^2) are greater than 0.99 for each band (Figure 4). Therefore, a pixel-based k image is developed with the polynomial regression model for each band. Figure 5 provides an example of a k image for ETM+ band 5. The flat areas, such as urban, agricultural lands, and water have high k values, but steeper slopes result in lower k values. A lower k value can reduce the topographic effects, especially for those areas with steep slopes. With the developed k image for each band, as well as the images of $\cos e$ and $\cos i$, the topographic correction for each ETM+ band is then conducted with Equation 1. Figure 6 provides part of the study area with color composites (i.e., ETM+ bands 4, 5, and 3 as red, green, and blue) as a comparison of before and after topographic correction. Visual examination of the images indicates that the topographic effects have been significantly reduced with the pixel-based Minnaert correction model.

Figure 7 provides a quantitative evaluation of topographic effects for each ETM+ band through a comparison of the mean homogeneity values between before and after topographic correction. For ETM+ bands 1, 2, 3, and 7, the mean homogeneity values increases gradually as slopes

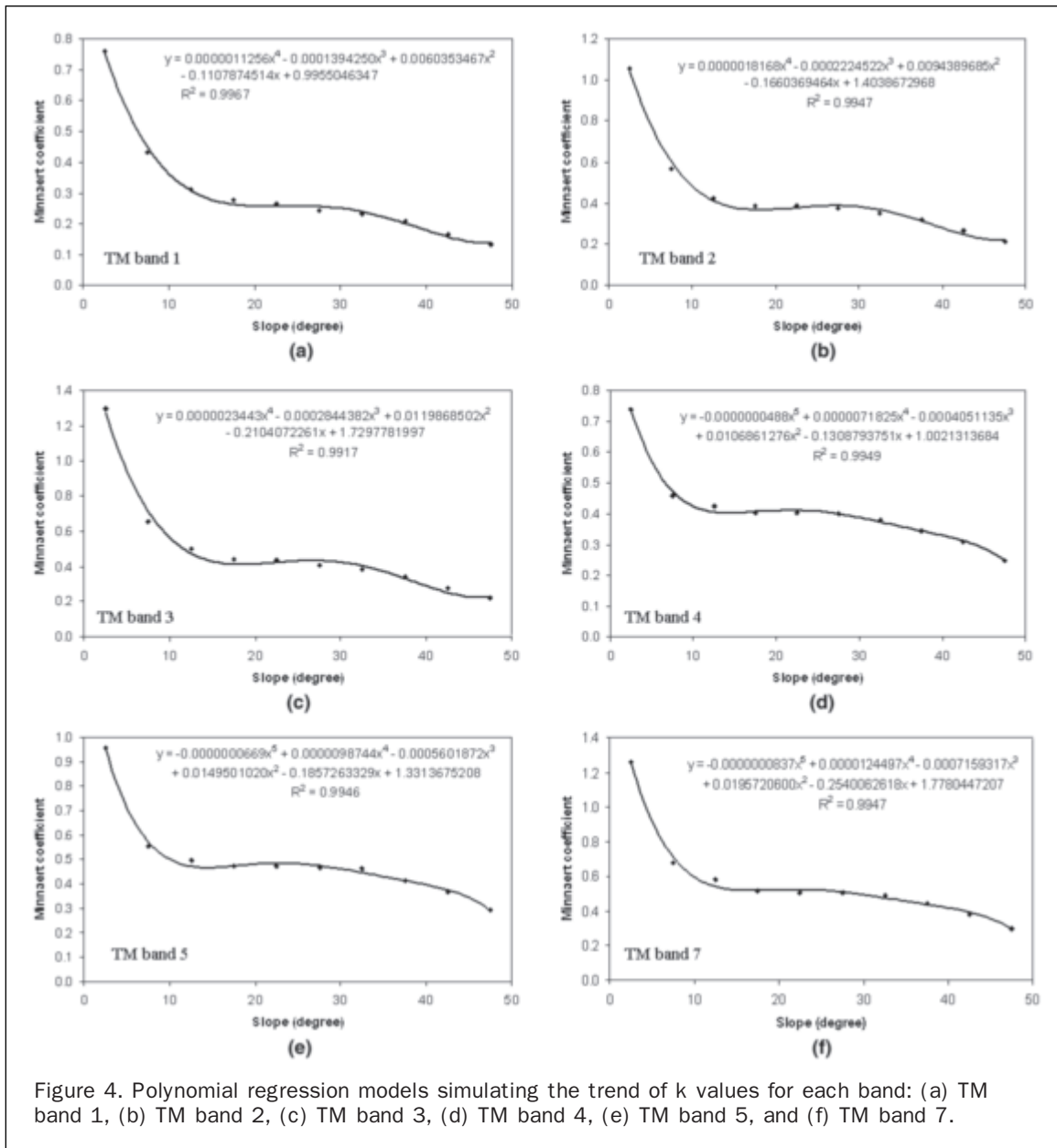


Figure 4. Polynomial regression models simulating the trend of k values for each band: (a) TM band 1, (b) TM band 2, (c) TM band 3, (d) TM band 4, (e) TM band 5, and (f) TM band 7.

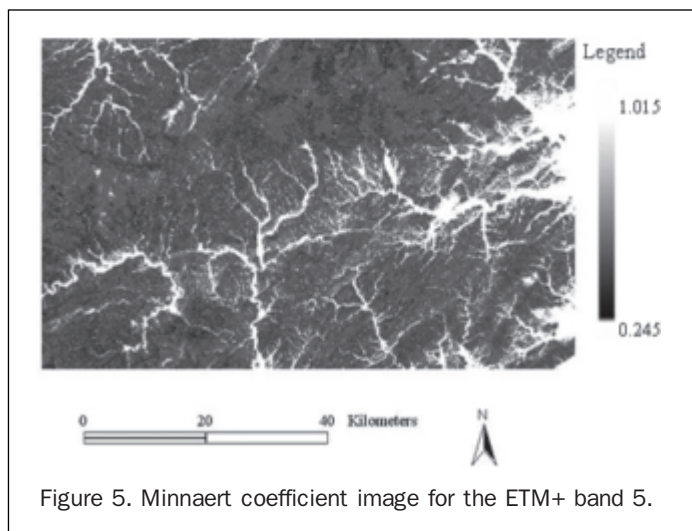
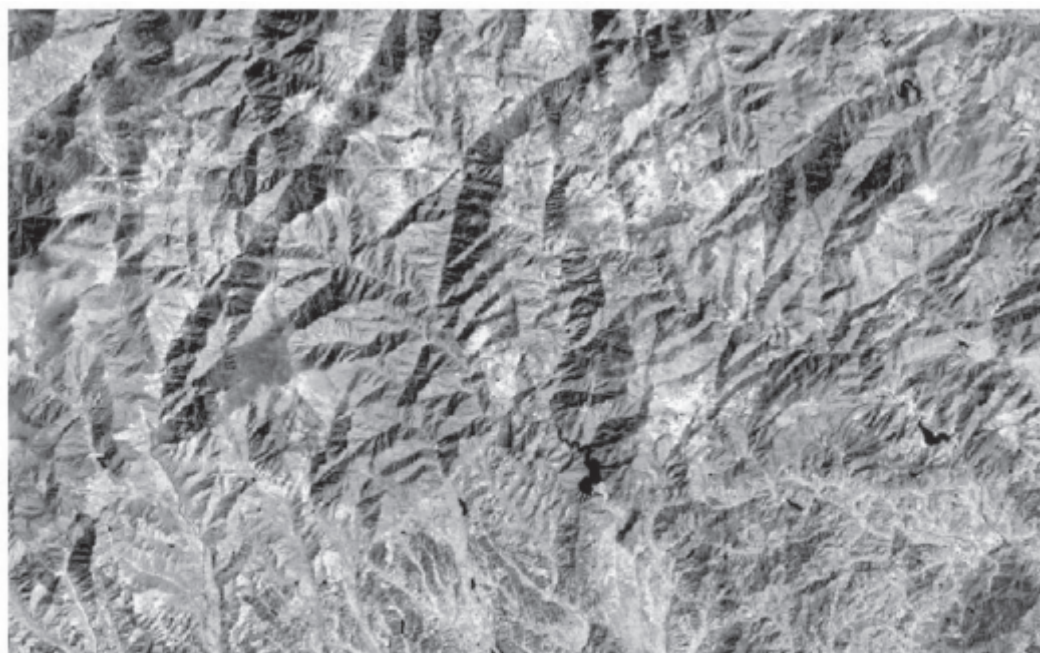


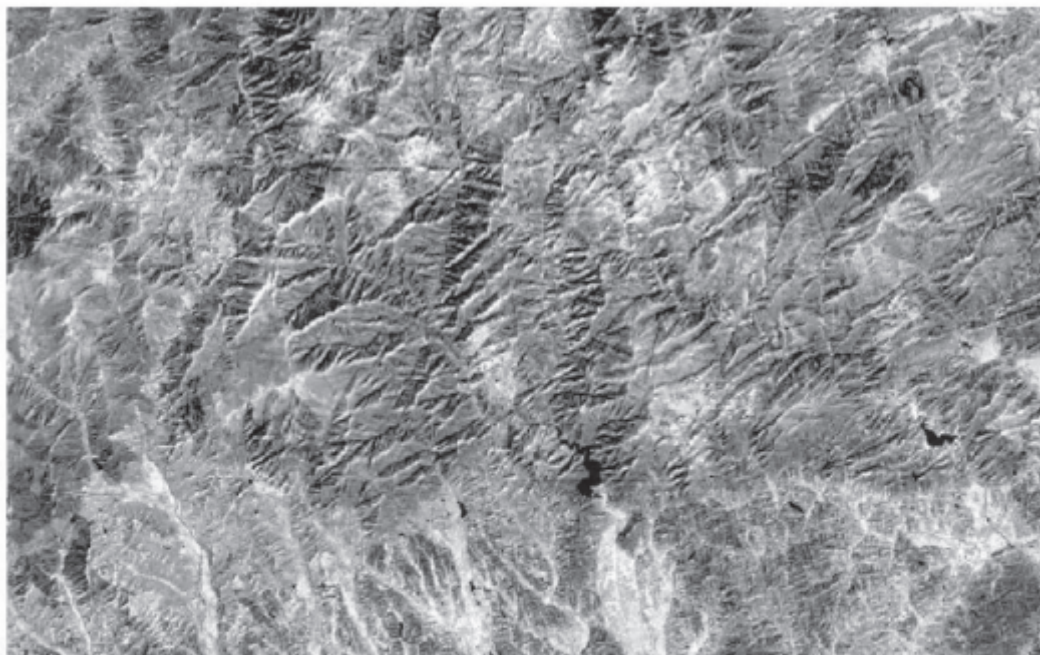
Figure 5. Minnaert coefficient image for the ETM+ band 5.

increase, especially when slopes are less than 30 degrees. The areas with gentle slopes are mainly in residential areas and agricultural lands. These areas are often very complex because of the mixture of buildings, trees, and grasses in residential areas, and different crops or cash trees with small sizes and shapes in agricultural areas. As slopes increase, different types of vegetation dominate in the mountainous areas, thus, the vegetation reflectance becomes more homogenous in these bands. An interesting occurrence is that the mean homogeneity value is somewhat independent of slopes in bands 4 and 5. In gentle slopes, the heterogeneous landscape in residential areas and agricultural lands makes less mean homogeneity values in land-cover reflectance in near-infrared (NIR) and shortwave infrared (SWIR) bands. As slopes increase, different vegetation stand structures and species composition also cause less homogeneity because of the greater reflectance differences in NIR and SWIR images.

A comparison of the mean homogeneity values between before and after topographic correction shows that



(a)



(b)

0 3 6 Kilometers



Figure 6. A comparison of ETM+ images between (a) before, and (b) after topographic correction (bands 4, 5, and 3 as red, green, and blue). A color version of this figure is available at the ASPRS [website: www.asprs.org](http://www.asprs.org).

the mean homogeneity values are higher in the ETM+ bands 1, 2, 3, and 7 after topographic correction than the corresponding bands before topographic correction. This indicates that topographic correction is effective in reducing the topographic influences on the derived apparent

reflectance (thus, also implicitly on derived surface reflectance) because these bands usually have less spectral variations. In contrast, the mean homogeneity values in bands 4 and 5, especially band 4, decreased after topographic correction comparing with the before topographic

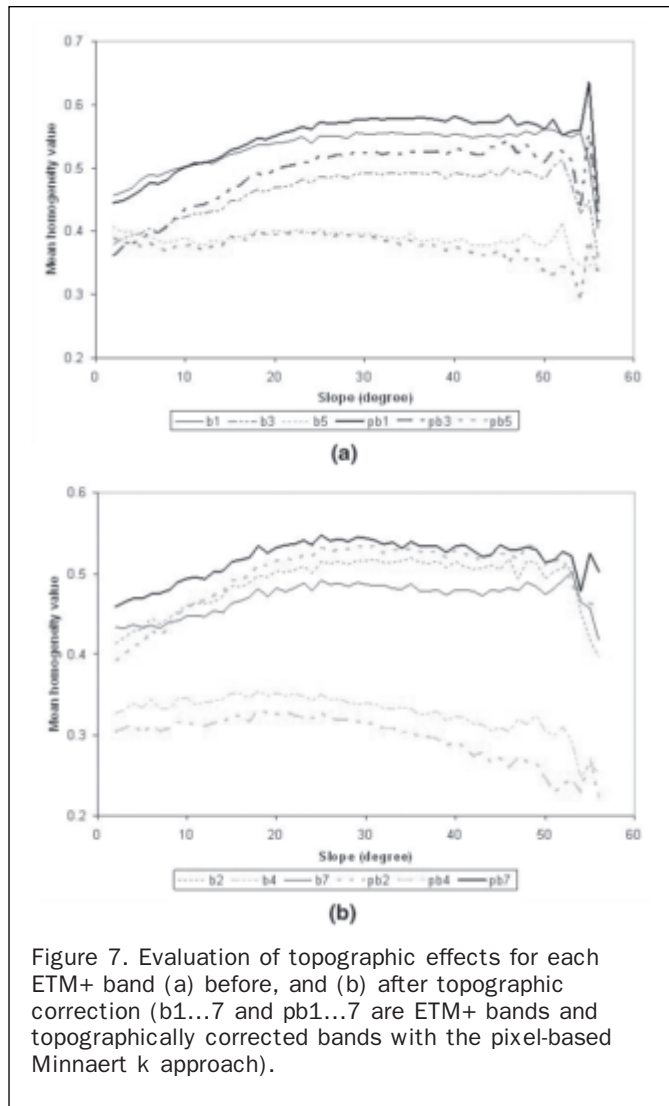


Figure 7. Evaluation of topographic effects for each ETM+ band (a) before, and (b) after topographic correction (b1...7 and pb1...7 are ETM+ bands and topographically corrected bands with the pixel-based Minnaert k approach).

correction image. This is because the topographic impact in gentle slopes (less than 15 degrees) is not an important factor in affecting land-cover reflectance. Thus, topographic correction for gentle slopes does not reduce the heterogeneity in bands 4 and 5. As slopes increase, the impacts of topographic slopes result in reduced vegetation reflectance and decrease the heterogeneity, even between different vegetation types. Therefore, one consequence of the topographic effects in mountainous areas is the difficulty in quantitative analysis of the vegetation types, such as vegetation classification. After topographic correction, the topographic impacts on the vegetation reflectance are decreased, thus highlighting the reflectance differences among different vegetation stand structure and species composition, and resulting in the improvement of classification performance of vegetation types after topographic correction. So the mean homogeneity values after topographic correction are decreased in ETM+ bands 4 and 5. When slopes are greater than 50 degrees, the mean homogeneity values become unstable because the k values with slopes of greater than 50 degrees are replaced with the k value at slope equal to 50 degrees. Higher slopes result in more severe topographic effects on the land-cover reflectance.

Discussion

In the Minnaert correction method, one critical element is to determine the k value. In previous research, a single global k value is the common way used for topographic correction for an entire image. This method is simple and easy to implement, but a single global k value has demonstrated a problem in correcting the topographic effects, especially in those areas with steep slopes, because the k value is dependent on the land-cover class and topographic conditions. Thus, multiple k values corresponding to land-cover classes have been used (Bishop and Colby, 2002; Bishop *et al.*, 2003). However, different topographic slopes have various impacts on the land-cover reflectance. Hence, a single k value corresponding to a land-cover type cannot effectively reduce the topographic effects either. A pixel-based k image, which is developed based on the relationships between k values and slopes, has shown more advantages in improving the topographic correction performance than a single k value or multiple k values. Considering the interactions of k, land-cover, and topographic conditions, the development of a pixel-based k image based on a combination of land covers and slopes may be the future direction in the topographic correction.

The selection of algorithms for development of k values is also important. The polynomial regression analysis used in this research can closely simulate the k trend within the data range, but has problems in extrapolation for the areas with high slopes when the slopes are beyond the range of selected samples. In this case, different models may combine, for example, use of polynomial model for estimation of k values with relative low slopes and use of exponential models for high slopes.

The evaluation of topographic correction results is an important part, but no universal approaches have been used in previous research. Many researchers evaluated the topographic correction success with the assistance of classification accuracies. The improvement of classification accuracy can be attributed to different factors, such as the selected classification algorithm, the image processing procedure used, the complexity of vegetation types and structures, and topographic impacts. An important reason that topographic correction can improve classification accuracy is that topographic correction reduces the topographic effects on the vegetation reflectance, and highlights the differences among different vegetation types or structures. Some previous research for evaluation of topographic correction effects using semivariogram or standard deviation is based on the assumption that topographic correction reduces the spectral variations. This assumption may be true for visible bands, but may be not true for NIR and SWIR images, especially in the vegetated areas with steep slopes and vegetation covers of different types.

Conclusions

Previous research has indicated the drawback of using a single global k value in topographic correction, but no effective approaches have been developed. This research develops a new approach for calculation of a pixel-based k image based on the relationship between k and slope and uses a homogeneity approach to evaluate the topographic correction result. This research has demonstrated the promising in using the pixel-based approach for topographic correction in a mountainous region. The homogeneity-based approach used in this research can be used to explain the topographic effects on the land-cover reflectance. More research is needed to develop the pixel-based k coefficient image for each band based on a combination of land covers and topographic slopes.

Acknowledgments

The authors wish to thank the National High Technology Research and Development Program of China (863 Program: #2006AA12Z109) for the financial support. We also wish to thank three anonymous reviewers for their constructive comments and suggestions.

References

- Allen, T.R., 2000. Topographic normalization of Landsat Thematic Mapper data in three mountain environments, *Geocarto International*, 15:13–19.
- Bishop, M.P., and J.D. Colby, 2002. Anisotropic reflectance correction of SPOT-3 HRV imagery, *International Journal of Remote Sensing*, 23:2125–2131.
- Bishop, M.P., J.F. Shroder Jr., and J.D. Colby, 2003. Remote sensing and geomorphometry for studying relief production in high mountains, *Geomorphology*, 55:345–361.
- Belsius, L., and F. Weirich, 2005. The use of the Minnaert correction for land-cover classification in mountainous terrain, *International Journal of Remote Sensing*, 26:3831–3851.
- Chavez, P.S. Jr., 1989. Radiometric calibration of Landsat Thematic Mapper multispectral images, *Photogrammetric Engineering & Remote Sensing*, 55(11):1285–1294.
- Chavez, P.S. Jr., 1996. Image-based atmospheric corrections – Revisited and improved, *Photogrammetric Engineering & Remote Sensing*, 62(9):1025–1036.
- Civco, D.L., 1989. Topographic normalization of Landsat Thematic Mapper digital imagery, *Photogrammetric Engineering & Remote Sensing*, 55(11):1303–1309.
- Colby, J.D., 1991. Topographic normalization in rugged terrain, *Photogrammetric Engineering & Remote Sensing*, 57(5):531–537.
- Colby, J.D., and P.L. Keating, 1998. Land-cover classification using Landsat TM imagery in the tropical highlands: The influence of anisotropic reflectance, *International Journal of Remote Sensing*, 19:1479–1500.
- Conese, C., M.A. Gilabert, F. Maselli, and L. Bottai, 1993. Topographic normalization of TM scenes through the use of atmospheric correction method and digital terrain models, *Photogrammetric Engineering & Remote Sensing*, 59(12):1745–1753.
- Ekstrand, S., 1996. Landsat TM-based forest damage assessment: Correction for topographic effects, *Photogrammetric Engineering & Remote Sensing*, 62(1):151–161.
- Franklin, S.E., D.R. Connery, and J.A. Williams, 1994. Classification of alpine vegetation using Landsat Thematic Mapper, SPOT HRV and DEM data, *Canadian Journal of Remote Sensing*, 20:49–56.
- Garcia-Haro, F.J., M.A. Gilabert, and J. Melia, 2001. Monitoring fire-affected areas using Thematic Mapper data, *International Journal of Remote Sensing*, 22:533–549.
- Gitas, I.Z., and B.J. Devereux, 2006. The role of topographic correction in mapping recently burned Mediterranean forest areas from Landsat TM images, *International Journal of Remote Sensing*, 27:41–54.
- Gu, D., and A. Gillespie, 1998. Topographic normalization of Landsat TM images of forest based on subpixel sub-canopy-sensor geometry, *Remote Sensing of Environment*, 64:166–175.
- Gu, D., A. Gillespie, J.B. Admas, and R. Weeks, 1999. A statistical approach for topographic correction of satellite images by using spatial context information, *IEEE Transactions on Geoscience and Remote Sensing*, 37:236–246.
- Holben, B.N., and C.O. Justice, 1980. The topographic effects on spectral response from nadir-point sensors, *Photogrammetric Engineering & Remote Sensing*, 46(10):1191–1200.
- Itten, K.L., and P. Meyer, 1993. Geometric and radiometric correction of TM data of mountainous forest areas, *IEEE Transactions on Geoscience and Remote Sensing*, 31:764–770.
- Jensen, J.R., 1996. *Introductory Digital Image Processing: A Remote Sensing Perspective*, Second edition, Prentice Hall, Upper Saddle River, New Jersey, 318 p.
- Jones, A.R., J.J. Settle, and B.K. Wyatt, 1988. Use of digital terrain data in the interpretation of SPOT-1 HRV multispectral imagery, *International Journal of Remote Sensing*, 9:669–682.
- Leprieur, C.E., J.M. Durand, and J.L. Peyron, 1988. Influence of topography on forest reflectance using Landsat Thematic Mapper and digital terrain data, *Photogrammetric Engineering & Remote Sensing*, 54(4):491–496.
- Markham, B.L., and J.L. Barker, 1987. Thematic Mapper bandpass solar exoatmospheric irradiances, *International Journal of Remote Sensing*, 8:517–523.
- Meyer, P., K.L. Itten, T. Kellenberger, S. Sandmeier, and R. Sandmeier, 1993. Radiometric corrections of topographically induced effects on Landsat TM data in alpine environment, *ISPRS Journal of Photogrammetry and Remote Sensing*, 48:17–28.
- Mitri, G.H., and I.Z. Gitas, 2004. A performance evaluation of a burned area object-based classification model when applied to topographically and non-topographically corrected TM imagery, *International Journal of Remote Sensing*, 25:2863–2870.
- Riano, D., E. Chuvieco, J. Salas, and I. Aguado, 2003. Assessment of different topographic corrections in Landsat-TM data for mapping vegetation types, *IEEE Transactions on Geoscience and Remote Sensing*, 41:1056–1061.
- Richter, R., 1997. Correction of atmospheric and topographic effects for high spatial resolution satellite imagery, *International Journal of Remote Sensing*, 18:1099–1111.
- Sandmeier, S., and K.I. Itten, 1997. A physically-based model to correct atmospheric and illumination effects in optical satellite data of a rugged terrain, *IEEE Transactions on Geoscience and Remote Sensing*, 35:708–717.
- Smith, J.A., L.L. Tzeu, and K.J. Ranson, 1980. The Lambertian assumption and Landsat data, *Photogrammetric Engineering & Remote Sensing*, 46(10):1183–1189.
- Teillet, P.M., B. Guindon, and D.G. Goodenough, 1982. On the slope-aspect correction of multispectral scanner data, *Canadian Journal of Remote Sensing*, 8:84–106.
- Tokola, T., J. Sarkeala, and M. van der Linden, 2001. Use of topographic correction in Landsat TM-based forest interpretation in Nepal, *International Journal of Remote Sensing*, 22:551–563.
- Vermote, E., D. Tanre, J.L. Deuze, M. Herman, and J.J. Morcrette, 1997. Second simulation of the satellite signal in the solar spectrum, 6S: An overview, *IEEE Transactions on Geoscience and Remote Sensing*, 35:675–686.
- Walsh, S.J., J.W. Cooper, I.E. von Essen, and K.R. Gallagher, 1990. Image enhancement of Landsat Thematic Mapper data and GIS data integration for evaluation of resource characteristics, *Photogrammetric Engineering & Remote Sensing*, 56(10):1135–1141.

(Received 01 August 2006; accepted 01 February 2007; revised 20 February 2007)

Orthogonal Transformation of Segmented SPOT5 Images: Seasonal and Geographical Dependence of the Tasselled Cap Parameters

Eva Ivits, Alistair Lamb, Filip Langar, Scott Hemphill, and Barbara Koch

Abstract

Brightness, Greenness, and Wetness Tasselled Cap parameters were derived for the SPOT5 sensor. Their robustness through space and time and their discrimination power in land-cover classes was investigated. Four images were acquired from March and September 2003, and in July and November 2004 over Germany. A fifth SPOT5 image was acquired from Cameroon, West Africa in January 2003. The Tasselled Cap parameters were extracted with the Gram-Schmidt orthogonalization technique for each image independently. One set of combined parameters was created for Germany using samples from the four SPOT5 images simultaneously. Each SPOT5 image was transformed into Brightness, Greenness, and Wetness with their own with the combined and the July parameters. Spearman's Rho correlation analysis was carried out between the Tasselled Cap counterparts acquired with the various parameters. Brightness exhibited nearly perfect correlations between the images in Germany; in Cameroon however, the images were inconsistent. Greenness and Wetness displayed a difference of up to 35 percent in November in Germany. The Wetness counterparts in Cameroon exhibited a 7 percent difference. Canonical discrimination analysis revealed that the components from July had the highest discrimination power and that Greenness expressed the highest association to the first canonical axis in all images. In March, July, and November, Brightness was the second most important Tasselled Cap component, in September the Wetness and in Cameroon the Greenness. These results indicate that the Tasselled Cap components are not stable between different seasons and geographical locations. They can be successfully used for land-cover discrimination if the images are transformed with parameters appropriate to the investigated season respective biogeographical zone.

Eva Ivits is with the Joint Research Centre, Institute for Environment and Sustainability, TP 460, Via E. Fermi 1, 21020 Ispra (VA), Italy, and formerly with the Department of Remote Sensing, University of Freiburg, Freiburg, Germany (eva.ivits-wasser@jrc.it).

Alistair Lamb is with Infoterra Ltd, Farnborough, UK.

Filip Langar, Scott Hemphill, and Barbara Koch are with the Department of Remote Sensing, University of Freiburg, Tennenbacherstr. 4, 79106 Freiburg, Germany.

Introduction

History and Spectral Rationale

Multispectral information from remotely sensed imagery provides a tool for the automatic classification of land-use and land-cover types. As the different spectral bands often contain highly correlated information, analyzing imagery using natural or false color may not distinguish the surface features in an optimal fashion (Horne, 2003). Crist and Cicone (1984a) state that the information contained in several discrete spectral bands needs to be on the one hand combined and on the other hand associated with the physical characteristics of landscape features. These priorities can be achieved by (a) understanding the relationships between the spectral bands and scene classes, (b) compressing the spectral bands into a lower number of channels, or (c) extracting physical scene characteristics from the spectral features. Many transformation techniques have been developed to overcome this problem and to distinguish stages of vegetation growth. Richardson and Wiegand (1977), for example, used the infrared and red Landsat channels to extract the Perpendicular Vegetation Index, which is based on finding an orthogonal vector from a "soil line" to a point representing green vigorous vegetation (Jackson, 1983). Wiegand and Richardson (1982) introduced the Soil Line Index, which is based on the location of vegetation points in a two-dimensional diagram of near infrared versus red reflectance.

Kauth and Thomas (1976) demonstrated that on any given date, Landsat MSS data for vegetation and soil would mostly occupy a two-dimensional data plane. The first dimension results from the correlation between the two visible bands, and the second dimension is defined through the correlated two infrared channels (Crist and Cicone, 1984b). The first dimension of the Tasselled Cap transformation, Brightness, is a weighted sum of all the four Landsat MSS channels and is a measure of overall scene reflectance. The transformation makes use of the "soil line" by selecting image points for dark and bright surfaces that will define the line. Greenness, the second dimension, is derived as the vector from the soil line to a dense vegetation image point calculated by the Gram-Schmidt orthogonalization

Photogrammetric Engineering & Remote Sensing
Vol. 74, No. 11, November 2008, pp. 1351-1364.

0099-1112/08/7411-1351/\$3.00/0
© 2008 American Society for Photogrammetry
and Remote Sensing

technique. Greenness contrasts the near-infrared and visible bands, and is a measure of the presence and density of green vegetation (Crist *et al.*, 1986). The third dimension, Yellowness, is orthogonal to both Brightness and Greenness, and is calculated to point towards senescing yellow vegetation. The fourth dimension is derived as an orthogonal vector to the other parameters and was called "Nonsuch" as no scene characteristics were evident in it. The four dimensional Tasselled Cap analysis was adapted to the Landsat TM sensor by Crist and Cicone (1984a). They performed a Tasselled Cap-like transformation of simulated Landsat Thematic Mapper data from a variety of soils and crops at a wide range of development stages. Unlike Kauth and Thomas, they used several principal component analyses instead of the Gram-Schmidt technique and found that the six bands data primarily occupy three dimensions: two of them are analogous to the MSS Tasselled Cap features Brightness and Greenness, and the Third component related to soil features including moisture status. This later component was called Wetness as Christ and Cicone (1984a) expanded the transformation to real Landsat TM datasets. Later, field observations and laboratory measurements conducted by Crist and Cicone (1984b) proved the sensitivity of the third component to wet surface conditions. Wetness contrasts the shortwave-infrared and near-infrared reflectance by providing a measure of soil moisture content, vegetation density, and improved delineation between fields that are greening up and those that are senescing. The last three Tasselled Cap dimensions have proven to be less important and will not be discussed further here.

Applications and Problems

The Tasselled Cap transformation has received acceptance in the scientific community. This is partly due to the effectiveness of the first two dimensions to typically capture 95 percent of the total variability in the visible and near infrared spectrum. On the other hand, the features can be directly correlated to physical characteristics of agricultural fields (Crist and Cicone, 1984a) and other land-cover classes. Cohen and Spies (1992), for instance, showed that the three Landsat TM Tasselled Cap features capture the majority of variations associated with forest conditions. Furthermore, Cohen and Spies (1992) and Fiorella and Ripple (1993) showed Wetness to be valuable for discrimination within closed forest canopies conditions. Additionally, Wetness proved to be independent of topographic variation. Cohen *et al.* (1995) could differentiate between the maturity and structure of closed conifer forest stands using Landsat TM Wetness. The Greenness/Wetness projection provides clear separation between forest/natural vegetation and cultivated vegetation scene classes, while the Brightness/Greenness feature space is often used to separate coniferous from deciduous stands (Crist *et al.*, 1986). As these classes are difficult to determine with original image channels, the use of Tasselled Cap features in image classification has reached widespread use. An advantage of Tasselled Cap features over spectral indices such as the NDVI is that the latter only uses a subset of the original channels, which results in the loss of spectral information. Cohen *et al.* (1995) reported that as much as 50 percent of the spectral information from the original Landsat TM channels is lost during the computation of an NDVI. Furthermore, noise due to soil background influences the detection of sparse vegetation cover resulting in NDVI values up to 0.3 for non-vegetated areas (Price, 1993).

Newer attempts are generally focused on the transformation of spectral data into more specific estimates of biophysical variables like the Leaf Area Index (LAI), Fraction of Absorbed Photosynthetically Active Radiation (FAPAR), Green

Vegetation Fraction (GVF), and moisture content. For the derivation of biophysical parameters however, long-term (in some cases over 20 years) remote sensing data are needed because long-term changes in vegetation phenology must be taken into account. This calls for the application of Time Series data with very high temporal resolution, which is only available on coarse spatial resolution (1 km) like the NOAA AVHRR satellite imagery. For the estimation of the LAI for instance, multi-temporal NDVI observations are needed because the maximum NDVI value in the season will correspond to the maximum LAI of vegetation cover (Justice, 1986). The absorption of the photosynthetically active radiation follows seasonal changes of some combinations of plant reflectance (Hipps *et al.*, 1983), and thus, multi-temporal satellite images for several years are needed for the estimation of its magnitude. Also, the GVF is derived from NDVI using a linear relationship with the assumption of dense vegetation (Gutman and Ignatov, 1997), and thus, the observation of seasonal variability is indispensable. Local scale phenological studies and habitat mapping exercises using biophysical variables are therefore not possible up to date, which explains the still great interest for the Tasselled Cap transformation of SPOT5 data.

However, some problems may arise when applying Tasselled Cap parameters to multi-temporal satellite images. First, changes in illumination geometry and variations in the composition of the atmosphere influence the magnitude of ground-leaving radiance, meaning that satellite-recorded radiances from a constant surface target will vary (Mather, 2004). Considering the soil line with its changing slope, the direction of the orthogonal vector to the green image point will also change. Thus, both Greenness and Brightness will be dependent on the reflectance properties of soils, and the soil line will be a mixture of the reflectance of different soils and atmospheric path radiance conditions (Jackson, 1983). For this reason, applying digital number (DN) based Tasselled Cap parameters is also problematic making it difficult to differentiate bright soil pixels from dark green pixels (Huang *et al.*, 2002). One solution to these problems is proposed by Huang *et al.* (2002), who suggest an at-satellite reflectance-based approach rather than digital number DN-based Tasselled Cap transformation of Landsat ETM images. This solves the problem of changing sun illumination geometry, which would otherwise strongly affect the DNS.

Secondly, it is often claimed that once the data have been normalized for haze level and viewing/illumination geometry, the Tasselled Cap features are consistent between different scenes (e.g., Crist and Cicone, 1984a). However, the extraction of MSS Tasselled Cap parameters was based on a small sample of North American soils and agricultural areas (Fayette County, Illinois). Field spectrometry measurements of crops and laboratory measurements of soil samples were initially used to extract the TM Tasselled Cap parameters, which were calibrated using subsets of Landsat TM data over Arkansas, Tennessee, Iowa, and North Carolina. As mentioned earlier, the slope of the soil line will be dependent on the type of soils sampled, as well as on their wet and dry condition. Depending on the slope of the line, the distance and angle to the dense vegetation image point will also change. Mather (2004) states that the application of the Tasselled Cap transformation parameters to agricultural areas in other parts of the world may not be successful if the defined Brightness axes do not correspond to the reflectance characteristics of soils in the North American calibration area. Crist and Cicone (1984a) state that, aside from atmosphere and illumination geometry, substantial deviation from a mid-latitude temperate environment will also affect Tasselled Cap parameters. It is also questionable as to

whether the dense vegetation image point behaves similarly when vegetation is sampled at different growth stages or from different biogeographical locations.

This paper attempts to address the above-mentioned problems by extracting SPOT5 Tasselled Cap parameters and testing their stability through space and time. Verdin *et al.* (1987) extracted Tasselled Cap parameters for the SPOT1 sensor while da Silva (1991) developed parameters for the SPOT2 satellite. These instruments are equipped with the HRVIS (High Resolution Visible Imaging System) sensor utilizing two visible bands and one near infrared band resulting in the Brightness, Greenness, and Yellowness parameters. The SPOT5 satellite is equipped with the HRVIR (High Resolution Visible Infrared) sensor, which includes a fourth band in the short wave infrared spectrum. Because of the different bands, the Tasselled Cap parameters derived for previous SPOT sensors cannot be applied and thus new parameters need to be extracted. The SPOT5 data are used in this study, because it is the first of the high-resolution satellites to truly balance large scene sizes with highly detailed imagery and with coverage of vast territories. Also, SPOT5 data are compatible with regular mapping standards and are indispensable tools for agriculture, urban planning, forest management, disaster management, and water resources. Furthermore, the SPOT5 bands in the visible and short-wave infrared portions of the spectrum are identical to those on the SPOT4 sensor, thus the derived Tasselled Cap parameters will also be applicable there.

Materials and Methods

SPOT5 Images Used and the Extraction of Tasselled Cap Parameters

Five SPOT5 images were acquired for the purposes of this analysis (Table 1). The four images of Germany were especially selected to cover a range of land-use features, including artificial surfaces, water, bare soil, agricultural, and forested areas from March, July, September, and November. The images from March and November are located in Schleswig-Holstein and mostly cover agricultural areas with some forest patches dominated by deciduous trees. The November image covers a very flat area and has almost no variation in topography. The July image is located in Thuringia and covers mostly agricultural areas with some deciduous forest patches. The SPOT5 image from September partly covers the area of Thuringia forest with mostly coniferous trees and patches of agricultural areas. This area is dominated by strong topography, with elevation differences of approximately 1,000 m. The Cameroon scene mostly covers vegetated areas (lowland tropical and mangrove forest and palm plantation) and part of the Gulf of Guinea of the Atlantic.

The Tasselled Cap parameters derived from the SPOT5 images are named Brightness, Greenness, and Wetness corresponding to the Landsat TM derivatives, as the corresponding channels occupy similar regions in the electromagnetic spectrum. Extraction of the Brightness and Greenness features is relatively straightforward, as Crist and

TABLE 1. DESCRIPTION OF THE SPOT5 IMAGES

| Notation | Location | Date of acquisition |
|----------|-----------------------------|---------------------|
| GER0303 | Schleswig-Holstein, Germany | 21 March 2003 |
| GER0704 | Thuringia, Germany | 07 July 2004 |
| GER0903 | Thuringia, Germany | 11 September 2003 |
| GER1104 | Schleswig-Holstein, Germany | 07 November 2003 |
| CAM0103 | Cameroon, Africa | 30 January 2003 |

Gicone (1984a) proved that the Vegetation and Soil Plane of TM Tasselled Cap are equivalent to the MSS Tasselled Cap Brightness and Greenness features. Extraction of the Wetness rather than the Yellowness component, however, requires some explanation. Stoner and Baumgardner (1980) proved that the third component of the TM Tasselled Cap is sensitive to soil moisture by showing the sensitivity of the middle infrared channel to soil moisture conditions. The third component of TM Tasselled Cap was called Wetness because it contrasts middle infrared reflectance with near-infrared (NIR) and visible reflectance. As SPOT5 images also contain a middle infrared band, and as the corresponding image channels are comparable to Landsat TM bands, the third Tasselled Cap component of a SPOT5 image should also become Wetness instead of Yellowness.

The digital numbers of the images were transformed to radiance values according to the reference information from Spotimage (Spotimage, 2004). Radiance values were converted to at-satellite reflectance based on the method presented by Markham and Barker (1986). The images were segmented using the software program eCognition® (Baatz and Schäpe, 2000) in order to obtain small and homogeneous clusters of pixels. Representative samples of bare soil, green vegetation, and water objects were selected to guide the Tasselled Cap Brightness, Greenness, and Wetness transformation, respectively. The samples were considered representative as being well distributed along the image and were chosen so that at least 10 percent of the segmented objects were selected. To obtain Brightness, two sets of soil segments considerably differing in reflectance values were selected: bright soils (X_{sb}) and dark soils (X_{sd}). First, the mean of the bright and dark soil values were differenced for each of the image bands (n) to acquire the image points b_i :

$$b_i = (\overline{X_{sb}} - \overline{X_{sd}})_i, i = 1 \dots n.$$

The Brightness coefficients (BRC_i) were acquired by dividing each of the vector components (b_1, b_2, \dots, b_n) by the normalization factor B , where:

$$B = \sqrt{\left(\sum_{i=1}^n b_i^2\right)}, n = \text{number of image bands, and } BRC_i = \frac{b_i}{B}.$$

The Brightness image (BRI) was then extracted by the linear transformation of the SPOT5 image bands (X_i) with the BRC_i :

TABLE 1. TECHNICAL DATA OF THE SPOT5 SATELLITE

| | green | red | nir | swir | pan |
|------------------|-----------------------------------|-------------------------|-------------------------|-------------------------|-------------------------|
| Wavelength | 0.50–0.59 μm | 0.61–0.68 μm | 0.78–0.89 μm | 1.58–1.75 μm | 0.49–0.69 μm |
| Resolution | 10m | 10m | 10m | 10m | 2.5m |
| Swath | | | 60 km | | |
| orbit | circular, sun-synchronous, 832 km | | | | |
| off-track | ± 27 degrees | | | | |
| viewing | | | | | |
| Launch | 04 May 2002 | | | | |
| Revisit interval | 5 days in oblique view | | | | |

$$BRI = \sum_{i=1}^n BRC_i * X_i.$$

For the extraction of the Greenness component, dense vegetation segments were selected in the SPOT5 images and their mean values were calculated for each band ($\bar{X}_{g,i}$). The NDVI was computed and was used as reference data for the collection of representative samples. The green vegetation and bright soil image points were then differenced for each SPOT5 band and subsequently the Gram-Schmidt orthogonalization was carried out by:

$$g_i = (\bar{X}_g - \bar{X}_{sb})_i - D_g * BRC_i, \text{ where}$$

$$D_g = \sum_{i=1}^n (\bar{X}_g - \bar{X}_{sb})_i * BRC_i.$$

This procedure ensures that the vector (g_1, g_2, \dots, g_n) is orthogonal to the soil line vector (b_1, b_2, \dots, b_n), (Jackson, 1983). The Greenness coefficients GRC_i for each SPOT5 band were then calculated by applying the normalization factor G to each of the components of g_i :

$$G = \sqrt{\sum_{i=1}^n g_i^2}, \text{ } n = \text{number of image bands, and } GRC_i = \frac{g_i}{G}.$$

The Greenness image (GRI) was then extracted by the linear transformation of the SPOT5 image bands (X_i) with the GRC_i :

$$GRI = \sum_{i=1}^n GRC_i * X_i.$$

The Wetness image was extracted following the method described above, where the vector towards the wetness image point was orthogonalized to both Brightness and Greenness. See the paper by Jackson (1983) for a more detailed description of the algorithm. The extracted Brightness, Greenness, and Wetness coefficients were tested against orthogonality by calculating the dot products of the coefficients. For instance, for the Brightness and the Greenness coefficients for the equation

$$\sum_{i=1}^n BRC_i * GRC_i = 0$$

needed to be fulfilled.

The Tasseled Cap parameters were extracted from each image individually, and thus five sets of parameters were obtained.

Analysis of the Robustness of Tasseled Cap Parameters

A sixth set of Tasseled Cap parameters was extracted combining image points of the four SPOT5 images of Germany. In order to establish the average soil line, the mean value of bright and dark soil objects was calculated from the four images. The resulting Brightness parameter is equivalent to the average value from soils with different wet and dry conditions. Similarly, the image points of Greenness and Wetness were obtained by averaging the segment values for dense vegetation and water surfaces through the four SPOT5 images, respectively. Using these combined parameters, new Tasseled Cap images were calculated from the four SPOT5 scenes of Germany. The original Brightness, Greenness, and Wetness images were correlated with their counterparts derived from the combined parameters. As in the literature, the Tasseled Cap transformation is often reported useful for classifying different vegetation surfaces, one might assume that Tasseled Cap parameters should only be calculated from imagery acquired during the vegetation period. How representative would these parameters be when applying them to images from other seasons? To answer this question, Tasseled Cap

parameters extracted from the SPOT5 image of July were applied to the March, September, and November images of Germany, and the resulting components were correlated with the original components. In order to test the geographical dependency of the Tasseled Cap parameters, the July and the combined parameters were applied to the SPOT5 image from Cameroon. These images were also correlated with the original Tasseled Cap components from Cameroon. All the Tasseled Cap images were segmented to obtain homogeneous clusters of pixels for the correlation analysis. The mean value of the Brightness, Greenness, and Wetness images, respectively, were calculated within each segment. From each Tasseled Cap image 900 random segments were selected by means of a random number generator. The corresponding Brightness, Greenness, and Wetness values of the segmented objects were correlated by means of Spearman-Rho correlation, as neither the variables nor their logarithm were normally distributed and thus a parametric test was not applicable. The Spearman-Rho (ρ) is a product-moment correlation coefficient that is used when the observations are ranked on both variables and is calculated as:

$$\rho = 1 - \frac{6 \sum d^2}{n(n^2 - 1)} \text{ where } n = \text{number of paired ranks, and } d = \text{difference between the paired ranks.}$$

The above-mentioned random segments were attributed to the water, forest, other vegetation (represented by dense agricultural crops and pastures), and bare soil classes in each Tasseled Cap image of Germany. In the Cameroon image, the 900 random segments were associated with water, palm plantation, mangrove forest, lowland tropical forest, and bare soil features. For the visual interpretation of the land-cover aerial photos were used. Canonical Discriminant Analysis (CDA) was applied in order to test the usefulness of the Tasseled Cap images in differentiating the major land-cover classes. The CDA maximizes the among-group variance explained by each canonical variates. A set of canonical discriminant functions (canonical variates) are derived, multiple axes that separate sets of groups. Canonical discriminant functions fit the equation:

$$Z_1 = a_{11}x_1 + a_{12}x_2 + a_{13}x_3 + \dots + a_{1n}x_n$$

where the "a" values are coefficients derived from Eigenanalysis of the matrix of between group variation, x_i devotes the image bands, and the Z values are scores (coordinates) along the derived axis. The Brightness, Greenness, and Wetness components entered the CDA models stepwise, based on the Monte Carlo permutation test with 999 permutations. The discriminative power of the models was tested with the percentage of variance in the samples that the first three canonical axes explained together. The significance of the axes was tested again with the Monte Carlo permutation test with 999 permutations. The discrimination power of the individual Tasseled Cap components was measured by the inter-set correlations of the components to the axes. The land-cover classes were plotted in the two-dimensional feature space of the first two discriminant axes in order to visualize the achieved separation among the groups and their association to the Tasseled Cap components.

Results

Properties of the Tasseled Cap Images

All spectral bands had positive loadings on the Brightness component, independent of the season or geographical position (Figure 1 and Appendix, Table 2). However, depending on the season and geographic location different

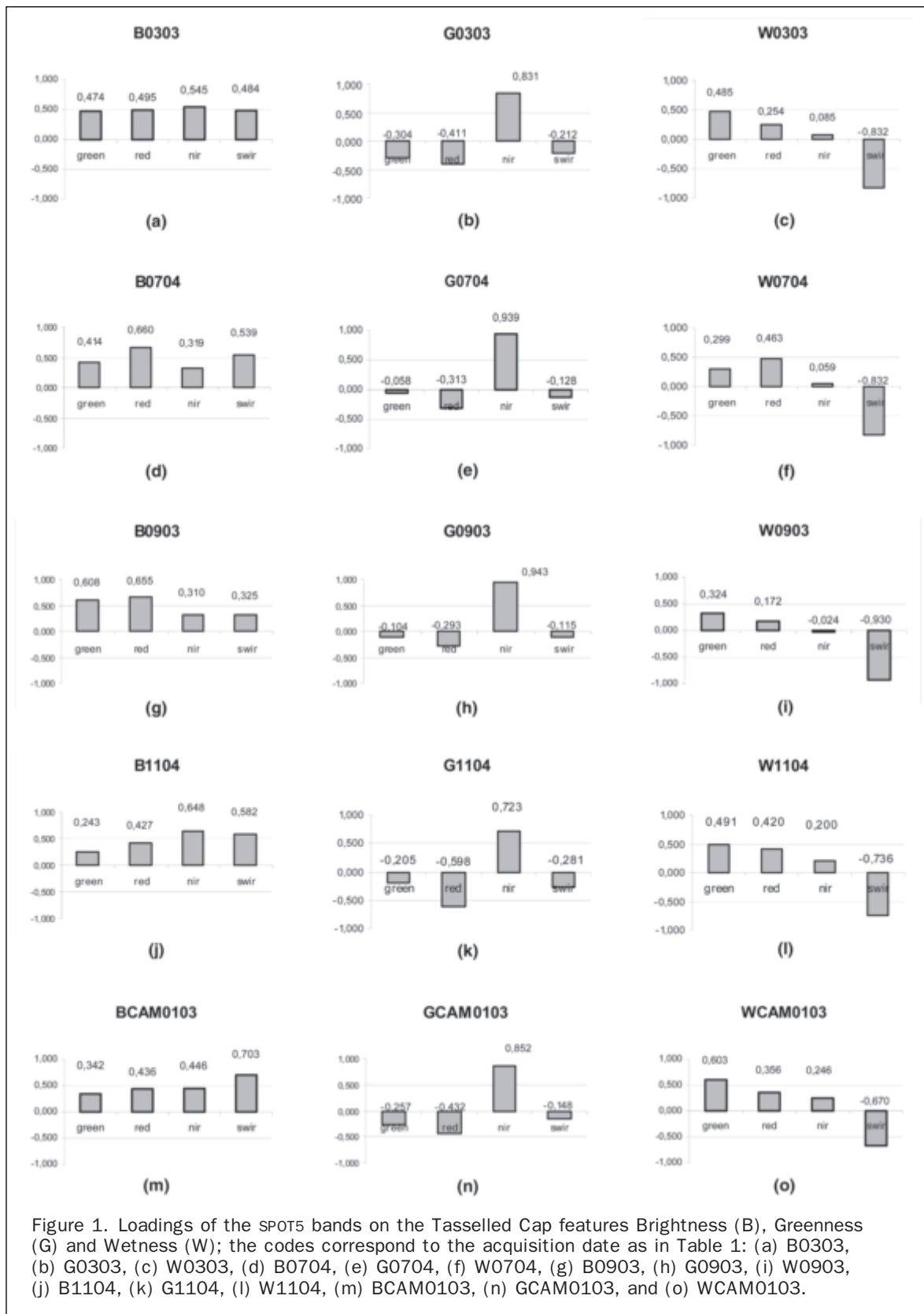


TABLE 2. TASSELLED CAP PARAMETERS (LOADINGS ON THE COMPONENTS) FOR THE SPOT5 IMAGES

| MARCH, GER0303 | | | | |
|---------------------|--------|--------|--------|--------|
| | GREEN | RED | NIR | SWIR |
| Brightness | 0,474 | 0,495 | 0,545 | 0,484 |
| Greenness | -0,304 | -0,411 | 0,831 | -0,212 |
| Wetness | 0,485 | 0,254 | 0,085 | -0,832 |
| JULY, GER0704 | | | | |
| | GREEN | RED | NIR | SWIR |
| Brightness | 0,414 | 0,660 | 0,319 | 0,539 |
| Greenness | -0,058 | -0,313 | 0,939 | -0,128 |
| Wetness | 0,299 | 0,463 | 0,059 | -0,832 |
| SEPTEMBER, GER0903 | | | | |
| | GREEN | RED | NIR | SWIR |
| Brightness | 0,608 | 0,655 | 0,310 | 0,325 |
| Greenness | -0,104 | -0,293 | 0,943 | -0,115 |
| Wetness | 0,324 | 0,172 | -0,024 | -0,930 |
| NOVEMBER, GER1104 | | | | |
| | GREEN | RED | NIR | SWIR |
| Brightness | 0,243 | 0,427 | 0,648 | 0,582 |
| Greenness | -0,205 | -0,598 | 0,723 | -0,281 |
| Wetness | 0,491 | 0,420 | 0,200 | -0,736 |
| COMBINED PARAMETERS | | | | |
| | GREEN | RED | NIR | SWIR |
| Brightness | 0,492 | 0,610 | 0,416 | 0,462 |
| Greenness | -0,196 | -0,389 | 0,896 | -0,084 |
| Wetness | 0,397 | 0,260 | 0,118 | -0,872 |
| CAMEROON, CAM0103 | | | | |
| | GREEN | RED | NIR | SWIR |
| Brightness | 0,342 | 0,436 | 0,446 | 0,703 |
| Greenness | -0,257 | -0,432 | 0,852 | -0,148 |
| Wetness | 0,603 | 0,356 | 0,246 | -0,670 |

channels gained importance on the components. In Germany, the near-infrared (NIR) channel contributes the most to the Brightness component in the March and November scenes, while the red channel is the most important in the high vegetation period of July and September (see the loadings). On the contrary, the short wave infrared (SWIR) band has the highest loading on Brightness in the Cameroon image. The importance of the green spectral band is the lowest in March and November in Germany and in Cameroon but is one of the highest in September. Regarding the extracted Brightness image, bare soil patches become very bright, grassland is displayed with light grey tones and forested areas appear very dark (Figure 2). The July and September images differentiate between different grassland and forest surfaces, while the images from March and

November express significantly less contrast. Water features are very dark in the Cameroon image, and also wet mangrove forest exhibits low spectral values. Lowland tropical forests are displayed with much brighter grey tones than forested landscape patches in Germany, while bare soil is very bright due to the dominance of the SWIR band.

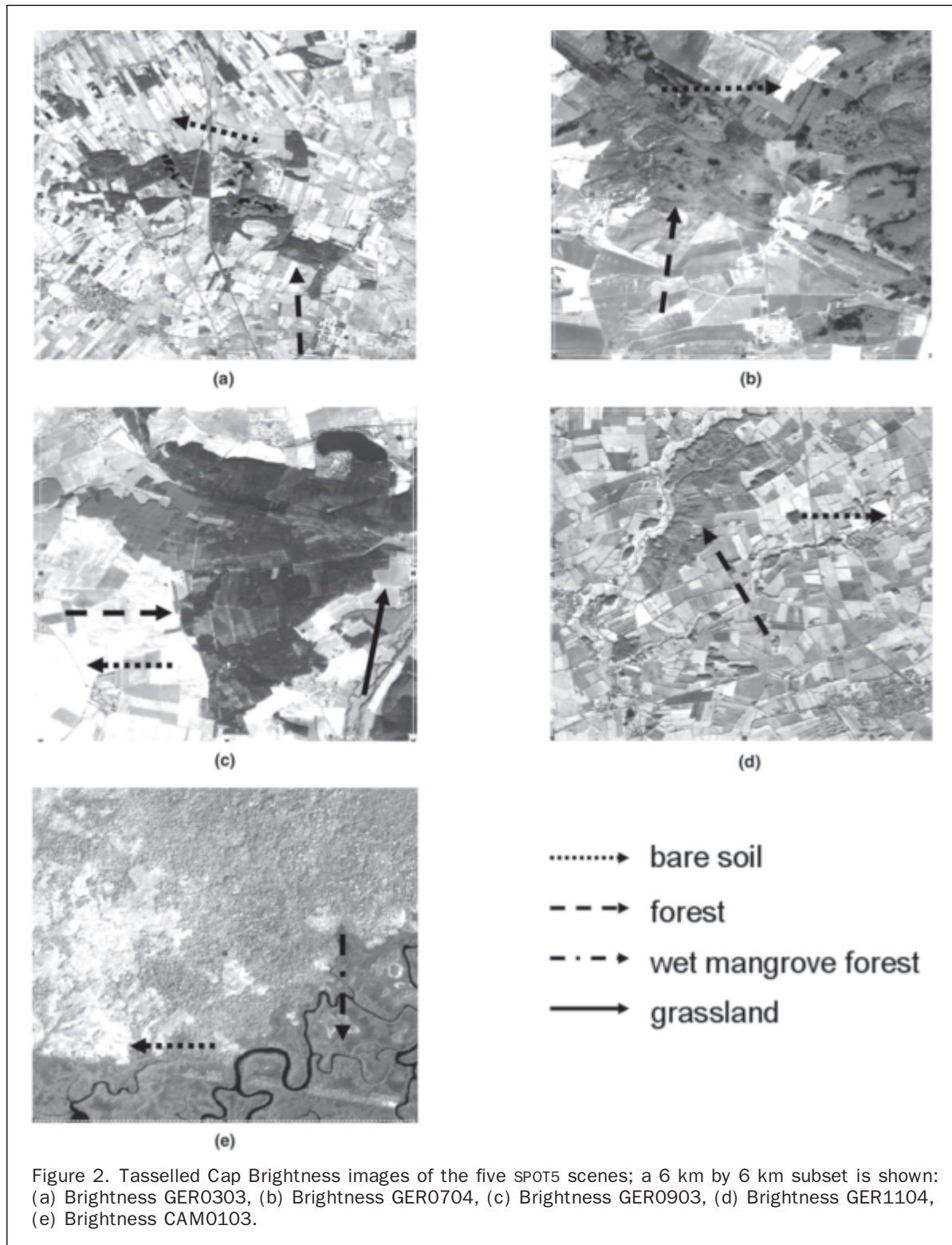
The loadings of the green, red, NIR, and SWIR bands on the Greenness component follow the same pattern in all images, independent on the seasonal or on the geographical differences (Figure 1). There is a strong contrast between the positive NIR and the negative visible and SWIR loadings, due to the high reflectance of green vegetation in this spectral range. The red channel loads higher (negatively) on Greenness than the green or SWIR bands. The Greenness image (Figure 3) exhibits high contrast between areas with and without vegetation. Water and bare soil areas are displayed with dark tones, while vegetation appears bright and white. The different grassland types are well distinguished in all seasons, however, coniferous (dark grey) and deciduous forest (bright grey) stands are only well defined in July and September. Wet mangrove and lowland tropical forests are the most clearly distinguishable land-cover features in the Cameroon Greenness image.

The SWIR band exhibits a high contrast to the visible and NIR channels in the Wetness component and has the highest and negative loading in all images. In the German March, September, and November and in the Cameroon scenes, the green channel has the highest positive loading while the loadings of the red and NIR channels are consecutively less. On the other hand, in July the red channel has the highest positive loading. While the loading of the near-infrared channel is very low in March, July, and September, it is moderate in November and in the Cameroon image. Clearly distinguishable land-cover features in the Wetness image (Figure 4) are water/wet surfaces and coniferous/deciduous vegetation types. Water surfaces appear white, wet mangrove forest and wet soils bright grey. Coniferous forest stands are very bright in September and July, and have darker grey tones in March and November. The deciduous forest patches are dark in July and September. Bare soil surfaces are very dark in March, July, and September, and become brighter in November.

Correlation Between the Tasseled Cap Components

Correlation coefficients of the Tasseled Cap images calculated with the original and the combined parameters from the German images are presented in Table 2. The original Brightness images exhibit a consistently high correlation with the Brightness images calculated through the combined parameters. The samples chosen for the correlation analysis stretch out in one line for March, July, and September, but exhibit some scatter in November (see Figure 1 in the Appendix). The Greenness counterparts for July and September are equal, and are very similar in March. In November however, almost 20 percent difference can be observed between the Greenness counterparts. The samples indicate some inconsistency between the images in March and a high number of outliers in November. The Wetness counterparts are almost equal in March and September, and are very similar in July, although here the samples are not positioned perfectly in one line. The original and the combined Wetness images only correlate 71 percent in November, and the scatter plot indicates a large number of outlier samples.

Table 3 presents the correlations between Tasseled Cap images calculated with the original and the July parameters. The correlation of Brightness is constantly high across all seasons, although in November the samples become slightly scattered (Appendix, Figure 1). The Greenness counterparts



of September are perfectly correlated, but the correlation between the Greenness pairs in March is somewhat lower and the scatter plot displays outliers. On the other hand, the corresponding Greenness components from November exhibit a correlation coefficient of only 0.654, and the scatter plot displays a large number of outlier samples. This reflects the seasonal dependency of the Tasseled Cap Greenness

parameter, which is to be expected, as Greenness is a strong indicator of vegetation vigor. Equal information content can be observed between the Wetness components from March, and in September the images are very similar although the samples scatter. In November nevertheless, there is only a 76 percent similarity between the Wetness counterparts and the scatter plot displays numerous outlier samples.

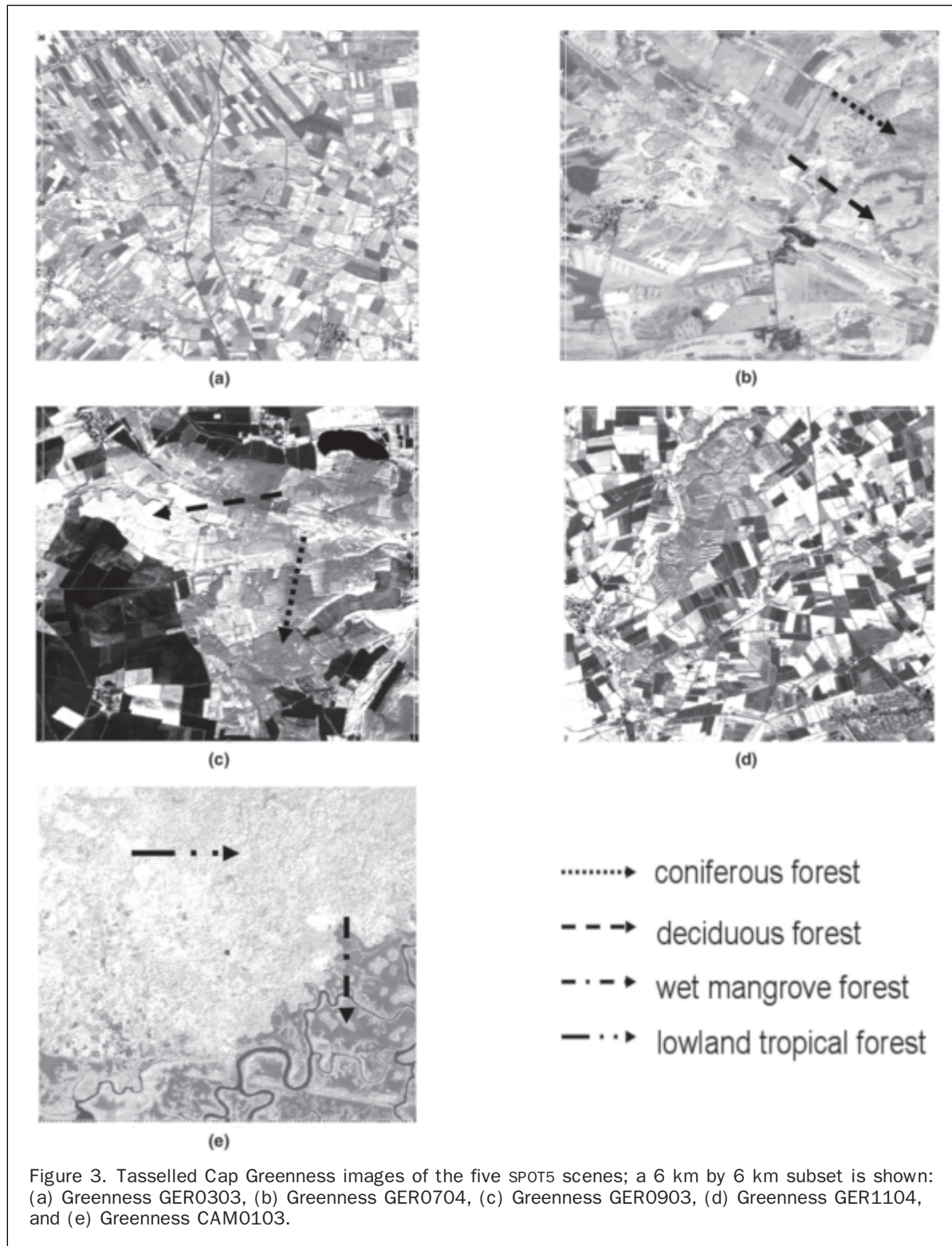


Table 4 presents correlation coefficients comparing the Tasseled Cap features from the Cameroon images calculated with the original, the combined, and the July parameters. The original Brightness image exhibits the same high correlation with the images calculated with the combined and the July parameters (0.959 and 0.952, respectively). On the other hand, the scatter plots indicate some inconsistencies between the samples in both cases.

The Greenness component exhibits 98 percent correlation with the aggregated parameter, the correlation with the July parameter is somewhat lower (0.94) with many outliers. The Wetness image correlates similarly with the images calculated through the combined and through the July Tasseled Cap parameters (0.93 and 0.95, respectively). The scatter plots of these two correlations exhibit numerous outlier samples.

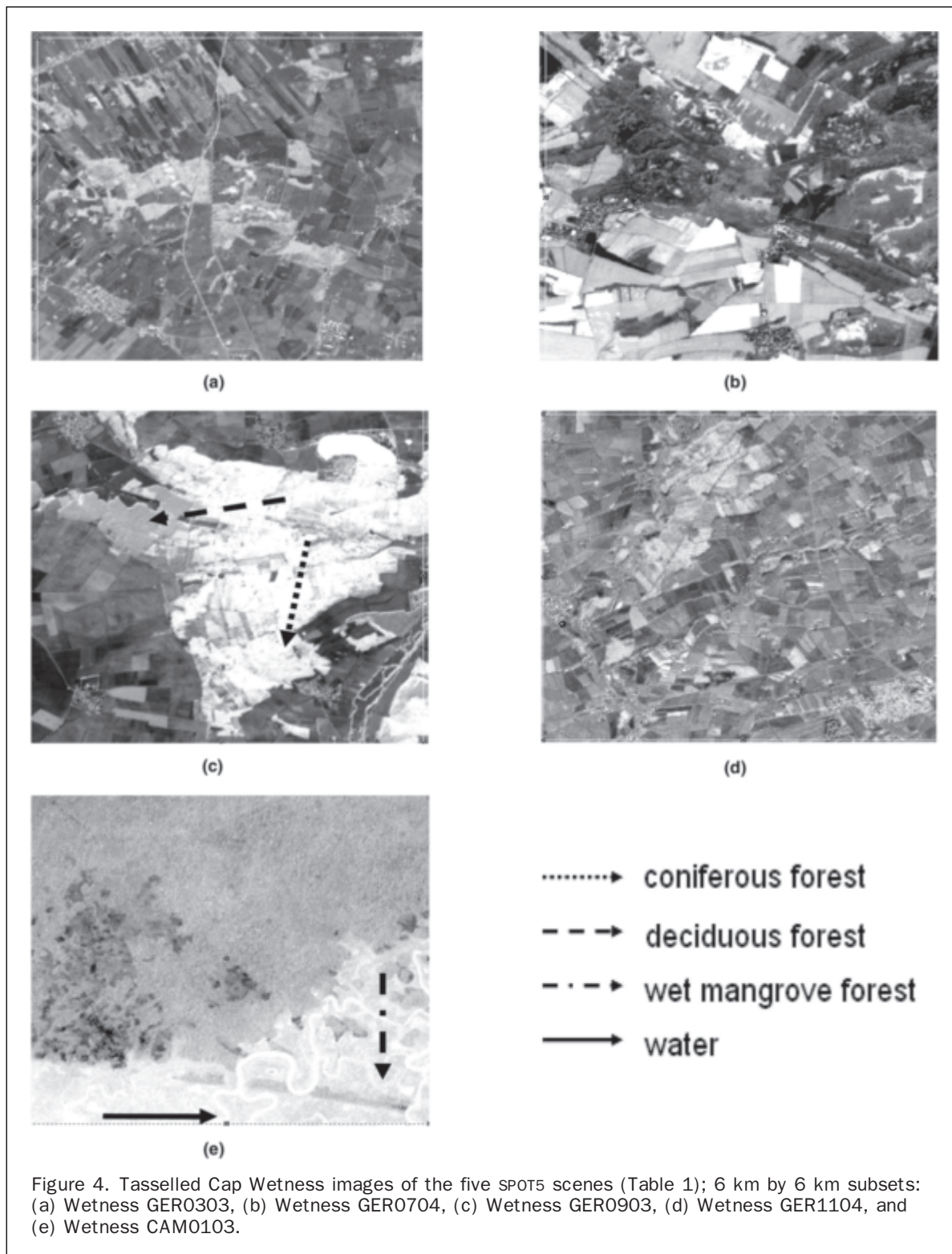


Figure 4. Tasseled Cap Wetness images of the five SPOT5 scenes (Table 1); 6 km by 6 km subsets: (a) Wetness GER0303, (b) Wetness GER0704, (c) Wetness GER0903, (d) Wetness GER1104, and (e) Wetness CAM0103.

Table 5 presents the goodness of fit measures of the CDA models to separate land-cover types using the original Tasseled Cap components. Figures 5 and 6 display random samples of the land-cover classes plotted against the first two canonical discriminant functions in Germany and in Cameroon, respectively. The best separation of bare soil, forest, grassland, and water classes was achieved in July and March (explained variance of 66.2 percent and

59.3 percent, respectively). The Tasseled Cap components of September explain the least variance in Germany and also the CDA biplot from September displays the most overlapping classes (Figure 5). The discriminative power of the Tasseled Cap images is the lowest from Cameroon. Accordingly, there is a great overlap between the lowland tropical forest, mangrove and palm plantation classes in the CDA biplot (Table 5 and Figure 6).

TABLE 2. SPEARMAN-RHO CORRELATIONS OF THE GERMANY TASSELLED CAP IMAGES (COLUMNS) WITH THE COMPONENTS CALCULATED THROUGH THE COMBINED PARAMETERS (ROWS)

| TC COMBINED | TCGER0303 | | | TCGER0704 | | | TCGER0903 | | | TCGER1104 | | |
|-------------------|-----------|-------|-------|-----------|---|-------|-----------|---|-------|-----------|-------|-------|
| | B | G | W | B | G | W | B | G | W | B | G | W |
| Brightness | 0.998 | | | 0.998 | | | 1 | | | 0.987 | | |
| Greenness | | 0.982 | | | 1 | | | 1 | | | 0.817 | |
| Wetness | | | 0.999 | | | 0.947 | | | 0.995 | | | 0.709 |

TC = Tasseled Cap, B = Brightness, G = Greenness, W = Wetness

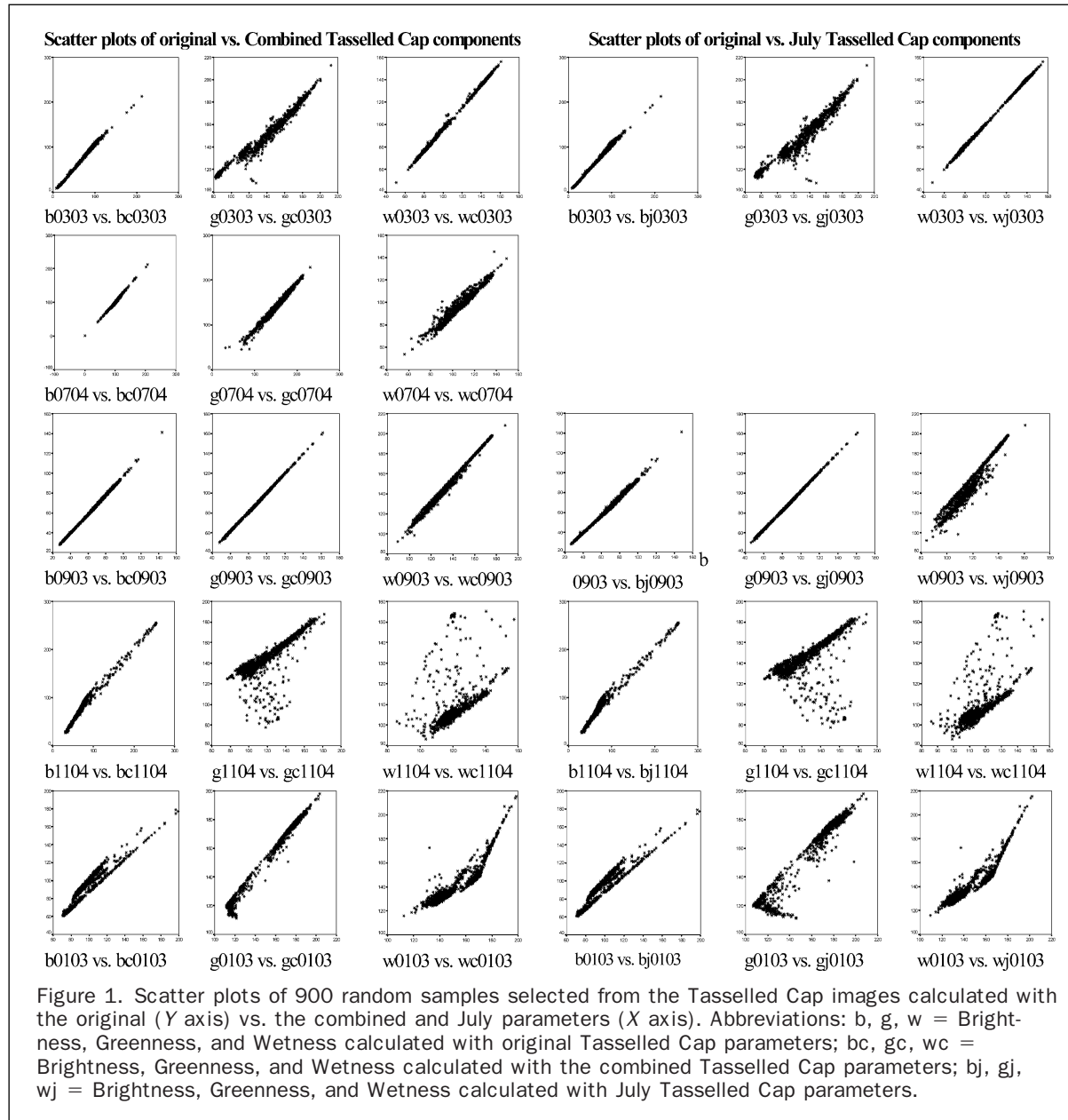


Figure 1. Scatter plots of 900 random samples selected from the Tasseled Cap images calculated with the original (Y axis) vs. the combined and July parameters (X axis). Abbreviations: b, g, w = Brightness, Greenness, and Wetness calculated with original Tasseled Cap parameters; bc, gc, wc = Brightness, Greenness, and Wetness calculated with the combined Tasseled Cap parameters; bj, gj, wj = Brightness, Greenness, and Wetness calculated with July Tasseled Cap parameters.

The variables entered into each of the CDA models in the following order: 1: Greenness, 2: Brightness, and 3: Wetness. Greenness exhibits the highest inter-set correlation to the first CDA axis in each image, indicating that this component has the highest explanatory power respecting the land-cover classes (Figures 5 and 6). In Germany, the component is positively associated with the other

vegetation and in Cameroon with the lowland tropical forest, mangrove, and palm plantation classes (see the position of the arrows). In March, July, and November, Brightness has the highest inter-set correlation to the second DCA axis and has a high explanatory power for the bare soil areas. In September, the Wetness component correlates the most with the second DCA axis. Wetness

TABLE 3. SPEARMAN-RHO CORRELATION OF THE GERMANY TASSELLED CAP IMAGES (COLUMNS) WITH THE COMPONENTS CALCULATED THROUGH THE JULY PARAMETERS (ROWS)

| TCGER0704 | TCGER0303 | | | TCGER0903 | | | TCGER1104 | | |
|-----------|-----------|-------|-------|-----------|---|-------|-----------|-------|-------|
| | B | G | W | B | G | W | B | G | W |
| B | 0.997 | | | 0.998 | | | 0.972 | | |
| G | | 0.965 | | | 1 | | | 0.654 | |
| W | | | 0.999 | | | 0.967 | | | 0.759 |

TC = Tasselled Cap, B = Brightness, G = Greenness, W = Wetness

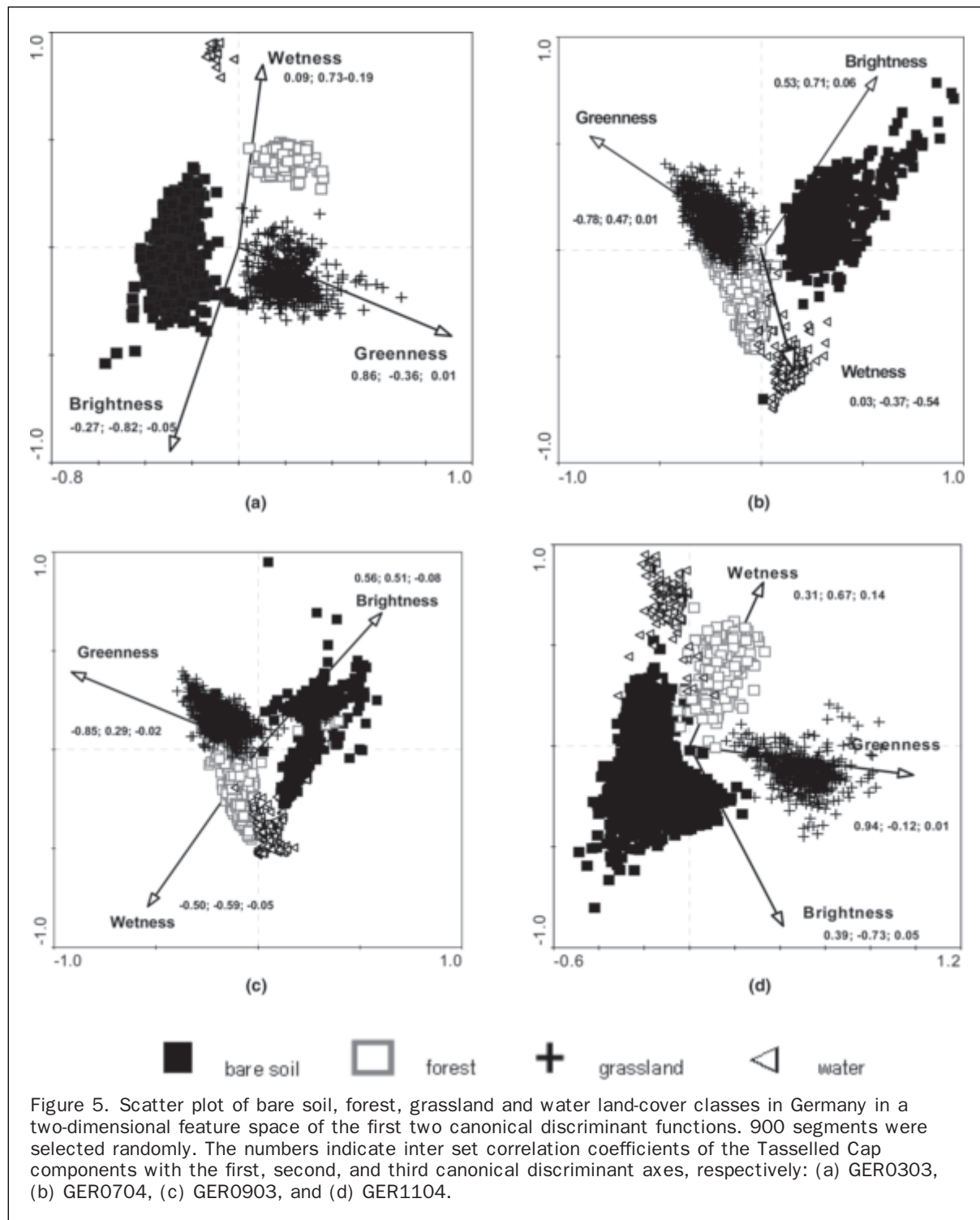
TABLE 4. SPEARMAN-RHO CORRELATION OF THE CAMEROON TASSELLED CAP IMAGES (ROWS) WITH THE COMPONENTS CALCULATED THROUGH THE COMBINED AND THE JULY PARAMETERS (COLUMNS)

| TCCAM0103 | TCCAM0103 calculated with the COMBINED parameters | | | TCCAM0103 calculated with the GER0704 parameters | | |
|-----------|---|-------|-------|--|-------|-------|
| | B | G | W | B | G | W |
| B | 0.952 | | | 0.952 | | |
| G | | 0.981 | | | 0.943 | |
| W | | | 0.952 | | | 0.949 |

TC = Tasselled Cap, B = Brightness, G = Greenness, W = Wetness

TABLE 5. GOODNESS OF FIT MEASURES OF THE CANONICAL DISCRIMINANT ANALYSES

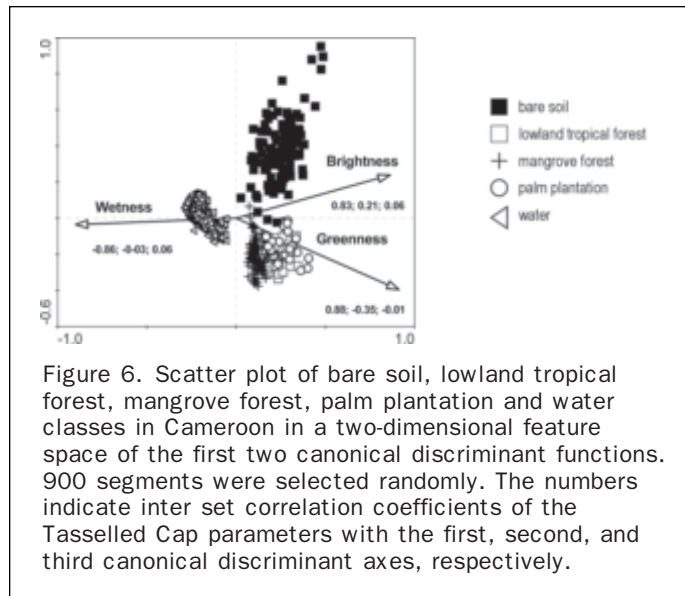
| | Canonical discriminant axes | | |
|---|-----------------------------|-------|-------|
| | CDA1 | CDA2 | CDA3 |
| | Germany, 0303 | | |
| Eigenvalues | 0.896 | 0.749 | 0.134 |
| Cumulative percentage of variance in the groups explained by the axes | 29.9 | 54.8 | 59.3 |
| Monte Carlo test of significance of all canonical axes together | | 0.001 | |
| | Germany, 0704 | | |
| Eigenvalues | 0.860 | 0.765 | 0.360 |
| Cumulative percentage of variance in the groups explained by the axes | 28.7 | 54.1 | 66.2 |
| Monte Carlo test of significance of all canonical axes together | | 0.001 | |
| | Germany, 0903 | | |
| Eigenvalues | 0.869 | 0.552 | 0.039 |
| Cumulative percentage of variance in the groups explained by the axes | 29.0 | 47.4 | 48.7 |
| Monte Carlo test of significance of all canonical axes together | | 0.001 | |
| | Germany, 1104 | | |
| Eigenvalues | 0.902 | 0.674 | 0.080 |
| Cumulative percentage of variance in the groups explained by the axes | 30.1 | 52.6 | 55.2 |
| Monte Carlo test of significance of all canonical axes together | | 0.001 | |
| | Cameroon, 0103 | | |
| Eigenvalues | 0.926 | 0.808 | 0.020 |
| Cumulative percentage of variance in the groups explained by the axes | 23.1 | 43.4 | 43.8 |
| Monte Carlo test of significance of all canonical axes together | | 0.001 | |



reached the highest correlation to the third DCA axis in March, July, and November, while in September its correlation is similar to that of Brightness. Wetness is closely related to the forested areas and to the water land-cover classes. The correlation of the Cameroon Tasseled Cap components with the first DCA axis is similarly high, while only Greenness and Brightness expressed moderate correlations (-0.35 and 0.21 , respectively) with the second axis (Figure 6). The importance of Wetness on the second and third axes can be ignored.

Discussion and Conclusion

Tasseled Cap components, calculated with the original, the July, and the combined parameters revealed differences within the seasons and between geographical locations. Although the Brightness components exhibited correlation coefficients above 97 percent in all cases and enhanced bare soil features in all images, no consistency was found in the loadings of the SPOT5 channels on this component. The highest loading of the NIR channel in March and November (Germany) can be explained by the high reflection of bare



soil surfaces. The vegetation growing period creates high contrast between vegetated and bare soil surfaces and brings up the red channel in the July and September images. In the Cameroon image, the SWIR band exhibited the highest loading on Brightness where in contrast to the German images vegetated surfaces dominated with high reflectance values. The reflectance of bare soil surfaces is not expected to change through seasons or between geometric locations, but as Brightness is a weighted sum of the SPOT5 image channels, it is plausible that vegetated surfaces influence this component.

The similar loading pattern of the SPOT5 bands observed on the Greenness component on the other hand is not necessarily an indicator of similar information content. In November, the correlation coefficients of 0.81 and 0.65 with the components calculated through the combined and July parameters, respectively, signalize considerable information differences of the images. It is plausible that the July Greenness parameter resulted in the lowest correlation coefficient with the November image because here information from vegetation high season was compared with information from senescent vegetation. The combined parameter's higher correlation coefficient with the November Greenness image is the consequence of including information also from the senescent vegetation surface. The highest loading of the NIR channel on the German Greenness component in July and September was due to the well-developed vegetation cover. Following the same logic, it is reasonable that the NIR channel reached the lowest loading in November; nevertheless, the difference when compared to the July and September loadings is significant. The second highest importance of the red channels on the Greenness components is due to bare soil and urban surfaces, seeing that Greenness separates vegetated from non-vegetated areas.

Of the Wetness components, the SWIR channels exhibited the highest and negative loadings in all images due to the absorbed reflection of water and wet surfaces. The relatively high loading of the green channel in the March, September, and November images of Germany and Cameroon can perhaps be explained by the high water content of plant leaves. The high Wetness values of coniferous forests in Figure 1 corresponds to the findings

of Cohen *et al.* (1995) who showed the importance of Landsat TM Wetness in the classification of coniferous forest stands. Wetness was a highly unstable Tasseled Cap component in Germany, which is most probably due to different rainfall events and water content of the vegetation throughout the seasons. In Cameroon, the similar correlations of the Wetness component with the July and combined components are somewhat surprising, as Wetness proved to be a highly unstable Tasseled Cap feature across the seasons.

Canonical Discriminant Analysis also provided an insight into the seasonal sensitivity of the Tasseled Cap parameters. The discrimination of the land-cover classes was most effective in March and July due to the fact that here also the second and third CDA axes exhibited relatively high eigenvalues. The importance of the third axis in September, in November, and in Cameroon was very low; the reason for that is unclear and would need further analyses. The high discriminative power in March and July can be attributed to the different reflection characteristics and water content of vegetated and non-vegetated surfaces. In March, broadleaved trees are still dormant and coniferous trees exhibit high contrast to bare soil, grassland, and agricultural crops, which explains the high importance of the Greenness and Brightness components. In July, the Greenness component is less powerful to separate coniferous, deciduous, and grassland areas due to their similar reflectance characteristics. However, the contrast of vegetated areas to bare soil features and the different water content of these areas give rise in the importance of the Brightness and Wetness components, so that the three CDA axes together explained the highest variance between land-cover types.

The highest explanatory power of Greenness in Germany was due to its correlation with the forest and other vegetation classes due to the high percentage of vegetation cover in these areas. The high importance of Wetness in March and November can most probably be explained by recent rainfall events creating generally wetter conditions than in summer, and by the sparse vegetation cover. In Cameroon, the dominance of wet mangrove forest land-cover brought Wetness high importance, and the sparse vegetation cover let the Brightness component equally important on the first axis. The high overlap between the samples from palm plantations, lowland tropical forests, and mangrove forest classes explains the lowest discrimination power of the Tasseled Cap parameters from Cameroon.

As the Brightness component proved to be very stable across the four seasons in Germany, it is reasonable to assume that this parameter can be extracted from one image and applied to another. On the other hand, Brightness was less stable in Cameroon suggesting inconsistencies between different biogeographical zones. The Greenness Tasseled Cap component was proved to carry the most unique and the highest amount of information in terms of discriminating between major land-cover types. However, the appropriateness of the application of the Greenness parameters on images from different seasons proved questionable, despite being an important parameter for the differentiation of land-cover features (Cohen *et al.*, 1995; Crist *et al.*, 1986; Cohen and Spies, 1992; Fiorella and Ripple, 1993). The same consequence can be drawn for the Wetness images. Therefore, the authors suggest care in applying Tasseled Cap parameters extracted from seasons different than the time of the study. It is highly advantageous to apply parameters derived from the time of the year with similar vegetation conditions and from similar biogeographic zones.

Acknowledgments

The analysis was carried out in the scope of the European Union Sixth Framework Program "Geoland" a joint initiative of European Commission and European Space Agency, which aims to build up a European capacity for Global Monitoring of Environment and Security. Furthermore, the authors thanks for Professor Mryka Hall-Beyer from the University of Calgary, Canada for the supporting comments.

References

- Baatz, M., and A. Schäpe, 2000. Multiresolution segmentation – An optimization approach for high quality multi-scale image segmentation, *Angewandte Geographische Informationsverarbeitung XII* (J. Strobl, T. Blaschke, and G. Griesebner, editors), Wichmann-Verlag, Heidelberg, Germany, pp. 12–23.
- Baatz, M., U. Benz, S. Dehghani, M. Heynen, A. Höltje, P. Hofmann, I. Lingenfelder, M. Mimler, M. Sohlbach, M. Weber, and G. Willhauck, 2001. *eCognition User Guide*, Definiens Imaging GmbH, München, Germany.
- Cohen, W.B., and T.A. Spies, 1992. Estimating structural attributes of Douglas-fir/western hemlock forests stands from Landsat and Spot imagery, *Remote Sensing of Environment*, 41:1–17.
- Cohen, W.B., T.A. Spies, and M. Fiorella, 1995. Estimating the age and structure of forests in a multi-ownership landscape of western Oregon, USA, *International Journal of Remote Sensing*, 16(4):721–746.
- Crist, E.P., and R.C. Cicone, 1984a. A physically-based transformation of Thematic Mapper data – The TM Tasseled Cap, *IEEE Transactions on Geoscience and Remote Sensing*, Vol. GE-22, No. 3.
- Crist, E.P., and R.C. Cicone, 1984b. Application of the Tasseled Cap concept to simulated Thematic Mapper data, *Photogrammetric Engineering & Remote Sensing*, 50(3):343–352.
- Crist, E.P., R. Laurin, and R.C. Cicone, 1986. Vegetation and soils information contained in transformed Thematic Mapper data, *Proceedings of IGARSS' 86 Symposium*, 08–11 September, Zürich, Switzerland (International Geoscience and Remote Sensing Symposium).
- da Silva, M.R.L.F., 1991. Determination of "Tasseled Cap" transformation parameters for images obtained by the SPOT satellite, *Proceedings of the Twenty-Fourth International Symposium on Remote Sensing of Environment*, 27–31 May, Rio de Janeiro, Brazil, Vol. 1.
- Fiorella, M., and W.J. Ripple, 1993. Determining successional stage of temperate coniferous forests with Landsat satellite data, *Photogrammetric Engineering & Remote Sensing*, 59(2):239–246.
- Gutman, G., and A. Ignatov, 1998. Derivation of green vegetation fraction from NOAA/AVHRR for use in numerical weather prediction models, *International Journal of Remote Sensing*, 19:1533.
- Hipps, L.E., G. Asrar, and E.T. Kanemasu, 1983. Assessing the interception of photosynthetically active radiation in winter wheat, *Agricultural Meteorology* 28:253–259.
- Horne, J.H., 2003. A Tasseled Cap transformation for Ikonos images, *Proceedings of the ASPRS Annual Conference*, 05–09 May, Anchorage, Alaska unpaginated CD-ROM.
- Huang, C., B. Wylie, L. Yang, C. Homer, and G. Zylstra, 2002. Derivation of Tasseled Cap transformation based on Landsat 7 at-satellite reflectance, *International Journal of Remote Sensing*, 23(8):1741–1748.
- Jackson, R.D., 1983. Spectral indices in n-space, *Remote Sensing of Environment*, 13:409–421.
- Justice, C.O., 1986. Monitoring east African vegetation using AVHRR data, *International Journal of Remote Sensing*, 6(8):1335–1372.
- Kauth, R.J., and G.S. Thomas, 1976. The Tasseled Cap – A graphic description of the spectral-temporal development of agricultural crops as seen by Landsat, *Proceedings of the Symposium of Machine Processing of Remotely Sensed Data*, 29 June – 01 July, Purdue University, West Lafayette, Indiana, pp. 41–51.
- Markham, B.L., and J.L. Barker, 1986. Landsat MSS and TM post-calibration dynamic ranges, exoatmospheric reflectances and at-satellite temperatures, *EOSAT Landsat Technical Notes*, 1:3–8.
- Mather, P.M., 2004. *Computer Processing of Remotely Sensed Images – An Introduction*, Third edition, John Wiley and Sons, Inc.
- Price, J.C., 1993. Estimating of leaf area index from satellite data, *IEEE Transactions on Geoscience and Remote Sensing*, 31(3):727–734.
- Richardson, A.J., and C.L. Wiegand, 1977. Distinguishing vegetation from soil background information, *Photogrammetric Engineering & Remote Sensing*, 43(12):1541–1552.
- Spotimage, 2004. URL: www.spotimage.fr/html/_167_224_584_.php (last date accessed: 10 July 2008).
- Stoner, E.R., and M.F. Baumgardner, 1980. Physiochemical, site, and bidirectional reflectance factor characteristics of uniformly moist soils, *Technical Report 11679*, Laboratory for Applications of Remote Sensing, Purdue University, West Lafayette, Indiana.
- Verdin, J.P., D.W. Eckhardt, and G.R. Lyford, 1987. Evaluation of SPOT imagery for monitoring irrigated lands, *Proceedings of the SPOT 1 Image Utilization, Assessment, Results*, Paris, France, Centre National D'Etudes Spatiales, pp. 81–91.
- Wiegand, C.L., and A.J. Richardson, 1982. Comparison among a new soil index and other two- and four-dimensional vegetation indices, *Proceedings of the 48th Annual Meeting*, American Society of Photogrammetry, pp. 211–227.

(Received 03 July 2006; accepted 07 December 2006; revised 28 March 2007)

A Polygonal Approach for Automation in Extraction of Serial Modular Roofs

Yair Avrahami, Yuri Raizman, and Yerach Doytsher

Abstract

This paper presents a novel approach for automation in roof extraction from two solved aerial images. The approach assumes that roofs are composed of several spatial polygons, and that they can be obtained by extracting all or even only some of them if the model is known. In view of this assumption, innovative algorithms for semi-automatic spatial polygon extraction were developed. These algorithms are based on a 2D approach to solving the 3D reality. Based on these algorithms, an interactive and semi-automatic model-based approach for automation in roof extraction was developed. The approach is composed of two phases: manual (interactive) and automatic. In the manual (interactive) phase, the operator needs to choose an Expanded Parameterized Model (EPM) from a knowledge base and select one pre-prepared Interactive Option for Extraction (IOE) of the roof. Then, the operator needs to point according to the guidelines of the chosen option in the left image space. In the automatic phase, the selected spatial polygons are extracted, the parameters of the selected model are calculated and the roof is reconstructed. The approach was examined and the results we obtained had standard accuracy. It appears that the approach can be implemented on many types of roofs and under diverse photographic conditions. In this paper, the algorithms, the experiments and the results are detailed.

Introduction

Generating 3D city models is a relevant and challenging task, both from a practical and a scientific point of view (Gruen and Wang, 1998). This type of data is extremely important in many areas such as municipal management, planning, communications, security and defense, and tourism. Most of the input data for these systems is entered manually ("point by point") on Digital Photogrammetric Workstations (DPW). This paper presents a novel approach to the automation of input data production (roofs) for these types of systems. The approach assumes that roofs are composed of several spatial polygons, and that they can be obtained by extracting all or even only some of them if the model is known. In view of this assumption, algorithms for semi-automatic spatial polygon extraction were developed. The suggested framework for enabling automation in the extraction, are two solved

aerial images, the interface and the reference. The interface image faces the operator, and it enables him to perform the measurements. The reference image exists only in the computer's memory in order to achieve the three-dimensional information and also to improve the information extracted from the interface image. In this paper, in order to simplify the explanation, the interface image was chosen to be the left image and the reference image as the right image.

The algorithms consist of several consecutive stages: (a) Manual pointing (by an operator) within a typical radiometric area to be extracted in the left image space. This stage defines the algorithms as semi-automatic and from here on the process is fully automatic; (b) Segmentation of the area and extraction of its bounding polygon in the left image space; (c) Calculation of the approximated average height of the polygon and transformation of the initial manual pointing to the right image space; (d) Segmentation of the area and extraction of its bounding polygon in the right image space; and (e) An iterative process which matches both polygons (in the right image space) followed by extraction of the spatial polygon.

These algorithms are based on a 2D approach for solving the 3D reality and can be employed in many feature extraction situations. In the current study, these algorithms are used for a novel approach for roofs extraction, which it presented in a semi-automatic interactive model-based approach. In the proposed approach there are two phases: manual interactive and automatic. In the manual interactive phase, the operator needs to choose an Expanded Parameterized Model (EPM) (explained below) from a knowledge base and to select one of prepared Interactive Option for Extraction (IOE) i.e., the roof. The prepared options are combination of spatial polygons and points, which are enablers for extracting the chosen EPM. Then, the operator needs to point according the guidance of the chosen option in the left image space. In the automatic phase, the selected spatial polygons are extracted, the parameters of the selected model are calculated, and the roof is reconstructed.

In the course of this study, a semi-automatic application for automation in roof extraction from aerial images was developed in order to examine algorithms efficiency. The results we obtained had a standard accuracy, and it appears that the algorithms can be implemented on many types of roofs and under diverse photographic conditions.

Yair Avrahami and Yerach Doytsher are with the Mapping and Geo-Information Engineering, Faculty of Civil and Environmental Engineering, Technion – Israel Institute of Technology (yaira@tx.technion.ac.il).

Yuri Raizman is with the Survey of Israel, 1 Lincoln St., Tel-Aviv, 65220 Israel.

Photogrammetric Engineering & Remote Sensing
Vol. 74, No. 11, November 2008, pp. 1365–1378.

0099-1112/08/7411-1365/\$3.00/0
© 2008 American Society for Photogrammetry
and Remote Sensing

This paper includes two main parts. The first one describes algorithms for a single spatial polygon extraction, which are based on an innovative criterion named the Overlapping Criterion. The second part describes a novel approach for modular roofs extraction, based on the algorithms described in the first part. The paper is arranged in the following manner: first, an overview of related work is provided; next, the algorithms for semi-automatic extraction of a single 3D spatial polygon are detailed; the next section demonstrates our approach for roof extraction which is based on the mentioned algorithms, while the subsequent sections discuss the implementation and the experiments, the analysis of the results, and ending with the summary and conclusions.

Related Works

Nowadays, extracting of buildings' roofs is carried out manually, employing digital photogrammetric workstations (DPW) or analytical stereoplotters. The advantage of the DPW environment is the ability to develop automation for photogrammetric assignments. In the last two decades, extensive research dealing with 3D building extraction from aerial images has been carried out by the photogrammetric and computer vision communities. However, full automation of object space extraction is still far from being implemented. The large amount of manual work required to extract buildings from aerial images, as well as the increased use of databases as 3D City Models and National GIS for control, management, and planning, necessitated the development of automation methods for establishing and updating these databases.

There is a great variety of algorithms for automation in building extraction depending on the type of building, level of required detail, number of images, kind of image cues and image primitives used, utilized external and *a priori* information, level of automation, and the operator interference (Gruen, 1997).

Usually, automation level is determined by the point of origin. In the automatic methods, the initial pointers or the rough locations of the buildings are automatically extracted. Cues such as color and DSM data have proved to be particularly valuable (Sibiryakov, 1996). In detection methods that exploit DSM or DEM data (Weidner and Forstner, 1995; Cord and Declercq, 2001; Ruther *et al.*, 2002), the initial pointers or the rough locations are three-dimensional. In other methods, they are two-dimensional when using classification or texture analysis (Kokubu *et al.*, 2001), shadow analysis (Irvin and McKoewn, 1989), or finding local maximums in a cumulative matrix of possible pointers (Croitoru and Doytsher, 2003). Semi-automatic methods use initial data provided by the operator, such as a pointer to the building, rough location of the building, or more detailed information, such as 3D point clouds and 3D spatial lines in the roof.

This paper focuses on developing semi-automatic algorithms whose sole input is a pair of color aerial images with known interior and exterior orientations. The reason for focusing on this input derives from the intellectual challenge in this research area and from a practical point of view. The current algorithms which rely on this input only can be divided into two types: those that extract a contour and height (2.5D) of the buildings (e.g., Gerke *et al.*, 2001; Ruther *et al.*, 2002; Oriot and Michel, 2004) and those that extract the detailed roof (3D) of the buildings (e.g., Gulch *et al.*, 1999; Gruen and Wang, 2001; Rau and Chen, 2003).

Gerke *et al.*, (2001) present algorithms for extracting 2.5d roof outlines of the buildings from orthophotographs and dsm in order to generate a building description which can be used in a simulation system for training emergency forces.

The process starts with a description of the coarse content of the given scene. Next, the knowledge about the surrounding of a building is used in order to support the detection of individual buildings. Finally, these buildings are reconstructed using invariant geometric moments leading to orthogonal geometric models. Ruther *et al.* (2002) focus on 2d flat roof mapping in informal settlement areas and suggest extracting the rough location from the dsm. The exact location is extracted from an orthophoto using the Snake method.

Oriot and Michel (2004) present a semi automatic approach for flat roof mapping. They suggest that the initial pointer would be 2D (i.e., on the left image) and performed manually. The rough location would be spotted by using Region Growing operations on the intensity and disparity images. The exact location and the matching of the photographs would be carried out using Hough Transform or Snake, according to the shape and the operator's decision.

Since creation of 3D City-Model datasets involves detailed extraction of elaborate roofs, it further complicates the problem. In order to scale-down the complexity and enable rapid and precise extraction, several methods which receive additional operator input were developed: Gülch *et al.* (1999) proposed a building extraction system which is model-based, and its automated features support the operator in adapting parametric models to multiple overlapping images. The operator's task is to fit to the photographs, in monoscopic viewing, to a wire-frame model of the selected type. The operator needs at least two photographs in order to adjust for the correct absolute height. If only one image is available, other external information is required. Several possibilities exist in their study: purely manual adaptation, guided adaptation, and automated adaptation.

Gruen and Wang (2001) proposed a semi-automatic topology generator for 3D objects named "CC-Modeler." In order to extract a building, a 3D point cloud for each building must be generated. The cloud is composed of boundary points (BP), arranged in a clockwise or counter-clockwise topological order, and interior points (IP). From this point, the process is fully automatic and the CC Modeler assigns appropriate surfaces to the point cloud and generates the building topology.

Rau and Chen (2003) proposed a method, which is called "SPLIT-MERGE-SHAPE," for constructing building models using 3D line segments which are measured manually. The method comprises five major stages: the creation of the Region of Interest (ROI) and preprocessing, splitting the model to construct a combination of roof primitives, merging connected roof primitives, shaping each building rooftop, and quality assurance. The amount of measurements in this method is of the same magnitude as that in the CC Modeler method, but this method has an advantage as it also deals with partial lines, and there is no need to estimate hidden corners.

Due to the complexity of automatic reconstruction of 3D reality from aerial images, each one of the last three methods attempts in its own way to minimize the dependency on radiometric parameters of the image. The algorithms proposed in this paper are based primarily on the radiometric parameters of the image and therefore can serve as a different approach or as an additional tool in combination with current methods.

Algorithms for a Single Spatial Polygon Extraction

Most of the published algorithms in object extraction are divided roughly into three parts: extracting image feature primitives such as image points, image edges, and image regions in each separate image; finding corresponding primitives between the images in order to achieve 3D

information; and extracting the desired 3D object by grouping methods, model-based methods, or other methods. For example, the Oxford Group (Baillard *et al.* 1999) started by extracting 2D lines in the image spaces, continued with line matching which led to 3D lines, and finally extracting the entire roof. In our research, different innovative algorithms were suggested according to the common paradigm of “divide and rule.” This method was implemented as follows: initially, the polygon is extracted from only one image; next, the corresponding polygon is extracted from the second image; and finally, the two are conflated in object space and the outcome is a final spatial polygon.

In order to extract the roof of a building, at least parts of the roof spatial polygons composing it must be extracted first. The following sections describe algorithms for extracting a spatial polygon (not only on a planar surface) from two solved aerial images. In order to facilitate a semi-automatic process, the working environment must be prepared beforehand. The preprocessing includes performing standard operations on the images in order to reduce noise and to emphasize the desired objects to be extracted in relation to their background. In order to start the semi-automatic spatial polygon extraction process, the operator needs to point, in the left image space, within a typical radiometric area of the desired polygon to be extracted. Pointing on the polygon is performed within a non-stereoscopic environment and without using 3D spectacles. This manual pointing defines the level of automation as semi-automatic. From this point on, the process is fully automatic and consists of the following stages: extraction of the polygon in the left image space, calculation of the approximated average height, transformation to the right image, extraction of the polygon in the right image, an iterative process based on the overlapping criterion for matching between the left and right polygons in the right image space, identification of “real” homologous points, and extraction of the spatial polygon. Figure 1 presents the flow chart of the spatial polygon extraction algorithms.

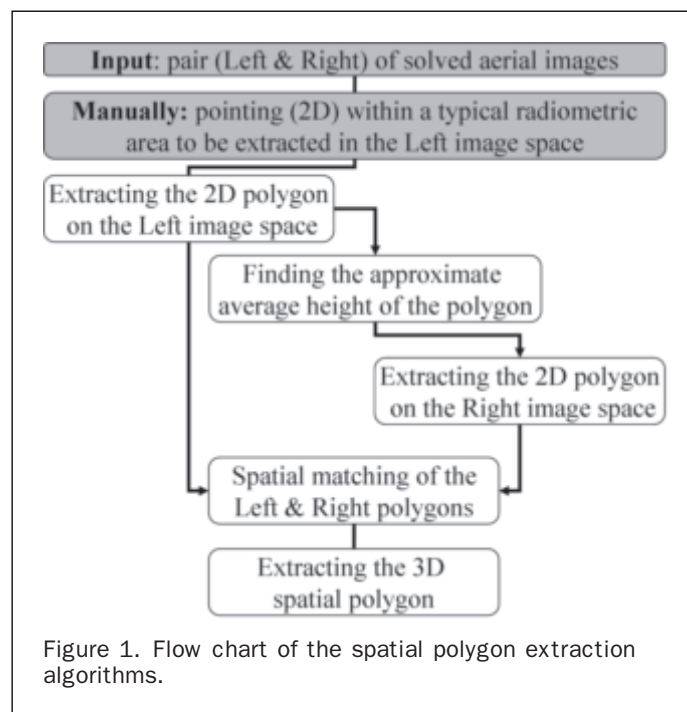


Figure 1. Flow chart of the spatial polygon extraction algorithms.

Left Polygon Extraction

The purpose of this stage is to extract the area which was identified by the operator in the left image space (segmentation). The algorithms utilized in this study are based on Region Growing methods combining morphological operators (“open” and “close”), a Flood Fill operator, and operators which eliminate “weak” and maintain “strong” edges. Following this process, the raster feature is converted to vector data using simplification methods, line adjustment, and intersection. The outcome is the 2D polygon in the left image space.

Approximated Average Height

In this stage, the average height of the polygon is approximated. Finding the average height is important because it enables for the transfer of the initial manual pointer from the left image space to a corresponding place in the right image space. For this purpose, we formulated several operations: dividing the left polygon into many points (for achieving many observations) and having each point from the left divided polygon find the homologue point in the right image space. The search for a homologous point is performed on the epipolar line in the right image space. When information about the possible range of heights of a polygon (minimum and maximum) is available, the search along the epipolar lines can be limited accordingly. This constraint can reduce the process computation time and improve the reliability of the results. All points on the polygon in the left image represent edge points and are subjectively defined as “interest points.” It would therefore be effective to use the ABM (Area Based Matching) method for finding their homologous points. From each pair of homologous points, we calculate the height; the outcome is a list of heights and their correlation criterion (between 0 and 1). The approximated average height is calculated by first reducing the list; only those heights which are higher than a defined criterion threshold are kept, and then the mean of the new list is determined.

Right Polygon Extraction

After calculating the average height of the polygon, it is possible to transfer the first initial manual pointer to the corresponding place in the right image in two steps: transferring to local coordinates and from these to the right image space (using the co-linear equations). From here on, the segmentation process around the transferred pointer can be applied (in the right image space) in the same way as in the left image. At the end of this process we obtain two polygons – one in the left image and one in the right image.

Matching the Left and Right polygons

Now that we have two polygons, one in the left image and one in the right image, a matching process between them is required. Matching between the polygons is very important for two reasons. First, in order to find the ground coordinates for each one of the polygon points. It is achieved by finding homologous points between the two polygons, which is easy to implement after the matching process. Secondly, in order to enable conflation and fusion between them by diluting the surplus points in the polygons (which exist due to the automatic segmentation).

One approach for matching between the polygons can use one of the common techniques in Object Recognition domain, such as Turning Function (Arkin *et al.*, 1991) or Geometric Hashing (Schwartz and Sharir, 1986). These techniques assume a global dissimilarity between shapes and cannot be efficient in our case. The reason is that in contrast to these methods which assume a global dissimilarity such as translation, rotation, scaling, and even projective. In our case,

the dissimilarity is not global due to the fact that in the projection of the polygon from the object space to the images, each one of the points is projected independently depending on its height.

A second approach for matching between the polygons can utilize the special geometric situation in which the polygons exist, derived from the fact that the polygons are the projective of the same spatial polygon. Basically, according to this approach, it is a simple process: for each point in the left polygon, we can find the corresponding homologous point in the right polygon by intersecting its epipolar line and the right polygon in the right image space. However, since extraction of polygons is performed automatically, the process often fails (explained below).

In this paper, algorithms for the matching between the polygons are presented. According to these algorithms the best matching is achieved by optimizing the Overlapping-Criterion, using the well-known optimization model the "adjustment by conditions" (Cooper, 1987). In the next sections, the difficulties in the matching process according to the second approach are discussed. Afterward, the developed algorithms which overcome these difficulties are presented.

Difficulties in Matching the Polygons

Since extraction of polygons is performed automatically, there are difficulties in finding corresponding points between the polygons. For example: (a) when there are a number of intersections per point (in the case of a convex polygon, there are two intersections, and in a concave polygon there might be more than two (Figure 2a)); (b) there is no intersection at all, e.g., when a polygon line is parallel to the epipolar line (Figure 2b), or when the epipolar line is imprecise due to impreciseness of the orientations (Figure 2c); or (c) there are more points than those existing in the "real" 3D polygon (because of occlusions in the images, the polygons may contain surplus points which are supposed to be eliminated in the matching process (Figure 2d).

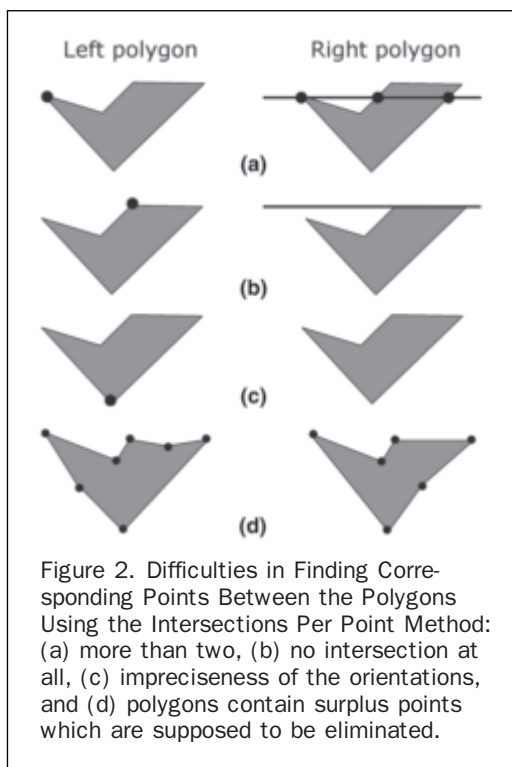


Figure 2. Difficulties in Finding Corresponding Points Between the Polygons Using the Intersections Per Point Method: (a) more than two, (b) no intersection at all, (c) impreciseness of the orientations, and (d) polygons contain surplus points which are supposed to be eliminated.

To overcome these difficulties, an iterative method for maximal matching between the two polygons was developed. After the polygons are in maximum overlap, a procedure which finds corresponding points and eliminates surplus points between the polygons is implemented. A spatial intersection of rays corresponding to the points enables the extraction of the spatial polygon.

Matching Based on the Overlapping Criterion

In this section, iterative innovative algorithms for maximal matching between the two polygons are presented. In our study, we defined the "Interior" and "Exterior" polygons as the result of the Boolean intersection and union operations. The matching process is based on the Overlapping-Criterion F (Equation 1): a minimum difference between the exterior and interior areas of the "transferred" left polygon and the right one in the right image space. The matching process between the polygons is based on the well-known optimization model called "adjustment by conditions" (Cooper, 1987). The unknowns in this model are the heights of each point in the left polygon. The conditional equation is F in Equation 1:

$$F = S_{out} - S_{in} \rightarrow \min \quad (1)$$

First, the points in the left polygon are assigned the approximate average height, which was calculated previously. In each one of the iterations, these heights of points in the left polygon are updated until the conditional equation is optimized. During the iterations, the left polygon "slides" in the direction of the epipolar line in the right image space. The "slide" rate is not constant because it depends on the varying height of each point. The iteration process stops when the polygons achieve maximum overlap in the right image space.

Algorithm 1 presents the pseudo code of the main iterative matching process between the polygons in the right

ALGORITHM 1. PSEUDO-CODE FOR THE ITERATIVE MATCHING PROCESS BETWEEN THE POLYGONS

Given:
 P_L, P_R
 $\{C_l\}_{1...i}; \{C_r\}_{1...j}; \bar{Z}_G$

Begin: Do until ($F \neq \text{Min}$)

(a) $\{C_l\}_{1...i} + \{Z_G\}_{1,i} \Rightarrow \{C_{l \rightarrow r}\}_{1...i}$
 (b) $\{C_r\}_{1...j} \cap \{C_{l \rightarrow r}\}_{1...i} \Rightarrow \{C_{out}\} \rightarrow S_{out}$
 (c) $\{C_r\}_{1...j} \cup \{C_{l \rightarrow r}\}_{1...i} \Rightarrow \{C_{in}\} \rightarrow S_{in}$
 (d) $F_{(Z_{1...i})} = S_{out} - S_{in} = [W]$

(e) $B = \begin{bmatrix} \frac{\partial F}{\partial(dZ_1)} & \frac{\partial F}{\partial(dZ_2), \dots} & \frac{\partial F}{\partial(dZ_i)} \end{bmatrix} \leftarrow \frac{\partial F_{(2)}}{\partial(dZ_1)} = \frac{(F_{(Z_i + \epsilon)} - F_{(Z)})}{\epsilon}$
 (f) $dZ_{1..i} = -B^T \cdot (B \cdot B^T)^{-1} \cdot W$
 (g) Update($Z_{1..i}$) $\rightarrow Z_{1..i} = Z_{1..i} + dZ_{1..i}$

End

image space. The input for the algorithm are two polygons, $\{C_l\}_{1...i}$ for the left image and $\{C_r\}_{1...j}$ for the right image, the projection matrix (P_L, P_R) for each one of the images (calculated from the orientation parameters) and the approximated average height \bar{Z}_G which was calculated previously. In line (a) the left polygon $\{C_l\}_{1...i}$ is transferred to the right image space using the average approximated height. In line (b) the area of the interior polygon (resulting from Boolean intersection) is calculated. In line (c) the area of the external polygon (resulting from Boolean union) is

calculated. Line (d) calculates the conditional function F which is supposed to be minimized. Line (e) describes the partial derivative matrix B , which is calculated in numerical fashion. Each matrix cell is a partial derivative of the conditional function for each point. In line (f), the corrections $dZ_{j...i}$ for the values from the former iteration is calculated according to the "adjustment by conditions" method. Finally in line (g), the heights from the former $Z_{j...i}$ iteration are updating by adding the corrections $dZ_{j...i}$.

Reconstruction of the 3D Spatial Polygon

When the iterative process is converged and the two extracted polygons overlap each other in an optimal manner (in the right image space), homologous points can be found using a compatibility scheme. The process requires building an adjacency matrix between all points in both polygons (in the right image space) and systematically extracts the two closest points. When a pair of points are found they are deleted from the matrix and the process is repeated until all pairs have been found. Thus, we have a list of pairs sorted by minimum distance, and all points which have no matching partners are automatically eliminated. From this list we select only those pairs that meet a user-predefined criterion, and these final points represent the 3D spatial polygon.

Synthetic Example

In this sub-section, an example is provided to fully explain the proposed solution for matching polygons from two different images. In Figure 3 there are two polygons, one in (a) gray, and one in (b) black. These polygons were created by projecting a spatial polygon on the image planes accordingly (the images are epi-polar rectified). Because of the difference in heights between the polygon points, their projection on the image planes causes substantial differences between the polygons. The differences between the polygons include area differences, changes in angles, and changes in lines lengths. In addition, due to problems in the segmentation, there are surplus points which do not belong to the original polygon (which is composed of only six points). Attempting to match these two polygons using common techniques in Object Recognition, which assume a global dissimilarity, are not efficient in our case. According to the proposed algorithm, the matching process is conducted in two stages: first, area-based matching between the polygons must be carried out in the right image. Next,

after the polygons are in maximum overlap, corresponding points between the polygons can be ascribed, surplus points can be eliminated, and the final polygon can be calculated.

Figure 3c shows the relationship between the two polygons after the left polygon is transferred to the right image space using the approximate height. Figure 3d shows the optimal overlap between polygons, after five iterations of the matching process. Table 1 shows the coordinates for the right polygon (first row) and the coordinates for the left polygon in the right image space before the iterations (second row). The next rows show the change in coordinates of the left polygon and the overlap rate, which was achieved throughout the five iterations. We can see that due to the fact that the surplus points are not present points on the spatial polygon, the maximum overlap is only 93 percent.

After the polygons have been matched and are in maximum overlap, the homologous points between the polygons must be extracted and the surplus points eliminated. Figure 4 shows the adjacency matrix which was calculated for this example. The matrix is presented six times according to the number of iterations which were needed to extract the six homologous points between the polygons. The horizontal axis contains point indices for the right polygon and the vertical axis contains point indices for the left polygon. In the first iteration (Figure 4a), the shortest distance was 0.04 between point No. 7 from the left polygon and point No. 6 from the right polygon and therefore the couple (7, 6) was chosen as homologous points. At this stage, the seventh row and sixth column must be deleted from the matrix (colored gray). In the next five iterations the couples (5, 3), (3, 2), (9, 7), (6, 5), and (1, 1) are chosen accordingly. The last distance chosen was 0.65, and the next shortest distance is 4.00 between point No. 2 from the left polygon and point No. 8 from the right polygon. This distance is significantly larger, and so the two points are not considered as homologous points, and the iterations end. We can see that six pairs of homologous points have been chosen. The points which have not been chosen (No. 2, 4, and 8 from the left polygon, and No. 4 and 8 from the right polygon) are automatically eliminated and do not participate in the calculation of the final polygon. After finding the point pairs, a spatial intersection is carried out between the points chosen from the two original polygons, and the result is the desired spatial polygon.

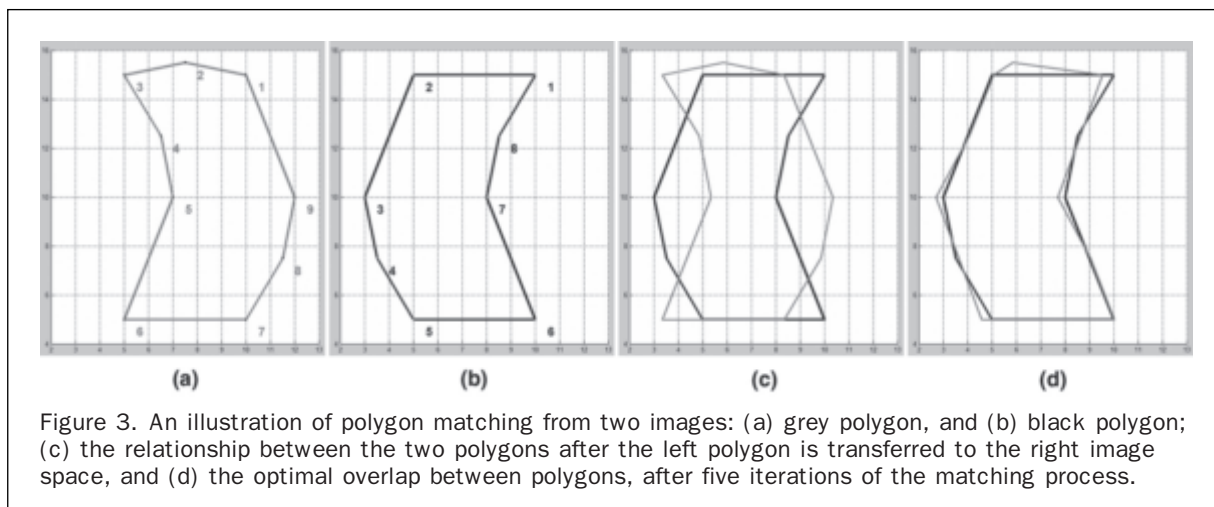


Figure 3. An illustration of polygon matching from two images: (a) grey polygon, and (b) black polygon; (c) the relationship between the two polygons after the left polygon is transferred to the right image space, and (d) the optimal overlap between polygons, after five iterations of the matching process.

TABLE 1. RESULTS OF THE ITERATIVE PROCESS FOR MATCHING POLYGONS

| | Point 1 | Point 2 | Point 3 | Point 4 | Point 5 | Point 6 | Point 7 | Point 8 | Point 9 | Overlap |
|-------------------|---------|----------|---------|----------|---------|---------|---------|----------|---------|---------|
| Right coordinates | 10,15 | 5,15 | 3,10 | 3.5,7.5 | 5,5 | 10,5 | 8,10 | 8.5,12.5 | | |
| Left coordinates | 10,15 | 7.5,15.5 | 5,15 | 6.5,12.5 | 7,10 | 5,5 | 10,5 | 11.5,7.5 | 12,10 | |
| Iteration No. 1 | 8.3 | 5.8 | 3.3 | 4.8 | 5.3 | 3.3 | 8.3 | 9.8 | 10.3 | 62(%) |
| Iteration No. 2 | 8.3 | 5.8 | 4.4 | 3.6 | 2.5 | 3.5 | 9.2 | 8.6 | 7.5 | 75(%) |
| Iteration No. 3 | 8.9 | 5.8 | 4.8 | 4.2 | 3.4 | 4.2 | 9.5 | 9.2 | 8.4 | 87(%) |
| Iteration No. 4 | 9.1 | 5.8 | 5.0 | 3.6 | 2.6 | 4.3 | 9.8 | 8.8 | 7.6 | 87(%) |
| Iteration No. 5 | 9.4 | 5.8 | 5.1 | 4.0 | 3.1 | 4.6 | 10.0 | 9.1 | 8.1 | 93(%) |

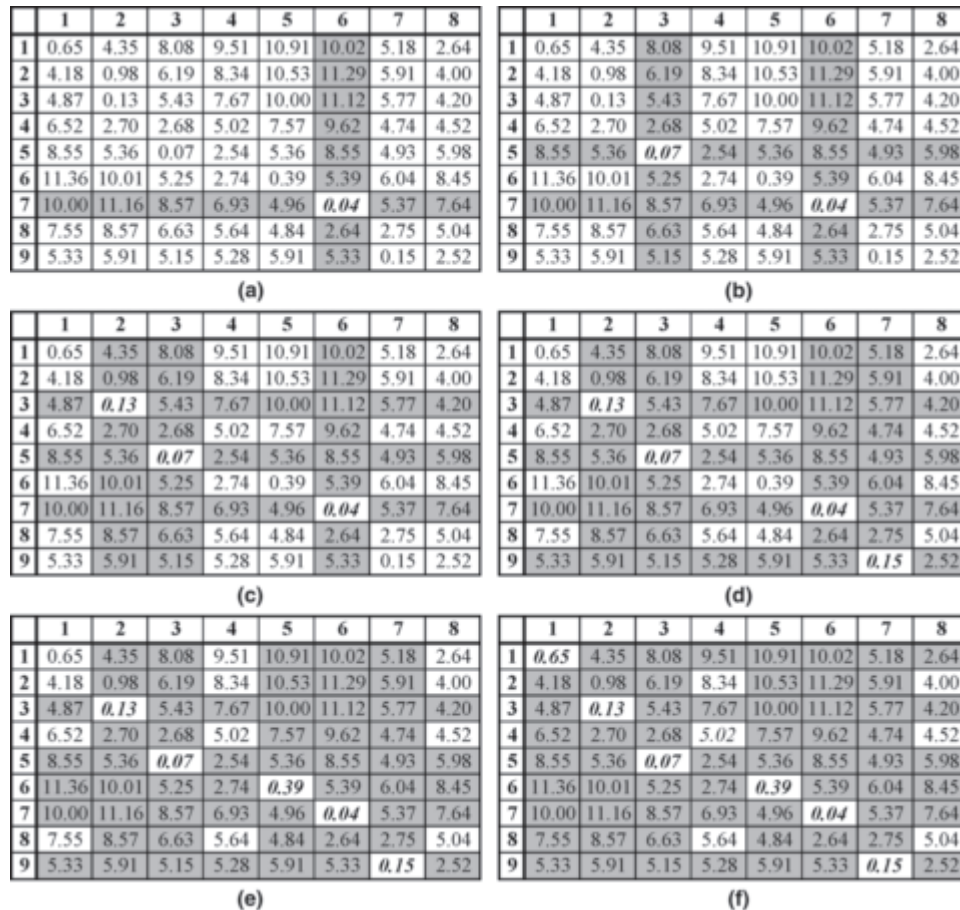


Figure 4. Using an adjacency matrix to find homologous points between polygons and to eliminate surplus points shown six times, (a) through (f) according to the number of iterations, respectively.

Automation in Roof Extraction

In the previous sections, algorithms for spatial polygon extraction were described. In this part, a novel interactive model based approach for automation in roof extraction is presented. Our approach utilizes the foreknowledge, interactive operations, and automatic tools to reduce the amount of measurements for extracting the roofs and to avoid the need for 3D measurements. This section is divided into three parts: first, we define two terms which are relevant for understanding the approach: Expanded Parameterized Model (EPM) and Interactive Option for Extraction (IOE); next, we describe the process for the extraction of a building roof, and finally, we bring several examples which illustrate the process.

Expanded Parameterized Model (EPM)

In the past two decades, numerous algorithms for semi-automatic extraction of roofs have been suggested. It is well accepted that the geometric data of roofs which are extracted manually or automatically are stored in one of the following ways: polyhedral models, prismatic models, parameterized polyhedral models, and CSG models (Tseng and Wang, 2003). Most of the research proposed model-based approaches and used the parametric model for describing and storing roofs. A parametric model of a structure is a rigid spatial body which has permanent topological relationships between the different faces which construct it. The spatial body is defined by a small number of parameters which help describe its shape. The advantage of parametric modeling of

structures is the fact that in order to calculate the shape of the model from the images, only the parameters which define it need to be calculated (it should be noted that along with the shape parameters, the position parameters, displacement, and rotation should be extracted). On the other hand, the disadvantage lies in reducing the extraction possibilities down to several basic models which are stored in a pre-defined library. In order to utilize the advantages of parametric models and overcome the disadvantage which is described above, a new model named Expanded Parameterized Model (EPM) is proposed in this research. This model is similar to the parametric model since the spatial body is defined by a small number of parameters which help define its shape. But, as opposed to the conventional parametric model, this model enables changes in the topological relationships between the faces which construct the body. Changes in the topological relationships are done by nullifying some of the model parameters during its extraction. In this way, a small library of EPMS can be created where each model consists of several sub-models.

Figure 5 shows an example of an expanded parametric model named G-Model (Generic-Model). In order to extract this model, we need to know the six horizontal parameters ($a_1, a_2, a_3, b_1, b_2, b_3$), the height parameter dz (the vertical difference between the upper and lower part of the roof), and the position parameters. This model is an expanded model because it contains many well-known basic parametric models. Figure 6 shows four well-known parametric models which are enclosed under the definition of G-Model. The transition from the expanded model to each one of the examples is possible by nullifying some of its parameters: (Figure 6a) parameters a_2 and b_2 are zero; (Figure 6b) parameter b_2 is zero; (Figure 6c) parameters a_1, a_3 and b_2 are zero; and (Figure 6d) parameters a_3 and b_2 are zero.

Figure 7 shows another expanded parametric model named L-Model. A primary point needs to be defined for each model so that the basic parameters and position parameters can be calculated according to them. In the G-Model, the primary point is defined as one of the corners of the rectangle (due to the symmetry of the rectangle, it doesn't matter which corner) and the axis are defined by the rectangle lines going out from the primary point. In the L-Model the axis are defined according to the two lines which pass on the upper part of each model part and the primary point is defined as the point of intersection of these two lines (shown in Figure 7 as the emphasized point). In order to extract this model we need to find 10 horizontal parameters ($a_1, a_2, a_3, b_1, b_2, c_1, c_2, c_3, d_1, d_2$), the vertical parameter dz , and the position parameters. As opposed to the G-Model where all of the horizontal parameters are positive, in this model there are two parameters a_1 and c_1 which can be positive or negative. In the

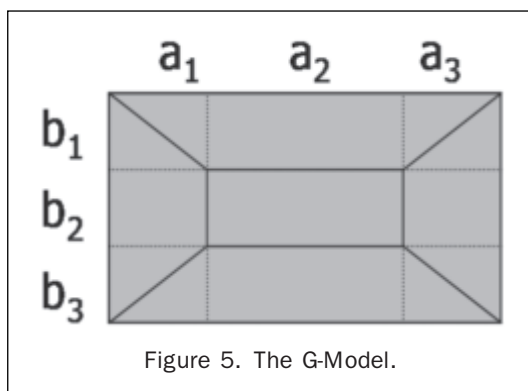


Figure 5. The G-Model.

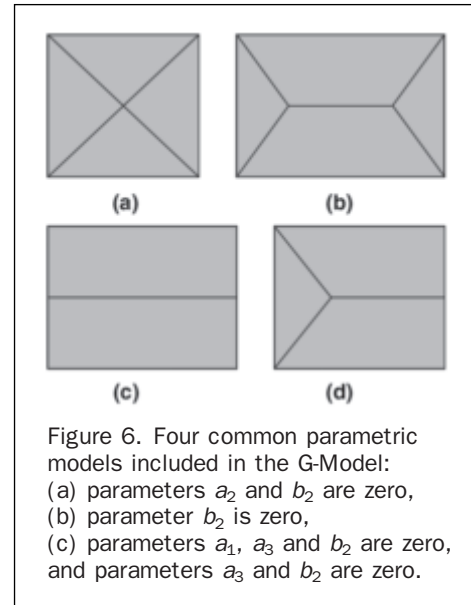


Figure 6. Four common parametric models included in the G-Model:
(a) parameters a_2 and b_2 are zero,
(b) parameter b_2 is zero,
(c) parameters a_1, a_3 and b_2 are zero,
and parameters a_3 and b_2 are zero.

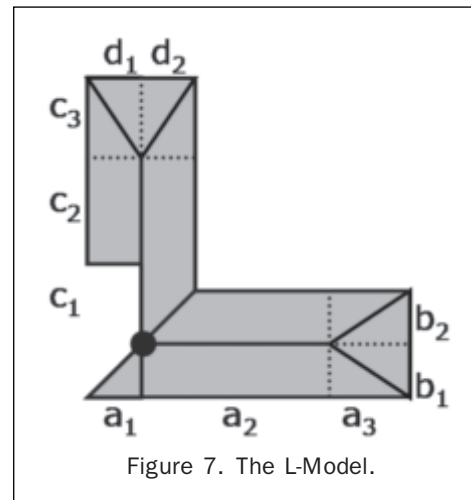


Figure 7. The L-Model.

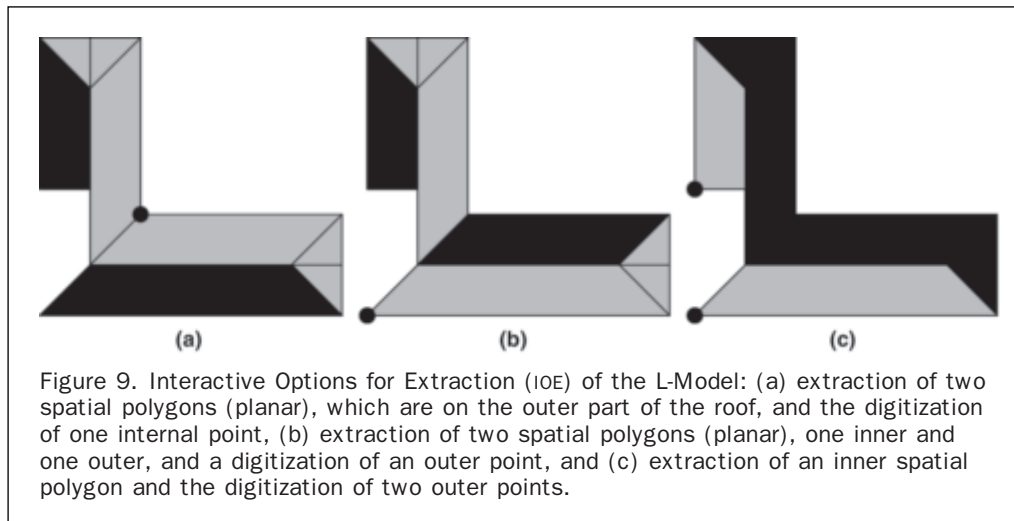
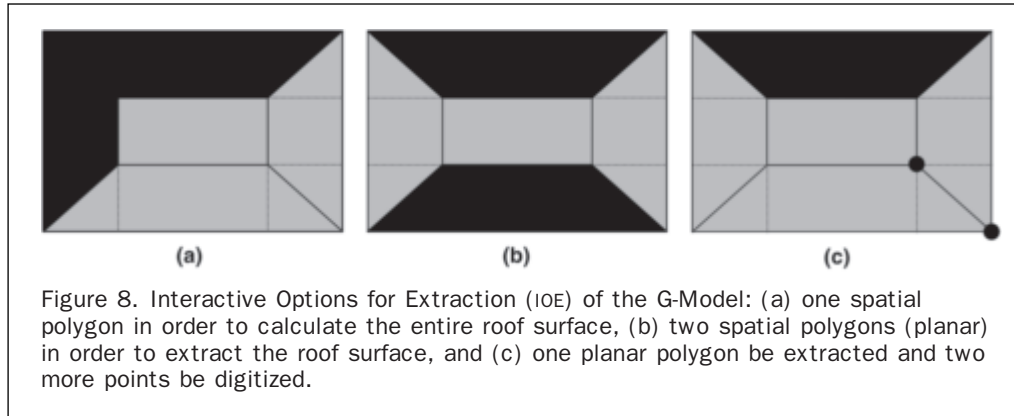
example presented in Figure 7, a_1 is defined as negative, and c_1 is defined as positive.

Interactive Option for Extraction (IOE)

The Interactive Option for Extraction is a minimal combination of spatial polygons and sometimes 2D points which enable a spatial extraction of a known EPM of a roof. The IOE is pre-defined for each EPM while setting up the model library.

Figure 8 shows three possible examples of IOE for the G-Model. The areas filled in black are the polygons which need to be extracted, and the emphasized points are those which should be digitized. According to the first option (Figure 8a), it is sufficient to extract one spatial polygon in order to calculate the entire roof surface. According to the second option (Figure 8b), we need to extract two spatial polygons (planar) in order to extract the roof surface. The third option (Figure 8c) requires that one planar polygon be extracted and two more points be digitized.

In Figure 9 we see three possible examples of IOE for the L-Model. The first option (Figure 9a) requires the extraction of two spatial polygons (planar), which are on the outer part of the roof, and the digitization of one internal point. The



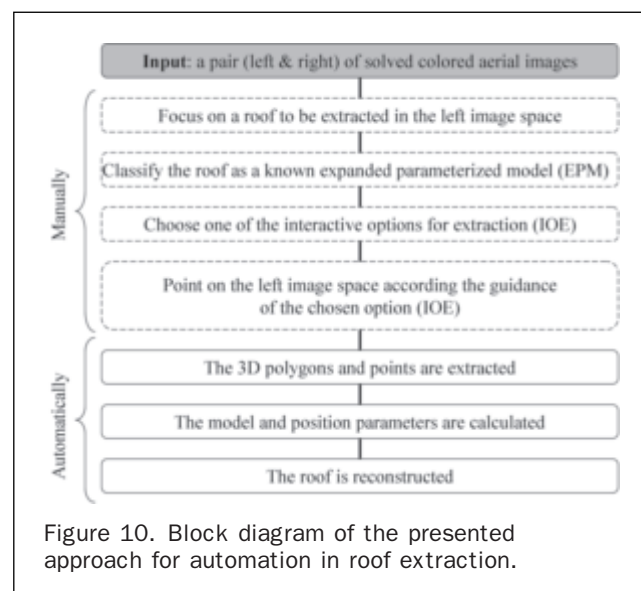
second option (Figure 9b) requires the extraction of two spatial polygons (planar), one inner and one outer, and a digitization of an outer point. The third option (Figure 9c) requires the extraction of an inner spatial polygon and the digitization of two outer points.

The selection of an IOE can be done immediately after a model has been chosen, but it is better to first examine the roof to be extracted and then choose the IOE so that the chosen option will be best suited to the specific roof according to the image conditions (photograph angle, occlusions, shadow, and light conditions).

The Extraction Process

Figure 10 shows a block diagram which describes the process of extracting a roof. The input is a pair of solved aerial images (left and right). The process for each roof is divided into two phases: the interactive phase which includes focusing on the roof to be extracted, choosing the appropriate Expanded Parameterized Model (EPM) for the chosen roof, choosing one of the Interactive Option for Extraction (IOE) which are defined for the chosen model, and finally digitization in the left image according to the directions of the chosen IOE. The automatic phase includes extraction of spatial information based on the digitized 2D information, calculation of the parameter models (the model parameters and position parameters) and calculation of the spatial coordinates of the roof's points.

The IOE includes guidance for the user leading him as to which spatial polygons and spatial points are needed in



order to extract the entire roof. The extraction of spatial polygons is carried out according to the semi-automatic algorithms described in the first part of the paper, algorithms which require, as input, a 2D manual digitization in

the left image space. However, there are three aspects in which the extraction of a spatial polygon applied here, as part of the roof extraction process, is different from the general algorithms described previously:

- As opposed to the general algorithms, where one pointer is needed for each polygon, as part of the roof extraction process, a characteristic point for each planar surface contained in the designated polygon, must be pointed. These points will serve as starting points for the segmentation process. More than one point is required for each polygon as often there is a “clear” edge between the surfaces in the image space. Even if the left image space does not appear to have these edges, it is possible that the right image, which is taken from a different direction, may have them. A pointer for each one of the surfaces can overcome this problem.
- As opposed to the general algorithms, where the final polygon is a “free” spatial polygon and thus do not satisfy any constraint in the suggested approach for roof extraction, the rough shape of the polygon is chosen interactively and therefore, the extracted polygon should satisfy some non-rigid constraints. Among these constraints are: an approximate knowledge about the number of points which consist the spatial polygon, points at the same height in the model have to be at closely heights in the extracted polygon, and parallel and perpendicular lines in the model must be roughly parallel and perpendicular in the extracted polygon. However, the final polygon does satisfy all these constraints due to the calculation process which takes into account the extracted polygon as observations and finds its parameters in the model’s context. For example, the lower height of the final polygon is calculated by averaging all the lower points in the extracted polygon.
- In the general algorithms, the certainty that the extracted polygon is the desired polygon is based only on the fact that the polygon is extracted independently from two images and that the matching process is achieving in reasonable Overlapping Criterion. As opposed to in the suggested roof extraction mechanism, the level of certainty is higher due to the pointing process which is done for each planar surface separately and due to the implementation of the constraints possibilities.

After the pointers for each planar surface, which is contained in the polygon, have been set in the left image, an automatic process for the extraction of a spatial polygon is executed. The automatic process includes the extraction of the polygon in the left image space, transferring the pointers to the right image space, extraction of the polygon in the right image space and the extraction of the final spatial polygon (according to the algorithms described in the next section).

In addition to the spatial polygons which are needed to be extracted according to the IOE in some cases, the guidance of the IOE requires a measurement of points. The extraction of these points is carried out by performing a manual pointing to the points in the left image space. These points can be transformed to the ground using the height taken from the relevant level in the spatial polygon extracted previously.

Examples

This section demonstrates examples which explain the proposed process. Two EPMs (G-Model and L-Model) and three IOEs were shown for each of the models. For each one of the six options mentioned, a characteristic example is demonstrated in the current section.

G-Model Examples

The following three examples present the extraction of G-Model roofs according to the guidance suggested in the first (Figure 11), second (Figure 12), and third (Figure 13) IOE. First, we focus on (shown as (a) in each figure) the roof and choose an EPM (G-Model) from an existing library; next,

we choose an IOE from (shown as (b) in each figure) one of the pre-defined options.

In the first example (Figure 11), the chosen IOE requires the extraction of only one spatial polygon comprised of two adjacent planar surfaces. Therefore, two points must be digitized in the left image space (Figure 11c). Next, the extraction of the polygon is performed automatically in the left (Figure 11c) and in the right (Figure 11d) image space. Then, the spatial polygon is reconstructed (Figure 11e). In the final stage, the model and position parameters are calculated from the spatial polygon, and the entire roof is reconstructed (Figure 11f).

In the second example (Figure 12), the chosen IOE requires the extraction of two opposite planar surfaces. Therefore, two points must be digitized in the left image space (Figure 12c). Next, the extraction of the polygons is performed automatically in the left (Figure 12c) and in the right (Figure 12d) image space. Then, the spatial polygons are reconstructed (Figure 12e). It should be noted that in this IOE the algorithms for extracting a spatial polygon are executed

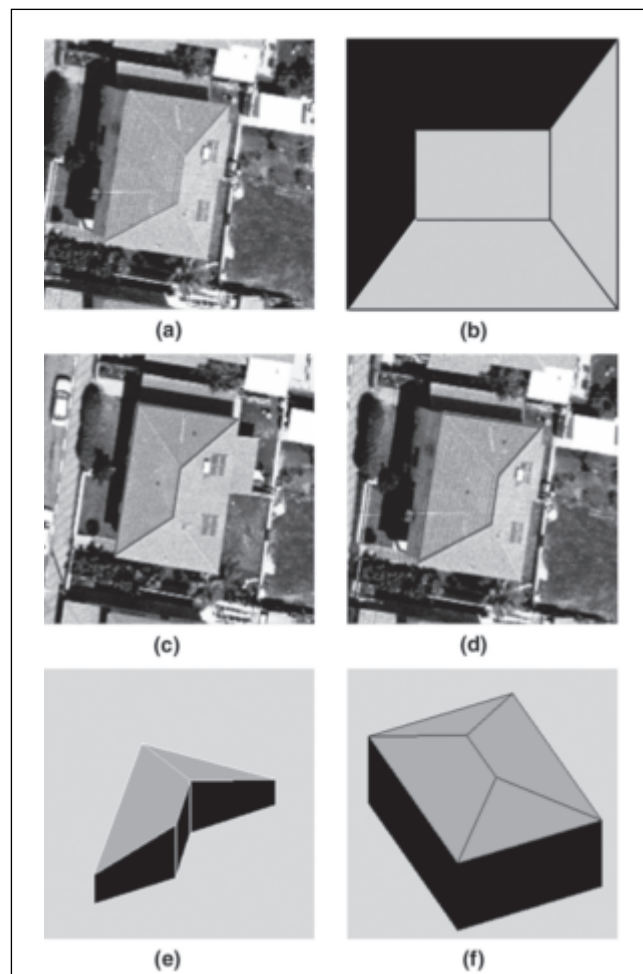


Figure 11. Extraction of G-Model roof using the first IOE: (a) the roof and an EPM (G-Model) from an existing library, (b) the roof and an IOE from one of the pre-defined options, (c) and (d) the extraction of the polygon is performed automatically, (e) the spatial polygon is reconstructed, and (f) the entire roof is reconstructed. A color version of this figure is available at the ASPRS website: www.asprs.org.

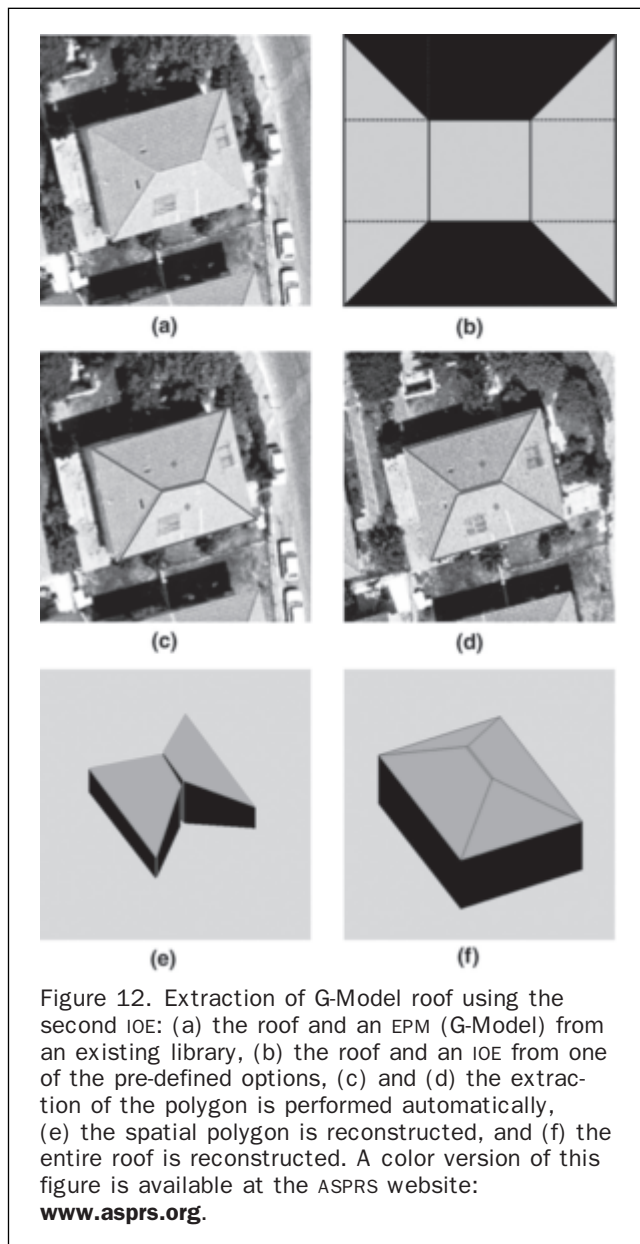


Figure 12. Extraction of G-Model roof using the second IOE: (a) the roof and an EPM (G-Model) from an existing library, (b) the roof and an IOE from one of the pre-defined options, (c) and (d) the extraction of the polygon is performed automatically, (e) the spatial polygon is reconstructed, and (f) the entire roof is reconstructed. A color version of this figure is available at the ASPRS website: www.asprs.org.

twice: once for each planar surface. In the final stage, the model and position parameters are calculated from the spatial polygons and the entire roof is reconstructed (Figure 12f).

In the third example (Figure 13), the chosen IOE requires the extraction of one spatial polygon (planar) and two spatial points. Therefore, three points must be digitized in the left image space. In (Figure 13c) we can see that only two points have been digitized instead of three according to the chosen IOE. This is due to the definition mentioned earlier where if only two points have been digitized, the parameter which defines the width of the upper planar part is zero, and then there is no need for the extra digitization. Next, the extraction of the polygon is performed automatically in the left (Figure 13c) and in the right (Figure 13d) image spaces. Then, the spatial polygon is reconstructed (Figure 13e), and the 2D digitized point is transferred to the object space while using the lower level height of the extracted polygon. In the final stage, the model and position parameters are calculated from the spatial polygon and from

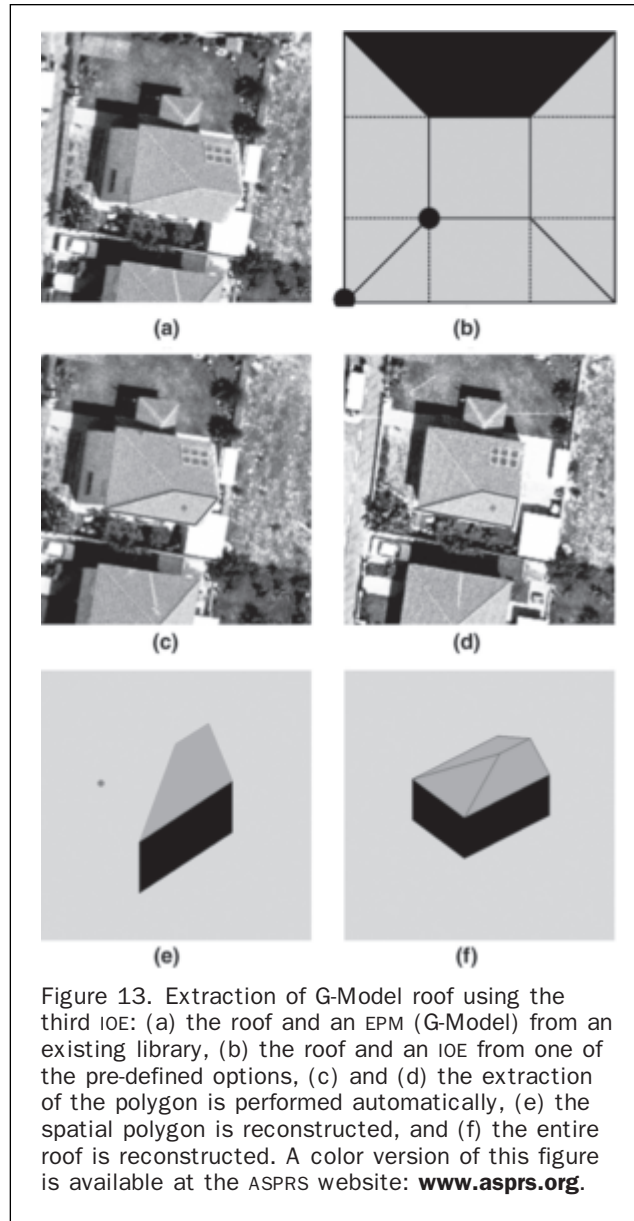


Figure 13. Extraction of G-Model roof using the third IOE: (a) the roof and an EPM (G-Model) from an existing library, (b) the roof and an IOE from one of the pre-defined options, (c) and (d) the extraction of the polygon is performed automatically, (e) the spatial polygon is reconstructed, and (f) the entire roof is reconstructed. A color version of this figure is available at the ASPRS website: www.asprs.org.

the transferred point and then, the entire roof is reconstructed (Figure 13f).

L-Model Examples

The following three examples present the extraction of L-Model roofs according to the guidance suggested in the first (Figure 14), second (Figure 15) and third (Figure 16) IOE. First, we focus on the roof (shown as (a) in each figure) and choose an EPM (L-Model) from an existing library; next, we choose an IOE from one of the pre-defined options (shown as (b) in each figure).

In the first example (Figure 14), the chosen IOE requires the extraction of two outer planar polygons and one inner point. Therefore, three points must be digitized in the left image space (Figure 14c). Next, the extraction of the polygons is performed automatically in the left (Figure 14c) and in the right (Figure 14d) image space. Then, the spatial polygons are reconstructed (Figure 14e), and the 2D digitized inner point is transferred to the object space while using the

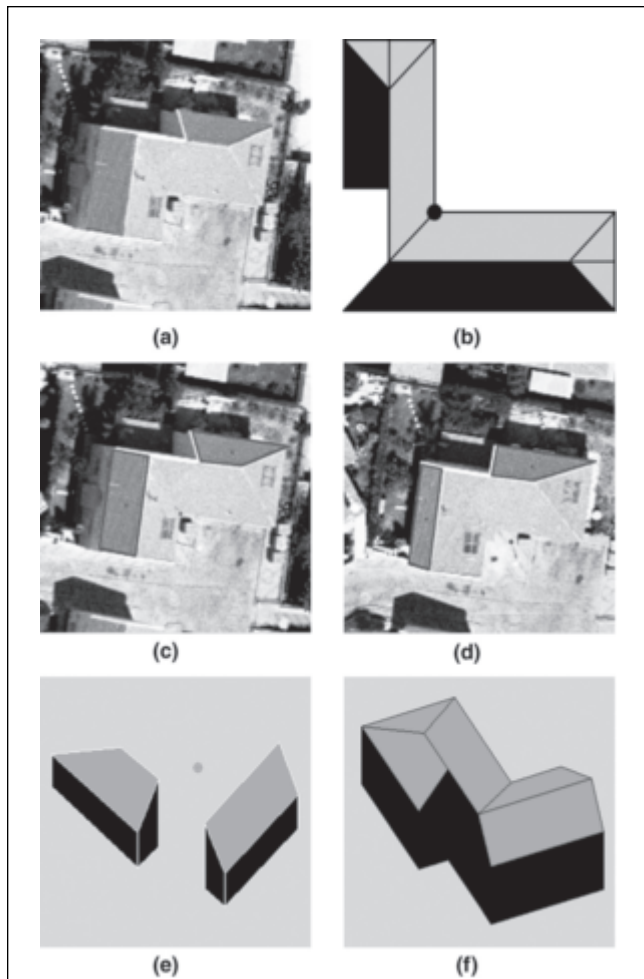


Figure 14. Extraction of L-Model roof using the first IOE: (a) the roof and an EPM (L-Model) from an existing library, (b) an IOE from one of the pre-defined options, (c) and (d) the extraction of the polygon is performed automatically, (e) the spatial polygon is reconstructed, and (f) the entire roof is reconstructed. A color version of this figure is available at the ASPRS website: www.asprs.org.

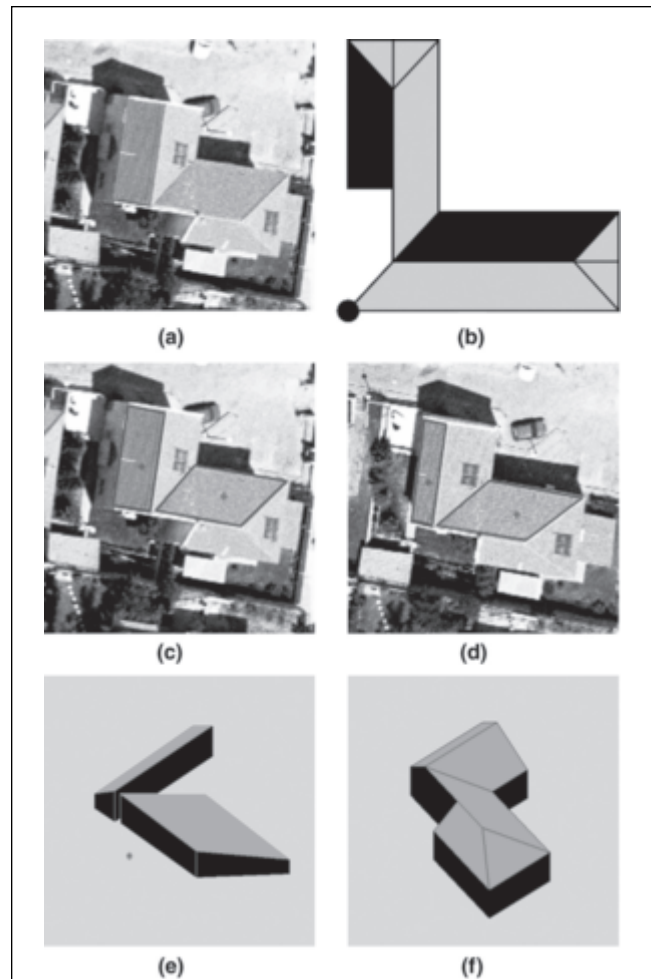


Figure 15. Extraction of L-Model roof using the second IOE: (a) the roof and an EPM (L-Model) from an existing library, (b) the roof and an IOE from one of the pre-defined options, (c) and (d) the extraction of the polygon is performed automatically, (e) the spatial polygon is reconstructed, and (f) the entire roof is reconstructed. A color version of this figure is available at the ASPRS website: www.asprs.org.

lower level height of the extracted polygons. In the final stage, the model and position parameters are calculated from the spatial polygons and from the transferred inner point and then, the entire roof is reconstructed (Figure 14f).

In the second example (Figure 15), the chosen IOE requires the extraction of two planar spatial polygons (inner and outer) and one outer point. Therefore, three points must be digitized in the left image space (Figure 15c). Next, the extraction of the polygons is performed automatically in the left (Figure 15c) and in the right (Figure 15d) image space. Then, the spatial polygons are reconstructed (Figure 15e), and the 2D digitized outer point is transferred to the object space while using the lower level height of the extracted polygons. In the final stage, the model and position parameters are calculated from the spatial polygons and from the transferred outer point and then, the entire roof is reconstructed (Figure 15f).

In the third example (Figure 16), the chosen IOE requires the extraction of one spatial polygon (in this case it comprises of three planar polygons) and two outer points. Therefore, five

points must be digitized in the left image space (Figure 16c). Next, the extraction of the polygon is performed automatically in the left (Figure 16c) and in the right (Figure 16d) image space. Then, the spatial polygon is reconstructed (Figure 16e), and the 2D digitized points are transferred to the object space while using the lower level height of the extracted polygon. In the final stage, the model and position parameters are calculated from the spatial polygon and from the transferred points and then, the entire roof is reconstructed (Figure 16f).

Implementation and Experiments

In order to examine the approach efficiency, a semi-automatic application for roof extraction from aerial images was developed. The system included an interactive guide, which enables to choose Expanded Parameterized Model from a knowledge base to choose one of the Interactive Options for Extracting the roof and to perform manual pointing in the left image space. After the manual interactive phase, the selected planes are

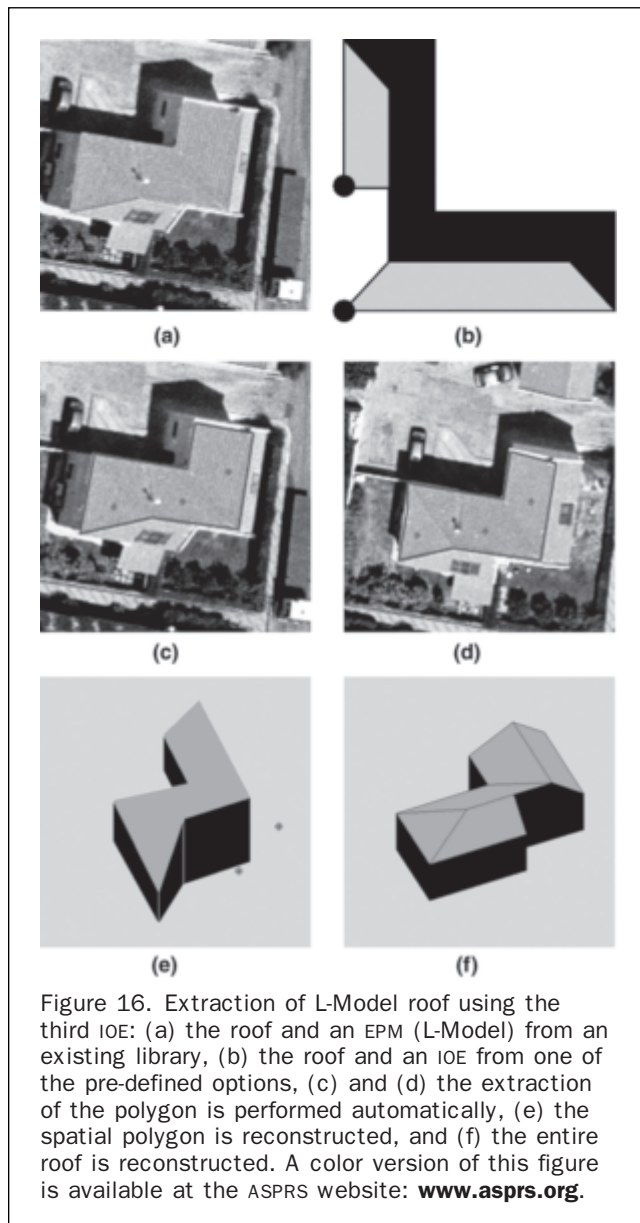


Figure 16. Extraction of L-Model roof using the third IOE: (a) the roof and an EPM (L-Model) from an existing library, (b) the roof and an IOE from one of the pre-defined options, (c) and (d) the extraction of the polygon is performed automatically, (e) the spatial polygon is reconstructed, and (f) the entire roof is reconstructed. A color version of this figure is available at the ASPRS website: www.asprs.org.

extracted, the parameters of the model are calculated and the roof is reconstructed in a local coordinate system. The implementation was carried out within the Matlab[®] environment. The extracting time was on average 10 second per roof, which might be significantly reduced while using real time programming.

In order to examine the accuracy of the proposed approach (compared to the manual extraction) and to assess the capabilities of the approach with different types of roofs, some experiments were performed. The test area was a small settlement in north Israel covered by two colored aerial images (Left and Right). The images scale was 1:5 200 and the ground resolution was 15 centimeters per pixel. The area contained 27 roof classified as G-Model and 16 roofs classified as L-Model. Figure 17 shows the results which were projected into the left and right image space, and Figure 18 presents the results in a local coordinate system. The algorithms enable only extraction of roofs and the presentation of the walls is only for visualization purpose. In order to generate walls, a point on the ground

must be known or calculated from an appropriate DTM (not included in the input data).

Analysis of the Results

The results for extracting roofs in the test area show that all roofs from the G-Model family were extracted (27 roofs). On the other hand, only 15 out of 16 roofs belonging to the L-Model family were extracted.

In order to evaluate the measurement accuracy, the roofs were measured manually by a skilled operator in the ERDAS Imagine[®] 8.6 software. Both extractions (manual and semi-automatic) were based on the same model solution with the same orientation errors and thus, there is no need to take them into consideration.

The semi-automatic extraction accuracy was calculated based on the RMS [$RMS = \sqrt{\sum(d^2)/n}$] of the deviation vectors, between the two extractions, and on the evaluated accuracy of the manual extraction.

The deviation vector of each corner on the semi-automatic extraction and the appropriate corner on the manual extraction were measured. Altogether 396 deviation vectors belonging to 42 extracted roofs in the test area were measured. The RMS of the deviation vectors is a "compared" accuracy between the manual and the semi-automatic proposed mechanisms for extraction.

The accuracy of the manual extraction can be evaluated according to Kraus (1993) using Equations 2 and 3, where: m is the image scale, m_q is an estimation of the photogrammetric measurement's accuracy (10 μ m), Z is the flight height, and B is the base line.

The accuracy of the semi-automatic extraction method can be calculated according to Equation 5 which implements the *variances propagation law* in Equation 4 representing the difference between the manual and semi-automatic extraction methods.

The accuracy was calculated for the roofs classified as G-Model, for the roofs classified as L-Model, and for both. The horizontal and vertical measurement accuracy in the test area is presented in Table 2: the evaluated accuracy of the manual measurements (column 2), the RMS of the deviation vectors between the mappings (column 3), and the semi-automatic mapping accuracy (column 4).

$$M_{xy} = m \times m_q \quad (2)$$

$$M_z = m \times m_q \times \frac{Z}{B} \quad (3)$$

$$Compared_{(H,V)} = Semiautomatic_{(H,V)} - Manual_{(H,V)} \quad (4)$$

$$M_{semi-automatic}^2 + M_{manual}^2 = M_{compared}^2 \quad (5)$$

As can be seen, the rate of success was approximately 98 percent (42 from 43 roofs) and the measurement accuracy of the proposed approach was 28 cm in the horizontal direction and 31 cm for the vertical direction. The semiautomatic results are lesser than the manual ones. This can be explained by the fact that in the suggested approach, we use the nature of modular buildings such as parallelism and perpendicularity and by using operations as mirror. These assumptions may not always be true. In addition, due to the fact that the roof is parameterized, a small error in a parameter such as size of line or its direction may have a considerable affect on the results.

Based on the research experiments, the main factor for successful results is the segmentation of the desired polygon in the images space. If the segmentation succeeds the matching always succeeds. The advantage of the suggested approach is that even if the segmentation of one part fails, the operator is able to start the process by extracting a different part of the roof.

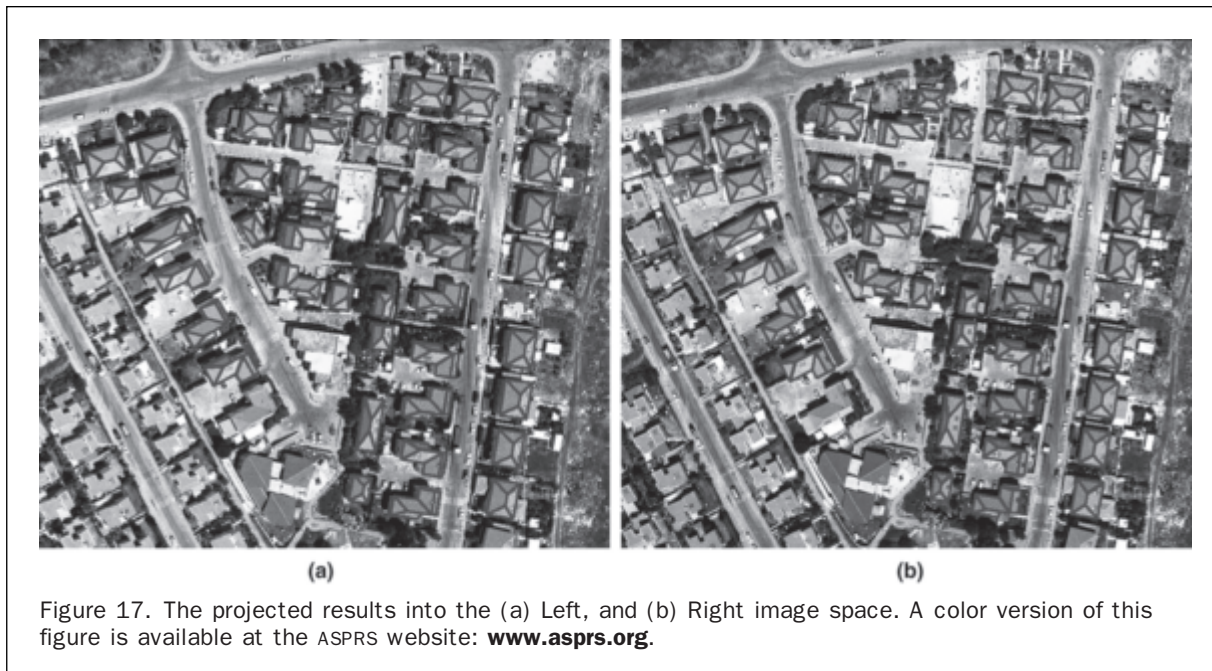


Figure 17. The projected results into the (a) Left, and (b) Right image space. A color version of this figure is available at the ASPRS website: www.asprs.org.

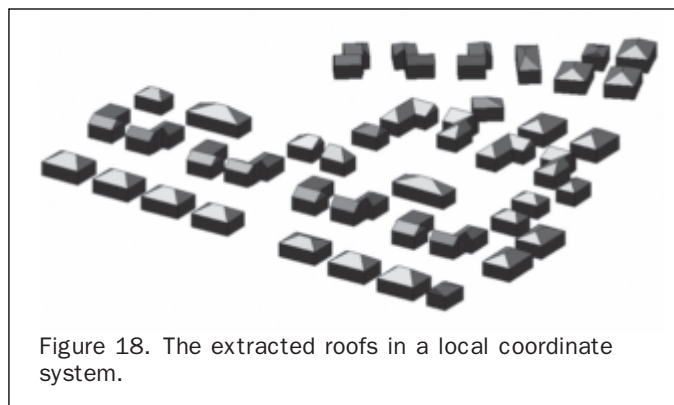


Figure 18. The extracted roofs in a local coordinate system.

TABLE 2. HORIZONTAL AND VERTICAL MEASUREMENT ACCURACY (M)

| Model | Manual | | Compared | | Semi-automatic | |
|-------|--------|-------|----------|-------|----------------|-------|
| | H | V | H | V | H | V |
| G | 0.05m | 0.09m | 0.35m | 0.35m | 0.34m | 0.33m |
| L | 0.05m | 0.09m | 0.20m | 0.29m | 0.19m | 0.27m |
| Both | 0.05m | 0.09m | 0.29m | 0.32m | 0.28m | 0.31m |

Summary and Conclusions

This paper presents innovative algorithms for semi-automatic extraction of 3D spatial polygons, based on an initial 2D manual pointing and their contribution towards roof extraction. The algorithms consist of several consecutive stages: initial pointing by a human operator which defines the algorithm as semi-automatic, extraction of a bounding polygon in the left image space, calculation of the estimated height and transformation to the right image space,

extraction of a bounding polygon in the right image space; an iterative process which matches both polygons by optimizing the Overlapping-Criterion using the well-known optimization model the “adjustment by conditions,” and, an iterative process which uses an adjacency matrix in order to achieve the polygons conflation and reconstruction of the 3D spatial polygon. These algorithms are based on a 2D approach to solving the 3D reality and can be employed in many feature extraction situations. The utilization of the

Overlapping Criterion for matching between two projected polygons is innovative.

In the suggested algorithms, the process starts by pointing on the left image space. Pointing at a different position on the left image space, as well as starting the process by pointing on the right image space, might cause to achieving other results. It should be noted that the differences between these different results are practically not important. Yet, one may decide to implement the process in both directions, from the left image (as interface) to the right image (as reference), and vice versa. This may slightly improve the results while having the disadvantage of doubling the process.

Based on these algorithms, a novel interactive and semi-automatic model-based approach for automation in roof extraction from two solved aerial images was developed. The main contributions of this approach are:

- Polygonal Approach: According to this approach, a roof can be extracted by extracting all the spatial polygons which comprise it or even only some of them if the parametric model is known.
- The Overlapping Criterion: Automatic matching between two projected polygons can be performed by optimizing the Overlapping Criterion between them.
- Divide and Conquer: The approach was adjusted to suit the case of extracting a spatial polygon from a pair of aerial images. According to this adjustment, we can separate the extraction process into three different sequential actions: extraction in left image, extraction in right image and fusion of the information from both images.
- Expanded Parametric Model (EPM): Expanding the use of parametric models by defining a new model, the Expanded Parametric Model, enclosing a number of parametric models.

This approach has several advantages: rapid extraction of roofs, a non-stereoscopic environment without the need for 3D spectacles, and the "Parallel" and "Perpendicular" nature of the results, thus fitting correctly "man-made objects." Moreover, this approach reduces the work required for roof extraction and thus having a better cost-effective solution; Success even in different conditions (varying illumination and varying photograph directions) enables identifying at a glance (by the operator) which roof can be extracted by this approach, thus permitting combining it with traditional manual extraction or other semi-automatic methods.

References

- Arkin, E.M., L.P. Chew, D.P. Huttenlocher, K. Kedem, and J.S.B. Mitchell, 1991. An efficiently computable metric for comparing polygonal shapes, *IEEE Transactions on Pattern Analysis and Machine Intelligence*, 13(3):209–216.
- Baillard, C., and A. Zisserman, 1999. Automatic reconstruction of piecewise planar models from multiple views, *Proceedings of CVPR 1999*, pp. 2559–2565.
- Cooper, M.A.R., 1987. *Control Surveys in Civil Engineering*, Collins, London, 381 p.
- Cord, M., and D. Declercq, 2001. Three dimensional building detection and modeling using a statistical approach, *IEEE Transactions on Image Processing*, 10(5):715–723.
- Croitoru, A., and Y. Doytsher, 2003. Monocular right-angle building hypothesis generation in regularized urban areas by pose clustering, *Photogrammetric Engineering & Remote Sensing*, 69(2):151–169.
- Gerke, M., C. Heipke, B.M. Straub, 2001. Building extraction from aerial imagery using a generic scene model and invariant geometric moments, *Proceedings of the IEEE/ISPRS Joint Workshop on Remote Sensing and Data Fusion over Urban Areas*, 08–09 November, University of Pavia, Rome, Italy, pp. 85–89.
- Gruen, A., and X. Wang, 1998. CC-modeler: A topology generator for 3D city models, *ISPRS Journal of Photogrammetry and Remote Sensing*, 53(5):286–295.
- Gruen, A., and X. Wang, 2001. News from CyberCity Modeler, *Automatic Extraction of Man-Made Objects from Aerial and Space Images (III)*, Balkema Publishers, Lisse, The Netherlands, pp: 93–101.
- Gruen, A., 1997. Automation in building reconstruction, *Photogrammetrische Woche*, pp. 175–186, URL: www.ifp.uni-stuttgart.de/publications/phowo97/gruen.pdf (last date accessed: 13 July 2008).
- Gulch, E., H. Muller, and T. Labe, 1999. Integration of automatic processes into semi-automatic building extraction, *International Archives of Photogrammetry and Remote Sensing*, 32(3–2W5):177–186.
- Irvin, R.B., and D.M. McKeown, 1989. Method for exploiting the relationship between buildings and their shadows in aerial imagery, *IEEE Transactions on Systems, Man, and Cybernetics*, 19(6):1564–1575.
- Kokubu, K., M. Kohiyama, F. Umemura, and F. Yamazaki, 2001. Automatic detection of building properties from aerial photographs using color and 3D configuration, *Presented at the 22nd Asian Conference on Remote Sensing*, November, Singapore.
- Kraus, K., 1993. *Photogrammetry, Volume 1*, Duenmiller, Bonn, 231 p.
- Oriot, H., and A. Michel, 2004. Building extraction from stereoscopic aerial images, *Applied Optics*, 43(2):218–226.
- Rau, J.Y., and L.C. Chen, 2003. Robust reconstruction of building models from three dimensional line segments, *Photogrammetric Engineering & Remote Sensing*, 69(2):181–188.
- Ruther, H., H. Martine, and E.G. Mitalo, 2002. Application of snakes and dynamic programming optimisation technique in modeling of buildings in informal settlement areas, *ISPRS Journal of Photogrammetry and Remote Sensing*, 56(4):269–282.
- Schwartz, J., and M. Sharir, 1986. Identification of partly obscured objects in two and three dimensions by matching noisy characteristic curves, *The International Journal of Robotic Research*, 5(4):38–55.
- Sibiryakov, A., 1996. House detection from aerial color images, *Internal Report, Institute of Geodesy and Photogrammetry, Swiss Federal Institute of Technology, Zurich (ETH)*.
- Tseng, Y., and S. Wang, 2003. Semi-automated building extraction based on CSG model, *Photogrammetric Engineering & Remote Sensing*, 69(2):171–180.
- Weidner, U., and W. Forstner, 1995. Toward automatic building reconstruction from high resolution digital elevation model, *ISPRS Journal of Photogrammetry and Remote Sensing*, 50(4):38–49.

(Received 06 May 2006; accepted 11 September 2006; revised 29 January 2007)

Conterminous U.S. and Alaska Forest Type Mapping Using Forest Inventory and Analysis Data

B. Ruefenacht, M.V. Finco, M.D. Nelson, R. Czaplewski, E.H. Helmer, J.A. Blackard, G.R. Holden, A.J. Lister, D. Salajanu, D. Weyermann, and K. Winterberger.

Abstract

Classification-trees were used to model forest type groups and forest types for the conterminous United States and Alaska. The predictor data were a geospatial data set with a spatial resolution of 250 m developed by the U.S. Department of Agriculture Forest Service (USFS). The response data were plot data from the USFS Forest Inventory and Analysis program. Overall accuracies for the conterminous U.S. for the forest type group and forest type were 69 percent (Kappa = 0.66) and 50 percent (Kappa = 0.57), respectively. The overall accuracies for Alaska for the forest type group and forest type were 78 percent (Kappa = 0.69) and 67 percent (Kappa = 0.61), respectively. This is the first forest type map produced for the U.S. The forest type group map is an update of a previous forest type group map created by Zhu and Evans (1994).

B. Ruefenacht and M.V. Finco are with the USDA Forest Service, Remote Sensing Applications Center, 2222 West 2300 South, West Valley City, UT 84119 (bruefenacht@fs.fed.us).

M.D. Nelson is with the USDA Forest Service, St. Paul, MN 55108.

R. Czaplewski is with the Rocky Mountain Research Station, Fort Collins, CO 80526.

E.H. Helmer is with the International Institute of Tropical Forestry USDA Forest Service, Río Piedras, PR 00926.

J.A. Blackard is with the U.S. Army Corps of Engineers, Fort Worth District, Fort Worth, TX 76102, and formerly with the Rocky Mountain Research Station, Ogden, UT 84401.

G.R. Holden is with the Cibola National Forest, Albuquerque, NM 87113, and formerly with the USDA Forest Service, North Central Research Station, St. Paul, MN 55108.

A.J. Lister is with the Northeastern Research Station, Newtown Square, PA 19073.

D. Salajanu is with the Southern Research Station, Knoxville, TN 37919.

D. Weyermann is with the Pacific Northwest Research Station, Portland, OR 97205.

K. Winterberger is with the Pacific Northwest Research Station, Anchorage, AK 99503.

Introduction

The United States Department of Agriculture Forest Service (USFS) Forest Inventory and Analysis (FIA) program has been in continuous operation since 1930. The mission of FIA is to inventory the renewable forest and rangeland resources of the U.S. To inventory these resources, FIA has placed plots throughout the U.S. at an intensity of approximately one plot per 2,000 ha (6,000 acres) (Forest Inventory and Analysis, 2004). FIA uses an annual rotating panel system where between 10 to 20 percent of each state's FIA plots are sampled every year. From this plot data, the FIA program produces annual reports in the form of tabular data at the county and state level. This information is freely available to the public, but the original plot locations are not available due to provisions of the Food Security Act of 1985 (7 U.S.C. 2276).

FIA is legally required to provide summarized or analyzed data that are readily available and targeted at different audiences. One of the ways to accomplish this objective is to provide geospatial modeled products using FIA plot data and remote sensing imagery. Blackard *et al.* (2008) developed a forest/non-forest map and an above-ground live forest biomass map for the conterminous U.S., Alaska, and Puerto Rico derived from modeling FIA plot forest/non-forest and biomass variables as functions of 250 m resolution geo-spatial database. Observed biomass values from an independent test data set were favorably correlated to the predicted biomass values with correlation coefficients ranging between 0.40 to 0.78. Additionally, 21 States' modeled biomass estimates fell within 10 percent of the plot-based biomass estimates. Classification accuracies for the forest/non-forest product ranged from 80 to 98 percent. Thus, modeling FIA plot attributes as functions of remote sensing images and GIS data layers effectively scales plot-based forest attributes to national maps.

Blackard *et al.* (2008) used classification and regression-trees (CART) to model biomass and forest/non-forest. Using CART for land-cover classification is becoming popular (DeFries and Chan, 2000; DeFries *et al.*, 1998; Friedl and Brodley, 1997; Friedl *et al.*, 1999; Hansen and DeFries, 1996). CART procedures have several advantages over more traditional classification procedures, such as, supervised and

Photogrammetric Engineering & Remote Sensing
Vol. 74, No. 11, November 2008, pp. 1379–1388.

0099-1112/08/7411-1379/\$3.00/0
© 2008 American Society for Photogrammetry
and Remote Sensing

unsupervised algorithms (Lillesand and Kiefer, 2000; Pal and Mather, 2003). Classification-trees are non-parametric, and as such, do not require assumptions about data distributions and can handle non-linear relationships between variables. They can also allow for missing data values, handle both numerical and categorical data, and incorporate many different data layers. The hierarchical structure of classification-trees makes interactions between data layers easier to interpret. Classification-trees are significantly less labor intensive than other classification techniques and can be used efficiently for large land-cover classifications (Friedl *et al.*, 1999; DeFries *et al.*, 1998). With quality training data, the accuracies of classification-trees are either similar to or better than supervised and unsupervised classification techniques (Lawrence and Wright, 2001; Friedl *et al.*, 1999; Friedl and Brodley, 1997; Hansen *et al.*, 1996).

Others have used remote sensing imagery and FIA plot data to create national mapping products. Zhu and Evans (1994) produced a forest type group map covering the entire

United States and Puerto Rico. This forest type group map was produced using Advanced Very High Resolution Radiometer (AVHRR) imagery collected in 1992 and FIA plot data, which was the first attempt to create a forest type group map of the U.S. The procedure used to create the forest type group map involved several iterations of unsupervised classification algorithms, spectral signature evaluation, masking, and recoding.

Forest type group and forest type are two FIA plot variables. Eyer (1980) defined 145 forest types, which are aggregations or pure stands of forest trees. The FIA program uses a modified version of Eyer's (1980) forest type classification scheme. FIA combined some of the Eyer (1980) forest types and others were redefined for a total of 142 forest types (Table 1). Eyer (1980) grouped the forest types into 20 forest type groups, which classification scheme came from the USFS Renewable Resources Evaluation Group program. FIA uses a similar forest type group classification scheme. FIA defined eight new forest type groups for a

TABLE 1. LIST OF THE USDA FOREST SERVICE FOREST INVENTORY AND ANALYSIS FOREST TYPE GROUPS AND FOREST TYPES WITH THEIR ASSOCIATED CODES

| | | | |
|---|------------|---|------------|
| White/Red/Jack Pine Group | 100 | Blue Spruce | 269 |
| Jack Pine | 101 | Mountain Hemlock | 270 |
| Red Pine | 102 | Alaska-yellow-cedar | 271 |
| Eastern White Pine | 103 | Lodgepole Pine Group | 280 |
| Eastern White Pine/Eastern Hemlock | 104 | Lodgepole Pine | 281 |
| Eastern Hemlock | 105 | Hemlock/Sitka Spruce Group | 300 |
| Spruce/Fir Group | 120 | Western Hemlock | 301 |
| Balsam Fir | 121 | Western Red Cedar | 304 |
| White Spruce | 122 | Sitka Spruce | 305 |
| Red Spruce | 123 | Western Larch Group | 320 |
| Red Spruce/Balsam Fir | 124 | Western Larch | 321 |
| Black Spruce | 125 | Redwood Group | 340 |
| Tamarack | 126 | Redwood | 341 |
| Northern White-cedar | 127 | Giant Sequoia | 342 |
| Longleaf/Slash Pine Group | 140 | Other Western Softwoods Group | 360 |
| Longleaf Pine | 141 | Knobcone Pine | 361 |
| Slash Pine | 142 | Southwest White Pine | 362 |
| Loblolly/Shortleaf Pine Group | 160 | Bishop Pine | 363 |
| Loblolly Pine | 161 | Monterey Pine | 364 |
| Shortleaf Pine | 162 | Foxtail Pine/Bristlecone Pine | 365 |
| Virginia Pine | 163 | Limber Pine | 366 |
| Sand Pine | 164 | Whitebark Pine | 367 |
| Table-mountain Pine | 165 | Misc. Western Softwoods | 368 |
| Pond Pine | 166 | California Mixed Conifer Group | 370 |
| Pitch Pine | 167 | California Mixed Conifer | 371 |
| Spruce Pine | 168 | Exotic Softwoods Group | 380 |
| Pinyon/Juniper Group | 180 | Scotch Pine | 381 |
| Eastern Red Cedar | 181 | Australian Pine | 382 |
| Rocky Mountain Juniper | 182 | Other Exotic Softwoods | 383 |
| Western Juniper | 183 | Norway Spruce | 384 |
| Juniper Woodland | 184 | Introduced Larch | 385 |
| Pinyon Juniper Woodland | 185 | Oak/Pine Group | 400 |
| Douglas-fir Group | 200 | Eastern White Pine/Northern Red Oak/White Ash | 401 |
| Douglas-fir | 201 | Eastern Redcedar/Hardwood | 402 |
| Port Orford Cedar | 202 | Longleaf Pine/Oak | 403 |
| Ponderosa Pine Group | 220 | Shortleaf Pine/Oak | 404 |
| Ponderosa Pine | 221 | Virginia Pine/Southern Red Oak | 405 |
| Incense Cedar | 222 | Loblolly Pine/Hardwood | 406 |
| Jeffrey Pine/Coulter Pine/Bigcone Douglas Fir | 223 | Slash Pine/Hardwood | 407 |
| Sugar Pine | 224 | Other Pine/Hardwood | 409 |
| Western White Pine Group | 240 | Oak/Hickory Group | 500 |
| Western White Pine | 241 | Post Oak/Blackjack Oak | 501 |
| Fir/Spruce/Mountain Hemlock Group | 260 | Chestnut Oak | 502 |
| White Fir | 261 | White Oak/Red Oak/Hickory | 503 |
| Red Fir | 262 | White Oak | 504 |
| Noble Fir | 263 | Northern Red Oak | 505 |
| Pacific Silver Fir | 264 | Yellow-poplar/White Oak/Northern Red Oak | 506 |
| Engelmann Spruce | 265 | Sassafras/Persimmon | 507 |
| Engelmann Spruce/Subalpine Fir | 266 | Sweetgum/Yellow-poplar | 508 |
| Grand Fir | 267 | Bur Oak | 509 |
| Subalpine Fir | 268 | Scarlet Oak | 510 |

| | | | |
|------------------------------------|------------|--------------------------------------|------------|
| Yellow-poplar | 511 | Paper Birch | 902 |
| Black Walnut | 512 | Gray Birch | 903 |
| Black Locust | 513 | Balsam Poplar | 904 |
| Southern Scrub Oak | 514 | Alder/Maple Group | 910 |
| Chestnut Oak/Black Oak/Scarlet Oak | 515 | Bigleaf Maple | 912 |
| Red Maple/Oak | 519 | Western Oak Group | 920 |
| Mixed Upland Hardwoods | 520 | Gray Pine | 921 |
| Oak/Gum/Cypress Group | 600 | California Black Oak | 922 |
| Swamp Chestnut Oak/Cherrybark Oak | 601 | Oregon White Oak | 923 |
| Sweetgum/Nuttall Oak/Willow Oak | 602 | Blue Oak | 924 |
| Overcup Oak/Water Hickory | 605 | Deciduous Oak Woodland | 925 |
| Atlantic White-cedar | 606 | Evergreen Oak | 926 |
| Baldcypress/Water Tupelo | 607 | Coast Live Oak | 931 |
| Sweetbay/Swamp Tupelo/Red Maple | 608 | Canyon Live Oak/Interior Live Oak | 932 |
| Elm/Ash/Cottonwood Group | 700 | Tanoak/Laurel Group | 940 |
| Black Ash/American Elm/Red Maple | 701 | Tanoak | 941 |
| River Birch/Sycamore | 702 | California Laurel | 942 |
| Cottonwood | 703 | Giant Chinkapin | 943 |
| Willow | 704 | Other Western Hardwoods Group | 950 |
| Sycamore/Pecan/American Elm | 705 | Pacific Madrone | 951 |
| Sugarberry/Hackberry/Elm/Green Ash | 706 | Mesquite Woodland | 952 |
| Silver Maple/American Elm | 707 | Cercarpus Woodland | 953 |
| Red Maple/Lowland | 708 | Intermountain Maple Woodland | 954 |
| Cottonwood/Willow | 709 | Misc. Western Hardwood Woodlands | 955 |
| Oregon Ash | 722 | Tropical Hardwoods Group | 980 |
| Maple/Beech/Birch Group | 800 | Sable Palm | 981 |
| Sugar Maple/Beech/Yellow Birch | 801 | Mangrove | 982 |
| Black Cherry | 802 | Other Tropical | 989 |
| Cherry/Ash/Yellow-poplar | 803 | Exotic Hardwoods Group | 990 |
| Hard Maple/Basswood | 805 | Paulownia | 991 |
| Elm/Ash/Locust | 807 | Melaluca | 992 |
| Red Maple/Upland | 809 | Eucalyptus | 993 |
| Aspen/Birch Group | 900 | Other Exotic Hardwoods | 995 |
| Aspen | 901 | | |

total of 28 forest type groups (Table 1). The forest type group and forest type are determined for a plot in the following manner. Each tree on the plot is placed into an appropriate forest type group. The stocking values, which are individual trees' contributions to the total stocking of the stand, of the trees within the forest type groups are summed. Using a decision tree, the final forest type is assigned to each plot (Arner *et al.*, 2003). Since the forest type group and forest type classification schemes are hierarchical, the final forest group is determined by the forest type.

The main objective of this study was to examine the feasibility of using low resolution imagery, such as 250 m Terra MODIS imagery, and FIA plot data to produce national mapping products in a timely, efficient, and accurate manner. The FIA plot variables chosen for this project were forest type group and forest type. Even though the forest type group is determined by the forest type, and thus, the forest type group can be obtained by simply aggregating the forest types, the variables were modeled separately. Since the forest type group is a more general classification scheme than the forest type classification scheme, the forest type group final result was expected to have higher accuracy than the forest type final result. If only the forest types were modeled and the forest type groups were created by aggregating the forest types, the inaccuracies of the forest types will be compounded negatively affecting the forest type group accuracies. For instance, it is expected that the forest types in the oak/hickory group to have low accuracies due to the spectral similarities between the types in that group. If the oak/hickory forest type group was created by aggregating the types within that group, the oak/hickory forest type group would have low accuracy as well. However, the forest type group might have a high accuracy value if classified separately. Furthermore, the forest type group and forest type products might be used by different groups

for different purposes. For these reasons, forest type groups and forest types were modeled separately creating two completely independent products. This means that a forest type pixel might not correspond to the forest type group assigned to the same pixel. If this is a concern or presents a problem to users, users can simply aggregate the forest types creating their own forest type group product.

Because CART does have the capability to handle large datasets and produce accuracies similar to other techniques, CART was chosen to model forest type groups and forest types for Alaska and the conterminous U.S. If the techniques developed for creating these spatial products are effective, perhaps additional FIA variables can be modeled and made available to the public.

Methods

The area of each FIA plot is categorized into a single condition or multi-conditions based on owner class and land class, which includes forest, non-forest, and water (Forest Inventory and Analysis, 2004). If an FIA plot is comprised of multi-conditions, the proportion of each condition occurring within the plot is calculated. For this study, all FIA plots with at least 50 percent of the plot area categorized into the land class forest condition were used for the modeling procedure. The land class forest condition is defined as greater than 0.4 ha (1 acre) in size, greater than 37 m (120 feet) in width, having or has been at least 10 percent stocked by trees of any size in the past or where stocking cannot be determined (e.g., western woodlands), having or has been at least five percent crown cover by trees of any size in the past, having an undisturbed understory, and not subjected to uses that prevent normal tree regeneration and succession (Forest Inventory and Analysis, 2004). According to this definition, transitional plots (i.e., plots temporarily

cleared of trees) are categorized under the forest condition even though few or no trees currently exist on the plot. Transitional plots were used in the modeling procedure. It is unknown exactly how many transitional plots were actually used, but transitional plots probably comprised less than one percent of the total number of plots.

For the mapping of the forest type group and forest type, the FIA plot data were collected between 1978 and 2004. The majority of the plot data (55 percent) were collected between 2000 and 2004; 36 percent of the plot data were collected between 1990 and 1999, and nine percent were collected pre-1990.

A geospatial data set consisting of 269 remote sensing images and GIS layers with a spatial resolution of 250 m served as the predictor variables in the modeling of the forest type group and forest type for the conterminous U.S. All images and layers were projected to the Albers Conical Equal Area NAD27 projection. For Alaska, 19 geospatial remote sensing images and GIS layers were available, and most of the images and layers had a native spatial resolution of 250 m. Those with a native spatial resolution greater than 250 m underwent either nearest neighbor resampling if the data were categorical or bilinear interpolation resampling if the data were continuous.

The National Land Cover Database (NLCD), elevation, slope, and aspect data were at 30 m spatial resolution. NLCD was recoded into five classes: deciduous, developed, evergreen forest, mixed forest, shrubland, and woody wetland (Vogelmann *et al.*, 2001). To rescale the NLCD to 250 m, the percent of each of these NLCD classes occurring within a 250 m pixel was calculated.

The 30 m elevation data set was rescaled to 90 m. Mean elevation was calculated for a 3×3 window resulting in a 270 m mean elevation data set, which was resampled to 250 m using bilinear interpolation. Slope and aspect were derived from the 90 m elevation data set. The 90 m slope data set was resampled to 250 m using bilinear interpolation. The aspect data set was recoded into four categories: (a) 0 to 90 degrees, (b) 91 to 180 degrees, (c) 181 to 270 degrees, and (d) 271 to 360 degrees. The maximum aspect for a 3×3 window was calculated resulting in a 270 m dominant aspect product, which was resampled to 250 m using nearest neighbor. Using the 90 m recoded aspect data set, a focal variety aspect data set was produced by calculating the number of unique values within a 3×3 window, resulting in a 270 m product, which was resampled to 250 m using nearest neighbor.

Soils (STATSGO), climate, and ecoregions variables were also included in the geo-spatial data set. The soils GIS layers were obtained from the National Resources Conservation Services (Miller and White, 1998). The climate data were obtained from DAYMET (Thornton *et al.*, 1997). The DAYMET variables used were annual and monthly average precipitation, monthly maximum and minimum temperature, and annual and monthly average temperature. The climate data resolution was 1 km. The climate data were rescaled to 250 m resolution using bilinear interpolation. For the conterminous U.S., Bailey's ecoregions (Bailey, 1989; Bailey and Hogg, 1986) were used and for Alaska, unified ecoregions of Alaska (Nowacki *et al.*, 2001) were used. The STATSGO, Bailey's ecoregions, and unified ecoregions of Alaska vector data were converted to raster data and scaled to 250 m.

The rest of the data layers consisted of Terra MODIS eight-day, Terra MODIS 32-day, and Terra MODIS-derived products such as enhanced vegetation index (EVI), normalized difference vegetation index (NDVI), and Terra MODIS vegetation continuous fields from 2001 (Hansen *et al.*, 2003). To capture phenology changes, each of these MODIS products, except for the Terra MODIS 32-day imagery, came from

three time periods: spring, summer, and fall. Because of the difficulty in finding cloud-free MODIS eight-day imagery, several 32-day MODIS images were used that covered spring, summer, and fall. Because of striping in band 5 in all the Terra MODIS eight-day and 32-day imagery, all Terra MODIS band 5 layers were excluded from analyses.

Many of these data layers are correlated. However, classification-trees can handle complex relationships between variables and can determine which data layers most accurately predict classes. Even though two data layers are correlated, there are differences between them. Classification-trees have the capability to use variations in data layers to develop models. The models that result are often complex. However, complex models are appropriate when the goal of a classification is accuracy rather than characterizing the relationships between the classes and the data layers. Consequently, correlated variables can be used.

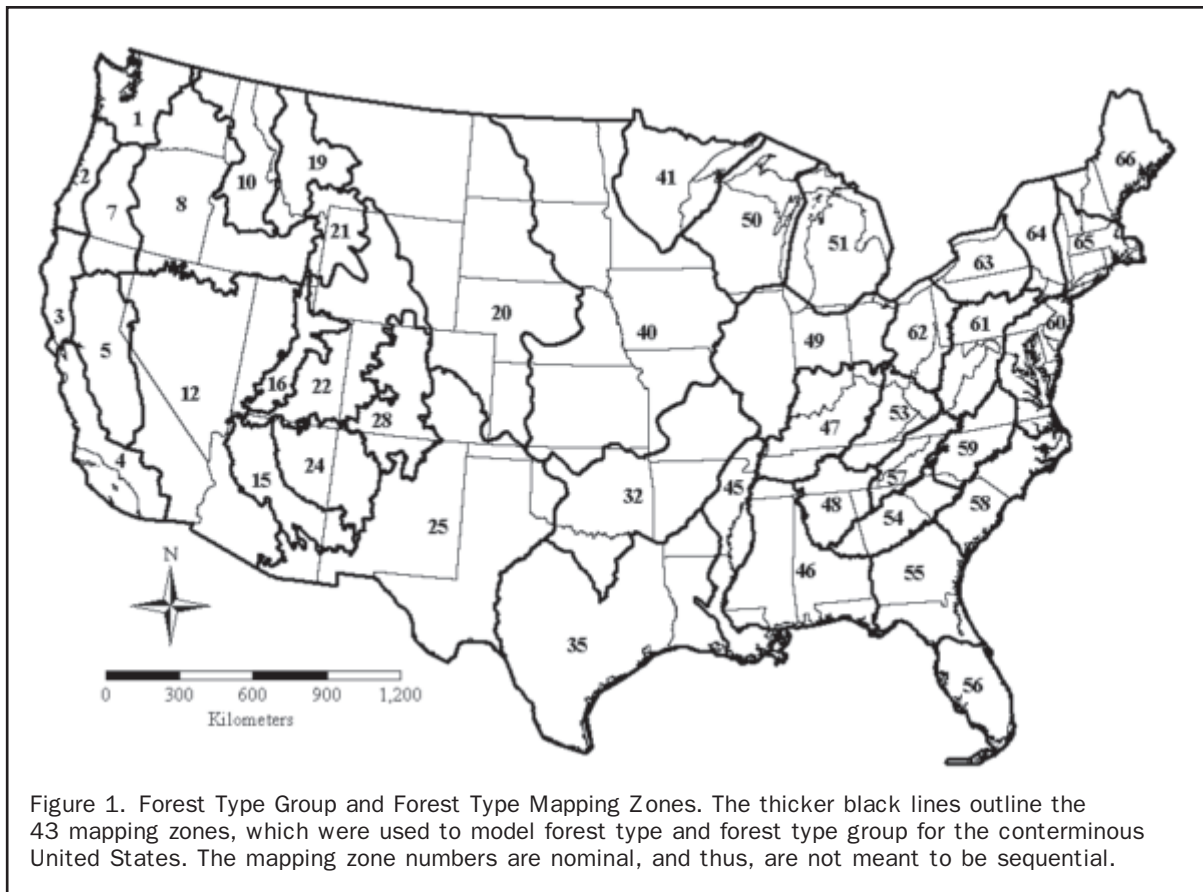
All imagery, except for Alaska, was pre-stratified in order to prevent errors such as an eastern U.S. forest type occurring in the western U.S. The imagery was stratified using the USGS NLCD 65 mapping zones for the conterminous U.S. (Homer and Gallant, 2001). The reason why the NLCD mapping zones were chosen as opposed to Bailey's or Omernik ecoregions (Omernik, 1987) is because the NLCD mapping zones, which are loosely based on Omernik ecoregions, were developed specifically for remote sensing classification. The NLCD mapping zones takes into account the spectral variability occurring within each mapping zone. Thus, using NLCD mapping zones for pre-stratification seems more appropriate than other ecoregions. Alaska was modeled separately from the conterminous U.S. and was not further stratified. The reason why Alaska was not stratified is FIA data does not exist for large portions of Alaska. If Alaska was stratified, there would be many strata with few or no points.

Some evidence suggests that increasing sample sizes increases classification-tree accuracy (Pal and Mather, 2003). Seventeen NLCD mapping zones had fewer than 200 FIA forested plots. To increase the number of FIA plots for these NLCD mapping zones, these 17 zones were merged with adjacent NLCD mapping zones creating a total of 43 mapping zones (Figure 1). Instead of re-ordering the mapping zones from 1 to 43, the original NLCD mapping zones numbers were retained because the numbers are nominal data and frequent users of the NLCD mapping zones associate the numbers to specific geographic areas. When merging the 17 zones, the lowest NLCD mapping zone number was retained, while the other numbers were eliminated. Even though Figure 1 displays mapping zones 1 to 66, there are actually only 43 mapping zones. Each mapping zone and Alaska was modeled independently of each other.

For each mapping zone and Alaska, the FIA plot data were intersected with the geo-spatial data set creating a modeling data set. For the conterminous U.S., 83,519 FIA forested plots were used, and 5,392 FIA forested plots were used for Alaska. A random ten percent of the plots were withheld from model development and were used for accuracy assessment purposes.

Rulequest's See5[®] software package (<http://www.rulequest.com>), which is a commercial version of C4.5 (Quinlan, 1993), was used to develop the classification-trees for the forest type group and forest type classifications. Classification-trees recursively divide data into smaller groups on the basis of tests performed at the nodes in the trees. The tests used are learning algorithms developed within the pattern-recognition and machine-learning communities. At the ends of the trees, a value is assigned.

Boosting can significantly increase classification-trees accuracies (Friedl *et al.*, 1999; Pal and Mather, 2003). Boosting creates multiple iterations of classification-trees.



For the first iteration, no weighting occurs. For all the other iterations, weights are assigned to each training observation. The weights assigned are based upon the misclassifications from the previous iteration. Each iteration tries to correct the errors from the previous iteration. Voting is used to generate the final classifier (DeFries and Chan, 2000; Freund and Schapire, 1996; Quinlan, 1996; Friedl *et al.*, 1999). Various studies have found 10 iterations to be the recommended number for both remote sensing studies and non-remote sensing studies (Friedl *et al.*, 1999; Freund and Schapire, 1997; Pal and Mather, 2003). For this study, the boosting option was set at 10 iterations.

Classification-trees can grow very large and complex, causing the classification-trees to overfit the training data. This can lead to poor accuracies when the classification-trees are applied if there were errors or noise in the training data. To alleviate this problem, classification-trees are pruned making them more general and flexible when classifying data not included in the training data set. The methodology See5[®] uses to prune is error-based pruning (Hall *et al.*, 2003; Mingers, 1989; Quinlan, 1987; Quinlan, 1993). To control the amount of pruning, the user can set the “pruning certainty factor.” Changing this value affects the size and accuracy of the classification-tree. For this project the pruning certainty factor was set at 25, which is the recommended value determined by Quinlan (1993), and corroborated by Hall *et al.* (2003).

Forest type group and forest type classifications were created from the See5[®] classification-trees and the geospatial data set by integrating the See5[®] public domain code available from <http://www.rulequest.com> with ERDAS Imagine[®] software (version 8.6). The See5[®] public domain

code has the ability to produce confidence values, which are expressions of the confidence of the classifications produced from the See5[®] models. Spatial confidence products for the forest type group and forest type were produced for the conterminous U.S. and Alaska. These spatial data products produced from See5[®], covered the conterminous U.S. and Alaska regardless of the presence of forest. The non-forest areas were masked using the forest/non-forest mask produced by FIA scientists (Blackard *et al.*, 2008).

If a testing data set is specified, See5[®] creates standard error matrices (Congalton and Green, 1999). Using these matrices, overall accuracies and kappas were calculated for each zone and for Alaska. As an additional accuracy assessment, using FIA’s mapmaker program (<http://ncrs2.fs.fed.us/4801/fiadb>) the current FIA state summaries of forest type group and forest type areas were compared to state summaries generated from the See5[®] modeled forest type group and forest type classifications.

Results and Discussion

The conterminous U.S. and Alaska forest type group classifications are shown in Plates 1 and 2. The conterminous U.S. and Alaska forest type classifications are not shown due to the amount of detail, but they along with the forest type group map, the confidence maps, associated metadata, and accuracy tables for each mapping zone are available at <http://fsgeodata.fs.fed.us>.

For the western U.S., the most abundant forest type group was pinyon/juniper group (22 million hectares) followed by Douglas-fir group (20 million hectares). The pinyon/juniper group occurred throughout the arid western U.S. and the

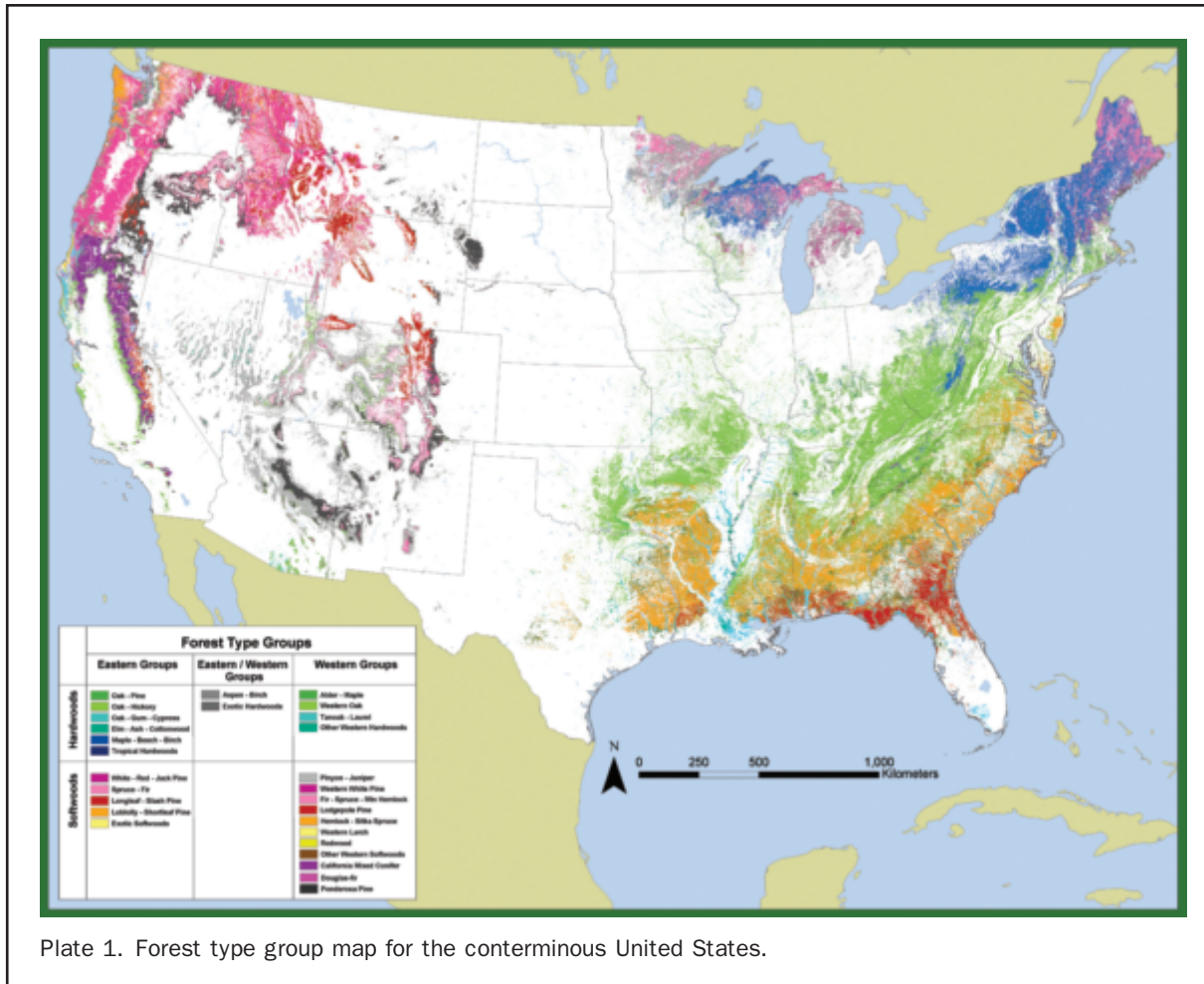


Plate 1. Forest type group map for the conterminous United States.

Douglas-fir group was prevalent in the Pacific Northwest and the northern Rocky Mountains. Other predominant western forest type groups included fir/spruce/mountain hemlock group (15 million hectares), ponderosa pine group (12 million hectares), and lodgepole pine group (7 million hectares).

The most abundant forest type in the western U.S. was Douglas-fir (22 million hectares) followed by pinyon/juniper woodland (18 million hectares). Other predominant western U.S. forest types were ponderosa pine (12 million hectares), lodgepole pine (7 million hectares), and California mixed conifer (5 million hectares). Note that the California mixed conifer forest type consists of a conglomerate of conifers including Douglas-fir (*Pseudotsuga menziesii*), ponderosa pine (*Pinus ponderosa*), sugar pine (*Pinus lambertiana*), incense cedar (*Libocedrus decurrens*), and white fir (*Abies concolor*). FIA only recognizes this type in California. Even though these tree species occur in neighboring states of California, the tree species are grouped into other types.

For the eastern U.S., the most abundant forest type group was oak/hickory group (67 million hectares) followed by loblolly/shortleaf pine group (31 million hectares), and maple/beech/birch group (24 million hectares). The oak/hickory group occurred throughout the eastern U.S., but primarily in the mid-eastern states. The loblolly/shortleaf pine group was predominant in the south and the maple/beech/birch group was predominant in the northeast. Other common eastern forest type groups included aspen/birch group (13 million hectares), oak/gum/cypress group

(11 million hectares), and oak/pine group (8 million hectares). The most abundant forest type in the eastern U.S. was loblolly pine (34 million hectares) followed by white oak/red oak/hickory (29 million hectares).

For Alaska, the most abundant forest type group was spruce/fir group (49 million hectares) followed by aspen/birch group (8 million hectares) and hemlock/Sitka spruce group (4 million hectares). The spruce/fir group and aspen/birch group occurred throughout the interior of Alaska and hemlock/Sitka spruce group occurred mainly in southeastern Alaska. The most abundant forest type in Alaska was white spruce (28 million hectares) followed by black spruce (20 million hectares) and paper birch (7 million hectares). All of these forest types occurred primarily in the interior of Alaska.

For the conterminous U.S., most forest type groups and forest types had low confidence values. The forest type group with the highest confidence was the pinyon/juniper group, which had 80 percent of the pixels with greater than 70 percent confidence. The next highest was the oak/hickory group with 61 percent of the pixels with greater than 70 percent confidence. That was followed by the maple/beech/birch group with 54 percent of the pixels with greater than 70 percent confidence. The forest type with the highest confidence was pinyon juniper woodland with 76 percent of the pixels with greater than 70 percent confidence. The next highest forest type was mesquite with 58 percent of the pixels with greater than 70 percent confidence.

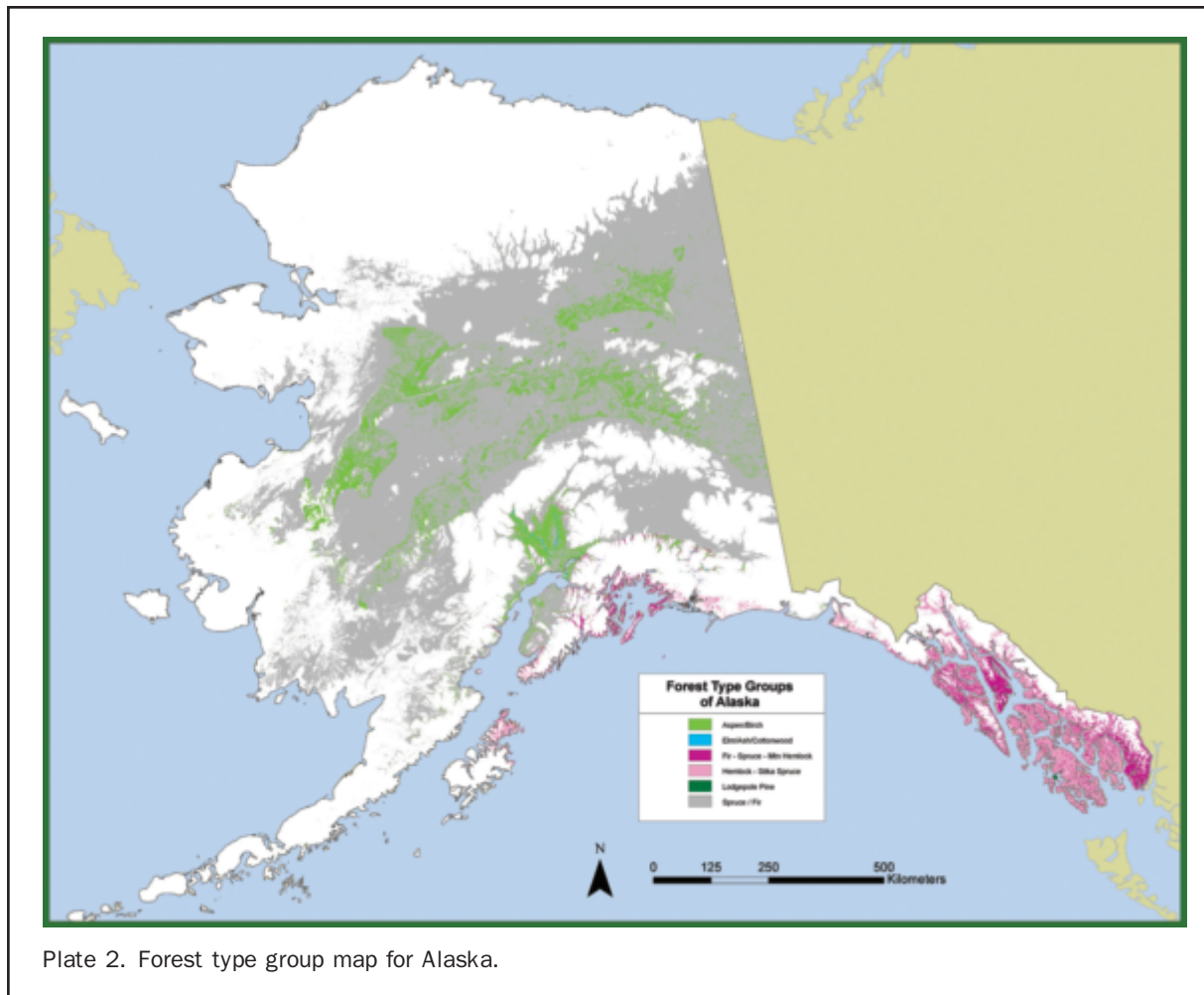


Plate 2. Forest type group map for Alaska.

For Alaska, the confidence values were higher. The forest type group with the highest confidence was the spruce/fir group, which had 85 percent of the pixels with greater than 70 percent confidence. The next highest was the hemlock/Sitka spruce group with 68 percent of the pixels greater than 70 percent confidence. That was followed by the fir/spruce/mountain hemlock group with 62 percent of the pixels greater than 70 percent confidence. The forest type with the highest confidence was Sitka spruce with 73 percent of the pixels with greater than 70 percent confidence. The next highest was mountain hemlock with 69 percent of the pixels with greater than 70 percent confidence. This was followed by white spruce with 64 percent of the pixels with greater than 70 percent confidence.

One of the advantages of using classification-trees is the ease of interpretation of the relationships between the independent variables and the dependent variable. For this project, the See5[®] output produced 88 classification-trees: a forest type group classification-tree and a forest type classification-tree for Alaska and for each of the 43 mapping zones. Each of these 88 classification-tree outputs consisted of ten classification-trees produced by the boosting option. Each individual classification tree consisted of more than 20 levels, and each of the 88 classification tree outputs are over 50 pages in length. Thus, the amount of data prohibits detailed examination of these classification-trees. For those interested in the models, they are available from the principal author. It is possible, however, to present

general summaries of the mapping zones and Alaska classification-trees.

For the forest type groups occurring in the western U.S., topography variables were the most frequently used variables in the classification-trees followed by the spring and fall dates of the MODIS EVI imagery and percent tree cover from the MODIS vegetation continuous fields. It is well known that temperature and precipitation play vital roles in the distribution and growth of vegetation (Burns and Honkala, 1990a; Burns and Honkala, 1990b). Topography in the western U.S. has a strong influence on precipitation and temperature. Topography variables should be prevalent in the classification-trees for the western U.S. mapping zones.

Topographical relief in the eastern U.S. is relatively minor compared to the western U.S., and climate is less influenced by topography in the eastern U.S. Variables associated with plant growth such as climate and soils should be used more frequently in the classification-trees for the eastern U.S. than the topography variables. However, instead of the climate variables being the most frequently used, the spring, summer, and fall dates of the MODIS EVI imagery as well as the fall date of the MODIS NDVI image were the most frequently used variables in the forest type group classification-trees for the eastern U.S. Topography variables were the second most frequently used variables in the classification-trees. NDVI indicates density of plant growth and is frequently used in vegetation mapping. EVI is similar to NDVI, but EVI optimizes the vegetation signal

improving sensitivity in high plant density regions. The differences in the EVI between the spring, summer, and fall could be surrogates for climatic data and this could explain the abundance of these variables in the forest type group classification-trees for the eastern U.S.

The forest type classification-trees for the western U.S. showed similar variable usage as the forest type group classification-trees for the western U.S. The topography variables were the most frequently used variables in the classification-trees followed by the spring, summer, and fall MODIS EVI imagery.

The topography variables were the most frequently used variables for the forest type classification-trees for the eastern U.S. This was unexpected because the topography variables were not expected to have a large influence in the eastern U.S. The second most frequently used variables for the forest type classification-trees for the eastern U.S. was the spring, summer, and fall MODIS EVI imagery, which

were also significant variables for the forest type group classification-trees for the eastern U.S.

For Alaska, the most frequently used variables for both the forest type group classification-trees and the forest type classification-trees were the topography variables. Alaska does have high topographical relief. The elevation ranges from 6,200 m (20,000 feet) to 0 m. Topography is expected to have a large influence in the forest type groups and forest type. The second most frequently used variable in both classification-trees was the unified ecoregions.

Table 2 shows the forest type group and forest type accuracies along with the associated kappas for each mapping zone. The highest forest type accuracy was 81 percent and the lowest was 34 percent. All of the mapping zones, except for one, with forest type accuracy greater than or equal to 75 percent occurred in the sparsely forested arid western U.S. All of the mapping zones with forest type accuracy less than 40 percent occurred in the northeast U.S., an area high

TABLE 2. FOREST TYPE GROUP AND FOREST TYPE OVERALL ACCURACIES AND KAPPAS FOR THE 43 MAPPING ZONES AND ALASKA. THE MAPPING ZONES REFER TO THE MAPPING ZONES IN FIGURE 1

| Zone | Forest Type Group Overall Accuracy | Kappa | Forest Type Overall Accuracy | Kappa |
|--------|------------------------------------|-------|------------------------------|-------|
| Alaska | 78% | 0.69 | 67% | 0.61 |
| 1 | 66% | 0.50 | 56% | 0.38 |
| 2 | 66% | 0.24 | 66% | 0.19 |
| 3 | 52% | 0.36 | 55% | 0.40 |
| 4 | 71% | 0.42 | 41% | 0.25 |
| 5 | 60% | 0.46 | 51% | 0.38 |
| 7 | 69% | 0.61 | 64% | 0.56 |
| 8 | 61% | 0.49 | 57% | 0.47 |
| 10 | 54% | 0.33 | 53% | 0.37 |
| 12 | 92% | 0.63 | 81% | 0.54 |
| 15 | 78% | 0.59 | 73% | 0.60 |
| 16 | 62% | 0.55 | 49% | 0.42 |
| 19 | 60% | 0.44 | 63% | 0.49 |
| 20 | 75% | 0.57 | 75% | 0.59 |
| 21 | 62% | 0.50 | 57% | 0.46 |
| 22 | 86% | 0.67 | 79% | 0.64 |
| 24 | 88% | 0.34 | 81% | 0.48 |
| 25 | 80% | 0.67 | 73% | 0.60 |
| 28 | 66% | 0.60 | 55% | 0.48 |
| 32 | 79% | 0.52 | 56% | 0.38 |
| 35 | 70% | 0.56 | 63% | 0.47 |
| 40 | 67% | 0.47 | 47% | 0.34 |
| 41 | 70% | 0.58 | 62% | 0.48 |
| 45 | 66% | 0.45 | 47% | 0.35 |
| 46 | 55% | 0.40 | 51% | 0.38 |
| 47 | 72% | 0.34 | 60% | 0.44 |
| 48 | 69% | 0.52 | 53% | 0.47 |
| 49 | 52% | 0.18 | 42% | 0.23 |
| 50 | 66% | 0.55 | 56% | 0.50 |
| 51 | 66% | 0.46 | 54% | 0.38 |
| 53 | 86% | 0.10 | 51% | 0.41 |
| 54 | 79% | 0.67 | 77% | 0.67 |
| 55 | 75% | 0.67 | 66% | 0.60 |
| 56 | 59% | 0.42 | 45% | 0.29 |
| 57 | 84% | 0.52 | 42% | 0.31 |
| 58 | 68% | 0.54 | 62% | 0.49 |
| 59 | 70% | 0.54 | 62% | 0.56 |
| 60 | 65% | 0.46 | 50% | 0.41 |
| 61 | 79% | 0.45 | 34% | 0.16 |
| 62 | 69% | 0.17 | 37% | 0.09 |
| 63 | 66% | 0.27 | 35% | 0.13 |
| 64 | 67% | 0.32 | 43% | 0.19 |
| 65 | 64% | 0.46 | 37% | 0.23 |
| 66 | 63% | 0.42 | 39% | 0.09 |

in tree species diversity. The eastern U.S. has a variety of pines and hardwoods, which are probably difficult to distinguish spectrally at a scale of 250 meters. The forest type group and forest type classification schemes were not designed for spectral analysis. There are forest types that are pure forest stands of a species, such as the longleaf pine forest type. These same species can also occur in mixed forests and be assigned a different forest type, such as the longleaf pine/oak forest type. These aforementioned forest types and others like them certainly reduced the accuracy. Forest type group and forest type classification schemes that considers spectral separability between classes would greatly improve the accuracy of these maps.

The highest forest type group mapping zone accuracy was 92 percent and the lowest was 52 percent. The forest type group mapping zone accuracies were always higher than the forest type mapping zone accuracies except for four mapping zones. The forest type groups are probably more easily distinguishable spectrally than the forest types. The forest type group accuracies showed no west to east trend of increasing accuracy.

The overall forest type group and forest type accuracies for the conterminous U.S. were 69 percent and 50 percent, respectively. For Alaska, the overall forest type group and forest type accuracies were 78 percent and 67 percent, respectively. To further verify the results, the total area for each forest type group and forest type was calculated for each state. These state area summaries were compared to FIA state summary tables. For the conterminous U.S., eight percent (40 out of 512) of the forest type groups and four percent (70 out of 1,777) of the forest types differed by more than ten percent in area between the FIA state summaries and the classification area estimates. For Alaska, three of the seven forest type groups and five of the 15 forest types differed by more than ten percent in area between the FIA state summaries and the classification area estimates. Thus, these forest type group and forest type mapping products compares favorably with other data sets at least at the state level.

The forest type group map produced by this project was compared to the forest type group map produced by Zhu and Evans (1994). Table 3 shows the percent agreement between the two forest type group maps. The oak/hickory forest type group had the high percent agreement at 74.38 percent

TABLE 3. PERCENT AGREEMENT BETWEEN THE ZHU AND EVANS (1994) FOREST TYPE GROUP MAP AND THE NEW FOREST TYPE GROUP MAP

| Forest Type Group Name | Percent Agreement |
|-----------------------------|-------------------|
| Oak/Hickory | 74.38% |
| Pinyon/Juniper | 69.01% |
| Maple/Beech/Birch | 64.16% |
| Fir/Spruce/Mountain Hemlock | 58.45% |
| Douglas-fir | 57.59% |
| Loblolly/Shortleaf Pine | 56.87% |
| Aspen/Birch | 46.90% |
| Longleaf/Slash Pine | 45.30% |
| Spruce/Fir | 39.31% |
| Oak/Gum/Cypress | 34.89% |
| Ponderosa Pine | 32.70% |
| Hemlock/Sitka Spruce | 32.24% |
| Lodgepole Pine | 31.70% |
| Redwood | 27.51% |
| Elm/Ash/Cottonwood | 16.16% |
| White/Red/Jack Pine | 15.64% |
| Oak/Pine | 8.53% |
| Western Larch | 3.58% |
| Other Western Hardwoods | 2.21% |
| Western White Pine | 0.01% |

and the western white pine forest type group had the lowest percent agreement at 0.01 percent. The western white pine forest type group is associated with forest types found within the Douglas-fir and the fir/spruce/mountain hemlock forest type groups (Forest Inventory and Analysis, 2004). The forest type group map produced by this project classified the western white pine forest type group into these other associated type groups. This occurred with all the other forest type groups with disagreements; the forest type groups were classified into other associated forest type groups. The Zhu and Evans (1994) forest type group map had a spatial resolution of 1 km. This new forest type group map with a spatial resolution of 250 m is able to distinguish finer differences in the forest type groups.

Conclusions

The forest type map is the first national forest type map. This map along with the forest type group map can be used for many different applications such as assisting in pre-stratification for other vegetation mapping projects, habitat analyses, and assisting policy and decision makers. One application for the forest type group map involves the updating of the forest risk maps. The Zhu and Evans (1994) forest type group map was one of the key components for the development of the forest risk maps published in 2000 by the USFS Forest Health Monitoring (FHM) program (Lewis, 2002). The forest risk maps were non-site-specific and identified broad areas that had potential high risk of forest mortality or growth/volume loss from insects and diseases. The intent of these forest risk maps was to provide national scale information to policy makers to help determine national priorities. The forest type group map developed as part of this project will also aid in the development and improvement of forest risk maps. Because this new forest type group map is at a higher resolution (250 m) than the Zhu and Evans (1994) forest type group map, which had a resolution of 1 km, this new forest type group map will allow future forest risk maps to be used more specifically at larger scales and finer grain analyses.

This project effectively demonstrated the possibility of deriving national mapping products using FIA data and a geo-spatial database. Software programs were written to facilitate communication between ERDAS Imagine and the See5[®] software, which greatly enhanced the development of these national mapping products. See5[®] produced highly accurate forest type group maps. The forest type maps were less accurate because of some of the difficulty in separating out types which have similar spectral signatures. The forest type maps were still fairly accurate especially at the state level where the area of the forest types were similar to the area estimated by FIA.

Acknowledgments

We would like to thank Michael Hoppus, Rachel Riemann, Dennis Jacobs, and Gretchen Moisen for their intellectual contributions and support. We also are grateful for the contributions and support of the USDA Forest Service Forest Inventory and Analysis and the Forest Health Protection programs. We appreciate the insightful comments of three anonymous reviewers, which greatly improved the manuscript.

References

- Arner, S.L., S. Woudenberg, S. Waters, J. Vissage, C. MacLean, M. Thompson, and M. Hansen, 2003. *National Algorithms for Determining Stocking Class, Stand Size Class, and Forest*

- Type for Forest Inventory and Analysis Plots*, U.S. Department of Agriculture Forest Inventory and Analysis, Washington, D.C., 65 p.
- Bailey, R.G., 1989. Explanatory supplement to ecoregions map of the continents, *Environmental Conservation*, 16(4):307–309.
- Bailey, R.G., and H.C. Hogg, 1986. A world ecoregions map for resource reporting, *Environmental Conservation*, 13(3):195–202.
- Blackard, J., M. Finco, E. Helmer, G. Holden, M. Hoppus, D. Jacobs, A. Lister, G. Moisen, M. Nelson, R. Riemann, B. Ruefenacht, D. Salajanu, D. Weyermann, K. Winterberger, T. Brandeis, R. Czaplewski, R. McRoberts, P. Patterson, R. Tymcio, 2008. Mapping U.S. forest biomass using nationwide forest inventory data and Terra MODIS-based information, *Remote Sensing of Environment*, 112(4):1658–1671.
- Breiman, L., J.H. Friedman, R.A. Olshen, and C.J. Stone, 1984. *Classification and Regression Trees*, Wadsworth International Group, Belmont, California, 358 p.
- Burns, R.M., and B.H. Honkala, 1990a. *Silvics of North America: 1. Conifers, Agriculture Handbooks 654*, U.S. Department of Agriculture, Forest Service, Washington, D.C., 675 p.
- Burns, R.M., and B.H. Honkala, 1990b. *Silvics of North America: 2. Hardwoods, Agriculture Handbooks 654*, U.S. Department of Agriculture, Forest Service, Washington, D.C., 877 p.
- Congalton, R.G., and K. Green, 1999. *Assessing the Accuracy of Remotely Sensed Data: Principles and Practices*, Lewis Publishers, New York, 137 p.
- DeFries, R.S., and J.C. Chan, 2000. Multiple criteria for evaluating machine learning algorithms for land cover classification from satellite data, *Remote Sensing of Environment*, 74(3):503–515.
- DeFries, R., M. Hansen, J.R.G. Townshend, and R. Sohlberg, 1998. Global land cover classifications at 8 km spatial resolution: The use of training data derived from Landsat imagery in decision tree classifiers, *International Journal of Remote Sensing*, 19(16):3141–3168.
- Eyre, F.H., 1980. *Forest Cover Types of the United States and Canada*, Society of American Foresters, Bethesda, Maryland, 148 p.
- Forest Inventory and Analysis, 2004. *Forest Inventory and Analysis National Core Field Guide, Volume 1: Field Data Collection Procedures for Phase 2 Plots*, version 2.0, U.S. Department of Agriculture Forest Inventory and Analysis, Washington, D.C., 208 p.
- Forest Health Protection, 2004. *Forest Insect and Disease Conditions in the United States 2003*, U.S. Department of Agriculture Forest Health, Washington, D.C., 156 p.
- Freund, Y., and R.E. Schapire, 1996. Experiments with a new boosting algorithm, *Machine Learning Proceedings of the Thirteenth International Conference*, Morgan-Kaufman, San Francisco, California, pp. 148–156.
- Freund, Y., and R.E. Schapire, 1997. A decision-theoretic generalization of on-line learning and an application to boosting, *Journal of Computer and System Sciences*, 55(1):119–139.
- Friedl, M.A., and C.E. Brodley, 1997. Decision tree classification of land cover from remotely sensed data, *Remote Sensing of the Environment*, 61(3):399–409.
- Friedl, M.A., C.E. Brodley, and A.H. Strahler, 1999. Maximizing land cover classification accuracies produced by decision trees at continental to global scales, *IEEE Transactions on Geoscience and Remote Sensing*, 37(2):969–977.
- Hall, L.O., K.W. Bowyer, R.E. Banfield, S. Eschrich, and R. Collins, 2003. Is error-based pruning redeemable?, *International Journal on Artificial Intelligence Tools*, 12(3):249–264.
- Hansen, M., R. DeFries, J.R. Townshend, M. Carroll, C. Dimiceli, and R. Sohlberg, 2003. *Vegetation Continuous Fields MOD44B, 2001 Percent Tree Cover, Collection 3*, University of Maryland, College Park, Maryland, 2001.
- Hansen, M., R. Dubayah, and R. DeFries, 1996. Classification-trees: An alternative to traditional land cover classifiers, *International Journal of Remote Sensing*, 17(5):1075–1081.
- Homer, C.G., and A. Gallant, 2001. *Partitioning the Conterminous United States into Mapping Zones for Landsat TM Land Cover Mapping*, U.S. Geological Survey, Sioux Falls, South Dakota, 7 p.
- Lawrence, R., A. Bunn, S. Powell, and M. Zambon, 2004. Classification of remotely sensed imagery using stochastic gradient boosting as a refinement of classification tree analysis, *Remote Sensing of Environment*, 90(3):331–336.
- Lawrence, R.L., and A. Wright, 2001. Rule-based classification systems using classification and regression tree (CART) analysis, *Photogrammetric Engineering & Remote Sensing*, 67(10):1137–1142.
- Lewis, J.W., 2002. *Mapping Risk from Forest Insects and Diseases, FS-754*, U.S. Department of Agriculture Forest Service, Washington, D.C., 62 p.
- Lillesand, T.M., and R.W. Kiefer, 2000. *Remote Sensing and Image Interpretation*, John Wiley and Sons, Inc., New York, 724 p.
- Miller, D.A., and R.A. White, 1998. A conterminous United States multi-layer soil characteristics data set for regional climate and hydrology modeling, *Earth Interactions*, 2(2):1–26.
- Mingers, J., 1989. An empirical comparison of pruning methods for decision tree induction, *Machine Learning*, 4(2):227–243.
- Omernik, J.M., 1987. Ecoregions of the conterminous United States: Map (scale 1:7,500,000), *Annals of the Association of American Geographers* 77(1):118–125.
- Pal, M., and P.M. Mather, 2003. An assessment of the effectiveness of decision tree methods for land cover classification, *Remote Sensing of Environment*, 86(4):554–565.
- Quinlan, J.R., 1987. Simplifying decision trees, *International Journal of Man-Machine Studies*, 27(3):221–234.
- Quinlan, J.R., 1993. *C4.5: Programs for Machine Learning*, Morgan-Kaufman, San Mateo, California, 302 p.
- Quinlan, J.R., 1996. Bagging, boosting and C4.5, *Proceedings of the Thirteenth National Conference on Artificial Intelligence*, American Association for Artificial Intelligence Press, Portland, Oregon, pp. 725–730.
- Thornton, P.E., S.W. Running, and M.A. White, 1997. Generating surfaces of daily meteorological variables over large regions of complex terrain, *Journal of Hydrology*, 190:214–251.
- Vogelmann, J.E., S.M. Howard, L. Yang, C.R. Larson, B.K. Wylie, and J.N. Van Driel, 2001. Completion of the 1990's National Land Cover Data Set for the conterminous United States, *Photogrammetric Engineering & Remote Sensing*, 67(6):650–662.
- Zhu, Z., and D.L. Evans, 1994. U.S. forest types and predicted percent forest cover from AVHRR data, *Photogrammetric Engineering & Remote Sensing*, 60(5):525–531.

(Received 06 June 2006; accepted 17 August 2006; revised 02 March 2007)

Leaf Area Index (LAI) Change Detection Analysis on Loblolly Pine (*Pinus taeda*) Following Complete Understory Removal

J.S. Iiames, R.G. Congalton, A.N. Pilant, and T.E. Lewis

Abstract

The confounding effect of understory vegetation contributions to satellite-derived estimates of leaf area index (LAI) was investigated on two loblolly pine (*Pinus taeda*) forest stands located in Virginia and North Carolina. In order to separate NDVI contributions of the dominant-codominant crown class from that of the understory, two *P. taeda* 1 ha plots centered in planted stands of ages 19 and 23 years with similar crown closures (71 percent) were analyzed for in situ LAI and NDVI differences following a complete understory removal at the peak period of LAI. Understory vegetation was removed from both stands using mechanical harvest and herbicide application in late July and early August 2002. Ikonos data was acquired both prior and subsequent to understory removal and were evaluated for NDVI response. Total vegetative biomass removed under the canopies was estimated using the Tracing Radiation and Architecture of Canopies (TRAC) instrument combined with digital hemispherical photography (DHP). Within-image NDVI change detection analysis (CDA) on the Virginia site showed that the percentage of removed understory (LAI) detected by the Ikonos sensor was 5.0 percent when compared to an actual in situ LAI reduction of 10.0 percent. The North Carolina site results showed a smaller percentage of reduced understory LAI detected by the Ikonos sensor (1.8 percent) when compared to the actual LAI reduction as measured in situ (17.4 percent). Image-to-image NDVI CDA proved problematic due to the time period between the Ikonos image collections (2.5 to 3 months). Sensor and solar position differences between the two collections, along with pine LAI increases through multiple needle flush, exaggerated NDVI reductions when compared to in situ data.

Introduction

Assessment of forest stand-level attributes has been required for the parameterization of many process-based ecological models. Specifically, the leaf surface area has been identified as the main surface of exchange between the plant canopy and the atmosphere and has been related to canopy interception; transpiration; net photosynthesis; gas, water,

carbon, and energy exchange; net primary productivity (NPP); biomass; rainfall interception; and dry deposition (Gholz, 1982; Pierce and Running, 1988; Chason *et al.*, 1991; Gower and Norman, 1991; Aber, 2001; Hall *et al.*, 2003). Leaf surface area has been quantified in the ratio of leaf area to ground surface area, a ratio termed the leaf area index (LAI). LAI has been defined here as one-half the total green leaf area per unit ground surface area (Chen and Black, 1992a).

LAI has been estimated from remote sensing satellites using empirical relationships between ground-estimated LAI and vegetation indices derived from primary spectral bands, especially the red and the near-infrared (NIR) wavelengths, taking advantage of the red-edge phenomenon existent within photosynthetically active vegetation (Chen *et al.*, 2002; Lee *et al.*, 2004; Schlerf *et al.*, 2005). The contrast between the visible and the NIR wavelengths forms a strong step in the electromagnetic spectrum of green vegetation between 680 and 750 nm that is often referred to as "the red edge." Many vegetation indices are predicated on this vegetative feature determined by leaf reflectance and transmittance properties, both which are affected by leaf pigments, internal scattering, and leaf water content (Gates *et al.*, 1965; Gausmann *et al.*, 1969; Myers, 1970; Peterson and Running, 1989; Jensen, 2000). Healthy vegetation absorbs approximately 80 percent of incoming solar radiation in the red and blue portions of the spectrum based on the presence of leaf pigments in the palisade mesophyll. However, scattering occurs in the NIR portion of the spectrum due to the presence of spongy mesophyll. The effect of this morphological characteristic may cause upwards of 76 percent scattering of the incoming solar radiation in the 700 to 1,200 nm region (Jensen, 2000).

The exploitation of this vegetative red-edge characteristic in remote sensing applications is tempered by the issue of saturation where an asymptotic increase in a vegetation index (VI) occurs with increasing LAI. The root of the LAI saturation problem with respect to satellite vegetation indices hinges on (a) leaf level differences (e.g., pigments, internal leaf structure, leaf orientation) (Baret and Guyot, 1991; Williams, 1991; Bouman, 1992; Yoder and Waring, 1994), (b) within tree

J.S. Iiames and A.N. Pilant are with the U.S. Environmental Protection Agency, 109 T.W. Alexander Drive, MD E243-05, RTP, NC 27709 (iiames.john@epa.gov).

R.G. Congalton is with the University of New Hampshire, Durham, NH.

T.E. Lewis is with the U.S. Army corps of Engineers, Vicksburg, MS.

Photogrammetric Engineering & Remote Sensing
Vol. 74, No. 11, November 2008, pp. 1389-1400.

0099-1112/08/7411-1389/\$3.00/0
© 2008 American Society for Photogrammetry
and Remote Sensing

crown differences (e.g., clumping and woody material contribution to total reflectance) (Williams, 1991; Huemmrich and Goward, 1997), and (c) differences in canopy level parameters (e.g., tree height heterogeneity and the size and number of tree gaps) (Cohen *et al.*, 1990; Cohen and Spies, 1992; Leblon *et al.*, 1996). The effect of the LAI saturation issue is seen in the poor correlations ($R^2 = 0.30$ to 0.52) reported between the normalized difference vegetation index (NDVI) and LAI (Spanner *et al.*, 1990; Nemani *et al.*, 1993; Chen and Cihlar, 1996). A variety of influences contribute to the poor correlations observed in the LAI-NDVI relationship, namely canopy closure, background materials (i.e., soil properties and soil moisture content), and understory contributions. Of the above mentioned three factors, canopy closure has been identified as the most important variable in determining canopy reflectance regardless of the understory component, due to the masking (i.e., occlusion of understory and ground cover) properties at varying canopy closure values (Spanner *et al.*, 1990; Stenback and Congalton, 1990; Danson and Curran, 1993). However, in forests stands where direct solar radiation is relatively non-occluded ($LAI < 3$), the contribution of understory vegetation has been shown to dramatically increase the NIR reflectance from conifer stands (Nemani *et al.*, 1993) thus affecting the overall response of NDVI.

Understory vegetation may contribute up to 60 percent of total stand LAI, yet detection of this component by various remote sensing platforms/sensors has been difficult due to a variety of influences on overall spectral behavior (i.e., seasonality, canopy structure, image scene dependency, etc.). Chen (1996) reported that the effective LAI (L_e), a canopy attribute influenced by the "effect" of nonrandom foliage spatial distribution on indirect measurements of LAI, varied by less than 5 percent in boreal conifer stands from spring to summer, however the red/NIR Ratio, or Simple Ratio (SR), changed dramatically from spring to summer due to the growth of the understory. This response is a result of the dramatic influence of hardwood understory to the overall NIR reflectance from conifer forests. On average, understory accounted for approximately 20 percent of the total LAI in both old growth ponderosa pine and young ponderosa pine regeneration (Law *et al.*, 2001). Understory LAI accounted for 35 to 60 percent of the total LAI within plots of naturally regenerated young trees (Law *et al.*, 2001). The broadleaved component in the understory with a conifer overstory showed a large effect in the NIR, a moderate effect in the red, and, little to no effect in the shortwave IR regions (Peterson and Running, 1989). Badhwar *et al.*, (1986) found that understory NIR reflectance dominated overall reflectance from open-canopied stands.

Separating the spectral signal from multi-layered forest canopies, especially those with a significant presence of understory, has proven difficult in the assessment of LAI in those forest stands (Franklin *et al.*, 1997; Carlson and Ripley, 1997). We investigated the confounding effect of understory contributions to satellite-derived estimates of LAI on two loblolly pine (*Pinus taeda*) plantations (ages 19 and 23 years) located in Virginia and North Carolina, USA. Understory vegetation was removed from 1-hectare (ha) plots ($100\text{ m} \times 100\text{ m}$) within both stands using mechanical harvest and herbicide application in late July and early August 2002. Ikonos multispectral imagery was collected both prior and subsequent to understory removal and was evaluated for change in VI response in the harvested and non-harvested areas. LAI change, a result of the removal of understory vegetation beneath the dominant *P. taeda* canopy, was estimated using an integrated optical LAI estimation technique combining measurements from the Tracing Radiation and Architecture of Canopies (TRAC; 3rd Wave Engineering, Ontario, Canada) instrument with digital hemispherical photography (DHP).

Methods

In situ broadleaf forest understory contributions to overall stand LAI were analyzed on two *P. taeda* sites located in the Albemarle-Pamlico Basin. On these same two sites, a VI change detection analysis was completed using 4 m multi-resolution Ikonos imagery. On both sites, within a 1 ha area, broadleaf understory and ground vegetation were removed using mechanical harvest and herbicide application in late July and early August 2002. Ikonos imagery was acquired pre-(IM-T1) and post-(IM-T2) harvest through the NASA Data Buy Program for analysis (Morissette *et al.*, 2003). *In situ* LAI was measured prior to and following the understory removal implementing the indirect optical estimation method integrating TRAC and DHP measurements (TRAC-DHP). IM-T1 and IM-T2 pair-wise Ikonos images for each site were first georectified then normalized using the localized relative radiometric normalization technique in order to assess change between the two dates (Elvidge *et al.*, 1995). Pair-wise images were then clipped to include the 1 ha site (UR region, i.e., understory removal) plus the unaltered *P. taeda* stand immediately surrounding the site (UA region, i.e., unaltered). VI using the red edge properties characteristic within photosynthetically active vegetation were utilized to assess LAI change. Comparisons between dates (image-to-image) and within-date (within-image) were made employing low-pass spatial filters at varying resolutions. An analysis of variance (ANOVA) was implemented to test for significant differences between dates (i.e., image-to-image) IM-T1 and IM-T2. A within-date (i.e., within-image) ANOVA was applied to test for differences in the IM-T2 image between the 1 ha UR and the UA regions.

Site Descriptions

Two sites chosen for this research were located on commercial forestland managed for pulp and paper production in Virginia and North Carolina. The Virginia (Appomattox) site is located in Campbell County, VA (37.219°N , -78.879°W) approximately 15.5 km SSW of Appomattox, VA (Figure 1). This upper piedmont region ranges in elevation of 165 to 215 m above mean sea level. The MeadWestvaco Corporation, a supporter of the Sustainable Forestry Initiative, permitted sampling access to the U.S. Environmental Protection Agency (EPA) for this *P. taeda* stand including a complete understory removal within the 1 ha UR region using mechanical harvest and herbicide application. *P. taeda* was planted in 1980. Predominant soil types within the county included both Typic Hapludults and Kanhapludults: Cecil (16.3 percent), Cullen (12.0 percent), Tatum (8.3 percent), and Appling (7.7 percent). Measurements of forest structural attributes (height [m] and diameter [cm]) were made at both sites within the 1 ha areas using a point sampling method (nine plots/ha) with a basal-area-factor 10 for trees larger than 5 cm diameter at breast height (DBH) (Avery and Burkhart, 1993). Three plots within both 1 ha UR regions were sampled for understory components (stems less than 5 cm DBH) using a 4.6 m radius fixed area sampling method. Canopy closure, defined as the percent obstruction of the sky by canopy elements, was estimated using a GRS Densitometer (Ben Meadows Co., Janesville, WI). Stocking values, expressed as trees per hectare (TPH), were 1,250 TPH for the dominant-codominant crown class and 3,790 TPH for all trees in the understory (suppressed). The Appomattox understory did not have one dominant species as found in the Hertford site understory, however all tree species were deciduous (Figure 2). The average diameter (DBH), measured 1.4 m above the base of the tree, was 21.6 cm. The average height of the dominant-codominant crown class was 15.9 m. This *P. taeda* stand supported a basal area (BA) per hectare of 36.7 m^2 , with BA defined as the cross-sectional

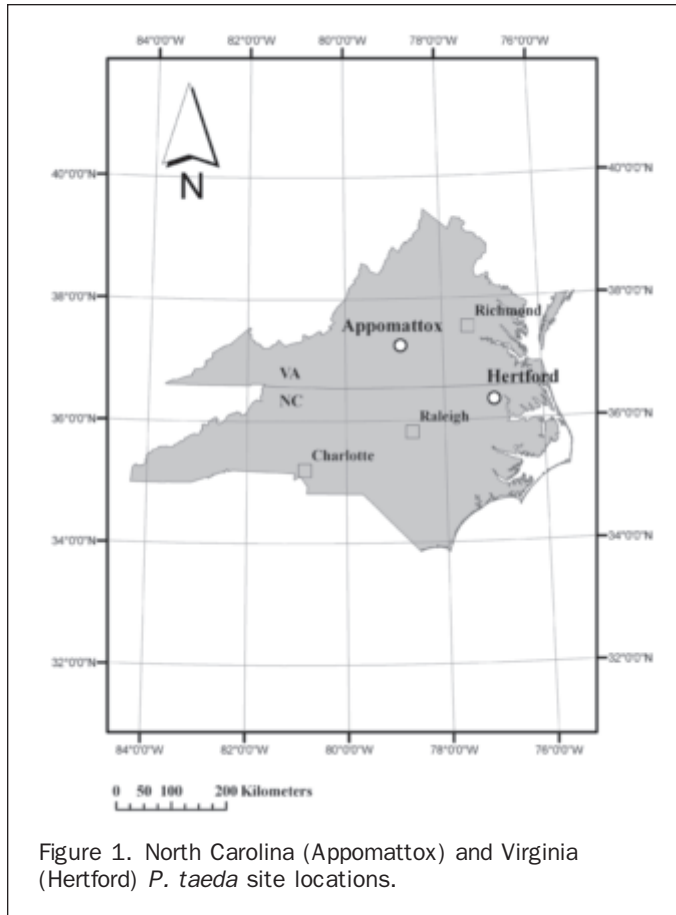


Figure 1. North Carolina (Appomattox) and Virginia (Hertford) *P. taeda* site locations.

area of a tree at 1.4 m above the tree base per unit area. The crown closure was 71 percent for this forest type (Table 1).

The North Carolina (Hertford) site, located in Hertford County, NC (36.383°N, -77.001°W), is approximately 5.8 km WSW of Winton, NC (Figure 1). This coastal plain site is 8 to 10 m above mean sea level with a moderately well drained thermic Aquic Hapludult soil type (Craven fine sandy loam). *P. taeda* was planted in 1983 and by

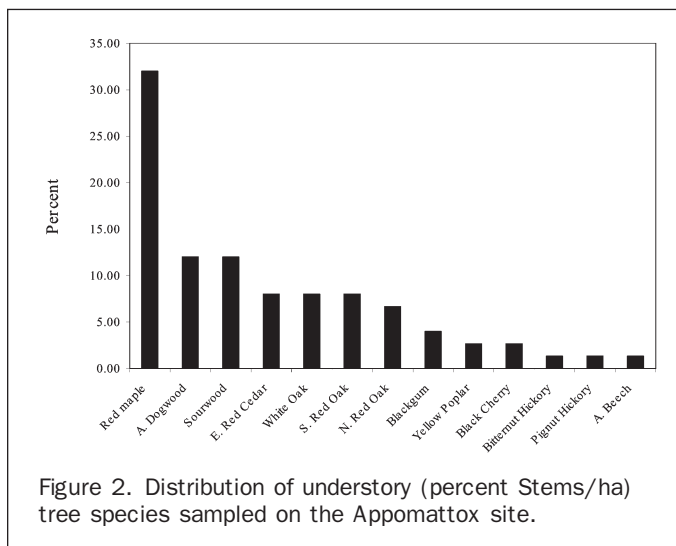


Figure 2. Distribution of understory (percent Stems/ha) tree species sampled on the Appomattox site.

TABLE 1. FOREST STAND STRUCTURE ATTRIBUTES FOR APPOMATTOX (VA) AND HERTFORD (NC)

| | Appomattox | Hertford |
|------------------------|------------|----------|
| TPH (overstory) | 1250 | 1740 |
| TPH (understory) | 3790 | 2830 |
| STAND AGE (years) | 23 | 19 |
| DBH (cm) | 21.6 | 18.5 |
| HEIGHT (m) | 15.9 | 14.3 |
| BA/H (m ³) | 36.7 | 37.3 |
| CC (%) | 71 | 71 |

2002 stocking values were 1,740 TPH for the dominant-codominant canopy class and 2,830 TPH for the suppressed canopy crown class. Understory was dominated (60 percent) by the broadleaf evergreen tree species *Ilex opaca* (American Holly) (Figure 3). The average diameter and height of this stand was 18.5 cm and 14.3 m, respectively. Measured basal area and crown closure was 37.3 m²/ha and 71 percent, respectively (Table 1).

Understory Harvest and Herbicide Application

Understory removal completion dates were 30 July 2002 (Hertford) and 02 August 2002 (Appomattox). The perimeters of both 100 m × 100 m plots on both sites were flagged and a mechanical harvest was applied, effectively shredding all understory. To ensure elimination of all photosynthetically active vegetation in the understory, including forbs, herbs, and grasses, an herbicide treatment of two quarts/acre of Accord Concentrate (Dow AgroSciences, Indianapolis, IN) was applied to both plots (Plate 1). This understory component was not significant (~10 to 15 percent) given the shading produced by the dominant-codominant and suppressed tree crown classes existent on both sites.

In situ LAI Measurements

A number of LAI validation studies have utilized the integration of optical instruments to capture gap fraction measurements and gap size distributions to estimate L_e and Ω_E . Leblanc and Chen (2001) combined the TRAC with LICOR PCA measurements for *in situ* LAI, as did Jonckheere *et al.* (2005). TRAC-DHP integration LAI estimation was assessed in the *P. taeda* pine forests of North Carolina and Virginia with good correlation to whole-tree harvest LAI estimates (Iiames, 2006). Recently, Ω_E has been extracted from gap size

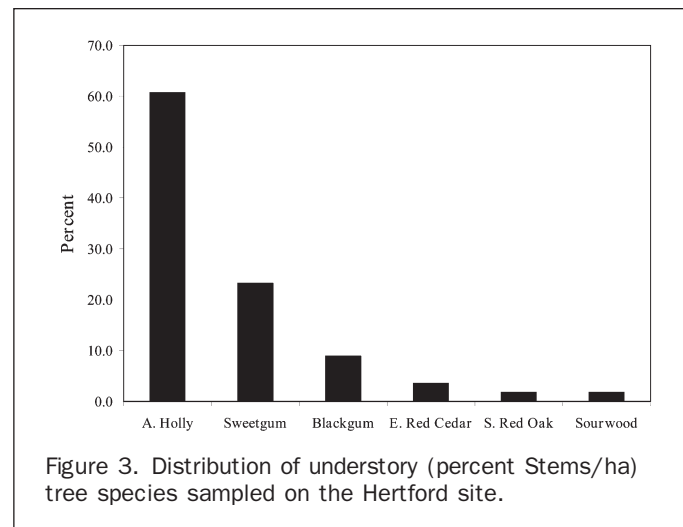


Figure 3. Distribution of understory (percent Stems/ha) tree species sampled on the Hertford site.



(a)



(b)



(c)

Plate 1. Appomattox, Virginia: (a) understory harvest, (b) pre-harvest conditions, and (c) post-harvest conditions.

distribution within DHP measurements, potentially eliminating the requirement of TRAC measurements to obtain the same parameter (Leblanc *et al.*, 2005). However, Chen *et al.* (2006) cautioned against exclusive use of DHP to estimate Ω_E due to (a) the effect of multiple scattering causing a loss of leaf/needle resolution in the vertical direction, and (b) the

distortion of the gap size distribution resulting from the loss of these small gaps.

Indirect optical estimation of LAI utilizing the TRAC-DHP method was completed on both sites immediately prior to (i.e., collection 2 [C2]: July 2002) and immediately following (i.e., collection 3 [C3]: August 2002) understory removal. *In situ* LAI change from these measurements would later be contrasted with NDVI change within-image for each site after harvest. In addition to the C2 and C3 LAI estimates, TRAC-DHP measurements were made on the Appomattox site in May 2002 (collection 1 [C1]) in order to assess LAI differences corresponding to the image-to-image NDVI change found during the same period. The TRAC-DHP indirect optical estimation method employs an equation (Equation 1) developed by Chen (1996) based on the Beer-Lambert (Beer, 1853) light extinction model, taking into account that the total amount of radiation intercepted by a canopy layer is dependent on the incident irradiance, canopy structure and optical properties of the site (Jonckheere *et al.*, 2005). This equation (modified Beer-Lambert light extinction model) solves for true LAI and is defined:

$$\text{LAI} = (1 - \alpha) \cdot [L_e(\lambda_E/\Omega_E)], \quad (1)$$

where LAI is the leaf area index representing one-half of the total leaf area per unit ground surface area, α is the woody-to-total area ratio, L_e is the effective LAI, λ_E is the needle-to-shoot area ratio, and Ω_E is the element clumping index. In summary, the effective LAI, L_e , is estimated from DHP gap fraction measurements; the element clumping index, Ω_E , is calculated from gap size distributions determined from TRAC measurements; the woody-to-total area and needle-to-shoot area ratios are calculated using a combination of field and laboratory methods.

The TRAC sunfleck-profiling instrument consists of three quantum photosynthetically active radiation (PAR) (400 to 700 nm) sensors (LICOR, Lincoln, NE, Model LI-190SB), two uplooking and one downlooking, mounted on a wand with a built-in datalogger (Leblanc *et al.*, 2002). The instrument is hand-carried approximately 1 m above the ground in direct sun conditions along a linear transect at a constant speed of 0.3 m/s. Typical transect lengths of 50 m to 100 m or greater are oriented close to perpendicular to the direction of the sun and are marked in fixed intervals, typically 10 m subdivisions. A user-defined time stamp initiates the transect collection with each intermediate 10 m subdivision also marked by the user progressing along the transect. The instrument records the downwelling solar photosynthetic photon flux density (PPFD) from one of the uplooking sensors in units of $\mu\text{mol}/\text{m}^2/\text{s}$ at a sampling frequency of 32 HZ. The datalogger records light-dark transitions as the direct solar beam is alternately transmitted and eclipsed by canopy elements. A 30° to 60° solar zenith angle (θ) is recommended for TRAC measurements in order to process gap fraction. TRAC data are processed by TRACWin software (Leblanc *et al.*, 2002) to yield the element clumping index (Ω_e) from the deviation of the measured gap size distribution from that of randomly distributed foliage (Morissette *et al.*, 2006).

DHP measurements were made with a Nikon Cool-Pix 995 digital camera with a Nikon FC-E8 fish-eye converter in diffuse light conditions. An image size of 1,600 pixels \times 1,200 pixels was selected at an automatic exposure. The camera was mounted on a tripod and was leveled over each stake at a height of 1.4 m using a combination of two bubble levelers, one on the tripod and one mounted on the lens cap. Proper leveling of the instrument ensured that the "true" horizon of the photograph was captured. The camera was oriented to true north in order to compare

metrics derived from other canopy gap instruments (e.g., TRAC, densitometer, etc.). The operator would select a delayed (3 to 10 second) exposure to eliminate any vibration incurred when depressing the shutter.

Gap Light Analyzer (GLA) software (Simon Fraser University, Burnaby, British Columbia, Canada) was used to process the DHP imagery. GLA relies on the accurate projection of a three-dimensional hemispherical coordinate system onto a two-dimensional surface. After downloading the images, a GLA configuration file was created for both sites. A configuration file contains information regarding image orientation, projection distortion and lens calibration, site location coordinates, length of growing season, sky-region brightness, and atmospheric conditions. GLA requires that each image be registered with respect to the location of due north on the image and the image circular area. This image registration process required that the FC-E8 fish-eye lens be recalibrated due to an actual field of view of 185°, not 180°. The image radius was reduced accordingly so that the 90° θ represented the true horizon. After the image was registered, an analyst-derived threshold value was assigned, delineating sky (white pixels) from no-sky (black pixels). GLA software returns gap fraction values for the following θ 's: 5.6°, 16.9°, 28.1°, 39.4°, 50.6°, 61.9°, 73.1°, and 84.4°. Miller (1967) found that gap fraction measurements made at 1 radian (~57.3°) for a variety of leaf or needle structures converge at a 0.5 projection coefficient (Beer-Lambert variable). This theoretical insensitivity of gap fraction to leaf angle distribution at 57.3° eliminates the requirement for gap fraction measurements over the entire range of θ 's. The gap fraction at 57.3° can be determined by plotting gap fraction values against the corresponding θ 's. Solving for L_e from the Beer-Lambert equation results in:

$$L_e = \ln P(\theta) / (-2\cos(\theta)) \quad (2)$$

where $P(\theta)$ is the gap fraction at θ .

The needle-to-shoot area (γ_E) and woody-to-total area (α) ratios were measured from samples taken from two additional sites located within the same physiographic provinces as the Appomattox and Hertford sites. The needle-to-shoot area ratio was obtained through laboratory analysis of shoot samples following the methodology of Chen and Black (1992a and b) and Fassnacht *et al.* (1994). The woody-to-total area ratio was estimated using ERDAS Imagine® image processing software through an unsupervised classification technique employing the ISODATA clustering algorithm (Iiames, 2006).

Sample Design

The primary sampling unit was the quadrant, a 100 m \times 100 m grid with five 100 m east-west TRAC sampling transects, labeled line 1 (L1) through line 5 (L5). The east-west grid layout aligned TRAC transects diagonal to the planted rows within both conifer sites, thereby minimizing the impact of clumping (Breda, 2003). Interspersed among the TRAC transects were five DHP transects (lines A through E; Figure 4). Quadrants were designed to approximate a Landsat ETM+ 3 pixel \times 3 pixel window. Quadrants on both sites were randomly selected within an area that allowed a 50 m minimum buffer to any road or open areas. The TRAC transect L1_0 m position was located using real-time (satellite) differentially corrected GPS to a horizontal accuracy of ± 1.0 m. From this point, TRAC transects were staked every 10 m with pre-labeled 18-inch plastic stakes. The stakes were used in TRAC measurements as walking-pace and distance markers. DHP transects were staked at the 10, 30, 50, 70, and 90 m positions located between the TRAC transects.

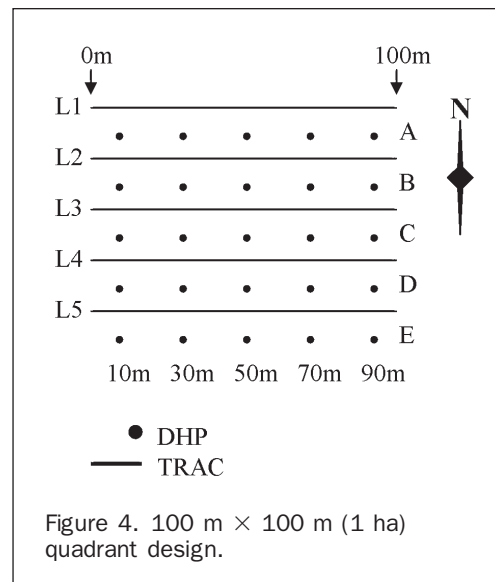


Figure 4. 100 m \times 100 m (1 ha) quadrant design.

Ikonos Image Processing

High-resolution (4 m) 11-bit Ikonos image pairs (IM-T1 and IM-T2) corresponding to pre- and post-understory harvest conditions were acquired from NASA's Scientific Data Purchase for both sites (Morissette *et al.*, 2003). IM-T1 Appomattox and Hertford images were obtained on 24 May and 12 May 2002, respectively, whereas IM-T2 images were acquired on 03 August (Appomattox) and 13 August (Hertford). Acquisition time occurred within a narrow morning window of 0957 to 1032 (UTC), with collection azimuth differing significantly (123.3°) between dates for both sites (Figure 5). Images were geometrically registered (georectified) to 1998 color infrared digital orthophotograph quarter-quadrangles (DOQQ) for both sites using ERDAS Imagine® 8.6 software. Prior to the geometric registration, field ground control points were collected using ± 1 m real-time differentially corrected GPS (Omnistar, Houston, TX) and compared to DOQQ locations of the same

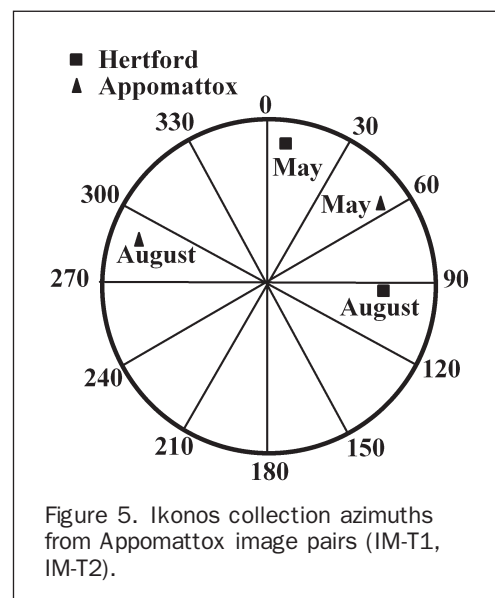


Figure 5. Ikonos collection azimuths from Appomattox image pairs (IM-T1, IM-T2).

point. Offsets in the X and Y direction were assessed for DOQQ accuracy prior to assuming this data layer as the base for georectification.

After the georectification process was completed image analysis was conducted to test: (a) image-to-image NDVI CDA using relative radiometric normalization technique (Appomattox site only), (b) within-image NDVI CDA (Appomattox and Hertford IM-T2 images), (c) spatial averaging unit appropriate for the *P. taeda* forest type, and (d) differences between NDVI and four other vegetation indices.

Image-to-Image NDVI Change Detection Analysis

To test IM-T1 and IM-T2 image-to-image NDVI change detection, the Appomattox image pair was subset to a 37.4 ha area centered about the 1 ha UR region (Plate 2). A relative radiometric normalization using an automatic scattergram-controlled regression was applied to the IM-T2 (August 2002) image in conjunction with the IM-T1 (April 2002) image (Elvidge *et al.*, 1995). Top-of-atmosphere reflectance-based NDVI images were created from these normalized image pairs. The 37.4 ha image pairs were then clipped to a 4.0 ha area completely contained within the *P. taeda* forest type, again centered about the 1 ha UR region. NDVI image subtraction was applied to both normalized images on an averaged 5 pixel by 5 pixel (i.e., 5×5 window) basis. This 5×5 spatial averaging window was chosen based on the spatial distribution of the trees within the two stands at Hertford and Appomattox. Stocking values of 1,250 TPH (Appomattox) translated into a nominal tree spacing of ± 3 m. Thus, a $20 \text{ m} \times 20 \text{ m}$ area (5×5 window) would theoretically contain 50 trees with the associated gaps, more than ample size to sample the variability within this crown type. NDVI change less than either positive or negative 0.01 was arbitrarily deemed as a "no-change" pixel. Descriptive statistics were generated for both the 1 ha UR and UA regions between the two dates.

Within-Image NDVI Change Detection Analysis (CDA)

To test within-image NDVI change, both site-specific (Appomattox and Hertford) IM-T2 top-of-atmosphere reflectance-based

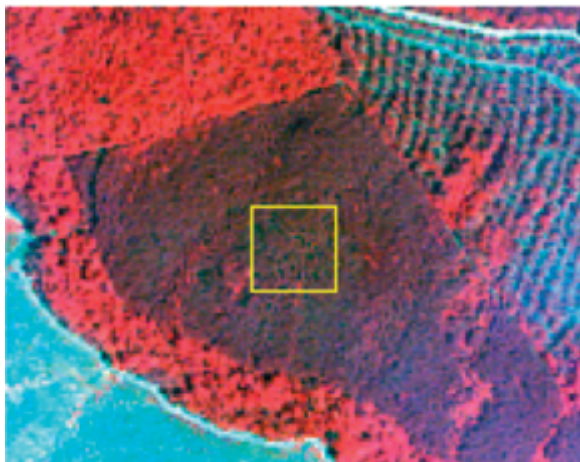


Plate 2. Color infrared subset (37.4 ha) of post harvest image (IM-T2) (Appomattox, Virginia) later normalized to pre-harvest (IM-T1) image. Yellow bounding box is 100 m \times 100 m harvested area.

NDVI images were subset to include both the 1 ha UR region and the similar surrounding *P. taeda* forest stand type (UA region). Change and no change was evaluated on an averaged 5 pixel by 5 pixel basis, employing an analysis of variance (ANOVA) to test for differences between the 1 ha UR and UA regions. While this test could be considered as a pseudo-replicated analysis (Hurlbert, 1984), the goal was not to provide an overall test in a formal experimental design, but to explain the difference beyond the pixel-to-pixel variability.

Spatial NDVI Averaging and Testing Other Vis

Spatial NDVI averaging window sizes of 3, 5, 7, and 9 pixels were evaluated on the Hertford IM-T2 image to test for optimal resolution capturing *P. taeda* crown variability. Finally, percent change within the Hertford IM-T2 image was evaluated using the vegetation indices: NDVI , $\sqrt{(\text{NIR}/\text{Red})}$, $\text{NIR} - \text{Red}$, and SR .

Results

In situ LAI Measurements

Collections of pre- and post-harvest TRAC measurements (Ω_E) for both sites were designed to acquire PPF values between the optimal sampling period of 30° to $60^\circ \theta$. However, due to limited atmospheric conditions (i.e., increased scattered clouds) or time-limited constraints associated with the distance between sites, some TRAC measurements were made outside the preferred 30° to 60° range and, therefore, the preferred time of day. TRAC measurements outside of this optimal θ range might bias Ω_E estimates only if the canopy was highly clumped (i.e., $\Omega_E \ll 1.0$). However, within these two stands *P. taeda* Ω_E values were close to unity indicating minimal clumping (Leblanc *et al.*, 2005).

For within-image and image-to-image NDVI CDA, three dates of TRAC measurements were made on the Appomattox site (23 May [C1], 30 July [C2], and 05 August [C3] 2002; Table 2). Because only within-image CDA was applied to the Hertford site, only two dates (27 July [C2] and 05 August [C3] 2002) of *in situ* LAI data were collected (Table 2). Corresponding DHP measurements were made on both sites on or within one day of the TRAC measurements within the $100 \text{ m} \times 100 \text{ m}$ sampling grid. The woody-to-total area ($\alpha = 0.25$) and the needle-to-shoot area ($\gamma_E = 1.21$) ratios were applied to both sites in the calculation of LAI.

Applying the input parameters into the modified Beer-Lambert light extinction model (i.e., Ω_E (TRAC), L_E (DHP), α , and γ_E), LAI (overstory and understory) was calculated for the three *in situ* collection periods for the Appomattox site (C1 to C3) and the two collection periods for the Hertford site (C2, C3). At the Appomattox site there was a 16.9 percent increase in *in situ* LAI between C1 (LAI = 2.01) and C3 (LAI = 2.35). However, within-image NDVI CDA revealed a 10.0 percent *in situ* LAI reduction between C2 (LAI = 2.61) and C3 (LAI = 2.35) (Table 3). At the Hertford site *in situ* LAI differences between C2 and C3 (within-image NDVI CDA) showed a 17.4 percent reduction (C1 = 2.41 LAI; C2 = 1.99 LAI; Table 3).

Ikonos Image Analysis

Georectification

Mean differences in geolocated GCPs compared to DOQQ points of the same location showed reasonable accuracy for both sites in the both the X and Y direction. The Appomattox site showed a mean deviation in the X and Y directions of 2.36 m and 2.13 m, respectively. The Hertford site showed a mean deviation in the X and Y directions of 2.07 m and 0.53 m, respectively. The georectification process for both sites (IM-T2

TABLE 2. *IN SITU* LAI PARAMETERS FOR APPOMATTOX AND HERTFORD SITES FOR THREE COLLECTION PERIODS (C1-MAY 2002; C2-JULY 2002; C3-AUGUST 2002)

| | C1 | | C2 | | C3 | |
|---------|--|---|--------------------|--------------------|---|---|
| | APPO | APPO | HERT | APPO | HERT | |
| W/IN-IM | | X | X | X | X | |
| IM-IM | X | | | X | | |
| TRAC | DATE | 23 May 2002 | 30 July 2002 | 27 July 2002 | 06 August 2002 | 05 August 2002 |
| | TIME (UTC) | 13:54–14:25 | 9:13–9:41 | 11:38–12:18 | 9:34–9:54 | 12:59–13:26 |
| | θ | 18.9–22.9° | 57.0°–51.3° | 27.2°–21.1° | 53.8°–49.9° | 19.8°–19.7° |
| | S. AZIMUTH | 211.6°–228.7° | 91.0°–95.6° | 122.9°–140.9° | 96.3°–99.8° | 169.4°–188.6° |
| | TRANSECTS (D) | L1–5 (W–E) | L1–5 (W–E) | L1–5 (W–E) | L1(10,50,90) (N–S) ¹ | L1–5 (W–E) |
| | PPFD ($\mu\text{mol}/\text{m}^2/\text{s}$) | 1850–1920 | 340–1013 | 585–928 | 401–668 | 1345–1416 |
| | $\Omega_E(\sigma)$ | 0.91 (0.04) | 0.89 (0.05) | 0.92 (0.03) | 0.90 (0.04) | 0.89 (0.03) |
| DHP | DATE | 23 May 2002 | 29 July 2002 | 25 July 2002 | 06 August 2002 | 05 August 2002 |
| | POINTS | A(10,50,90) C(10,50,90) E(10,50,90) | All (A,B,C,D,E) | All (A,B,C,D,E) | B(30,50,70) C(30,50,70) D(30,50,70) | B(30,50,70) C(30,50,70) D(30,50,70) |
| | $L_E(\sigma)$ | 1.79 (0.21) | 2.25 (0.28) | 2.21 (0.28) | 2.07 (0.20) | 1.78 ((0.10) |

Note: TRAC lines were run N-S due to solar position. TRAC runs began at L1_10 then proceeded south through L2, L3, L4, and L5_10. The next TRAC run began at L5_50, then proceeded north along the 50 m markers. The same process was repeated for L1_90, proceeding south.

TABLE 3. CALCULATION OF *IN SITU* LAI (TRAC-DHP) FOR APPOMATTOX (VA) AND HERTFORD (NC) SITES

| Site | Collection | Month/Year | Ω_E | L_E | γ_E | α | LAI | ¹ ADJ LAI |
|------|------------|-------------|------------|-------|------------|----------|------|----------------------|
| APPO | C1 | MAY 2002 | 0.91 | 1.79 | 1.21 | 0.25 | 1.78 | 2.01 |
| APPO | C2 | JULY 2002 | 0.89 | 2.25 | 1.21 | 0.25 | 2.30 | 2.61 |
| APPO | C3 | AUGUST 2002 | 0.90 | 2.07 | 1.21 | 0.25 | 2.08 | 2.35 |
| HERT | C2 | JULY 2002 | 0.92 | 2.21 | 1.21 | 0.25 | 2.13 | 2.41 |
| HERT | C3 | AUGUST 2002 | 0.89 | 1.78 | 1.21 | 0.25 | 1.76 | 1.99 |

Note: ADJ LAI (i.e., adjusted LAI): LAI estimates were adjusted upward by a factor of 1.132 to adjust for the differences accounted between *in situ* TRAC-DHP estimated LAI and allometrically-derived LAI estimates from destructive harvests (Iiames, 2006).

images) resulted in root mean square error (RMSE) within one-half pixel (i.e., approximately 2 m). RMSE was below one-half pixel for the Hertford site (RMSE = 0.27 m) and close to one-half pixel for the Appomattox site (RMSE = 2.10 m). The IM-T1 images (Appomattox and Hertford) were registered to the corrected IM-T2 images for georectification.

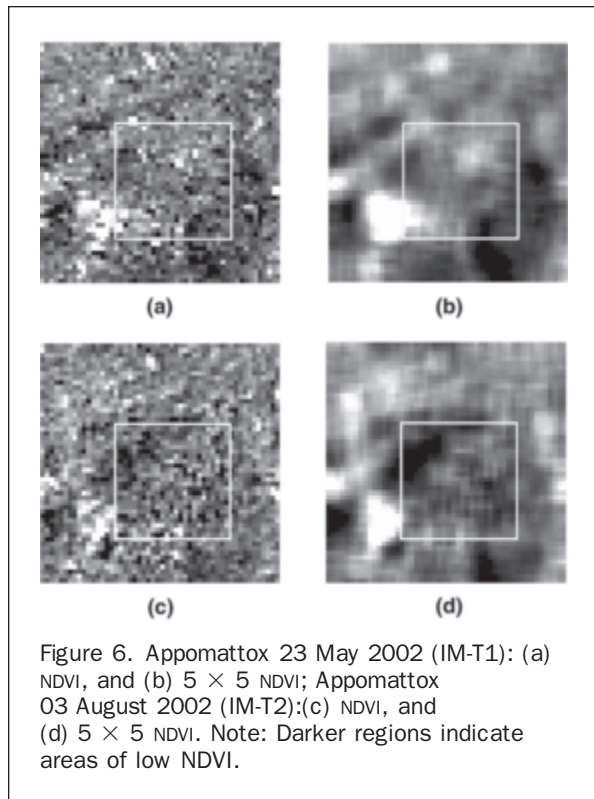
Image-to-Image NDVI Change Detection Analysis

Testing image-to-image NDVI change at both sites was problematic in that the time between the two image dates (IM-T1 and IM-T2) was lengthy (73 days: Appomattox; 94 days: Hertford). Also, the nominal collection azimuths differed within the Appomattox image pairs (236.7°) and the Hertford image pairs (83.8°). Therefore, this method was applied only to the Appomattox image pair to determine if any change could be detected.

The mean UA region NDVI for the IM-T1 (May 2002) image was reduced 9.1 percent between image acquisition dates (Table 4). Within the 1 ha UR region, a 14.3 percent decrease in NDVI was observed between the IM-T1 image and the IM-T2 image. Between-date ANOVA results indicate that there were significant differences between the 1 ha UR ($p = <0.0001$, $F = 1303.9$, $df = 1$) and the UA regions ($p = <0.0001$, $F = 3010.2$, $df = 1$). Within the 1 ha UR region an NDVI image subtraction (pre-harvest image NDVI minus post harvest image NDVI) resulted in 81.2 percent of the area exhibiting a decrease in NDVI greater than 0.01 NDVI change threshold. The remaining 18.8 percent of the 1 ha UR region indicated no change in NDVI. Within the UA region 11.9 percent of the area showed an NDVI decrease (>0.01), 8.5 percent resulted in an NDVI increase (>0.01), and the rest of the area was unchanged.

TABLE 4. IMAGE-TO-IMAGE NDVI CDA (5×5 AVERAGED) OF 23 MAY (IM-T1) AND 03 AUGUST 2002 IMAGES (IM-T2) (APPOMATTOX)

| | UR ($n = 16$) | | | UA ($n = 60$) | | |
|----------|-----------------|--------|-------------|-----------------|--------|-------------|
| | 5/23/02 | 8/3/02 | % Reduction | 5/23/02 | 8/3/02 | % Reduction |
| μ | 0.58 | 0.49 | 14.3 | 0.57 | 0.52 | 9.1 |
| σ | 0.004 | 0.004 | | 0.009 | 0.006 | |



Within-image NDVI Change Detection Analysis

Significant differences were detected between the 1 ha UR and the UA regions within the IM-T2 (Appomattox) NDVI image ($p = <0.0001$, $F = 300.9$, $df = 1$) and the IM-T2 (Hertford) NDVI image ($p = <0.0001$, $F = 30.3$, $df = 1$) (Figures 6 and 7). A 5.0 percent decrease in NDVI was detected between the 1 ha UR and the UA regions of the IM-T2 (Appomattox) NDVI image (UR NDVI = 0.493; UA NDVI = 0.519), whereas only a 1.8 percent decrease was detected between the 1 ha UR and UA regions within the IM-T2 (Hertford) NDVI image (UR NDVI = 0.425; UA NDVI = 0.433; Table 5).

Spatial Averaging Window Size

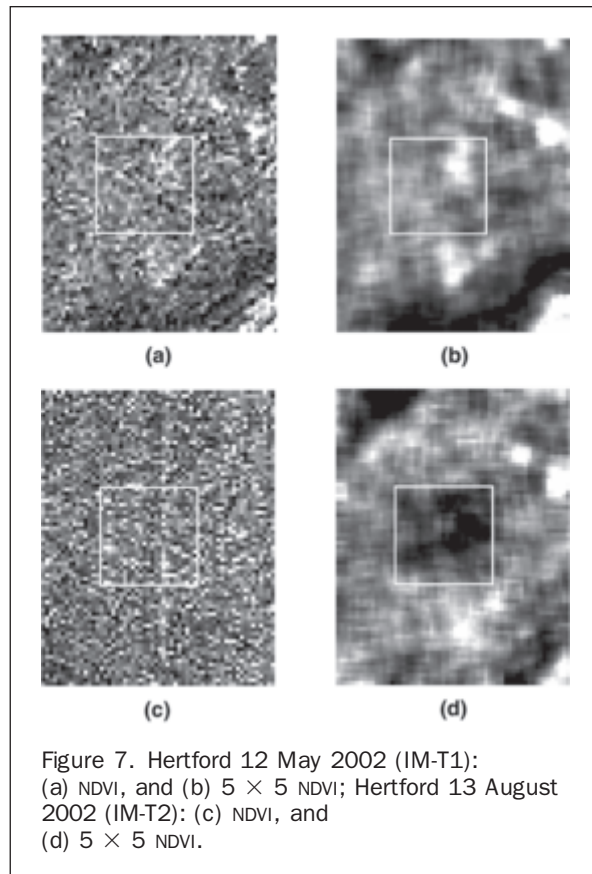
The mean values between four spatial averaging window sizes (3×3 , 5×5 , 7×7 , and 9×9) for both the 1 ha UR and the UA regions were identical (Figure 8). All p-values indicated significant differences in the means for the two regions (UR versus UA) within each window size ($p < 0.001$). Note the random noise associated with image A in Figure 8 that resulted from the 4 m NDVI values occurring over canopy gap areas with no understory vegetation (darker pixels) and other 4 m NDVI values occurring over crown tops (light pixels). The spatial averaging in panels B through E (Figure 8) resolve NDVI decreases at the canopy level.

Other Vegetation Indices

Analysis of the four additional vegetation indices besides NDVI revealed that NDVI and NIR - Red resulted in the detec-

TABLE 5. WITHIN-IMAGE NDVI CDA (5×5 AVERAGED) OF 03 AUGUST 2002 (IM-T2) (APPOMATTOX) AND 13 AUGUST 2002 (IM-T2) (HERTFORD) IKONOS IMAGERY

| | UR | UA | Reduction % |
|------------|-------|-------|-------------|
| Appomattox | 0.493 | 0.519 | 5.0 |
| Hertford | 0.425 | 0.433 | 1.8 |

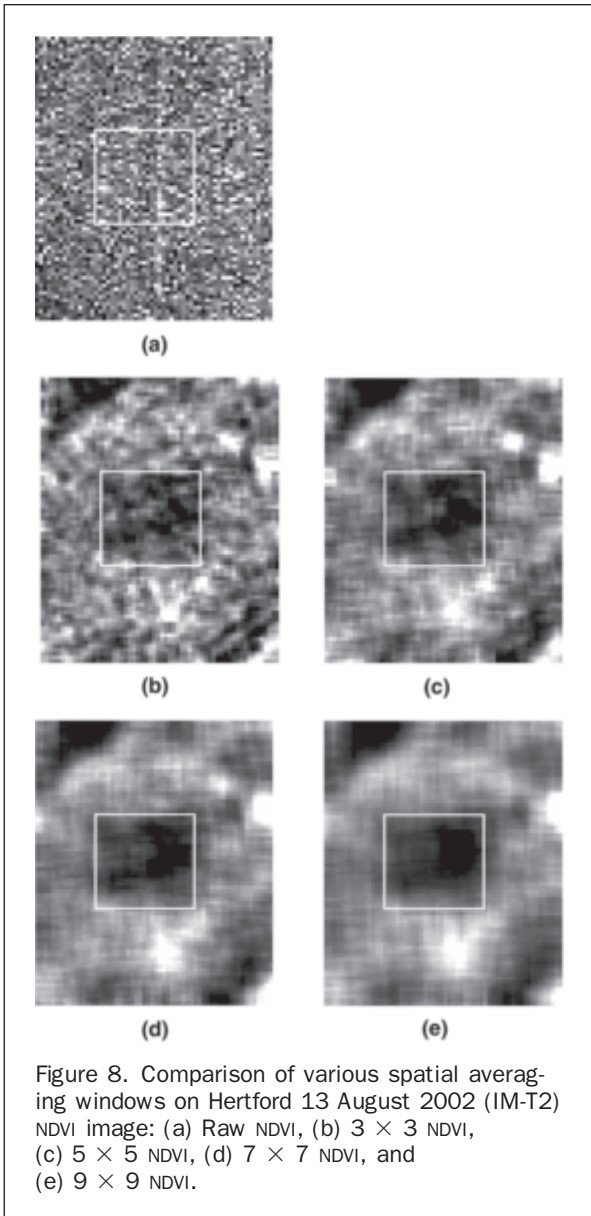


tion of the largest change across all four indices (Table 6). The vegetation index tNDVI was the least sensitive detector of change.

Discussion

Understory effects on spectral signal to the sensor are confounded by a number of factors including the spatial distribution of variable illumination conditions (direct sunlight, sunflecks, penumbra, shade) (Miller *et al.*, 1997). For example, in the Boreal Ecosystem-Atmospheric Study (BOREAS), these illumination variables affected VI response dependent on forest stand type when evaluating over seasons and time-of-day (Miller *et al.*, 1997). Gamon *et al.* (2004) suggested that optical signature variability in the boreal conifer forests render LAI derived from Vis into question. It has also been shown that understanding the understory contribution to overall LAI has significance in the evaluation of ecosystem flux data. Ponderosa pine carbon-water interactions as well as Slash pine water and energy exchange have been aided by the assessment of the understory LAI contributions (Williams *et al.*, 2001; Powell *et al.*, 2005).

With our research, the image-to-image NDVI CDA within the Appomattox site did show a larger decrease in NDVI within the 1 ha UR region between image dates (14.3 percent) than did the IM-T2 within-image NDVI decrease between the 1 ha UR and UA regions (5.0 percent). However, the image-to-image processing technique had some underlying issues in that the IM-T1 Ikonos acquisition was 2.5 to 3 months prior to the IM-T2 acquisition. Ikonos acquisition azimuthal differences between the two image dates (123.3°) could affect shadowing and the



amount of NIR reflectance received at the sensor. Also, *P. taeda* incurs tremendous change over the growing season, with the addition of two to three needle flushes common within this species. Sampson *et al.* (2003) found that *P. taeda* LAI varied twofold inter-annually with a minimum LAI in March to April and a maximum in September. This trend is evident when comparing the increase of *in situ* LAI (29.9 percent) from May 2002 (C1), to July 2002 (C2), then

the expected decrease (10 percent) between C2 and C3. Viewing only *in situ* LAI change between C1 and C3, an increase of 16.9 percent was recorded, even though significant leaf biomass had been removed (Figure 9). NDVI, contrary to the *in situ* LAI trend, exhibited a continually decreasing tendency between C1 to C2 (9.7 percent), then C2 to C3 (5.0 percent), with an overall NDVI decrease from C1 to C3 of 14.3 percent (Figure 9). Possible explanations for this decrease in NDVI with a corresponding increase in *in situ* measured LAI may result from higher NIR reflectivity and red absorption from planophile broadleaf foliage in the understory compared to erectophile foliage typical of conifer needles (Turner *et al.*, 1999) (Table 4). Another possible explanation may be related to the relative visibility of the deciduous understory in the low LAI *P. taeda* conditions typical for the early-late spring period. A direct comparison of empirically-derived LAI, i.e., the correlation of spectral data with *in situ* estimated LAI, and *in situ* LAI was not possible due to the narrow range of LAI values within this stand.

Within-image NDVI CDA compared the 1 ha UR and UA regions for both sites within each corresponding IM-T2 (August 2002) image. Significant differences between both regions (UR and UA) were detected. However, within the 1 ha UR region, the Appomattox and Hertford sites behaved differently with respect to the percent reduction in NDVI and the *in situ* estimated reduction in LAI. The Appomattox site showed a larger decrease in NDVI than the Hertford site within the 1-ha UR regions (5 percent versus 1.8 percent), yet the Hertford site exhibited a greater reduction in LAI (17.4 percent versus 10.0 percent). One possible explanation for this result may be the large percentage of *Ilex*

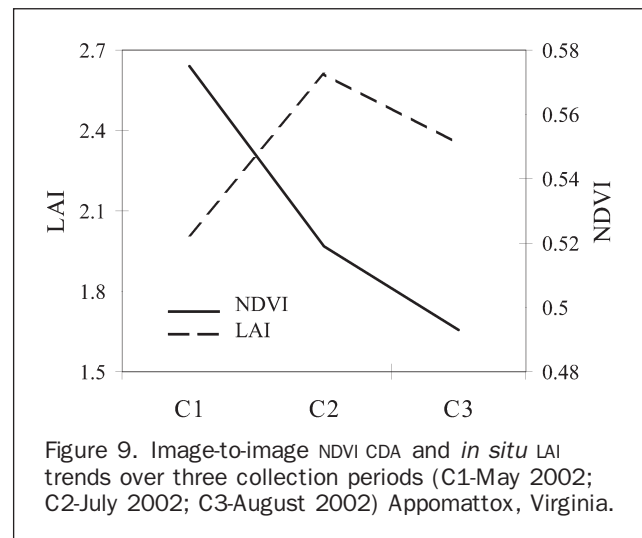


TABLE 6. VEGETATION INDICES DIFFERENCES EVALUATING BIOMASS CHANGE DETECTION FOR THE 13 AUGUST 2002 (IM-T2) HERTFORD IKONOS NDVI IMAGE (H = HARVESTED; NH = NON-HARVESTED)

| | NDVI | tNDVI | NIR/Red | NIR-Red | NIR/Red |
|----------|-------------|-------------|-------------|-------------|-------------|
| | (H:NH) | (H:NH) | (H:NH) | (H:NH) | (H:NH) |
| μ | 0.425:0.433 | 0.963:0.966 | 1.580:1.591 | 401.4:408.8 | 0.426:0.434 |
| σ | 0.004:0.005 | 0.003:0.002 | 0.010:0.009 | 7.79:7.56 | 0.004:0.004 |
| % Diff | 1.80 | 0.33 | 0.73 | 1.80 | 1.72 |
| <i>p</i> | <0.001 | <0.001 | <0.001 | <0.001 | <0.001 |

opaca (American Holly) existent within the Hertford understory (60 percent). This species is extremely shade tolerant, thus exhibits characteristics typical of this shade class (increased photosynthetic and respiratory efficiency, increased light use efficiency, and, increased leaf surface area). There is a visible difference between the leaf underside and top of leaf. The non-Lambertian surface (leaf and canopy) could produce significantly spectral differences dependent on the image acquisition angle. In addition to the *Ilex opaca* issue, returned reflectance to the sensor may further have been reduced by the larger presence of organic soils in this coastal plain site compared to the piedmont site (Appomattox).

The question arises on how other sensor-derived NDVI might detect subtle changes in forest stand structure. Spectral vegetation indices may not be comparable due to sensor spectral and spatial characteristics (Hill and Aifadopoulou, 1990; Teillet *et al.*, 1997; Steven *et al.*, 2003; Soudani *et al.*, 2006). The primary issue affecting NDVI differences between sensors was the spectral characteristic of the red band (i.e., width, location) (Teillet *et al.*, 1997; Soudani *et al.*, 2006). Ikonos-derived NDVI was observed to be systematically lower than Landsat ETM+ -and SPOT HRVIR-derived NDVI, with an observed offset approximately 0.11 and 0.20 NDVI units dependent on image preprocessing techniques (i.e., atmospheric corrections) (Soudani *et al.*, 2006). No generalized Ikonos NDVI-LAI regression model was found in the literature for *P. taeda* in the southeastern U.S. However, a general comparison was made between within-image Ikonos-derived NDVI change observed on both sites and retrieved NDVI differences from a species-specific nonlinear regression model developed from the HyMap (Integrated Spectronics Pty Ltd., 1997) sensor (Flores, 2003). This equation was developed by regressing *in situ* estimated LAI with HyMap-retrieved NDVI on two *P. taeda* stands located in the North Carolina Sandhills and Coastal Plain regions. Flores (2003) found this equation to be transferable across sites, stand structures, and seasons. By applying C2 and C3 *in situ* LAI estimates into the Flores regression model, predicted NDVI values were retrieved for both the Appomattox and Hertford sites. The HyMap NDVI was shown to be 0.21 (Appomattox) and 0.28 (Hertford) NDVI units above those observed with the Ikonos sensor, values similar to differences observed between the Landsat ETM+ and SPOT HRVIR sensors. Results were indifferent as to which sensor might have more appropriate detection abilities. On the Appomattox site, a 2.8 percent NDVI reduction was predicted by the Flores regression model as compared to a larger NDVI reduction (5.0 percent) observed with the Ikonos-derived NDVI. On the other site, the Flores regression model predicted a larger NDVI reduction than that observed with Ikonos sensor (5.0 percent versus 1.8 percent). It would be expected that, if available, actual observed HyMap-derived NDVI values would be more highly detectable due to the higher spectral resolution and the corrections for atmospheric interference.

The 5×5 spatial averaging window was chosen to offset issues inherent within higher spatial resolution sensors: (a) the introduction of heterogeneity at a finer scale than that from which *in situ* LAI is measured, and (b) the resolving of canopies at the individual tree level (Cohen *et al.*, 1990; Turner *et al.*, 1999). Regarding the comparison of the various VIS, NDVI detected the most change in biomass compared to the other four indices. Both sites had yet to reach the asymptotic point in the NDVI-LAI relationship; thus, the relationship was described as linear. However, the SR vegetation index may be more useful in areas of higher biomass due to the linear relationship with LAI (Flores, 2003).

Conclusions

Appomattox results showed that the percentage of removed understory detected by the Ikonos sensor in a piedmont site was 5.0 percent when compared to an actual *in situ* LAI reduction of 10.0 percent. The Hertford results showed that a larger percentage of NDVI change was undetected by the Ikonos sensor (1.8 percent) when compared to the actual LAI reduction as measured *in situ* (17.4 percent). Possible reasons for these differences may be based upon underlying soil types (organic) and/or bi-directional reflectance distribution functions for the non-Lambertian *Ilex opaca* canopy. Off-nadir image acquisitions for both sites would inhibit view of understory conditions for both sites (solar elevation $\approx 65^\circ$).

Acknowledgments

The authors wish to express their gratitude to Jerry Hansen of International Paper Corporation and Vick Ford of Mead-Westvaco who facilitated access to the Appomattox and Hertford sites. Ikonos imagery was provided through the NASA Data Buy Program managed by Jeff Morissette and Jaime Nickeson. In addition, John Duncan, Malcolm Wilkins, Milton Bowen, and Govind Gawdi provided network and logistical support. Administrative, statistical, and technical support was given by John Lyon, L. Dorsey Worthy, Ross Lunetta, David Holland, Megan Mehaffey, Jayantha Ediriwickrema, and Joe Knight. Lastly, we would like to thank three anonymous reviewers who provided input to this article as well as the UNH Dissertation Committee who critiqued the initial study design and results: John D. Aber, Mark J. Ducey, Mary E. Martin, and M.L. Smith. The U.S. Environmental Protection Agency funded and conducted the research described in this paper. It has been subject to the Agency's programmatic review and has been approved for publication. Mention of any trade names or commercial products does not constitute endorsement or recommendation for use.

References

- Aber, J.D., and J.M. Melillo, 2001. *Terrestrial Ecosystems*, Academic Press, San Diego, California, 556 p.
- Avery, T.E., and H. Burkhardt, 1993. *Forest Measurements*, New York, McGraw Hill Text, 331 p.
- Baret, F., and G. Guyot, 1991. Potentials and limits of vegetation indices for LAI and APAR assessment (absorbed photosynthetically active radiation), *Remote Sensing of Environment*, 35:161-173.
- Beer, A., 1853. *Einleitung in die höhere Optik*, Vieweg und Sohn, Braunschweig, Germany, 430 p.
- Badhwar, G.D., R.B. MacDonald, F.G. Hall, and J.G. Carnes, 1986. Spectral characterization of biophysical characteristics in a boreal forest: relationship between Thematic Mapper band reflectance and leaf area index for aspen, *IEEE Transactions on Geoscience and Remote Sensing*, GE-24:322-326.
- Bouman, B.A., 1992. Accuracy of estimating the leaf area index from vegetative indices derived from crop reflectance characteristics, A simulation study, *International Journal of Remote Sensing*, 13:3069-3084.
- Breda, N.J.J., 2003. Ground-based measurements of leaf area index: A review of methods, instruments and current controversies, *Journal of Experimental Botany*, 54(392):2403-2417.
- Carlson, T.N., and D.A. Ripley, 1997. On the relation between NDVI, fractional vegetation cover and leaf area index, *Remote Sensing of Environment*, 62:241-252.
- Chason, J.W., D.D. Baldocchi, and M.A. Huston, 1991. A comparison of direct and indirect methods for estimating forest canopy leaf area, *Agricultural and Forest Meteorology*, 57:107-128.

- Chen, J.M., and T.A. Black, 1992a. Defining leaf-area index for non-flat leaves, *Plant Cell and Environment*, 15(4):421-429.
- Chen, J.M., and T.A. Black, 1992b. Foliage area and architecture of plant canopies from sunfleck size distributions, *Agricultural and Forest Meteorology*, 60:249-266.
- Chen, J.M., and J. Cihlar, 1996. Retrieving leaf area index of boreal conifer forests using Landsat TM images, *Remote Sensing of Environment*, 55:153-162.
- Chen, J.M., 1996. Optically-based methods for measuring seasonal variation of leaf area index in boreal conifer stands, *Agricultural and Forest Meteorology*, 80:135-163.
- Chen, J.M., G. Pavlic, L. Brown, J. Cihlar, S.G. Leblanc, H.P. White, R.J. Hall, D.R. Peddle, D.J. King, J.A. Trofymow, E. Swift, J. Vander Sanden, and P.K.E. Pellikka, 2002. Derivation and validation of Canada-wide coarse-resolution leaf area index maps using high-resolution satellite imagery and ground measurements, *Remote Sensing of Environment*, 80:165-184.
- Chen, J.M., A. Govind, O. Sonnentag, Y. Zhang, A. Barr, and B. Amiro, 2006. Leaf area measurements at Fluxnet-Canada forest sites, *Agricultural and Forest Meteorology*, 140:257-268.
- Cohen, W.B., T.A. Spies, and G.A. Bradshaw, 1990. Semivariograms of digital imagery for analysis of conifer canopy structure, *Remote Sensing of Environment*, 34:167-178.
- Cohen, W.B., and T.A. Spies, 1992. Estimating structural attributes of Douglas-fir/western hemlock forest stands from Landsat and SPOT imagery, *Remote Sensing of Environment*, 41:1-17.
- Danson, F.M., and P.J. Curran, 1993. Factors affecting the remotely sensed response of coniferous forest plantations, *Remote Sensing of Environment*, 43:55-65.
- Elvidge, C.D., D. Yuan, R.D. Weerackoon, and R. Lunetta, 1995. Relative radiometric normalization of Landsat Multispectral Scanner (MSS) data using an automatic scattergram-controlled regression, *Photogrammetric Engineering & Remote Sensing*, 61(11):1255-1260.
- Fassnacht, K.S., S.T. Gower, J.M. Norman, and R.E. McMurtrie, 1994. A comparison of optical and direct methods for estimating foliage surface area index in forests, *Agricultural and Forest Meteorology*, 71:183-207.
- Flores, F., 2003. *Using Remote Sensing Data to Estimate Leaf Area Index and Foliar Nitrogen of Loblolly Pine Plantations*, Ph.D. dissertation, North Carolina State University, Raleigh, North Carolina, 115 p.
- Franklin, S.E., M.B. Lavigne, M.J. Deuling, M.A. Wulder, and E.R. Hunt, 1997. Estimation of forest leaf area index using remote sensing and GIS for modelling net primary production, *International Journal of Remote Sensing*, 18(16):3459-3471.
- Gamon, J.A., K.F. Huemmrich, D.R. Peddle, J. Chen, D. Fuentes, F.G. Hall, J.S. Kimball, S. Goetz, J. Gug, K.C. McDonald, J.R. Miller, M. Moghaddam, A.F. Rahman, J.L. Roujean, E.A. Smith, C.L. Walthall, P. Zarco-Tejadan, B. Hui, R. Fernandes, and J. Cihlar, 2004. Remote sensing in BOREAS: Lessons learned, *Remote Sensing of Environment*, 89(2):139-162.
- Gates, D.M., J.J. Keegan, J.C. Schleiter, and V.R. Weidner, 1965. Spectral property of plants, *Applied Optics*, 4(1):11-20.
- Gausmann, H.W., W.A. Allen, and R. Cardenas, 1969. Reflectance of cotton leaves and their structure, *Remote Sensing of Environment*, 1:110-122.
- Gholz, H.L., 1982. Environmental limits on above-ground net primary production, leaf-area, and biomass in vegetation zones of the Pacific Northwest, *Ecology*, 63(2):469-481.
- Gower, S.T., and J.M. Norman, 1991. Rapid estimation of leaf-area index in conifer and broad-leaf plantations, *Ecology*, 72(5):1896-1900.
- Hall, R.J., D.P. Davidson, and D.R. Peddle, 2003. Ground and remote estimation of leaf area index in Rocky Mountain forest stands, Kananaskis, Alberta, *Canadian Journal of Remote Sensing*, 29(3):411-427.
- Hill, J., and D. Aifadopolou, 1990. Comparative analysis of Landsat-5 TM and SPOT HRV-1 data for use in multiple sensor approaches, *Remote Sensing of Environment*, 34:55-70.
- Huemmrich, K.F., and S.N. Goward, 1997. Vegetation canopy PAR absorbance and NDVI and assessment for ten tree species with the SAIL model, *Remote Sensing of Environment*, 61:254-269.
- Hurlbert, S.H., 1984. Pseudoreplication and the design of ecological field experiments, *Ecological Monographs*, 54:187-211.
- Iiames, J.S., 2006. *Assessing the Accuracy of the MODIS LAI 1-KM Product in Southeastern United States Loblolly Pine Plantations: Accounting for Measurement Variance from Ground to Satellite*, Ph.D. dissertation, University of New Hampshire, Durham, New Hampshire, 184 p.
- Jensen, J.R., 2000. *Remote Sensing of the Environment: An Earth Resource Perspective*, Prentice-Hall, Upper Saddle River, New Jersey, 544 p.
- Jonckheere, I., B. Muys, and P. Coppin, 2005. Allometry and evaluation of in situ optical LAI determination in Scots pine: a case study in Belgium, *Tree Physiology*, 25:723-732.
- Law, B.E., S. Van Tuyl, A. Cescatti, and D.D. Baldocchi, 2001. Estimation of leaf area index in open-canopy ponderosa pine forests at different successional stages and management regimes in Oregon, *Agricultural and Forest Meteorology*, 108:1-14.
- Leblon, B., L. Gallant, and H. Grandberg, 1996. Effects of shadowing types on ground-measured visible and nearinfrared shadow reflectances, *Remote Sensing of Environment*, 58:322-328.
- Leblanc, S.G., and J.M. Chen, 2001. A practical scheme for correcting multiple scattering effects on optical LAI measurements, *Agricultural and Forest Meteorology*, 110:125-139.
- Leblanc, S.G., J.M. Chen, and M. Kwong, 2002. *Tracing Radiation and Architecture of Canopies. TRAC Manual*, version 2.1.3., Natural Resources Canada, Canada Centre for Remote Sensing, Ottawa, Ontario, Canada, 25 p.
- Leblanc, S., J.M. Chen, R. Fernandes, D.W. Deering, and A. Conley, 2005. Methodology comparison for canopy structure parameters extraction from digital hemispherical photography in boreal forests, *Agricultural and Forest Meteorology*, 129:187-207.
- Lee, K.-S., W.B. Cohen, R.E. Kennedy, T.K. Maiersperger, and T. Gower, 2004. Hyperspectral versus multispectral data for estimating leaf area index in four different biomes, *Remote Sensing of Environment*, 91:508-520.
- Miller, J.B., 1967. A formula for average foliage density, *Australian Journal of Botany*, 15:141-144.
- Miller J.R., H.P. White, J.M. Chen, D.R. Peddle, G. Mcdermid, R.A. Fournier, P. Shepherd, I. Rubinstein, J. Freemantle, R. Soffer, and E. Ledrew, 1997. Seasonal change in understory reflectance of boreal forests and influence on canopy vegetation indices, *Journal of Geophysical Research*, 102(d24):29,475-29,482.
- Morisette, J.T., J.E. Nickeson, P. Davis, Y.J. Wang, Y.H. Tian, C.E. Woodcock, N. Shabanov, M. Hansen, W.B. Cohen, D.R. Oetter, and R.E. Kennedy, 2003. High spatial resolution satellite observations for validation of MODIS land products: IKONOS observations acquired under the NASA Scientific Data Purchase, *Remote Sensing of Environment*, 88:100-110.
- Morisette, J.T., F. Baret, J.L. Privette, R.B. Myneni, J. Nickeson, S. Garrigues, N. Shabanov, M. Weiss, R. Fernandes, S. Leblanc, M. Kalacska, G. Sánchez-Azofeifa, M. Chubey, M.B. Rivard, P. Stenberg, M. Rautiainen, P. Voipio, T. Manninen, A. Pilant, T. Lewis, J. Iiames, R. Colombo, M. Meroni, L. Busetto, W. Cohen, D. Turner, E. Warner, G.W. Petersen, G. Seufert, and R. Cook, 2006. Validation of global moderate-resolution LAI Products: A framework proposed within the CEOS land product validation subgroup, *IEEE Transactions of Geoscience and Remote Sensing*, 44(7):1804-1817.
- Myers, V.I., 1970. Soil, water, and plant relations, *Remote Sensing with Special Reference to Agriculture and Forestry*, National Academy of Sciences, Washington, D.C., pp. 253-297.
- Nemani, R., L. Pierce, and S. Running, 1993. Forest ecosystem processes at the watershed scale: Sensitivity to remotely sensed leaf area index estimates, *International Journal of Remote Sensing*, 14(13):2519-2534.
- Peterson, D.L., and S.W. Running, 1989. Applications in forest science and management, *Theory and Application of Optical Remote Sensing* (G. Asrar, editor), Wiley, New York, 429-473 p.
- Pierce, L.L., and S.W. Running, 1988. Rapid estimation of coniferous leaf-area index using a portable integrating radiometer, *Ecology*, 69(6):1762-1767.

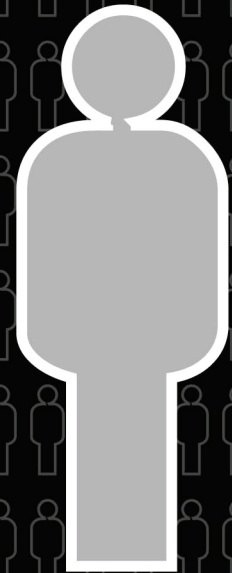
- Powell, T.L., G. Starr, K.L. Clark, T.A. Martin, and H.L. Gholz, 2005. Ecosystem and understory water and energy exchange for a mature, naturally regenerated pine flatwoods forest in north Florida, *Canadian Journal of Forest Research*, 35:1568–1580.
- Sampson, D.A., T.J. Albaugh, K.H. Johnsen, H.L. Allen, and S.J. Zarnoch, 2003. Monthly leaf area index estimates from point-intime measurements and needle phenology for *Pinus taeda*, *Canadian Journal of Forest Research*, 33:2477–2490.
- Schlerf, M., C. Atzberger, and J. Hill, 2005. Remote sensing of forest biophysical variables using HyMap imaging spectrometer data, *Remote Sensing of Environment*, 95:177–194.
- Soudani, K., C. Francois, G. le Maire, V. Le Dantec, and E. Dufrene, 2006. Comparative analysis of IKONOS, SPOT, and ETM+ data for leaf area index estimation in temperate coniferous and deciduous forest stands, *Remote Sensing of Environment*, 102:161–175.
- Spanner, M.A., L.L. Pierce, D.L. Peterson, and S.W. Running, 1990. Remote sensing of temperate coniferous forest leaf area index: The influence of canopy closure, understory vegetation and background reflectance, *International Journal of Remote Sensing*, 11(1):95–111.
- Stenback, J.M., and R.G. Congalton, 1990. Using Thematic Mapper imagery to examine forest understory, *Photogrammetric Engineering & Remote Sensing*, 56(9):1285–1290.
- Steven, M.D., T.J. Malthus, F. Baret, H. Xu, and M.J. Chopping, 2003. Intercalibration of vegetation indices from different sensor systems, *Remote Sensing of Environment*, 88(4):412–422.
- Teillet, P.M., K. Staenz, and D.J. Williams, 1997. Effects of spectral spatial and radiometric characteristics of remote sensing vegetation indices of forested regions, *Remote Sensing of Environment*, 61:139–149.
- Turner, D.P., W.B. Cohen, R.E. Kennedy, K.S. Fassnacht, and J.M. Briggs, 1999. Relationships between leaf area index and Landsat TM spectral vegetation indices across three temperate zone sites, *Remote Sensing of Environment*, 70:52–68.
- Williams, D.L., 1991. A comparison of spectral reflectance properties at the needle, branch, and canopy level for selected conifer species, *Remote Sensing of Environment*, 35:79–93.
- Williams, M., B.E. Law, P.M. Anthoni, and M.A. Unsworth, 2001. Use of a simulation model and ecosystem flux data to examine carbon-water interactions in ponderosa pine, *Tree Physiology*, 21:287–298.
- Yoder, B.J., and R.H. Waring, 1994. The normalized difference vegetation index of small Douglas-fir canopies with varying chlorophyll concentrations, *Remote Sensing of Environment*, 49:81–91.

(Received 21 August 2006; accepted 06 February 2007; revised 04 April 2007)

Stand out from the rest— earn ASPRS Certification

"ASPRS Certification is a highly sought after credential by employers and clients. Since receiving my certification, I find I get more respect from my peers and clients."

Raquel Charols, Certified Photogrammetrist 1240



Apply now for one of these ASPRS Certifications:

- **Photogrammetrist**
- **Mapping Scientist - Remote Sensing**
- **Mapping Scientist - GIS/LIS**
- **Photogrammetric Technologist**
- **Remote Sensing Technologist**
- **GIS/LIS Technologist**

An Initial Study on Vehicle Information Extraction from Single Pass QuickBird Satellite Imagery

Zhen Xiong and Yun Zhang

Abstract

Vehicle information is useful in many fields. In this paper, a technique is presented to extract vehicle information from single pass QuickBird images. While passing a target area, the satellite acquires panchromatic (PAN) and multi-spectral (MS) images simultaneously. Because of a small time interval difference between the PAN and MS images, it is theoretically possible to extract two sets of vehicle ground positions from the PAN and MS images, respectively, to identify whether or not a vehicle is in motion, and to calculate the vehicle's velocity and direction. Practically, however, this extraction and calculation are challenging. Since the time interval is very short, a small error in information extraction will result in an unacceptably large error in the calculated vehicle position and velocity. Another challenge is that satellite image pairs (PAN and MS) do not have the same resolution. Therefore, traditional change detection techniques are incapable of providing reliable results, due to varying scales and relief distortions in the co-registered images or slight pixel shifts in the orthorectified images caused by resampling of the PAN and MS images. In order to avoid these errors, this research presents an algorithm through which a vehicle's ground positions can be directly calculated from the raw PAN and MS images. Experiments demonstrate that it is feasible to use this technique to extract vehicle information from high-resolution images obtained from a single satellite pass.

Introduction

Vehicle information (i.e., position, velocity, and direction) is very important for transportation management, security surveillance, and military applications. In order to extract vehicle information, a sequence of vehicle positions is normally acquired in a fixed time interval. These vehicle positions and time intervals are then used to calculate vehicle velocity and direction. The equipment that is usually used for vehicle information extraction includes radar (Liu *et al.*, 2001; Nag *et al.*, 2003; Liu and Jen, 1992), SAR (Dias *et al.*, 2003; Sun *et al.*, 2002; Pettersson, 2004; Soumekh, 2002), and video cameras (Munno *et al.*, 1993). The system platforms are almost always ground-based (Castellano *et al.*, 1999; Nag *et al.*, 2003; Munno *et al.*, 1993; Pettersson, 2004) or aircraft based (Liu *et al.*, 2001; Sun *et al.*, 2002; Soumekh, 2002). To date, satellites have seldom been used.

Radar, SAR, and video cameras can acquire a sequence of images over a relatively long duration (i.e., several seconds to several hours). Each image has the same resolution. Typically the images are registered, and then the vehicle's position change is calculated. Therefore, for Radar, SAR, and video cameras, geometric processing is not a problem. The research focus for such equipment is on automatic target detection and extraction. Some researchers have used a generalized likelihood ratio as a threshold to judge which target is in motion (Liu *et al.*, 2001; Dias *et al.*, 2003; Pettersson, 2004). Others have used a filter (Nag *et al.*, 2003), or have applied a fractional Fourier transformation (Sun *et al.*, 2002) for digital target detection. Munno *et al.* (1993) utilized Victor's frequency domain spatio-temporal filtering and spatio-temporal constraint error of image frame pairs to detect and track vehicles or people in natural scenes in spite of challenges such as low image contrast, changes in the target's infra-red image pattern, sensor noise, or background clutter (Munno *et al.*, 1993).

The method presented here is completely different, and is based on information obtained from high-resolution imagery provided by a single satellite pass. Some high-resolution satellites such as Ikonos and QuickBird have two sensors. These sensors can therefore acquire two sets of images for the same target area in one pass. For example, the QuickBird satellite can acquire one panchromatic (PAN) image and one multispectral (MS) image in a single pass. The time that the PAN sensor passes through the nadir point is different from that of MS sensor. Therefore, there is a time interval between the PAN image and the MS image (less than one second). If the target vehicle is in motion, the PAN image and MS image will record two different positions of the same vehicle. So theoretically, from a single satellite pass, two different positions of a vehicle can be extracted from the PAN image and MS image, respectively. Thus the vehicle's velocity and direction can be calculated.

This method presents challenges for image processing. First, unlike radar, SAR, and video cameras, QuickBird satellites can only acquire one image pair (a PAN image and a MS image) during each pass, and each image has a different resolution. This makes image registration more difficult than usual. Second, the time interval between the PAN image and MS image is very short. A very small error in

Department of Geodesy & Geomatics Engineering, University of New Brunswick, 15 Dineen Drive, P.O. Box 4400, Fredericton, NB, Canada E3B 5A3 (v009v@unb.ca).

Photogrammetric Engineering & Remote Sensing
Vol. 74, No 11, November 2008, pp. 1401-1411.

0099-1112/08/7411-1401/\$3.00/0
© 2008 American Society for Photogrammetry
and Remote Sensing

registering the vehicle's position will cause a very large error in calculating its velocity. Third, traditional equipment can acquire many images and the vehicle's velocity can therefore be adjusted using the image sequence, but for the QuickBird satellites, only one pair of images can be used to calculate vehicle's position and velocity. Without redundant data, the velocity error is very difficult to find and correct.

Our focus is on how to reduce the error in registering the vehicle's position. Traditionally, the image change detection technique is used for vehicle information extraction. But the accuracy of this technique is directly affected by image scale, ground relief, and image resampling. In order to avoid this problem, a direct location algorithm to calculate vehicle's ground position from its image position based on a Digital Elevation Model (DEM) is developed below.

We believe that this technique offers a new choice for extracting vehicle information. We begin this paper by describing traditional methods and discussing their limitations for use with QuickBird images. We then present our new methodology and test it using QuickBird satellite imagery. Finally, we discuss the results and present our conclusions.

Traditional Methods

Fundamentally there are two different ways to extract vehicle information from images. One is to extract vehicle information in the image domain, and the other is to extract vehicle information in the object domain. These methods use a change detection algorithm to extract the change in the vehicle's position, but as shown below, if these methods are used to process the high-resolution satellite images, there will be many difficulties. These two traditional methods are described in more detail in the following sections, and their limitations for extracting vehicle information from QuickBird satellite imagery are described.

Vehicle Information Extraction in Image Domain (Method 1)

In this method, images are first registered, and then the change detection method is used to extract vehicle's position change. Finally, the vehicle's position, velocity, direction, and acceleration/deceleration are calculated and adjusted (Munno *et al.*, 1993; Nag *et al.*, 2003); Figure 1 shows the flowchart.

After acquiring a sequence of images, the vehicle's speed between two neighboring images can be calculated.

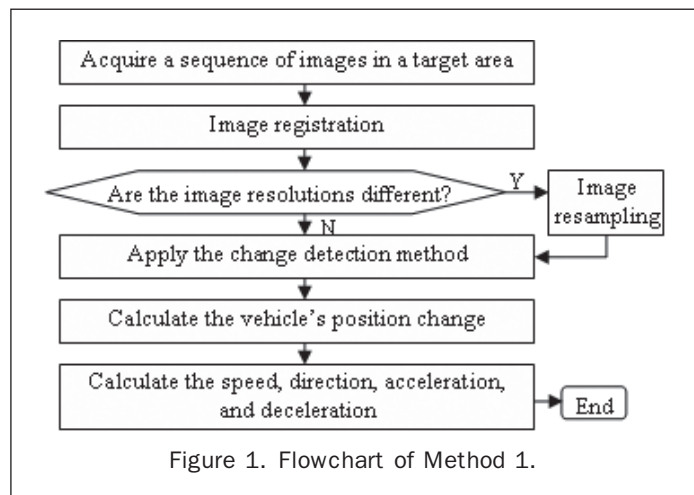


Figure 1. Flowchart of Method 1.

Using this information, the vehicle's acceleration or deceleration can be calculated. From all the vehicle's positions and the time interval, the vehicle's average speed can be calculated (Figure 2).

If this method is applied to QuickBird image pairs, one should first resample the PAN and MS images to the same resolution, then register the resampled images together. Next, one can extract the vehicle's image position from the resampled images. Finally, the vehicle's velocity and direction can be calculated.

For example, if a vehicle moves from point $A(I_A, J_A)$ to point $B(I_B, J_B)$ (Figure 3), in image space, the distance S that vehicle has moved during the time interval is calculated as:

$$S = \sqrt{(I_B - I_A)^2 + (J_B - J_A)^2} \quad (1)$$

where S is distance (pixels), (I_A, J_A) and (I_B, J_B) are image coordinates (pixels); J_A is the column of point A , I_A is the row of point A , J_B is the column of point B , and I_B is the row of point B .

Then, the velocity can be calculated as following:

$$v = \frac{S}{t} \quad (2)$$

where v is speed (pixels/second) and t is time (seconds);

$$\theta = \tan^{-1} \left(\frac{J_B - J_A}{I_B - I_A} \right) \quad (3)$$

where θ is the moving direction angle (degrees) (See Figure 3).

Vehicle Information Extraction in the Object Domain (Method 2)

In this method, the images are first registered, then the PAN and MS images are orthorectified to the same resolution. Next, the change detection method is used to extract

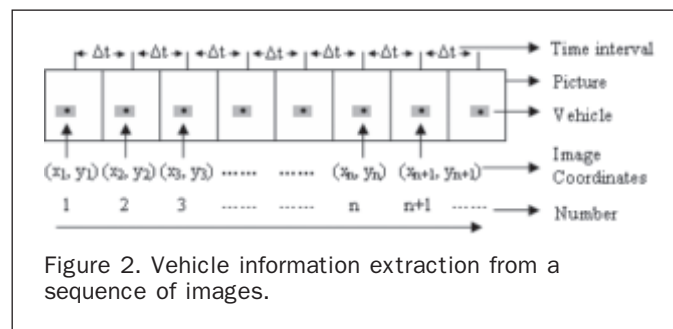


Figure 2. Vehicle information extraction from a sequence of images.

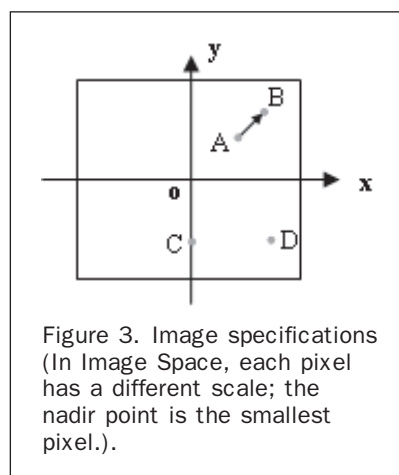


Figure 3. Image specifications (In Image Space, each pixel has a different scale; the nadir point is the smallest pixel.)

the vehicle's position change. Finally, the vehicle's velocity, direction, and acceleration/deceleration are calculated and adjusted. Figure 4 shows the flowchart of Method 2.

The Drawbacks of the Traditional Methods

If Method 1 is used to extract vehicle information from QuickBird images, three factors affect the accuracy of the final result: scale change, ground relief variation, and image resampling error. Because Method 2 includes a process of image orthorectification, it can effectively avoid the error of scale change and ground relief variation, but Method 2 is still affected by the image resampling error. Each of the three types of error is described below.

Scale Change

Before orthorectification, each image pixel on a QuickBird image has a different scale. The nadir point on the image is the smallest pixel. The farther the pixel is from the nadir point, the bigger it is. For QuickBird, the nadir point resolution on the PAN image is 0.61 meters and the 25° off-nadir point resolution is 0.72 meters. The nadir point resolution on the MS image is 2.44 meters and the 25° off-nadir point is 2.88 meters (QuickBird Product Guide, 2003). Therefore, if vehicle C (in Figure 3) moves at a speed of five pixels per second at the nadir point and vehicle D (in Figure 3) also moves at five pixels per second at the off-nadir point, vehicle D is moving faster than vehicle C.

Ground Relief Variation

Before orthorectification, the pixel size on a QuickBird image changes with the ground relief. In Figure 5, from similar triangles ΔLCa and ΔLDA , we can get Equation 4:

$$\frac{Ca}{DA} = \frac{f}{H-h} \quad (4)$$

From similar triangles ΔLCb and ΔLDB , we can get Equation 5:

$$\frac{Cb}{DB} = \frac{f}{H-h} \quad (5)$$

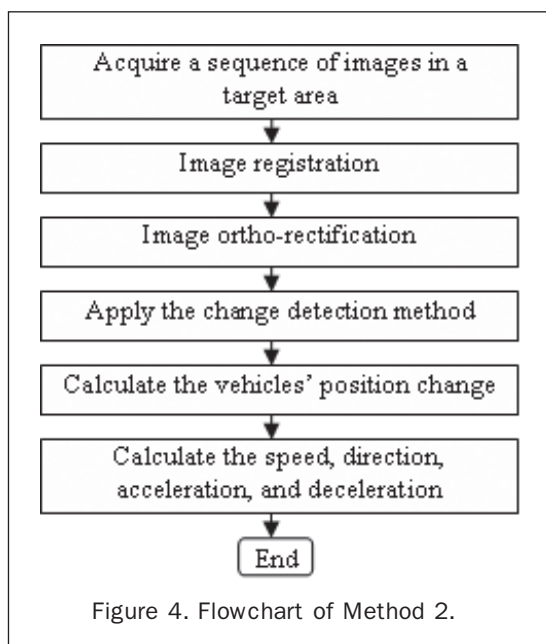


Figure 4. Flowchart of Method 2.

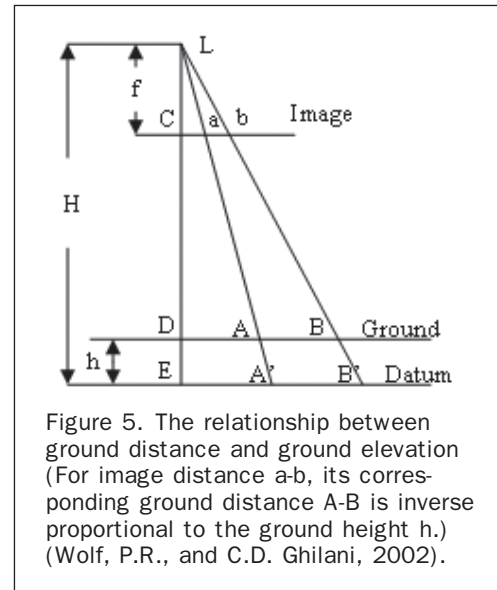


Figure 5. The relationship between ground distance and ground elevation (For image distance $a-b$, its corresponding ground distance $A-B$ is inverse proportional to the ground height h .) (Wolf, P.R., and C.D. Ghilani, 2002).

From Equation 4 and Equation 5, we can get:

$$\frac{Ca}{DA} = \frac{Cb}{DB} \Rightarrow \frac{Cb}{Ca} = \frac{DB}{DA} \Rightarrow \frac{Cb - Ca}{Ca} = \frac{DB - DA}{DA} \Rightarrow \frac{ab}{Ca} = \frac{AB}{DA} \quad (6)$$

From Equation 4 and Equation 6, we can get:

$$\frac{ab}{AB} = \frac{Ca}{DA} = \frac{f}{H-h} \quad (7)$$

From Equation 7, we can get Equation 8:

$$AB = \frac{H-h}{f} ab \quad (8)$$

For a satellite image, the focal length f and flying height H are constants. For a line ab on the image, its distance AB on the ground is inversely proportional to the ground height h . The greater the ground height h , the smaller the ground distance AB .

Image Resampling Error

Image resampling error can reach 0.5 pixels and directly affects the accuracy of a vehicle's position, velocity and direction. Such an error will result in a 0.3 m position error (for PAN image) and 1.22 m position error (for MS image), respectively.

The Proposed Method for Vehicle Information Extraction

Because the time interval between the PAN and MS images is so small, even a small error in the image position will result in a very large error in the ground position, velocity, and direction. Therefore, every factor that can reduce error and improve accuracy should be considered. In order to avoid the error from image scale, ground relief, and image resampling, a Direct Location Algorithm (DLA) is suggested. This method extracts vehicle information in the object domain, but it does not require image resampling. This method consists of three main components: the DLA, sensor model refinement, and vehicle image position refinement (Figure 6).

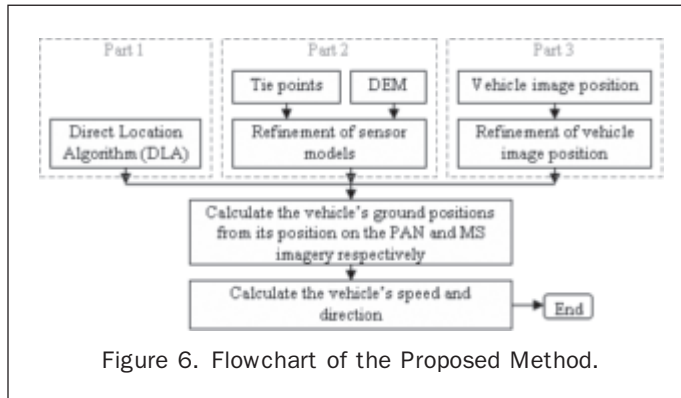


Figure 6. Flowchart of the Proposed Method.

Developing the Direct Location Algorithm (DLA)

In photogrammetry, space intersection can be used to calculate a tie point's ground position. In the current example, this is not feasible. First, the air base is too short (about 7.5 km) compared to the flight height (450 km), and the intersection angle is therefore too small, about two degrees (QuickBird Product Guide, 2003; <http://www.digital-globe.com>). This means that a small error with an intersection angle will result in very large error in the ground position. Second, the target vehicle is in motion. Therefore, the two points on the PAN and MS images are not tie points. They are actually two different points.

In this research, an algorithm is developed to calculate a vehicle's ground position from its image position based on a DEM. Figure 7 is the flowchart of the DLA.

The steps used to develop this direct location algorithm are described below:

1. From the QuickBird sensor model (RPB), obtain the approximate region (A1, B1, C1, D1) that the image covers (Figure 8). Within this region, select four points (A2, B2, C2, D2) that are near the four corners and obtain the ground position of each corner: A2(X1, Y1), B2(X2, Y2), C2(X3, Y3), and D2(X4, Y4).
2. Interpolate the elevation (Z) of each corner from the DEM. Then, obtain each corner's three-dimensional position: A2(X1, Y1, Z1), B2(X2, Y2, Z2), C2(X3, Y3, Z3), and D2(X4, Y4, Z4).
3. Use the sensor model (Equations 12a and 12b) and each corner's ground position (X, Y, Z) to calculate the image position of the four corners: a2(I1, J1), b2(I2, J2), c2(I3, J3), and d2(I4, J4).
4. Use these four points' image coordinates (I, J) and ground coordinates (X, Y, Z) to build a conformal transformation between the image coordinate system and the ground coordinate system:

$$X = f(I, J) = a_1 I + b_1 J + c_1 \quad (9a)$$

$$Y = g(I, J) = a_2 I + b_2 J + c_2 \quad (9b)$$

where (X, Y) are ground coordinates, and (I, J) are image coordinates.

5. For an image point (I, J), use Equations 9a and 9b to calculate its ground position (X, Y).
6. Then, from (X, Y), each point's height Z is interpolated from the DEM.
7. Then, use the ground position (X, Y, Z) and sensor model (Equations 12a and 12b) to calculate the image coordinates (I', J'). Because the conformal transformation (Equations 9a and 9b) just gives a coarse ground position (X, Y), this position (X, Y) has error. Therefore, the image coordinates (I', J') calculated from this coarse position (X, Y, Z) also contain error and are different from the initial position (I, J).
8. Calculate the difference between these two sets of image coordinates:

$$\Delta I = I - I' \quad (10a)$$

$$\Delta J = J - J' \quad (10b)$$

9. If these differences are less than the threshold, perhaps 0.0001 pixel, stop the iterations and output the ground position (X, Y, Z);
10. Otherwise, use $\Delta I, \Delta J$ to correct the ground coordinates (X, Y).

$$\Delta X = a_1 \cdot \Delta I + b_1 \cdot \Delta J \quad (11a)$$

$$\Delta Y = a_2 \cdot \Delta I + b_2 \cdot \Delta J \quad (11b)$$

$$X = X + \Delta X \quad (11c)$$

$$Y = Y + \Delta Y \quad (11d)$$

11. Go to step 6.

Sensor Model Refinement

Every satellite has a positioning system that can determine each pixel's ground position (on an ellipsoid surface) based on its image position. Each satellite type has a different physical geometric sensor model and different positioning accuracy. Some satellite image vendors, such as SPOT, provide users with a physical sensor model, but others, such as Ikonos and QuickBird, do not because of commercial secrecy. These latter satellite image vendors only release a

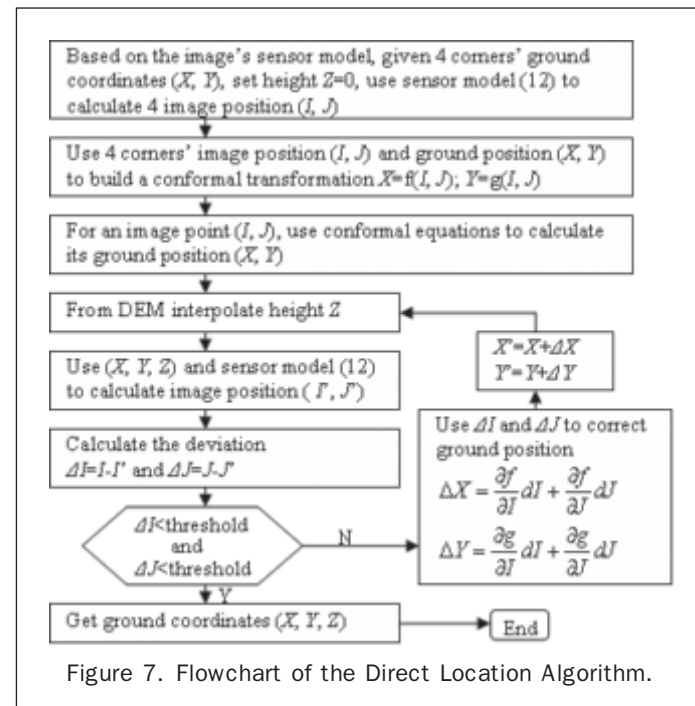


Figure 7. Flowchart of the Direct Location Algorithm.

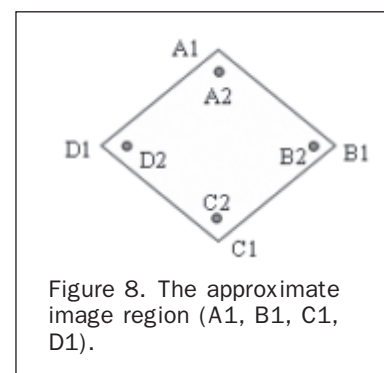


Figure 8. The approximate image region (A1, B1, C1, D1).

rational polynomial coefficient (RPC) as their geometric sensor model, such as the following:

$$\begin{cases} I = \frac{P_1(X,Y,Z)}{P_2(X,Y,Z)} \\ J = \frac{P_3(X,Y,Z)}{P_4(X,Y,Z)} \end{cases} \quad (12a)$$

$$\begin{cases} I = \frac{P_1(X,Y,Z)}{P_2(X,Y,Z)} \\ J = \frac{P_3(X,Y,Z)}{P_4(X,Y,Z)} \end{cases} \quad (12b)$$

$$P(X,Y,Z) = \sum_{i=0}^{m_1} \sum_{j=0}^{m_2} \sum_{k=0}^{m_3} a_{ijk} X^i Y^j Z^k \quad (12c)$$

$$0 \leq m_1 \leq 3, 0 \leq m_2 \leq 3, 0 \leq m_3 \leq 3, m_1 + m_2 + m_3 \neq 3 \quad (12d)$$

where (I, J) are the image coordinates, (X, Y, Z) are the ground coordinates, and a_{ijk} is the polynomial coefficient.

Both the physical sensor model and RPC have a definite value of absolute positioning error. For example, according to the test we conducted, before refinement with ground control points (GCPs), the sensor model provided with SPOT1, SPOT2, and SPOT4 has about a 300-meter absolute positioning error, and the sensor model for SPOT5 has about a 50-meter absolute positioning error. The sensor models for Ikonos and QuickBird each have about a 20-pixel absolute positioning error. If these sensor models are used to calculate a vehicle's ground position, the error of the sensor model will be propagated to the position. Therefore, the sensor model error will affect the final result.

Many researchers have done substantial work on sensor model refinement. Di *et al.* (2003) have proposed two methods to improve the geopositioning accuracy of Ikonos GEO products. One method is to use a large number of GCPs to compute new RPCs. Another method is to use a linear polynomial to correct RPCs in the object domain. Grodeki and Dial (2003) have also proposed the use of a polynomial to correct RPCs in the image or object domain.

Generally, the polynomial correction method can effectively correct the satellite sensor model and provide a relatively good result. For Ikonos imagery, Di *et al.* (2003) improved the ground position accuracy to one to two meters after the sensor model refinement and Grodeki and Dial's results also showed that ground position accuracy had been improved to one to two meters (2003).

In the present research, vehicle velocity and direction are the most important information data to be extracted. Therefore, relative position accuracy is our focus. Other than GCPs, only tie points are used to refine the sensor models. An iteration algorithm was therefore developed to refine the linear polynomial. Finally this polynomial is used to correct the RPCs:

$$\begin{cases} X = a_0 + a_1 X_{RF} + a_2 Y_{RF} + a_3 Z_{RF} \\ Y = b_0 + b_1 X_{RF} + b_2 Y_{RF} + b_3 Z_{RF} \\ Z = c_0 + c_1 X_{RF} + c_2 Y_{RF} + c_3 Z_{RF} \end{cases} \quad (13a)$$

$$\begin{cases} X = a_0 + a_1 X_{RF} + a_2 Y_{RF} + a_3 Z_{RF} \\ Y = b_0 + b_1 X_{RF} + b_2 Y_{RF} + b_3 Z_{RF} \\ Z = c_0 + c_1 X_{RF} + c_2 Y_{RF} + c_3 Z_{RF} \end{cases} \quad (13b)$$

$$\begin{cases} X = a_0 + a_1 X_{RF} + a_2 Y_{RF} + a_3 Z_{RF} \\ Y = b_0 + b_1 X_{RF} + b_2 Y_{RF} + b_3 Z_{RF} \\ Z = c_0 + c_1 X_{RF} + c_2 Y_{RF} + c_3 Z_{RF} \end{cases} \quad (13c)$$

where (X, Y, Z) are the ground coordinates after correction, (X_{RF}, Y_{RF}, Z_{RF}) are ground coordinates derived from RPC, and (a_i, b_i, c_i) are correction coefficients. Figure 9 shows the flowchart of sensor model refinement.

The steps used to refine the polynomial coefficients are described below:

1. Use the DLA (Figure 8) to calculate each tie point's ground position. For each tie point, two sets of ground coordinates can be obtained from the PAN and MS images, respectively. They are: $X_{RF}^{(PAN)}, Y_{RF}^{(PAN)}, Z_{RF}^{(PAN)}$, and $X_{RF}^{(MS)}, Y_{RF}^{(MS)}, Z_{RF}^{(MS)}$.
2. Calculate the relative deviation between these two sets of ground coordinates. Their average values are used as the final ground coordinates (X, Y, Z) for each tie point.
3. If the biggest relative deviation is less than a threshold ε , stop the iterations and output the polynomial coefficients (a_i, b_i, c_i) .

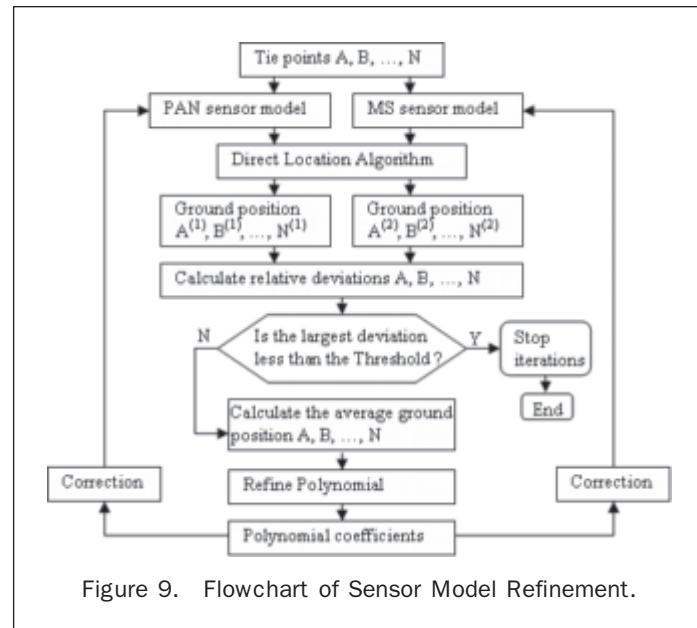


Figure 9. Flowchart of Sensor Model Refinement.

4. A set of average ground positions (X, Y, Z) and the ground positions derived from RPC (X_{RF}, Y_{RF}, Z_{RF}) are used to refine the correction coefficients (a_i, b_i, c_i) in Equation 13.
5. Go to step 1.

Refinement of Vehicle Image Position

Because the vehicle's ground position is calculated from its image position, a "region growing" method is used to refine the vehicle's image position, so as to improve its accuracy. Figure 10 shows the flowchart of the refinement of the vehicle image position.

On a QuickBird image, some long vehicles consist of many pixels (Plate 1a). Normally a vehicle image consists of several pixels (Plate 1b). The problem is to determine which pixel represents the vehicle's central position. Plate 1b shows two vehicles on a QuickBird MS image. One vehicle (A) consists of two pixels, and the other one (B)

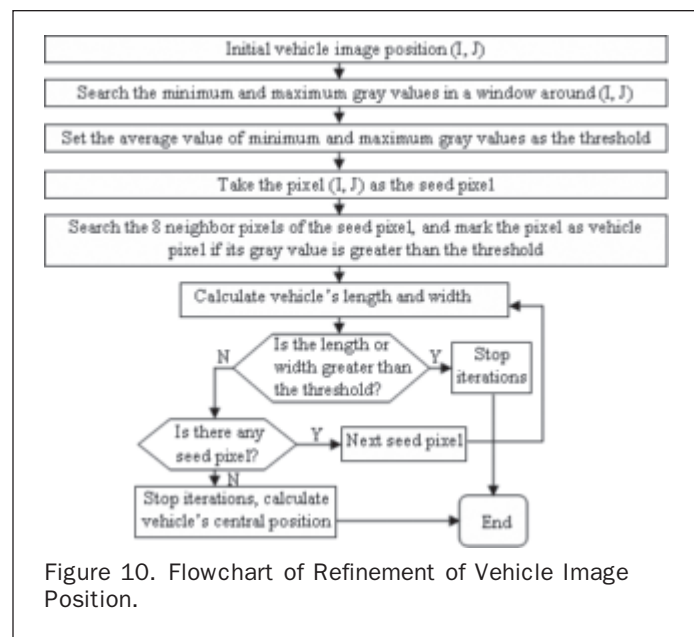


Figure 10. Flowchart of Refinement of Vehicle Image Position.

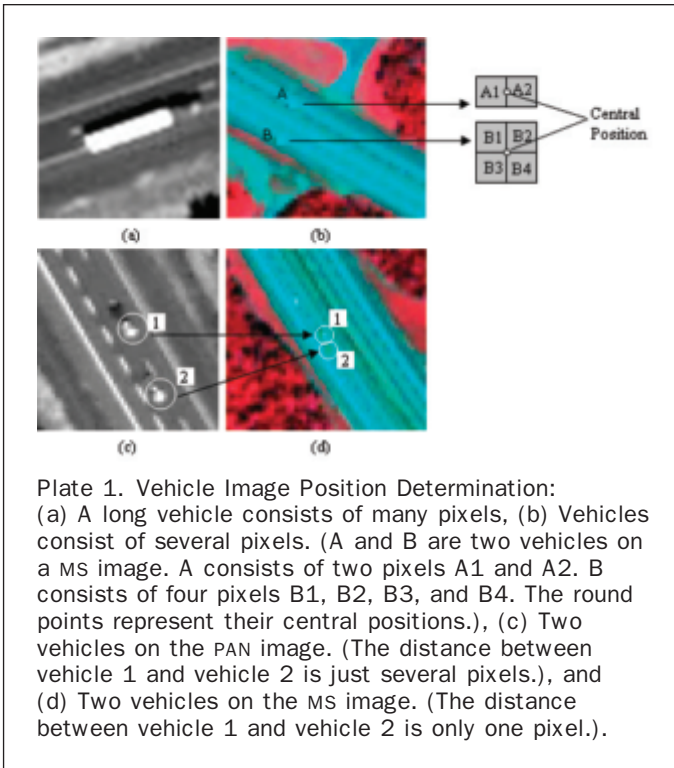


Plate 1. Vehicle Image Position Determination: (a) A long vehicle consists of many pixels, (b) Vehicles consist of several pixels. (A and B are two vehicles on a MS image. A consists of two pixels A1 and A2. B consists of four pixels B1, B2, B3, and B4. The round points represent their central positions.), (c) Two vehicles on the PAN image. (The distance between vehicle 1 and vehicle 2 is just several pixels.), and (d) Two vehicles on the MS image. (The distance between vehicle 1 and vehicle 2 is only one pixel.).

consists of four pixels. Table 1 shows the image position of vehicle pixels and their central image position. Their central positions are (126.5, 552) and (123.5, 560.5), respectively. Obviously, no single pixel can represent the vehicle's central position.

In order to use the vehicle's central image position to calculate its ground position, a "region growing" method is used to collect all the vehicle pixels. The average value of the vehicle's image position is then used as the vehicle's central position.

When the region growing method is used to collect pixels, a threshold should be set up to judge whether or not a pixel represents the vehicle. Here a 5 by 5 window is used for a statistical calculation. The minimum and maximum gray values are searched within this window. The average value of these two gray values is used as the threshold.

TABLE 1. IMAGE COORDINATES OF VEHICLE PIXELS AND VEHICLE CENTRAL POSITION

| Point | Image Coordinates | |
|-----------------------------|-------------------|-------|
| | Column | Row |
| A1 | 126 | 552 |
| A2 | 127 | 552 |
| Central position of point A | 126.5 | 552 |
| B1 | 123 | 560 |
| B2 | 124 | 560 |
| B3 | 123 | 561 |
| B4 | 124 | 561 |
| Central position of point B | 123.5 | 560.5 |

Different vehicles may be in close proximity and, therefore, the vehicle pixels may be overlapping (Plate 1c and 1d). In order to avoid mixing two or more vehicles together, only the connected pixels are considered as belonging to the same vehicle. Some vehicles are very long (Plate 1a), so another threshold corresponding to the long vehicle is used. For example, for a threshold of 20 pixels, if the vehicle length is greater than 20 pixels, then stop region growing and output non-vehicle information.

Test Using QuickBird Images

A pair of level 1A (basic) QuickBird images, which includes a 2.44 meter resolution multispectral image (Plate 2) and a 0.61 meter resolution panchromatic image (Figure 11), was used to test our program. These images were acquired on 26 July 2002 in Gagetown, New Brunswick, Canada. Only a portion of each image was used. Table 2 shows the detailed data clipping information. Because the sensor model RPB is for the whole image, the local image coordinates must include the upper left coordinates of each image before we use the sensor model to calculate a vehicle's ground position from its image position.

The direct location algorithm requires a Digital Elevation Model (DEM) to deliver the third dimension height (Z). In our experiment, a free Global DEM was used, having a resolution of 30 seconds (about 1,000 meters). Figure 12 shows the DEM corresponding to the images, interpolated using a cubic sampling algorithm.

The maximum elevation of this area is 64 meters and the minimum elevation is -5 meters. In the Gagetown area, the elevation of the river water is above mean sea level. Therefore, this DEM has an absolute error of at least 5 meters.

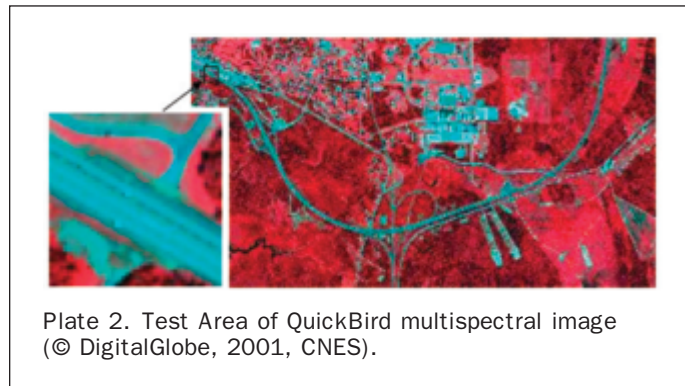


Plate 2. Test Area of QuickBird multispectral image (© DigitalGlobe, 2001, CNES).

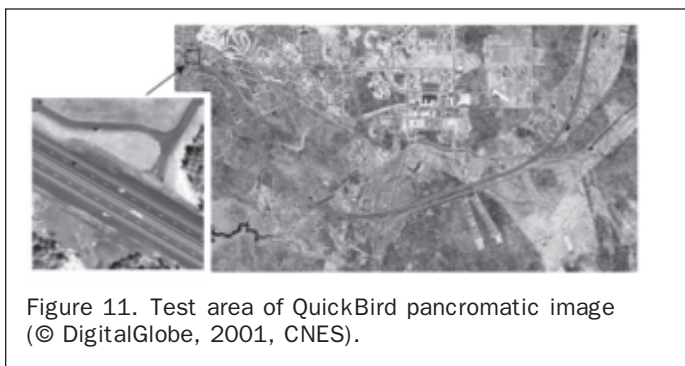


Figure 11. Test area of QuickBird panchromatic image (© DigitalGlobe, 2001, CNES).

TABLE 2. DATA CLIPPING INFORMATION

| Point | MS Data | | PAN data | |
|-------------|---------|------|----------|-------|
| | Column | Row | Column | Row |
| Upper Left | 2865 | 5047 | 11200 | 20000 |
| Lower Right | 5937 | 7007 | 24000 | 29000 |

Because the QuickBird level 1A (Basic) PAN and MS images are not registered, 15 tie points were used to refine the sensor models and register the images together. Table 3 shows image coordinates of the 15 tie points. Table 4 shows the relative position deviation before sensor model refinement, and Table 5 shows the relative position deviation after sensor model refinement. These tables show that after sensor model refinement, the mean deviation of the tie points has been reduced from 3.47 meters to 1.33 meters (Figure 13).

Figure 14 shows 24 vehicles we selected for testing on the panchromatic imagery. Each vehicle's image position was first manually measured. The region growing method was then used to collect all vehicle pixels. Next, these pixels were used to calculate each vehicle's average image coordinates. Table 6 shows each vehicle's initial image coordinates and their final image coordinates after refinement. These refined vehicle image coordinates were then used to calculate their ground coordinates, velocity, and direction. Table 7 shows the result.

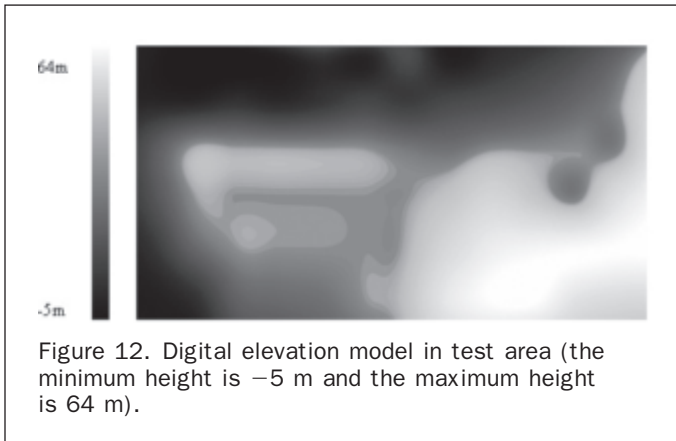


Figure 12. Digital elevation model in test area (the minimum height is -5 m and the maximum height is 64 m).

TABLE 3. IMAGE COORDINATES OF TIE POINTS

| No. | MS Image | | PAN Image | |
|-----|----------|------|-----------|------|
| | Column | Row | Column | Row |
| 1 | 333 | 612 | 1616 | 1162 |
| 2 | 2730 | 570 | 11186 | 999 |
| 3 | 241 | 1711 | 1245 | 5561 |
| 4 | 2844 | 1487 | 11638 | 4664 |
| 5 | 1333 | 1778 | 5608 | 5827 |
| 6 | 1887 | 503 | 7817 | 730 |
| 7 | 93 | 506 | 655 | 738 |
| 8 | 99 | 509 | 681 | 750 |
| 9 | 91 | 497 | 648 | 702 |
| 10 | 96 | 500 | 669 | 714 |
| 11 | 101 | 503 | 689 | 726 |
| 12 | 94 | 493 | 659 | 687 |
| 13 | 95 | 490 | 665 | 672 |
| 14 | 101 | 493 | 687 | 685 |
| 15 | 106 | 496 | 707 | 696 |

TABLE 4. GROUND COORDINATES AND RELATIVE DEVIATION OF TIE POINTS BEFORE SENSOR MODEL REFINEMENT

| No. | MS | | PAN | | Deviation |
|-----|----------|-----------|----------|-----------|-----------|
| | X | Y | X | Y | |
| 1 | 694451.0 | 5079302.1 | 694449.7 | 5079302.4 | 1.7 |
| 2 | 700473.8 | 5079713.1 | 700472.6 | 5079712.5 | 1.7 |
| 3 | 694302.5 | 5076471.4 | 694298.9 | 5076470.2 | 5.3 |
| 4 | 700826.9 | 5077380.9 | 700823.7 | 5077382.7 | 5.0 |
| 5 | 697053.7 | 5076440.0 | 697052.0 | 5076441.4 | 2.6 |
| 6 | 698351.0 | 5079777.3 | 698347.8 | 5079776.3 | 4.7 |
| 7 | 693837.4 | 5079541.1 | 693834.4 | 5079540.9 | 4.3 |
| 8 | 693852.8 | 5079534.2 | 693851.0 | 5079534.1 | 2.4 |
| 9 | 693831.6 | 5079563.8 | 693829.2 | 5079563.7 | 3.4 |
| 10 | 693844.5 | 5079556.8 | 693842.7 | 5079556.7 | 2.4 |
| 11 | 693857.3 | 5079549.8 | 693855.6 | 5079549.7 | 2.4 |
| 12 | 693838.8 | 5079574.4 | 693835.9 | 5079573.6 | 4.3 |
| 13 | 693841.1 | 5079582.2 | 693839.3 | 5079583.4 | 2.7 |
| 14 | 693856.5 | 5079575.3 | 693853.5 | 5079575.8 | 4.2 |
| 15 | 693869.3 | 5079568.3 | 693866.3 | 5079569.5 | 4.3 |

Mean Deviation = 3.47 m

Note: (1) Unit of X, Y, and Deviation: Meters.
(2) Coordinate System: UTM WGS84

TABLE 5. GROUND COORDINATES AND RELATIVE DEVIATION OF TIE POINTS AFTER SENSOR MODEL REFINEMENT

| No. | MS | | PAN | | Deviation |
|-----|----------|-----------|----------|-----------|-----------|
| | X | Y | X | Y | |
| 1 | 694449.9 | 5079301.6 | 694451.0 | 5079301.8 | 1.6 |
| 2 | 700472.0 | 5079712.6 | 700473.2 | 5079711.9 | 1.7 |
| 3 | 694301.4 | 5076470.8 | 694300.2 | 5076469.3 | 2.3 |
| 4 | 700825.4 | 5077380.2 | 700824.2 | 5077381.8 | 2.2 |
| 5 | 697052.4 | 5076439.4 | 697053.0 | 5076440.4 | 1.3 |
| 6 | 698349.5 | 5079776.8 | 698348.6 | 5079775.8 | 1.6 |
| 7 | 693836.4 | 5079540.6 | 693835.8 | 5079540.5 | 0.9 |
| 8 | 693851.8 | 5079533.7 | 693852.4 | 5079533.7 | 0.9 |
| 9 | 693830.6 | 5079563.4 | 693830.6 | 5079563.2 | 0.1 |
| 10 | 693843.5 | 5079556.3 | 693844.1 | 5079556.3 | 0.9 |
| 11 | 693856.3 | 5079549.3 | 693857.0 | 5079549.2 | 0.9 |
| 12 | 693837.9 | 5079574.0 | 693837.2 | 5079573.2 | 1.1 |
| 13 | 693840.1 | 5079581.8 | 693840.7 | 5079582.9 | 1.4 |
| 14 | 693855.5 | 5079574.9 | 693854.9 | 5079575.4 | 0.9 |
| 15 | 693868.3 | 5079567.9 | 693867.7 | 5079569.0 | 1.4 |

Mean Deviation = 1.33 m

Note: (1) Unit of X, Y, and Deviation: Meters.
(2) Coordinate System: UTM WGS84

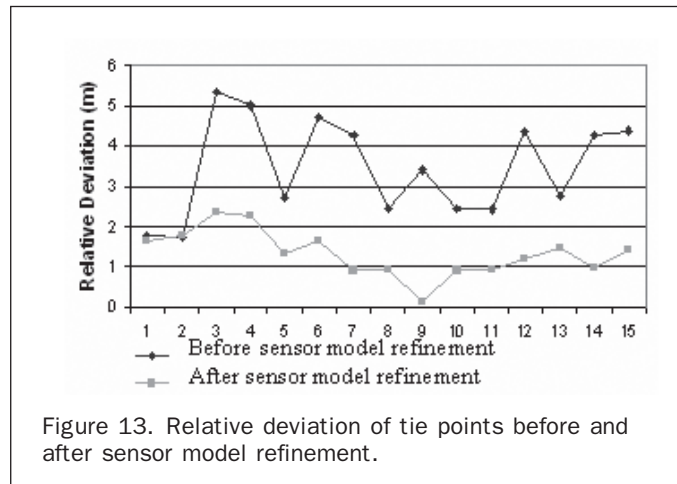


Figure 13. Relative deviation of tie points before and after sensor model refinement.

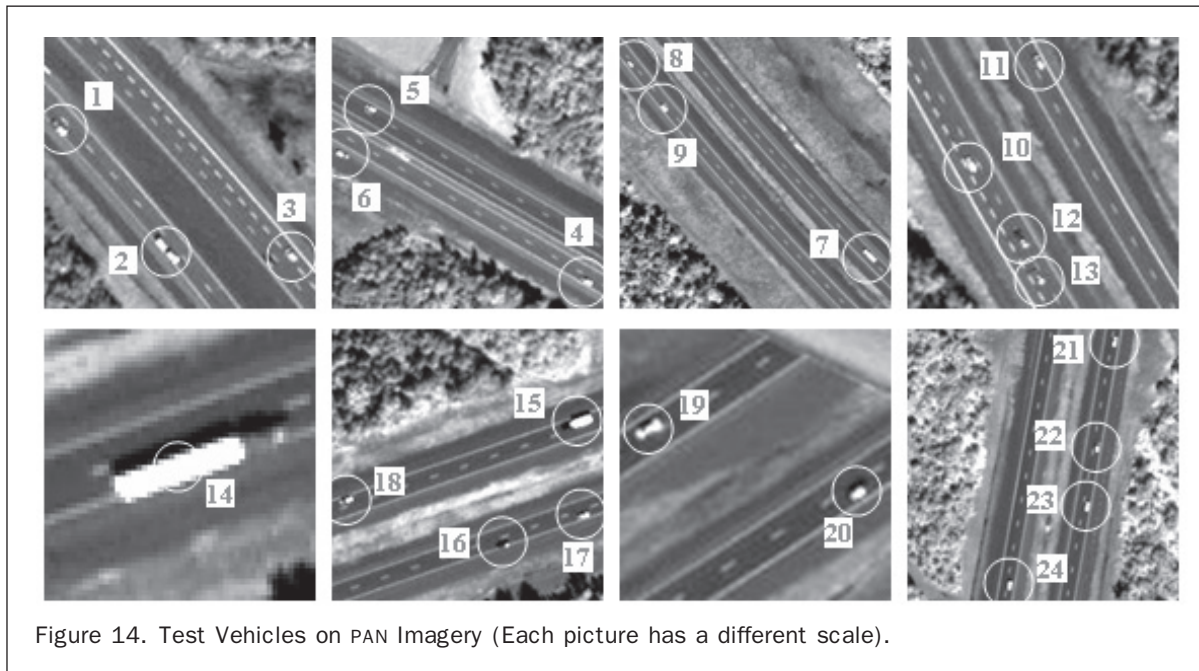


Figure 14. Test Vehicles on PAN Imagery (Each picture has a different scale).

TABLE 6. COORDINATES OF TEST VEHICLES

| No. | Initial Position | | | | After Refinement | | | | |
|-----|------------------|------|-----------|------|------------------|--------|-----------|---------|--------|
| | MS Image | | PAN Image | | MS Image | | PAN Image | | |
| | Column | Row | Column | Row | Column | Row | Column | Row | |
| 1 | 331 | 706 | 1599 | 1531 | 1 | 330.7 | 706.3 | 1599 | 1531.5 |
| 2 | 345 | 723 | 1657 | 1597 | 2 | 344.7 | 722 | 1657.1 | 1596.8 |
| 3 | 358 | 719 | 1718 | 1596 | 3 | 357.5 | 718.5 | 1718 | 1596 |
| 4 | 166 | 583 | 939 | 1039 | 4 | 165.8 | 582.6 | 938.5 | 1038.6 |
| 5 | 127 | 552 | 798 | 927 | 5 | 126.5 | 552 | 797.7 | 926.7 |
| 6 | 124 | 560 | 777 | 955 | 6 | 123.5 | 560.5 | 776.9 | 955.3 |
| 7 | 723 | 1362 | 3179 | 4172 | 7 | 723 | 1362.2 | 3179 | 4172.3 |
| 8 | 670 | 1322 | 2955 | 3993 | 8 | 670.5 | 1321.5 | 2955.7 | 3993.3 |
| 9 | 679 | 1332 | 2987 | 4034 | 9 | 678.7 | 1332.3 | 2986.9 | 4034.3 |
| 10 | 608 | 1230 | 2707 | 3626 | 10 | 608 | 1229.5 | 2707.9 | 3626.3 |
| 11 | 614 | 1212 | 2741 | 3576 | 11 | 614 | 1212 | 2740.8 | 3576.2 |
| 12 | 615 | 1240 | 2733 | 3664 | 12 | 615 | 1239.5 | 2733.3 | 3663.9 |
| 13 | 616 | 1244 | 2742 | 3682 | 13 | 616 | 1244 | 2741.2 | 3681.8 |
| 14 | 1788 | 1449 | 7418 | 4516 | 14 | 1788.7 | 1449.2 | 7417.7 | 4516.2 |
| 15 | 1939 | 1383 | 8035 | 4247 | 15 | 1938.8 | 1383.4 | 8035 | 4247.2 |
| 16 | 1933 | 1400 | 7991 | 4320 | 16 | 1933 | 1400 | 7990.5 | 4320.5 |
| 17 | 1944 | 1396 | 8037 | 4303 | 17 | 1944 | 1396 | 8037.6 | 4302.8 |
| 18 | 1904 | 1395 | 7897 | 4294 | 18 | 1904 | 1395 | 7896.4 | 4294 |
| 19 | 2344 | 1221 | 9653 | 3597 | 19 | 2344 | 1221 | 9652.2 | 3596.9 |
| 20 | 2365 | 1224 | 9717 | 3617 | 20 | 2364.5 | 1224 | 9717.4 | 3616.9 |
| 21 | 2722 | 579 | 11151 | 1044 | 21 | 2722.5 | 578.5 | 11150.5 | 1045 |
| 22 | 2719 | 599 | 11137 | 1127 | 22 | 2719 | 599.5 | 11137.2 | 1126.7 |
| 23 | 2717 | 611 | 11130 | 1172 | 23 | 2716.7 | 610.7 | 11129.3 | 1172.7 |
| 24 | 2701 | 631 | 11069 | 1233 | 24 | 2701 | 631 | 11069.1 | 1232.6 |

Figure 15 shows the position, velocity, and direction of motion of the vehicles.

Table 7 and Figure 15 show that the mean speed is about 100 km/h. We noted that some vehicles were moving at speeds quite different from the mean. We investigated these vehicles in more detail (Table 8). Most of the slow vehicles were found to be either on the road shoulder (vehicle 6) or in the slow lane. In the latter cases, the slow vehicle had either just been passed by another

vehicle (vehicle 8 and 15) or was being passed (vehicle 13). For the fast vehicles, they either were passing other vehicles (vehicle 12) or had just passed on other vehicle (vehicle 9 and 18). Some vehicles were in the slow lane, but moving at high speed (vehicles 4, 9, 11, 16, 18, 19, 20, and 22). It is interesting to note that vehicle 24 is in the fast lane, but its speed is only 77.5 km/h. In a real time transportation management or security screening, vehicle 24's speed might be worthy of investigation.

TABLE 7. GROUND COORDINATES, SPEED, AND AZIMUTH ANGLE OF TEST VEHICLES

| No. | X(m) | Y(m) | H(m) | Speed(km/h) | Azimuth(°) |
|-----|----------|-----------|------|-------------|------------|
| 1 | 694447.8 | 5079066.2 | 29.5 | 118.5 | 133.8 |
| 2 | 694485.7 | 5079025.9 | 30.3 | 109.9 | 150.1 |
| 3 | 694524.2 | 5079028.5 | 30.5 | 68.1 | 323.1 |
| 4 | 694021.1 | 5079358.1 | 18.0 | 133.6 | 126.3 |
| 5 | 693929.8 | 5079424.8 | 15.4 | 93.1 | 306.8 |
| 6 | 693917.1 | 5079406.3 | 15.7 | 23.8 | 74.0 |
| 7 | 695493.5 | 5077424.5 | 30.5 | 135.7 | 317.7 |
| 8 | 695349.1 | 5077532.0 | 30.6 | 113.8 | 152.4 |
| 9 | 695370.0 | 5077506.8 | 30.6 | 149.7 | 134.3 |
| 10 | 695185.9 | 5077759.2 | 30.3 | 107.4 | 150.1 |
| 11 | 695206.4 | 5077792.3 | 30.2 | 145.6 | 337.5 |
| 12 | 695203.0 | 5077735.7 | 30.3 | 145.4 | 146.1 |
| 13 | 695209.0 | 5077724.5 | 30.3 | 83.8 | 164.7 |
| 14 | 698168.0 | 5077339.5 | 37.8 | 71.2 | 52.9 |
| 15 | 698551.6 | 5077532.6 | 43.5 | 120.4 | 254.5 |
| 16 | 698525.3 | 5077484.4 | 43.6 | 162.6 | 74.1 |
| 17 | 698553.9 | 5077496.8 | 44.0 | 127.1 | 75.3 |
| 18 | 698465.6 | 5077497.8 | 42.2 | 150.2 | 249.1 |
| 19 | 699557.0 | 5078000.1 | 42.4 | 144.7 | 243.9 |
| 20 | 699597.5 | 5077989.3 | 42.3 | 143.5 | 68.1 |
| 21 | 700452.3 | 5079682.3 | 27.9 | 96.3 | 4.3 |
| 22 | 700445.0 | 5079628.6 | 28.1 | 138.3 | 11.2 |
| 23 | 700441.4 | 5079599.5 | 28.2 | 100.2 | 10.3 |
| 24 | 700404.1 | 5079558.5 | 28.5 | 77.5 | 183.2 |

Note: (1) Coordinate System: UTM WGS84.

(2) The vehicle's ground position (X, Y, H) are derived from its PAN image position.

TABLE 8. VEHICLE INFORMATION EXTRACTED FROM ITS SPEED, POSITION, DIRECTION, AND IMAGE INTERPRETATION

| No. | Speed(km/h) | Lane | Note |
|-----|-------------|----------|---------------------------|
| 1 | 118.5 | Slow | |
| 2 | 109.9 | Slow | |
| 3 | 68.1 | Slow | A dark car is passing it |
| 4 | 133.6 | Slow | |
| 5 | 93.1 | Slow | |
| 6 | 23.8 | Shoulder | Parked there |
| 7 | 135.7 | Fast | |
| 8 | 113.8 | Slow | Vehicle 9 just passed it |
| 9 | 149.7 | Slow | Just passed vehicle 8 |
| 10 | 107.4 | Slow | |
| 11 | 145.6 | Slow | |
| 12 | 145.4 | Fast | It is passing vehicle 13 |
| 13 | 83.8 | Slow | Vehicle 12 is passing it |
| 14 | 71.2 | Slow | Long vehicle |
| 15 | 120.4 | Slow | Vehicle 18 just passed it |
| 16 | 162.6 | Slow | |
| 17 | 127.1 | Slow | |
| 18 | 150.2 | Slow | Just passed vehicle 15 |
| 19 | 144.7 | Slow | |
| 20 | 143.5 | Slow | |
| 21 | 96.3 | Slow | |
| 22 | 138.3 | Slow | |
| 23 | 100.2 | Slow | |
| 24 | 77.5 | Fast | Strange ! |

Error Analysis and Discussion

The accuracy of vehicle information is dependent on the DEM, vehicle image position, the satellite sensor model, and the time interval between capture of the PAN and MS images. The time interval can be considered as constant, since it cannot be changed.

A DEM is used in our method to deliver the third dimension, i.e., height. The DEM's accuracy will directly affect the accuracy of vehicle position. For example, vehicle

P's ground position is calculated using its PAN and MS image positions. Then, we can obtain its ground position A. If the DEM has error h , the vehicle's ground position is calculated with height 0, and the vehicle's ground position B and C can then be obtained (Figure 16).

From Figure 16, we can obtain the following equations:

$$S_{PC} = \frac{h}{\cos\alpha} \quad (14)$$

TABLE 9. VEHICLE ERROR CAUSED BY DEM, SATELLITE SENSOR MODEL, AND VEHICLE IMAGE POSITION

| | Caused by DEM | Caused by sensor model | Caused by the vehicle's image position (MS) | Caused by the vehicle's image position (PAN) |
|---|---------------|------------------------|---|--|
| Error with the vehicle's relative deviation | ±0.18 m | ±1.33 m | ±1.22 m | ±0.3 m |
| Error with the vehicle velocity | ±3.31 km/h | ±23.94 km/h | ±21.96 km/h | ±5.4 km/h |

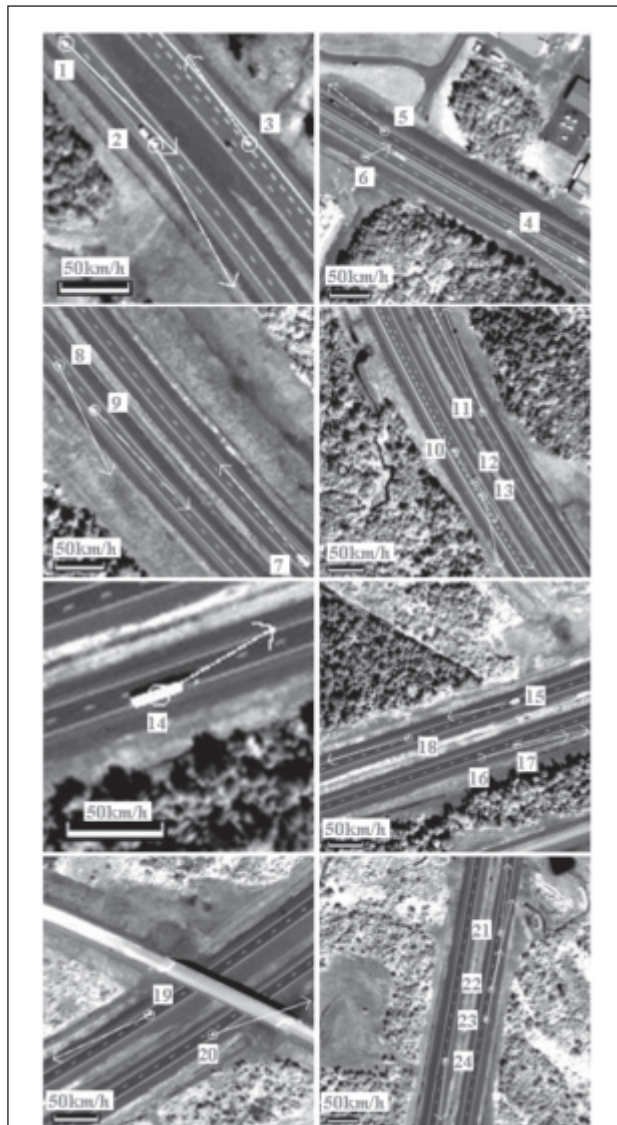


Figure 15. Vehicle velocity and direction extracted from a single pass of QuickBird imagery. Note: Each picture has a different scale, and the arrow length is proportional to the vehicle's speed.

$$S_{AC} = h \cdot \tan \alpha \tag{15}$$

$$S_{BC} = S_{PC} \cdot \varphi \tag{16}$$

The intersection angle φ (Figure 16) can be calculated from the time interval t , satellite flight speed v , and satellite flight altitude H :

$$\varphi = \frac{vt}{H} \tag{17}$$

From Equations 16 and 17, we can get Equation 18:

$$S_{BC} = \frac{h}{\cos \alpha} \cdot \frac{vt}{H} \tag{18}$$

where S_{AC} is the vehicle's position error caused by DEM error, and S_{BC} is the relative deviation caused by the DEM error. In this experiment, a Global DEM with a resolution of 30 seconds was used. We assume that the error of this DEM is 10-meters. Here, if the incidence angle is 25 degrees and intersection angle is one degree, then the position error will be 4.66 m and relative deviation will be 0.18 m. Obviously, the position error is much greater than the relative deviation. Because it is the relative deviation, not the ground position that directly affects the vehicle's velocity calculation, the

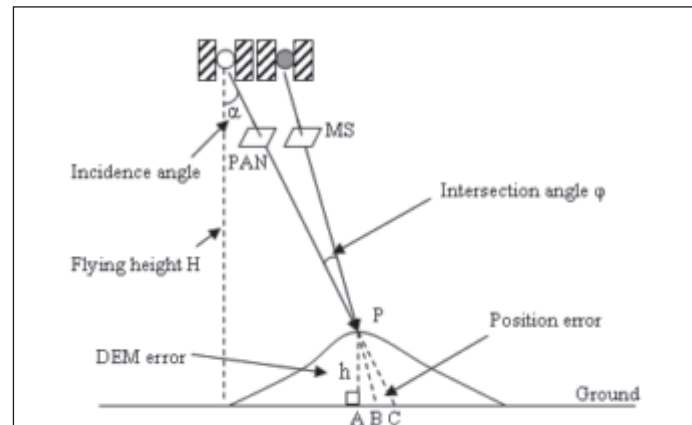


Figure 16. Position error caused by DEM error. DEM error "h" will result in ground position error A-B (when calculated from MS image position) and A-C (when calculated from PAN image position).

effect of DEM error on the vehicle's ground position is much more severe than that of the vehicle's velocity.

Besides the DEM, another factor that affects the accuracy of the vehicle position is the satellite sensor model. In our method, a linear polynomial was used to correct the sensor model. After refinement, the mean relative deviation of tie points was reduced from 3.47 m to 1.33 m.

The third factor affecting accuracy is the vehicle's image position. If the vehicle's image position has a 0.5 pixel error, the vehicle's ground position will be 0.3-meters (for the PAN image) and 1.22-meters (for the MS image). Although a region growing method is used to collect all the vehicle pixels and all these pixels are used to calculate the vehicle's central position because a threshold for image segmentation is used to judge whether a pixel is a vehicle or not, the image segmentation is pixel accuracy. If a sub-pixel segmentation method is used here, the accuracy of the vehicle image position will be improved.

Table 9 shows the vehicle's error caused by DEM, satellite sensor model, and the vehicle's image position. Compared these three error sources, it is very obvious that the vehicle error mainly comes from the satellite sensor model, and the vehicle image position, especially the vehicle image position on the MS image. The DEM error contributes the smallest part to the vehicle error.

Conclusions

A new method of vehicle information extraction from a single pass of QuickBird imagery is presented. It includes three major components: (a) A new approach using tie points to refine sensor models, (b) a method to refine vehicle's image position, and (c) a new direct location algorithm to calculate a vehicle's ground position from its image position. The experimental results show that this technique can effectively extract a vehicle's position, velocity, and direction. Most of the high-resolution satellites can now acquire both PAN and MS images. So this technique potentially offers a new cost-effective choice to extract vehicle information.

We also recognize that there is still potential for further improvement in the vehicle image coordinates calculation and sensor model refinement. A more precise DEM is another way to improve the accuracy. Because the satellite time interval is very small, even a marginal improvement in the vehicle image coordinates, say 0.1-pixel, will yield a very large contribution to the accuracy of vehicle information. This will be the focus of our future research.

References

- Castellano, G., J. Boyce, and M. Sandler, 1999. CDWT optical flow applied to moving target detection, *IEEE Colloquium on Motion Analysis and Tracking* (Ref. No. 1999/103), 10 May, pp. 17/1–17/6.
- Di, K.R. Ma, and R. Li, 2003. Rational functions and potential for rigorous sensor model recovery, *Photogrammetric Engineering & Remote Sensing*, 69(1):33–41.
- Dias, J.M.B., and P.A.C. Marques, 2003. Multiple moving target detection and trajectory estimation using a single SAR sensor, *IEEE Transactions on Aerospace and Electronic Systems*, 39(2):604–624.
- Grodecki J., and G. Dial, 2003. Block adjustment of high-resolution satellite images described by rational polynomials, *Photogrammetric Engineering & Remote Sensing*, 69(1):59–68.
- Liu, C.-M. and C.-W. Jen, 1992. A parallel adaptive algorithm for moving target detection and its VLSI array realization, *Signal Processing, IEEE Transactions on Acoustics, Speech, and Signal Processing*, 40(11):2841–2848.
- Liu, G., and J. Li, 2001. Moving target detection via airborne HRR phased array radar, *IEEE Transactions on Aerospace and Electronic Systems*, 37(3):914–924.
- Munno, C.J., H. Turk, J.L. Wayman, J.M. Libert, and T.J. Tsao, 1993. Automatic video image moving target detection for wide area surveillance, *Security Technology Proceedings, Institute of Electrical and Electronics Engineers 1993 International Carnahan Conference*, 13–15 October, pp. 47–57.
- Nag, S., and M. Barnes, 2003. A moving target detection filter for an ultra-wideband radar, *Proceedings of the IEEE Radar Conference 2003*, 05–08 May, pp. 147–153.
- Pettersson, M.I., 2004. Detection of moving targets in wideband SAR, *IEEE Transactions on Aerospace and Electronic Systems*, July, 40(3):780–796.
- Reed, I.S., R.M. Gagliardi, and L.B. Stotts, 1988. Optical moving target detection with 3-D matched filtering, *IEEE Transactions on Aerospace and Electronic Systems*, July, 24(4):327–336.
- Soumekh, M., 2002. Moving target detection and imaging using an X band along-track monopulse SAR, *IEEE Transactions on Aerospace and Electronic Systems*, January, 38(1):315–333.
- Sun, H., G. Liu, H. Gu, and W. Su, 2002. Application of the fractional Fourier transform to moving target detection in airborne SAR, *IEEE Transactions on Aerospace and Electronic Systems*, October, 38(4):1416–1424.
- Wolf, P.R., and C.D. Ghilani, 2002. *Elementary Surveying: An Introduction to Geomatics*, Tenth edition.

(Received 18 January 2006; accepted 10 January 2007; revised 28 March 2007)

Calendar

November

17-20, **The William T. Pecora Memorial Symposium**, *ASPRS*, Denver, Colorado. For more information, visit www.asprs.org.

❖ 17-20, **Coastal Cities Summit 2008 — Values and Vulnerabilities**, *International Ocean Institute-USA*, St. Petersburg, Florida. For more information, visit www.coastalcities.org.

❖ 19-20, **Geomatics Atlantic 2008 — Discovering the Way to a Sustainable Future**, *The Canadian Institute of Geomatics*, Saint John, New Brunswick. For more information, visit www.geomaticsatlantic.com.

January 2009

26-28, **ILMF 2009**, *International Lidar Mapping Forum*, New Orleans, Louisiana. For more information, visit www.lidarmap.org.

February 2009

❖ 17-18, **2009 Indiana GIS Conference**, *Indiana Geographic Information Council*, Bloomington, Indiana. For more information, visit www.in.gov/igic/conference/index.html

March 2009

8-13, **ASPRS 2009 Annual Conference - 75th Anniversary of ASPRS**, *ASPRS*, Baltimore, Maryland. For more information, visit www.asprs.org.

22-27, **The Association of American Geographers 2009 Annual Meeting**, *AAG*, Las Vegas, Nevada. For more information, visit www.aag.org/annualmeetings/2009/index.htm.

April 2009

❖ 19-22, **2009 Geospatial Infrastructure Solutions Conference**, *Geospatial Information & Technology Association (GITA)*, Tampa, Florida. For more information, visit www.gita.org/gis.

❖ = indicates a new listing

July 2009

❖ 7-10, **GI Forum 2009 — Geoinformatics Forum Salzburg**, *Z-GIS Centre for Geoinformatics * Salzburg University*, Salzburg, Austria. For more information, visit www.gi-forum.org.

❖ 10-13, **AG 2009 — The 2nd International Symposium on Academic Globalization**, Orlando, Florida. For more information, visit <http://www.iiis2009.org/wmsci/website/default.asp?vc=22>.

❖ 28-30, **MultiTemp-2009 — Fifth International Workshop on the Analysis of Multitemporal Remote Sensing Images**, Groton, Connecticut. For more information, visit <http://clear.uconn.edu/multitemp09>.

September 2009

9-12, **ISDE6 - Digital Earth in Action**, *International Society for Digital Earth (ISDE)* and *Chinese Academy of Sciences (CAS)*, Beijing, China. For more information visit www.isde6.org.

November 2009

16-19, **ASPRS/MAPPS 2009 Fall Conference**, *ASPRS* and *MAPPS*, San Antonio, Texas. For more information, visit www.asprs.org.

April 2010

26-30, **ASPRS 2010 Annual Conference**, *ASPRS*, San Diego, California. For more information, visit www.asprs.org.

May 2011

1-5, **ASPRS 2011 Annual Conference**, *ASPRS*, Milwaukee, Wisconsin. For more information, visit www.asprs.org.

How Do I Contact ASPRS?

5410 Grosvenor Lane, Suite 210
Bethesda, MD 20814
301-493-0290, 301-493-0208 (fax)
www.asprs.org

| | |
|---------------------------------|--|
| Accounting | x115 |
| Awards | x101, awards@asprs.org |
| Calendar | x107, calendar@asprs.org |
| Certification | x101 certification@asprs.org |
| Exhibit Sales | 301-215-6710 asprs@townsend-group.com |
| General/Miscellaneous | x101 asprs@asprs.org |
| Meeting Information | x106 meetings@asprs.org |
| Membership | x109 members@asprs.org |
| PE&RS Advertising | 301-215-6710 asprs@townsend-group.com |
| PE&RS Editorial | x103 |
| PE&RS Manuscripts | 402-472-7531 jmerchant1@unl.edu |
| PE&RS Subscriptions | x104 sub@asprs.org |
| Proceedings - Paper Submissions | x103 kimt@asprs.org |
| Publications/Bookstore | x103 asprspub@pmcs.com |
| Scholarship | x101 scholarships@asprs.org |
| Web Site | homepage@asprs.org |

Read articles on-line!

PE&RS is now available on-line.

Grids & Datums • Direct Georeferencing
Peer-review Articles • Software Reviews
Calendar Notices • Classifieds
Book Reviews • and much more...

www.asprs.org

A Comparison of Coincident Landsat-5 TM and Resourcesat-1 AWiFS Imagery for Classifying Croplands

David M. Johnson

Abstract

A comparison of land-cover maps, emphasizing row crop agriculture, resulting from independent classifications of coincident Landsat-5 Thematic Mapper (TM) and Resourcesat-1 Advanced Wide Field Sensor (AWiFS) imagery is presented. Three agriculturally intensive study areas within the midsection of the United States were analyzed during the peak of their growing season. For each region the data were collected within the same hour during August 2005. Identical decision tree style classification methodologies relying on ground truth from the June Agricultural Survey were applied to the image pairs for each of the three cases. The direct comparison of mapping accuracy results show, on average, the TM output to perform slightly better than that of the complimentary AWiFS. It is concluded AWiFS is a valid alternative to TM for classifying cultivated agriculture in areas with reasonably large field sizes. Furthermore, AWiFS offers increased benefits due to larger swath widths and shorter revisit frequencies.

Introduction

The mission of the National Agricultural Statistics Service (NASS) is to providing timely, accurate, and useful statistics in service to United States agriculture. To meet the goal, NASS implements hundreds of annual surveys, plus a comprehensive census every five years, which continually compile and tabulate information on domestic crops and livestock. Demographic, environmental, and economic data related to agriculture is also gathered. The information is collected by a variety of methods including mail, phone, Internet, or personal interview.

The flagship survey effort within NASS is the June Agricultural Survey (JAS). Annually, enumerators visit over 11,000 sample sites, encompassing roughly 85,000 land tracks, distributed across the U.S. Data is collected on planted crop acreage, livestock inventories, and farm economics. Each site is usually one square mile in size and location determined from a stratified random sample selected from a probability-based area frame. The samples are primarily drawn from agriculturally intensive regions and amount to a ground sampling rate of one half percent or denser in those areas. The data from all of the visited sites is ultimately aggregated to state and national levels and used to make agricultural planted acreage estimates for the current year.

The need often arises for the June collected statistical information to be compiled at a geographically finer level than what the JAS can provide. Remotely sensed imagery used in conjunction with concurrent JAS land-use data presents a means for identifying the spatial distribution of crops down to the level of individual fields. This is employed through a “supervised” image classification methodology and is made robust because of the geographically and randomly distributed nature of the JAS. Thus, for several years NASS has leveraged the JAS ground truth information and produced categorized land-cover image products, known as Cropland Data Layers (CDL) (Craig, 2001; Mueller, 2000). Focus for the CDL program has been on select central and southern U.S. states dominated by intensive agriculture and has grown in scope since inception during the late-1990s.

The CDL products have a variety of applications, especially when integrated into a geographic information system (GIS). Primary benefits within NASS include the ability to tighten confidence intervals for the state level acreage estimates derived from the JAS, derivation of county level acreage estimates, and feedback for the defining and updating of the land-use strata for which the JAS is based. Beyond NASS, examples of known uses include assessing regional scale environmental impacts from farming, detection of land-use changes in agricultural fringe areas, validation of crop classifications derived from coarser-scaled imagery, and time series analysis of cropping patterns. Additionally, since the CDLs are tailored to cropland mapping, the information from it can also be used to supplement other land-cover mapping efforts which in themselves may lack sufficient detail in agricultural classes.

Landsat-5 and -7 have been the primary source of the remotely sensed data for the CDL program (Craig, 2002). Reasons for utilizing Landsat data include its appropriate pixel size and spectral bands for mapping agricultural cover types, sufficient revisit rate usually allowing for one or more cloud-free image acquisitions during ideal times of the growing season, cost effectiveness, and operational nature. Furthermore, land-cover mapping applications with Landsat are common given a large user community (USDIO, 2006). There is a particularly large following specifically for monitoring agriculture and natural resources. Within the U.S. Department of Agriculture (USDA) Landsat imagery is analyzed

United States Department of Agriculture, National Agricultural Statistics Service, 3251 Old Lee Highway, Suite 305, Fairfax, VA 22030
(dave_johnson@nass.usda.gov).

Photogrammetric Engineering & Remote Sensing
Vol. 74, No. 11, November 2008, pp. 1413–1423

0099-1112/08/7411-1413/\$3.00/0
© 2008 American Society for Photogrammetry
and Remote Sensing

by the Foreign Agricultural Service, Natural Resources Conservation Service, Forest Service, Farm Service Agency, and Risk Management Agency, in addition to NASS.

However, with the uncertainty of the Landsat program due to limited remaining lifespan expectancy with the greater than 20-year age of the Landsat-5 TM platform, degradation of the Enhanced Thematic Mapper Plus (ETM+) sensor because of the Scan Line Corrector (SLC) failure in 2003 aboard Landsat-7, and doubts about the likeliness and timeliness of follow on missions, NASS began exploring other data sources. The most appropriate and Landsat-like imagery to be found was that from the Indian Remote Sensing's (IRS) Resourcesat-1 AWIFS. Appealing characteristics included a large swath width, inclusion of spectral bands important to crop identification and monitoring, and cost effectiveness per unit area. Additionally, the geographically wide images had the added benefit of creating large overlap areas between adjacent scenes which in effect shortened revisit times.

In 2004, NASS tasked the Resourcesat AWIFS sensor to collect data over much of the upper and lower Mississippi River basin during the month of August. About 150 scenes were obtained with a general objective to assess the quality and timeliness of the data. A more targeted goal was to evaluate the suitability of the data to build a CDL and test the acreage estimate accuracy. Quantitative assessment of the 2004 data's utility within the CDL program was limited, but AWIFS was thought to be promising as a compromise because derived classifications and acreage estimates for major crops were comparable (Boryan and Craig, 2005). Minimally, AWIFS satisfied the goal of providing supplemental information in regions where a high-quality Landsat scene was not available due to cloud cover.

The next year NASS committed further to collecting AWIFS imagery to better explore and document its utility. Again, data was collected for the central and southern portions of the U.S. Data collection times coincided with late spring and middle summer of 2005. More detailed comparative assessments were undertaken and further boosted the notion that Resourcesat-1 could be a suitable alternative to Landsat for crop type mapping. Still lacking however was a direct quantitative comparison of coincident, in date and location, imagery which would in effect control for differences in classifications that could otherwise arise from changes in atmospheric and ground conditions.

Even outside of NASS, very little known research has been published to assess the utility of AWIFS data, whether for agricultural applications or disciplines beyond. Reasons may be varied, but likely a result of the newness, limited availability, unfamiliarity, degraded imagery specification compared to Landsat TM and ETM+, or competition from other sensors such as SPOT or ASTER. Of note however, are publications from Kiran-Chand *et al.* (2006) who utilized AWIFS imagery in conjunction with MODIS to validate a Defense Meteorological Satellite Program fire detection product over India, and from Kulkarni *et al.* (2006) who applied AWIFS data for snow cover monitoring in the Himalayas.

Thus, the goal of this study is straightforward: to quantitatively assess the utility of AWIFS imagery for land-cover mapping, specifically targeting crop type identification, and determine whether AWIFS is a valid replacement data source for Landsat. TM data will be used as a benchmark from which to compare AWIFS, because TM has been used nearly exclusively for the NASS CDL program since the SLC problem arose on the ETM+ sensor. Furthermore, TM is currently considered the *de facto* data source in much of the land-cover monitoring community.

Background

The Resourcesat-1 (IRS-P6) satellite imaging system is a relative newcomer as a source for spaceborne remotely sensed imagery. The platform was launched in 2003 and follows a long lineage of IRS land imaging satellites dating back to 1988. Resourcesat-1 represents increased capabilities over previous generation IRS satellites and carries three imaging instruments with complimentary characteristics (NRSA, 2003; Lutes, 2005). The sensor with the broadest areal coverage is AWIFS. It has a nadir ground sample distance (GSD) of 56 m and a swath width of 740 km. The wide field-of-view imaging is accomplished by two separate but identical AWIFS multispectral cameras which are oppositely titled approximately 12 degrees with respect to nadir with scenes that overlap by 8.4 km. They each contain a linear charge coupled device (CCD) array utilizing 6,000 pixels capturing data in four spectral bands (green, red, near-infrared, and shortwave-infrared).

The other two Resourcesat-1 sensors are the high resolution Linear Imaging Self-Scanner (LISS-IV) which has a GSD of 5.8 m and the medium resolution Linear Imaging Self Scanner (LISS-III) with a GSD of 23.5 m. LISS-III's CCDs are identical to those of AWIFS and collect data in parallel. This setup affords the ability to create a higher resolution reference set of data within the middle of the AWIFS strip. LISS-IV is more specialized and can collect imagery 4,000 pixels wide in multispectral mode (green, red, and near-infrared) or 12,000 pixels wide in mono mode (normally the red band). NASS has not studied the utility of LISS-III or LISS-IV specifically for regional scale mapping of agriculture partially due to their limited swath widths, 141.0 and 23.9 km, respectively, and in the case of LISS-III, temporal repeat coverage of only 24 days. LISS-IV, however, can be pointed up to 26 degrees from nadir to improve revisit times to only five days over limited areas.

Specifics about Landsat-5 TM and Resourcesat-1 AWIFS are highlighted in Table 1. Notable similarities of the sensors are the overlap of green, red, near-infrared (NIR), and shortwave-infrared (SWIR) spectral bands. Not only are the spectral ranges for each nearly identical, but the AWIFS designers went as far as labeling the bands to correspond to those of TM. Overpass times are also similar, with Resourcesat-1 lagging Landsat-5 by

TABLE 1. SENSOR SPECIFICATIONS

| | Landsat-5 TM | Resourcesat-1 AWIFS |
|---------------------|--|---|
| Launch | 01 March 1984 | 17 October 2003 |
| Altitude | 705 km | 817 km |
| Orbit | circular, sun-synchronous | circular, sun-synchronous |
| Inclination | 98.2° | 98.7° |
| Period | 99 minutes | 101 minutes |
| Equatorial crossing | 9:45 AM ± 15 minutes | 10:30 AM ± 5 minutes |
| Revisit rate | 16 days | 24 days |
| Pixel size | 30 m (reflective) 120 m (thermal) | 56 m — |
| Quantization: | 8-bit | 10-bit |
| Spectral bands | 1: Blue (0.45–0.52 μ m) 2: Green (0.52–0.60 μ m) 3: Red (0.63–0.69 μ m) 4: NIR (0.76–0.90 μ m) 5: SWIR (1.55–1.75 μ m) 6: Thermal (10.40–12.50 μ m) 7: MIR (2.08–2.35 μ m) | — 2: Green (0.52–0.59 μ m) 3: Red (0.62–0.68 μ m) 4: NIR (0.77–0.86 μ m) 5: SWIR — (1.55–1.70 μ m) — |
| Field of view | 14.7° | 42.1° |
| Swath width | 185 km | 737 km |
| Scene size | 184 × 185.2 km | 370 × 370 km |

about 45 minutes. A key dissimilarity between the sensors is the exclusion of the blue, mid-infrared (MIR), and thermal-infrared channels on AWIFS. Also, an important difference is the sampled ground size of the pixels. AWIFS's pixels are 56 m squared versus 30 for TM. As a result, AWIFS pixels are approximately 3.5 times larger in area than TM pixels. The swath width of AWIFS is about four times wider than TM, but because of the bigger pixel sizes, the overall numbers of pixels per scene are comparable. AWIFS has a large field of view so the native area of the pixels increases to approximately 70 m resolution at off-nadir scene edges. At these edges the resulting view angle is over 20 degrees from nadir. TM's maximum off-nadir viewing angle is only about seven degrees so native pixel size increase on the scene edges is minimal. From the specifications in the table alone, one might conclude AWIFS has less ability to acquire repeat scenes over the same location since it takes 24 days versus 16 to duplicate its orbital path. However, because AWIFS has very wide footprints, the side overlays create repeat frequencies for a given area every five days. Additionally, 80 percent of a path is overlapped by a successive orbit, and as a result, it is common to get even greater repeat coverage for smaller geographic areas. In some cases, overlap occurs the very next day.

Study Area

In order to directly assess cropland map classification outcomes of TM versus AWIFS data, coincident scenes, in both time and location, were deemed most desirable. Images collected at the same time control for differences that often arise from changed atmospheric (e.g., haze, humidity) or ground conditions (e.g., plant phenology, soil moisture) which could alter otherwise similar classification efforts. By chance, coincident data collects occurred several times during the summer of 2005 within the midsection of the U.S. Three scene intersections were chosen as best and further utilized for evaluating cropland detection between sensors. Factors in selecting the test imagery were based on their location residing in an agriculturally dominant setting, proper timing for crop phenology, minimal amounts of clouds and haze, and sufficient overlap area between scenes. Additionally, given the large variation of view angle and GSD across track with AWIFS and two overlapping imaging sensors, it was also seen desirable to include different combinations of view angle and test both AWIFS cameras when possible.

The first example presented was based on imagery collected 20 August 2005. Geographically, the data resided over a section of the agriculturally intensive Mississippi River Alluvial Plain, locally known as the Delta, centered over the eastern portion of the state of Arkansas (Figure 1). A small portion of the study site extended south into Louisiana, and to a lesser extent, north into Missouri. The majority of the data was in Arkansas though and thus how referred to here for discussion. The Arkansas imagery originally spanned west of the Delta region, but that portion was excluded from analysis because the region is almost exclusively non-cropland in nature, and thus little ground truth data was collected. Based on the 2005 JAS statistics, about two-thirds of the land in this Arkansas study area was dedicated to field crop agriculture dominated by soybeans, rice, and cotton (Table 2). Corn was also found, but in lesser amounts. During mid-August, the time for which the data were collected, soybeans and cotton were in the middle of their growing season while rice and corn were nearing harvest (USDA, 1997). Scene quality was very good with only a few cumulous clouds present along the south and western edges of the study area. Because the images were collected within an hour of one another, the clouds had only shifted slightly between scenes. The Resourcesat-1 data were along the mid-scene of

the west-sided AWIFS camera, and thus represented pixel reflectances oriented away from the sun at an angle averaging roughly ten degrees from nadir (Table 3). Oppositely, the corresponding Landsat-5 TM data angled slightly into the sun, albeit only about five degrees on average, because of its location along the eastern edge of its scene.

The second study area was found in south-central Iowa. It was the smallest geographically of the three examples. The overlap area originally extended south into Missouri but was excluded because of little training data and cloud issues in that region. The data for Iowa were captured on 18 August 2005, two days prior to the Arkansas example. In terms of agriculture, this region was predominately made up of corn and soybean row cropping, particularly toward the northern extent. These crops were in the midst of their growing season during mid-August. There was also a sizable amount of land, particularly toward the south, dedicated to forage like alfalfa, hay, and pasture. Non-agriculture cover types were a mix of urban and woodland. The city of Des Moines was nearly centered vertically within the resulting strip of coincident data. A few cumulous clouds appeared in the scenes concentrated along the northern extent, but otherwise the data was of high quality. The AWIFS imagery was from Resourcesat-1's eastward facing camera and represented the greatest off-nadir viewing angle possible, trending toward the sun by about 20 degrees. The result was a native ground sample distance of approximately 70 m. In contrast, the reflectances from the TM data were oriented away from the sun, given the area of interest fell onto its western scene edge. Also, the TM viewing angle was much less extreme because of its narrower field of view. The Iowa example presented a scenario with the most opposed viewing geometry possible between the AWIFS and TM data.

The final case of coincident data was from northeastern Illinois and collected on 29 August 2005. In terms of geographic area, the Illinois site was about twice as large as the Arkansas study case and four times that of Iowa. Corn and soybeans were the majority crop cover type, as was in Iowa. A portion of the Chicago metropolitan area was found in the northeastern section and accounted for about ten percent of the land-cover over the examined region. The late-August date was still well within the heart of the growing season and appropriate for cropland mapping. Cumulous clouds were present toward the northern edge of the area along with a thick cirrus band in the extreme southeast. The AWIFS imagery was from the eastern Resourcesat-1 camera centered along the scene's midsection and thus presented an example of moderate view angle toward the sun. The TM swath was used almost in entirety, so the average pixel view angle was near zero with an equal number of pixels oriented toward the sun as away.

Methodology

A classification tree analysis (CTA) methodology (Friedl and Brodley, 1997, Lawrence and Wright, 2001) was used to perform identical but independent classifications on the three coincident image pairs. Leica Geosystems ERDAS Imagine® 9.0 was used for imagery preparation, NASS PEDITOR software for digitization and attribution of the NASS JAS enumerated field boundaries, ESRI ArcGIS® 9.1 for further analysis and management of those polygons, and See® 5.0 2.0 for derivation of the decision tree classification rules (Quinlan, 1993). The Imagine® "NLCD Mapping Tool" extension provided by the U.S. Geological Survey (USGS) (Homer *et al.*, 2004) was used to more easily interface See® 5.0 with Imagine's tools.

The first step consisted of compiling for each of the study areas the intersecting 2005 JAS data. In raw form, the

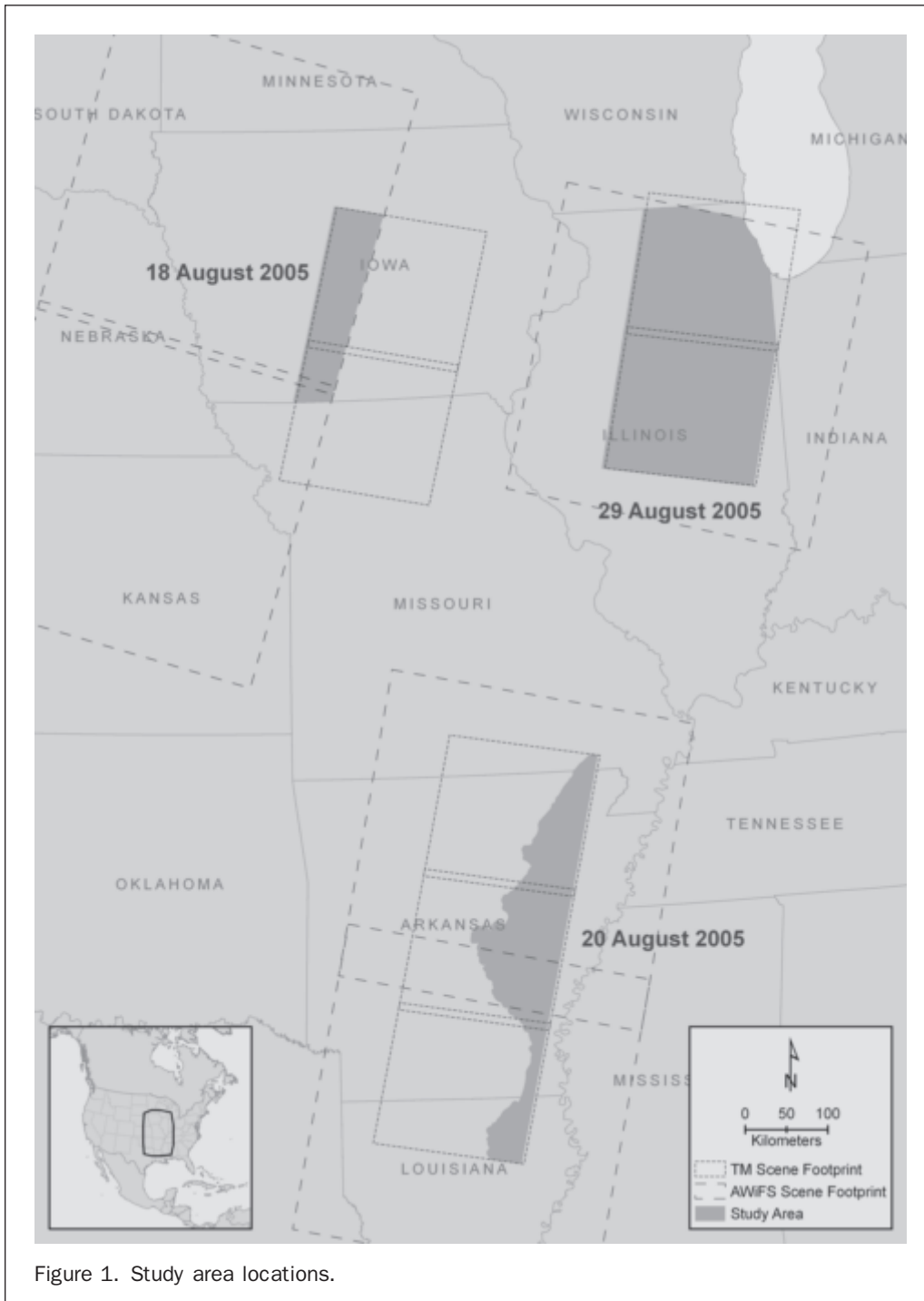


Figure 1. Study area locations.

TABLE 2. DOMINANT COVER TYPES AND ESTIMATED AREA DERIVED FROM 2005 NASS JAS

| Arkansas | | Iowa | | Illinois | |
|---------------|--------|------------------|--------|----------------|--------|
| Cover Type | Area % | Cover type | Area % | Cover type | Area % |
| Corn | 3 | Alfalfa | 7 | Alfalfa | 2 |
| Cotton | 10 | Corn | 28 | Corn | 45 |
| Rice | 24 | Soybeans | 20 | Soybeans | 32 |
| Soybeans | 32 | Idle cropland | 9 | Other cropland | 2 |
| Idle cropland | 3 | Pasture/Hay | 16 | Idle cropland | 1 |
| Pasture/Hay | 7 | Non-agricultural | 20 | Pasture/Hay | 3 |
| Woodland | 14 | | 100 | Woodland | 4 |
| Developed | 4 | | | Developed | 11 |
| Water | 3 | | | | 100 |
| | 100 | | | | |

TABLE 3. SCENE GEOMETRIES

| | Arkansas | Iowa | Illinois |
|-----------------------|-----------|-----------|-----------|
| Scene area (ha) | 2,578,086 | 1,240,869 | 5,597,249 |
| Average view angle | | | |
| TM | +5° | -7° | 0° |
| AWiFS | -10° | +20° | +10° |
| AWiFS camera | west | east | east |
| Average AWiFS GSD (m) | 60 | 70 | 60 |

annual JAS instrument consists of 24-inch by 24-inch paper-based maps with an accompanying questionnaire containing attribute information. The map component contains the boundary of a one square mile area sample unit known internally to NASS as a "segment." Recent aerial photography is depicted in the background for reference and scaled at 1:8 000. The questionnaire contains, among other things, a list of possible land-cover types and a place to record estimated acreage for each. Explaining the breadth of the JAS further, each segment is randomly selected from a NASS-defined area frame of contiguous segments spanning the entire U.S. To improve the efficiency of the sampling, the segments are stratified into a few categories based on the percentage of the land-cover dedicated to agriculture. Thus, minimally intensive agricultural regions are sampled less frequently than those from highly intensive areas. For example, in 2005 the state of Iowa, which has a very high percentage of land dedicated to agriculture, had 452 area segments chosen for the JAS. Arid Nevada on the other hand, had only 26 segments, even though the total land area is twice the size. In terms of the total amount of land area sampled, the Iowa study subset area had approximately three-fourths of one percent JAS coverage. The Illinois study area had a similar sampling frequency. More intense though was the Arkansas Delta region which had nearly two percent of the land area sampled.

During the first two weeks of June, trained enumerators visit each segment and delineate by colored pencil onto the survey map the current land-cover boundaries. Alongside, the questionnaire is completed describing what cover type was found within each of the defined homogeneous areas. The information is determined visually and by interviewing someone responsible with the land management at that location. The NASS survey process places more emphasis and detail on discriminating agricultural cover types, particularly cropland, versus those of non-agriculture classes. Thus, while differentiation between crop types is always expected within the data, no effort is made to place non-agricultural classes into more than just simple categories such as "urban," "woodland," and "water." Furthermore; in some cases an enumerator may simply lumped anything not agriculture into a single class, "non-agricultural."

The land track boundary information is not archived digitally, since NASS only needs the tabular information to produce its state and nation-wide estimates of planted acreage for the U.S. crop commodities. So next, the 2005 JAS field boundaries from the paper maps were "heads-up" digitized into a GIS for use as ground truth polygons. Same season map projected Landsat TM images were used for spatial referencing of the field boundaries within the GIS. Topology was checked to assure no gaps or overlaps existed between adjacent land-cover units within a segment. Linked to each polygon was the attribute information about cover type and estimated acreage recorded from the corresponding JAS questionnaire. The reported acreage value was compared against the drawn acreage to improve confidence the field were properly delin-

eated. If a large discrepancy was found, then the polygon was flagged as bad and ignored for later use. In total, the Arkansas study region contained 199 segments, Iowa 38, and Illinois 163. Respectively, they contained 1,793, 563, and 3,648 homogenous cover type polygons.

Next, the land tract level polygons were refined. Each -digitized field was manually inspected to see if it intersected a cloud top or shadow in either the coincident TM or AWiFS imagery, and if so, discarded from any further analysis. Also eliminated from the ground truth polygons were double-cropped fields (those with more than one planting per year) since only single date summer imagery was being used in the comparison. Furthermore, only majority cover type categories were utilized since often there were not enough samples from minority ones to be reasonably depicted across the scene. This involved combining smaller classes into more generalized ones and occurred more commonly for non-cropland categories. For example, in Iowa, all non-agriculture classes were collapsed together because there were deemed too few samples of urban, woodland, and water to be representative alone.

With the complete GIS of the JAS in place, the polygons for each of the three study cases were randomly sampled by record and divided into two sets of equal length. One set of the JAS polygons were tasked for training the image classifier and the other placed aside for validation of the output later. The training-set half of the polygons were further refined. To create spectrally pure ground truth training signatures, the polygons were buffered inward by a distance of 50 m. The distance was chosen as compromise between being sufficiently large enough to rid spectrally mixed edge pixels in either the 30 m TM and 56 m AWiFS data, yet not so large as to completely eliminate training polygons from fields that were small to begin with. Finally, the buffered training polygons were rasterized to a 15 m grid, assuring increased spatial precision beyond either imagery dataset, from which to draw training samples used for the CTA.

The Arkansas study area analysis was performed in the USGS-defined Continental U.S. Albers Equal Area projection. The Iowa dataset was analyzed in Universal Transverse Mercator, Zone 15 north, and the Illinois dataset in Zone 16. All reprojections were done using a cubic convolution resampling with the output grid preserved to the original pixel size of 30 m for TM and 56 m for AWiFS. The JAS vector information was map projected to the same extents as the corresponding satellite imagery before being converted to raster form.

Classification of the raw imagery was performed first using the JAS data in conjunction with the TM and then with the AWiFS data for each case. All bands of data were used as input other than TM's thermal (band 6) due to its coarse spatial resolution of only 120 m. The TM imagery was analyzed in its native 8-bit color depth. AWiFS was also analyzed in 8-bit, but after having been linearly rescaled from the native 10-bit. Random point samples, at a rate of 10 percent of the total, were drawn from within the training pixels and used to derive the decision trees. See[®]5.0's boosting (Quinlan, 1996) option was set to 10 trials and global pruning at 25 percent. Analysis was performed on a per pixel basis and thus no neighboring contextual information added.

Finally, output from each classification was assessed against the fifty percent of JAS data that was withheld for validation. The validation polygon data was not buffered, unlike with the training data, but were again rasterized to 15 m preserving a reasonable amount of edge detail. For each of the cases the classified image was then intersected with the validation data to produce an error matrix defining

how the predicted classification fared against the ground truth (Congalton and Green, 1999).

Results

Overall map accuracy and Kappa statistics are presented in Table 4. Comparative statistics were similar for each study area. For Iowa, the classification scenario resulted more favorably to the AWiFS analysis. Overall accuracies were 59.1 percent for TM and 61.6 percent for AWiFS, a difference of 2.5. Also, similarly trending were the Kappas with TM yielding 0.491 and AWiFS 0.520, a difference of 0.029. Within the Arkansas focus region, the overall accuracies and Kappas were greater than for Iowa. Results from Landsat's sensor showed a modest edge over Resourcesat's with a 1.0 accuracy difference (69.4 percent versus 68.4 percent, respectively) and a Kappa difference of 0.014 (0.590 versus 0.576). Finally, the best results overall came from the Illinois subset utilizing TM which showed an even larger mapping performance gap over AWiFS. TM was a whole five percentage points better than AWiFS in map accuracy (75.8 percent versus 70.8 percent) and 0.082 for the Kappa statistic (0.612 versus 0.530). Of note, across the study areas the TM Kappa was better in Illinois than for Arkansas, but the reverse was found for AWiFS. Taking a general average of accuracy and Kappa differences between the three study cases implies classifications from TM outperformed AWiFS, albeit modestly. All differences were found to be statistically significant at the pixel level.

Table 5 breaks out the accuracies by major cover types to provide a more detailed look at how the classifications performed. Within Table 5a, the values represent the producer's accuracies, or how well the general classification predicted within the validation areas. Expressed inversely, subtracting the producer's accuracy from 1.0 gives the omission error. Equally important, Table 5b shows the user's accuracies. The inverse of the user's accuracy is the commission error. For most classes across sensors the producer's and user's accuracies were similar and within class trends tended to mimic those of the overall statistics. In general, the dominant classes related to the major crop types performed the best. Soybeans, corn, rice, and cotton categorized more easily than non-cropland classes. Herbaceous cover types like alfalfa and pasture/hay struggled to give even marginal results. Idle cropland accuracies were even worse on average. Overall, the non-agricultural classes performed relatively poorly while row crop classes did the best.

Subset examples of the final output maps are shown in Plate 1 to provide a geographical perspective of the classification differences. In general, all three examples showed similar patterns, especially at the agricultural field level, and thus reinforced the tabular results from Tables 4 and 5. Major differences within the dominant crop cover types of corn, soybeans, and rice were difficult to find. However, transitions between land-cover boundaries were more sharply defined in the TM maps and non-agricultural classes appeared more reasonable. For example, in Iowa's TM classification there was better definition of roads (classed as non-agricultural) and no suggestion of pasture/hay incorrectly classified within the urban region. Additionally, the overall percentage of "speckling" was about the same for all classifications but more noticeable within AWiFS when viewed at the same scale as TM.

As noted earlier, the main discrepancy in the sensors' design comes from the lack of blue (band 1) and MIR (band 7) reflectance channels and the decreased pixels resolution of 56 m on AWiFS. More insight could be gained on the relative importance of each by altering the TM data to meet

the same specifications as AWiFS. Thus, three more classifications were performed on each study area. First, the TM data were analyzed without bands 1 and 7, but keeping with the original spatial resolution of 30 m. Next, all six TM bands were used in the analysis, but after degrading them to the 56 m resolution using cubic convolution resampling. And finally, the TM data was both stripped of bands 1 and 7 and resampled to 56 m, thus matching the characteristics of AWiFS. Each of the new data sources was reclassified with the same methodology as before and accuracies computed.

Results for each test are presented in Table 6. The original TM and AWiFS classification numbers are shown again for direct reference. The accuracies and Kappas were reduced at all three study sites with the degradation of the TM data, and in some cases the differences were more pronounced than for others. In Iowa for starters, very little change occurred. The withholding of the blue and MIR bands only created a 0.2 point difference drop in accuracy percentage and 0.003 in Kappa. Spatial degradation to the 56 m resampling effort impacted the results more with a drop of 0.9 in accuracy and 0.012 in Kappa. The impact of the combined band removal and pixel resampling was 56.6 percent, or five percentage points below the raw numbers for the AWiFS classification. If all else were equal, it may have been expected for the accuracies of the degraded TM data to improve and match that of the true AWiFS for Iowa. However, that was not the case and thus further variables must have been affecting the differences. For Arkansas the drops in accuracy were increased over that of Iowa but still relatively minor. Both the band stripping and pixel degradation methodologies resulted in similar accuracy reductions. The 4-band scenario was down 1.9 percentage points from the original and the degraded pixel test lowered by a similar 1.7. Kappas trended down nearly equally as well. With the effects combined, the overall accuracy was 66.0 percent, down 3.4 points from the original TM. All of the degradation schemes for Arkansas yielded assessment values a bit lower than that produced from the raw AWiFS data outright. Finally, for the Illinois example there was a decrease in accuracy of only 0.6 for the 4-band scenario but almost three times greater with 1.7 for the 56 m simulation. The Kappa difference varied in the same manner and thus was more pronounced in change for the 56 m run. The combined impact to the two effects resulted in an accuracy drop of 2.2 percentage points. Unlike for the other study sites though, the compromised TM data for Illinois yielded impacts that were not damaging enough to reduce it below the output created from the raw AWiFS data. Taking a general average of all three cases, it appears that the change in spatial resolution has more impact on the classifier accuracy than the combined exclusion of the two spectral bands.

To boost the notion that the blue (band 1) and MIR (band 7) reflectance channels from TM were of little significance to the classification output, the relative importance of those spectral bands can be inferred by

TABLE 4. OVERALL CLASSIFICATION ASSESSMENTS

| | Arkansas | | Iowa | | Illinois | |
|--------------|----------|-------|-------|-------|----------|-------|
| | TM | AWiFS | TM | AWiFS | TM | AWiFS |
| Pixel based | | | | | | |
| Accuracy (%) | 69.4 | 68.4 | 59.1 | 61.6 | 75.8 | 70.8 |
| Kappa | 0.590 | 0.576 | 0.491 | 0.520 | 0.612 | 0.530 |

TABLE 5. CLASS SPECIFIC (a) PRODUCER'S, AND (b) USER'S ACCURACIES (%)

| (a) | | | | | | |
|------------------|----------|-------|------|-------|----------|-------|
| Class | Arkansas | | Iowa | | Illinois | |
| | TM | AWiFS | TM | AWiFS | TM | AWiFS |
| Alfalfa | — | — | 12.1 | 16.2 | 8.0 | 6.3 |
| Corn | 43.7 | 42.7 | 80.2 | 82.8 | 88.4 | 85.1 |
| Cotton | 71.7 | 75.3 | — | — | — | — |
| Rice | 82.6 | 84.1 | — | — | — | — |
| Soybeans | 79.4 | 76.5 | 76.1 | 71.4 | 82.9 | 75.1 |
| Idle Cropland | 14.4 | 10.1 | 54.0 | 49.2 | 4.3 | 1.4 |
| Other Cropland | — | — | — | — | 30.5 | 36.4 |
| Pasture/Hay | 34.0 | 29.3 | 61.9 | 66.1 | 7.9 | 14.1 |
| Non-agricultural | — | — | 37.2 | 45.4 | — | — |
| Woodland | 52.1 | 49.2 | — | — | 41.9 | 39.1 |
| Developed | 6.0 | 3.4 | — | — | 35.7 | 26.2 |
| Water | 17.3 | 20.4 | — | — | — | — |

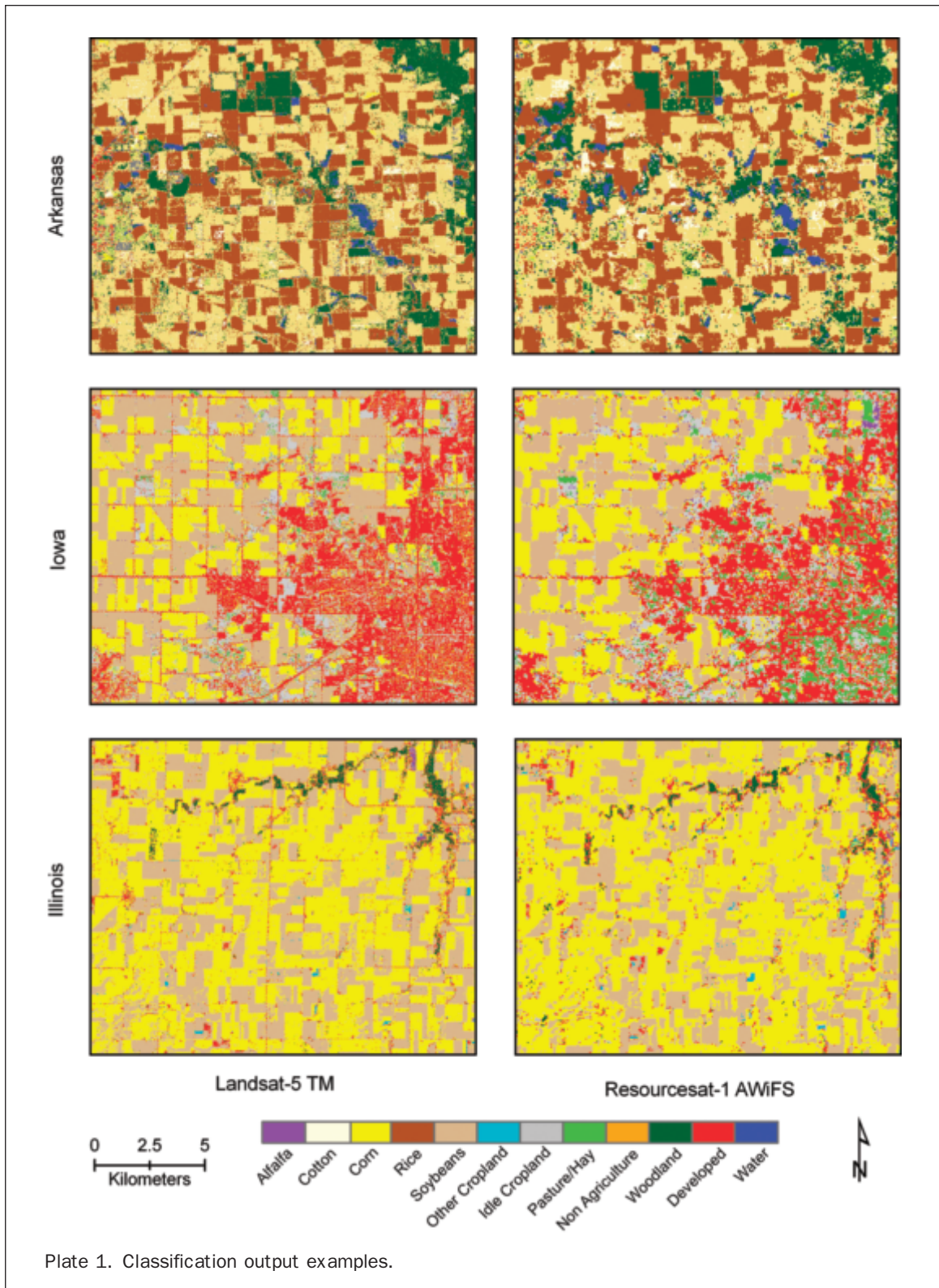
| (b) | | | | | | |
|------------------|----------|-------|------|-------|----------|-------|
| Class | Arkansas | | Iowa | | Illinois | |
| | TM | AWiFS | TM | AWiFS | TM | AWiFS |
| Alfalfa | — | — | 37.0 | 41.3 | 17.4 | 7.7 |
| Corn | 62.4 | 54.2 | 73.3 | 71.9 | 79.7 | 74.3 |
| Cotton | 69.9 | 74.1 | — | — | — | — |
| Rice | 83.1 | 84.5 | — | — | — | — |
| Soybeans | 69.1 | 66.1 | 68.5 | 72.9 | 80.3 | 74.3 |
| Idle Cropland | 40.8 | 26.5 | 44.3 | 42.3 | 4.1 | 1.1 |
| Other Cropland | — | — | — | — | 41.2 | 38.1 |
| Pasture/Hay | 29.8 | 22.6 | 37.6 | 42.0 | 35.1 | 39.3 |
| Non-agricultural | — | — | 69.1 | 73.5 | — | — |
| Woodland | 64.8 | 66.4 | — | — | 63.9 | 67.6 |
| Developed | 9.5 | 5.9 | — | — | 45.6 | 45.3 |
| Water | 17.9 | 23.2 | — | — | — | — |

studying the decision rules derived during the CTA. In other words, the bands with the least ability to discriminate between class types would be expected farther down the decision tree structure than the bands that were important. Within Iowa, and for both the raw TM and AWiFS data sources, NIR (band 4) was where the first decision was made and red (band 3) was the next most important. Blue was not needed until a split at the fourth level, and the MIR unused until even farther down the tree. This is consistent with there being little impact from those bands, since there was little change in the accuracy when they were taken out. For the Arkansas case, the primary split was based on the SWIR channel (band 5) in both TM and AWiFS. The NIR

band was the next most important decision in the tree. Like with Iowa, the blue band was not called upon within the TM analysis until the fourth level of split, and the MIR layer was buried farther down. However, for Illinois, the story was different. Within the normal TM classification the blue band was utilized at the second level of the decision tree and the MIR band at the fourth. The red and near-infrared were found at the first and third split. For the corresponding AWiFS analysis, the SWIR band was called upon first and then the NIR. The overall implication was that the blue band provided more information than the MIR, and sometimes the blue band was as important as the red, NIR, and SWIR bands.

TABLE 6. SIMULATION OF AWiFS DATA FROM TM

| | TM | 4-band TM | 56 m TM | 4-band, 56 m TM | AWiFS |
|-----------------|-------|-----------|---------|-----------------|-------|
| <u>Arkansas</u> | | | | | |
| Accuracy (%) | 69.4 | 67.5 | 67.7 | 66.0 | 68.4 |
| Kappa | 0.590 | 0.564 | 0.569 | 0.546 | 0.576 |
| <u>Iowa</u> | | | | | |
| Accuracy (%) | 59.1 | 58.9 | 58.2 | 56.6 | 61.6 |
| Kappa | 0.491 | 0.488 | 0.479 | 0.456 | 0.520 |
| <u>Illinois</u> | | | | | |
| Accuracy (%) | 75.8 | 75.2 | 74.1 | 73.6 | 70.8 |
| Kappa | 0.612 | 0.599 | 0.586 | 0.575 | 0.530 |



Discussion

The key classification objectives for NASS of good discrimination between cropland and non-cropland classes, and the within-cropland discrimination of major commodities, were met in most cases. The poorly performing non-cropland classes, regardless of sensor, may have seemed a disappointment, but are actually of little concern. Those categories are

better served by more sophisticated classification efforts (e.g., NLCD or Gap Analysis) which may have been derived from ancillary raster or vector data (e.g., roads, water, field boundaries, and topography) and multiple scenes of time appropriate imagery (time series analysis over winter and summer). Even from a NASS perspective, cropland discrimination is known to improve with the availability of two or more scenes within the

same growing season. This is how analysis within the CDL program is performed when possible.

Accuracy differences in general varied more widely across class categories than across sensor types. This was likely a reflection of insufficient training data or the spectral inconsistency of certain cover types. For example, the major row crop categories are usually planted, managed, and harvested similarly, and thus have steady multi-spectral reflectances ideal for classification. On the flip side, herbaceous cover types like alfalfa and hay often vary spectrally due to a range of cutting or grazing practices and thus were more difficult to properly categorize. Idle cropland-cover types often vary even more widely in practice because fallow fields can have vastly differing cover types, from bare soil to thick vegetation. Too few or non-representative training data was probably coming into play in the case of the mediocre result of the water class for Arkansas, which can vary from shallow aquaculture ponds to deep natural water bodies. For both the TM and AWIFS analysis, all of the poorly performing classes would likely be improved with the collection of more training data to better account for the true variability of those landscapes.

Furthermore, the pixel-based classification methodology used here was simplistic in nature and has room for improvement. An easy way to increase overall and within class accuracies is by taking spatial context into perspective through post processing of the results using a minimum mapping unit (MMU) filter to reduce spurious misclassified pixels. For example, applying a cropland appropriate MMU of 20 acres (8.1 hectares, or 90 TM pixels and 26 AWIFS pixels) to all of the example scenarios improved overall accuracies on average by a 5.2 percentage point difference for the TM examples and 4.0 with AWIFS. Kappas were also better for all cases averaging improvements of 0.064 for TM and 0.046 for AWIFS. The overall suggestion is TM has somewhat more to gain than AWIFS when increasing the MMU beyond the native pixel size due to its finer spatial resolution.

The overall accuracies in Iowa, with AWIFS outperforming the TM analysis, were somewhat surprising and perplexing. The explanation may be found in Iowa's uniqueness in terms of average surface incident angle of the scene pixels, compared to those from the Arkansas and Illinois study areas. Again, the Iowa TM data's area of interest was towards the left edge of the scene, facing away from the sun, while the corresponding AWIFS's data was angled oppositely, toward the sun. The resulting average difference in viewing angle was about 25 degrees. Given the better outcomes of AWIFS for Iowa, it can be speculated that the optimal bi-directional reflectance for discriminating cropland was looking into the sun and that the off-nadir increase in GSD was more than compensated for. The logic being impact from longer shadows found in certain cover types are mixing into pixels and thus increased contrast. This would be especially true for a crop like corn which in mid-August was tall and leafy versus a low lying category like pasture/hay. Analysis of full swath width AWIFS imagery does subjectively suggest that pixels towards the sun facing scene edges show more contrast between differing cover types, especially in the NIR and SWIR spectral bands. The wide range of view angles with AWIFS is something that should be taken into consideration more heavily than when utilizing a relatively nadir looking system like TM. Viewing angle impacts on classification efforts is a research topic in its own right and needs to be further explored.

For agriculture regions outside those studied here, the negative impact of AWIFS larger pixels may become more dramatic in areas having smaller field sizes, such as those

found in the eastern half of the U.S. It is speculated that the gap between AWIFS and TM performance would widen because scale would become more of an issue. Obviously, the larger and more uniform the field the less need there is for a high-resolution pixel to capture its difference from neighboring cover types. For data users that are focused on deriving non-agricultural classes, differences between TM and AWIFS may also become more apparent. Spatially detailed and texturally complex classes such as urban will likely suffer inferior classification results with AWIFS.

Only TM data in relation to AWIFS was compared within this study. Landsat-7 ETM+, scan-gap problem aside, is known to have better sensor performance than TM in terms of signal-to-noise ratio and the inclusion of the 15 m panchromatic band in addition to a 60 m thermal infrared. TM lacks both of these, and thus cropland classifications derived from a normally functioning ETM+ sensor would probably outperform TM, and thus AWIFS even more (Craig, 2002).

The large scene sizes of AWIFS are appealing because a large amount of training data can be employed, but they can have the unintended consequence of stretching training data information across the image to areas where they are not appropriate. Keeping agriculture as an example, training data from one scene corner of a particular commodity may have a difference spectral signature from that same commodity data several hundred kilometers away. This would be especially pronounced during the times of green-up or senescence where one portion of an image leads or lags another due to seasonal onsets. Also, crops may behave differently across scenes due to other geographic factors such as changes in soil types, soil moisture, elevation, climate, and crop management practices.

AWIFS offers compelling benefits over TM not addressed directly in a side-by-side classification comparison. For one, AWIFS has a much greater temporal repeat frequency. In a region like the mid-section of the U.S., one can expect cloud cover about fifty percent of the time during the summer. Haze is even more common. Often the biggest obstacle to being able to identify crops from space comes not from limitations due to sensor design, data infrastructure, or processing algorithms, but from the non-availability of suitable time appropriate imagery. NASS often finds occasions when not a single cloud-free TM scene is available during the growing season over certain areas. This results in an inability to produce a consistent wide area cropland classification. AWIFS with its five-day revisit rate more than triples the 16-day repeat of TM, and thus the likelihood of obtaining useable data. Furthermore, the same five-day repeat also increases the ability to capture multi-temporal data over the same location. Although only analysis of single scenes was shown here, improved classifications often result when two or more scenes from different times of the same growing season are used.

Second, because of the large AWIFS footprints, state-wide or regional scale classifications are simpler and more efficient to construct. For a typical U.S. state it takes several Landsat scenes to build a mosaic large enough to cover the entire area, and managing a large number of scenes with differing capture dates and atmospheric conditions increases the complexity and workload of a classification. With AWIFS, the potential exists for many state level projects to only need a couple of scenes to complete an entire analysis. Or thought of another way, utilizing the same amount of resources onto the larger scene footprints increases the scope of land in area that is classifiable. AWIFS is a tool that brings NASS closer to being able to rapidly identify planted locations of the major commodities beyond just a state level.

Another advantage to AWIFS is in regards to data intercomparability that can be had with the other LISS-III multi-spectral sensor on the Resourcesat-1 platform. It is collected simultaneously and has the identical sensor characteristics to AWIFS, other than a finer pixel size and narrower field of view. LISS-III allows for a direct method to obtain some of the AWIFS scene information spectrally calibrated at an increased resolution of 23.5 m. The JAS provides NASS with a rich training set of ground truth information, but other classification efforts might need to rely on inspection of higher resolution data that is collected in parallel.

Further utility of AWIFS data that TM cannot provide may arise in the form of time series analysis. Sensors such as AVHRR, MODIS, and SPOT Vegetation have typically been used for this work because they have a daily repeat frequency. However, their pixels have relatively low resolutions (250 m to 1 km) which are too large to provide detail at the crop field level for which Landsat is better suited. AWIFS represents a compromise between the low and medium resolution sensors in terms of temporal coverage and pixel size so has the potential for spatially detailed phenology analysis that is currently not possible.

Conclusions

A comparison of coincident Landsat-5 TM and Resourcesat-1 AWIFS imagery for deriving independent land-cover classifications emphasizing row crop agriculture has been presented for three study sites. TM data was found to be on average slightly superior to AWIFS in terms of overall, and within category, map accuracies. Differences were typically within five percentage points of one another and not considered major. TM performed better likely because of its spatial resolution being three and one half times finer than that of AWIFS and, to a lesser extent, the added spectral information provided through its blue and MIR bands. However, implying the only differences in the data sources were due to pixel sizes and spectral bands is likely over simplifying the comparison. This is true because it was shown degrading the TM data to match the AWIFS created larger, not smaller, dissimilarities between the outputs for two of the three cases.

It is speculated that the classification performance gap would widen if the study sites contained cultivated areas with fields smaller than those typically found within the central U.S. This is a logical next topic for research and would help document the usability of 56 m pixels in more spatially complex land-cover areas. Additionally, impacts to classification outcomes by AWIFS due to the wide field of view need to be explored in further detail. However, no evidence was found showing AWIFS edge pixels to be more compromised than those at nadir, and there is even suggestion that off-nadir viewing angles might have benefits.

For cropland classification purposes, it is believed the any loss in map accuracy from switching to AWIFS from TM will be compensated for by the threefold or better revisit rate. As such, Resourcesat offers real opportunity for temporal analysis of agriculture that Landsat cannot match. Answers to further crop questions, such as condition or yield, may become more obtainable from remotely sensed imagery than ever before.

Finally, while crop detection over the central U.S. was the focus here, there are obviously other applications and regions around the globe reliant on remotely sensed imagery of the earth's land surface. It is believed the large footprints and better than weekly overpass coverage of AWIFS can significantly increase the capacity of land-cover monitoring and evaluation for a variety of disciplines, particularly at

regional scales. Users that will likely benefit most are those that have a difficult time obtaining imagery because of high likelihood of cloud cover in their area of interest such as in tropical, mountainous, or high latitude regimes. Additionally, because the large scene sizes simplify analysis, AWIFS data should be appealing to those in the land-cover monitoring community trying to map large regional or even continental-sized extents.

Acknowledgments

The author would like to thank Claire Boryan, Mike Craig, Bob Seffrin, and in particular Rick Mueller, all from the Spatial Analysis Research Section of NASS, for helpful remarks and suggestions on the paper. Comments from the anonymous reviewers were appreciated as well and helped to improve the manuscript. Thanks also go to Bob Tetrault of the Foreign Agricultural Service for continued support and promotion of Resourcesat-1 imagery within the USDA's Satellite Image Archive and James Lutes of GeoEye as technical lead for the processing of the North American collected data.

References

- Boryan, C., and M. Craig, 2005. Multiresolution Landsat TM and AWiFS sensor assessment for crop area estimation in Nebraska, *Proceedings from Pecora 16*, Sioux Falls, South Dakota (American Society for Photogrammetry and Remote Sensing, Bethesda, Maryland), unpaginated CD-ROM.
- Congalton, R.G., and K. Green, 1999. *Assessing the Accuracy of Remotely Sensed Data: Principles and Practices*, CRC Press, Boca Raton, Florida, 137 p.
- Craig, M.E., 2001. A resource sharing approach to crop identification and estimation, *Proceedings of the 2001 Annual Conference*, St. Louis, Missouri (American Society for Photogrammetry and Remote Sensing, Bethesda, Maryland), unpaginated CD-ROM.
- Craig, M.E., 2002. Comparing 30 meter imagery from Landsat 5 and 7 for crop area estimation, *Proceedings of the ACSM-ASPRS Conference 2002*, Washington, DC (American Society for Photogrammetry and Remote Sensing, Bethesda, Maryland), unpaginated CD-ROM.
- Friedl, M.A., and C.E. Brodley, 1997. Decision tree classification of land-cover from remotely sensed data, *Remote Sensing of Environment*, 61:399-409.
- Homer C., C. Huang, L. Yang, B. Wylie, and M. Coan. 2004. Development of a 2001 national land-cover database for the United States. *Photogrammetric Engineering and Remote Sensing* 70(9):829-840.
- Kiran-Chand, T.R., K.V.S. Badarinath, V.K. Prasad, M.S.R. Murthy, C.D. Elvidge, and B.T. Tuttle, 2006. Monitoring forest fires over the Indian region using Defense Meteorological Satellite Program-Operational Linescan System nighttime satellite data, *Remote Sensing of Environment*, 103:165-178.
- Kulkarni, A.V., S.K. Singh, P. Mathur, and V.D. Mishra, 2006. Algorithm to monitor snow cover using AWiFS data of Resourcesat-1 for the Himalayan region, *International Journal of Remote Sensing*, 27:2449-2457.
- Lawrence, R.L., and A. Wright, 2001. Rule-based classification systems using Classification and Regression Tree (CART) analysis, *Photogrammetric Engineering & Remote Sensing* 67(10):1137-1142.
- Lutes, J., 2005. Resourcesat-1 Geometric Accuracy Assessment, *Proceedings of the ASPRS 2005 Annual Conference*, Baltimore, Maryland (American Society for Photogrammetry and Remote Sensing, Bethesda, Maryland), unpaginated CD-ROM.
- Mueller, R., 2000. Categorized mosaicked imagery from the National Agricultural Statistics Service crop acreage estimation program, *Proceedings of the ASPRS 2000 Annual*

- Conference*, Washington, D.C. (American Society for Photogrammetry and Remote Sensing, Bethesda, Maryland), unpaginated CD-ROM.
- National Remote Sensing Agency (NRSA), 2003. *IRS-P6, Data Users Manual*, Department of Space, Government of India, Balanagar, Hyderabad, 141 p.
- Quinlan, J.R., 1993. *C4.5 Programs for Machine Learning*, Morgan Kaufmann Publishers, San Mateo, California, 302 p.
- Quinlan, J.R., 1996. Bagging, Boosting, and C4.5, *Proceedings of the Thirteenth National Conference on Artificial Intelligence*, Portland, Oregon (American Association for Artificial Intelligence Press, Menlo Park, California), pp. 725–730.
- United States Department of Agriculture (USDA), National Agricultural Statistics Service, Crops Branch, 1997. *Usual Planting and Harvesting Dates for U.S. Field Crops*, Agricultural Handbook No. 628, Washington, D.C., Government Printing Office.
- United States Department of Interior (USDOI), United States Geological Survey, 2006. *Landsat Project*, URL: <http://landsat.usgs.gov/>, Washington, D.C. (last date accessed: 24 July 2008)
- (Received 29 November 2006; accepted 09 March 2007; revised 14 May 2007)

OPEN NEW CAREER DOORS...

"...official recognition by one's colleagues and peers that an individual has demonstrated professional integrity and competence in their field..."

- ✓ **Photogrammetrist**
- ✓ **Remote Sensing Mapping Scientist**
- ✓ **GIS/LIS Mapping Scientist**
- ✓ **Photogrammetric Technologist**
- ✓ **Remote Sensing Technologist**
- ✓ **GIS/LIS Technologist**

ASPRS Certification validates your professional practice and experience. It differentiates you from others in the profession. For more information on the ASPRS Certification program contact certification@asprs.org or visit <http://www.asprs.org/membership/certification/>.

WITH ASPRS CERTIFICATION

ASPRS Mission Statement

The mission of the ASPRS is to advance knowledge and improve understanding of mapping sciences and to promote the responsible applications of photogrammetry, remote sensing, geographic information systems (GIS), and supporting technologies.

Announcement and Call for Papers

MultiTemp 2009 Fifth International Workshop on the Analysis of Multitemporal Remote Sensing Images Mystic Marriott Hotel & Spa July 28-30, 2009 • Groton, Connecticut

The design of new instruments to acquire multi-temporal or even hyper-temporal earth observation imagery and the development of effective methods to analyze these data sets, represent some of the more challenging issues the remote sensing community faces today. At issue is the temporal dimension of the imagery that allows for linkages to the dynamic character of systems, processes, function and other phenomena under study.

The Fifth International Workshop on the Analysis of Multi-temporal Remote Sensing Images (MultiTemp-2009) will continue the objective of the previous editions to assess the state-of-the-art in the analysis of multi-temporal remote sensing and geo-spatial data. The workshop will have oral and interactive poster presentations dealing with both the theoretical and applied issues surrounding the use of multi- and hyper-temporal information in support of the sustainable management of earth's resources to maximize societal benefits (<http://clear.uconn.edu/multitemp09>).

MultiTemp-2009 is soliciting papers in the following topic areas:

- phenology product development and monitoring applications
- innovative approaches to multi-temporal data handling
- novel multi-temporal and hyper-temporal applications
- image registration, calibration and correction techniques
- change detection analysis methods and applications
- land-cover and land-use mapping and monitoring
- drought monitoring and predictive modeling
- ecosystem process monitoring and modeling
- multitemporal SAR and InSAR data analysis
- change detection validation and assessment
- multitemporal imagery analysis techniques
- water resources monitoring and modeling
- environmental security applications
- plant production system monitoring
- multitemporal LIDAR data analysis

Contributions are welcome from the scientific community dealing with innovation as well as from the applications' sector focusing on using the resulting methods in practical settings. The workshop will include papers accepted for oral and interactive poster presentation. Only presented papers will appear in the workshop proceedings. A Special Issue of the IEEE Journal of Selected Topics in Applied Earth Observations and Remote Sensing (J-STARS) focusing on "Multitemporal Imagery Analysis", will be open to participant contributions.

Prospective contributors are invited to submit an extended abstract of 2-3 pages at the dedicated MultiTemp-2009 website.

Abstract Submission is available at <http://clear.uconn.edu/multitemp09/abstract.html>.

Important Dates

- January 31, 2009 deadline for extended abstract submission
- March 1, 2009 notification of acceptance
- April 30, 2009 due date for camera-ready proceedings manuscripts
- May 31, 2009 registration deadline
- July 28-30, 2009 MultiTemp-2009 at Groton, CT

Hosted by the University of Connecticut and Co-sponsored by US EPA, NASA, USGS, ASPRS, and IEEE.

Using a Binary Space Partitioning Tree for Reconstructing Polyhedral Building Models from Airborne Lidar Data

Gunho Sohn, Xianfeng Huang, and Vincent Tao

Abstract

During the past several years, point density covering topographic objects with airborne lidar (Light Detection And Ranging) technology has been greatly improved. This achievement provides an improved ability for reconstructing more complicated building roof structures; more specifically, those comprising various model primitives horizontally and/or vertically. However, the technology for automatically reconstructing such a complicated structure is thus far poorly understood and is currently based on employing a limited number of pre-specified building primitives. This paper addresses this limitation by introducing a new technique of modeling 3D building objects using a data-driven approach whereby densely collecting low-level modeling cues from lidar data are used in the modeling process. The core of the proposed method is to globally reconstruct geometric topology between adjacent linear features by adopting a BSP (Binary Space Partitioning) tree. The proposed algorithm consists of four steps: (a) detecting individual buildings from lidar data, (b) clustering laser points by height and planar similarity, (c) extracting rectilinear lines, and (d) planar partitioning and merging for the generation of polyhedral models. This paper demonstrates the efficacy of the algorithm for creating complex models of building rooftops in 3D space from airborne lidar data.

Introduction

Today, there are increasing demands for rapid and timely compilation of three-dimensional building models from remotely sensed data. Accurate acquisition and frequent up-dating of such models becomes more important source of information for decision making in support of numerous applications, including geospatial database compilation, urban planning, environmental study, and military training (Ameri, 2000). Traditionally, three-dimensional compilation of urban features has been manually conducted under guidance of a human operator using a Digital Photogrammetry Workstation (DPW). Automation of such resource-intensive tasks has been

a major focus of Photogrammetry and Remote Sensing for many years.

In recent years, topographic airborne lidar (Light Detection and Ranging) has been rapidly adopted as an active remote sensing system that uses near-infrared laser pulses (typically 1 to 1.5 μm) to illuminate man-made or natural features on the terrain. The up-to-date lidar system can collect elevation data at a vertical accuracy of 15 cm, at a rate of higher than 100,000 pulses per second. This ability allows the system to produce a dense array of highly accurate and precise three dimensional elevation models, which is a useful property for automating the sophisticated tasks involved in building reconstruction. This paper focuses on the issue of automated construction of 3D building models from lidar data.

It is well understood that a general solution to the building reconstruction system entails the collection of modeling cues (e.g., lines, corners, and planes), which represent the major components of building structure. By correctly grouping those cues, geometric topology between adjacent cues, describing a realistic roof shape, can be created. A significant bottleneck hindering the reconstruction process is caused by the fact that extraction of modeling cues is always disturbed by noise inherited from imaging sensors and objects. The most disadvantageous feature of lidar is characterized by irregular data acquisition, which often makes extraction of modeling cues difficult. As shown in Figure 1, the salient boundaries comprising building roof structures, which are easily recognizable in the optical imagery, are often distorted due to a variety of factors, most notably: scanning pattern, point spacing, surface material properties, and object complexity. For this reason, 3D building reconstruction systems have performed most effectively by constraining the knowledge of building geometry either explicitly (model-driven reconstruction) or implicitly (data-driven reconstruction) in order to recover incomplete modeling cues.

The model-driven approach pre-specifies particular types of building models so that geometric relations (topology) across modeling cues are provided. By fitting the model to observed data, the model parameters are determined. A good example of model-driven reconstruction was presented by Maas and Vosselman (1999), who were able to determine the parameters of a standard gable

Gunho Sohn and Vincent Tao are with the GeoICT Lab, Department of Earth and Space Science and Engineering, York University, 4700 Keele St., Toronto, ON, Canada, M3J 1P3 (gsohn@yorku.ca).

Xianfeng Huang is with the State Key Laboratory of Information Engineering in Surveying, Mapping and Remote Sensing (LIESMARS), Wuhan University, 129 Luoyu Road, Wuhan, China.

Photogrammetric Engineering & Remote Sensing
Vol 74 No. 11, November 2008, pp. 1425–1438.

0099-1112/08/7411-1425/\$3.00/0
© 2008 American Society for Photogrammetry
and Remote Sensing

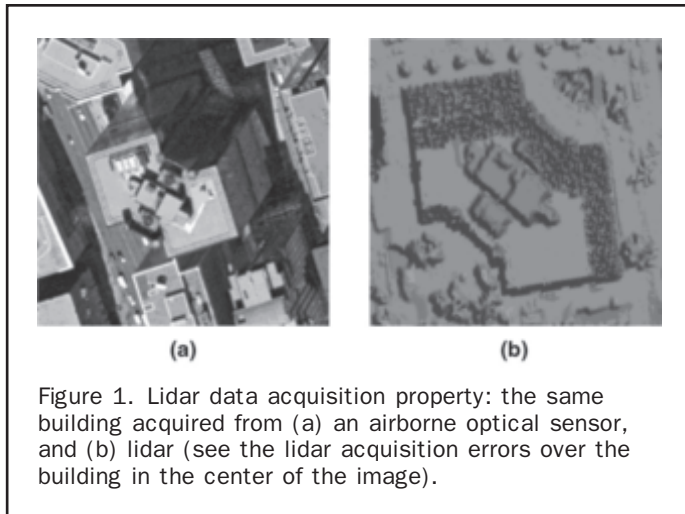


Figure 1. Lidar data acquisition property: the same building acquired from (a) an airborne optical sensor, and (b) lidar (see the lidar acquisition errors over the building in the center of the image).

roof with small dorms through the analysis of invariant moments from lidar points. In order to cope with more complicated models, a number of different building models are hypothesized and tested within partitioned rectangles of existing ground planes, and a full description of the roof model is generated by integrating the verified parametric models (Brenner and Haala, 1998; Vosselman and Dijkman, 2001).

The data-driven method reconstructs the boundary of polyhedral building models by grouping extracted lines, corners and planes with minimal use of prior knowledge of the generic building model. As the modeling cues, plane clusters are obtained by the Hough transformation (Vosselman, 1999); RANSAC (Brenner, 2000); orthogonal projection of point clouds (Schwalbe *et al.*, 2005); and region growing (Rottensteiner *et al.*, 2005). Also, linear features are extracted by intersecting planes detected and the analysis of height discontinuity (Vosselman, 1999); approximating the boundary of planes (Alharthy and Bethel, 2004). The Gestalt laws (proximity, symmetry, parallelism, and regularity) are often used for bridging the gaps between extracted features in order to reconstruct the model topology (Hu, 2003) or to snap adjacent planes (Alharthy and Bethel, 2004). In order to impose geometric regularity on reconstructed models, additional constraints are used in which: (a) a set of rules for intersecting adjacent planes are pre-determined (Hofman, 2004); (b) the roof structure is restricted to the dominant building orientation (Vosselman, 1999; Schwalbe *et al.*, 2005); or (c) orientations of building outlines are derived from an existing ground plan (Brenner, 2000). A global optimality of shape regularity is achieved by the Minimum Description Length (MDL) principle (Weidner and Förstner, 1995).

Many buildings in modern cities exhibit a very high degree of shape complexity, being comprised of a mixture of various building primitives, with multiple stories and many roof super-structures (chimneys, air vents, water tanks, roof fences, etc.). Under these circumstances, particular types of pre-defined models become problematic to accommodate high variations in building shapes (Brenner, 2005). On the other hand, strong constraints in analyzing topological relations and grouping adjacent model cues, which are commonly used in data-driven reconstruction, may degrade the robustness of reconstruction systems if the fragmentary level of cue extraction becomes higher and roof super structures are located around the border of adjacent roof primitives. Using an existing ground plan to sub-divide

a building region of interest into a set of rectangles can greatly reduce the complexity of the building reconstruction process (Brenner 2000; Vosselman and Suveg 2001). However, as building complexity becomes higher, pre-assumptions of coherent relations between roof structures and the ground plan may be invalid

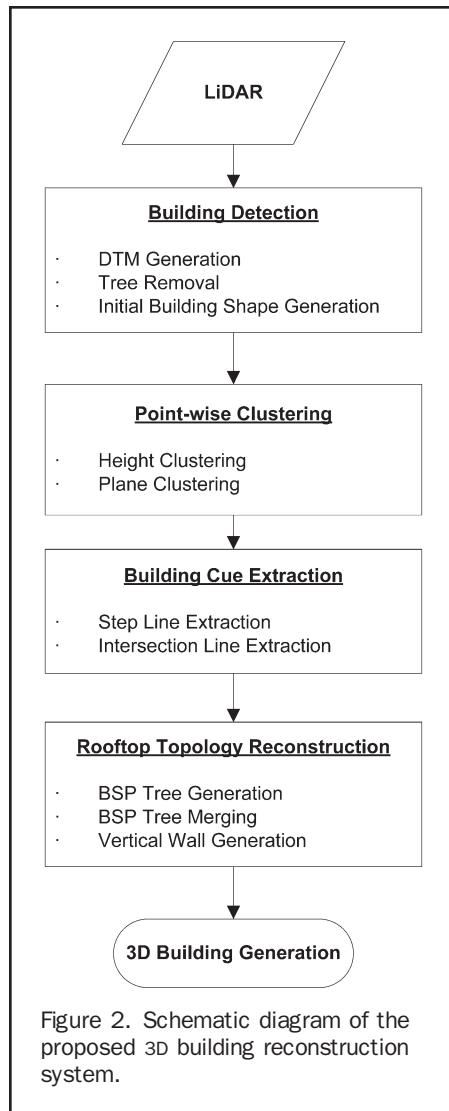
The main objective of this paper is to present a new partitioning framework, where data-driven linear features optimally subdivide a building object into piecewise plane clusters with no use of existing ground plans. Thus, 3D roof structures are reconstructed by collecting plane clusters so that fragmented linear cues can be implicitly recovered. In the following section, the major components comprising the suggested building reconstruction system are explained. Afterwards, experimental results from topographic lidar data containing various types of building objects are discussed. Finally, we draw conclusions with recommendations for future work.

Proposed Method

Overview

The boundary of a building object with planar facets is decomposed into collections of more primitive elements (i.e., modeling cues) such as facets, edges, and vertices. A generic model of 3D buildings can be represented based on a combined topological and geometric description of the building object. Here, the topology of building models is obtained by recovering a set of relations that indicate how the faces, edges, and vertices are connected to each other, while the geometry can be specified by estimating appropriate geometric parameters (perimeter, intersecting angle, area, orientation, location, etc.) of modeling cues. The purpose of our research is to automatically model building objects by recovering both topological and geometrical relations across modeling cues, primarily relying on the information driven from lidar data only, but with minimal use of *a priori* knowledge on targeted building shapes. This data driven approach is more amenable to describing variants of building shapes than is the use of pre-specified model primitives. However, a scientific challenge in the data-driven technique may lie in a reliable grouping of modeling cues that are fragmented with unpredictable order. This fragmentation can be due to many reasons, including the noise inherited from the sensor, disadvantageous backscattering properties and object complexity. In order to resolve this problem, we suggest a unique framework for globally grouping incomplete features extracted from a given data space that yields successively finer approximations of the building object.

The method consists of four steps: (a) building detection, (b) point-wise clustering, (c) linear cue extraction, and (d) building rooftop reconstruction. The functional elements of the proposed building reconstruction system are schematically illustrated in Figure 2. The main purpose of the building detection process are to classify the lidar data into building and non-building points, and to provide coarse building models for individual building objects by bounding each isolated building region with a rectangle for the subsequent reconstruction processes. Two interesting low-level features, including plane clusters and linear features, are extracted in order to serve as modeling cues to delineate rooftop structures. The classified building points are clustered by the similarity criterion of either height (height cluster) or planar property (planar cluster). An edge is a significant local change in lidar data, usually associated with a discontinuity in either height (step line) or principal curvature (intersection line). The step lines are obtained by approximating the boundary shared with adjacent height clusters. On the other hand, the intersection of adjacent



planar clusters with different slopes produces intersection lines. As the coarse building shape (rectangle) is hierarchically sub-divided by the extracted linear features, convex polygons with more fine scales are produced. Finally, a geometric topology between adjacent polygons (i.e., planes) is reconstructed when all partitioned polygons are verified as building planes. This topology reconstruction is implemented by optimally controlling the generation of the Binary Space Partitioning (BSP) tree.

Extracting Initial Building Models

Our building reconstruction system starts to extract coarse building models from lidar data, which bound individual building regions by simple rectangles. These initial building models will be later partitioned to finer models that become closer to real building shapes. An important element to create the initial building models is to reliably isolate laser points that only belong to building objects from the ones located over non-building features. Rather than directly detecting building points (Filin, 2002), we followed a hierarchical focusing strategy (Baillard, 1999) where the targeted foreground objects (i.e., buildings) are detected by removing the background features including terrain and trees. The first step was to apply a model-based filtering algorithm to airborne lidar data (Sohn and Dowman, 2008),

in order to automatically identify laser points hit on the ground only. This technique was developed, in particular to allow a lidar filter to be self-adaptive to various landforms of different slopes. This terrain filter employed a tetrahedral model to generally represent a terrain surface with single slope (homogeneous terrain). A model-fitness between lidar points and the tetrahedral terrain model was measured in a framework of Minimum Description Length (MDL). In a coarse-to-fine scheme, this model-fitness scores triggered to recursively fragment a lidar DEM convolved with heterogeneous terrain slopes into piecewise homogeneous sub-regions where underlying terrain can be well characterized by the terrain model. Once these homogeneous terrains were obtained, the separation of non-terrain points from the ground can be simply made by a height threshold, as terrain characteristics over sub-regions are uniformly regularized. Then, the building points were retained by removing points over the tree objects from non-terrain points. In order to eliminate the tree points, (a) laser points showing large height difference between first and last returns were first removed, and (b) the connected component analysis was then applied to spatially clustered non-terrain points for investigating average height, boundary regularity, and surface smoothness. A non-point cluster is removed as the tree object if the aforementioned criteria are less than thresholds. After removing tree features from the non-terrain ones, individual buildings comprising only building points are bounded by the rectangles which will be feedback as initial building models to the following building reconstruction procedures.

Height Clustering

Since we aim to reconstruct 3D buildings with a mixture of multiple flat and sloped planes containing rooftop furniture, extracting modeling cues directly from an entire building may result in difficulties due to such a high degree of shape complexity. In order to reduce this complexity, lidar points collected for individual buildings are first decomposed into a set of clusters based on height similarity. A maximum height deviation for each point is measured from its neighboring points in a triangulated irregular network (TIN), which contributes to producing a height histogram of a certain bin size. After applying a simple moving box filter to the height histogram, a maximum height peak, δ_h , is automatically found from the histogram, within a height range between 1 m to 3 m. Similarly to a conventional region growing algorithm, lidar points are grouped in one height cluster if a height discrepancy between a point and those connected to it in a TIN is less than δ_h . As a consequence, the data domain R of lidar points P located over a building rooftop are divided into a set of height clusters $\{R_i; i = 1, \dots, N\}$ so that $R = \cup_{i=1}^N R_i$, $R_i \cap R_j = \phi$ if $i \neq j$, and P satisfies a homogeneity criterion on each R_i . Note that one height cluster may include several different planes or corresponds to only one plane if it is isolated from neighboring building parts in terms of height difference (Figure 3a). During the process, all of the cue extraction algorithms are independently applied to each height cluster (local process), but a building reconstruction based on locally collected cues will be conducted regardless of this height clustering result over the entire building region (global process).

Plane Clustering

This section describes a plane clustering process that segments lidar points into a set of clusters which uniquely represent planar surfaces. In current research, these planar cues play an important role in either extracting intersection lines or in optimally partitioning the data space, thereby reconstructing the rooftop topology across the extracted

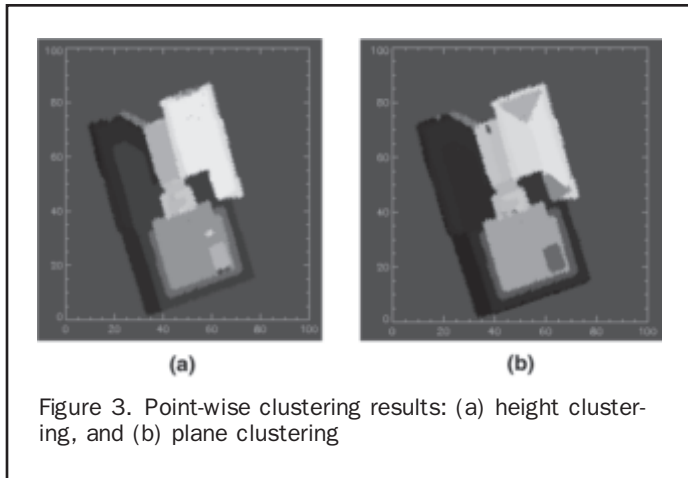


Figure 3. Point-wise clustering results: (a) height clustering, and (b) plane clustering

linear features. Thus, obtaining a reliable planar clustering result from lidar points is important. The implemented clustering process follows a hierarchical voting process in the parameter space discussed by Vosselman *et al.* (2004). In general, a three-dimensional plane passing through a point (x,y,z) in the data space can be represented by:

$$x \cos \alpha + y \cos \beta + z \cos \gamma = \rho \quad (1)$$

where (α, β, γ) is the plane normal vector angles measured between the plane and the x -, y - and z -axis, respectively, satisfying $\cos^2 \alpha + \cos^2 \beta + \cos^2 \gamma = 1$, and ρ is the distance of the plane from the origin of the coordinate system. The voting process quantizes the plane parameter $(\alpha, \beta, \gamma, \rho)$ in a discrete parameter space with certain bin sizes. The position of a particular bin in the parameter space uniquely represents a plane in the data space. The plane parameter locally estimated from the data space votes for a corresponding bin in the parameter space. Thus, by searching maximum peaks in the parameter space, the dominant planes passing through laser points of interest can be found (Vosselman *et al.*, 2004)

Rather than clustering the four plane parameters simultaneously, two separate parameter spaces for clustering (α, β, γ) , and ρ , respectively, are used in order to reduce the dimensions of the parameter space. The normal vector angles (α, β, γ) are computed for all the points using a conventional least squares method. An error of this local planar parameter estimation is measured by an orthogonal residual between the point and the plane estimated. Only for those points with an estimation error of less than 1 m, the normal vector angles are mapped in the parameter space with one unit. The maximum peak of (α, β, γ) is determined in the parameter space if the voting score is larger than a certain threshold. We collect neighboring points from the maximum peak, by which the average values of planar parameters can be determined from neighboring points, including maximum peak. The remaining parameter ρ for all points with a normal vector similar to the maximum is calculated by Equation 1 and is mapped to a one-dimensional parameter space. The maximum in this space determines the orthogonal distance of the plane from the origin. This process continues until all of the maximum peaks of the plane parameters can be found.

The previously mentioned plane clustering algorithm works on each height cluster independently. After assigning the plane parameters to the entire building, a plane adjacency graph is created for analyzing the connectivity of adjacent planes. The connected planes are merged if the

plane parameters $(\alpha, \beta, \gamma, \rho)$ are almost the same and are recomputed using all of the points of the merged plane. This plane merging process continues until no similar adjacent planes are found. Figure 3b shows a plane clustering result obtained when the presented method was applied to Figure 3a.

Step Line Extraction

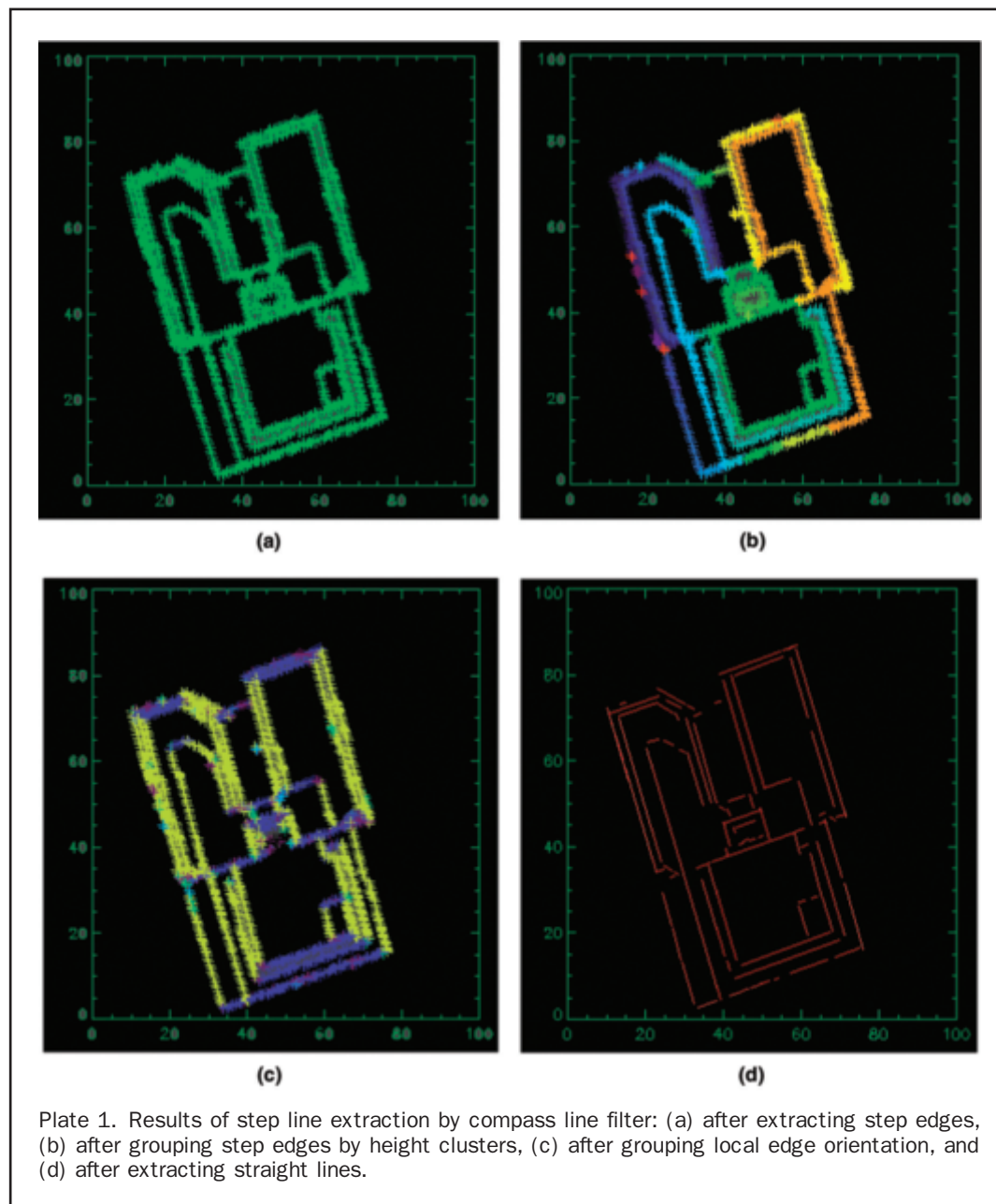
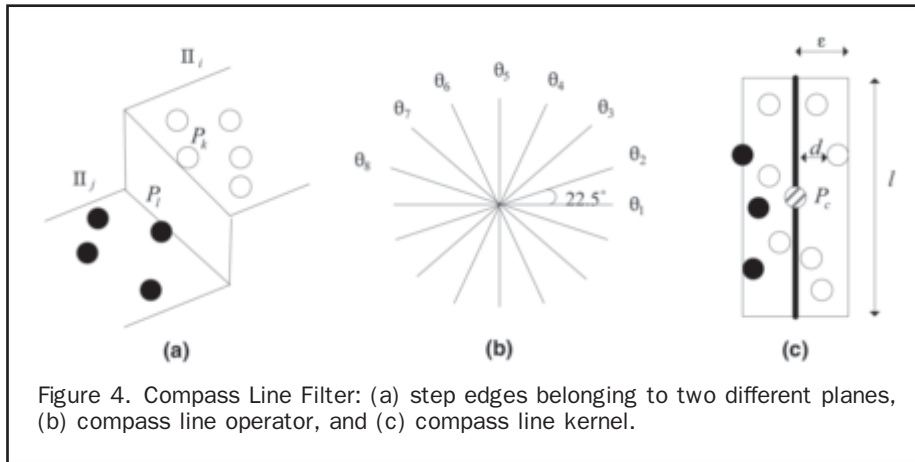
A step line is produced where the height continuity changes abruptly over rooftop surfaces. The line can be found around the building boundary or the rooftops of multiple story buildings where two planes are adjacent to each other, but with a large height discontinuity. As discussed by Vosselman (1999), compared to the optical sensors, extracting the step line by detecting the height discontinuity from lidar is not a trivial job due to the nature of discrete and irregular data acquisition. He suggested a sequential algorithm for extracting step lines from lidar data. After the connected component of the points on all roof surfaces is determined, the contour of this component is then approximated by step lines that are either parallel or perpendicular to the main building orientation. The method showed a successful result for reconstructing a row of houses with small sheds. However, it is limited to delineating only two directions, which are determined depending on the main building orientation. Obviously step lines with more than two directions are required in order to reconstruct complex buildings.

In the current experiment, we develop a step line extractor, called a Compass Line Filter (CLF), for extracting straight lines from irregularly distributed lidar points. The process starts to collect step edges, which are points showing abrupt height discontinuities relative to their neighborhoods in the TIN. Since the data R is already segmented into N height clusters $\{R_i\}_{i=1}^N$, the step edges can be simply collected by tracing all the boundaries where adjacent height clusters with different IDs share. However, as shown in Figure 4a, this process produces double step edges on the common border of two adjacent planes, (e.g., recognize P_k and P_l of planes Π_i and Π_j as step edges in Figure 4a). Since the proposed algorithm generates step lines by approximating the step edges contour, obtaining a thinner contour yields better approximation result. Thus, a thinning process is considered to a point P_c as the step edge if its neighboring points P_n belongs to more than one height cluster, and P_c is the member of the highest plane. This relation can be described by a signed height difference function, $H(P_c, P_n) = P_c - P_n$ as follows:

$$\left| \max_{\forall P_n} H(P_c, P_n) \right| > \left| \min_{\forall P_n} H(P_c, P_n) \right| \quad (2)$$

Once all the step edges are extracted (Plate 1a) and grouped by each height cluster (Plate 1b), the next step is to determine the local edge orientation for each step edge using a compass line filter. The local edge orientation provides directional information of the change of height discontinuity at a particular point. However, due to the nature of irregular data sampling, implementing a first-order of gradient operator to detecting height discontinuity from lidar is not as trivial as is using optical imagery with fixed pixel size.

We modified Kirsch's compass kernels, which can be applied to irregularly distributed point space. Instead of employing the gradient kernel with fixed size and gradient coefficients, we employ a compass line operator shown in Figure 4b) that has the whole set of eight filtering lines with different slopes $\{\theta_i; i = 1, \dots, 8\}$, each of which, as illustrated in Figure 4c, is equally separated in steps of 22.5° (the first compass line corresponds to the horizontal line). Each line has two virtual boxes (line kernel) where length l is the same as the one of line and width corresponding to ϵ .



Suppose that a height jump edge P_c belonging to a height cluster R_i is convolved with the whole set of eight line kernels. The local edge gradient is measured by the sum of distances d between the compass line θ_i and N kernel member points that are located within the line kernel K_i and belonging to R_i . A final local edge orientation θ^* is determined with the orientation of the kernel that yields the maximum local edge gradient. The values for the output orientation lie between one and eight, depending on which of the eight kernels had produced the maximum response. The computation of this local orientation for height jump edges is described by:

$$G(\theta_i) = \sum_{k=1}^N \frac{2}{1 + e^{\varepsilon \times d_k}}, \theta^* = \arg \max_{\forall \theta_i} (G(\theta_i)), i = 1, \dots, 8. \quad (3)$$

Once the local edge orientation is determined by the compass line operator, step edges with similar local edge orientation, belonging to the same height cluster, are grouped (Plate 1c). The local edge orientation angle is explicitly assigned by a pre-specified compass line filter. Finally, the real orientations for θ_i are newly determined by the well-known Hough transformation (Plate 1d).

Intersection Line Extraction

Once all of the planes are detected by the plane clustering process for each height cluster, the intersection lines are obtained by intersecting two adjacent planes. Thus, accuracy of the intersection line computation is subjective to the plane clustering result. The major problem of the plane clustering method presented in the previous section is that the process follows a *winner-take-it-all* approach, which does not take into account of a retro-validation in the hierarchical voting scheme. Suppose that we try to extract intersection lines over a simulated hip roof with certain amount of white noise (Figure 5a). If a plane Π_i is detected with higher scores, more numbers of points (white dots in Figure 5b) are clustered to Π_i (over-clustering), but less numbers of points (black dots in Figure 5b) are clustered to Π_j (under-clustering) with lower votes as the plane is later selected. In particular, this over- or under-clustering problem produces errors around the boundary as those points, for instance the ones inside dashed circle in Figure 5b, has similar height differences from both Π_i and Π_j . This clustering ambiguity leads to the mis-location of the intersection lines (Figure 5c). To avoid this problem, a post-validation process is conducted before extracting intersection lines. First, points located around the boundary between adjacent planes are collected, and then orthogonal distances from each boundary point to adjacent planes are measured. A true planar membership of the point is now determined by selecting the plane having the shortest distance measure of adjacent planes. This process continues until no boundary points change their planar membership. By re-estimating the result of planar clustering, more accurate intersection line computation can be obtained (Figure 5d).

Binary Space Partitioning

A key issue of modeling 3D building objects is to recover the geometrical and topological relations between adjacent planar or linear segments that are usually fragmented or missed. Instead of pre-specifying a set of explicit relations of adjacent features as *a priori* knowledge, this section employs the well-known data structure of the BSP tree as a mid-level feature grouping tool for object reconstruction.

The BSP is a method for recursively subdividing n -dimensional space into convex sets with homogeneous property by $(n-1)$ -dimensional hyperplane. A consequence

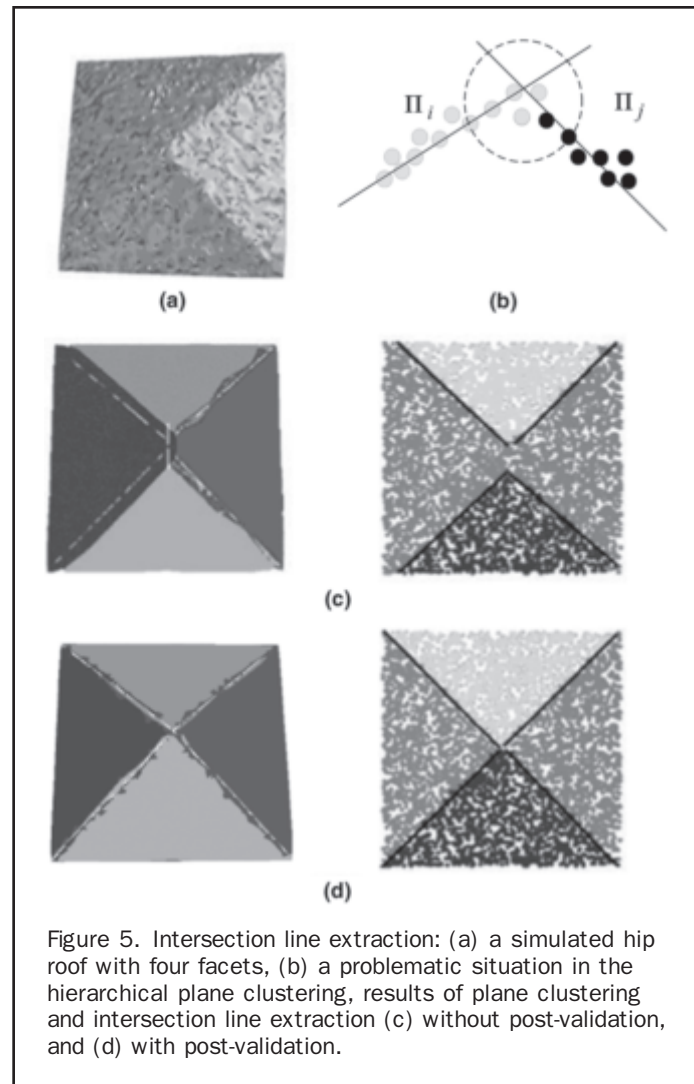


Figure 5. Intersection line extraction: (a) a simulated hip roof with four facets, (b) a problematic situation in the hierarchical plane clustering, results of plane clustering and intersection line extraction (c) without post-validation, and (d) with post-validation.

of this hierarchical subdivision is formulated as a representation of the complex spatial scene by means of a binary tree data structure. The BSP tree is a widely used representation of solid geometry, and is extremely versatile due to its powerful classification structure. The most traditional application of the BSP tree is in 3D computer graphics in order to increase rendering efficiency including solid modeling, hidden surface removal, shadow generation, visibility orderings, and image representation (Fuchs *et al.*, 1980; Gordon and Chen, 1991; Naylor, 1990). Instead of utilizing the tree structure as a pre-processor to store a virtual environment comprising polygonal solid models, Sohn and Dowman (2001 and 2007) has presented potentials of the BSP tree as an object reconstruction tool to produce prismatic models, either using monocular high-resolution satellite, or by combining it with airborne lidar data. The methods were successfully applied to urban city models, but limited to the reconstruction of building outlines with no detailed description of building rooftop structures. In this section, we further exploit the BSP tree for reconstructing complex rooftop models by involving new types of modeling cues including linear features and plane clusters comprising the shape of building rooftop. To deal with increased numbers of modeling cues with different properties, we investigate a new partitioning function and strategy to obtain the

optimality in the generation of the BSP tree. The BSP tree serves as a special data structure consisting of convex hierarchical decompositions of 3D lidar points. With this tree structure, a polyhedral building model is represented by the union of convex regions, which correspond to segmented planar roof-facets that are delineated by a rectilinear boundary with maximum response to real edges. In other words, the convex decompositions of the lidar space induced by the BSP method serve as a fusion framework for integrating area-features (i.e., planar clustering result) and edge-features (line extraction result) for representing the boundary of 3D building rooftops.

Figure 6 illustrates a general idea for the construction of the BSP tree. As discussed earlier, the rectangle bounding each building object is given as the initial building model P_0 . The entire member points of P_0 are labeled, shown by different colors in Figure 6, based on the planar clustering result. Both step and intersection lines $\{l_i\}$ extracted by the line detectors are formulated as the hyperlines $\{h_i\}$, each of which will be involved in the subdivision of the given building polygon, which is described by:

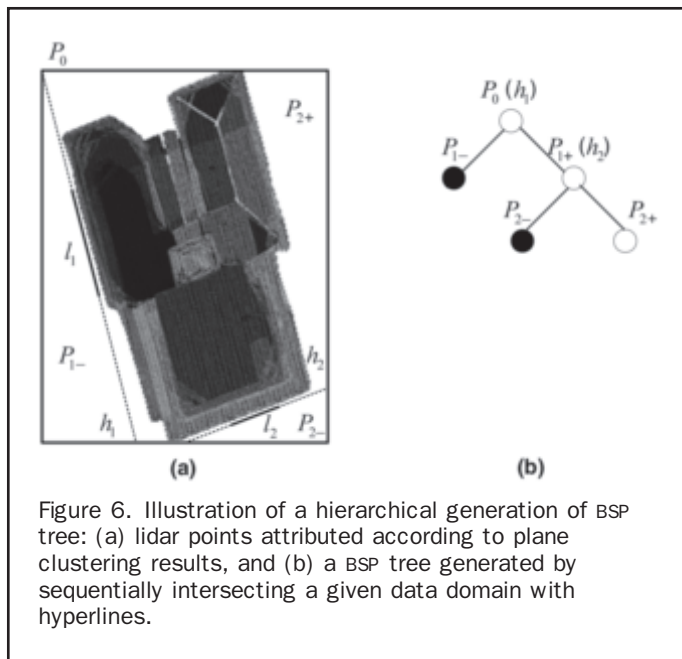
$$h_i(\rho_i, \theta_i) = \{(x, y) \in R \mid x \cos \theta_i + y \sin \theta_i - \rho_i = 0\} \quad (4)$$

where (ρ_i, θ_i) means the distance of the origin from a line segment l_i , and the slope angle measured between the edge normal and x-axis, respectively. A hyperline h_i is then chosen to halve planar clustered points into the positive and negative region, P_{i+} and P_{i-} such that at least one of the two polygons retains relatively higher planar homogeneity and more favorable geometric properties than the ones produced by the other hyperlines; more detailed criteria for the hyperline selection will be described later in this section. Each of sub-polygons is expressed by:

$$P_{i+}(h_i; \rho_i, \theta_i) = \{(x, y) \in R \mid x \cos \theta_i + y \sin \theta_i - \rho_i > 0\}$$

$$P_{i-}(h_i; \rho_i, \theta_i) = \{(x, y) \in R \mid x \cos \theta_i + y \sin \theta_i - \rho_i < 0\} \quad (5)$$

The normal vector of the hyperline h_i is defined by $(\cos \theta_i, \sin \theta_i)$. The positive polygon P_{i+} corresponds to the one that lies in the direction of the normal vector of l_i , the

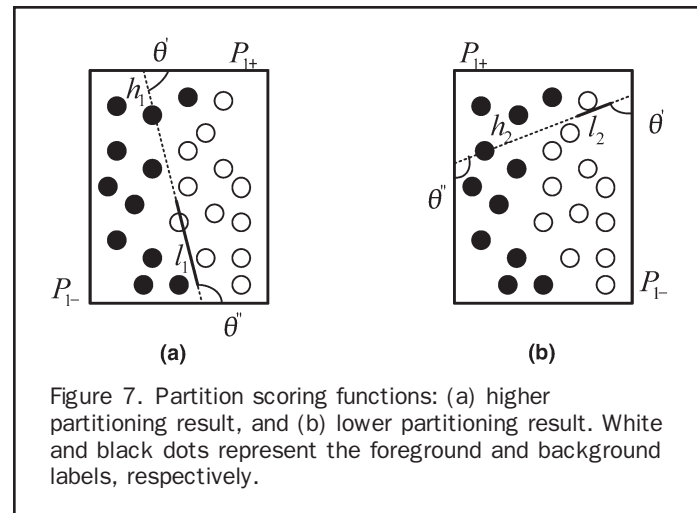


negative polygon P_{i-} is located in the opposite direction. A BSP tree is now constructed as the root node holds the hyperline h_1 , where all vertices comprising P_0 and the two sub-polygons are represented by leaf nodes. Each leaf of the BSP tree contains binary attributes, closed and open polygon, according to a degree of co-planar homogeneity over a given polygon. A convex region will be represented as the open polygon (node) in the BSP tree if, within the polygon, the member points are attributed with more than one planar cluster and also any part of the line segments is found; in other cases, the node will be attributed as the closed polygon. This node classification determines a triggering and terminating condition of the BSP over the node. That is, when a successive hyperline h_i is selected as presented in Figure 7, the line continues to partition an un-partitioned (open) polygon P_{i+} . However, the partitioning process will be terminated to a closed polygon P_{i-} . This process continues until no open leaf is generated by BSP.

The partitioning result will be different when a different sequence of line segments is employed. Thus, it is necessary to have the hyperline selection criterion which provides an optimal partitioning result over P_i . This optimality is achieved by the hypothesize-and-test scheme with a partition scoring function. The partitioning score for a hyperline h_i is measured by three criteria: (a) plane homogeneity, (b) geometric regularity, and (c) edge correspondence.

Plane Homogeneity

This criterion controls hierarchical generation of the BSP tree by maximizing the numbers of points with similar planar properties for partitioned polygons. Suppose that an arbitrary polygon P_i contains points with N different plane labels $L_p - \{L_i; i = 1, \dots, N\}$ by the plane clustering method presented in previous section. A representative plane label of P_i is determined as L_r to which maximum numbers of plane labels of P_i are assigned. The plane labels L_p are then binarized into either foreground label L_{fore} or background label L_{back} . A member point of P_i is labeled as L_{fore} if its plane label corresponds to L_r , otherwise as L_{back} . As an arbitrary hyperline h_i partitions P_i into two sub-polygons P_{i+} and P_{i-} , a higher score of the plane homogeneity is given for h_i if maximum labeling homogeneity of both L_{fore} and L_{back} is



obtained in each partitioned sub-polygon. This normalized strength of the plane homogeneity SH is measured by:

$$SH(P_i; h_i) = \max(SH(P_{i+}; h_i), SH(P_{i-}; h_i))$$

$$SH(P_{i+}; h_i) = \frac{1}{2} \left\{ \frac{N_{fore}(P_{i+}; h_i)}{N_{fore}(P_i; h_i)} + \frac{N_{back}(P_{i+}; h_i)}{N_{back}(P_i; h_i)} \right\}$$

$$SH(P_{i-}; h_i) = \frac{1}{2} \left\{ \frac{N_{fore}(P_{i-}; h_i)}{N_{fore}(P_i; h_i)} + \frac{N_{back}(P_{i-}; h_i)}{N_{back}(P_i; h_i)} \right\} \quad (6)$$

Edge Correspondence

A better partitioning result can be achieved when the boundary between two partitioned regions strongly corresponds to real edges. The strength of edge correspondence SE is measured by the ratio of lengths of a physical line l_i extracted from lidar data and the corresponding hyperline h_i . A higher score for the edge correspondence is assigned to h_i if a longer length of l_i is found in the polygon by

$$SE(P_i; h_i, l_i) = \frac{Length(l_i)}{Length(h_i)} \quad (7)$$

Geometric Regularity

Most building models have regular geometry (i.e., orthogonal, parallel, symmetric properly), rather than sharp corners. This heuristic preference on the geometric regularity SG is measured by the minimum intersecting angle between P_i and h_i . A lower score is given for h_i when h_i intersects P_i with sharper intersecting angles; scores increase as the minimum intersecting angle increases. Note that the intersecting angles are measured only for one of two child polygons of P_i which contains larger numbers of the foreground labels (Figure 7);

$$SG(P_i; h_i) = Ang(P_i; h_i)$$

$$Ang() = [0(0^\circ \leq \vartheta \leq 30^\circ), 0.5(30^\circ \leq \vartheta \leq 60^\circ), 1(60^\circ \leq \vartheta \leq 180^\circ)] \quad (8)$$

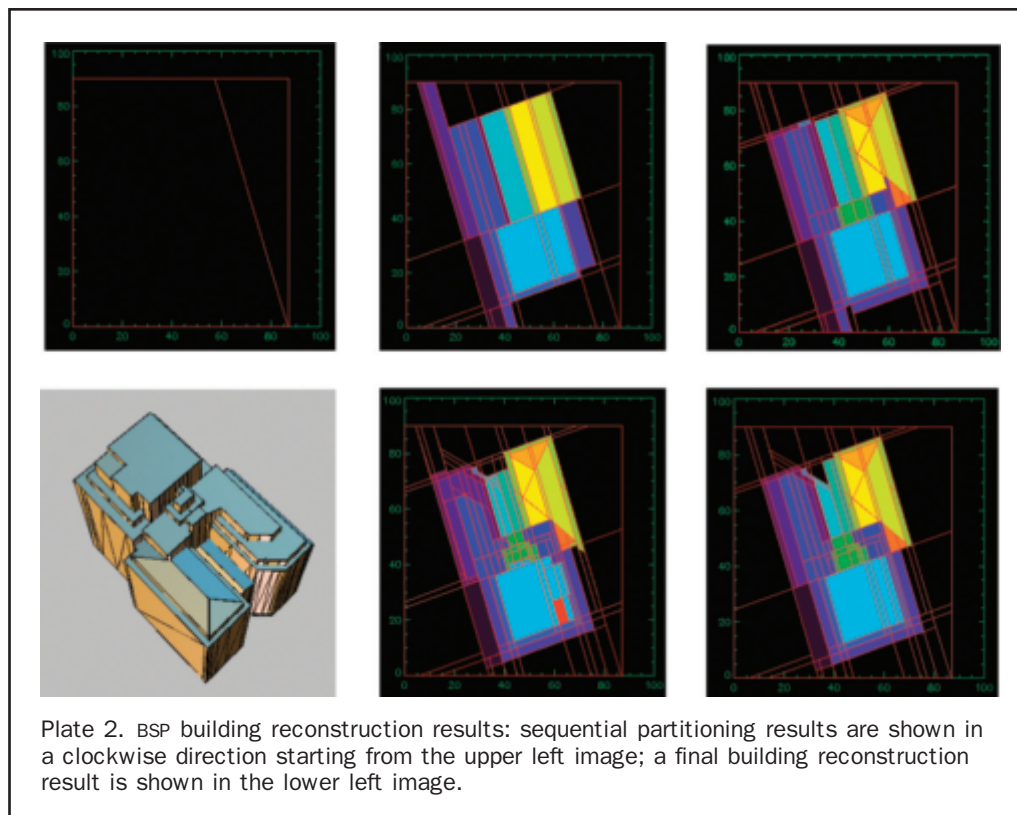
All the hyperlines are tested to partition P_i , and the partitioning result generated by each hyperline is evaluated by a partitioning scoring function. A hyperline, h^* , with the highest partitioning score is finally selected to partition P_i by:

$$h^* = \arg \max_{\forall(h)} (\alpha \times SH(P_i; h_i) + \beta \times SL(P_i; h_i, l_i) + \gamma \times SG(P_i; h_i)) \quad (9)$$

where $\alpha + \beta + \gamma = 1$ and usually (α, β, γ) is chosen as $(0.5, 0.3, 0.2)$, respectively. After constructing the BSP tree, a plane adjacency graph is created by collecting final leaves of the BSP tree where each node represents a planar roof-facet and each arc represents the connectivity between neighboring planes. Starting from the node with the largest area in the plane adjacency graph, a simple validation of normal vector compatibility is applied to its adjacent planes. The planes having similar normal vector angles are merged and planar parameters for merged planes are re-estimated. This merging process continues until no plane can be accepted by the co-planar similarity test. Once all polygons are merged together, building boundaries are reconstructed. Plate 2 shows a sequence of the building reconstruction results obtained by the presented method based on the BSP tree.

Experimental Results

In this section, we discuss and evaluate the performance of the building reconstruction technique we propose here. Figure 8a shows an elevation model over downtown Toronto. The data was acquired with an Optech Incorporated ALTM-2050 airborne laser scanner with a pulse



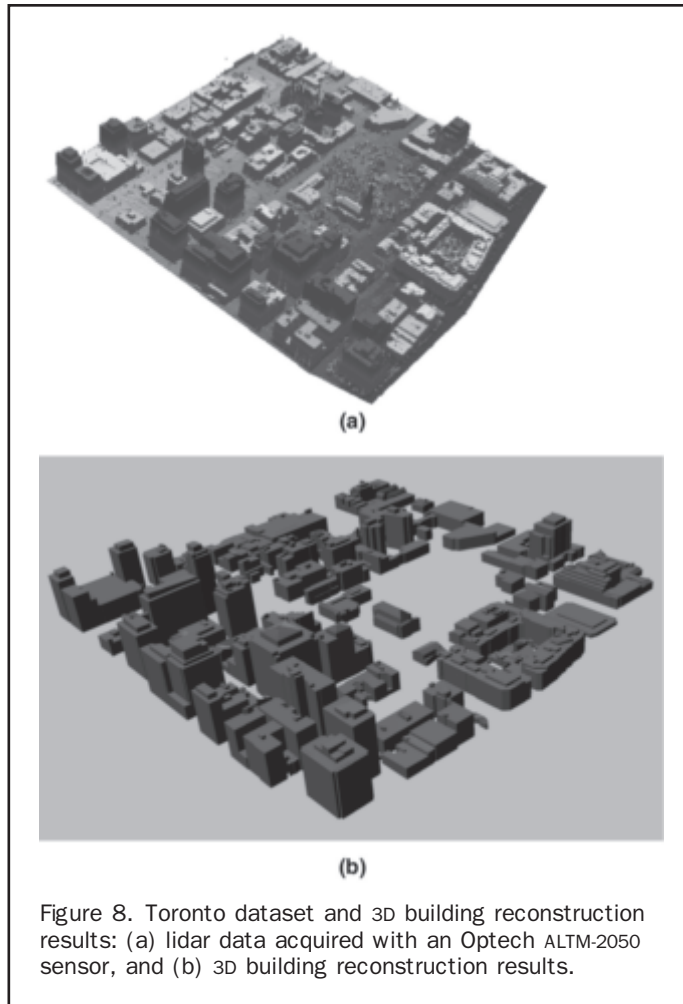


Figure 8. Toronto dataset and 3D building reconstruction results: (a) lidar data acquired with an Optech ALTM-2050 sensor, and (b) 3D building reconstruction results.

repetition rate of 50 KHZ at a flying height of 850 m above ground level. The Toronto test dataset covers approximately 1 km by 1 km where a total 2,741,684 laser points were acquired with a mean density of 2.74 points/m² (~0.6 m point spacing). According to the sensor and flight specifications, 0.43 m horizontal and 0.15 m vertical accuracies are expected. The overall elevation is almost flat, and the northern part of the data is slightly higher (approximately 100m) than the southern area. The test scene was chosen to include many buildings with different orientations and roof structures; consequently it is a good region to test our reconstruction algorithm.

Figure 8b shows a final result of 3D building reconstruction from the Toronto dataset based on the proposed method. As a prerequisite processing step for achieving the result of Figure 8b, all the building objects were isolated using the building detection procedure described in the previous section. As a consequence, a total of 53 buildings comprising 182,450 points were detected, each of which was bounded by an initial building model (i.e., rectangle). All the member points in each rectangle were attributed as non-building and building points, and were sequentially clustered by height similarity and planar similarity, through which step and intersection lines were extracted. As those initial models were hierarchically partitioned by extracted rectilinear lines, convex polygons representing roof-facets were produced with finer scales and rooftop models were reconstructed as similar roof-facets were merged. All of the parameters used for this experiment were described in the previous section.

In Figure 8b, a total of 529 roof-facets were reconstructed. Since the Toronto dataset includes buildings with a wide range of shape complexity, the number of roof facets reconstructed varies from one to 43 and an average of 10 planes per building with the standard deviation of 12.3 planes. Out of a total 182,450 points, 94.48 percent (172,378 points) were recognized as *planar* points by the planar clustering algorithm (i.e., representing a particular planar roof-facet), while 5.52 percent (10,072 points) were not clustered as the *planar* points, but were eliminated during the planar clustering process. Also, 87.7 percent (160,078 points) of the *planar* points were actually utilized for the final reconstruction of the roof-facets as the foreground points (those points are termed *pure planar* points), while 5.5 percent *planar* points (10,072 points), namely *impure planar* points, remained as the background points in under-partitioned roof-facets. We evaluated the overall *pure* accuracy of the roof-facet reconstruction by measuring the residual of the *pure* planar points from a plane reconstructed in the Root Mean Squared Error (RMSE). The *pure* plane reconstruction accuracy was measured as the mean $\mu = 0.38$ (m), and standard deviation $\sigma = 0.22$ (m).

The proposed algorithms were implemented and performed on a Desktop PC with a Pentium-4 processor at a clocked speed of 2.40 GHZ and with 512 MB RAM. We attempt to evaluate the efficiency of our method by measuring the total time consumed in reconstructing the entire test scene. The execution time of building reconstruction on this platform was a total of 461.1 seconds, which corresponds to 8.5 seconds per building. The most of buildings (79 percent buildings) were reconstructed in less than 10 seconds, while the maximum execution time reached to 85.3 seconds over a building, with the largest area of 8,270 m² and the maximum number of planes (43 planes). Note that this figure does not include all the time taken for building detection. (Figure 9a)

Since the ground truth of 3D building rooftops was not available over the test site, an absolute comparison of reconstruction accuracy between the ground truth and reconstructed polygons was not possible. Thus, we examined the accuracy of the building reconstruction results in two relative measures, by measuring the residuals of the *impure planar* points from a reconstructed plane (*impure planar fitness*) and the ratio of the number of the *impure planar* points against the total numbers of *pure planar* points in a roof-facet reconstructed (*planar impurity*). This plane reconstruction accuracy cannot estimate in an absolute scale the geometric accuracy and the topological consistency of the reconstructed roof polygons. However, these measures can indirectly indicate an overall quality of the reconstruction performance, in a sense that lower residuals, and a lower ratio of *impure planar* points can be achieved as the roof polygons are reconstructed by maximizing the planar homogeneity, and thus with the minimum numbers of the *impure planar* points. If the reconstructed building model does not preserve original building boundaries or misses some part of building structures, more numbers of the *impure planar* points are produced and thus, both measurements are increased. Figure 9b and 9c shows histograms of the measurements of the *impure planar fitness* and the *planar impurity* respectively. The RMSE of the *impure planar fitness* for all the buildings was measured as 1.1 m, and $\sigma = 1.2$ m, while the average ratio of the *planar impurity* was measured as 5.1 percent with $\sigma = 4.4$ percent. As described earlier, the amount of the *impure planar points* increases both measures. It was observed that most of the *impure planar points* were produced around roof boundary regions where adjacent roof-facets were not correctly delineated by reconstructed models due to geometrically erroneous hyperlines or over roof-facets which were under-partitioned due to a lack

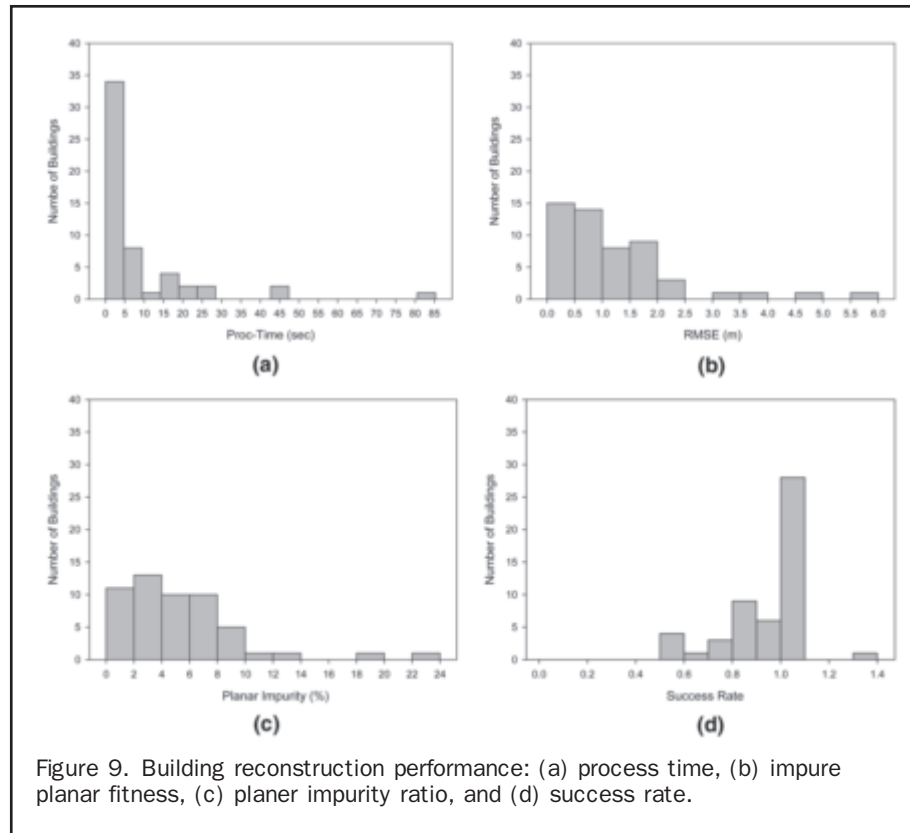


Figure 9. Building reconstruction performance: (a) process time, (b) impure planar fitness, (c) planer impurity ratio, and (d) success rate.

of hyperlines extracted. A large *impure planar fitness*, higher than 3 m, were found over four buildings as planar roof-facets comprising those buildings are connected each other with large height differences.

Finally, we also evaluated the reliability of our building reconstruction system by comparing the number of automatically reconstructed roof-facets to the one that was manually counted. The success rate of the algorithm is defined by:

$$R = 1 - \frac{N_t - N_r}{N_t} \quad (10)$$

Here, N_r is the total number of planes reconstructed by our method, and N_t is the total number of planes that are visually found by a human operator. In the tests, accuracy is only judged by the human operator with a comparison to the manual results. The success rate R will be larger than 1 if the algorithm over-reconstructs building roof-facets, but is less than 1 if roof-facets are under-reconstructed by the method. A perfect success rate of 1 will be achieved if no roof plane is missed by our method, but R will be 0 if the algorithm cannot reconstruct any roof-facet at all. Figure 9d shows the statistical result of the test of the reliability of the automatic building reconstruction method. The success rate R is measured as $\mu = 0.92$ ($\mu_{\min} = 0.5$ and $\mu_{\max} = 1.3$) with $\sigma = 0.2$. The experiments indicate a great potential for the developed method for practical GIS data production. This suggests that when a building is comprised of 10 roof-facets, our method fails to reconstruct one plane. As seen in the figure, the algorithm tends to under-reconstruct building rooftops, rather than over-reconstruct the models. It has been visually confirmed that the over-reconstruction of building models occurred in cases when either a small flat roof or super-structure was hard to distinguish in

height from the neighboring large-area planes during the height clustering process; or step lines, usually having a short length of 1 m to 3 m, could not be detected by the edge detector due to high irregular density of lidar data.

In Figures 10, 11, and 12, we visualized several examples of 3D buildings that had been reconstructed in order to discuss the characteristics of the proposed building reconstruction system. Table 1 shows the information of presented buildings and reconstructed models. The most of prismatic buildings with single flat roofs were reconstructed with the highest performance. For instance, two buildings in Figure 10 show a simple "T" and a rectangular shape. A slightly higher performance in the planar fitness and the planar impurity was measured for the building in the second row of Figure 10b in which there are more numbers of roof super-structures. It was confirmed that most of the prismatic buildings with one or two planar roof facets show a similar level of planar fitness and impurity. This is because low-level modeling cues of planar clustering and linear features can be extracted with higher quality (i.e., less fragmentary or missing levels with higher geometric accuracy). It is worthwhile to point out that the developed reconstruction method can deal with irregular deficiency of laser-scanning acquisition. It was observed that there are many regions occluded by building objects so that lidar data are missing near to the building roof boundary. As seen in the second row of Figure 10b, the left-hand side of the building in the lidar data was a little intruded from the original rectangular shape since the lidar data were missing due to the occlusion effect. Nevertheless, there were no missing parts in 3D building model reconstructed. This is one of the advantages as the reconstruction algorithm is directly applied to irregular points, rather than to the gridded format.

In Figures 11 and 12, the buildings show more complicated shapes than in Figure 10, where several building primitives are horizontally or vertically connected to each other. It is

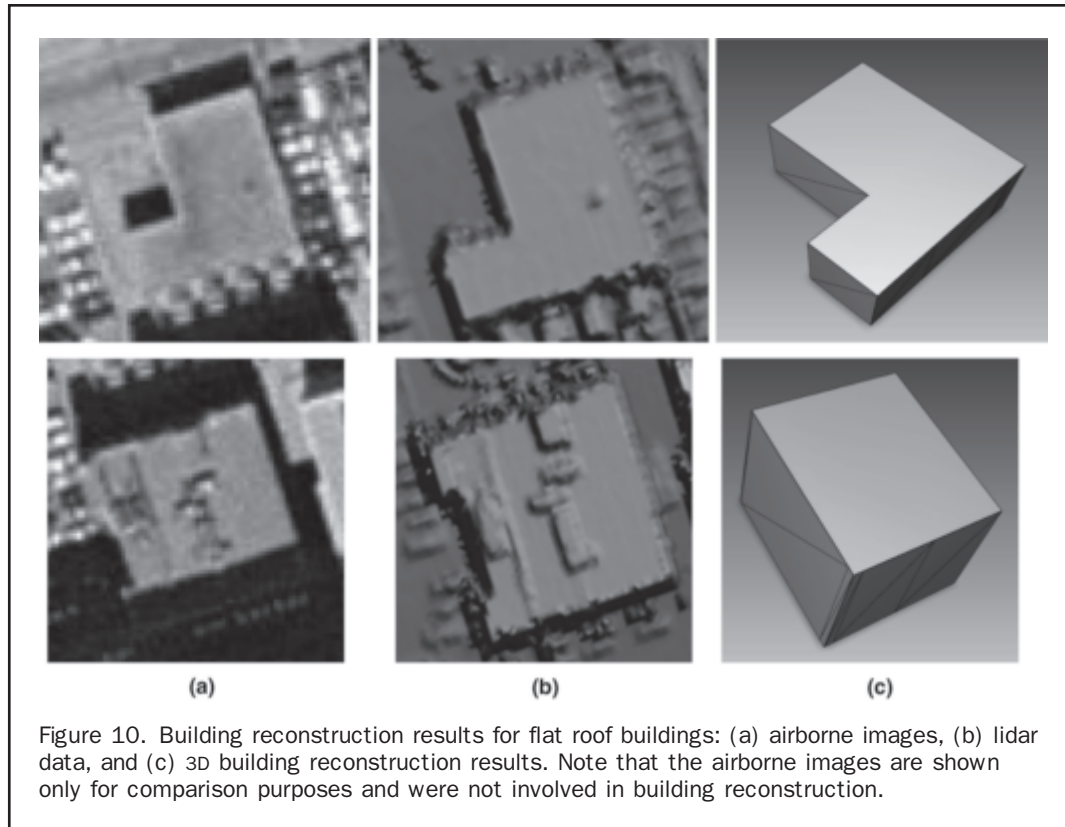


Figure 10. Building reconstruction results for flat roof buildings: (a) airborne images, (b) lidar data, and (c) 3D building reconstruction results. Note that the airborne images are shown only for comparison purposes and were not involved in building reconstruction.

evident that all of the buildings in the figures contain large amounts of data acquisition errors due to the small coverage. These errors may make it difficult to recognize some of the rooftop structures and sharp boundaries. Although the shape complexity and data irregularity have increased, Figures 11 and 12 showed that the overall quality of the reconstruction result based on the proposed technique is satisfactory, and that the reconstructed models effectively preserve the original geometry. In fact, 3D structures of the buildings presented in these figures were not very easily interpreted by visual investigation, either from the optical imagery or lidar data. Also the reconstruction results were achieved without requiring *a priori* knowledge of specific building models or of the topological relations between adjacent planes. Thus, it can be concluded that the developed techniques would be useful to quickly provide an initial, yet fine rooftop model with very high shape complexity. However, it is also evident that the reconstructed models are not perfect. As seen in the first row of Figure 11, details of the structures around the corners were lost and most of them were generalized too much as rectangular corners. Also, a super-structure in the middle of the building was wrongly reconstructed, although the original shape of this structure is not certain, even by visual investigation. Those problems may be caused by a significant lack of point density covering those particular regions, which results in missing linear features.

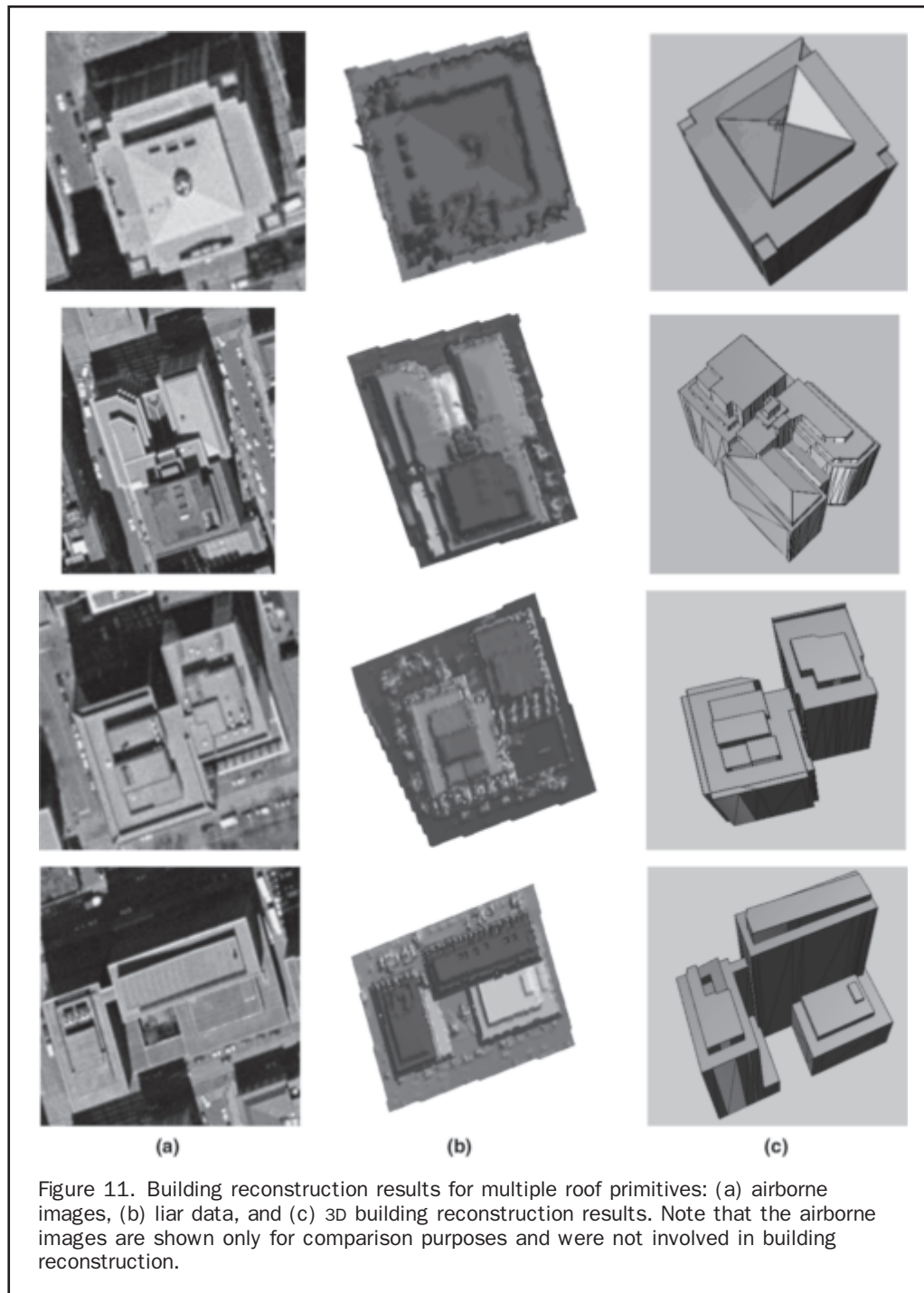
Summary and Conclusions

We have proposed and presented a new algorithm for automatic 3D reconstruction of building rooftops from airborne lidar data. In the current research, this task has been achieved through the development of a unique data-driven framework that employs the BSP tree algorithm. The BSP-based method was used to reconstruct polyhedral building models by implicitly grouping fragmentary linear features

between adjacent roof-facets. The results show that the method can represent highly complicated building structures, where multiple building primitives are horizontally and/or vertically connected with, and occluded from, each other. Starting from a coarse description, the developed techniques incrementally refine the model at different modeling scale by maximizing the co-planarity, edge correspondence and geometric regularity. By this nature of global optimization, the system can simultaneously reconstruct a large number of connected roof-facets, but does not require a local analysis of the primitive connectivity between adjacent facets that are independently generated. These characteristics are the most beneficial compared to existing model-driven techniques which may suffer difficulties under these circumstances. Another advantage of BSP algorithm, which has not been studied yet in current analysis, is the ability to combine a search structure with a representation scheme into one unique data structure. For instance, a building model can be represented in a different scale, i.e., by controlling the depth of BSP tree. This useful property can be further exploited for generalizing building shapes according to the level of detail (LoD). Due to the irregular nature of laser scanning and building occlusion problems, it is usually difficult to provide a complete set of linear features for representing building models from lidar data. The proposed BSP algorithm provides an alternative approach to the traditional feature grouping approaches to overcoming the difficult problem of when linear features are fragmented into an unpredictable order.

Although the method was successfully applied for reconstructing buildings from lidar, there are still some drawbacks that indicate our future work could be extended in order to improve the method:

- The modeling accuracy of roof-facets reconstructed based on our method is mainly subject to the extraction quality of linear features. Improper location of extracted linear features leads to unsatisfactory or erroneous results. Also, some parts



of building shapes are under-modeled if linear features over those regions are not detectable. During the current experiments, these problems have been observed over the region where the irregularity of point density is so high that some parts of buildings are not well represented by the laser acquisition. One solution to the problem is to devise a compensatory process for recovering missing features of interest by partly combining additional geometric information driven from specific building models. For instance, a hypothetical prediction of symmetrical shape can locate a new conjugate line feature as suggested by Sohn and Dowman (2007).

- In general, height clustering is effective for decomposing a group of connected buildings into simpler regions where the

complexity of planar clustering problems can be reduced. However, as discussed in the previous section, we observed that some small flat roof-facets were not isolated from adjacent ones using this process. This problem is due to the height difference of those roof-facets from the entire building is too weak to be detected by a pre-fixed bin size of the height histogram. As a consequence, 3D roof modeling over those regions fails, which decreases the success rate. To deal with these problems, we need to develop a more adaptive algorithm for the height clustering to varying heights. This will help in reconstructing more building structures with small scales.

- In the current experiment, a geometric regularization has been devised by quantizing line slopes in a limited number

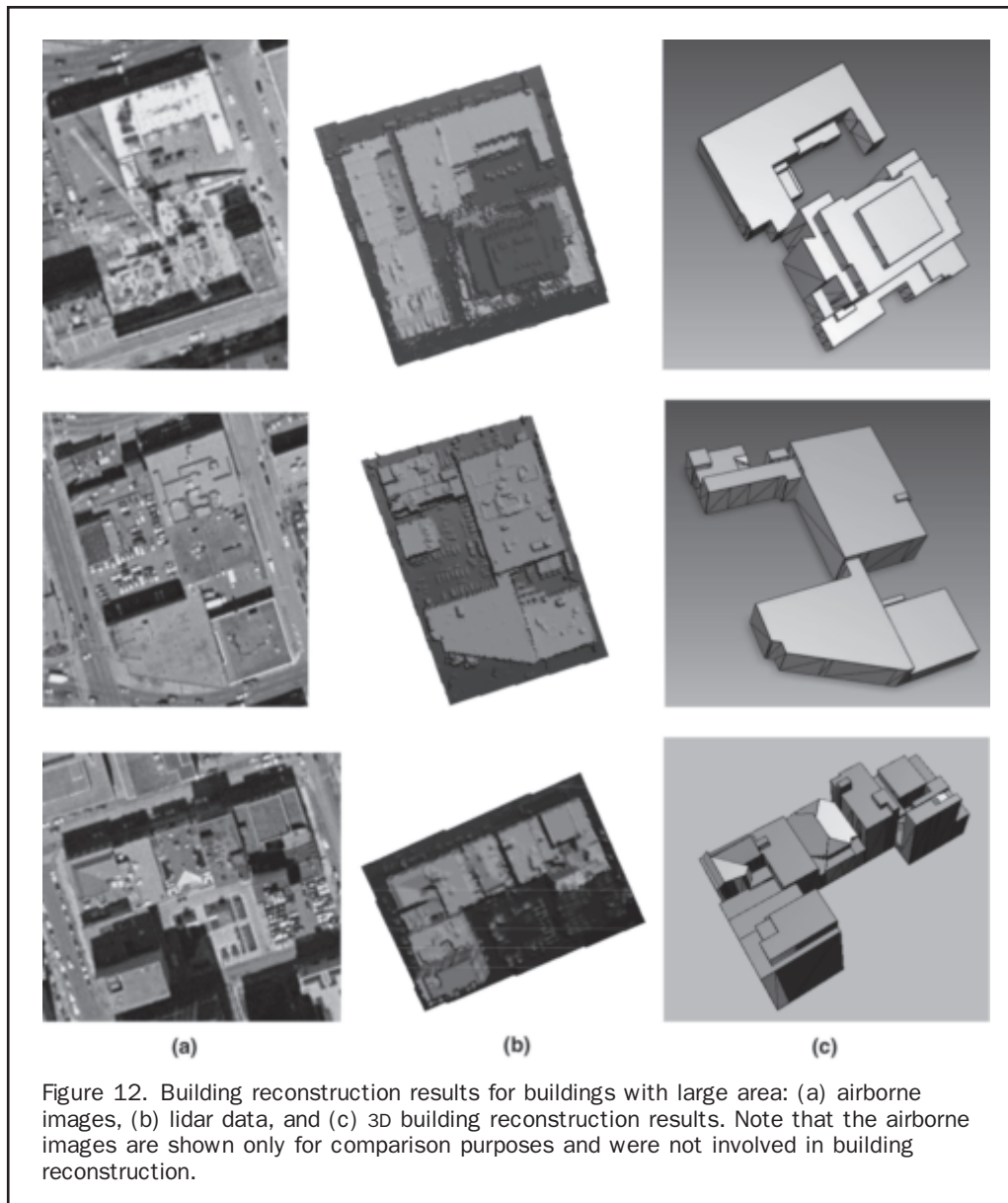


Figure 12. Building reconstruction results for buildings with large area: (a) airborne images, (b) lidar data, and (c) 3D building reconstruction results. Note that the airborne images are shown only for comparison purposes and were not involved in building reconstruction.

of angular ranges during the early stage of feature extraction. However, incorrect reconstruction of building models with irregular and sharp corners was still present in current experiments in case that a few erroneous lines were inevitably involved in the BSP partitioning process. Thus, a future research direction towards this problem, a post-processing procedure to refine data-driven models produced by BSP by combining parametric models will be conducted.

References

- Alharthy, A., and J. Bethel, 2004. Detailed building reconstruction from airborne laser data using a moving surface method, *International Archives of Photogrammetry and Remote Sensing*, 35(Part B3):85–92.
- Ameri, B., 2000. *Automatic Recognition and 3D Reconstruction of Buildings from Digital Imagery*, Ph.D. dissertation, Institute of Photogrammetry, University of Stuttgart, 110 p.
- Baillard, C., and H. Maitre, 1999. 3D reconstruction of urban scenes from aerial stereo imagery: A focusing strategy, *Computer Vision and Image Understanding*, 76(3):244–258.
- Brenner, C., 2000. Towards fully automatic generation of city models, *International Archives of Photogrammetry and Remote Sensing*, 33(Part B3):85–92.
- Brenner, C., and N. Haala, 1998. Fast production of virtual reality city models, *International Archives of Photogrammetry and Remote Sensing*, 32(4):77–84.
- Brenner, C., 2005. Building reconstruction from images and laser scanning, *International Journal of Applied Earth Observation and Geoinformation*, 6(3–4):187–198.
- Chen, S., and D. Gordon, 1991. Front-to-back display of BSP trees, *IEEE Computer Graphics and Applications*, 11(5):79–85.
- Filin, S., 2002. Surface clustering from airborne laser scanning data, *International Archives of Photogrammetry and Remote Sensing*, 34(Part 3):119–124.
- Fuchs, H., Z.M. Kedem, and B.F. Naylor., 1980. On visible surface generation by a priori tree structures, *Computer Graphics*, 14(3):124–133.
- Hofmann, A.D., 2004. Analysis of TIN-structure parameter spaces in airborne laser scanner data for 3-D building model generation, *International Archives of Photogrammetry and Remote Sensing*, 35(B3):302–307.

TABLE 1. BUILDING RECONSTRUCTION PERFORMANCE

| | Area (m ²) | Nr | Nt | Impure Planar Fitness | Planar Impurity | Success Rate (R) |
|------------|------------------------|----|----|-----------------------|-----------------|------------------|
| Figure 10a | 279.63 | 1 | 1 | 0.0967 | 0 | 1 |
| Figure 10b | 526.73 | 1 | 2 | 0.6684 | 0.1030 | 0.5 |
| Figure 11a | 2,116.59 | 10 | 10 | 0.9504 | 4.5141 | 1 |
| Figure 11b | 3,269.09 | 23 | 25 | 1.9776 | 13.6801 | 0.92 |
| Figure 11c | 3872.45 | 9 | 9 | 4.6757 | 9.2088 | 1 |
| Figure 11d | 2,329.86 | 16 | 14 | 0.8770 | 2.5537 | 0.88 |
| Figure 12a | 3,486.09 | 15 | 18 | 3.1449 | 3.3127 | 0.83 |
| Figure 12b | 5,794.29 | 15 | 11 | 0.6208 | 2.3137 | 0.80 |
| Figure 12c | 4,329.66 | 38 | 42 | 2.2703 | 7.3140 | 0.91 |

Hu, Y., 2003. *Automated Extraction of Digital Terrain Models, Roads and Buildings Using Airborne Lidar Data*, Ph.D. dissertation, University of Calgary, Calgary, Alberta, 206 p.

Maas, H.-G., and G. Vosselman, 1999. Two algorithms for extracting building models from raw laser altimetry data, *ISPRS Journal of Photogrammetry and Remote Sensing*, 54(2-3):153-163.

Rottensteiner, F., J. Trinder, S. Clode, and K. Kubik, 2005. Using the Dempster-Shafer method for the fusion of LIDAR data and multi-spectral images for building detection, *Information Fusion*, 6(4):283-300.

Schwalbe, E., H.-G. Maas, and F., Seidel, 2005. 3D building model generation from airborne laser scanner data using 2D GIS data and orthogonal point cloud projections, *International Archives of Photogrammetry and Remote Sensing*, 36(Part 3/W19):209-214.

Sohn, G., and I.J. Dowman, 2001. Extraction of buildings from high resolution satellite data, *Automatic Extraction of Man-Made Objects from Aerial and Space Images (III)* (A. Grün, E.P. Baltsavias, and O. Henricsson, editors), Balkema Publishers, Lisse, pp. 345-356.

Sohn G., and I. Dowman, 2007. Data fusion of high-resolution satellite imagery and lidar data for automatic building extraction, *ISPRS Journal of Photogrammetry and Remote Sensing*, 62(1):43-63.

Sohn, G., and I. Dowman, 2008. A model-based approach for reconstructing terrain surface from airborne LiDAR data, *The Photogrammetric Record*, 23(122):170-193.

Suveg, I., and G. Vosselman, G., 2004. Automatic 3D reconstruction of buildings from aerial images, *ISPRS Journal of Photogrammetry and Remote Sensing*, 58(3-4):202-224.

Vosselman, G., 1999. Building reconstruction using planar faces in very high density height data, *International Archives of Photogrammetry and Remote Sensing*, 32(Part 2):87-92.

Vosselman, G., and S. Dijkman, 2001. 3D building model reconstruction from point clouds and ground plans, *International Archives of Photogrammetry and Remote Sensing*, 33(3/W4):37-44.

Vosselman, G., B.G.H. Gorte, G. Sithole, and T. Rabbani, 2004. Recognising structure in laser scanner point clouds, *International Archives of Photogrammetry and Remote Sensing*, 36(8/W2):33-38.

Weidner, U., and W. Förstner, 1995. Towards automatic building reconstruction from high resolution digital elevation models, *ISPRS Journal of Photogrammetry and Remote Sensing*, 50(4):38-49.

(Received 29 January 2007; accepted 11 May 2007; revised 06 September 2007)

Certification Seals & Stamps

- Now that you are certified as a remote sensor, photogrammetrist or GIS/LIS mapping scientist and you have that certificate on the wall, make sure everyone knows!
- An embossing seal or rubber stamp adds a certified finishing touch to your professional product.
- You can't carry around your certificate, but your seal or stamp fits in your pocket or briefcase.
- To place your order, fill out the necessary mailing and certification information. Cost is just \$35 for a stamp and \$45 for a seal; these prices include domestic US shipping. International shipping will be billed at cost. Please allow 3-4 weeks for delivery.

SEND COMPLETED FORM WITH YOUR PAYMENT TO:

ASPRS Certification Seals & Stamps, 5410 Grosvenor Lane, Suite 210, Bethesda, MD 20814-2160

| | | | |
|--|--------------|--------------------|----------------|
| NAME: _____ | | PHONE: _____ | |
| CERTIFICATION #: | | EXPIRATION DATE: | |
| ADDRESS: _____ | | | |
| CITY: _____ | STATE: _____ | POSTAL CODE: _____ | COUNTRY: _____ |
| PLEASE SEND ME: <input type="checkbox"/> Embossing Seal..... \$45 <input type="checkbox"/> Rubber Stamp..... \$35 | | | |
| METHOD OF PAYMENT: <input type="checkbox"/> Check <input type="checkbox"/> Visa <input type="checkbox"/> MasterCard <input type="checkbox"/> American Express | | | |
| CREDIT CARD ACCOUNT NUMBER _____ | | EXPIRES _____ | |
| SIGNATURE _____ | | DATE _____ | |

Celebrating 75 Years



This celebration would not be happening in 2009 if 12 men, led by Col. Claude Birdseye, had not met in July 1934 in Washington, D.C. to discuss forming a photogrammetric society in the United States that came to be called The American Society of Photogrammetry (ASP). The Society founders represented the U.S. Corps of Engineers, U.S. Forest Service, U.S. Geodetic Survey, U.S. Geological Survey, U.S. Soil Erosion Service, Fairchild Aerial Survey and W.N. Brown, Inc. Most of these agencies and companies and their successors are still driving forces of the Society today.

The founders' vision for this organization included, a newsletter that would discuss photo mapping activities in the U.S. and abroad and furnish members with a means of communication. *PE&RS*, an outgrowth of the early newsletter, continues today as a top journal in the scientific world. Another goal of the newly founded Society was periodic meetings of members that would provide an opportunity to meet and know those interested in the same subjects and promote a frank exchange of opinions. Again, this objective continues to be met with the annual and fall conferences. The recently instituted "Hot Topics" segment at the annual conference harkens back to the founding fathers ambition of a "frank exchange of opinions."

In the early years of 1934-1935, the ASP boasted 354 members. Due to this ever evolving field, in the late 1980s the ASP Board of Directors agreed to a name change for the organization, incorporating the words "Remote Sensing" to become the American Society for Photogrammetry and Remote Sensing (ASPRS). Today ASPRS boasts more than 6,000 members who continue to carry the same strong dedication to the profession that the founders had 75 years ago.

ASPRS proudly celebrates its 75th Anniversary throughout 2009, with special events taking place at the 2009 Annual Conference in Baltimore.

The ASPRS 2009 Annual Conference *Reflection of the Past, Vision for the Future* will be held March 9-13, 2009 at the Baltimore Marriott Waterfront Hotel at Baltimore, Maryland's Inner Harbor.

This conference will have an outstanding set of technical presentations on all aspects of imaging and geospatial information. Following the theme of the conference, *Reflection of the Past, Vision for the Future*, we will feature sessions on the evolution and future of geospatial data collection, processing and analysis, and information derivation in ways that are useful in making local, national and global decisions, whether it is for homeland security, resource management, business, or other purposes.

For more information on exhibiting, advertising, or sponsoring an event, contact

Jim Perrus
The Townsend Group
7315 Wisconsin Avenue, Suite West 750
Bethesda, MD 20814
(301) 215-6710 ext. 107
(301) 215-7704 Fax
asprs@townsend-group.com

"Come and be a pixel!"



In preparation for the celebration, more than 400 attendees at the ASPRS 2008 Annual Conference in Portland gathered for this photograph. "Come and be a pixel!" said in-coming President, Kass Green, President, The Alta Vista Company.

We invite you to join us for the Celebration! Come and be part of history as ASPRS turns 75-years old.

Bergman Photographic Services, Inc. donated their services to fly over and take the image.

Classifieds

For Sale:

FOR SALE: IMA analytical stereoplotter, ABC setup software, (2) computers. Best offer. Buyer to pay for shipping. Call 530-582-8499.

Complete DITEM Summit Evolution w/Autocad 2006, Survcadd, Dell XEON Computer, monitors, Z-screen, Stealth Mouse, etc. - \$22,000 - 770-722-8459

Who Do I Contact to Advertise with ASPRS?

5410 Grosvenor Lane, Suite 210
Bethesda, MD 20814
301-493-0290, 301-493-0208
(fax), www.asprs.org

Calendar
x107, calendar@asprs.org

Exhibit Sales
301-215-6710,
asprs@townsend-group.com

Meeting Information
x106, meetings@asprs.org

PE&RS Advertising
301-215-6710,
asprs@townsend-group.com

Positions Wanted:

Assistant Professor: Remote Sensing/GIS (Job #7435)

Humboldt State University, Arcata, California, seeks applications for a full time (academic year) tenure track Assistant Professor starting August 2009.

Ph.D. in Forestry, Natural Resources, or related field, with specialization in remote sensing and GIS from an accredited university, is required prior to the start of the subsequent probationary year following initial appointment. Additional expertise in spatial statistics is desirable.

This position is open until filled; first consideration will be given to applications received no later than November 17, 2008. Early response is encouraged.

For the full vacancy announcement and application instructions please visit: <http://www.humboldt.edu/~aps/employment/tenure.html>.

Humboldt State University employs only individuals authorized to work in the United States. HSU is an EO/Title IX/ADA employer.

ASPRS Meeting Schedule

Save the dates!!!

ASPRS 2009 Annual Conference

75th Anniversary of ASPRS

March 8 – 13, 2009

Baltimore Marriott Waterfront Hotel, Baltimore, Maryland

ASPRS/MAPPS 2009 Fall Conference

November 16 – 19, 2009

Crowne Plaza Hotel, San Antonio, Texas

ASPRS 2010 Annual Conference

April 26 – 30, 2010

Town and Country Hotel, San Diego, California

ASPRS 2011 Annual Conference

May 1 – 5, 2011

Midwest Airlines Center/Hyatt Hotel, Milwaukee, Wisconsin

Check www.asprs.org for updates and important program information.

Is your contact information current?

Contact us at members@asprs.org or log on to <https://eserv.asprs.org> to update your information.

We value your membership.

See your Ad HERE

Each year, more and more businesses of all sizes realize that PE&RS advertising gets results. The reason is simple: people look to PE&RS on a regular basis to find the latest and best products and services.

Jim Perrus
to discuss your
advertising needs.

301-215-6710x107

(fax) 301-215-7704

asprs@townsend-group.com

PE&RS BACK ISSUES SALE

- **2002-2007: ANY SET OF 12 ISSUES** \$150
For USA Addresses (postage included)
Non-USA Addresses Add \$60 for postage.

- **ANY 2006/2007 SPECIAL ISSUE/
RESOURCE DIRECTORY** \$30

- **OTHER SINGLE ISSUES (2002-2006)** \$10

- **OTHER SINGLE ISSUES (2006-2007)** \$25

Add \$5.00 postage per issue for Non-USA addresses.

GST is charged to residents of Canada only (GST #135123065). Tax is calculated at 6% x (subtotal + shipping charges).

Availability: 2002 – 2007

Some individual issues are out of print.

TO ORDER, CONTACT:

ASPRS Distribution Center
301-617-7812, 301-206-9789 (fax)
asprspub@pmds.com

VISA, MasterCard, and American Express are accepted.

Professional Directory

ALABAMA

SOUTHERN RESOURCES MAPPING CORPORATION
 2884 MCFARLAND BOULEVARD
 NORTHPORT, ALABAMA 35478
 PHONE: (205) 333-8900
 FAX: (205) 333-8915
 WEB: www.srmcorp.com
 EMAIL: srmc@srmcorp.com

**Aerial Photography
 Digital Orthophotos
 Digital Mapping
 Stockpile Inventories
 Reprographics**

ARIZONA

KENNEY AERIAL MAPPING, INC.

PHOTOGRAMMETRIC SERVICES SINCE 1963

Airborne GPS Control GIS Applications/Services
 Softcopy & Analytical Color and B&W Photo Lab
 Certified Photogrammetrists Registered Land Surveyors

www.kam-az.com www.kam-az.com
 Phoenix, AZ 602-258-6471 Las Vegas, NV 702-260-3033

CALIFORNIA

ADI AERIAL DIGITAL IMAGES, LLC.
 Complete Aerial Photography, Airborne GPS, & Photo Lab Services

Beechcraft Bonanza, Navajo Chieftain
 Zeiss Digital Mapping Camera (DMC)
 Zeiss Top 15/30 Camera W/FMC
 Zeiss Precision Scanner
 Gyro Stabilized Mount
 Airborne LIDAR Sensor/ Optech Gemini
 Airborne GPS - IMU
 Aerial Photography
 Panoramic Oblique
 Photo Lab

21062 Brookhurst St. Suite 102 Huntington Beach, CA 92646
 Tel: 714-593-8530, 866-593-8530 Fax: 714-593-8529
 adi_al@adimagesllc.com www.adimagesllc.com

DMI DIGITAL MAPPING, INC.
 Complete GIS Photogrammetric Services

Digital Aerial Photography - Intergraph DMC
 LIDAR Acquisitions & Processing - Optech Gemini 167
 Airborne GPS - IMU
 Photogrammetric Mapping
 Digital Orthophotography
 Digital Terrain Modeling - DTM/DSM/DEM
 GPS Survey Services
 GIS Services

Off the shelf high resolution imagery
 www.gisbank.com

21062 Brookhurst St. Suite 101 Huntington Beach, CA 92646
 Tel: 714-968-5459, 866-968-5459 Fax: 714-968-2429
 admi@admap.com www.admap.com

HJWgeospatial
 PACIFIC AERIAL SURVEYS

Photogrammetric Mapping
 LiDAR Terrain Modeling
 Orthoimagery
 Aerial & Satellite Imagery
 QA/QC Oversight
 GIS / Spatial Data Fusion

2001 Broadway, Third Floor
 Oakland, CA 94612
 P: 510.834.2001 F: 510.834.2101
 www.hjw.com

Innovative Geospatial Solutions with Uncompromised Quality

I.K. Curtis Services, Inc.
 "Image is Everything"

Aerial Photography
 Photogrammetric Flying
 Extensive Stock Library
 Airborne GPS
 4 Aircraft
 7 Cameras

2501 Burbank Blvd. #301
 Burbank, CA 91505 1-800-842-1816 www.ikcurtis.com

AERIAL PHOTOGRAPHY • DIGITAL DATABASE MAPPING • DIGITIZING SERVICES
 DIGITAL ORTHOPHOTOS • CONVENTIONAL TOPOGRAPHIC MAPPING
 DIGITAL IMAGING



1161 EAST MAIN ST. TEL: (619) 631-1366
 SUITE 102 FAX: (619) 631-1375
 EL CAJON, CA. WEB: www.photogeodetic.com
 92021-7150 EMAIL: maps@photogeodetic.com

Skyview Aerial Photo Inc.
 www.skyairphoto.com
 Email: info@skyairphoto.com

Precision Aerial Photography
 Multiple Aircraft
 Two Leica RC30's
 Airborne GPS

1050 Calle Cordillera, Suite 104
 San Clemente, CA 92673
 Tel: (800) 498-9757
 Fax: (949) 498-9751

Aerial Surveys | Color & B/W Photolab | Photogrammetric Scanning

COLORADO

Aerial Surveys International, LLC

P.O. Box 130
 37500 Astra Way, Unit 3E
 Watkins, CO 80137
 Shop Phone (303) 261-9990
 Fax (303) 261-9996
 Mark Schubert (303) 261-9990

Precision Aerial Photography LMK 2000 (ABGPS)
 Z/I Scanning & B&W/ Color Lab

When you're serious about digital image mosaicking

ORTHOVISTA Direct

- Digital Image Dodging
- Image & Color Mosaicking
- Automatic Seam Placement

www.orthovista.com

WINDOWS LINUX IRIX SOLARIS

IDAHO

VALLEY AIR PHOTOS
 CATHY GRAVILLE
 Owner / Operator

TEL: 208-454-4344 P.O. BOX 1118
 FAX: 208-454-4345 CALDWELL, IDAHO 83406-1118
 EMAIL: cathy@valleyairphotos.com www.valleyairphotos.com

ILLINOIS

ALT-TERRA SURVEY

LARGE FORMAT VERTICAL PHOTOGRAPHY

DIMAC Digital Aerial Camera
 3 Leica RC 30 FMC Cameras
 2 IMUs, Airborne GPS/Glonass
 4 survey aircraft, 2 Gyro Mounts

Alt-Terra Survey, Inc.
 Sheboygan Falls, WI 53085
 (920) 467-6720

w.phebus@alt-terra.com
 www.alt-terra.com

KANSAS

Western Air Maps, Inc.
 "Imagery and Mapping Solutions"

Aerial Photography - ABGPS - Aerial Triangulation
 Stereo Compilation - Digital Orthophotography
 GIS - Film Processing

1-800-643-5177
 www.westernair.com

OHIO

Kenneth R. Stiller Voice: 937-222-3856

HAS Images, Inc.

FULL SERVICE AERIAL PHOTOGRAPHIC LABORATORY
 Including Scanning & Digital Photographic Output

136 North St. Clair Street • Suite 300 • Dayton, Ohio 45402
 Fax: 937-222-2443 • www.hasimages.com
 e-mail: info@hasimages.com

OKLAHOMA

ADS

Where Innovation And Service Take Flight

Full-Service Aerial Photography & Photogrammetry

Aerial Photography
 Airborne GPS and IMU Camera Positioning
 Photo Lab & Scanning
 GPS Surveying
 Digital Mapping
 Digital Terrain Modeling (DTM)
 3D City Modeling
 Laser Scanning
 LIDAR
 Digital Orthophoto Rectification
 Geographic Information Systems (GIS)
 Satellite Image Processing

8201 E. 51st St., Suite 100 918-622-4144
 Tulsa, Oklahoma 74148 Fax: 918-622-4118
 www.aerialdata.com

Aerial Data Service, Inc.
 1-800-888-9163

Professional Directory

OREGON

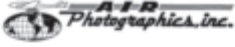


503.239.6010
503.239.4637 (fax)
Info@BergmanPhotographic.com

- Aerial Photography
- Airborne GPS
- Zeiss Top 15 FMC
- Zeiss Top 30 FMC
- Wild RC-10 8.25"
- 4 Survey Aircraft/2 Person Crews
- 9x9 & Medium Format Obliques
- Full Lab Services
- Photogrammetric Scanner
- Historical Files Available

BERGMAN PHOTOGRAPHIC SERVICES, INC.
7816 SE 13TH - PORTLAND, OREGON - 97202

WEST VIRGINIA



Aerial Photography / Airborne GPS
Airborne IMU Data Collection & Processing
5 Leica Cameras with FMC
5 Stabilized Camera Mounts
Photogrammetric Scanning

Arlie Winters, III, President/CEO
2115 Kelly Island Road
Martinsburg, WV 25405

Toll Free: (800) 624-8993
Fax: (304) 267-0918
www.airphotographics.com

EUROPE



Aerial Photography -
ULTRACAMX,
Photogrammetry,
GPS and Laser Scanning

Linke Wienzeile 4, A-1060 Vienna, Austria
www.meixner.com meixner@meixner.com
T: +43 1 587 96 16 F: +43 1 587 34 32

PENNSYLVANIA



14 Survey Aircraft
8 Leica RC30 Cameras
4 Leica DSW Scanners

3 Microsoft UltraCamX
Gryo Stabilized Mounts
ABGPS/IMU Processing

Conventional/Digital Color & BW Products
Extensive Library of Digital & Film Imagery

Mary Potter, President
Tel: 215.677.3119
Fax: 215.464.2889

Philadelphia, PA • Benson, AZ
www.keystoneaerialsurveys.com
info@keystoneaerialsurveys.com

TEXAS



Specializing in Vertical Aerial Photography & Related Services

Customized Aerial Survey Projects
Leica RC-30 Cameras/Gyro Mount/Airborne GPS Capability
Twin Engine Aircraft
Color, Color IR & B&W Lab Services
Digital Photographic Products
Current & Historical Aerial Photos
Houston Based—Serving Entire U.S.

800-784-5801
Grady Owens, 8319 Thora Ln. #E3, Spring, Texas 77379
gowens@aerialviewpoint.com, www.aerialviewpoint.com



FLYING SERVICES FOR MAPPING

LEICA RC30's STABILIZED MOUNTS AIRBORNE GPS

210 497-4260 Voice
830 438-3023 Fax
email: krawietz@gvtc.com

P O Box 191
Bulverde, Texas 78163

Serving the southwestern United States since 1966

VIRGINIA



First Time Right
Geospatial Products
and Services

Geospatial Data Acquisition
Remote Sensing
Photogrammetric Services
Geographic Information Systems

www.3001inc.com 866.GEO.3001

Professional Directory Advertising Reaches a Large U.S. and International Network

Companies providing specific services for the geospatial and mapping community gain new customers by advertising in the PE&RS Professional Directory section with a business cardsized ad. Readers looking to contract (or subcontract) services in a state or region turn to the Professional Directory section of PE&RS to find the company that can fulfill their requirements.

Contact Jim Perrus to discuss your advertising needs;
301-215-6710x107, (fax) 301-215-7704,
asprs@townsend-group.com

Index to Advertisers

| | |
|--|---------|
| BAE Systems • 858-592-1046 • www.baesystems.com | Cover 4 |
| Cardinal Systems, LLC. • 386-439-2525 • www.cardinalsystems.net | 1319 |
| DAT/EM • 907-522-3681 • www.datem.com | 1312 |
| DIMAC Systems • 303-651-2018 • www.dimacsystems.com | 1309 |
| ERDAS Inc. • 770-776-3400 • www.erdas.com | Cover 2 |
| ESRI • 800-447-9778 • www.esri.com | 1281 |
| GeoEye • 1-800-232-9037 • www.geoeye.com | 1296 |
| ITT Visual Information Solutions • 303-786-9900 • www.itvis.com | 1281 |
| Leica Geosystems AG • 0041-71-727-31-31 • www.leica-geosystems.com | 1285 |
| Marsh Affinity Group • 1-800-424-9883 • www.insurancetrustsite.com/ASPRS | 1306 |
| Novatel Inc. • 1-800-NOVATEL or 1-800-295-4900 • www.novatel.com | 1310 |
| Optech Incorporated • 905-660-0808 • www.optech.ca | Cover 3 |
| Wehrli & Associates • 914-831-9821 • www.wehriassoc.com | 1316 |

Volume 74, No. 11, pp. 1281-1444 PHOTogrammetric ENGINEERING & REMOTE SENSING November 2008